

12th Workshop on Crystalline Silicon Solar Cell Materials and Processes

Extended Abstracts and Papers

Workshop Chairman/Editor: B. L. Sopori

Program Committee:

J. Kalejs, T. Saitoh, R. Sinton, M. Stavola,
D. Swanson, T. Tan, E. Weber, J. Werner,
B. Sopori, and M. Al-Jassim

*Beaver Run Resort
Breckenridge, Colorado
August 11-14, 2002*



National Renewable Energy Laboratory

1617 Cole Boulevard
Golden, Colorado 80401-3393

NREL is a U.S. Department of Energy Laboratory
Operated by Midwest Research Institute • Battelle • Bechtel

Contract No. DE-AC36-99-GO10337

12th Workshop on Crystalline Silicon Solar Cell Materials and Processes

Extended Abstracts and Papers

Workshop Chairman/Editor: B. L. Sopori

Program Committee:

J. Kalejs, T. Saitoh, R. Sinton, M. Stavola,
D. Swanson, T. Tan, E. Weber, J. Werner,
B. Sopori, and M. Al-Jassim

*Beaver Run Resort
Breckenridge, Colorado
August 11-14, 2002*

Prepared under Task No. WO97.A700



National Renewable Energy Laboratory

1617 Cole Boulevard
Golden, Colorado 80401-3393

NREL is a U.S. Department of Energy Laboratory
Operated by Midwest Research Institute • Battelle • Bechtel

Contract No. DE-AC36-99-GO10337

NOTICE

This report was prepared as an account of work sponsored by an agency of the United States government. Neither the United States government nor any agency thereof, nor any of their employees, makes any warranty, express or implied, or assumes any legal liability or responsibility for the accuracy, completeness, or usefulness of any information, apparatus, product, or process disclosed, or represents that its use would not infringe privately owned rights. Reference herein to any specific commercial product, process, or service by trade name, trademark, manufacturer, or otherwise does not necessarily constitute or imply its endorsement, recommendation, or favoring by the United States government or any agency thereof. The views and opinions of authors expressed herein do not necessarily state or reflect those of the United States government or any agency thereof.

Available electronically at <http://www.osti.gov/bridge>

Available for a processing fee to U.S. Department of Energy
and its contractors, in paper, from:

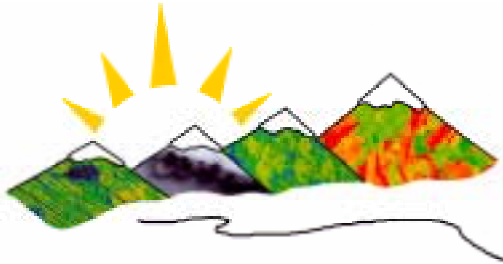
U.S. Department of Energy
Office of Scientific and Technical Information
P.O. Box 62
Oak Ridge, TN 37831-0062
phone: 865.576.8401
fax: 865.576.5728
email: reports@adonis.osti.gov

Available for sale to the public, in paper, from:

U.S. Department of Commerce
National Technical Information Service
5285 Port Royal Road
Springfield, VA 22161
phone: 800.553.6847
fax: 703.605.6900
email: orders@ntis.fedworld.gov
online ordering: <http://www.ntis.gov/ordering.htm>



Printed on paper containing at least 50% wastepaper, including 20% postconsumer waste



12th Workshop on Crystalline Silicon Solar Cell Materials and Processes

TABLE OF CONTENTS

Title/Author(s):	Page
Workshop Theme: <i>Fundamental R&D in c-Si: Enabling Progress In Solar-Electric Technology</i> Bhushan Sopori, National Renewable Energy Laboratory	1
Characterization of Silicon-Film™ Sheet Material James Rand, George Rozgonyi, Ralf Jonczyk, Sarbajit Datta, Jinggang Lu, Robert Reedy, and Renhua Zhang	3
Ribbon-Growth-on-Substrate: Status, Challenges and Promises of High Speed Silicon Wafer Manufacturing A. Schönecker, L. Laas, A. Gutjahr, M. Goris, P. Wyers, G. Hahn, and D. Sontag	7
Solar Grade Silicon Feedstock: Recent Assessment Results and A Cost Effective Chemical Path Wolfgang Koch, Armin Raeuber, Armin Mueller, Karsten Wambach, and Holger Kirchner	15
Development of Cast Technology for High Quality Multicrystalline Silicon Ingot of Solar Cells Seiko Nara and Yasuhiko Sakaguchi	27
The Technology of Modern Wiresaw in Silicon Wafer Slicing for Solar Cells Imin Kao	35
50µm Wafering Techniques – First Experimental Results Daniel Kray and Gerhard P. Willeke	43
Practical Aspects of Wire Sawing Process for Solar Cells Kensho Miyata	51
Wafer Slicing Using Improved Fixed Abrasive Slicing Technology (FAST) Frederick Schmid, Maynard B. Smith, and Chandra P. Khattak	57
Light-Induced Degradation in CZ Silicon Solar Cells: Fundamental Understanding and Strategies for Its Avoidance Jan Schmidt and Rudolf Hezel	63

<i>A Feasibility Study on Gallium Doping for Higher Quality Multicrystalline Silicon Cast Wafers</i>	71
Marwan Dhamrin and Tadashi Saitoh	
<i>Low-Cost Crystalline Silicon Wafers and Ribbons for Solar Cells (KOSI): A German Research Program</i>	79
D. Karg, G. Hahn, and K. Roy	
<i>Front-Side Surface Recombination Analysis of 18%-Efficient Multicrystalline Silicon Solar Cell</i>	86
Yuji Komatsu, Yoshiro Takaba, Shuji Yasukawa, Satoshi Okamoto, and Masafumi Shimizu	
<i>Review on PV Low Concentration Devices</i>	94
Carlos del Cañizo	
<i>A Contactless Technique for Measuring Minority-Carrier Parameters in Silicon</i>	103
R. K. Ahrenkiel and S. W. Johnston	
<i>Application of Synchrotron Radiation Based X-Ray Microprobe Techniques for the Analysis of Recombination Activity of Metals Precipitated at Si/SiGe Misfit Dislocations</i>	110
O. F. Vyvenko, T. Buonassisi, A. A. Istratov, E. R. Weber, M. Kittler, and W. Seifert	
<i>Locating Losses Due to Contact Resistance, Shunts and Recombination by Potential Mapping With the Corescan</i>	116
A. S. H. van der Heide, J. H. Bultman, J. Hoornstra, A. Schönecker, G. P. Wyers, and W. C. Sinke	
<i>Quantitative Shunt Investigations on Solar Cells by Lock-In Thermography</i>	124
O. Breitenstein	
<i>Efficient Characterisation Techniques for Industrial Solar Cells and Solar Cell Materials</i>	135
C. Ballif, S. Peters, T. Zerres, J. Isenberg, D. Borchert, and G. Willeke	
<i>Microscopic Properties of Copper in Silicon: Theoretical Predictions</i>	146
S. K. Estreicher and D. West	
<i>Interstitial H₂ in Si: A Nearly Free Rotator After All</i>	154
Michael Stavola, E. Elinor Chen, W. Beall Fowler, J. Anna Zhou, and Peter Walters	
<i>Industrial Systems for Hydrogen Passivation Using Hydrogenated Amorphous SiNx Layers</i>	162
Silvia Roth, Roth and Rau Oberflächentechnik AG	
Poster Papers	
Title/Author(s)	
<i>Isolated N and N Pairs in Silicon</i>	170
J. L. McAfee and S. K. Estreicher	
<i>Theory of Copper Impurities in Silicon</i>	174
D. West and S. K. Estreicher	

<i>Hot Wire Chemical Vapor Deposition of Silicon Nitride Films for Crystalline Silicon Cell Emitter Passivation</i>	175
J. K. Holt, M. Swiatek, D. G. Goodwin, A. M. Gabor, and Harry A. Atwater	
<i>New Method of Solar Grade Silicon Production</i>	179
V. V. Zadde, A. B. Pinov, D. S. Strebkov, E. P. Belov, N. K. Efimov, E. N. Lebedev, E. I Korobkov, D. Blake, K. Touryan	
<i>A Luminescent Anti Reflective Coating</i>	190
Stephan Nicoletti, Robert Engelken, Roger M. Hawk	
<i>Hot-Wire Chemical Vapor Deposition for Epitaxial Silicon Growth on Large-Grained Polycrystalline Silicon Templates</i>	195
M. Swiatek Mason, C. M. Chen, and H. A. Atwater	
<i>Process for Production of Silane</i>	199
Marat F. Tamendarov	
<i>Injection-Dependent Lifetime Studies of Copper Precipitates in Silicon</i>	201
Daniel Macdonald, Willi Brendle, Andres Cuevas, and A. A. Istratov	
<i>Nanoscale Investigations of Polycrystalline Silicon for Photovoltaic Applications</i>	205
R. Zhang, G. Duscher, J. Rand, and G. A. Rozgonyi	
<i>Infrared Residual Stress Polariscopic for Solar Cell Inspection</i>	209
Shijiang He, Steven Danyluk, and Sergei Ostapenko	
<i>Achieving High Dopant Concentrations in Si: First Principles Simulations</i>	211
Scott A. Centoni, Babak Sadigh, Maria-Jose Caturla, George H. Gilmer, and Tomas Diaz de la Rubia	
<i>Solar-Grade Silicon by a Direct Route Based on Carbothermic Reduction of Silica: Requirements and Production Technology</i>	215
L. J. Geerligs, G. P. Wyers, R. Jensen, O. Raaness, A. N. Waernes, S. Santén, A Reinink, and B. Wiersma	
<i>Rapid Anodic Oxidation for Depth Profiling of Silicon</i>	219
Oleg V. Sulima, Ralf Jonczyk, Neil L. Kirpalani, Puther D. Paulson, Sarbajit Datta, and James A. Rand	
<i>Direct Write Processing for Photovoltaic Cells</i>	223
Tanya Rivkin, Calvin Curtis, Alex Miedaner, John Perkins, Jeff Alleman, and David Ginley	
<i>Effects of Dislocations on Minority Carrier Lifetime in Dislocated Float Zone Silicon</i>	227
A. Karoui, R. Zhang, G. A. Rozgonyi, and T. F. Ciszek	
<i>Partitioning Effects in Recrystallization of Silicon From Silicon-Metal Solutions</i>	231
E. A. Good, T. H. Wang, T. F. Ciszek, R. H. Frost, M. R. Page, and M. D. Landry	

<i>Measurement of Lattice Vacancy-Type Defects in Crystalline Si by a Au Labeling Technique</i>	235
A. T. Fiory, N. M. Ravindra, R. Kalyanaraman, V. C. Venezia, and B. L. Sopori	
<i>Comparison of Shunt Imaging by Liquid Crystal Sheets and Lock-in Thermography</i>	239
O. Breitenstein, J. P. Rakotoniaina, and J. Schmidt	
<i>Leakage Current in P-N Junctions Contributed by Metallic Precipitates Via the Schottky Effect</i>	243
M. D. Negoita and T. Y. Tan	
<i>Resonance Acoustic Diagnostics as a Characterizing Tool for Solar-Grade Cz-Si Wafers</i>	247
A. Belyaev, S. Ostapenko, and T. L. Jester	
<i>Rapid Thermal Processing Enhanced SiN_x-Induced Defect Passivation in 15.9% Efficient Screen-Printed EFG Silicon Solar Cell</i>	250
J-Weon Jeong, Ajeet Rohatgi, B. R. Bathey, J. P. Kalejs	
<i>Measurement of the Current Distribution in the Emitter Region of Solar Cells by Magnetic Methods</i>	254
R. Buchwald, E. Soika, M. Zschorsch, H. J. Möller, D. Drung, and T. Schurig	
<i>Analysis of Shunts in Multicrystalline Silicon Solar Cells Using Microprobe X-Ray Fluorescence Technique</i>	258
T. Buonassisi, O. F. Vyvenko, A. A. Istratov, E. R. Weber, R. Schindler, and G. Hahn	
<i>Application of X-Ray Fluorescence Technique to Studies of Aluminum Gettering in Silicon</i>	263
O. F. Vyvenko, T. Buonassisi, A. A. Istratov, and E. R. Weber	
<i>Investigation of Oxygen Precipitates and Associated Stacking Faults in Polycrystalline Sheet Silicon and Their Impact on Solar Cell Performance</i>	267
Jinggang Lu, James Rand, Ralf Jonczyk, and George Rozgonyi	
<i>A Study of Contact Resistance and Cell Performance of Selective-Emitter Screen-Printed Silicon Solar Cells Using a Self-Doping Paste</i>	271
M. Hilali, J. – W. Jeong, and A. Rohatgi	
<i>Greater Than 15% Efficient Screen Printed Solar Cells with Porous Silicon Anti-Reflection Coating</i>	275
Ben Damiani and Ajeet Rohatgi	
<i>mc-Si: Relation Between Ingot Quality and Cell Efficiency</i>	280
L. J. Geerligs	

<i>Development of a Novel Phosphorus Spray Diffusion System for Low Cost Silicon Solar Cells</i>	284
K. Nakano, A. Hariharan, K. Matthei, D. S. Kim, A. D. Upadhyaya, and A. Rohatgi	
<i>Two-Dimensional Simulations of Thin-Silicon Solar Cells</i>	291
T. H. Wang, M. R. Page, and T. F. Ciszek	
<i>Wafer and Solar Cell Characterization by GT-PVSCAN6000</i>	295
Bhushan Sopori, Jamal Madjpour, Chris Auriemma, Keith Matthei, Kengo Nakano, and Keiko Moritz	
<i>Production Technology for Passivation of Polycrystalline Silicon Solar Cells</i>	300
Julio A. Bragagnolo, Bhushan Sopori, Erten Eser, Tohru Hashimoto, and Ichiro Sugiyama	
<i>GT Reflectometer: Performance Testing/Error Analysis</i>	308
Bhushan Sopori, Chris Auriemma, Jamal Madjpour, Keith Matthei, Kengo Nakano, and Heiko Moritz	

Fundamental R&D in c-Si: Enabling Progress in Solar Electric Technology

Bhushan Sopori
National Renewable Energy Laboratory
1617 Cole Boulevard
Golden, CO 80401

With increasing acceptance of photovoltaic (solar electric) energy as a solution to many energy needs of the world, PV production has grown at about 20%/year in recent years. Worldwide shipments of PV modules reached about 400 megawatts (MW) in 2001. Because Si continues to be the dominant technology, solar cell manufacturing using c-Si (single or multicrystalline) has reached new pinnacles. Shipments of solar electric power products based on c-Si materials reached about 320 MW in 2001, representing more than 80% of total solar cell shipments. Because of the increasing demands of PV energy use, much of the current activity in the PV industry is heavily geared for increasing manufacturing capabilities. Nearly all major manufacturers are installing new production lines.

The industry expansion and attempts toward reducing production costs are guiding the production technologies in several directions:

- Development of automated processing-equipment such as infrared furnaces, and wafer/cell handling machines
- Fabrication of crystal-growth furnaces for larger ingots and higher chemical purity
- Sawing (cutting) thinner wafers (faster edge removal for ribbons)
- Encapsulation and module fabrication machines
- Testing and process monitoring instrumentation.

Many of these technologies implement the latest knowledge from fundamental research programs. These areas of science and technology that were topics of discussions in previous workshops include:

- Improved material quality through better thermal profiles and reduced impurity content
- Methods of mitigating deleterious effects of impurities and defects in Si through gettering and passivation
- Metallization techniques, screen printing with finer fingers, and fire-through SiN
- Minimizing the number of process steps.

These technologies are promising >17% solar cell efficiencies in commercial production.

With the tremendous push for manufacturing growth, there is a certain degree of danger in that installing these technologies may prevent the entry of newer scientific results into production. Such a stagnation of technologies can also diminish the interest in fundamental research and may promote a tendency to devote R&D resources to more applied research.

One may ask: have we run out of fundamental research? Clearly, the answer is NO.

The theme of this workshop reflects a need to establish directions for the future R&D—directions that can take Si PV beyond 17%-efficient commercial solar cells to 20% cells and further lower the processing costs.

Some of the important R&D areas are identified and are included in this workshop for further discussions. The various sessions are:

- Advances in rapid crystal growth and material issues
- Wire sawing and future wafering techniques
- Defects/light degradation
- Solar cell fabrication
- Characterization techniques
- Shunting in solar cells: mechanisms and diagnostics
- Hydrogen passivation and processing.

The discussions in this workshop will pave the way for R&D efforts that will enable future progress in the solar electric technology, particularly in Si PV. This workshop provides a forum for informal exchange of scientific and technical information among international researchers and industry representatives. Traditionally, this workshop has helped define the R&D objectives of the NREL/U.S. Department of Energy Silicon program. Attaining the objectives of this workshop is greatly helped by devoted efforts of all participants — many people who help in organizing, planning the program, making presentations, and participating in discussions. The workshop also recognizes the need to involve young scientists who will shape the future of the solar electric discipline. We are particularly thankful to PV companies who have contributed to the Graduate Student Awards; this year, seven students will share these awards.

CHARACTERIZATION OF SILICON-FILM™ SHEET MATERIAL

James Rand¹, George Rozgonyi², Ralf Jonczyk¹, Sarbjit Datta¹, Jinggang Lu², Robert Reedy³, Renhua Zhang²

¹AstroPower, Inc., Newark, DE, ²North Carolina State University, Raleigh, NC;

³National Renewable Energy Laboratory, Golden, CO

INTRODUCTION

The Silicon-Film™ process produces a continuous sheet of polycrystalline silicon for use in the production of solar cells. This is a relatively new material for the industry considering the growth method, the relatively high level of impurities, and small grain size. This paper reports on the progress in characterizing this relatively new material. The conversion efficiency for Silicon-Film™ solar cells is presently approximately 80% of those achieved with the industry standard CZ or large grain cast materials. The smaller grain size and the lower purity are the logical explanations for performance differences. With advances in the understanding of critical high temperature processes, such as gettering, views on impurity requirements have changed. Similarly, conventional grain size limits are shown to be inaccurate, allowing higher performance than thought possible from smaller grains. To delve into these and other specific material issues, an industry – academic – government team has been established. This paper reports on some of the results found by that team and highlights some of the conclusions that have been drawn as regards impurities and gettering.

Sheet Growth and Solar Cell Processing

AstroPower presently has the fifth and sixth generation of its Silicon-Film™ machines in production. The top surface of the polycrystalline silicon sheet has columnar grains, ranging in size from 100 µm to 5 mm. The total sheet thickness ranges from 600 to 800 µm. Each machine has a production capacity of 15MW per year and a linear sheet speed of 3.1 meters/min [1].

Silicon-Film™ wafers are processed into solar cells using a conventional industrial process sequence. After the sheet is cut square, which is done by laser or a conventional saw, the process sequence is a NaOH-based etch, continuous phosphorus diffusion on a belt furnace, continuous HF etch, SiN anti-reflection coating, and screen-printed metallization [1]. In addition, two novel, high temperature gettering steps are being evaluated as part of the standard processing sequence.

Characterization Requirements

In its pure, single crystal state, silicon is a well understood and predictable semiconductor material, ac-

cordingly it is tempting to attribute all the deleterious effects seen in polycrystalline material to grain boundaries and impurities. Historically, it was believed that small grains (100 µm in diameter) limited solar cell performance to efficiencies less than 8% [3]. Similarly, impurity studies in CZ ingots found that certain impurities in concentrations as low as 10^{12} ppma could devastate solar cell performance [4]. Both of these conventional models are inadequate to explain the performance of Silicon-Film™.

To fully understand the impact of defects and impurities on efficiency, a hierarchy of contributing factors is presented in Figure 2. The starting contributing factor remains impurities in the feedstock – with a special delineation for dopants (intentionally added) and high temperature compounds that may react differently than their elemental components. Examples are oxygen, carbon, and nitrogen, and their high temperature sili- cides.

Extensive studies of the impurity impact on CZ grown wafers were reported in 1980, some details of which are shown in Figure 1. The ranges of some critical impurities found in Silicon-Film™ material are also shown. The levels found are well in excess of the quantity expected to strongly impact efficiency, yet Silicon-Film™ efficiencies remain at roughly 80% of the baseline 14% efficiency reported in that work [4].

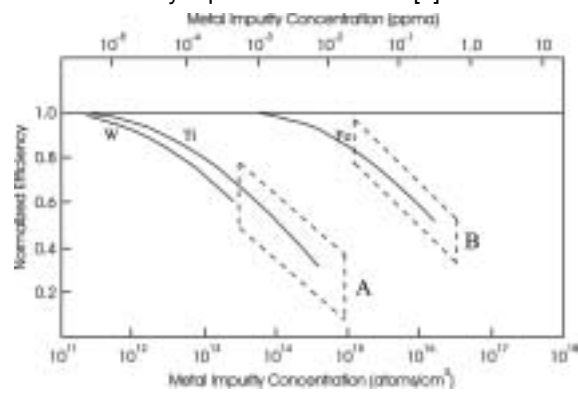


Figure 1. Impact of impurities on CZ ingots as reported in 1980 [4]. The dashed boxes represent the range of impurities found in Silicon-Film™ for Ti and W (box A) and Fe (box B).

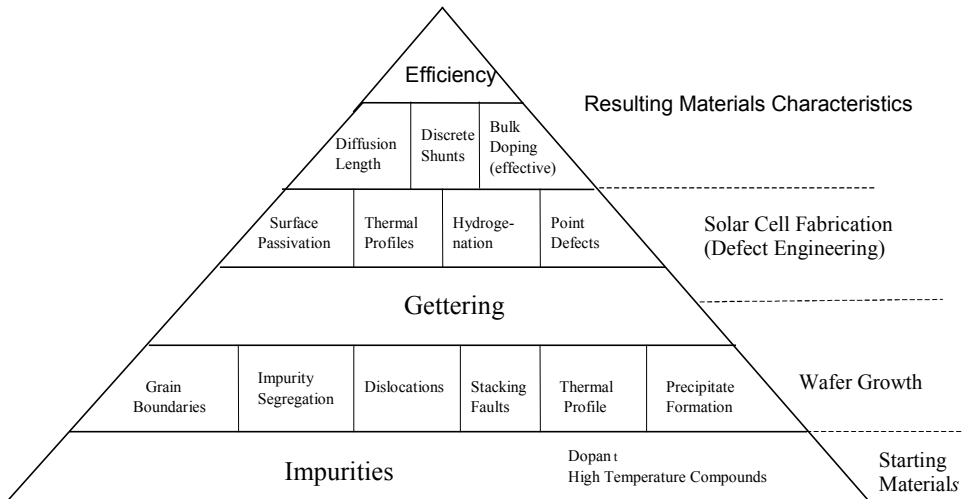


Figure 2. A hierarchical table of the materials factors contributing to solar cell efficiency.

The next tier of contributing factors shown in Figure 2 are those occurring in the wafer formation process. Again, these are very well understood for the CZ and FZ methods, but not yet well known for the Silicon-Film™ sheet process. Critical controlling variables are the impurity segregation effects and the role of inclusions. Critical results are the density of grain boundaries, dislocations, precipitates, stacking faults and the role of point defects in their formation.

Gettering is highlighted in Figure 2, as it spans both wafer formation and solar cell processing. Many exciting advances have occurred in the past decade in gettering for wafers used in the integrated circuits field and photovoltaics [5]. This area holds great promise for the proactive engineering of impurities. The impact in Silicon-Film™ material is actively under study. In addition to gettering, other areas of defect engineering include: surface passivation, hydrogenation, and optimized thermal profiles. The material characteristics resulting from these contributing factors are the minority carrier diffusion length, the effective doping level, and the level of discrete shunts, which when taken as a whole, determine solar cell efficiency.

Impurity Studies by SIMS

Our objective has been to determine the impact of each of the contributing factors shown in Figure 2 to the overall device performance. The first step was to measure the bulk impurity concentration. ICP-MS, NAA, and GDMS have all been evaluated. GDMS was determined to have needed detection limits and also the ability to measure impurities in only the active region of the device. Methods that determine an "average" measurement over the wafer from front to back give misleading results for Silicon-Film™ material. The range of GDMS results for Silicon-Film™ is shown in Figure 1 for Fe, Ti, and W. Analysis of the data shows that there is more than enough Fe, W, Al, Mo and Ti to account for all the lifetime degradation in Silicon-Film™ individually, let alone in total. The level of the impurity

did not track lifetime in careful comparisons of material with high and low lifetimes. The question then becomes which impurities are detrimental and which are benign.

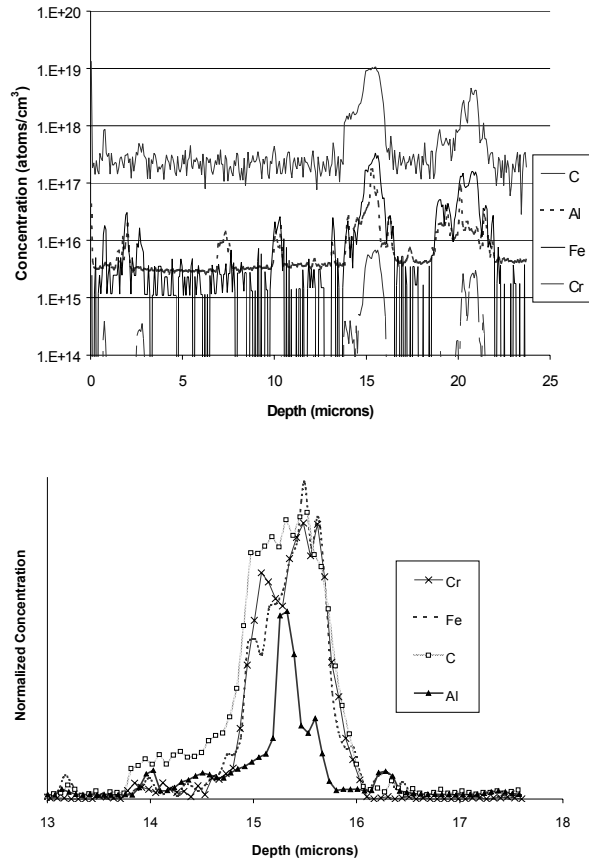


Figure 3. SIMS depth profiles showing a large carbon precipitate, with high levels of chromium, aluminum, and iron at the same site. The lower scan shows an expanded view of a single precipitate containing C, Cr, Fe, and Al with the peak concentrations normalized. The striking similarity in the C, Cr, and Fe scans led to the conclusion that the particulate was an inclusion, as opposed to being precipitated in the process. (SIMS done at NREL).

In an attempt to quantify the role of the impurities, SIMS (Secondary Ion Mass Spectroscopy) depth profiles were taken at the National Renewable Energy Laboratories. An example of a SIMS depth profile is shown in Figure 3 where a number of precipitates can be found.

One plausible conclusion from the SIMS data is that the transition metals are gettering to the larger carbon precipitate. The similarity of shape of the profiles in Figure 4 implies that the impurities are uniform through the precipitate, which is not what would be expected from a gettered impurity. A detailed analysis was carried out on 13 different carbon precipitates by calculating the total concentration of Al, Fe, and Cr, and comparing it to the concentration of carbon. Figure 4 shows the relative impurity concentrations are surprisingly uniform in both raw sheet samples (virgin) and processed materials. This has led to the conclusion that the particulates are not precipitated from the melt at all, but are inclusions. The characteristic impurity profile has been traced to certain insulation materials in the Silicon-FilmTM furnace.

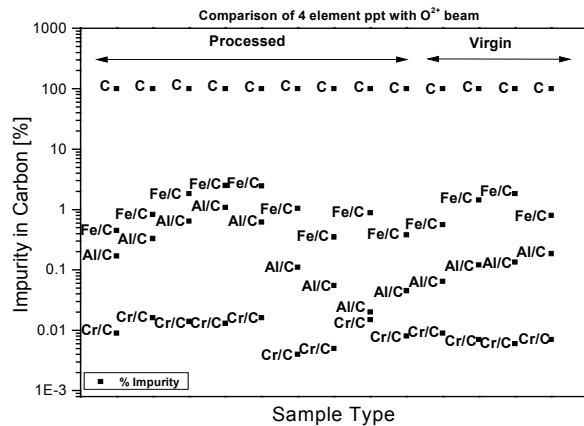


Figure 4. Analysis of 13 different carbon precipitates as identified by SIMS. The impurity concentration for Fe, Al, and Cr was calculated and compared with C. The data shows that the ratio of Fe to C, and ratio of Cr to C, varies over a relatively narrow range, where the ratio of Al to C varies greatly. Combined with the inconsistent shape of the Al peak, this has lead to the conclusions that the Al is gettered to the site, and the Cr and Fe are present in the carbon inclusion.

TEM Results

TEM studies have been carried out at both at NREL and at NCSU. A review of the NCSU findings is presented in a separate paper at this workshop [6]. Carbon particulates were identified in Silicon-Film™ material through TEM analysis done by NREL. One example is shown in Figure 5. The image shows a particulate surrounded by a network of dislocations. Clusters such as these have also been identified in EBIC images and have a significant impact on device performance.

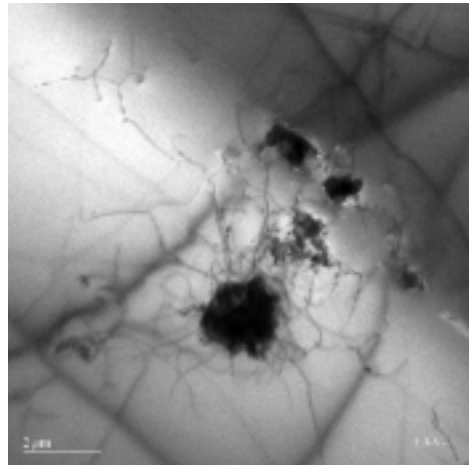


Figure 5. A TEM image of a particulate with a corresponding network of dislocations (work done by NREL).

Similar large dislocation networks have been identified by NCSU with precipitates, inclusions, and voids at their core. Utilizing EELS analysis, C and O have been found to be present in these particles. There is also evidence of transition metal gettering to these sites. As sample sizes and areas are small with TEM studies, further studies are required before conclusions with regard to overall material performance can be drawn.

Oxygen Precipitates

Work done at North Carolina State University (NCSU) has focused on direct observation of defects through polishing and defect etching. An example of that work is shown in Figure 6. This sample shows a clearly delineated denuded zone (DZ) and a uniform distribution of stacking faults inside the grain.

A detailed study of this effect has focused on oxygen levels and is presented at this workshop in a separate paper [7]. In that study stacking fault formation in samples with high and low oxygen levels were analyzed after gettering and phosphorus diffusion steps. Stacking fault formation was evident in the high oxygen samples and missing in the low oxygen sample. Minority carrier properties correlated with stacking fault presence. A conclusion is drawn that for Silicon-Film™ material with the annealing schedule presently in use, initial interstitial oxygen concentrations need to be below about $12 \times 10^{17} \text{ cm}^{-3}$ to avoid the formation of stacking faults.

The size of the denuded zone in Figure 6 indicates that the mechanism causing the nucleation of the oxygen precipitates has the ability to diffuse on the order of 50 microns during the thermal schedule of the growth and processing sequences. This distance rules out slowly diffusing interstitial oxygen, but includes carbon,

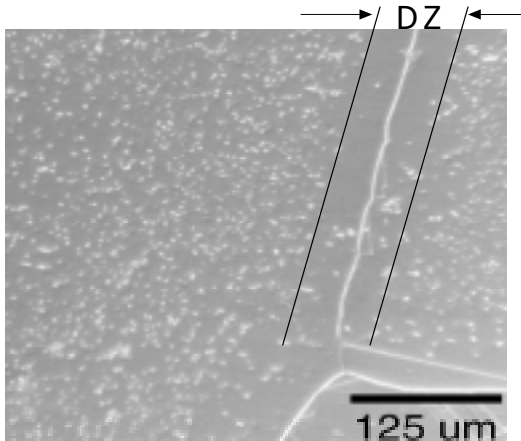


Figure 6. Optical micrograph of an annealed sample SECCO etched for 1 minute. A clearly defined denuded zone (DZ) can be seen around the grain boundary. High initial interstitial oxygen levels have been associated with the high density of stacking faults formed in the intergrain regions. This work was done at NCSU.

nitrogen, and iron – all known to enhance oxygen precipitation, and all present at high levels in Silicon-Film™ material. Following this theory, the nucleation causing agent is gettered to the grain boundary, leaving an oxygen precipitation free zone. The gettering of self-interstitials is another plausible cause for the formation of the denuded zone put forth in [7].

The impact of the denuded zone can be seen qualitatively in the EBIC image of Figure 7. If the stacking fault defects dominate device performance, a conclusion could be drawn that smaller grain material would make better solar cells. The impact of the grain boundaries on shunt conduction needs to be taken into consideration.

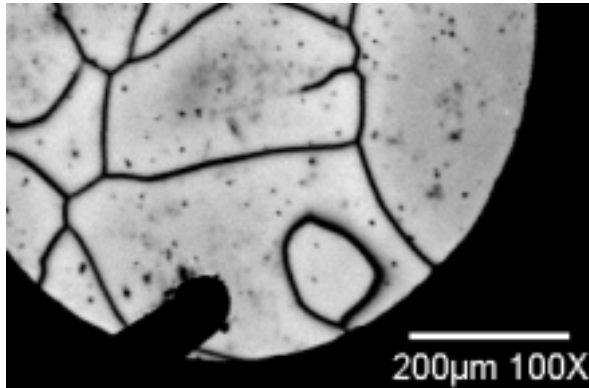


Figure 7. EBIC of a sample showing enhanced performance near grain boundaries.

Conclusion

The application of new processing steps and better understanding of defect and impurity interactions is allowing small grain polycrystalline silicon sheet mate-

rial to produce solar cell efficiencies approaching that of cast material and CZ. To realize the full benefit of working with this highly defected, impure material, a thorough understanding of which impurities and defects are benign and which are limiting performance is needed. Several characterization techniques are being evaluated and their effectiveness in addressing these issues reviewed.

Acknowledgements

The majority of this work was initially presented at the 29th IEEE PVSC in New Orleans, USA, in May 2002. Large teams at NREL, NCSU, and AstroPower have all contributed to this work. From NREL, Kim Jones did the TEM work, Bhushan Sopori and Pete Sheldon have supported the effort. At NCSU, significant contributions were made by Magnus Wagener, Indrajeet Sen, and Ludwik Kordas. At AstroPower, characterization work was performed by Brian Gremm, Brian Huebner, and Ernest Addo.

References

- [1] J. S. Culik et al., "Progress in 15-MW Single-Thread Silicon Film Solar Cell Manufacturing Systems", 17th EC PVSEC, Munich, October 2001
- [2] J. Bernreuter, Photon International, September 2001, p. 26.
- [3] A. K. Ghosh et al, J. Appl. Phys., Vol 51, No 1, January 1980, p 446.
- [4] J. R. Davis et al, 13th IEEE PVSC, 1978, pg 490.
- [5] S. M. Myers et al, Journal of Appl. Physics, Vol 88, No 7, October 2000, Pg. 3795
- [6] R. Zhang et al, 12th Crystalline Silicon Workshop, Aug, 2002.
- [7] J. Lu et al, 12th Crystalline Silicon Workshop, Aug, 2002.

Ribbon-Growth-on-Substrate: Status, Challenges and Promises of High Speed Silicon Wafer Manufacturing

A. Schönecker*, L. Laas, A. Gutjahr, M. Goris, P. Wyers

ECN Solar Energy, P.O. Box 1, 1755 ZG Petten, The Netherlands

* phone: +31-(0)224 564740, fax: +31-(0)224 563214, e-mail: schonecker@ecn.nl

G. Hahn, D. Sontag

University of Konstanz, Faculty of Physics, P.O. Box 5560, 78434 Konstanz, Germany

ABSTRACT

The Ribbon-Growth-on-Substrate (RGS) silicon wafer manufacturing technology is a very promising high-speed wafer production technique under development at the moment. It has the promise to lead to a manufacturing technology, which allows silicon wafer manufacturing at the 25 MWp/a to 50 MWp/a level.

A future development of this technology in the areas, RGS machine prototyping, wafer quality improvement and solar cell process optimization should lead to a commercialization of this technology in 2005.

In the following an outline of the past developments, a status of the RGS technology today and the most probable road ahead is presented.

Motivation

In the last years a remarkable growth of the PV industry with annual growth rates well above 25% was achieved [1]. It is expected that PV can and will maintain growth rates at 25 to 35% in the foreseeable future [2]. This also means that the PV industry has to adjust its manufacturing capacities to satisfy the market.

Table 1: Production speed and capacity of different silicon ribbon production technologies. The last column shows the number of furnaces for a 100 MWp production line. [3] (EFG: edge defined film fed growth, SR: string ribbon)

Material	Pull speed (cm/min.)	Throughput (cm ² /min.)	Furnaces per 100 MWp
EFG	1.7	165	100
SR	1 – 2	5 – 16	1175
RGS	600	7500	2 – 3

To fulfill this market demand is the main challenge for PV manufacturing technology in the next years. Although it is expected that the world PV market will approach GWp module shipment levels shortly after 2006, the technology to produce PV modules efficiently on the

100 MWp scale is not available yet. Thus technological developments can be expected in all parts of the PV module production chain, from solar grade silicon, over wafer and solar cell manufacturing to module production. In the field of wafer production, the ribbon-growth-on-substrate silicon wafer technology promises the effective production of silicon wafers at low manufacturing costs, at high production rate (see table 1) and with almost 100% silicon usage.

During the late 70's and 80's a number of potentially high-speed crystal growth technologies were developed in laboratories in the US and in Europe. Their main difference were the way how the crystallization heat was removed from the liquid silicon and how the geometrical definition of the wafer was realised. Although a number of these technologies were very promising and successfully demonstrated on the lab-scale, most of the developments were stopped in the late 80's in a development state, where major investment into a production prototype became necessary.

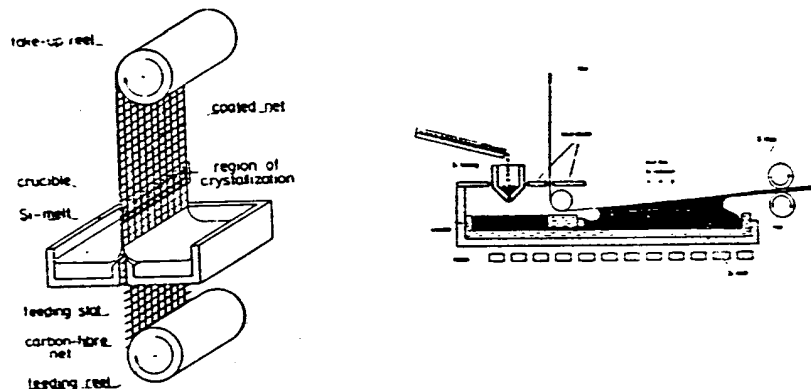


Figure 1: Web supported silicon ribbon (S-Web) pulling was under development by Siemens. High throughput and 12% efficiency were demonstrated in the early 90's. The major problem was the single use of the supporting web, which was made of very pure and expensive graphite. Brandl GmbH in Germany now owns this technology. [4]

Among these processes, there were a number of methods where silicon was solidified in contact with another material (substrate or inlay). Wacker, as an example, at that time developed the so-called RAFT technology, which is similar to the RGS technology in the way that a re-usable substrate material was used to grow the silicon wafer. Other technologies under development were the LASS (low angle silicon sheet) technology or the S-web technology as outlined in figure 1.

None of the above mentioned high-speed silicon ribbon technologies made it into production yet. However driven by the strong market pull and the expectation of a rapidly expanding silicon PV industry, some technological development are started (Sharp's rotational solidification), speeded up (RGS) or revived (S-Web).

Ribbon-Growth-on-Substrate wafer manufacturing

Promises

Compared to all other high-speed wafer manufacturing technologies the Ribbon-Growth-on-Substrate technology was under continuous development since its start in 1984 at Bayer

AG in Germany. But similar to the other technologies there was a strong dedication into the RGS development in the late 80's and early 90's resulting in the building of an RGS laboratory infrastructure and two laboratory scale RGS machines. In the time period between 1994 and 1999 major steps in RGS technology development were realized with respect to wafer quality and solar cell efficiency but it was never decided to invest into the pilot scale RGS machine. Nevertheless this situation resulted in a unique possibility for RGS in the late 90's due to the following:

- It is a very promising high-speed silicon wafer manufacturing technology, which demonstrated continuous improvements throughout its development.
- RGS is well understood from a scientific point-of-view, and a number of advanced solar research laboratories are supporting the further development with their know-how.
- Reasonable solar cell efficiencies are demonstrated and there is sufficient know-how available to justify the development of the pilot machine.

This formed the base for a co-operation between Deutsche Solar (as successor of Bayer Solar) and ECN on one side and a Dutch development consortium with support from S'Energy on the other side for a further development of the technology. [5]

RGS principle

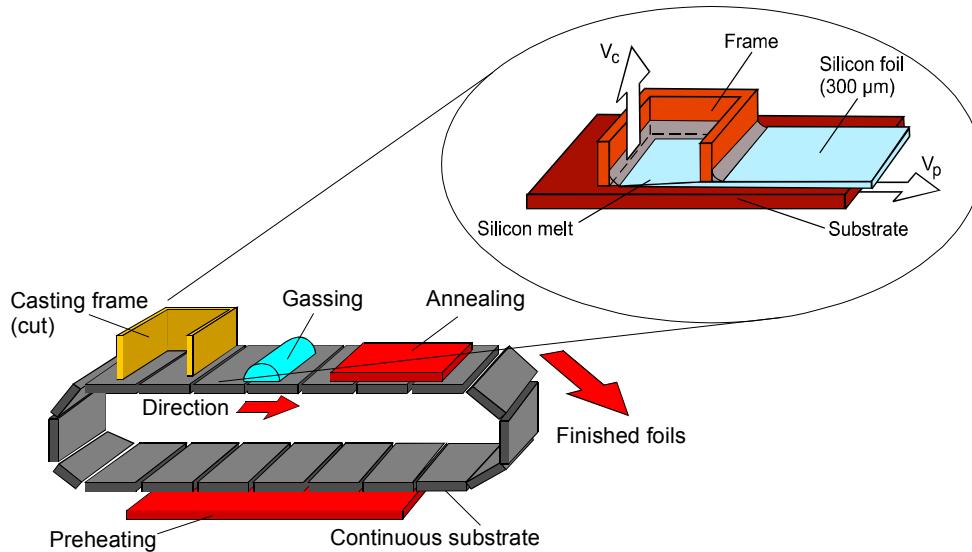


Figure 2: Principle of the RGS process and schematic drawing of the continuos RGS machine built by Bayer. The most important process feature is the de-coupling of the crystal growth velocity (V_c) from the production speed (V_p) (src. Bayer AG).

The principle of the RGS wafer casting process is simple. A 'cold' (below silicon melting temperature) substrate is moved underneath a casting frame filled with liquid silicon (melting point 1414°C). Thus heat is extracted from the silicon melt forcing a crystallization process of silicon from the substrate into the silicon melt. During this process the substrate is moved underneath the casting frame and crystal growth is stopped at the moment the substrate leaves the casting frame. Thus crystal growth direction and silicon wafer production direction are perpendicular to each other, which allows the independent control of both. Therefore

relatively slow crystal growth can be combined with high substrate transport speed and thus high production volume.

After the casting frame, the wafers and the substrates are cooled down. During this process the wafer and the substrate separate, forced by their different thermal expansion coefficients. This allows the substrate to be re-used after the wafer has been picked-up. The RGS process as shown in figure 2 was demonstrated on Bayer's lab-scale machines.

Silicon crystal growth process

Silicon crystal growth in contact with a cold substrate can be described by mathematical models, which belong to a class of transient heat transfer problems with a moving boundary condition, the solidification interface. The simplest case of this important class of problems is called the 'classical Stefan problem' [6]. It assumes that a liquid at uniform temperature T_l , which is higher than the melting temperature T_m is confined to a half space $x>0$. At time $t=0$ the boundary surface ($x=0$) is lowered to a temperature T_0 below the melting temperature (i.e. contact with the cold substrate) and maintained at this temperature. As a result solidification starts at the surface $x=0$ and a solid liquid interface $s(t)$ moves into positive x -direction. Under these assumptions the heat conduction equations can be solved and the position of the solid-liquid interface in time is described by:

$$s(t) = \lambda \sqrt{\alpha_s t}$$

with α_s being the thermal diffusivity of the solid phase and λ being the solution of equation:

$$\frac{\exp(\lambda^2/4)}{\operatorname{erf}(\lambda/2)} + \frac{b}{\sqrt{a}} \frac{T_m - T_l}{T_m - T_0} \frac{\exp(-\lambda^2/4a)}{\operatorname{erfc}(\lambda/2\sqrt{a})} - \frac{\lambda\sqrt{\pi}h_{sf}}{2c_{ps}(T_m - T_0)} = 0$$

with the parameters:

b: ratio of liquid and solid heat conductivity

a: ratio of liquid and solid heat diffusivity

h_{sf} : solidification heat

c_{ps} : specific heat capacity of the solid phase.

Although this model is much too simple to describe the crystal growth in the RGS case, its solution can be useful for the qualitative understanding of crystal growth velocity and wafer thickness.

In dependence of the substrate temperature, the following two figures show the wafer thickness grown after a certain time and the growth velocity of the solid liquid interface.

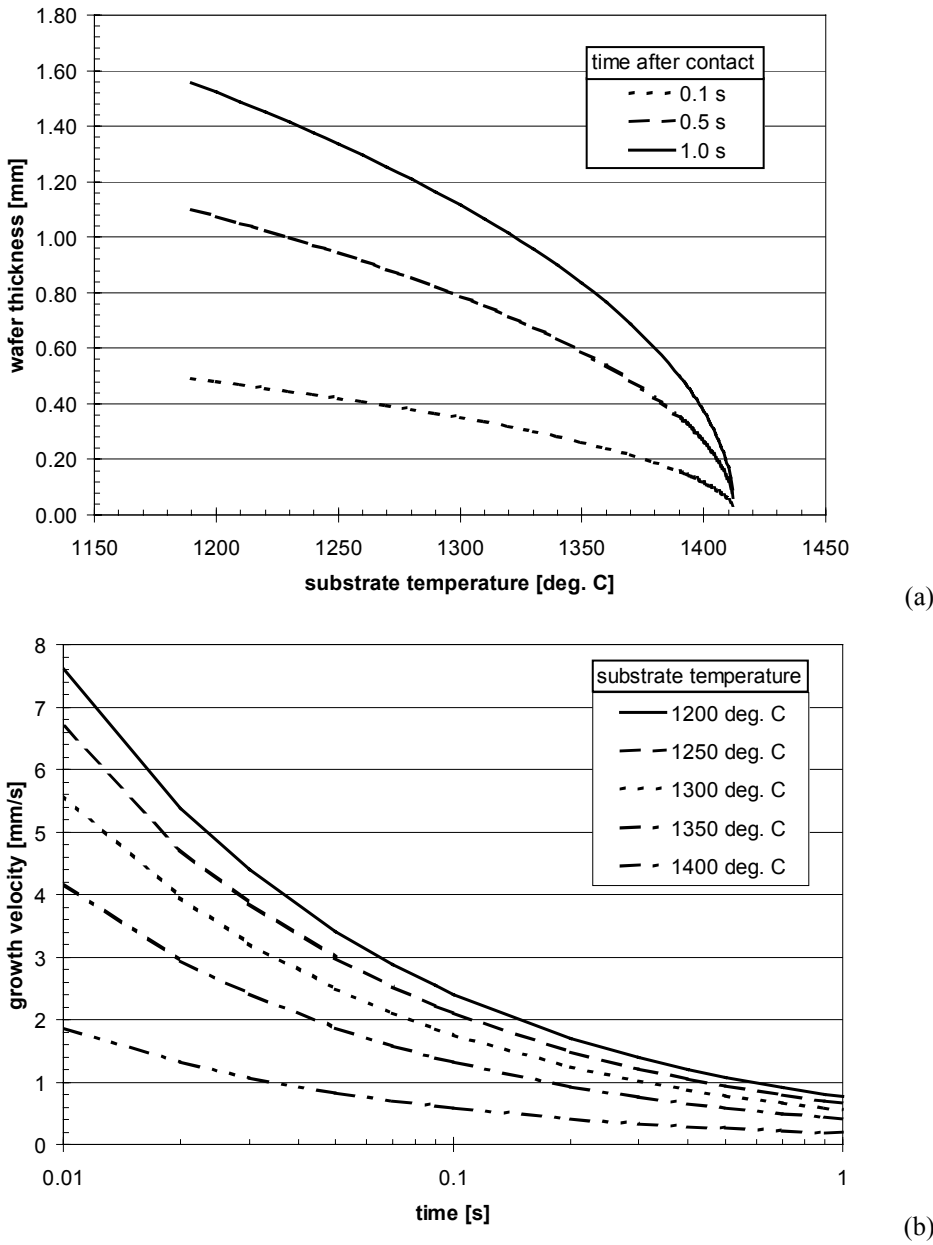


Figure 3: (a) Wafer thickness in dependence of the initial substrate temperature after 0.1s, 0.5s and 1.0s. (b) Growth velocity as a function of time depending on substrate temperature. Note that the analytical expression approaches infinity for $t>0$.

As indicated in the figures above, silicon wafer thickness in the range of 0.8 mm up to more than 1.6 mm for reasonable substrate temperatures can be reached in 1 s, with typical growth velocities in excess of a few mm/s range. Compared to other silicon crystallisation methods the silicon crystal growth rate in such a process is very high.

The experimental results from RGS runs are in qualitative agreement with the picture as outlined above, although for a detailed quantitative analysis a much more sophisticated model is needed. In agreement with the classical Stefan problem, the initial crystal growth velocity is high in the beginning of the process and decreases rapidly. However, after a growth period of 1 s, the typical wafer thickness is in the range of 0.3 mm to 0.4 mm, which is much thinner

than predicted by the model. The reason for the overestimation of the wafer thickness by the model is caused by the facts,

- that the substrate temperature is not constant during crystal growth but increasing,
- that there is a finite heat transfer between liquid silicon and substrate, which slows down the crystallisation speed and
- that the liquid silicon melt is most probably in turbulent flow, transporting heat from the hotter top surface of the melt to the liquid-solid interface.

All extensions to the simple Stefan problem solution slow down the crystallisation process, which means, that the solutions above can be regarded as upper limit. In reality, crystallisation speed and wafer thickness is lower, depending on system properties such as silicon-substrate properties, melt temperature and melt behaviour.

RGS wafer technology and solar cell process development

Record solar cell efficiencies achieved with RGS wafer based solar cells show a remarkable trend over the last 10 years. One of the main reasons for this development was the good co-operation between wafer manufacturer (Bayer AG), solar cell process developers as well as basic silicon material research and development (HEXSi, KoSi projects). This led to an increased understanding of the material characteristic and the behavior of the RGS wafer in a solar cell process. The consequences of this development can be seen by the steady efficiency increase as shown in figure 4.

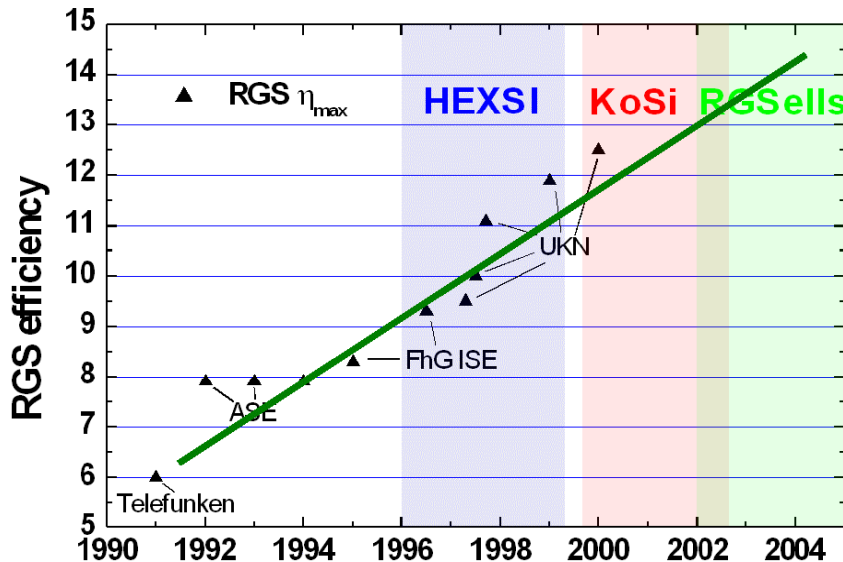


Figure 4: Record RGS solar cell efficiencies. Earliest results were from Telefunken and its successor ASE. In later projects the Fraunhofer Institute for Solar Energy Systems (FhG-ISE) and the University of Konstanz (UKN) held the efficiency records.

In the future, it is expected that this development can be continued at the same or even increased speed. In order to do so, the next improvements in wafer manufacturing will be:

- A reduction of the high oxygen content of the wafers by better silicon melt treatment. The oxygen concentration in the wafer limits at the moment the effect of hydrogen in-

diffusion and thus the efficiency of an RGS solar cell in an industrial-type cell process. The high oxygen content also leads to the formation of oxygen related recombination centers during the cell process (thermal and new donors) [7, 8, 9].

- The application of results from the silicon growth modeling to lower the wafer growth speed further and to improve crystal quality.
- In a second phase the casting process will be optimized to allow better thickness variation control and to lower the amount of liquid silicon film extraction from the casting frame.

Initial steps taken to implement the improvements as outlined above, resulted in the manufacturing of RGS wafers without major shunts, which were regularly seen in the past. These shunts were most probably caused by inversion channels of highly oxygen decorated extended defects, which could in the most extreme cases result in a carrier collecting network in the RGS wafer [10]. In a similar way series resistance problems, which were often lowering the fill factor of RGS wafers, could be solved. Both improvements resulted in the production of the first RGS based solar cell with efficiencies above 10% using an industrial-type solar cell process (i.e. screen printed contacts, firing through silicon nitride ARC, no texturisation).

Table 2: Cell parameters of an RGS wafer based solar cell produced by an industrial type screen-printing process (cell size 5x5 cm²).

Voc [mV]	Jsc [mA/cm ²]	FF [%]	efficiency [%]
563	24.0	75.1	10.1

Summary

Ribbon-Growth-on-Substrate silicon wafer manufacturing technology is one of the most promising technological developments for the further improvement of silicon wafer based PV modules. Its productivity rate in the 25 MWp to 50 MWp range allows the construction of a 100 MWp wafer production facility with only 2-4 RGS machines.

In two R&D projects RGSolar and RGSELLS, the three important areas of machine development, RGS wafer manufacturing and solar processing are developed in parallel. In the area of machine development, design phase and technical drawing phase is finished resulting in a technical product documentation of the RGS prototype machine. Improvements in wafer manufacturing process development and solar cell processing techniques resulted in better wafer characteristics and a deeper understanding of the factors influencing wafer quality. Main near term challenges are decreasing the oxygen concentration and controlling the crystal growth velocity. Both are accompanied and guided by model forming in the fields of solution and evaporation behavior of impurities in the silicon melt and silicon crystal growth during the casting process.

First steps in reducing the oxygen content resulted in RGS wafers and solar cells, which showed reasonable good cell parameters in a screen-printing process. Promising efficiencies of more than 10% could be achieved. Future improvements in melt treatment should result in further reduction of oxygen concentration and to an increase in solar cell efficiency. Additionally, this new material should react much faster on hydrogen passivation, which makes the material even more compatible with a standard firing through silicon nitride solar cell process.

These results and the promises of high-speed, low-cost silicon wafer manufacturing are the driving force to push this technology forward to commercialization in 2005.

Acknowledgements

We highly appreciate the excellent co-operation with the R&D groups working on silicon material in Europe. The enthusiastic support from the former Bayer RGS team and the very motivated work of the ECN engineering department during the training and technology transfer phase is highly appreciated. Their excellent work formed the base for a fast and continuous development of the RGS technology in a new surrounding. We also thank the engineers from the professional industrial equipment group of Philips ETG for all the effort and motivation they brought in during the development of the RGS machine design.

We gratefully acknowledge the support from the Dutch Economy, Ecology and Technology program (E.E.T.) under contract number EETK99150 and of the European Commission under contract number ENK6-CT2001-00574.

References

- 1 P.D. Maycock, Photovoltaic News, **Vol. 21**, No 3, ISSN 04739-4829, 2002
- 2 NCPV, "PV industry roadmap", <http://www.nrel.gov/ncpv>
- 3 J. P. Kaleijs, Solar Energy Materials and Solar Cells, **Vol. 72**, p. 139, 2002
- 4 A. Briglio et al, Flat plate solar array project final report: Vol. 3, NASA-CR-180661, DOE/JPL-1012-125, 1986
- 5 A. Schönecker et al., to be published Proc. 29th IEEE PVSC, New Orleans 2002
- 6 R. H. Rangel, X. Bian, Int. Jour. of Heat and Mass Transfer, Vol. 39, No. 8, p. 1591, 1996
- 7 T. Pernau, et al., Proc. 17th European PVSEC, p. 1764, 2001
- 8 B. Sopori, et al., Journal of Electronic Materials, Vol. 30, No 12, 2001, p. 1616
- 9 A. Kananmori, M. Kanamori, Journal Applied Physics, 50, 1979, p. 8095
- 10 Giso Hahn et al., Proc. 17th European PVSEC, p. 1371, 2001

**SOLAR GRADE SILICON FEEDSTOCK
RECENT ASSESSMENT RESULTS AND A COST EFFECTIVE CHEMICAL PATH**

Wolfgang Koch[†], Armin Raeuber[‡], Armin Mueller*, Karsten Wambach*, Holger Kirchner^Δ

[†]Bayer AG, Rheinuferstr. 7-9, D-47829 Krefeld,

Phone +49 2151 883370, Fax +49 2151 887503, wolfgang.koch.wk2@bayer-ag.de

*PSE Projektgesellschaft Solare Energiesysteme mbH, Christaweg 40, D-79114 Freiburg

*Deutsche Solar AG, Berthelsdorfer Str. 113, D-09599 Freiberg (Sachsen)

^ΔDegussa AG, Weissfrauenstr. 9,D-60287 Frankfurt/Main

ABSTRACT

To reach the cost and volume goals of the rapidly developing photovoltaic industry it is inevitable, to create an independent feedstock supply with Solar Grade High Purity Silicon (SGS), because the availability of the hitherto used by-products of the Electronic Silicon Industry is limited and will not increase reasonably within the next 10-15 years. The growing feedstock demand today is already irritating the PV market but a true shortage must not be expected. Recent results of a global assessment will be presented here.

One of the conclusions implies that a new, cost effective Silicon feedstock, not depending on Electronic Grade Silicon production chain, must be available on the market by 2005 to meet the cost objectives.

The implementation of a new technology jointly pursued by SolarWorld AG and Degussa AG will make the production of solar silicon substantially more efficient and cost-effective while maintaining the same high quality level. The vigorously expanding solar industry will thus be able to draw on a source for its supply of solar silicon that will be reliable in the long run.

Keywords: Solar Silicon, Feedstock, Production

INTRODUCTION

All PV experts are well aware that Silicon and Oxygen are the most abundant elements looking at 16 km of the earth's crust. 50 % Oxygen and 25 % Silicon are guarantees that Silicon is available forever. So there is an abundant amount of Silicon, why not for photovoltaic devices at reasonable costs?

The explanation for it is a high-energy demand for the reduction to elemental Silicon and the purity needed because the cleaning processes request a lot of investment for the plants.

Reviews of the present situation have been given by us earlier in two past studies carried out by BAYER and LIFE within EPIA the first denominated "Photovoltaics in 2010" [ALTN1] in 1995-1997 and the second denominated "Present and likely future bottlenecks analysis for a sustainable photovoltaic policy" [ALTN2, Woditsch1, Koch1] in 1998-1999 and by Hubert Aulich [AULICH1]. Not to mention the NREL and EPIA roadmap considerations.

A part of Aulich's conclusions was: "EG-Si produced by gas-phase decomposition of SiHCl₃ and SiH₄ represents the only source material for all crystalline silicon solar cells.

There are only 7 companies producing Prime Poly Silicon material today and 6 out of 7 are producing crystals and wafers as a forward-integrated product as well. Comparing these

conventional microelectronic technologies used by e.g. Wacker, ASiMi, MEMC and Hemlock, the production cost is high, with 30-45 \$/kg too high for a mass product of the PV industry. Because of area related efficiency PV is not in a position to lower the cost by minimising the amount of feedstock like the electronic industry going into higher integration making more and more chips out of one wafer.

A new global assessment of the „solar feedstock situation“ has been finished just recently (June 2002) by the EU-SAHARA project (A Task Force for the Creation of a Consortium to Set-up a SoG-Si Production Plant) and some results will be presented here. The SAHARA task force partners were: Deutsche Solar, ECN, Netherlands, JRC, Ispra, Italy, Scatec, Norway and Transenergie, France. Main objective of the SAHARA project was to set up a task force to act as a leverage towards the setting up of Solar Grade Silicon (SoG-Si) production plants.

From those studies, and in particular from the feedstock bottleneck study in 98-99, clearly emerged that a feedstock crisis would have happened towards 2005 unless something was done towards the production of SoG-Si. In fact at that time no industrial Si producers would have thought to produce Silicon for the PV Industry also in view of the very good electronic market in the same period against the crisis which hit it later.

A complete assessment at world-wide level of the current status of accomplished and on-going researches and industrial developments in the field of silicon production processes for solar cells applications has been tried. It has been the aim of the SAHARA Project to get the most updated, clear and objective document existing in the sector. This evaluation was on one side the basis for the analysis/revision of the [ALTN2] Study which was critically reviewed and validated in its main statements and on the other side it assisted into the definition of the most suitable technologies for further industrial development.

Main fundamental objectives (the SAHARA 'a priori' project goals) were :

1. At technical level, to review state of the art of current industrial and R&D activities on Solar Grade Silicon production to ascertain if one or more technologies exist mature for industrial production or for pilot phase and a complete definition of the same technologies.
2. At economic and commercial level, to update and validate [ALTN 2] study previously carried out by BAYER and LIFE within EPIA in 1999 to ascertain if a shortage of feedstock is confirmed and therefore if the need of a SoG-Si production still remains.
3. In case of positive answers for points 1 and 2 above, to promote some kind of association actions (Joint-ventures, Consortia, Link-agreements etc.) among mainly European partners for the R&D development first, the industrial development later and the commercial phase to immediately follow for those viable SoG-Si production routes.
4. At policy level, to understand what role can Public Organisations play (National Governments, European Union, etc.) and which policy could be suggested, to sustain the risk and the huge investments of the actions described in 3 above.

GENERAL ASSUMPTIONS

1. The expectation in the **market growth makes it worthwhile** considering big efforts. The development in the past will be shown in Fig. 1 (next page) and the prognosis for market growth for the time 2002 and 2010 may be discussed in terms of three different models.

Model 1	Growth rate +11,6%/year, starting in 2002 (average growth rate up to 1996)
Model 2	Growth rate +21,9%/year, starting in 2002 (average growth rate 1990 to 2001)
Model 3	Growth rate +34,3%/year for 2002 and 2003, levelling off to 11,6% (Model 1) from 2004 (34,3% was the average growth rate from 1997 to 2001, Japanese and German funding programmes end after 2003)

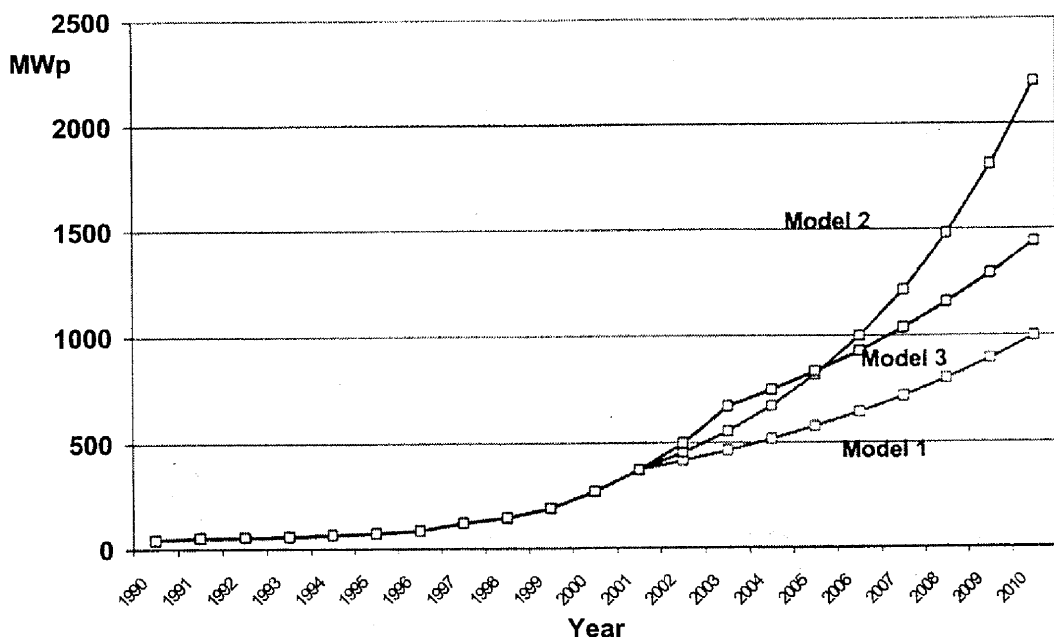


Fig. 1: History and projection of market growth of solar cell

2. Crystalline Silicon is the workhorse of the global PV Industry at least for a decade. The distribution of the market shares of different solar cell technologies since 1980 (Fig. 2) demonstrates it's growing dominance. The growth of thin film technology is unlikely to have an impact on the demand of silicon feedstock over the time period considered."

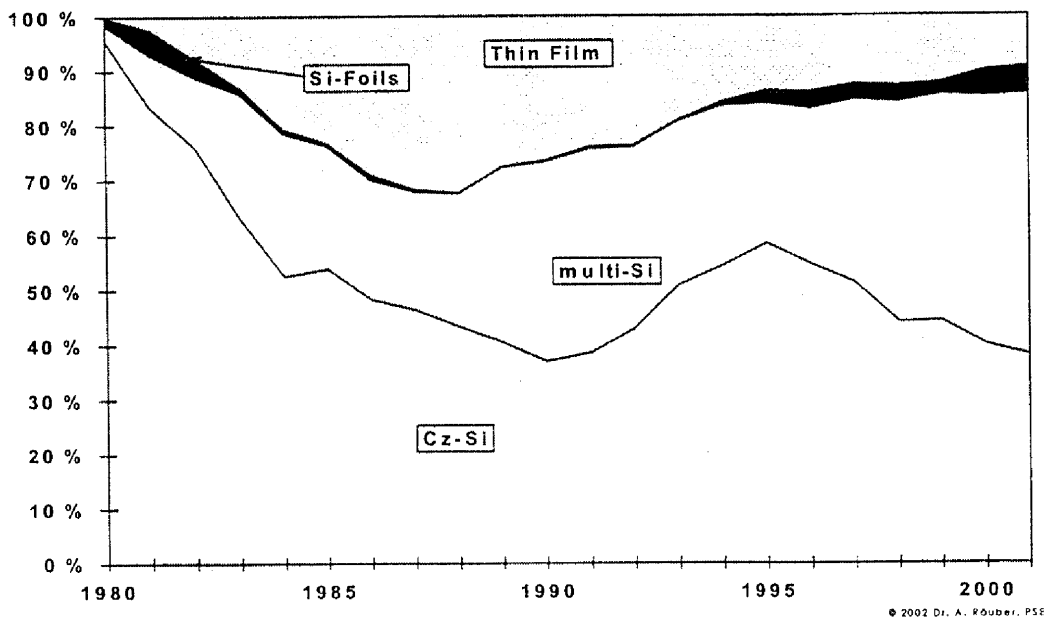


Fig. 2: relative market shares of different solar cell technologies (in percent of total turnover)

3. The **specific consumption of silicon decreased** from about 20 g/Wp in 1995 to about 15 g/Wp nowadays and will decrease further to about 10 g/Wp in 2010.
4. Some **Solar Grade Silicon Qualities** can be defined and used in different wafer and cell processes which go somewhere **in between electronic grade and upgraded metallurgical** specifications of the maximum allowable impurity content as sketched in Fig. 3.

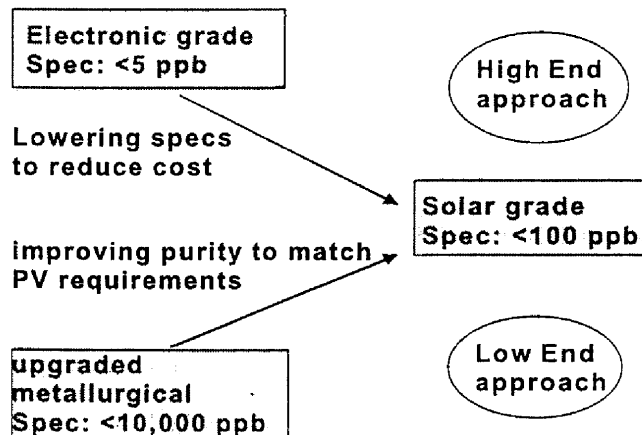


Fig. 3: Different principles to approach Solar Grade Silicon

SOLAR SILICON DEMAND

Taking the above mentioned assumptions into account together with the decrease of the specific feedstock use and some assumption concerning some growing market penetration of thin film modules. The silicon demand will grow dependent on the different models presented in fig. 1 to ca. 6.000 to 9.000 t by the year 2005 roughly.

The capacities for Electronic Grade Silicon (EG-Si) will been shown, together with some statements that are describing the present knowledge of the feedstock supply situation for electronic and PV business.

The idle capacities of EG-Si are used today to follow the demand for Silicon by the PV companies. As the Prime Poly Silicon production in 2000 was 18.200 t there should be a Silicon supply for PV industry of 6.370 t if 35 % of the Silicon used in the production chain is recovered for PV wafer production. This amount of Silicon is reduced to 13 % by losses of recovering by subtracting highly doped material and by loosing material during sorting and cleaning as well as internally recycling. Total off spec Silicon together with MEMC granular for PV industry today is available up to 2.100 t in 2001 as will be shown in Fig 4.

The demand for a Solar Grade Silicon will rise up to at least 8,000 tons in 2010 on the 15 % growth rate scenario and to more than 12.000 tons in case that all announced capacities are going on stream. The data are evaluated under the premises that 20 % of the market in 2010 is covered by Thin Film and technology development will reduce the demand of Silicon per Wp by 70 % to 10 g per Wp in 2010.

The supply/demand balance is shown in fig. 4 for the three different growth scenarios.

The capacities announced for 2003 and the coming years of the entirely PV dedicated feedstock part are presented by hatched fields.

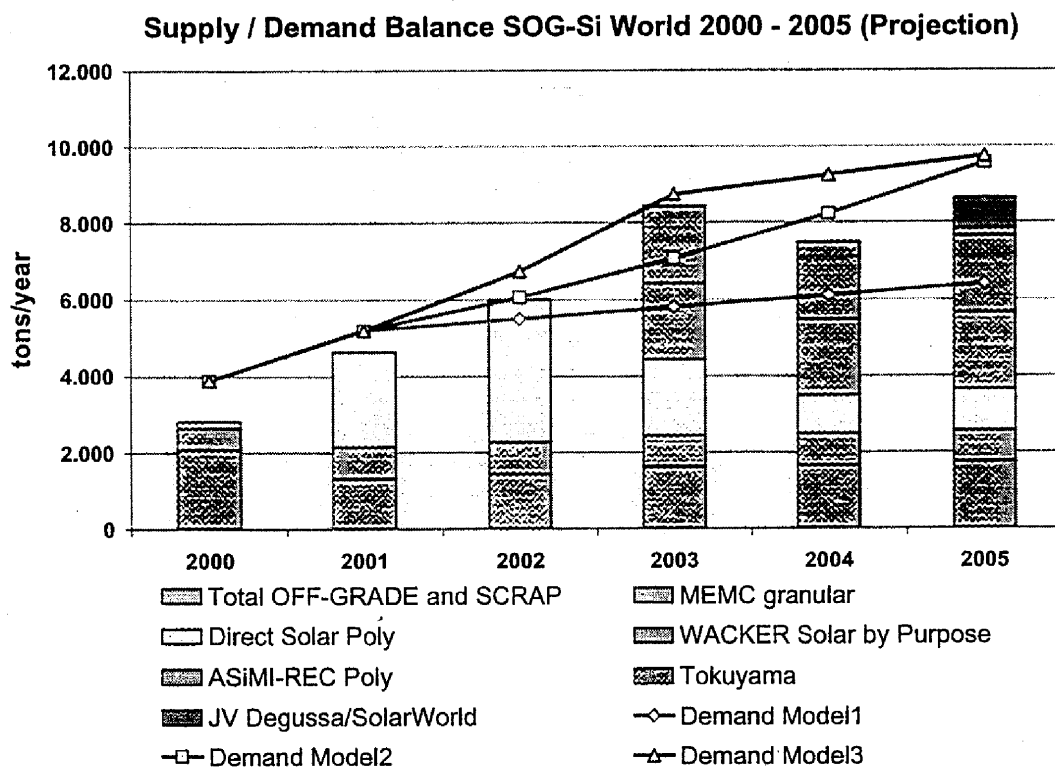


Fig. 4: Supply/Demand Balance for Solar Grade Silicon in the PV Industry 2000-2005 (moderate scenario)

The scheduled amounts in tons/year can be seen in the next table:

Year	2003	2004	2005
ASiMI-REC Poly	2,000	2,000	2,000
WACKER Solar by Purpose	2,000	2,000	2,000
JV Degussa/SolarWorld	0	0	800
Tokuyama	10	10	200

The challenge and the solution to meet the coming demand is visible: the PV industry needs a Solar Grade Silicon production of at least 5,000 tons per year in 2005 and up to 10,000 to 15,000 tons per year in 2010 independent from the electronic industry.

Let's look to the market development as a function of module price. The decrease of price from 19 \$ per Wp in 1980 to about 4 \$ in 2000 means an average price reduction by more than 7 % per year connected with a strong market growth. The scenario for the future development shows the uncertainties of any prognosis. In 1999 the PV society expected a growth up to 650 MW in 2010, today the capacities announced predict 1.000 MW already in 2005.

The price and the demand are connected. If the price does not come down as expected the market would not grow as announced and vice versa. This means that along the whole production chain cost has to be lowered at least to 50 % in the forthcoming ten years.

DEMAND FOR COST REDUCTION

Calculating the feedstock price influence along our own cost structure at Deutsche Solar AG [Woditsch1, Koch1] or the European APAS Study we will define a target price for the Silicon feedstock of 12 to 13 Euro per kg as the challenge of the feedstock supply for the future.

The summary of the supply for the PV market with feedstock comes up with six theses for a Solar Grade Silicon Production Facility shown below. Point 5 has to be solved and point 6 means: start immediately.

1. Off spec materials and side products of the electronic Wafer production are limited
2. Rapid growth of PV Market needs additional 5.000 t of Silicon in 2005 (moderate scenario) or already in 2004 (cell capacities announced)
3. The growing PV Market is connected to an expected price reduction and vice versa
4. The Module price reduction to 1,5 - 2,0 \$ per Wp needs cost reduction along the value chain
5. Silicon feedstock should be available in the range of 12 to 13 € per kg at least lower than 25 € per kg (20 ¢ per Wp)
6. The schedule for development is more than tight

NEW ROUTES To SOLAR GRADE SILICON PRODUCTION

All attempts for the production of an SGS-production in the past and the present show that there was no solution of the problem around the corner, joint efforts are necessary.

All considered new routes to a cheaper Solar Grade Silicon can be summarised under five HEADLINES

1. Purification of Metallurgical Grade Silicon (MGS)
2. Reaction of Silicon dioxide and Carbon with high purity
3. Chloroilane reduction with high purity reduction materials
4. Development of existing technologies to reduce cost
5. Design of new processes on existing technologies

For more than 20 years the purification of MGS to SGS was the dream of different groups working hard succeeding hardly. The activities have been manifold as has been presented earlier.

No production was realised until today because of economical reasons. The reduction of Silicon dioxide with Carbon of high purity is started again by Sintef/ECN in a two-step process with Carbon removal afterwards.

Starting in the period from 1975 to 1985 there was a lot of attempts to look to new chemical routes to an SGS-product. Besides a lot of money that was spent for evaluating these processes no solution of the feedstock problem was at the horizon.

Normally when there is a promising new technology coming up old technologies show their strength and potential of fighting for the market. Even in case of PV there is no real stress on old technologies, producers of Prime Poly Silicon look for technologies to reduce cost.

Cost reduction possibilities of the existing technologies and the companies involved are considered. There are efforts to market a SGS material, but the estimated cost reduction is not enough for the long-term need of the PV industry and the long-term commitment of the companies involved is at least on doubt, when the electronic industry is recovering and higher prices are possible in the chip production.

There was a sign of hope when Bayer entered the stage with a new approach. Looking at existing technology the critical path was discussed, defined and developed by a project team looking to the cheapest way for the production of a SGS. Calculating with the optimistic eyes of an R&D-team they believed to come up with a new plant for an SGS-product within 54-57 month, in an amount of 5.000 tons per year and with a price of 12 to 13 Euro per kg. Due to Core Business Considerations Bayers Solar Silicon Branch got sold to SolarWorld AG. A rough principal sketch of a special PV supply route can be found in fig. 5.

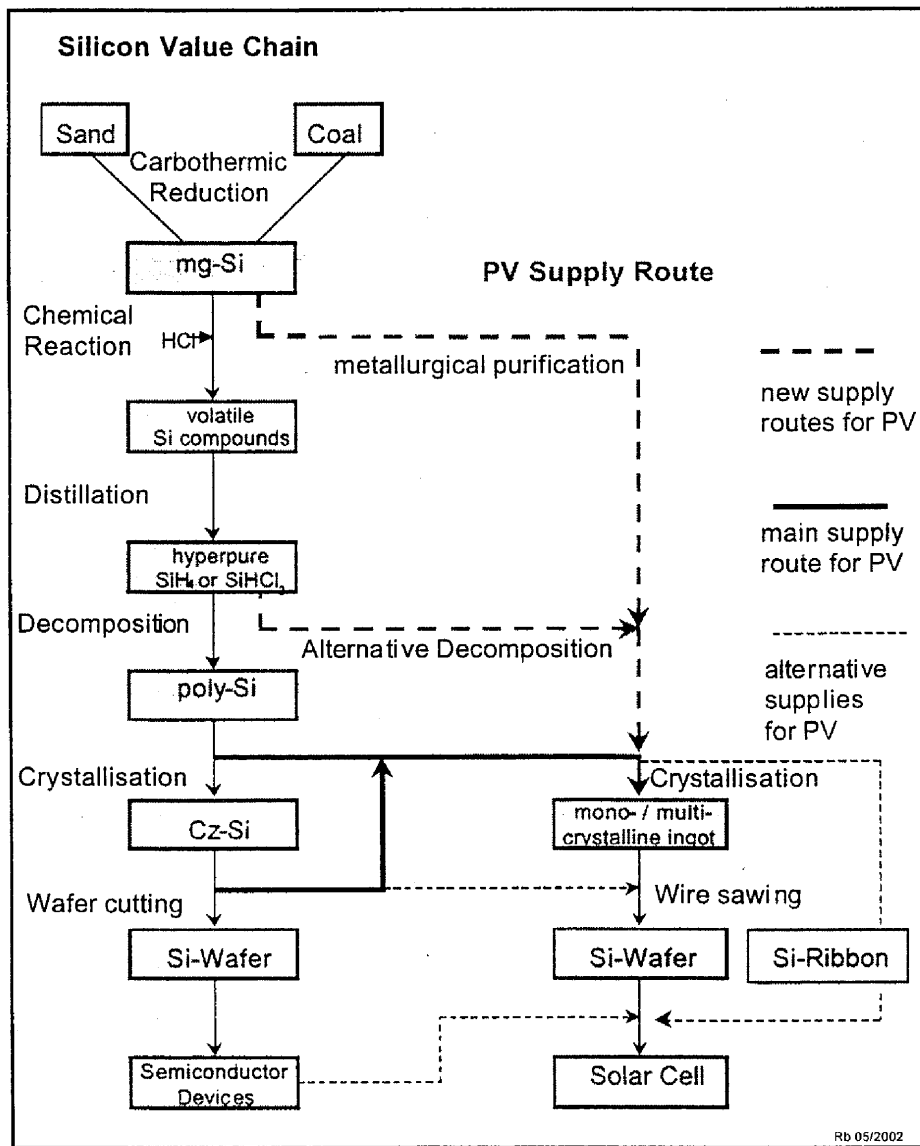


Fig 5. Value chain of semiconducting silicon and the related PV branch

Due to the numerous discussions about a solar silicon supply an efficient de-bottlenecking shows up to happen by various projects of different companies or consortia. Some of them

coming from the microelectronic side will bridge the gap at reasonable prices. Others will go further aiming at the necessary cost goals.

Six projects were considered (SAHARA a posteriori projects results) for further development and described shortly below:

- The Wacker Chemie project plus a Fluidised Bed Reactor (FBR) development project
- The Tokuyama project with a new type of deposition reactor
- The ASiMI/REC project plus a FBR development project
- The Degussa/SolarWorld project with tube deposition
- The SOLSILC/SPURT project with direct reduction and a melt purification cycle
- The ELKEM project based on purification of metallurgical grade silicon

In particular those directly or indirectly initialized by SAHARA and some other bottleneck and roadmap discussions are:

The ASiMI/REC project, which is “ready to go” into industrial production with their relaxed Siemens process in 2003, whereas their REC Fluidised Bed Reactor (FBR) project still has to go through the pilot phase to aim for a lower product price.

The JV Degussa/SolarWorld project, which is considered as the most ambitious project (high end technology from the world biggest producer of Chlorosilane with a high end product at a price target in the range of 20 €/kg along the guidelines set forth by the “Feedstock Bottlenecks Analysis” Study), which needs a pilot phase prior to industrialisation.

The SOLSILC/SPURT project, which is already now conducted by a European consortium made of research institutions and industrial companies. This process is presently operated partly at pilot scale, partly at lab scale, and the whole process is planned for pilot phase in 2004 having as a goal a product at a price below 20 €/kg.

A “ranking” of these different technologies is not possible at the current state of development. All projects should go through the state of pilot production or industrial production; as appropriate, to allow a more detailed judgement.

Projects 3 and 4 use, indeed, a very similar technology for the production of Chlorosilane but the foreseen deposition techniques are different. Project 5 is completely different and it is an alternative to the gas phase processes.

The SPURT consortium will deliver a different product of probably lower grade and lower price than the gas phase technologies, and they will probably address at least partly another market segment than the other producers.

Of the six projects above SAHARA certainly gave its strong contribution in promoting the Degussa/SolarWorld Joint Venture, the ASiMI/REC Joint Venture and the SPURT Consortium, by means of, among others, several meetings, two European Round Tables and a European Workshop. In view of the fast moving sector, LIFE, will continue working on this project.

Two of the projects: Wacker Chemie and ASiMI/REC, are already at the industrial stage level with their relaxed Siemens process with Wacker Chemie already producing and ASiMI/REC to start production in 2003. They can bridge the feedstock gap of the coming years at somewhat higher prices than the PV cost-goals. Both Wacker Chemie and ASiMI/REC Fluidised Bed Reactor (FBR) projects still have to go through a pilot phase. SPURT is scheduled for the pilot phase in 2004. Above projects pilot phases are certainly recommended together with the Degussa/SolarWorld project ready for the pilot phase now.

THE JV DEGUSSA/SOLARWORLD

On May 24th 2002 Degussa AG and SolarWorld AG announced a joint venture for the future-oriented production of solar silicon. They thus pool their competencies in developing and establishing a cost-effective technology for the manufacture of solar silicon. In the consistently high demand for solar silicon as the raw material for the photovoltaic (PV) industry the two companies see a significant potential for their joint activities. Degussa AG holds 51 per cent and SolarWorld AG has a 49 per cent stake in the new company. Entrepreneurial decisions will be taken jointly by the two partners.

Degussa is world market leader in speciality chemicals. With sales of EUR 12.9 billion and a workforce of some 53,400, in fiscal 2001, the corporation generated operating profits (EBITA) of more than EUR 1 billion. Degussas Organization plan is shown in fig 6.

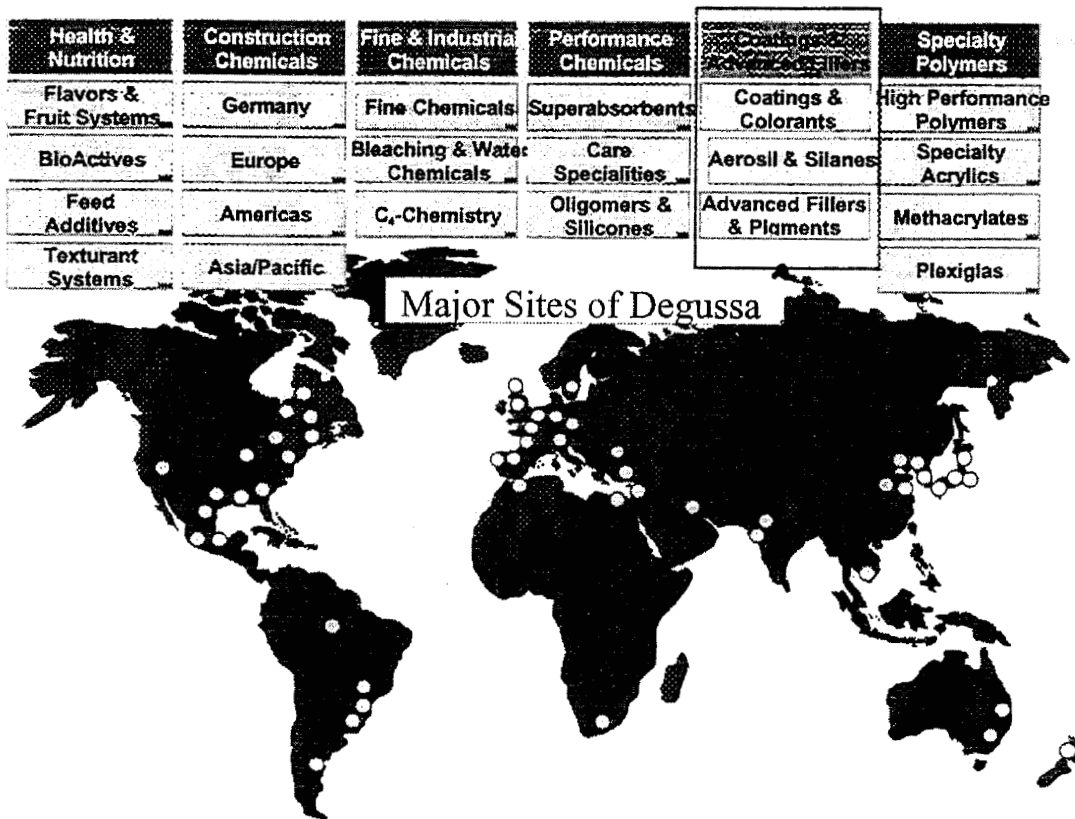


Fig. 6: Organisation Plan of Degussa AG. The Business Unit Aerosil & Silanes of the Division Coatings & Advanced Fillers section is highlighted

Degussa being the World market leader in Chlorosilanes since many decades can be considered as the ideal partner to a company being specialised in Solar Silicon PV.

The leading World Market Positions in the Sector of Aerosil and Silanes and the production places can be taken from fig. 7. Antwerp, Belgium is foreseen as the location for the planned Solar Silicon pilot plant.

Aerosil & Silanes

Product	Applications	World Market Position
Fumed silicas (Aerosil®)	Silicone rubber, paints and coatings, adhesives, sealants, plastics, pharmaceuticals, cosmetics, high temperature insulation, electronics	1
Organosilanes	Glass fiber, paints and coatings, adhesives and sealants, wire and cable, silicones, pharmaceuticals, building protection, fillers and pigments, thermosets	2
Chlorosilanes	Optical fibers, fumed silicas, organosilanes, silicic acid esters	1

The map shows the European continent with several industrial sites marked. In the north, Waterford (Ireland) and Bitterfeld (Germany) are indicated. In the center, Antwerp (Belgium) and Rheinfelden (Germany) are marked. In the south, Tokkaichi (Japan) is shown, suggesting an international context for the market positions.

Fig. 7: World Market Positions in the Sector of Aerosil and Silanes and their production places

The co-operation concept between Degussa and SolarWorld and their Joint Venture company JV Degussa/SolarWorld (51/49) bundles the expertise of both partners and their backgrounds.

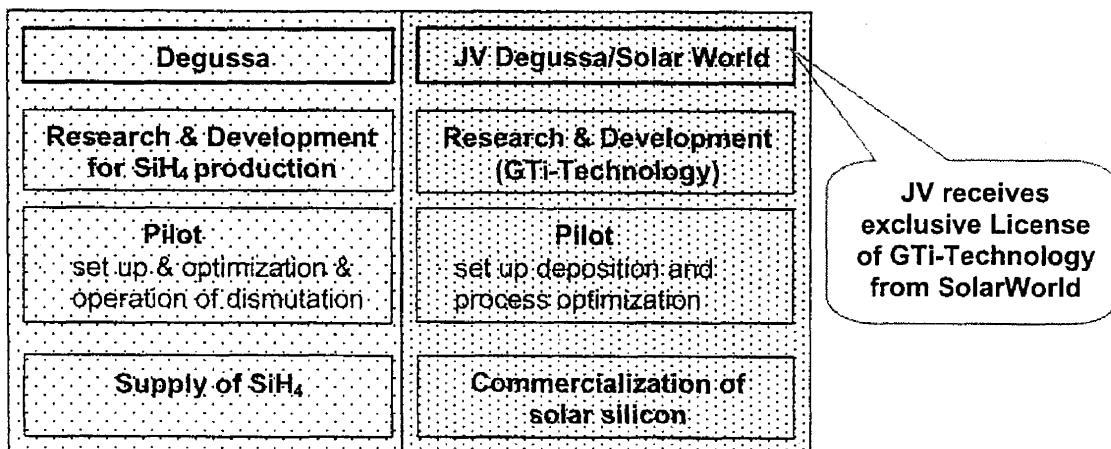


Fig. 8: Co-operation between Degussa and SolarWorld and their Joint Venture company JV Degussa/SolarWorld (51/49)

The advantages of an integrated chlorosilanes production facility, an inexpensive dismutation process and an efficient deposition technology* will lead to a competitive costs position

A flow-chart of the planned Pilot-Plant; app.800 t p.a. can be seen in fig. 9.

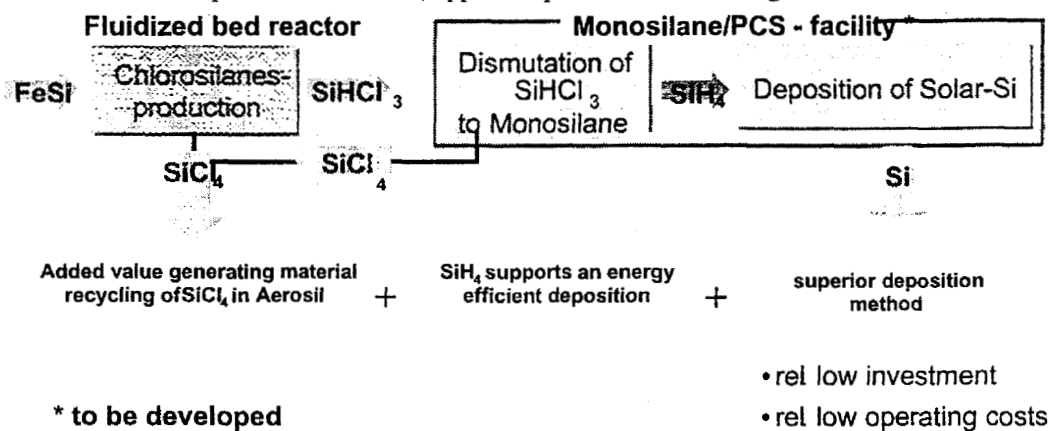


Fig. 9: Flow-chart of the planned JV Degussa/SolarWorld Pilot-Plant; app.800 t p.a.

The objective of the joint venture is to produce silicon from silane, a gas consisting of silicon and hydrogen. The silane will be provided by Degussa AG, one of the world's leading supplier of speciality chemicals. The decomposition of silane to silicon takes place in tube-type reactors whose technology will be contributed to the joint venture by SolarWorld AG which holds the world-wide and exclusive license to this process developed by the US technology group GT Equipment Technologies Inc. (GTI), Nashua/New Hampshire. This technology provides for the silicon from the silane to be precipitated on the walls of silicon tubes.

The joint venture will optimise and establish this innovative silicon technology to the point where a pilot plant with an annual capacity of initially 800 tons of silicon can be built at the Degussa AG location in Antwerp by the year 2005. SolarWorld will use up to 85 per cent of the solar silicon of the pilot plant capacity for the group's own production of solar silicon wafers. The remainder will be made available to the world-wide solar wafer industry.

The implementation of the new JV will make the production of solar silicon substantially more efficient and cost-effective while maintaining the same high quality level. The vigorously expanding solar industry will thus be able to draw on a source for its supply of solar silicon that will be reliable in the long run. Once the new technology has been established prices can be expected to come down in all parts of the PV industry.

CONCLUSIONS

The time of assessments, meetings and discussions is over. On an existing profound technical basis joint ventures, some being concluded right now, are necessary and will solve the main problems of the PV community.

1. Strong growth of PV industry needs an own feedstock supply independent from electronic industry (10.000 tons in the next 10 years).
2. Feedstock must be of high quality for the production of mono- and multicrystalline Si - wafers with the potential for high efficient Solar cells (17 %).
3. Cost target is below 20 €, maximum 25 € per kg (20 ¢ Wp).
4. SGS from traditional Silicon producers will be available to compensate the fading supply of EG-Si capacities which will be used more and more for the semi conductor industry.
5. High risk of the projects needs joint efforts and public financial support.
6. Schedule for an independent SGS not before the end of 2005.

ACKNOWLEDGEMENTS

The Contributions of Hans-Dieter Block, Bayer AG, Holger Kirchner, Degussa AG and Werner Warmuth, PSE are gratefully acknowledged. This work has been partially funded by the Northrhine -- Westphalian Ministry of Schools and Research, the Federal Ministry of Economics and Technology and the European Commission (DG-TREN) within the Altener II Programme of the European Union 1998-2002) Contract n. 4.1030/Z/00-. This SAHARA project has been very professionally managed by Lorena Franceschi, LIFE.

REFERENCES

ALTN2

"Present and Likely Future Bottlenecks Analysis for a Sustainable Photovoltaic Policy"
Final Report of a study within the ALTENER Programme, written by Bayer AG and
LIFE Ltd, November 1999

Aulich1

"Solar Grade Silicon Feedstock: The Global Perspective"
H. A. Aulich, Paper presented at the EPIA Round Table on Solar Grade Silicon
Feedstock, 24 October 2001, Munich

Roadmap1

"Silicon for PV Applications: Roadmap Meeting"
Preliminary Results of a Meeting sponsored by SEIA, 6 March 2002, Washington DC, USA,
Minutes by Melissa Eichner, Energetics, Inc.

Silicon3

"Polycrystalline Silicon – World Demand and Supply"
J. Mauritius, Proc. 8th Workshop on Crystalline Silicon Solar Cell Materials and Processes, 17
–19 August 1998, Copper Mountain, CO, USA, NREL/CP-520-25232

SU2

Strategies Unlimited, Solar Flare 2002-01

Wacker1

Polysilicon Market Update April 2002, R. Huber, Wacker Siltronic
Data presented at the EPIA Spring Meeting 2002 in Barcelona

Woditsch1

"Solar Grade Silicon Feedstock Supply for PV Industry"
Peter Woditsch and Wolfgang Koch, Paper E1.2, E-MRS Spring Meeting 2001,
Strasbourg, France, June 5 – 8, 2001

Koch1

Wolfgang Koch , Peter Woditsch, "Solar Grade Silicon Feedstock Supply for PV Industry"
17th European Photovoltaic Solar Energy Conference, Munich, Germany, 22-26 October
2001, p. 73-76

Development of cast technology for high quality multicrystalline silicon ingot of solar cells

Seiko Nara, Yasuhiko Sakaguchi
Technical Research Laboratories,
Kawasaki Steel Corporation,
Kawasaki-dori 1-chome, Mizushima, Kurashiki, 712-8511, Japan

Abstract

Silicon ingot casting conditions, including purification of the mold, mold coating material, and atmosphere gas and the ingot solidification rate, were investigated in order to improve the efficiency of photovoltaic cells of multicrystalline silicon with an optical conversion efficiency of 20% as a final target. As a result, it was possible to obtain high quality silicon ingots and produce wafers (wafer thickness, 3mm; resistivity, $0.5\Omega\text{cm}$) with an average diffusion length of $250\mu\text{m}$ or more from these ingots. The conversion efficiency of cells produced from these silicon wafers reached 18.3% (cell area, 25cm^2).

1. Introduction

Various research and development on photovoltaic systems is now underway with the aim of encouraging wider use of this technology as a form of clean energy, which is now desired. As part of this trend, research and development of a manufacturing technology for high quality multicrystalline silicon has also been carried out in order to achieve a substantial improvement in the conversion efficiency of cells in photovoltaic systems using multicrystalline silicon, as this material is produced in relatively large quantities.

The quality of silicon wafers is very important for improving the conversion efficiency of photovoltaic systems which use multicrystalline silicon. It is difficult to improve the conversion efficiency of a cell by the cell manufacturing process if inferior wafers are used. This means that improved wafer quality is indispensable for improving conversion efficiency.

To date, various methods have been employed to improve the quality of multicrystalline silicon wafers. It is well known that impurities¹⁻⁹⁾ in silicon wafers have an especially strong negative effect on conversion efficiency. Improvements have been realized in the silicon wafer purification process. However, since it is also clear that defects¹⁰⁻¹⁵⁾ in silicon crystals influence efficiency, research aimed at reducing defects has been carried out, and in some cases, the results have been applied in commercial production.

The difference between multicrystalline silicon and single crystal silicon is in the grain boundary. Investigations of the influence of the grain boundary¹⁶⁻¹⁸⁾, including simulations, have been carried out, but additional research and development are still considered necessary in order to achieve further gains in multicrystalline silicon efficiency.

In the present work, a casting technology for manufacturing high quality multicrystalline silicon ingots was developed to improve wafer quality and thereby contribute to high conversion efficiency in cells of multicrystalline silicon. This report presents results from a project entitled “Development of a practical technology for high efficiency multicrystalline silicon solar cells,” which was supported by Solar-Grade Silicon Technology Research Association (SOGA) and sponsored by New Energy and Industrial Technology Development Organization (NEDO).

2. Experimental Procedure

In this research, the casting method was used as the manufacturing method for multicrystalline silicon. Experiments were conducted with emphasis on the following points in the casting process.

- 1) Purification: In particular, purification of the mold, mold coating material, and atmosphere gas (argon).
- 2) Solidification rate control: The size of silicon grains is controlled by control of the solidification rate itself when manufacturing multicrystalline silicon by the multi-stage solidification control method.

However, the purpose of solidification rate control was not limited to control of the grain size, but also included reduction of defects in crystal grains.

The experimental conditions are shown below in Table 1.

Table 1 Experimental conditions

Ingots size	440mm X 440mm X 170mm (75kg)
Silicon resource	Semiconductor grade (over 1kΩcm)
Target resistivity	0.5Ωcm
Solidification rate	0.1-0.5mm/min

3. Results and Discussion

3.1 Crystal configuration of solidification ingots

Figure 1 shows the cross-sections of multicrystalline silicon ingots obtained by (a) the conventional multicrystalline silicon manufacturing method and (b) the multi-stage solidification control method (MUST process).

In the conventional ingot shown in Fig. 1(a), the crystal grains increase in size from small grains at the bottom to large grains in the upper part. In other words, it was found that the grain size is dependent on the height position in the ingot. The lines in the upper and lower parts of the ingot are traces of the cutting process.

In contrast, the MUST process ingot in Fig. 1(b) shows a virtually uniform grain size from the bottom of the ingot to the top.

Figure 2 shows the distribution of the number of grains and grain size in the ingot height direction, in other words, the solidification direction dependency of grain size. Because ingots solidify from the bottom to the top, these results may be understood as showing the dependency of grain size on the solidification direction. In the conventional ingot in Fig. 2(a), a large number of grains were observed at the ingot bottom. This number decreased at higher positions in the ingot, and became even smaller in the top area, near the final solidification position. In the MUST process ingot in Fig. 2(b), the grain size is constant at approximately 10mm, and the number of grains is also constant.

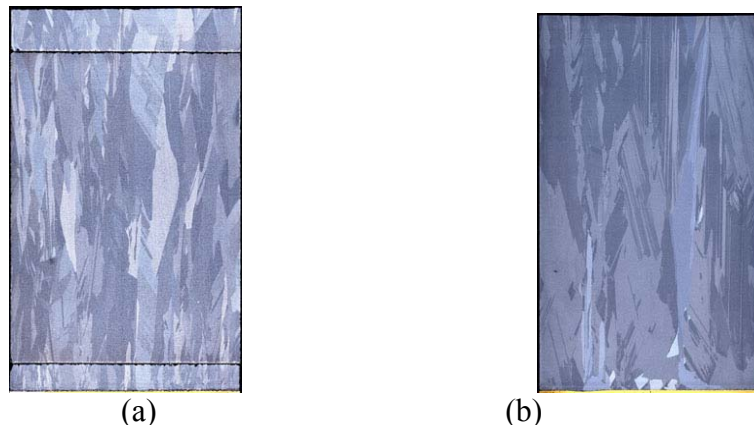


Fig. 1 Cross section of ingots by (a) conventional method and (b) MUST method

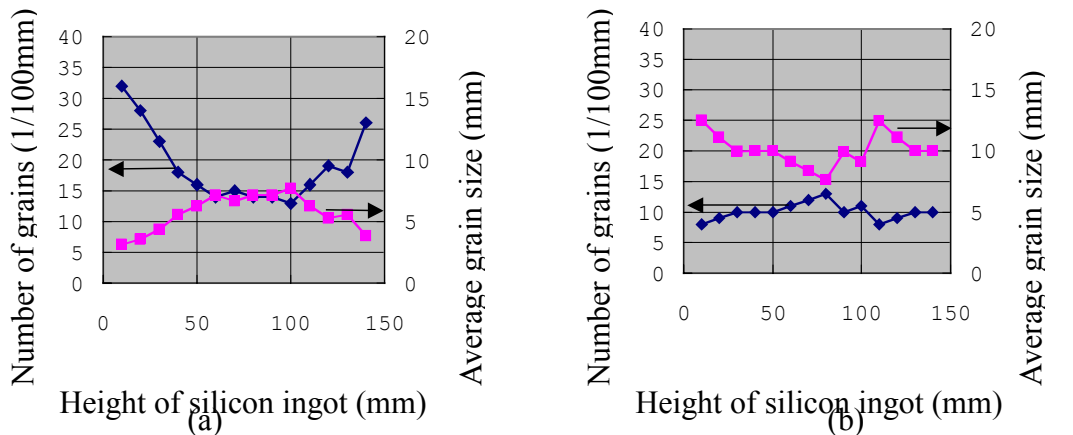


Fig. 2 Distribution of number of grains and grain size in ingot height direction in (a) conventional method and (b) MUST process ingot

3.2 Analysis of impurities

Figure 3 shows the results of an analysis of the impurity element iron in (a) conventional and (b) MUST process silicon ingots. The concentration of Fe is low in the central part in the ingot height direction. Table 2 shows the analysis values of other impurities. The analysis position in Table 2 was the central part in the height direction at the center of diameter of the ingot. The improvements shown here are the result of high purification.

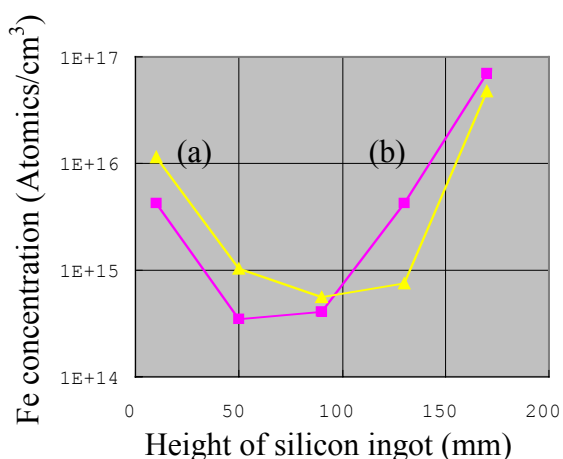


Fig.3 Distribution of impurity element iron in ingot height direction in (a) conventional ingot and (b) MUST process ingot

Table 2 Concentrations of impurities

	(a) (Atoms/cm ³)	(b) (Atoms/cm ³)
Aluminum	< 5.2X10 ¹⁴	< 5.2X10 ¹⁴
Oxygen	1.5-4.2X10 ¹⁸	< 4.3X10 ¹⁷
Carbon	1.2X10 ¹⁸	1.2X10 ¹⁸

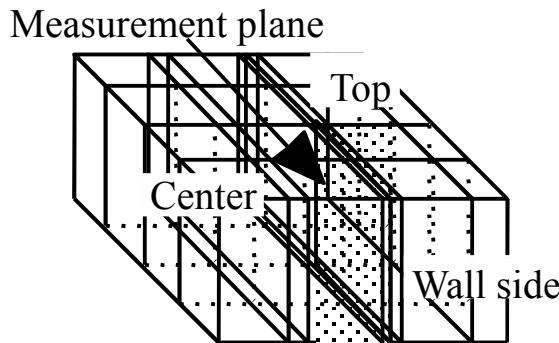


Fig. 4 Position of diffusion length measurement in silicone ingot

0.4-0.6Ωcm, the average diffusion length was 250 μm or more, and in some portions, the maximum diffusion length reached more than 400 μm. Wafers were manufactured from this ingot and used to produce high efficiency cells¹⁹⁾. As shown in Table 3, a measured conversion efficiency (EFF) of 18.3% was obtained in a 25cm² area. Table 3 also shows other values such as the open-circuit voltage, short-circuit current, etc.

3.3 Measurement of diffusion length

Figure 4 shows the diffusion length measurement position. Figure 5 shows the diffusion length measurement results for (a) conventional and (b) MUST process ingots. From Fig. 5, it is clear that the diffusion length of the ingots obtained as a result of this research and development project was MUST process greater than with the conventional method.

Figure 6 shows the measured diffusion length of wafers produced from a MUST process ingot. Although the resistivity of the wafers was

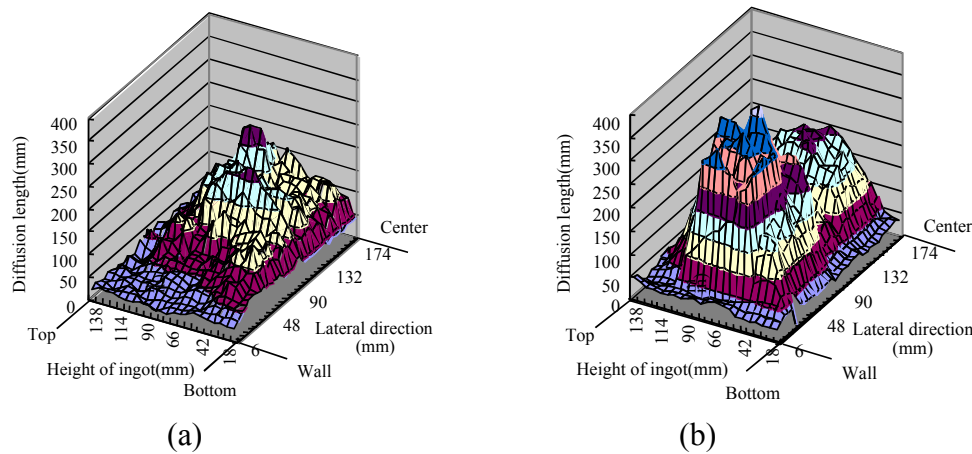


Fig. 5 Distribution of diffusion length in measurement plane (from Fig. 4) in (a) conventional ingot and (b) MUST process ingot

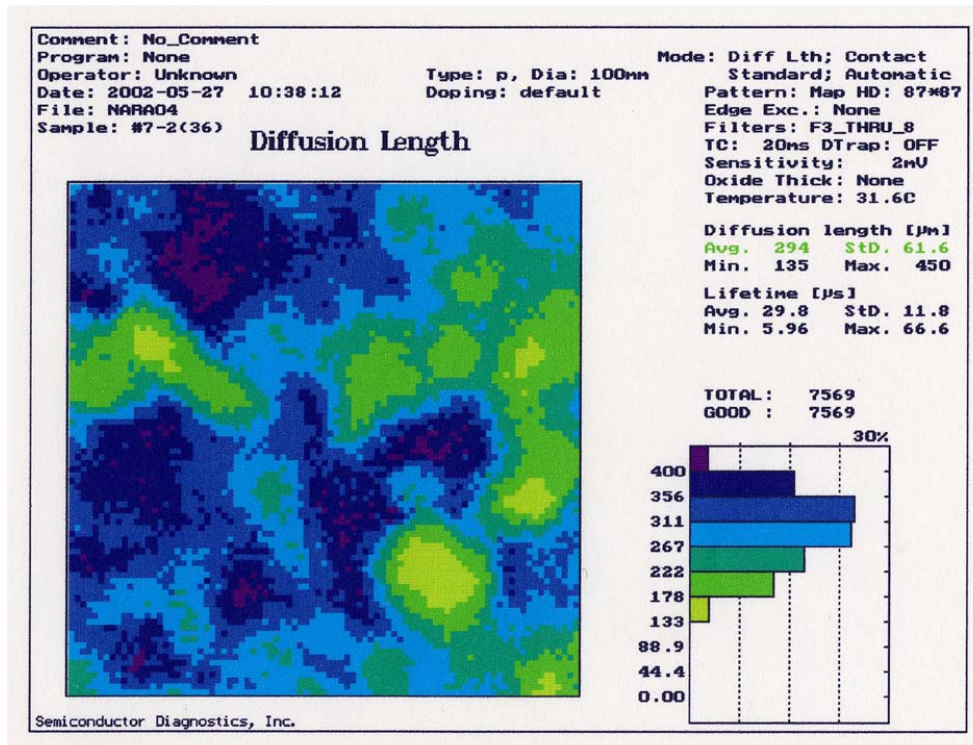


Fig. 6 Distribution of diffusion length in MUST process wafer

Table 3 Cell properties¹⁹⁾ (25cm^2)

Jsc (mA/cm ²)	Voc (mV)	FF	EFF (%)
<hr/>			
36.9	634	0.782	18.3

3.4 Measurement of etch pits

Etch pits were measured to investigate the reason why the diffusion length was greater with the MUST process than with the conventional method. However, no clear tendency could be observed, as the etch pits were under approximately $10/\text{cm}^2$ in both cases. Typical etch pits in

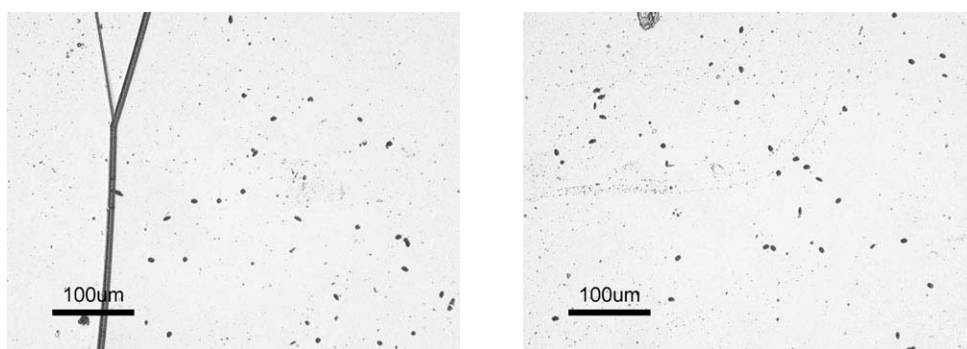
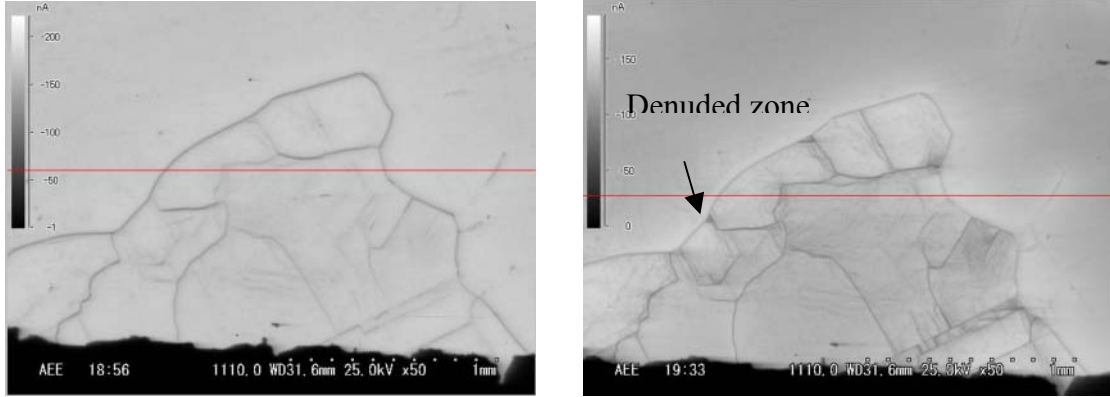


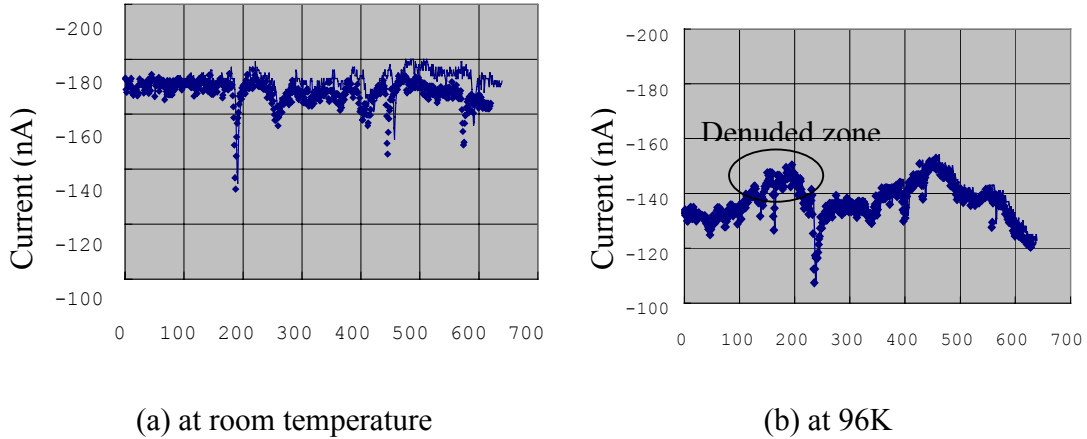
Fig. 7 Etch pits on MUST process wafer



(a) At room temperature

(b) At 96K

Fig. 8 EBIC photographs of wafer



(a) at room temperature

(b) at 96K

Fig. 9 EBIC current at lines in photos in Fig. 8

an ingot produced by the MUST process are shown in Fig. 7. The etch pit density of the ingot in this figure was 4×10^5 ($/\text{cm}^2$).

Comparing the MUST process ingot and conventional ingot, the concentrations of all impurities except oxygen are of virtually the same order. The fact that only the crystal particle diameter differed in the two methods suggests that some defect related to the crystal size or structure causes reduced quality. The authors will continue to investigate this point.

3.5 Observation of Electron Beam Induced Current method (EBIC)

Wafers were analyzed by the EBIC method to ascertain the cause of the extremely long diffusion length in MUST process ingots.

Figure 8 shows EBIC photographs of the grain boundary area of wafers produced by the conventional method. Although the grain boundary is only shown in the photograph in Fig. 8(a), which is an EBIC photo at room temperature, the current rose near the grain boundary at the low temperature of 96K. This high current area is called the “denuded zone.” Moreover, internal defects can be seen in the crystal grain at low temperature.

Figure 9 shows the absolute current of the red lines shown in the photo in Fig. 8. When the denuded zone is compared with the interior of a crystal grain, the current is clearly higher in the denuded zone at low temperature. Based on the fact that the denuded zone shows less

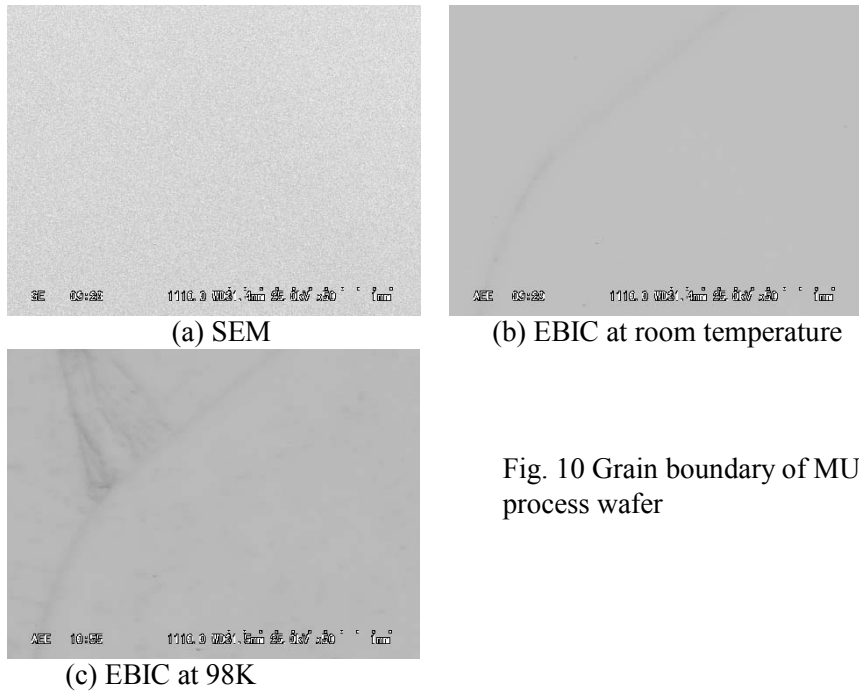


Fig. 10 Grain boundary of MUST process wafer

current drop at low temperature, it is considered that no deep-level defects exist in this zone, and further, that shallow-level defects have been reduced in comparison with the grain interior.

Figure 10 shows the results of observation of the grain boundary of a MUST process wafer. Within the grain, degradation of the current was observed at low temperature (98K), but was not clearly seen at room temperature. Furthermore, the current values showed basically the same tendencies at the grain boundary. Based on these results, it is thought that the grain boundary has little influence on the properties of the wafers obtained in the present work, and in particular, the grain boundary tends not to become a recombination site at room temperature.

3.6 Observation of Transmission Electron Microscope (TEM) and Secondary Ion Mass Spectrometry (SIMS)

The TEM sample was taken from the grain boundary area observed by EBIC using the FIB (Focused Ion Beam) method and observed by TEM and SIMS. Although the sample was investigated by EDX (Energy Dispersive X-ray spectrometer) in TEM observation, no impurities were detected in the grain boundary and the grain. Likewise, no special elements were detected

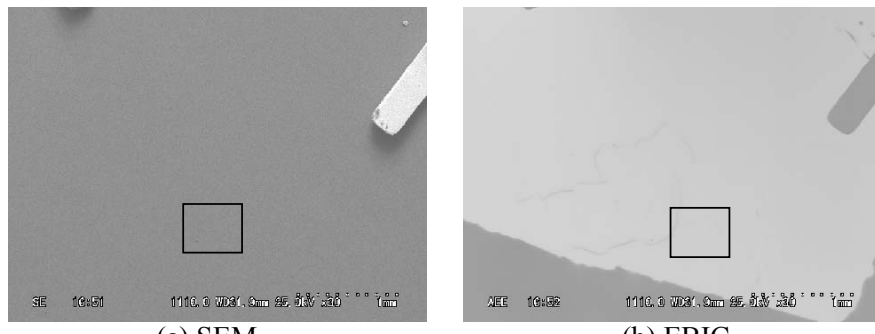


Fig. 11 Analysis areas for TEM-EDX and SIMS

by SIMS. Thus, even assuming that impurities may exist at the grain boundary, based on these results it can be said that their extent is limited to the grain interior, or their levels are below the respective detection limits.

4. Conclusion

A new multi-stage (MUST) solidification control method was developed in this research and development work and used to produce silicon ingots. The ingots showed a virtually uniform crystal grain size. Experimental photovoltaic cells produced from these ingots by a high efficiency process showed a conversion efficiency of 18.3%.

A denuded zone was detected at the grain boundary of the silicon wafers by EBIC analysis. Measurement at low temperature showed few recombination sites in this denuded zone in comparison with the grain interior. Wafers manufactured by the MUST process showed no current degradation at the grain boundary.

Reference

- 1) K. Graff, Aggregation Phenomena of Point Defects in Silicon p. 121, The Electrochemical Society (1982)
- 2) E.R. Weber, N. Wiehl, Defects in Semiconductors, p.19, North-Holland (1983)
- 3) W.T. Read, W. Shockley, Phys. Rev., 78, 275(1950)
- 4) G. Hasson, J.Y. Boos, I. Herbeauval, M. Biscondi, C. Goux, Surf. Sci., 31, 115(1972)
- 5) J.W. Christian, The Theory of Transformations in Metals and Alloys, p.353, Pergamon (1981)
- 6) J.C. Fisher, J. Appl. Phys., 22, 74 (1951)
- 7) A.D. Le Claire, Phil. Mag., 42, 468 (1951)
- 8) J. Fally, F. Faber, B. Chabot, Review Phys. Appl. 22 (1987) 529-534
- 9) R. H. Hopkins, R.G. Seidensticker, J. R. Davis, P. Rai-Choudhury, P. D. Blais, J. R McCormik, Journal of Crystal Growth 42 (1997) 493-498
- 10) M. Apel, I. Steinbach, Preprint 2nd World Conference and Exhibition on Photovoltaic Solar Energy Conversion, Vienna, 1998
- 11) C. Hassler, W. Koah, W. Krumbe, S. Thum, Preprint 2nd World Conference and Exhibition on Photovoltaic Solar Energy Conversion, Vienna, 1998
- 12) C.P. Khattak, F. Schmid, Preprint 2nd World Conference and Exhibition on Photovoltaic Solar Energy Conversion, Vienna, 1998
- 13) A. Lowerenz, M. Rinio, S. Riedel, M. Ghosh, M. Werner, H. J. Moller, 16th European Photovoltaic Solar Energy Conference and Exhibition 2000
- 14) C. Hassler, W. Koch, W. Krumbe, A. Muller, A. Schertlich, Preprint 2nd World Conference and Exhibition on Photovoltaic Solar Energy Conversion, Vienna, 1998
- 15) E.T. Yu, K. Barmak, P. Ronsheim, M.B. Johnson, P. MacFarland, J. M. Halbout, J. Appl. Phys. 79(4), 15, February 1996
- 16) D. Franke, T. Rettelbach, F. Pezzolla, J. Liebermann, M. Apel, Preprint 2nd World Conference and Exhibition on Photovoltaic Solar Energy Conversion, Vienna, 1998
- 17) D. Franke, M. Apel, C. Hassler, W. Koch, 16th Photovoltaic Solar Energy Conference and Exhibition 2000
- 18) D. Franke, C. Hassler, W. Koch, J. Liebermann, Preprint 2nd World Conference and Exhibition on Photovoltaic Solar Energy Conversion, Vienna, 1998
- 19) Yuji Komatsu, et al, 12th Crystalline Silicon Solar Cell Materials and Processes, 2002

The Technology of Modern Wiresaw in Silicon Wafer Slicing for Solar Cells

Imin Kao,* Associate Professor
Manufacturing Automation Laboratory (MAL)
Department of Mechanical Engineering
State University of New York at Stony Brook
Stony Brook, NY 11794-2300

Abstract

The modern wiresaw has emerged as the technology for slicing both single and ploy crystalline silicon wafers, replacing the ID saw which has been the tool for wafer slicing in the past 20 years. The ability to slice very thin silicon wafers effectively with minimum kerf loss and good surface finish has made the modern wiresaw an indispensable tool for photovoltaic (PV) wafer production. In this paper, an overview of fundamental research in modeling of modern wiresaw manufacturing process will be presented, with the objectives to better understand the cutting mechanism and to make it relevant via experiments for improving industrial processes. To this end, investigation has been carried out on the modeling, optimization, and control of the modern wiresaw manufacturing processes to meet the requirements of the PV and semiconductor industry. Research results in mathematical modeling, numerical simulation and experiments are presented.

1 Introduction

Slicing is a very important step in wafer preparation for photovoltaic (PV) industry. Since early 1990's, wiresaws have emerged in the scene for wafer slicing in PV industry. Subsequently, more wiresaws arrived at the manufacturing floors for PV wafer slicing—replacing ID saws as the technology for wafering. The modern wiresaw has the following advantages: (*i*) efficient cutting with low kerf loss, (*ii*) high throughput of wafer production, and (*iii*) high quality surface finish, ready for the subsequent processes. Investigation has been carried out on the fundamental understanding of the cutting process, modeling of the wiresaw slicing mechanism, optimization and control of the manufacturing processes, and experiments. A comparison between the wiresaws and ID saws is offered in Table 1. From the table, it is clear that wiresaw has much higher throughput and yield with less kerf loss and sub-surface damage.

The modern wiresaw slicing process belongs to the category of Free Abrasive Machining (FAM). A schematic of wiresaw is shown in Figures 1(a), which consists of one wire moving, either uni-directionally or bi-directionally, on the surface of silicon ingot. The single wire is wound carefully on wire guides with grooves of constant pitch to form a "wire web," as shown in Figure 1(a). The wire guides are rotated by a pair of master-slave drives, causing the entire wire web to move at high speed (typically 5 m/s – 12 m/s) on ingot surface, while carrying the abrasive slurry to remove materials. The ingot is fed in the direction perpendicular to the wire web as shown by the arrow, resulting in a net normal force and causing the hydrodynamic effect to act upon the contact interface. The wire is maintained at constant tension (typically

*The author has a web site for wiresaw related research: <http://dove.eng.sunysb.edu/~kao/wiresaw>.

Property	Wiresaw	ID Saw
Cutting method	FAM/lapping	ploughing/grinding
Typical cut surface features	periodic wire marks	chipping & surface fracture
Depth of sub-surface damage	uniform 2 to 12 μm	variable 20 to 30 μm
Productivity	110 to 220 cm^2/hr	10 to 30 cm^2/hr
Wafers per run	200 to 400 wafers	one wafer
Kerf loss	210 μm	300 to 500 μm
Minimum thickness of wafer	200 μm	350 μm
Yield of 300 μm -thick wafers	580 per 30cm ingot length	375 per 30cm ingot length
Maximum ingot size/diameter	300 mm and higher	up to 200 mm (8")

Table 1: Comparisons of various properties between the modern wiresaw and ID saw.

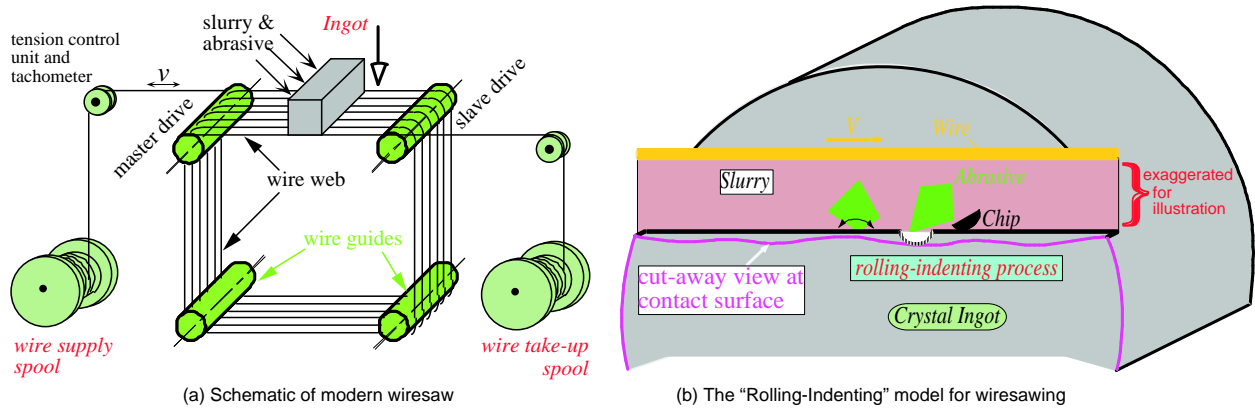


Figure 1: (a) A schematic diagram of modern wiresaw, and (b) the “rolling-indenting” wiresaw manufacturing model. Note the exaggeration in the cut-away view for illustration. [15]

20-30 N for steel wire of 175 μm diameter) during the cutting process. A spool of plain carbon steel wire is used to continuously supply the wire necessary for cutting.

The mechanism of wiresaw manufacturing process is described by the *rolling-indenting* process [4, 3, 6, 8, 7, 14, 2, 5]. The process of wiresaw slicing with slurry is theoretically more efficient and less brutal than cutting with the ID and diamond saws, under the condition of the same energy input, because of the inherent difference in the cutting mechanism viz. rolling and indenting in the former as opposed to ploughing in the latter. In this paper, an overview of the wiresaw technology in silicon wafering will be presented. Important parameters including: speed and tension of wire, slurry composition and viscosity, size and material of abrasive grits, carrier fluid, kerf loss, real-time wire management, ... etc, which influence the subsurface damage, total thickness variation (TTV), and warp of wafers will be discussed.

It is important to note that the modern wiresaw (slurry wiresaw) is entirely different from the diamond impregnated wire saw. The diamond impregnated wire saw, utilizing diamonds coated on the surface of wire to remove the materials by the ploughing machining process, is essentially an ID saw with linear cutting edge instead of an annular one. Unlike the FAM wiresaw where the “free” abrasives will re-join the cutting process, the diamond coated wire will lose its cutting capability once the bonding between the surface of the wire and diamond is lost.

2 Modeling of the Wiresaw Manufacturing Process

Before we started our research in wiresaw seven years ago, we found very little work done in this field other than a few patents and technical notes. Since then, our research objective has been to develop a relevant and integrated process model for this manufacturing process. Our ongoing research activities include modeling and simulation, as well as experiments on both industrial and laboratory wiresaws. The analytical solutions and finite element simulation are combined with boundary conditions to establish the integrated model. Most of these research activities are related to the improvement of the manufacturing process such as reduction of kerf loss and better surface finish. In the following, an overview of various aspects of research in our wiresaw will be provided.

2.1 The “rolling-indenting” model

The fundamental cutting process of a modern wiresaw is built upon the rolling and indenting process with the abrasives acting as the third party agent in the FAM process. A schematic of the model is shown in Figure 1(b). During the manufacturing process, the abrasive particles in slurry are the free agents carried by high speed wire. These abrasives are constrained to roll and indent on the surface of the ingot, as shown in Figure 1(b). The brittle materials under an indenter develop vertical and surface cracks when indenter approaches the surface to make contact. More interestingly, the subsurface horizontal cracks will start to form when the indenter is retreating. Hence, the *rolling-indenting* process causes the formulation and concatenation of such subsurface cracks, leading to the removal of materials. Equations of stress due to contact and indentation are formulated with boundary conditions [4, 3, 6, 7]. The results, expressed with dimensionless stress measures and normalized by the depth of indentation and angle of contact, suggest the regions of removal for the ingot and the optimal shape of abrasives. It is recommended that the abrasive have a conical indenting angle between 90° to 120° to optimize the slicing process. The *rolling-indenting* process is also aided by the high-speed wire carrying abrasive slurry.

2.2 Vibration analysis

While the vibration behavior of a stationary wire, as that in a violin, is very well understood for centuries, the solution of vibration of a moving wire is not derived until early 1990’s [9, 5, 11, 12]. Vibration analysis is very useful in predicting the behaviors of the wire during the slicing process. Careful study of the vibration of moving wire can help us to predict the kerf loss due to vibration.

In the analysis of vibration, the wire is subject to multiple excitations at the contact surface caused by the abrasives and contact. The natural frequencies of a moving wire are [5]

$$\Omega_n = \frac{n\pi(P - \rho V^2)}{L\sqrt{\rho P}}, \quad (1)$$

where L is the length of wire, ρ is the mass density per unit length, P is the tension, and $n = 1, 2, 3, \dots$ represents the modes of vibration. When the velocity V is zero, Ω_n will be reduced to the well-known form of the natural frequencies of a stationary string. The velocity of wire when Ω_n in equation (1) vanishes is defined as the critical speed. When the speed of the wire is near this speed, the wire will experience divergence instability. For the industrial wiresaws which use steel wire, ρ is very small while tension P is high (around $20N$) which results in very high critical speed (typically over $300m/s$). The wiresaw operating speed is normally less than $20m/s$; hence, the divergence instability is generally not a concern.

The magnitude of vibration of a moving wire will also affects the kerf loss. The research in frequency response, as that in Figure 2, reveals that the tension is a more important parameter than the speed of wire,

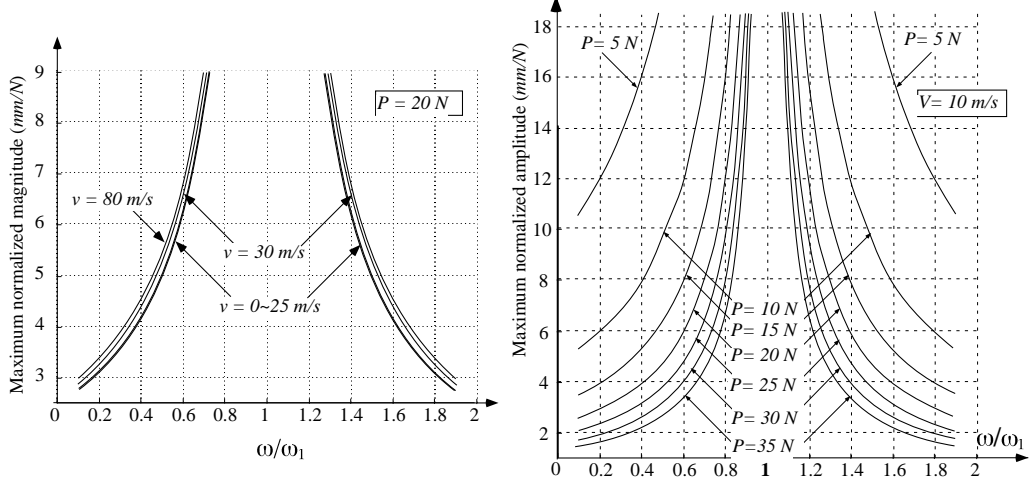


Figure 2: Magnitude of the frequency response of a moving wire with respect to (a) various translating speeds of wire, and (b) tensions. [12]

as far as the amplitude of vibration and kerf loss are concerned. Essentially, increasing the speed of wire does not significantly change the kerf loss.

2.3 Hydrodynamic modeling at contact interface

A hydrodynamic model is developed to determine the hydrodynamic pressure and slurry thickness during wafer slicing. Such results have direct bearing on the choice of abrasive size and viscosity properties of the slurry base [2, 1]. The work focuses on the elasto-hydrodynamic interactions prevalent in wiresaw free abrasive wafer slicing. During the wiresaw slicing process, an elasto-hydrodynamic film is formed between the wire and the abrasive carrying viscous slurry, squeezed between an axially moving semi-compliant wire under tension and the ingot being sliced. This phenomenon is analyzed by using finite element analysis. In addition, the analysis of coupled hydrodynamic effect with the vibration of wire was conducted for a better understanding of interaction at slicing [16, 17]. Numerical algorithm is used to simulate the process. The analysis yields the profiles of film thickness and pressure distribution along the region of line contact as a function of wire speed, slurry viscosity and process parameters. This information helps in demarcating between the regimes of “slicing” and “polishing” in any “free abrasive machining” (FAM) process. The results can be used to promote technological improvements in the productivity and efficiency of wiresaw slicing.

3 Experiments and Results

Various experiments were performed pertaining to the wiresaw research. The size of grits and properties of carriers will affect the hydrodynamic and vibration characteristics, and subsequently the performance of cutting process and parameters such as viscosity of slurry. In addition, the ratio with which the grit and carrier (oil-based or water-soluble) is mixed also have significant influence on the viscosity of slurry. In the following sections, we discuss and summarize some results of research.

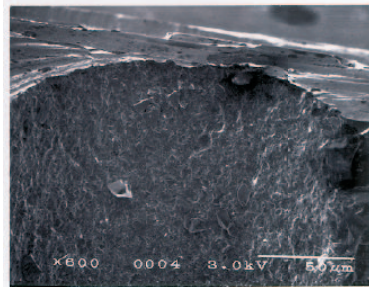
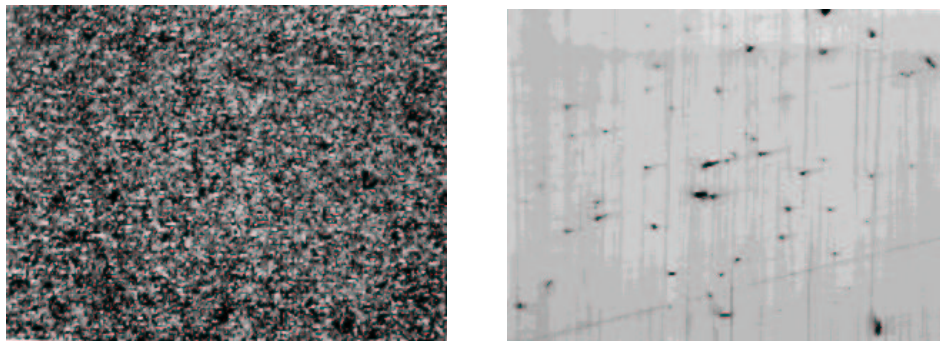


Figure 3: A typical SEM photo of wiresaw sliced wafer surface. Note the abrasive grit indented onto the surface.



(a) surface of wiresaw sliced wafer

(b) surface of polished wafer

Figure 4: Comparison of wiresawed and lapped wafer surfaces. [1]

3.1 Rolling-indenting model and surface characteristics

Scanning Electron Microscope (SEM) are used to examine surfaces of as-sliced wafers. The results of a typical wafer surface is shown in Figure 3. The SEM photo suggests that the rolling-indenting process is random as revealed by the homogeneous pits on the surface (also see Figure 4a). Abrasive grit can be seen to remain indented unto the surface of silicon substrate. In another figure, typical surfaces of wiresaw-sliced and lapped wafers are compared in Figure 4. A well-controlled wiresawing process, unlike some lapping processes, will not have scratches on the surface of wafer.

3.2 Abrasive grits and carriers

As mentioned earlier, oil-based and water-soluble slurries are frequently used in industrial wiresaws. Oil-based slurry has two major problems: oil breakdown and environmental concerns. More operations have turned to water-soluble or water-based carriers. Silicon Carbide (SiC) has been widely accepted as abrasive grits for wiresaw due to its lower cost and high hardness. Green SiC is often preferred to black SiC in semiconductor wafer slicing operations due to lower levels of metal and contaminants such as aluminum, calcium, sodium, and iron. Table 2 summarizes data of SiC abrasives. Although slight discrepancy exists between the two measurements on size of abrasive, data from Measurement I is usually used for analysis. Note that the medium size reflects the average value. The actual particle size varies within designated distributions. The green SiC also has slightly smaller surface area per unit mass. Typical abrasive geometry and composition of kerf particles after slicing is shown in Figure 5. The figure also shows typical silicon particles which are removed during the slicing process.

When slurry is made, certain ratio between the mass of the grits (in *kg*) and the volume of the carrier (in *liter*) is established. Naturally, the viscosity of the slurry is related to the ratio between the grits and

FEPA Grade	Medium size (μm)		Surface area (m^2/g)	
	Measurement I	Measurement II	black SiC	green SiC
F400	17.3	20.7	0.282	0.257
F500s	11.7–14.7	13.1	0.400	0.324
F600	9.3	12.3–13.3	0.516	0.428
F800	6.5	9.6	0.700	0.500
F1000	4.5	6.6	1.272	1.201
Fujimi GC600WS	-	22	-	-

Table 2: Grit sizes for different grades of SiC and surface areas for green and black SiC. Measurement I is done by the Coulter Multisizer capacitance principle; measurement II is by the Coulter LS laser diffraction. The “F” prefix of the different grits designates the FEPA, European standard, average particle size. A larger number indicates a finer average size.



Figure 5: Comparison of wiresawed and lapped wafer surfaces. [1]

carrier. A typical chart for different mixing ratios (*kg* of grit per *liter* of carrier) of SiC in water-soluble carrier is shown in Figure 6. In the figure, the viscosity (in *cP*) is plotted in logarithmic scale with respect to the shear rate. Four different mixing ratios are plotted. The mixing ratio of 1.25 results in the maximum viscosity of 14000*cP* at low shear rate. It is clear from Figure 6 that higher ratio results in higher viscosity. On the other hand, if the ratio is too low the slurry will lose its viscosity, resulting in poor cut. A commonly accepted mixing ratio is between 0.75 and 1.0.

3.3 Wafer surface measurements

A new methodology built upon the shadow moiré technique with the Talbot effect is developed to measure the surface topology of sliced wafers. The methodology of shadow moiré employs a fine grating to cast shadow on surface of wafer with a He-Ne laser. The interference between the grating and the shadow casted by the reference grating causes fringe patterns to formulate [14, 13]. The technique is non-contact and does not require spinning the wafers, and thus will not introduce dynamic stresses and vibrations to the wafers during the measurement process. Consequently, this technique will enhance the fidelity of surface measurements. In addition, the measurement is done on the entire wafer surface simultaneously, eliminating non-collocated discrepancies. The resolution of such surface measurement technique is enhanced by the *phase-shifting* technique to submicron resolution [10].

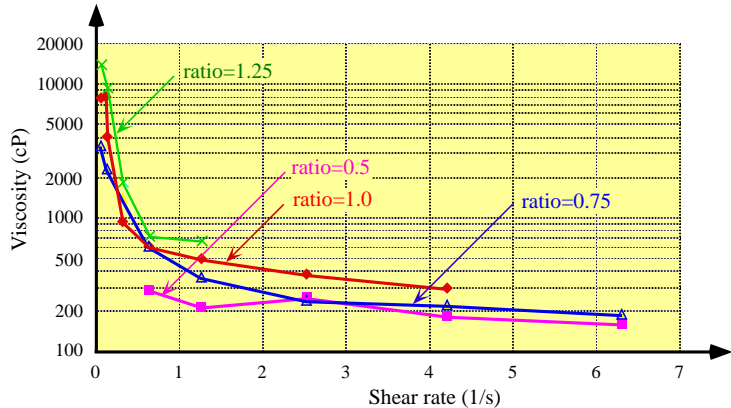


Figure 6: Experimental results on the relationship of the viscosity and shear rate for water-soluble carrier with SiC. The four different mixing ratios represent *kg* of SiC abrasive grit per *liter* of carrier.

4 Future of Wiresaw in Wafer Production

The ability of wiresaw in cutting ingots of various materials as well as the capability of slicing large crystals with small kerf loss have made it indispensable for wafer preparation in the future. As the modern wiresaw technology matures in the 21st century, it will play an even more important role in wafer preparation. In addition, the wiresaw is capable of cutting harder materials such as III-V compounds and ceramics.

The future development in the improvement of yield is important. Many sliced wafers are broken during the handling and shipping process due to (1) inherited residual stress on the wafers, and (2) additional stress applied due to handling. These issues can be studied using optical metrology method, such as those in Section 3.3, to find the residual stress pattern as a function of slicing parameters.

Wire rupture causes wafer surface discontinuity and typically results in the entire ingot being discarded. A real-time, on-line monitoring and metrology of wire during wiresaw operation is needed to ensure the quality and success of slicing.

Reclamation and recycling of abrasive grits have been developed for water soluble carriers. This remains a very exciting and beneficial area that can be improved for efficiency and productivity.

5 Summary

In this paper, we presented recent research results on wiresaw manufacturing process for wafer preparation. Theoretical modeling and experiments were performed to advance the technology and knowledge of this critical technology. The existing technology of ID saw and the modern wiresaw are compared.

The “*rolling-indenting*” model of the wiresaw manufacturing process is presented, as well as the shape of abrasives for optimal cutting performance. Individual vibration and hydrodynamic analysis are studied, as well as the interaction between the two. The results can be used to predict the amount of kerf loss and pressure distribution. Experimental results on various aspects of wiresaw and slicing process are also presented. A non-contact, whole-wafer wafer surface measurement technique using the shadow moiré technique with Talbot effect is also described.

6 Acknowledgment

This research has been supported by the National Science Foundation grant DMI-0085021.

References

- [1] M. Bhagavat, V. Prasad, and I. Kao. Elasto-hydrodynamic interaction in the free abrasive wafer slicing using a wiresaw: Modeling and finite element analysis. *the ASME Journal of Tribology*, 122(2):394–404, April 2000.
- [2] I. Kao, M. Bhagavat, and V. Prasad. Integrated modeling of wiresaw in wafer slicing. In *NSF Design and Manufacturing Grantees Conference*, pages 425–426, Monterey, Mexico, January 5-8 1998.
- [3] I. Kao, V. Prasad, J. Li, and M. Bhagavat. Wafer slicing and wire saw manufacturing technology. In *NSF Grantees Conference*, pages 239–240, Seattle, Washington, January 7–11 1997.
- [4] I. Kao, V. Prasad, J. Li, M. Bhagavat, S. Wei, J. Talbott, and K. Gupta. Modern wiresaw technology for large crystals. In *Proceedings of ACCGE/east-97*, Sept. 28 – Oct. 1 1997.
- [5] I. Kao, S. Wei, and F.-P. Chiang. Vibration of wiresaw manufacturing processes and wafer surface measurement. In *NSF Design and Manufacturing Grantees Conference*, pages 427–428, Monterey, Mexico, January 5-8 1998.
- [6] J. Li, I. Kao, and V. Prasad. Modeling stresses of contacts in wiresaw slicing of polycrystalline and crystalline ingots: Application to silicon wafer production. In *Proceedings of ASME IMECE '97*, pages 439–446, Dallas, Texas, November 16–22 1997. ASME Press.
- [7] J. Li, I. Kao, and V. Prasad. Modeling stresses of contacts in wiresaw slicing of polycrystalline and crystalline ingots: Application to silicon wafer production. *ASME Journal of Electronics Packaging*, 120(2):123–128, June 1998.
- [8] R. K. Sahoo, V. Prasad, I. Kao, J. Talbott, and K. Gupta. An integrated approach for analysis and design of wafer slicing by a wire saw. *ASME Journal of Electronics Packaging*, 120:16–21, March 1998.
- [9] S. Wei and I. Kao. Analysis of stiffness control and vibration of wire in wiresaw manufacturing process. In *Proceedings of the Manufacturing Engineering Division, IMECE 98*, pages 813–818. ASME Press, 1998.
- [10] S. Wei and I. Kao. Hight-resolution wafer surface topology measurement using phase-shifting shadow moiré technique. In C. Sahay, B. Sammakia, I. Kao, and D. Baldwin, editors, *the Proceedings of IMECE'99: DE-Vol 104, Electronics Manufacturing Issues*, pages 15–20, Three Park Ave., New York, NY 10016, November 1999. ASME Press.
- [11] S. Wei and I. Kao. Free vibration analysis for thin wire of modern wiresaw between sliced wafers in wafer manufacturing processes. In *the Proc. of IMECE'00: EEP-Vol 28 packaging of electronic and photonic devices*, pages 213–219, Orlando, Florida, November 2000. ASME Press.
- [12] S. Wei and I. Kao. Vibration analysis of wire in free abrasive machining of the modern wiresaw manufacturing process. *International Journal of Vibration and Sound*, 231(5):1383–1395, 2000.
- [13] S. Wei, S. Wu, I. Kao, and F. P. Chiang. Wafer surface measurements using shadow moiré with Talbot effect. *ASME Journal of Electronics Packaging*, 120(2):166–170, June 1998.
- [14] S. Wu, S. Wei, I. Kao, and F. P. Chiang. Wafer surface measurements using shadow moiré with Talbot effect. In *Proceedings of ASME IMECE'97*, pages 369–376, Dallas, Texas, November 16–22 1997. ASME Press.
- [15] F. Yang and I. Kao. Free abrasive machining in slicing brittle materials with wiresaw. *ASME Journal of Electronics Packaging*, 123(3):254–259, September 2001.
- [16] L. Zhu, M. Bhagavat, and I. Kao. Analysis of the interaction between thin-film fluid hydrodynamics and wire vibration in wafer manufacturing using wiresaw. In *the Proc. of IMECE'00: EEP-Vol 28 packaging of electronic and photonic devices*, pages 233–241, Orlando, Florida, November 2000. ASME Press.
- [17] L. Zhu and I. Kao. Equilibrium elastohydrodynamic interaction analysis in wafer slicing process using wiresaw. In *the Proc. of IMECE'01*, pages No. EEP-24715, NYC, New York, November 11-17 2001.

50 μ m WAFERING TECHNIQUES – FIRST EXPERIMENTAL RESULTS

Daniel Kray and Gerhard P. Willeke

Fraunhofer Institute for Solar Energy Systems, Heidenhofstr. 2, D-79110 Freiburg,
Phone: ++49 761 4588 5266, Fax: ++49 761 4588 9250, email: willeke@ise.fhg.de

INTRODUCTION

Today, the typically 320 μ m thick crystalline silicon wafer sawn from an ingot with a kerf loss of 180 μ m represents more than 40 % of the solar module cost. A reduction of this major cost share is therefore an important and very effective measure towards lower cost goals. In principle, thinner wafers with better surface quality have to be cut from a crystal at high yield with less silicon material wasted. The outstanding electronic quality of a pulled or cast silicon crystal leads to a 20 % solar cell conversion efficiency capability even in a 50 μ m thin silicon wafer [1]. At present the multi-wire slurry saw (MWSS) method is the only wafering technique on the market. Because of the abrasive nature of this cutting process, which involves mechanical stress and surface damage, there are physical limitations concerning the wire diameter, the size of SiC grains used in the slurry and the minimum thickness of the wafers that can be prepared under high yield conditions. It appears that a wire spacing (i.e. a wafer thickness plus kerf loss) of 250 μ m may eventually be obtained in the probable limit of this method [2], representing a twofold increase in the number of wafers obtainable from the same ingot. Further progress with this technique will be barred effectively by the extremely fragile nature of 100–150 μ m thin surface-damaged silicon wafers. In order to overcome this limit, at Fraunhofer ISE there are at present different methods under consideration which may be suitable for a stress- and damage-free cutting of 50 μ m thin wafers with ready-to-use surfaces and a cutting loss of below 100 μ m [3]. The proposed chemical cutting of silicon by means of *stream etching* and *laser-assisted thermochemical etching* does not suffer from mechanical stress-related limitations since they are non-abrasive techniques. The idea for the former was taken from an old patent by Barry and Seeley [4], where it was extensively tested for cutting 25 μ m thin wafers of Germanium with a 175 μ m cutting width. In the present paper, the first experimental results of the application of the *stream etching* technique to silicon cutting as well as the involved theory of silicon etching will be described in some detail.

STREAM ETCHING PRINCIPLE

Fig. 1 shows the principle of *stream etching* (after ref. [4]). A stretched metal wire is used to electrochemically slice a crystal ingot. A suitable electrolyte flows down the wire and wets the crystal locally as indicated on the right hand side. When a DC voltage is applied between the wire and the ingot, electrochemical etching starts in the neighbourhood of the wire. The electrical conductivity of the elec-

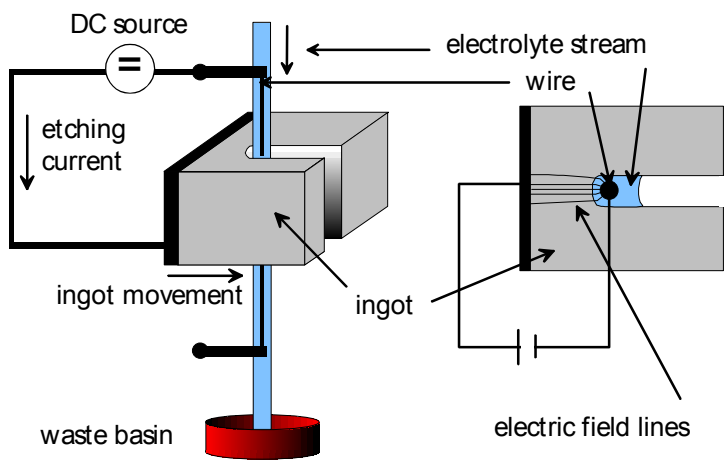


Fig. 1: Stream Etching principle

troyte should be low in order to concentrate the electric field lines and therefore the etching action in the direction of the intended ingot movement. The electrical resistivity of the electrolyte needs to be indeed much higher than that of the crystal, otherwise the cut would be widened considerably, and eventually the ingot would be etched nearly isotropically in all parts where the electrolyte wets the ingot.

When a groove has been etched – which can be monitored by a decreasing etching current – the wire or the ingot has to be moved forward in order to maintain a constant distance between the wire and the crystal to be etched. In principle, it should be possible to control the process quite well by monitoring the etching current at constant voltage and feeding the wire electrode at a constant rate towards the ingot.

Cutting germanium by stream etching

In ref. [4] Barry and Seeley have listed several application examples of their cutting method for the production of germanium wafers. The electrolyte used was 0.00087 – 0.002 % KOH in DI water, the wire material was tungsten or platinum with diameters from 25 – 85 µm. They sliced $2.5 \Omega \text{ cm}$ p-Ge and n-Ge crystals into $2.8 \times 2.8 \text{ mm}^2$ sized wafers with thicknesses as small as 25 µm and with a cutting width in the range of 127-241 µm. In most of their experiments they applied a constant voltage of 90 – 100 VDC, which resulted in current densities of 9–28 mA per mm of cut length. The wire feed rate was between 178 and 432 µm/min, the optimum cutting speed for the smoothest surfaces ranged from 178 to 305 µm/min.

What Barry and Seeley observed was that the etching factor, which is defined as the ratio between the volume of the material etched per minute and the corresponding etching current, decreased from 3.0 to $2.5 \text{ mm}^3/\text{A min}$ when the wire was fed at a higher speed. Faster cutting resulted also in increased cutting widths. The authors suggested to maintain the temperature as well as the concentration of the continuously agitated electrolyte constant and to vary only the cutting speed and the applied voltage. In fact they observed that at constant voltage conditions, the process became self-stabilizing. Since there is a very steep, non-linear inverse relationship between the local current density (and therefore the local etch rate) and the gap between the wire and the material to be removed, the actual gap between the wire and the front of the cut is maintained constant when cutting at a constant feed rate. If for example there is a local reduction of the etch rate due to a higher local resistivity (due to possible fluctuations) in the material to be cut, the gap between the wire and the crystal decreases locally with a resultant considerable increase in the local etching current such that this particular area is preferentially etched away.

The above etching principle could be reproduced in an experiment, as shown in Fig. 2. A surface profile of a germanium wafer is shown that has been etched in 0.004 % KOH without wire movement. As can be seen, a clear image of the wire has been etched with macroscopically smooth surfaces. The scan has been performed with an FRT MicroProf® optical surface profiler.

Considering the quite high etch rates obtained by Barry and Seeley which are at least one order of magnitude larger than those obtained with conventional wet etches, an ingot of 100 mm diameter could at least theoretically be cut completely in less

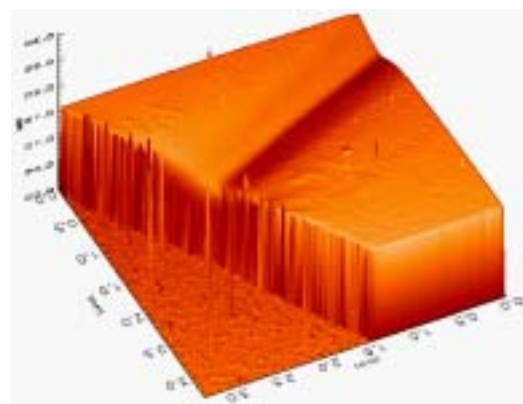


Fig. 2: Germanium stream etching

than 6 hours which is about half the cutting speed of a MWSS. The problem however in just extrapolating the results of [4] for larger ingots is the electrical current that has to be supported by the fine metal wire. For example the necessary current for cutting a $125 \times 125 \text{ mm}^2$ ingot instead of a $2.8 \times 2.8 \text{ mm}^2$ one is about 45 times higher, namely 3.5 A . This means that the $84 \mu\text{m}$ diameter wire would have to carry a current density of approximately 630 A/mm^2 . Such large currents would of course instantly vaporize any wire material. However, this problem could be overcome by utilizing cutting foils rather than wires. Through a suitable foil of the same thickness, which must be rigidly arranged, the current densities could be reduced to about 0.33 A/mm^2 . Another important advantage in using a foil rather than a wire is that a means for wafer separation - a time-consuming and wafer-breaking step in MWSS wafer production - is already included in the cutting process.

Cutting silicon by stream etching

Transferring the cutting principle from germanium to silicon may appear straightforward since both semiconductors have a number of material parameters in common: they are both members of the IVth group of elements in the periodic table with similar atomic radii, ionization energies, work functions and bandgaps. However there is an important difference between Si and Ge that makes a fundamental change in the cutting electrolyte necessary: germanium oxide is soluble in water whereas silicon oxide is not. This fact is so important because all etching processes in aqueous solutions proceed in two steps whose first is an oxidation of the surface. If the oxidized species is soluble in the etchant, a net material removal is observed. A diluted KOH solution in DI water is therefore the optimum for Ge etching since the water – which is abundantly found everywhere in the solution – has the double function of oxidizing Ge and dissolving the oxide. The KOH is only added to increase the conductivity and to act as a carrier for water molecules which are transported as solvation shells to the germanium surface through the electric field. This is the reason why Ge *stream etching* does not work with pure DI water.

However, this interdependence means that diluted KOH cannot be used as a silicon etchant since the intermediate product SiO_x is not soluble in strongly diluted KOH or other alkali hydroxide solutions. The surface would rapidly be oxide passivated and no etching action would occur. Therefore a specially adapted electrolyte has to be found for successful silicon stream etching. The silicon oxide etch rates of alkali hydroxides in water are in general too low to reach economic cutting speeds. It therefore becomes immediately apparent that only fluorine-based etchants can be applied in the case of silicon. Before the respective experiments are described, we will focus first on the theory of electrochemical and chemical etching of silicon.

THEORY OF ELECTROCHEMICAL ETCHING OF SEMICONDUCTORS

Many publications focus on the electrochemistry of semiconductor etching in aqueous solutions. A comprehensive review article has been published by Gerischer [5]. Additional valuable information can be found in [6]. When a semiconductor and an electrolyte are brought into contact, an equilibrium charge distribution in the semiconductor (electrons and holes) and the electrolyte (ions) is established and the so-called electrical double layer is formed. Depending on the process parameters, charge-transfer reactions through the interface of the two phases can occur. These reactions may include electron transfer, i.e. redox reactions, or ion formation and therefore corrosion.

Surface electrochemistry

The theory of metal electrodes in contact with an electrolyte was developed by several scientists and much later applied to semiconductor electrodes. In the electrolyte, the ionic charge balancing the excess charge in the (metal) electrode is distributed in different layers. In the concept of the Helmholtz double layer this opposing charge is concentrated as a surface charge at the distance of a solvation shell. In dilute solutions however, the charge is distributed over a wider range which led to the Gouy-Chapman model of the diffuse ionic double layer. On the other hand, some ions approach the electrode surface even until part of their solvation shell is lost and that they can partially be chemisorbed (Stern model).

These concepts had to be adapted to semiconductor electrodes since in contrast to metal electrodes, there exists a space charge region also in the semiconductor which can dominate the overall capacitance of the system if the conductivity in the semiconductor is not too high. Depending on the materials used and the external voltage, three different situations can occur, as shown in Fig. 3 for an n-type semiconductor. At the flatband potential, the bands are not bent so that there is no charge density gradient. In the case of anodic or cathodic polarization of the semiconductor, majority carriers are depleted or accumulated at the interface with the electrolyte such that the bands are bent and the surface carrier concentration is modified. Due to the fixed position of the ionized donor centers, the excess charge of the depletion layer has a much larger extension than that of the accumulation layer.

It could be shown that for concentrated electrolytes, a semiconductor doping below 10^{19} cm^{-3} and a low surface state density, the electrical potential variation in the electrolyte can be neglected and the applied voltage modifies mainly the surface charge concentration in the semiconductor.

Charge transfer reactions

Whether a current flows through the semiconductor - electrolyte interface depends on the relative position of the Fermi energy E_F in the semiconductor and the redox potential E_{redox} in the electrolyte. The current density is determined by the number and the occupation of energy states at the same energy level in the semiconductor and the electrolyte. Due to the bandgap in the semiconductor there can only be large exchange currents when the redox potential in the electrolyte is located at the band edges. Depending on the position of E_{redox} hole transfer via the valence band or electron transfer via the conduction band can be observed.

Additionally, activation barriers may exist between the different intermediate states that influence the charge transfer considerably. The realistic chemical reactions are not yet fully understood because of many intermediate steps so that simplified two-step processes have to be assumed. At non-equilibrium conditions (external voltage), the transfer currents are mainly determined by the carrier surface concentrations.

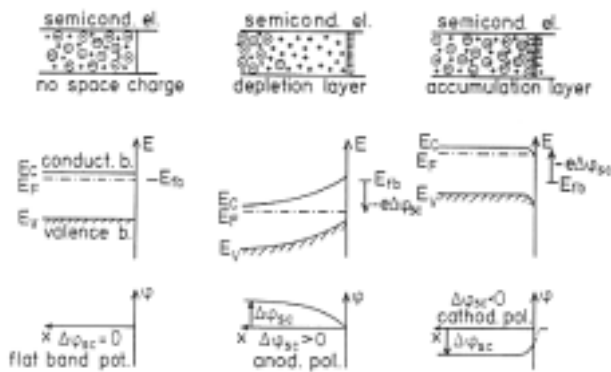


Fig. 3: Charge distribution, band bending and electrical potential in n-type semiconductors in contact with electrolytes (from ref. [5]).

Ion formation and corrosion

The charge transfer through the interface can involve chemical variations at the semiconductor surface, ranging from changes in the oxidation state to corrosion of the electrode. These variations occur preferably at crystal planes with more than one surface bond. The anodic breaking of a surface covalent bond happens in two steps (see Fig. 4). First, the surface bond is weakened by the capture of a hole h^+ . The positive charge attracts nucleophilic reactants A^- that attach themselves to the surface atom and leave one electron unpaired.

This electron which is in a surface energy state within the bandgap can escape in a second step through a hole capture or thermal elevation into the conduction band. Cathodic decomposition processes are much less common and not yet well understood.

The solubility of the formed reaction products determines whether the electrode corrodes or only the oxidation state is changed. The oxidation of the electrode can occur without a chemical mechanism, independent of the applied voltage or with a net electrical charge production, i.e. an electrochemical reaction. For silicon, holes from the valence band are needed to oxidize the surface. These holes can be generated in different ways. For p-type Si, an anodic polarization is sufficient, whereas n-type Si has to be additionally illuminated in order to produce excess holes by photoexcitation. In addition, a hole-injecting redox system can also be used.

Silicon in fluoride solutions

The silicon surface in fluoride solutions at open circuit potential (OCP) is hydrogen terminated due to the fact that a fluoride or hydroxyl termination induces a strong polarization of the surface bond. Polar molecules such as H_2O can attack the back bond, leaving essentially unpolar Si-H bonds at the surface. This hydrogen terminated surface acts as a weak acid such that the etch rate is strongly dependent on the pH of the solution as well as on the crystal orientation and therefore on the density of mono- and dihydrides on the surface. At OCP and low pH, the hydrogen termination is very inert and etching is virtually stopped. For anodic polarization and $pH < 4$, a likely model for the etching process [6] is illustrated in Fig. 5. First, the capture of a hole weakens the surface bond and attracts the negatively charged F^- species (probably as HF_2^-), leaving one surface electron in an unpaired state. This bond can be saturated by another F^- , injecting the surplus electron into the conduction band of the semiconductor. The back bonds are strongly polarized such that the polar HF molecule can

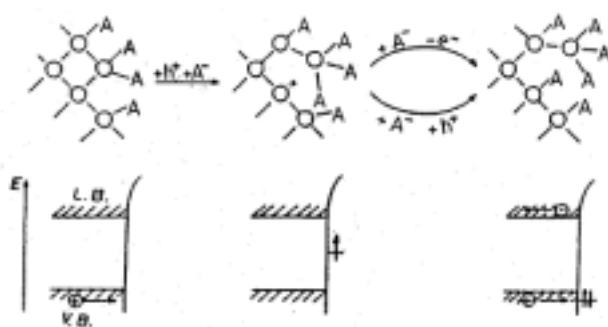


Fig. 4: Surface bond breaking for anodic polarization (from ref. [5]).

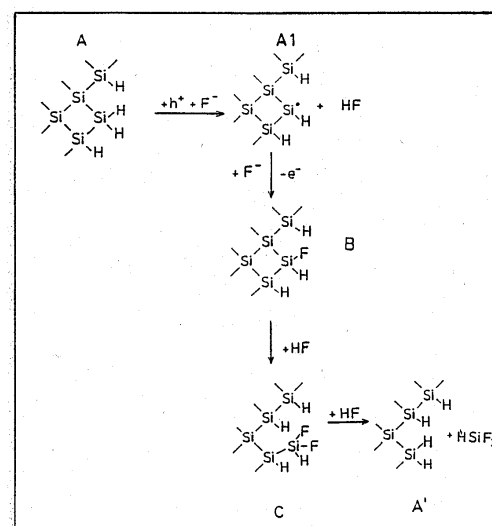


Fig. 5: Anodic decomposition of silicon in fluoride solutions with $pH < 4$ (from ref. [6]).

attack them. Repeating this step 4 times results in a soluble HSiF_3 molecule that is detached and the surface is again left hydrogen terminated.

For higher pH-values, the behaviour of the system is not completely understood, since there seem to be several competing reactions. The same problem exists for anhydrous solutions with e.g. methanol as a solvent. The etch rates here are much higher than for aqueous solutions, possibly because of the missing competing oxidation by hydroxyl groups.

EXPERIMENTAL RESULTS

After several tests with diluted and concentrated KOH as stream etching electrolyte for silicon cutting, which led only to an oxidation of the surface, fluoride solutions were tested. NH_4F salt was dissolved in water / ethylene glycol mixtures with varying ratios. The pH-value was adjusted by adding concentrated H_2SO_4 . The reduction of the water content by adding ethylene glycol had different reasons. First of all, the competing oxidation by water was reduced, thus favoring the fluoride surface reactions. Secondly, the electrical conductivity of the solution was lowered in order to increase the localisation of the etching action.

Experimental setup and results

The experiments with fluorine-based electrolytes were conducted in a PTFE beaker. $0.5\text{-}1 \Omega\text{cm}$ boron-doped silicon samples of $25\text{x}25 \text{ mm}^2$ size and small evaporated TiPdAg or Al contacts were used. DC voltages between 30 and 95 V were applied for 3-5 minutes. A PTFE sample holder held the wafer firmly in place and included suitable spacers such that the $80 \mu\text{m}$ thin Pt wire, that acted as a counter electrode, could be wrapped around the sample at a distance of about 1-2 mm.

Since these first experiments were aimed at quickly finding a suitable electrolyte that enables localized etching of silicon, no elaborate measurement techniques were used. In addition, different water to ethylene glycol ratios were obtained by simply adding the respective chemicals. The conclusions drawn from the experiments were qualitative in terms of successful localized etching or not. The following six sets of experiments have been realised:

Series No.	Fluorine concentration	Solvent	pH	Stirring	Additives
1	Low	Ethylene glycol (EG)	6-7	No	5% HF (var.)
2	Medium	EG + water (var.)	6-7	No	
3	High	EG + water (var.)	6-7	No	
4	High	EG + water (var.)	2	No	H_2SO_4 for pH
5	High	EG + water (var.)	4-5	No	H_2SO_4 for pH
6	High	EG + water (var.)	1	Yes/No	H_2SO_4 for pH

The first series showed that water-free or nearly water-free solutions with a low F- concentration (approx. 0.1g of NH_4F in 150ml of solvent) resulted in very pitted surfaces without localised etching. The addition of some water-containing 5% HF to the solution favoured localisation but the etching result was still unsatisfactory. As can be seen in the surface profile shown in Fig. 6a, the wire position can hardly be guessed. Apparently the resistivity of the electrolyte is not the most important factor but local crystal dislocations and scratches that lower local activation barriers which determine the current flow through the solid-liquid interface.

Increasing the F-concentration to 2g of NH₄F in 150ml of solvent resulted in smoother surfaces that appeared grey to the eye. The surface layer formed is in fact a porous silicon layer (PSL). Horányi et al. [7] have studied electropolishing silicon and described the different reaction products depending on the current density. They found that a critical minimum current density must be reached before electropolishing occurs. At low currents, a PSL is formed which

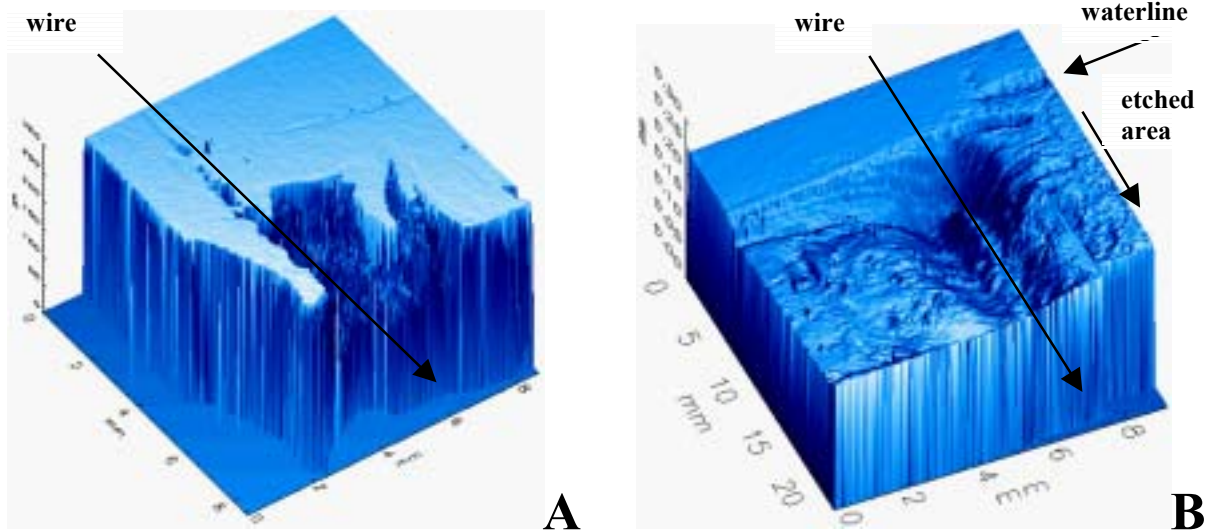


Fig. 6: Surface profile scans of different silicon etch experiments. See text for details.

is exactly what was observed in series 2. When starting from pure water solvent and adding ethylene glycol, the etching current decreases since the electrolyte resistivity increased and the etched surface became more and more porous.

In the next experimental set 3 with a further increased F-concentration of 10g of NH₄F in 150ml of solvent, the appearance of the PSL changed to darker colours, indicating that the mean pore diameter changed. Still no satisfactory surface morphologies could be produced, neither was there a localisation of the etching action. This result is probably due to the too high pH of the solution. As described in [8], high pH in NH₄F containing solutions favours fluoride speciation into F⁻ (to the disadvantage of HF and HF₂⁻) which seems not to be participating in silicon etching. Also, since the hydrogen terminated surface acts as a weak acid, there is a general tendency of the entire immersed surface to become devoid of protons, a situation that also does not favour localised etching.

As a result, in the next series 4 the high fluorine concentration was maintained but the pH-value was adjusted to 2 by means of adding 10ml of concentrated H₂SO₄. Starting from 100ml of pure water solvent and adding up to 60ml of EG, an interesting effect could be seen: The waterline as well as the neighbourhood of the wire are etched by electropolishing, the rest of the wafer is covered by some coloured or porous layer. The more EG is added, the larger is the electropolished region. This can be understood by the work of Turner [9]. The critical current density necessary for electropolishing is inversely proportional to the fourth root of the viscosity. Therefore lower current densities are needed to electropolish when EG is added, such that regions far from the wire and waterline that were PSL covered can be polished by adding further EG and thus increasing the viscosity of the electrolyte.

However, the fact that the etch depth at the waterline is comparable to that near the wire – cf. Fig. 6b – means that the resistivity of the silicon also plays an important role and is not to be neglected. In a stream etching application, the relative arrangement of the two or more electrodes is more favourable such that this fact is not very disturbing.

The last two experiment series 5 and 6 with a pH of 4-5 and 1 point in the same direction as the results of Osseo-Asare [8] in the sense that a pH of 2.5 is best for electrochemical etching of silicon dioxide since the results at higher pH were not as promising. In series 6 the effect of stirring the electrolyte was briefly studied. Two consecutive samples were etched with and without stirring. The results differed considerably since the etching effect was much reduced on the stirred sample.

DISCUSSION, CONCLUSIONS AND OUTLOOK

Diluted KOH is an unsuitable electrolyte for the stream etching of silicon and adapted etchants have to be developed. The first series of experiments with NH₄F based solution in water/ethylene glycol resulted in several requirements:

- At least small amounts of water are needed since water-free etchants result in pitted surfaces.
- If the solvent contains too much water, the competing oxidizing reactions by water molecules are dominant which disfavours localised etching.
- If the fluorine concentration and therefore the solvent conductivity is too low, the critical current densities may not be reached and PSL forms.
- There exist many process parameters to be optimized as pH and stirring of the electrolyte.

Even though NH₄F dissociates partially into HF, the chemistry of NH₄F solutions seems to be less favourable. As described by Uhlir [10], 50% HF in ethylene glycol may be a better choice for stream etching silicon. First attempts have been encouraging, especially the water-line dependence of the etch rate seems to be overcome which indicates that the conductivities of HF solutions in EG are in general lower. Further experiments will be conducted in that direction in order to see if a suitable electrolyte can be found. It appears however, in particular when comparing it with the rather straightforward stream etching of Ge with the quite ideal etchant of dilute KOH being just as fast as needed in an industrial production, that it may be a long way to reach this for silicon.

Acknowledgements

The authors would like to thank Ute Schubert as well as Marion Steuder for technical assistance with the electrochemical etching. The use of the experimental facilities of the FMF of the University of Freiburg is gratefully acknowledged.

REFERENCES

- [1] G. P. Willeke, Thin crystalline silicon solar cells, Sol. En. Mat. Solar Cells **72** (2002) 191-200
- [2] G. P. Willeke, The Fraunhofer ISE roadmap for crystalline silicon solar cell technology, Proc. 29th IEEE PVSC, New Orleans, May 20-24, 2002, in print
- [3] G. P. Willeke and D. Kray, A new route towards 50 µm thin crystalline silicon wafer solar cells, Proc. 17th EUPVSEC, Munich, Germany, 22-26 October 2001, B. McNelis, W. Palz, H.A. Ossenbrink and P. Helm (eds.), WIP-Renewable Energies, Munich and ETA, Florence, (2002) 1621-1624
- [4] J.F. Barry and N.C. Seeley, Method of shaping semiconductive bodies, US Patent 2827427, (1958)
- [5] H. Gerischer, The impact of semiconductors on the concepts of electrochemistry, Electrochim. Acta, **35**, pp. 1677-99, 1990
- [6] V. Costa-Kieling, Untersuchung zum Ätzen von Silizium in alkalischen und fluoridhaltigen Elektrolyten, Dissertation, TU Berlin, 1992
- [7] T. S. Horányi and P. Tüttö, Electrochemical etching and profiling of silicon, Applied Surface Science 63 (1993), p. 316-21
- [8] K. Osseo-Asare, Etching kinetics of silicon dioxide in aqueous fluoride solutions: a surface complexation model, J. Electrochem. Soc., **143**, pp. 1339-47, 1996
- [9] D. R. Turner, Electropolishing silicon in hydrofluoric acid solutions, J. Electrochem. Soc., **105**, pp. 402-8, 1958
- [10] A. Uhlir Jr., Electrolytic shaping of germanium and silicon, The Bell System Technical Journal, March 1956

Practical Aspects of Wire Sawing Process for Solar Cells

Kensho Miyata

Nippei Toyama Corporation

1-15, Shinmei-cho, Yokosuka, Kanagawa, Japan

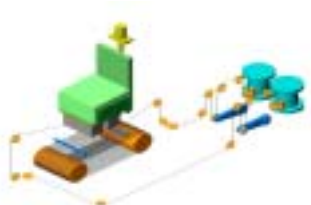
miyata.k@tk.nippeitoyama.co.jp

Wire Sawing process has taken over the I. D. (Inner Diameter) sawing process for cutting PV wafers and IC wafers. Due to the above change of the process, the Kerf loss has drastically reduced, and productivity per machine has been improved by more than 3 times. However, the reduction of the process cost, which is the material cost, the running cost and the environmental cost, is endless demands from the industry and marketplace. Under the above circumstance, wire diameter and abrasive grain size are getting finer, and Slurry Recycle System of the abrasive grain and cutting fluid is applied for reducing the operation cost. This paper presents introductory mechanism, technical trend and efficiency of wire sawing process.

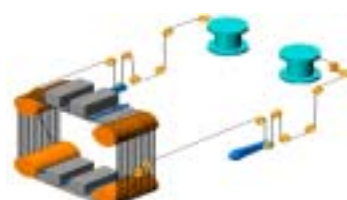
1. Machining Mechanism of Wire Saw

Wire Saw was developed in 1960s, and started to be applied to a process of cutting an ingot of a large diameter, more than 6 inches in around 1990. Compared with a conventional ID saw, this Wire Saw features a less cutting allowance (Kerf loss), an easy cutting of thin sheet, and a high productivity by slicing many wafers per one batch production.

For the Wire Saw to cut a brittle material like silicon, a web of wires (piano wires) are wound around the rollers, which have 300 to 1000 engraved grooves each, and make the web of wires move in high speed (reciprocating or one-way movement). While a mixture of abrasive-grain and dispersant, which is called Slurry, in a form of oil is poured onto the wires. By the above Slurry on the wire in high speed running, silicon is to be cut.



2 Roller Type

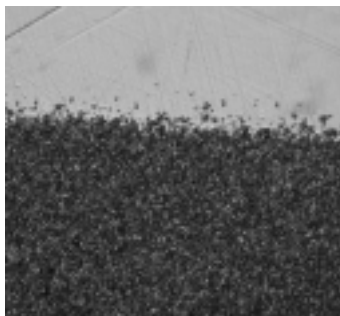


4 Roller Type

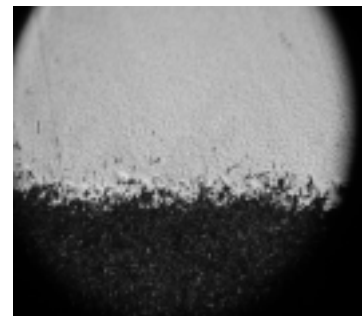
2. Machining Distortion by Wire Saw Process

The machining method by Wire Saw is to cut an ingot by means of suspended abrasive-grain as mentioned above, so machining distortion caused by this method resembles the lapping process in behavior. The distortion on the wafer was reported by our engineer Mr. Hasegawa* as under:

He measured a distortion of the wafer in case of using the abrasive-grain of GC600 to GC2000 and set a machining condition so that the slicing load can be constant to slice a mono-crystal silicon. After an oblique grinding, a machining distortion was measured by etching it.



Distortion by Lapping Process



Distortion by GC#2000

As Fig 2-1 below clearly shows:

- (1) The higher the grain count is, the lower the machining distortion is.
- (2) Machining distortion of nearly the same size as abrasive-grain diameter occurs.
- (3) Generally, in a lapping process, the bigger the grain size of the grit becomes, the bigger the machining distortion and roughness become in proportion. On the other hand, a similar tendency can be observed also with the Wire Saw machining process to make this process and the lapping process similar each other in the machining mechanism.

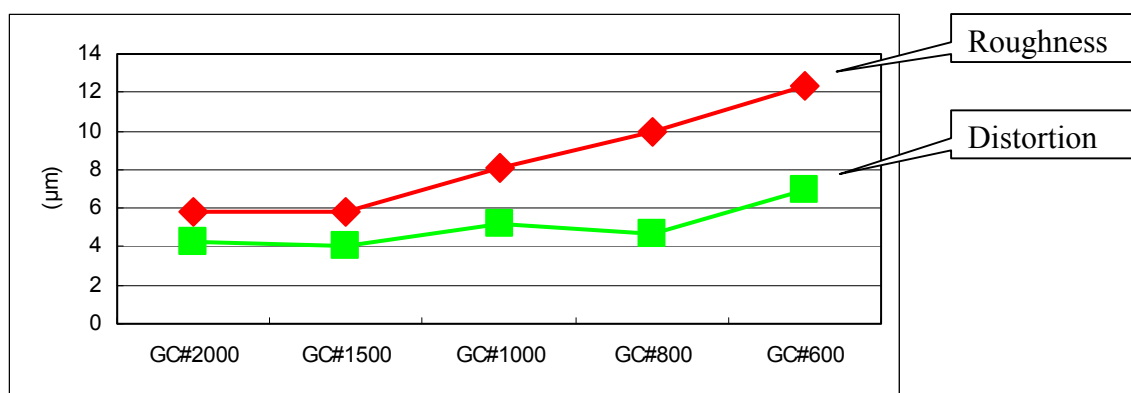


Fig. 2-1 “Relation between Machining Distortion and Roughness by Abrasive Grain”

3. Wafering Process for Solar Cell

In a slicing process with Wire Saw, the wafering for solar cells gives a very heavy load to the equipment to make the slicing very tough although the demanded accuracy differs.

We have to optimize machining conditions by considering the equipment ability according to uneven machining load due to a multi-crystal material, change of machining performance caused by a change of cutting chips quantity during the slicing process, and tendency that demanded wafers are getting thinner, and the sizes of the wire, and of abrasive-grain are getting smaller.

For setting machining parameters, the followings items are listed up:

- (1) Thickness of the wafer
- (2) Length of the block
- (3) Wire diameter
- (4) Grain size of the abrasive-grain
- (5) Specific gravity of the slurry
- (6) Viscosity of the slurry
- (7) Flowrate of the slurry
- (8) Temperature of the slurry
- (9) Speed of the feed unit
- (10) Wire speed
- (11) Wire tension

From the viewpoint of the limit of the wire ability, it is necessary for us to review the wire consumption per machining area (km/m²).

In the mean time, the sizes of the wire and of the abrasive-grain are getting smaller for the kerf loss to reduce. At present, the abrasive-grain of GC800 to GC1000 is being used, however, the grain size of GC1500 is expected to be used in the very near future. As to the wire size, the wire of 0.16mm is mainly used now, however, the size is inclining toward 0.14mm hereafter. Therefore, we find it necessary for us to review the specifications of the equipment so that the above wire and abrasive-grain can be used for the equipment.

4. Cost Efficiency by means of Various Models

For the line-up of our Wire Saws for slicing wafers for solar cell, we could expand the range of our

supply from the compact model to the large-sized model by releasing MWM442DS last year. By this expanded line-up, we were able to supply the most optimal equipment according to production environments of our customers.



MWM442DS



PV400



MWM452W

Model	MWM442DS	PV400	MWM452W
Capacity	150 x 150 x 300 x 2pcs	127 x 127 x 400 x 3pcs 150 x 150 x 400 x 2pcs	150 x 150 x 400 x 4pcs
Roller Number	2 pcs	2 pcs	4 pcs
Machine Dimension	2200W x 1500L x 2400H	3000W x 2700L x 2780H	2400W x 4100L x 3600H

In the process of wafering for a solar cell, a mass production by means of a large-sized machine is generally supposed to be of cost efficiency because the mass production can reduce a unit price of wafers, however, the larger the machine is, the more time is needed for setups and changeovers, the more wire must be used per one batch, and an increasing load on the big machine becomes difficult to reuse the wire, which results in an increase of the wire consumption to the disadvantage of our customers.

The big machine can increase an efficiency per a foot print of the machine due to a high production capacity per unit, and can decrease the number of operators to the advantage of our customers, but controlling technique for its operation is needed.

Therefore, if labor cost and land prices are low or if a customer uses the Wire Saw for the first time, the compact machine can increase productivity and more economical than the big machine. In addition, the compact machine has an advantage in avoiding a risk at the wire-break. Accordingly, please keep it in mind that a service condition must be studied for a selection of the model, otherwise, cost efficiency cannot be improved, and the wafering cost will go up. Thus, we cannot say the mass production by the large-sized machine is always economical.

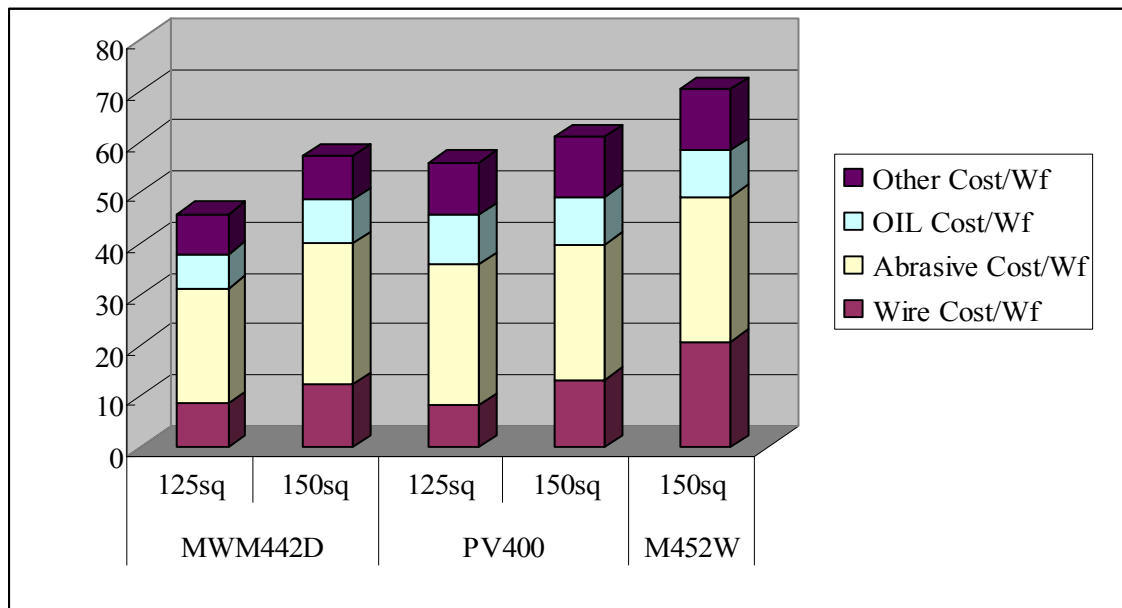


Fig 4-1: Running Cost Comparison at Each Model

5. Cost Reduction by Slurry Recycle System

Our slurry recycling system recovers dispersant and abrasive-grain from the used slurry by using two units of a horizontal centrifuge which is named a decanter, and re-mixes the recovered elements with new slurry so that the recycled slurry is of the specific gravity that is needed by the Wire Saw. (US Patent #US6161533)

By means of this system, slurry can be recovered to reduce a running cost drastically. Furthermore, it is significant for this system to stabilize a cutting quality by supplying the slurry of stable quality.

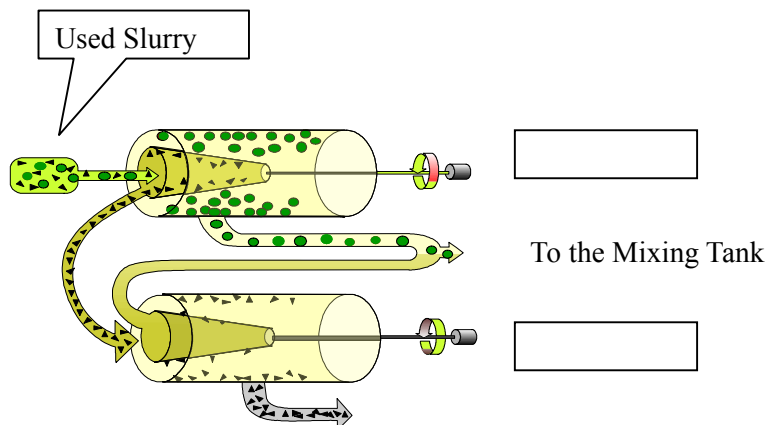


Fig. 5-1: Conceptual Diagram of Slurry Recycle System

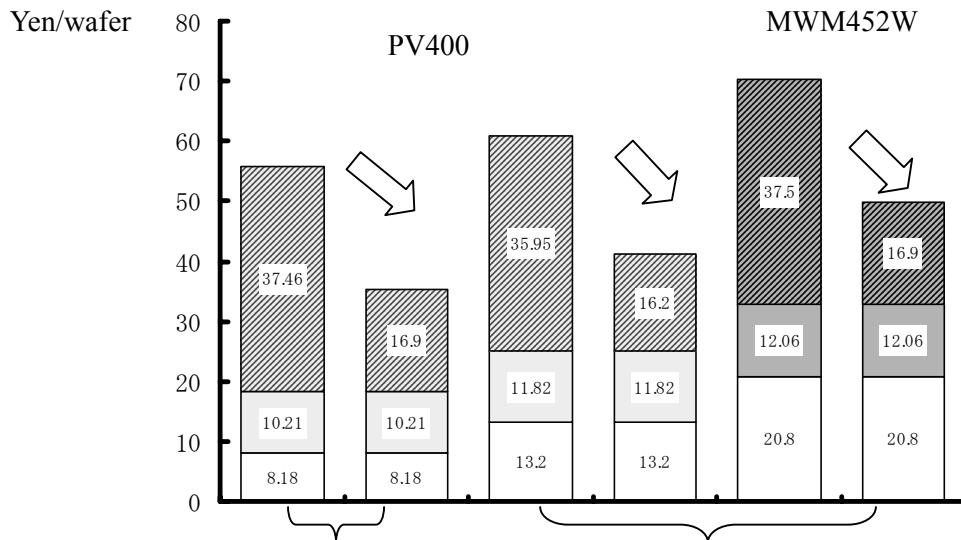


Fig5-2: Running Cost Reduction by Slurry Recycle System

Conclusion

A wafer for a solar cell is tending to be thinner, and sizes of the wire and of the abrasive-grain are tending to be smaller. Equipment maker have to promote a development of equipment, and an optimization of processing software, and parameter which meet this tendency. At the same time, from the viewpoint of using this equipment, we would like for you to select the most suitable model by considering operation circumstances so that you can exploit the maximum efficiency from the equipment you selected.

Wafer Slicing Using Improved Fixed Abrasive Slicing Technology (FAST)

Frederick Schmid, Maynard B. Smith and Chandra P. Khattak

Crystal Systems, Inc., 27 Congress Street, Salem, Massachusetts 01970 USA

Phone 978 745 0088, Facsimile 978 744 5059, email chandra@crystalsystems.com

ABSTRACT

An emerging slicing technique, Fixed Abrasive Slicing Technology (FAST), has so far been used for effective slicing of soft, fragile crystals. Recent improvements in FAST allow it to be utilized for effective slicing of hard materials at low cost. The most significant improvement involves high-speed rotation of the workpiece during slicing. The results of slicing silicon and sapphire are discussed. FAST has been used in prototype production of 50-mm diameter sapphire wafers for over a year.

INTRODUCTION

Most high technology materials are produced in ingot form and have to be sliced into wafers or plates for utilization in a wide range of applications. The microelectronics industry is the largest user of wafers of silicon, gallium arsenide and other compound semiconductor materials. A recent addition is photovoltaic application, which requires even larger quantities of silicon wafers. An emerging high-volume market is for light-emitting diodes (LEDs) for which large volumes of substrates such as sapphire, silicon carbide, etc., are required. In almost all high-volume applications, cost considerations are very important. Therefore, it is necessary to produce thin wafers with low kerf, high wafer accuracy and low cost. A number of wafering techniques have been used to slice different materials, and these technologies have been adopted by the industry for different reasons. An emerging technique, Fixed Abrasive Slicing Technology (FAST), has been under development for some time¹⁻³. This technology has been effective for slicing soft, fragile crystals, but the slicing effectiveness was limited when harder materials or very large sizes were sliced. This paper reports recent improvements in FAST, which allow it to be utilized for effective slicing of hard materials at low cost. Results of slicing silicon and sapphire are discussed. Based on this data, FAST slicing of sapphire crystals has been carried out in prototype production mode for producing substrates for LED applications.

FIXED ABRASIVE SLICING TECHNOLOGY (FAST) APPROACH

FAST has been developed as a multiwire slicing technique in which a wirepack plated with diamonds is reciprocated in a frame across the workpiece³. Typically, grooved rollers are placed on either side of the workpiece to guide the wires and thereby improve wafer accuracy. The workpiece is forced against the reciprocating wires. The feed forces that could be utilized were rather limited for such a configuration. It was necessary to minimize the contact areas between the wire and the workpiece so that higher feed forces could be achieved at the cutting edge of the diamonds on the wire. This was achieved by rocking the workpiece during slicing. A major effort involved development of the technology and the slicer to slice silicon for photovoltaic application.

FAST slicing showed many advantages and had the potential of being developed into a low cost, effective slicing method. This process combines all the major advantages of other slicing processes. For example, kerf was minimized as with multiwire slicing (MWS), low expendable material costs were achieved as with internal diameter (ID)slicing, and the equipment was simple as with multiblade slurry (MBS) slicing. In addition, thin slices could be produced with high wafer accuracy. FAST slicing was carried out using low feed forces to achieve high wafer quality.

A major emphasis in FAST development was to produce silicon wafers for solar cell applications. Multiwire Slicing (MWS) using a continuous wire wrapped around rollers and using a silicon carbide slurry was developed and adopted by the microelectronics and the solar cell industry. The MWS method had higher cutting rates than FAST because the surface speed of the wire was much higher.

To achieve high surface speed of wire, FAST was modified to incorporate high-speed rotation of the workpiece, as shown in Figure 1. A diamond-plated wirepack with equal spacing and tension of wires is stretched in the bladehead of the slicer and reciprocated. A cylindrical workpiece is rotated at high speeds of up to 5,000 rpm and with a feed force pushed downward against the wires. Grooved rollers are placed on either side of the workpiece below the wirepack to minimize wire wander and improve wafer accuracy. This approach minimizes the contact length between the workpiece and the wires, increases effective feed force on the diamond tip against the workpiece and allows diamonds to plow into the workpiece to achieve effective slicing. In this configuration, slicing is achieved from the circumference of the cylinder toward the interior. When the wires reach the central hub, a bridge is attached to the circumference of the workpiece to hold the wafers together and the crystal rotation is changed to a rocking mode to complete slicing the central core of the workpiece. In this stage, only a small central hub is sliced in rocking mode. With these improvements, FAST slicing is three times faster than MWS for slicing sapphire with one-third of the consumable cost. As the hardness of the material increases, the rotation rates for the crystal can be increased. The size of the workpiece that can be sliced will be limited by the degradation of diamonds on the wirepack. These improvements in FAST have opened a new era of slicing many crystals more efficiently and particularly large hard crystals that could not be effectively sliced until now.

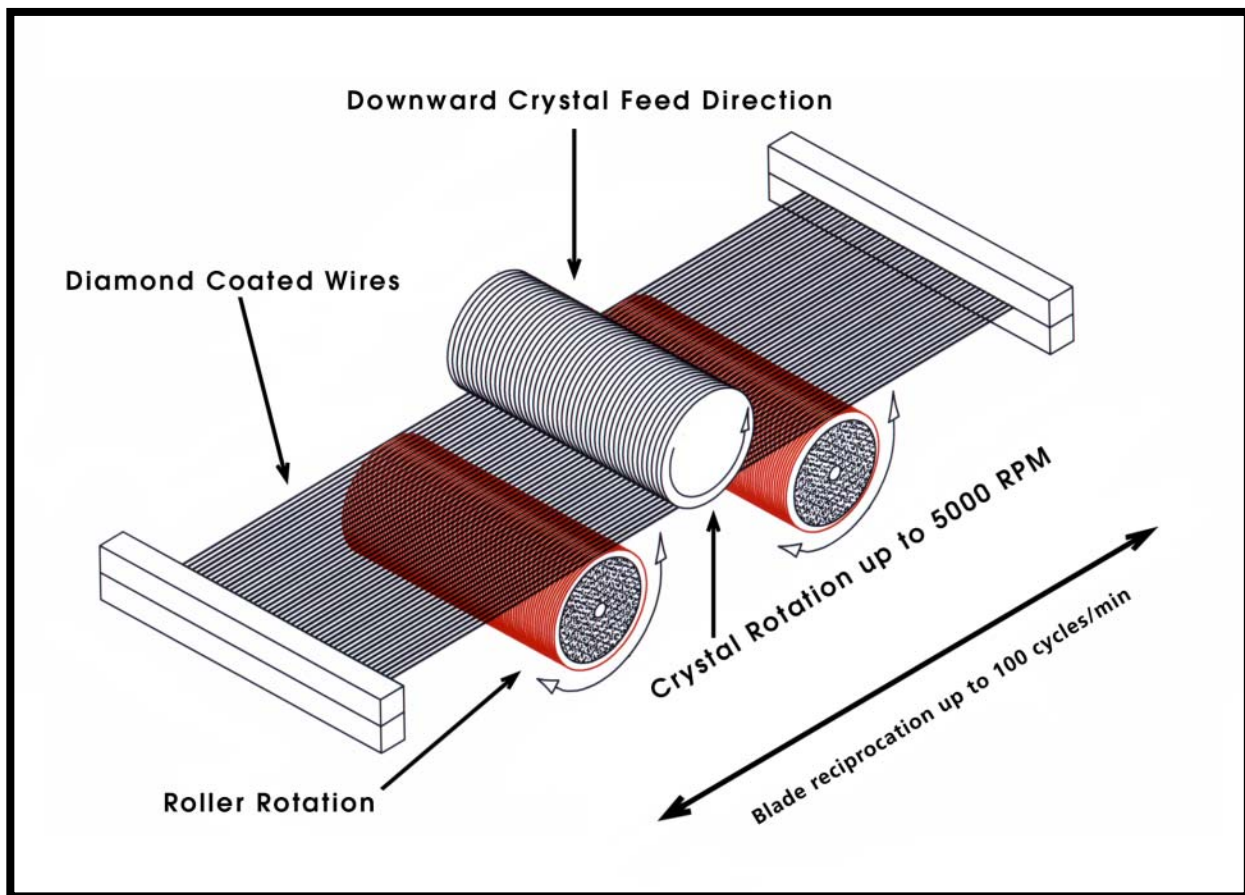


Figure 1. Schematic of a modified FAST slicer.

Silicon Slicing

Using conventional FAST, silicon ingots of 100 mm square cross section were sliced in a rocking mode at less than 0.1mm/minute⁴. The total time to slice such a workpiece was about 20 hours and diamond degradation of the wires during such a long period of slicing caused loss of slicing effectiveness as slicing progressed. The wirepack could not be used for slicing more than one silicon ingot because during subsequent cuts the slicing rate decreased and the cycle time increased dramatically. A 76-mm diameter silicon workpiece was rotated at 3,000 rpm and the infeed rate was 2.5 mm/minute. Therefore, the diameter of the workpiece was reduced 5 mm/minute. This cutting rate was 50 times greater than the cutting rate established during rocking mode. The yield of these wafers was 100%. A lapped surface was produced as a result of the rotation, and the thickness variation during this initial test was <50 μm . During another test, a 76-mm diameter, 100-mm long silicon workpiece was mounted and rotated at 5,000 rpm. Using the same feed rate of 2.5 mm/minute, 100% yield of wafers was achieved. These wafers showed a thickness variation of only 20 μm . This data showed that effective silicon slicing at high rotation rates can be achieved with an infeed rate of 2.5 mm/minute. At this infeed rate, a 100-mm square-cross-section silicon bar could be sliced in less than one hour. This is a dramatic improvement over any conventional slicing technology. Even higher infeed rates can be used, but it will be necessary to develop a more effective coolant system which can be used to carry coolant at the cutting site.

Sapphire Slicing

After it was demonstrated that slicing effectiveness can be achieved with the improved FAST and rotation of the workpiece, slicing of sapphire crystals was evaluated. Using FAST in the rocking mode, even 6-mm diameter sapphire could not be sliced into wafers. Initially improved FAST was used to slice 25-mm diameter sapphire rods and they could be sliced easily. The workpiece size was scaled up to 50-mm diameter as this size was needed commercially for use as substrates for LED applications. Optimization of 50-mm diameter sapphire was carried out with a 100-mm long workpiece. It was sliced with the center-to-center wire spacing of 1-mm as well as 0.75 mm. Figure 2 shows the 50-mm diameter sapphire substrates produced using improved FAST slicing. During this period, optimization of diamond plated wire was also carried out. Currently, 50-mm diameter sapphire workpieces slice in less than 8 hours and one bladepack can slice up to four workpieces. These results have been achieved in prototype production mode for over a year and several thousand wafers have been supplied from production to commercial customers.

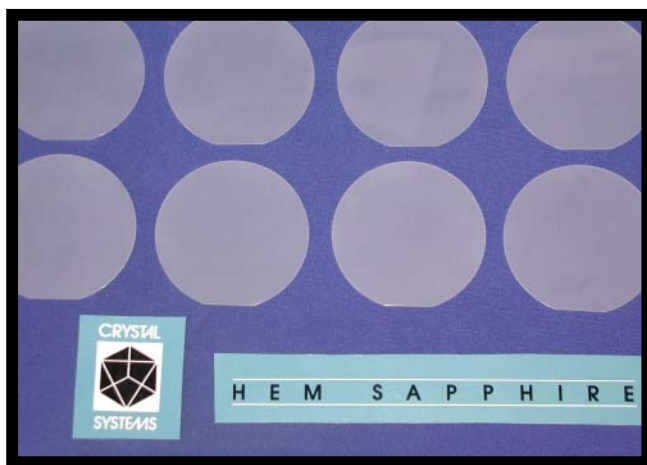


Figure 2. 50-mm diameter sapphire substrates produced using improved FAST slicing.

The LED substrate market is proceeding toward using 76-mm diameter size. Samples of 76-mm diameter sapphire substrates have been produced using improved FAST without any problems.

FAST PRODUCTION SLICER

Based on prototype production of sapphire substrates using high-speed rotation of the workpiece, an automated FAST production slicer was designed, fabricated and tested. Slicing of the workpiece can be carried out in rotation or rocking mode. Most effective slicing is carried out during high-speed rotation of the workpiece or for wafers with a central hole for an arbor. For such samples, a mandrel can be attached to the central hole of the workpiece and slicing can be carried out in rotation mode only without resorting to the rocking mode. For other wafers, the central hub is sliced in a rocking mode of the workpiece.

To achieve effective slicing and minimization of chips on the edge of wafers, it is desirable to introduce the wires into the workpiece from the outside diameter gradually. Thereafter, during slicing from the outside to the central hub, the feed rate can be gradually increased as the effective diameter for slicing decreases. The FAST slicer is designed to program the feed rate during slicing.

A forced coolant system is used on the FAST slicer so that it can be transported to the cutting site. Other features such as ease of installation of the workpiece, removal of the wafers and alignment of the wires can be easy operations. The slicer is designed for ease of maintenance, a guard system along with other safety features is installed for use in production mode. The production FAST slicer is shown in Figure 3.



Figure 3. Photograph of a production FAST Slicer.

FUTURE CONCEPTS FOR SLICING

It has been demonstrated that effective FAST slicing can be achieved for hard crystals of varying sizes. For smaller size crystals required in large quantities, the setup of the workpiece and the slicer can account for a large portion of the total cycle time. In addition, most wafers do not have a central hole. Therefore, the slicing has to be finished in the rocking mode which can be a significant portion of the cycle time, even though the amount of material cut in this mode is small. Several concepts have been tried successfully to slice smaller workpiece sizes and without resorting to the rocking mode during slicing. An approach to slicing several small diameter rods simultaneously is shown in Figure 4. These concepts can be used even for slicing several 50-mm sapphire workpieces bundled to achieve simultaneous slicing, as shown in Figure 5. Using this concept, several square workpieces can be bundled to achieve more effective slicing (Figure 6). These concepts may have more value for slicing silicon for solar cell applications.

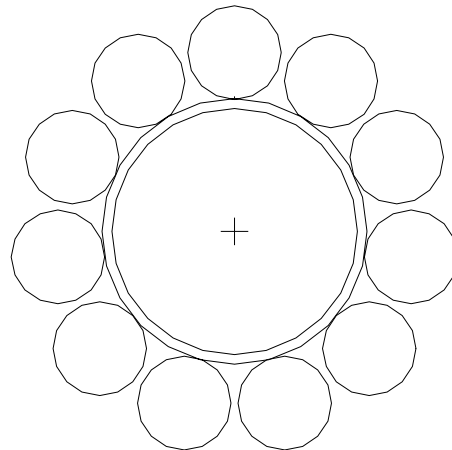


Figure 4. Schematic of small diameter workpieces bundled to achieve more effective slicing.



Figure 5. Configuration of three 50-mm diameter sapphire crystals bundled together for slicing without the need to enter into rocking mode.

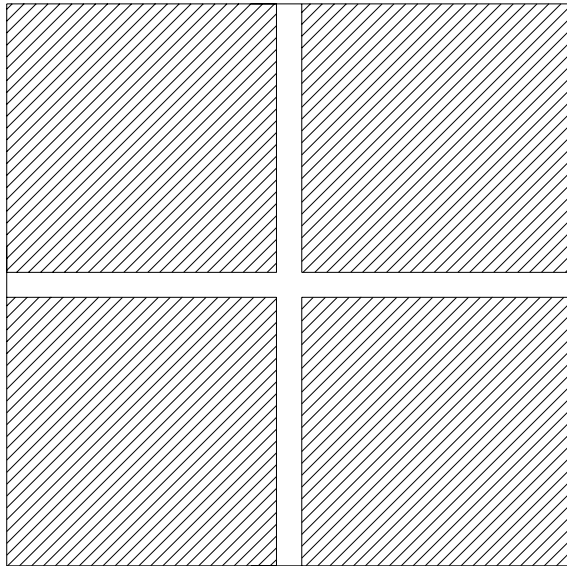


Figure 6. Bundling of 100-mm square-cross-section silicon bars for simultaneous slicing for solar cell applications using a modified FAST slicer.

CONCLUSIONS

Recent improvements in FAST using high-speed rotation of the workpiece have opened up the technology for slicing hard crystals and larger sizes. This approach has been used for slicing 50-mm diameter sapphire in prototype production for over a year. The improved slicing involves rotation of the workpiece and slicing from the circumference of the cylinder toward the interior until only a small hub remains. Thereafter, a bridge is attached to the wafers and further slicing is completed by rocking the workpiece. Newer concepts involve bundling of smaller size workpieces so that the central hub does not have to be sliced. These concepts will make FAST slicing even more efficient and cost effective. FAST can be utilized to slice four 100-mm square-cross-section silicon bars simultaneously for photovoltaic applications.

REFERENCES

1. C.P. Khattak and F. Schmid, *Low-Cost, High-Efficiency Silicon by Heat Exchanger Method and Fixed Abrasive Slicing Technique*, Proc. 2nd E.C. Photovoltaic Specialists Conference, D. Reidel Publ. Co. p. 106 (1979).
2. F. Schmid and C.P. Khattak, *Cutting Silicon Wafer Costs for Photovoltaics*, Optical Spectra 15 (5), p. 65 (1981).
3. F. Schmid, M.B. Smith, and C.P. Khattak, *Overview of a New Slicing Method-Fixed Abrasive Slicing Technique*, Proc. of the Low-Cost Solar Array Wafering Workshop, Phoenix, AZ, June 1981, DOE/JPL-1012-66, p. 233 (1982).
4. C.P. Khattak, F. Schmid, and M.B. Smith, *Wire-Blade Development for Fixed Abrasive Slicing Technique (FAST) Slicing*, Proc. of the Low-Cost Solar Array Wafering Workshop, Phoenix, AZ, June 1981, DOE/JPL-1012-66, p. 111 (1982).

LIGHT-INDUCED DEGRADATION IN CZ SILICON SOLAR CELLS: FUNDAMENTAL UNDERSTANDING AND STRATEGIES FOR ITS AVOIDANCE

Jan Schmidt and Rudolf Hezel

Institut für Solarenergieforschung Hameln/Emmerthal (ISFH)
Am Ohrberg 1, D-31860 Emmerthal, Germany

Abstract: Solar cells manufactured on boron-doped Czochralski-grown silicon (Cz-Si) degrade in performance when exposed to light or minority carriers are injected in the dark until a stable efficiency is reached. This effect, which is now known for almost 30 years, is due to the activation of a specific metastable defect in the Cz-Si material. Although a conclusive explanation of the effect is still to be found, recent investigations have clearly revealed that the Cz-specific defect is correlated with the boron and the oxygen concentration in the material. The first part of this paper reviews the current status of the physical understanding of the effect and gives an overview of the defect models proposed in the literature. In the second part, an overview of different strategies for avoiding or reducing the light-induced degradation in Cz-Si solar cells is presented.

1. INTRODUCTION

Approximately 90% of the present world solar cell production is based on boron-doped crystalline silicon, with Czochralski-grown monocrystalline silicon (Cz-Si) having a market share of about 40% and cast multicrystalline silicon (mc-Si) having a share of approximately 50%.¹ The main problem of solar cells manufactured on Cz-Si is that their initial efficiency degrades under illumination until a stable performance level, well below the initial efficiency, is reached. In the case of high-efficiency laboratory solar cells, like the PERL cell, the efficiency was found to degrade by up to 10% relative,² while in commercially manufactured solar cells an efficiency degradation by typically 3-7% (relative) has been reported.³ Despite the fact that the efficiencies obtained on monocrystalline Cz-Si are initially much higher compared to those attained on the cheaper cast mc-Si materials, efficiencies closely approach after a few hours of illumination. This is due to the fact that mc-Si solar cells are, in most cases, stable under illumination. Since, in general, Cz-Si is more expensive than mc-Si, the future of solar-grade Cz-Si crucially depends on whether it is usable for the mass-production of high-efficiency solar cells or not. Hence, in recent years, a lot of research has been devoted to the light-induced degradation (LID) problem, which is presently the main obstacle for making solar-grade Cz-Si a perfect high-efficiency solar cell material. This paper discusses the present physical understanding of the LID effect and gives an overview of the different approaches for reducing or even completely avoiding it.

2. FUNDAMENTAL UNDERSTANDING

2.1 Discovery of the effect and early models

To our knowledge, the first observation of LID in non-particle-irradiated solar cells fabricated on boron-doped Cz-Si wafers was made by Fischer and Pschunder in 1973.⁴ Figure 1 shows the evolution of the power output P_m , the short-circuit current I_{sc} , and the open-circuit voltage V_{oc} of a Cz-Si solar cell under illumination, as published in the original paper by Fischer and Pschunder.⁴ The initial cell parameters were measured directly after cell fabrication and are characterized by an intermediate state, labeled X. After only a short period of light exposure, all three cell parameters degrade until a stable level B is reached. Interestingly, it was found that the cell performance can be completely recovered by a low-temperature annealing treatment at 200°C (state A). By additional photoconductance decay measurements it was shown that the observed effect is due to a bulk carrier lifetime varying between two values, corresponding to two different states, A and B, of the material. State A is associated with a high lifetime and requires low-temperature annealing to be activated, while state B is associated with a

low carrier lifetime and is caused by illumination. Both levels were found to have the tendency to saturate and can reversibly be changed by applying the appropriate treatment.⁴

While the study performed by Fischer and Pschunder was more of phenomenological nature, in the following years, several attempts were made to develop a defect model which explains the observed lifetime instabilities in boron-doped Cz-Si solar cells. Weizer et al.⁵ proposed a model where the effect was attributed to a complex of a lattice defect and a silver atom or a cluster of atoms. Graff and Pieper⁶ proposed a vacancy-gold complex as the lifetime-limiting recombination center in the material. However, none of these models was capable of explaining the complete degradation/recovery cycle observed in boron-doped Cz silicon. Corbett et al.⁷ noted that the lifetime variations in Cz silicon are probably not due to a direct creation of the metastable defect by photons and suggested that the lifetime degradation might be due to the dissociation of donor-acceptor defect pairs caused by excess carriers via a recombination-enhanced mechanism. A recombination-enhanced defect reaction (REDR) was believed to be the responsible physical mechanism for the defect formation, as it explains the experimental observation that the degradation of the carrier lifetime occurs not only under light exposure, but also in the dark if a forward bias voltage is applied.^{5,8,9}

One of the probably best studied donor-acceptor complexes in crystalline silicon is the iron-boron pair. This defect pair dissociates under illumination and interstitial iron is formed.¹⁰ Interstitial iron is, under low-injection conditions, a more effective recombination center than the iron-boron pair, and hence leads to a strong degradation in the carrier lifetime. Reiss et al.¹¹ investigated solar cells fabricated on boron-doped Cz silicon wafers with comparatively high iron contamination levels and hence very low bulk lifetimes ($\sim 4 \mu\text{s}$). They observed a pronounced degradation in cell performance during illumination, during the application of a forward bias voltage in the dark, and during thermal treatment above $\sim 250^\circ\text{C}$. In order to recover the cell efficiency, the cell had to be stored in the dark at temperatures below 100°C . The authors clearly showed that this behavior can undoubtedly be explained by iron-boron pairs.

The annealing behavior of the material investigated by Reiss et al.¹¹ is very different to the one reported by Fischer and Pschunder⁴ who measured a complete lifetime recovery during annealing at temperatures above about 200°C and no lifetime recovery when storing the cells at room temperature in the dark. The latter researchers investigated Cz silicon with negligible iron content. Hence, it is very likely that the fundamental LID effect reported in Ref. 4 was screened in the solar cells of Reiss et al. by the superimposed iron-related effect. At this point it should be noted that several inconsistencies in the literature are due to the fact that often no clear distinction between both effects is made. The present paper only deals with the fundamental LID observed even in highest-purity electronic-grade boron-doped Cz-Si with virtually no metal contamination.

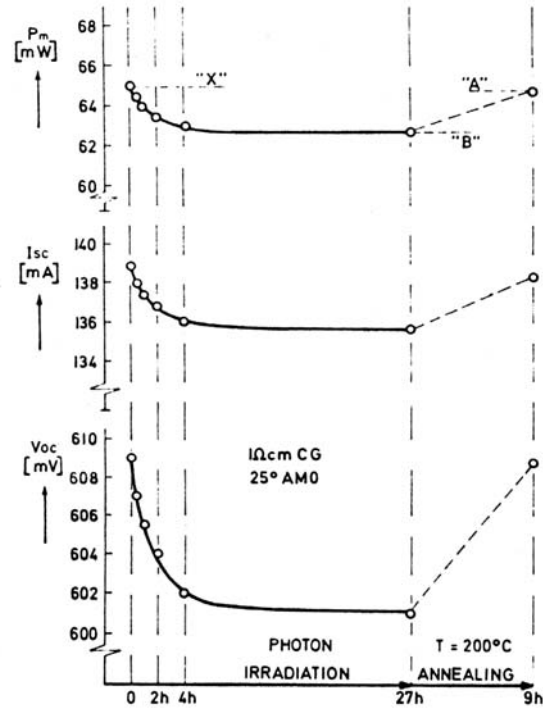


Figure 1: First observation of light-induced degradation in B-doped Cz-Si solar cells (from Ref. 4).

2.2 Structure of the metastable defect and mechanism of defect transformation

While all former attempts to clarify the LID of the carrier lifetime in Cz-Si were based on the formation of metal-containing defect complexes, it was not until 1997 that a complete defect reaction model was proposed by Schmidt et al.¹² that did not involve any metallic impurities. This was also the first model capable of explaining the lifetime degradation under illumination (or, alternatively, minority-carrier injection in the dark) as well as the lifetime recovery during annealing at temperatures above ~200°C. The most important feature of this model is the formation of a defect pair composed of one interstitial boron and one interstitial oxygen atom (B_iO_i) during illumination of the Cz silicon. The qualitative correlation of the magnitude of degradation with the boron and the oxygen concentration in the material was demonstrated by means of carrier lifetime measurements performed before and after LID on Cz wafers with different boron and oxygen concentrations.¹² Furthermore, photoconductance decay measurements on gallium-doped *p*-type Cz silicon and on phosphorus-doped *n*-type Cz material did not show any lifetime degradation.¹² Based on these results, several methods for reducing the lifetime degradation in Cz silicon solar cells were proposed, which will be discussed in Section 3. According to recent theoretical considerations of Ohshita et al.,¹³ the B_iO_i pair could only exist in a stable configuration if a substitutional silicon atom is sited between the boron and the oxygen atom.

In 1998, Glunz et al.¹⁴ confirmed the strong correlation between the LID in Cz-Si and the boron as well as the oxygen concentration by means of lifetime measurements on a very large number of boron-doped Cz-samples. Whereas they found an approximately linear increase of the lifetime degradation with boron doping concentration, a strongly superlinear increase with interstitial oxygen concentration, approximately to the power of five, was observed. It is important to note that, in the study of Glunz et al.,¹⁴ surface recombination of the Cz-Si wafers was suppressed by a high-temperature oxidation step at 1050°C and a subsequent deposition of corona charges on top of the thermally grown silicon dioxide layer, while in the upper study of Schmidt et al.¹² silicon nitride films deposited at low temperature (375°C) were used for surface passivation. The results of Glunz et al.¹⁴ gave rise to the suspicion that the Cz-specific recombination center is probably associated with a defect complex different from the B_iO_i pair. Besides, it is questionable if any interstitial boron exists in non-particle-irradiated silicon at all. These considerations were supported by measurements of Schmidt and Cuevas¹⁵ using injection-dependent lifetime spectroscopy (IDLS). They showed that the energy level of the light-induced recombination center is relatively close to the middle of the silicon band gap and hence it is very different from that of the B_iO_i pair (Fig. 2). On the basis of these results, they proposed a new structure consisting of one substitutional boron B_s and several oxygen atoms. Rein et al.¹⁶ determined the energy level of the metastable Cz-specific defect in its passive state (Fig. 2) by means of temperature-dependent lifetime spectroscopy (TDLS) and combined their own TDLS measurements with the IDLS measurements published in Ref. 15 to obtain a narrower range for the energy level of the active state.

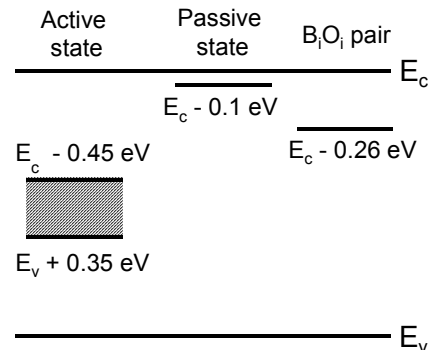


Figure 2: Energy levels of the metastable Cz-defect in its active and passive state, as determined by means of lifetime spectroscopy.^{15,16} For comparison, the energy level of the B_iO_i pair is shown.

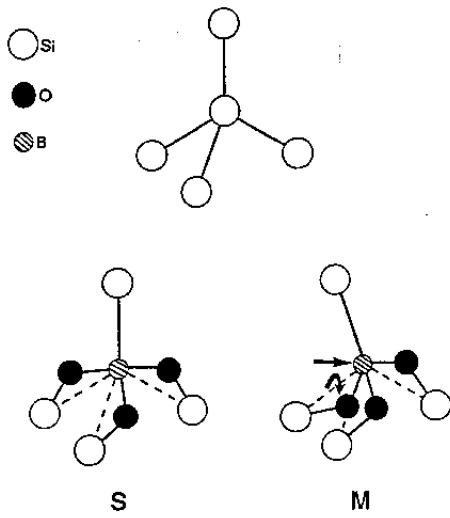


Figure 3: Stable (S) and metastable (M) configuration of the boron-oxygen complex proposed by Bourgoin et al. (from Ref. 17).

points towards a diffusion-limited defect formation process, where the minority-carrier injection plays merely an indirect role.

The defect annihilation process has been shown to be thermally activated as well.^{16,19} Isothermal annealing experiments were performed by different groups using different experimental approaches and revealed barrier energies of $E_{\text{ann}} = 1.3 \text{ eV}$ ¹⁶ and $E_{\text{ann}} = 1.8 \text{ eV}$,¹⁹ respectively, which are both well above the barrier energy of the defect generation process of $E_{\text{gen}} = 0.4 \text{ eV}$. It was also shown that the defect annihilation rate decreases approximately linearly with the doping concentration N_{dop} , while E_{ann} seems to be independent of N_{dop} .¹⁹

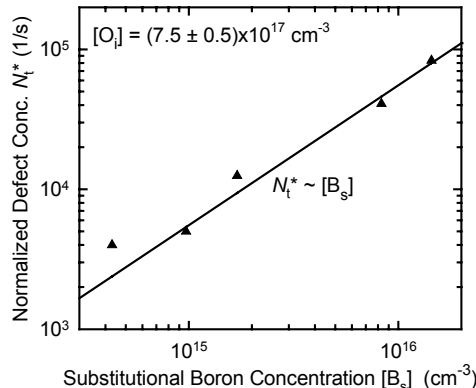


Figure 4: Measured normalized defect concentration N_t^* as a function of the substitutional boron concentration $[B_s]$ (from Ref. 19).

Most recently, the impact of boron and oxygen on the light-induced metastable defect concentration in Cz-Si was re-examined¹⁹ using the quasi-steady-state photoconductance method,²⁰ enabling the accurate measurement of carrier lifetimes at defined injection levels. Figure 4 shows the measured normalized defect concentration N_t^* , determined by subtracting the inverse lifetimes after and before light soaking $N_t^* \equiv 1/\tau_d - 1/\tau_0$, as a function of the substitutional boron concentration $[B_s]$ for Cz-Si wafers with similar levels of oxygen contamination $[O_i] = (7.8) \times 10^{17} \text{ cm}^{-3}$. In perfect agreement with previous

Bourgoin et al.¹⁷ proposed a possible atomic configuration of the boron-oxygen complex where the B_s atom is surrounded by three O_i atoms (Fig. 3). They also suggested a new degradation mechanism where electron trapping induces a Jahn-Teller distortion, shifting one of the energy levels of the defect to the middle of the silicon band gap. However, an experimental verification of the proposed mechanism was not performed.

Rein et al.¹⁶ investigated the defect generation as a function of doping concentration and found that it shows a quadratic increase with doping level, excluding the previously proposed REDR mechanism. Moreover it was shown, in good agreement with results of Hashigami et al.,¹⁸ that the defect generation rate is virtually independent of the light intensity. These somewhat surprising results led to the hypothesis that the mechanism of defect transformation might be a simple charging process. More recently, it was discovered that the defect generation is a thermally activated process with a relatively low barrier energy of $E_{\text{gen}} = 0.4 \text{ eV}$.¹⁹ This finding

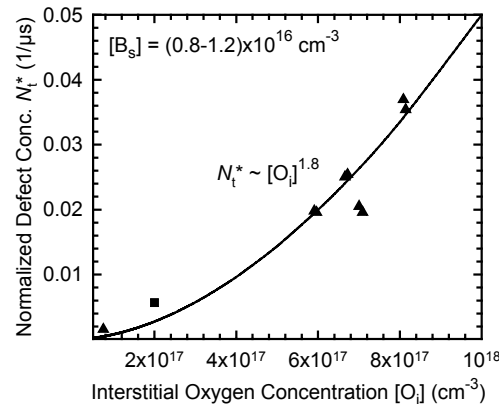


Figure 5: Measured normalized defect concentration N_t^* as a function of the interstitial oxygen concentration $[O_i]$ (from Ref. 19).

studies,^{14,15} a *linear* increase of N_t^* with increasing $[B_s]$ was found. Figure 5 shows the measured N_t^* values as a function of the interstitial oxygen concentration $[O_i]$. The boron concentration, as determined from resistivity measurements, was chosen to be approximately the same for all samples $[B_s]=(0.8\text{--}1.2)\times 10^{16} \text{ cm}^{-3}$. The most striking result of Fig. 5 is the fact that N_t^* shows an approximately *quadratic* increase with $[O_i]$, which is a much weaker dependence compared to that found by Glunz et al.¹⁴ This discrepancy might be due to the fact that in Ref. 14 a high-temperature oxidation, which could lead to a change of the bulk properties, was performed to passivate the surfaces, whereas in Ref. 19 low-temperature silicon nitride films were used for surface passivation.

Based on their experimental lifetime data, a new defect reaction model was developed by Schmidt et al.¹⁹ In this model, fast-diffusing oxygen dimers O_{2i} are captured by substitutional boron B_s to form a B_s - O_{2i} complex, acting as highly effective recombination center (Fig. 6). The defect formation process is governed by the diffusion of the oxygen dimer and, hence, is a thermally activated process, in good agreement with the experimental results of Ref. 19. The role of the minority-carrier injection could not be fully revealed. However, it was conjectured that the diffusivity of O_{2i} in silicon might depend on its charge state, which could change under illumination or minority-carrier injection. The defect formation process suggested in Ref. 19 is similar to the thermal donor (TD) formation mechanism proposed by Gösele and Tan,²¹ where the O_{2i} molecules are captured by other oxygen atoms or clusters to form the different TDs. In fact, a detailed theoretical and experimental analysis²² shows that during the first few hours of TD formation, the concentration of the O_{2i} dimer shows a pronounced decrease. As less O_{2i} molecules are available, the model proposed in Ref. 19 predicts a decrease in the B_s - O_{2i} concentration and hence a reduced light degradation of the carrier lifetime after TD formation. In order to verify this hypothesis, Bothe et al.²³ have annealed different boron-doped Cz-Si wafers at 450°C for up to 32 h. These conditions are ideal for the formation of TDs. After TD formation they measured a pronounced reduction of the metastable defect concentration by up to a factor of 3, giving an indirect confirmation of the proposed defect reaction model.

3. STRATEGIES FOR SUPPRESSING THE LIGHT-INDUCED DEGRADATION

3.1 Alternative Cz-Si materials

The correlation of the magnitude of degradation with the boron and the oxygen concentration in the Cz material had been proven by means of carrier lifetime measurements on a large number of Cz wafers from different manufacturers.^{12,14,19} Furthermore, measurements on Ga-doped *p*-type Cz silicon as well as on P-doped *n*-type Cz material had shown no degradation of the carrier lifetime.¹² Based on these experimental results, several methods for reducing the lifetime degradation in Cz silicon solar cells were proposed.¹² The two most promising approaches were: (i) replacement of B with another dopant element, like Ga or P, and (ii) reduction of the oxygen concentration in the Cz material. In a recent international joint research project, organized by Saitoh,²⁴ a large number of Cz-Si wafers with different dopant elements (B, Ga) and different oxygen concentrations (including conventional and magnetic Cz-Si) were manufactured by Shin-Etsu Handotai (SEH) and supplied to various international institutions (Sharp Co., Hitachi Ltd., FhG-ISE, Georgia Tech, ISFH, UNSW, TUAT) for characterization and solar cell fabrication. Figure 7 shows the typical behavior of the different Cz materials: while the carrier lifetime of conventional B-doped Cz-Si (solar-grade as well as electronic-grade material) degrades under illumination, Ga-doped Cz-Si of similar doping concentration has a stable lifetime on a much higher level, comparable to that of B-doped float-zone (FZ) silicon, even if the interstitial oxygen con-

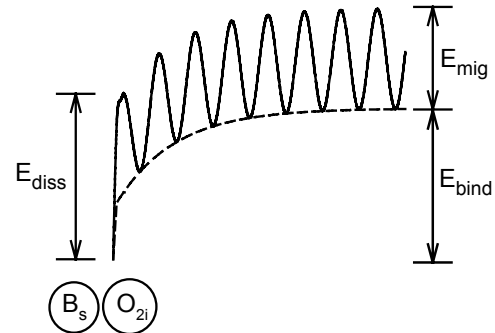


Figure 6: Schematic energy diagram of the B_s - O_{2i} interaction (from Ref. 19).

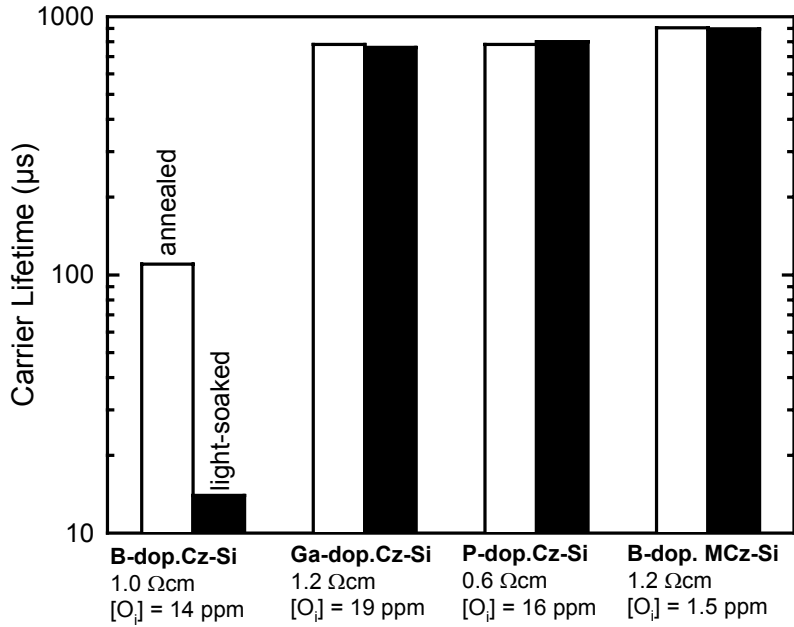


Figure 7: Measured carrier lifetimes of of B-, Ga-, and P-doped Cz-Si and B-doped MCz-Si before and after light soaking (data taken from Refs. 12, 27).

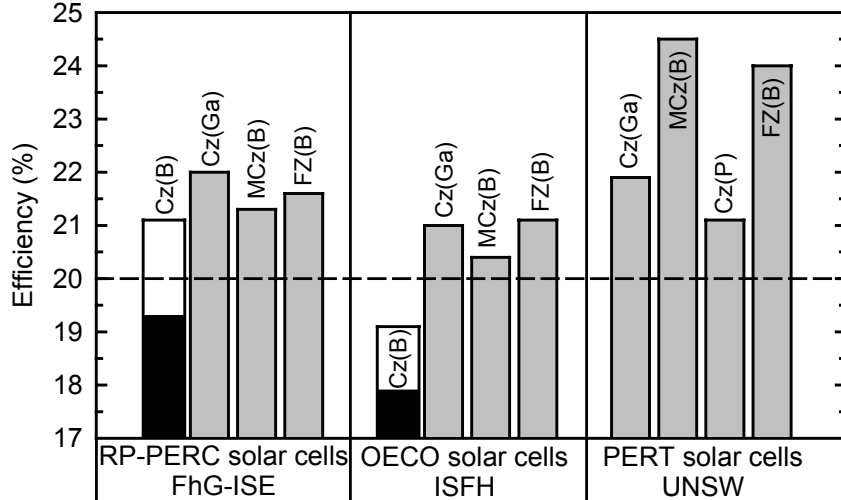


Figure 8: Stable efficiencies of solar cells manufactured on alternative Cz-Si and FZ-Si (gray boxes). For comparison, cell efficiencies obtained on conventional B-doped Cz-Si before (white boxes) and after (black boxes) light degradation are shown (data taken from Refs. 25–30).

centration is approximately as high as in the case of the B-doped Cz material. The high oxygen concentration in silicon ingots grown with a conventional Cz single crystal puller is due to the partial dissolution of the silica crucible during the growth process. The oxygen content can be strongly reduced by damping the melt flows with magnetic fields. This so-called magnetic Cz (MCz) silicon with strongly reduced O_i concentration shows an almost vanishing light degradation (see Fig. 7) and has bulk lifetimes which are comparable to that of Ga-doped Cz-Si. Also included in Fig. 7 is a P-doped Cz-Si material with high O_i content, which is also completely stable under illumination. However, since the latter material is an *n*-type semiconductor and most industrial solar cell processes have been developed for *p*-type base material, at present the most promising alternative Cz silicon materials seem to be Ga-doped Cz-Si and B-doped MCz-Si.

High-efficiency solar cell processes were applied to the alternative Cz materials at different institutes and stable efficiencies well above 20% were obtained on Ga-doped Cz-Si, B-doped MCz material, and

P-doped *n*-type Cz-Si (Fig. 8).²⁵⁻³⁰ For comparison, cell results obtained on B-doped FZ-Si and B-doped Cz-Si are also included in Fig. 8. Solar cell efficiencies above 20% can only be achieved with the new Cz materials, while the stable efficiency of cells fabricated on conventional 1-Ωcm B-doped Cz-Si is always well below 20%. Note that the degree of complexity of the three cell processes compared in Fig. 8 is very different, with the PERT process being by far the most complex manufacturing process, whereas the OECO process, on the other hand, is completely avoiding any photolithography and alignment steps. The latter process is currently transferred to industrial pilot production.

The segregation coefficient of gallium in silicon is two orders of magnitude lower compared to that of boron in silicon. Hence, Ga-doped Cz-Si crystals exhibit a considerably higher variation in resistivity along their growth axis compared to B-doped crystals. Metz et al. have investigated the usability of a complete 6" Ga-doped Cz-Si crystal in their high-efficiency OECO solar cell process.²⁸ The resistivity of the crystal varied from 1.3 Ωcm at the top to 0.4 Ωcm in the tail region. Figure 9 shows the measured OECO solar cell efficiencies as a function of the base resistivity. Peak efficiencies of up to 21% were obtained on 0.4-Ωcm material and, more important, in the broad resistivity range between 0.25 and 1.34 Ωcm, cell efficiencies were found to reach more than 97% of the peak value, demonstrating that the inherent resistivity variations in Ga-doped Cz-Si crystals are well within the range tolerable for the manufacturing of high efficiency solar cells.

3.2 Process optimization

Several approaches aiming at reducing the concentration of the Cz-specific metastable defect in B-doped Cz-Si during the solar cell manufacturing process have been investigated. In particular, certain high-temperature steps, optimized for Cz-Si, were found to be capable of significantly reducing the magnitude of degradation. In a recent comprehensive study, the high-temperature (~1050°C) thermal oxidation process required for the growth of masking oxides and passivation layers was studied in detail.^{14,31} It was found that the concentration of the Cz-specific metastable defect can be reduced by up to a factor of 4 if the ramping conditions are chosen properly. However, the absolute values of the stable lifetimes of conventional B-doped Cz-Si materials were still found to be on a relatively low level between about 20 and 45 μs after the optimized oxidation step, which is well below the lifetimes measured on Ga-doped Cz-Si and MCz materials. In a more recent study, a phosphorus emitter diffusion step at ~850°C with optimized ramping conditions was also found to have a beneficial effect on the LID, leading to a maximum reduction in the light-induced defect concentration by a factor of 3.5.²³ This effect was attributed to the temperature profile only and was shown to be not due to a gettering of impurities.²³ A permanent improvement of the carrier lifetime in Cz-Si is not only possible using conventional quartz-tube furnaces. A short annealing step of a few seconds at temperatures around 800°C in a belt furnace was found to halve the light-induced defect concentration.³² Similar results were also obtained using rapid thermal processing.³³

3.3 Other approaches

An alternative method to reduce the harmful effects of lifetime degradation on cell efficiency is to modify the cell design. By simply reducing the thickness of their solar cells to 100 μm, Münzer et al.³⁴

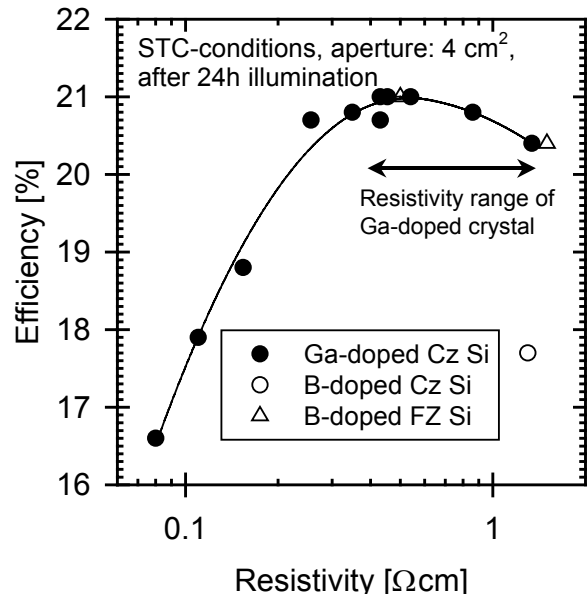


Figure 9: Measured efficiencies of OECO solar cells manufactured on Ga-doped Cz-Si as a function of base resistivity (from Ref. 28).

obtained a reduced degradation and an improved stable efficiency. However, this approach requires a very efficient rear surface passivation of the solar cell.^{34,35} Other solar cell structures, like the Emitter-Wrap-Through (EWT) cell, have also the potential to reduce the light degradation considerably.³⁶

On the basis of the novel defect reaction model proposed in Ref. 19, it was suggested that carbon-rich B-doped Cz-Si may exhibit a reduced lifetime degradation, because the formation of carbon-oxygen complexes could be a competitive process to the formation of the lifetime-limiting boron-oxygen complex. However, an experimental verification of this promising new way of reducing the metastable defect concentration in B-doped Cz-Si has not been published up to now.

Acknowledgements

The support by the State of Niedersachsen and the German Bundesministerium für Bildung und Forschung (BMBF) is gratefully acknowledged. The ISFH is a member of the German *Forschungsverbund Sonnenenergie*.

References

- ¹ P.D. Maycock, *PV News*, April 2002.
- ² J. Knobloch, S. Glunz, V. Henninger, W. Warta, W. Wetling, F. Schomann, W. Schmidt, A. Endrös, K. Münzer et al., *Proc. 13th European PVSEC*, 1995, p. 9.
- ³ S. Sterk, K. Münzer, and S. Glunz, *Proc. 14th European PVSEC*, 1997, p. 85.
- ⁴ H. Fischer and W. Pschunder, *Proc. 10th IEEE PVSC*, 1973, p. 404.
- ⁵ V.G. Weizer, H.W. Brandhorst, J.D. Broder, R.E. Hart, and J.H. Lamneck, *J. Appl. Phys.* **50**, 1979, p. 4443.
- ⁶ K. Graff and H. Pieper, *phys. stat. sol. (a)* **49**, 1978, p. 137.
- ⁷ J. W. Corbett, A. Jaworowski, R.L. Kleinhenz, C.B. Pierce, and N.D. Wilsey, *Solar Cells* **2**, 1980, p. 11.
- ⁸ J. Knobloch, S.W. Glunz, V. Henninger, W. Warta, W. Wetling, F. Schomann, W. Schmidt, A. Endrös, and K.A. Münzer, *Proc. 13th European PVSEC*, 1995, p. 9.
- ⁹ J. Knobloch, S.W. Glunz, D. Biro, W. Warta, E. Schäffer, and W. Wetling, *Proc. 25th IEEE PVS*, 1996, p. 405.
- ¹⁰ K. Graff and H. Pieper, *J. Electrochem. Soc.* **128**, 1981, p. 669.
- ¹¹ J.H. Reiss, R.R. King, and K.W. Mitchell, *Appl. Phys. Lett.* **68**, 1996, p. 3302.
- ¹² J. Schmidt, A.G. Aberle, and R. Hezel, *Proc. 26th IEEE PVSC*, 1997, p. 13.
- ¹³ Y. Ohshita, T. Khanh Vu, and M. Yamaguchi, *J. Appl. Phys.* **91**, 2002, p. 3741.
- ¹⁴ S. W. Glunz, S. Rein, W. Warta, J. Knobloch, and W. Wetling, *Proc. 2nd WCPSEC*, 1998, p. 1343.
- ¹⁵ J. Schmidt and A. Cuevas, *J. Appl. Phys.* **86**, 1999, p. 3175.
- ¹⁶ S. Rein, T. Rehrl, W. Warta, S. Glunz, and G. Willeke, *Proc. 17th European PVSEC*, 2001, p. 1555.
- ¹⁷ J. C. Bourgoin, N. de Angelis, and G. Strobl, *Proc. 16th EU PVSEC*, 2000, p. 1356.
- ¹⁸ H. Hashigami, Y. Itakura, A. Takaki, S. Rein, S. Glunz, and T. Saitoh, *Proc. 17th European PVSEC*, 2001, p. 1483.
- ¹⁹ J. Schmidt, K. Bothe, and R. Hezel, *Proc. 29th IEEE PVSC*, 2002, in press.
- ²⁰ R. A. Sinton and A. Cuevas, *Appl. Phys. Lett.* **69**, 1996, p. 2510.
- ²¹ U. Gösele and T. Y. Tan, *Appl. Phys. A* **28**, 1982, p. 79.
- ²² D. Åberg, B. G. Svensson, T. Hallberg, and J. L. Lindström, *Phys. Rev. B* **58**, 1998, p. 12944.
- ²³ K. Bothe, J. Schmidt, and R. Hezel, *Proc. 29th IEEE PVSC*, 2002, in press.
- ²⁴ T. Saitoh, H. Hashigami, X. Wang, T. Abe, T. Igarashi, S. Glunz, S. Rein, W. Wetling, A. Ebong, B.M. Damiani, A. Rohatgi, I. Yamasaki, T. Nunoi, H. Sawai, H. Ohtuka, T. Warabisako, J. Zhao, M. Green, J. Schmidt, A. Cuevas, A. Metz, and R. Hezel, *Proc. 16th EU PVSEC*, 2000, p. 1206.
- ²⁵ S. Glunz, S. Rein, J. Knobloch, W. Wetling, and T. Abe, *Prog. Photovolt.* **7**, 1999, p. 463.
- ²⁶ S. Glunz, S. Rein, J. Lee, and W. Warta, *J. Appl. Phys.* **90**, 2001, p. 2397.
- ²⁷ A. Metz and R. Hezel, presented at the *1st Workshop on Light Degradation of Carrier Lifetimes in Cz-Si Solar Cells*, Sapporo, Japan, 1999.
- ²⁸ A. Metz, T. Abe, and R. Hezel, *Proc. 16th EU PVSEC*, 2000, p. 1189.
- ²⁹ J. Zhao, A. Wang, and M. Green, *Proc. 16th EU PVSEC*, 2000, p. 1100.
- ³⁰ J. Zhao, A. Wang, and M. Green, *Prog. Photovolt.* **8**, 2000, p. 549.
- ³¹ S. Glunz, S. Rein, W. Warta, J. Knobloch, and W. Wetling, *Sol. Energ. Mat. Sol. Cells* **65**, 2001, p. 219.
- ³² H. Nagel, A. Merkle, A. Metz, and R. Hezel, *Proc. 16th EU PVSEC*, 2000, p. 1197.
- ³³ J. Lee, S. Peters, S. Rein, and S. Glunz, *Prog. Photovolt.* **9**, 2001, p. 417.
- ³⁴ K. Münzer, K. Holdermann, R. Schlosser, S. Sterk, *IEEE Trans. Electron Dev.* **46**, 1999, p. 2055.
- ³⁵ B. Damiani, A. Ristow, A. Ebong, and A. Rohatgi, *Prog. Photov.* **10**, 2002, p. 185.
- ³⁶ S. Glunz, J. Dicker, J. Lee, R. Preu, S. Rein, E. Schneiderlöhner, J. Sölter, W. Warta, and G. Willeke, *Proc. 17th European PVSEC*, 2001, p. 1287.

A Feasibility Study on Gallium Doping for Higher Quality Multicrystalline Silicon Cast Wafers

*Marwan Dhamrin and Tadashi Saitoh
Tokyo A&T University*

Contents

- * Background
- * Light degradation of B-doped Cz-silicon
- * Elimination of degradation in Cz-Si by Ga doping
- * Light degradation of B-doped mc-Si cast wafers
- * Effect of Ga doping for mc-Si wafers
- * Conclusions

ABSTRACT:

In recent years, light degradation research has been extensively conducted for B-doped, Cz-silicon crystals and solar cells. The degree of the degradation depends on the metastable B-On defects created under light irradiation. Gallium doping was successfully applied to eliminate the defects for Cz-silicon. In addition, the Ga doping was effective to grow high-quality single crystals with higher carrier lifetimes in low-resistivity regions.

Multicrystalline cast silicon crystals were also investigated under simulated sunlight irradiation. Carrier lifetimes in commercial wafers decreased to 60% of the initial values and cell efficiencies decreased relatively about 2 to 3 % after 3hr irradiation.

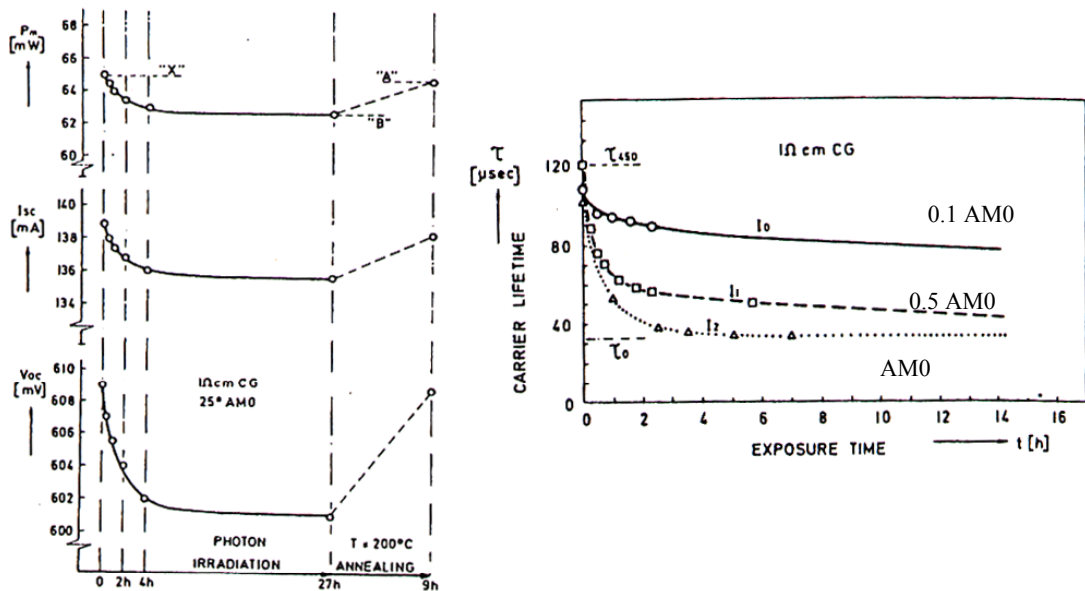
By fabricating an experimental cast ingot, gallium doping in the multicrystalline silicon was firstly found to be very effective to suppress the light-induced degradation of carrier lifetimes. It is expected to fabricate highly efficient solar cells and to provide more reliable silicon PV modules.

Light Degradation Research

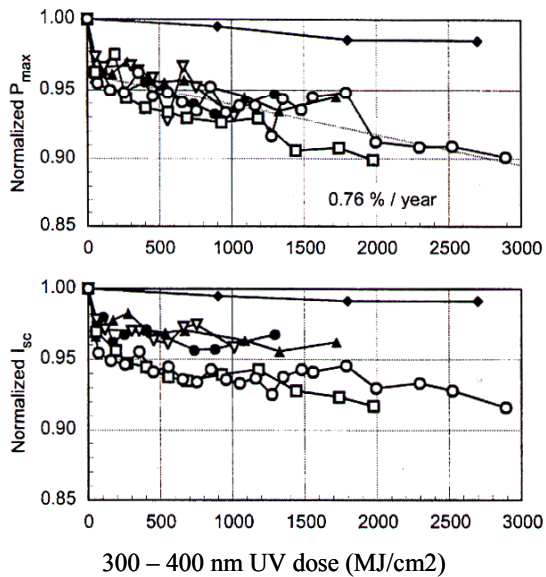
- First paper on the light degradation by Fischer and Pschunder (1973)
→ use of medium range resistivity for solar cell production.
- Light degradation of high efficiency-Cz Si cells by Knobloch (1995)
- A first model for light degradation : Bi-Oi pair by J. Schmidt (1997)
- International joint research organized by T. Saitoh and T. Abe (1998-1999)
(Effect of Ga and O impurities)
- B-On model
Light-induced defects increase super-linearly with Oi contents.
 $n = 5$ (Glunz, 1998), $n = 3$ (J. Bourgoin, 2000), $n=2$ (Schmidt, 2002)
 $n = \text{variable}$ (Hashigami, 2001, 2002)
- Light degradation of multicrystalline Si wafers (Takaki 2001, Marwan 2002)

Investigation of Photon and Thermal Induced Changes in Silicon Solar Cells

H. Fischer and W. Pschunder, 10th IEEEPVSC, 1973



Degradation of Weathered c-Si PV Modules
 C. Osterwald, 29th IEEE PVSC, 2002

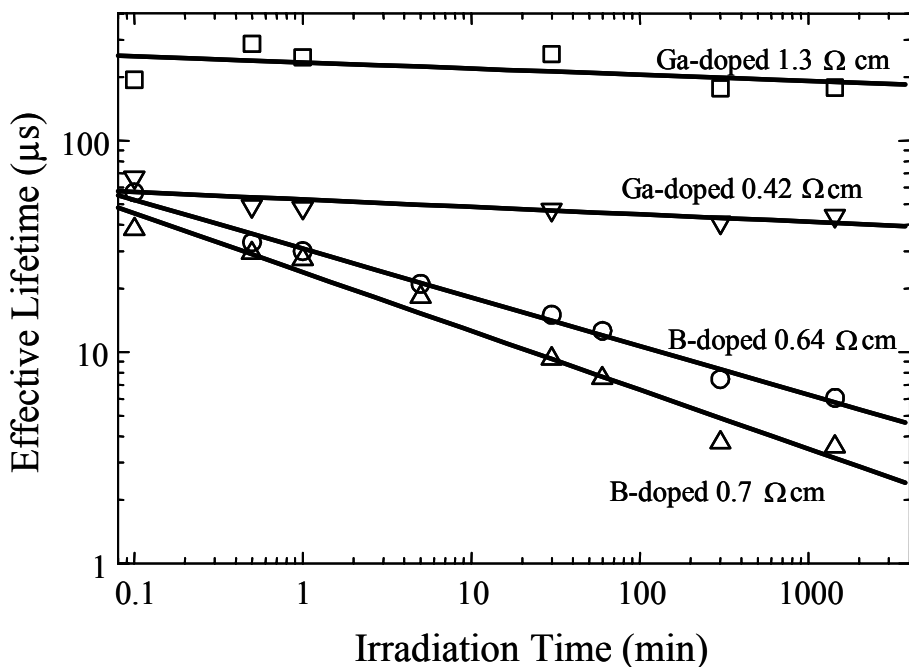


A summary of degradation rates

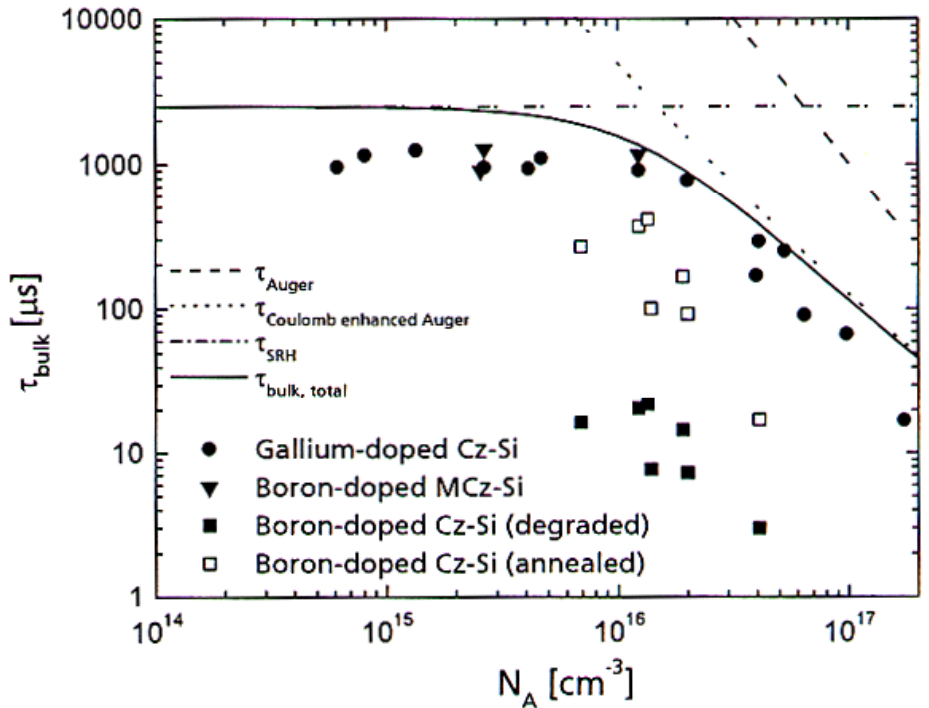
Module type	P_{max} rate (%/year)	I_{sc} rate (%/year)	P_{max} init. Loss (%)	I_{sc} init. Loss(%)
Single	-0.88	-0.59	-2.75	-2.26
	-0.76	-0.60	-3.87	-3.34
Multi	-0.76	-0.25	-2.34	-2.25
	-0.53	-0.24	-2.56	-2.34

Normalized P_{max} and I_{sc} for Cz-Si module #2
 ◆ control, ▽ Outdoor, real time
 ● Outdoor 1X, ▲ Outdoor 3X
 ○ Indoor XR260, □ Indoor UV

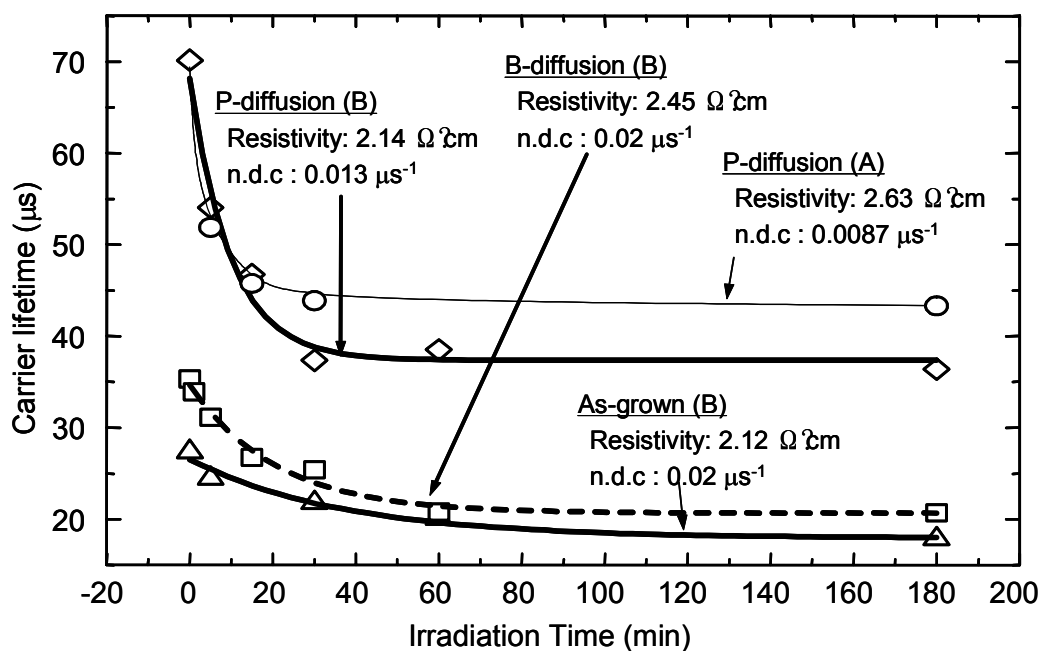
Variation of Carrier Lifetimes for as-received CZ-Si Wafers under AM 1.5 Illumination (Saitoh et al, 1999)



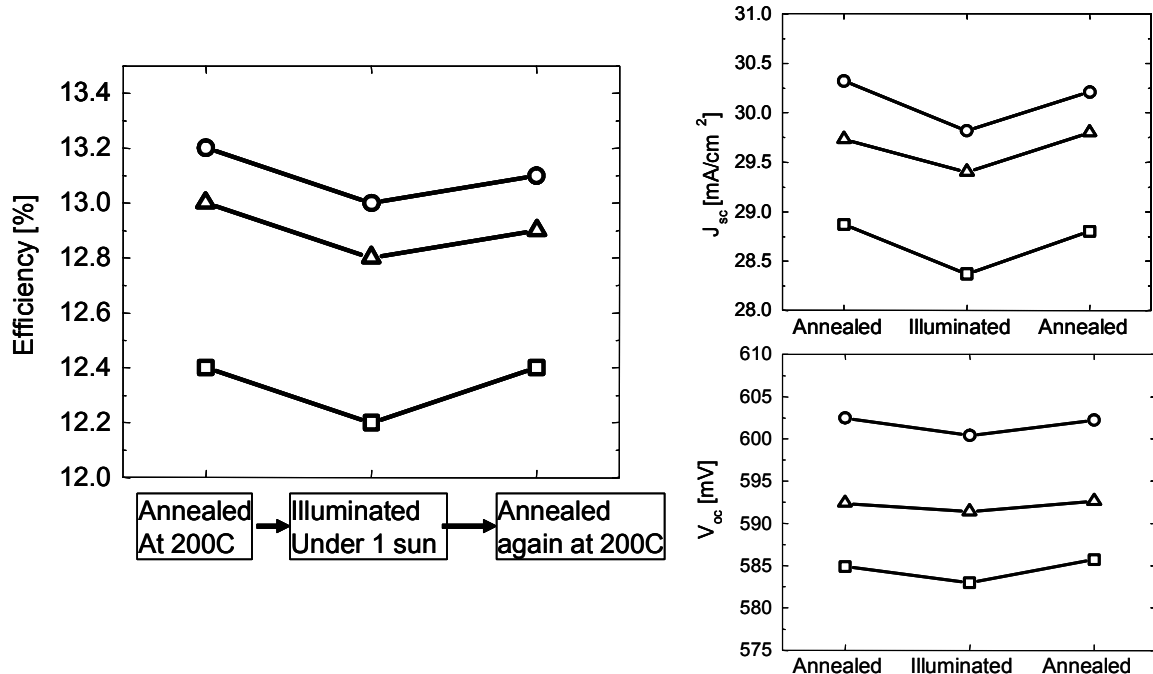
Carrier Lifetime vs Resistivity for Ga-doped Cz-Si
 (S. Glunz, 16th EU PVSC, 2000)



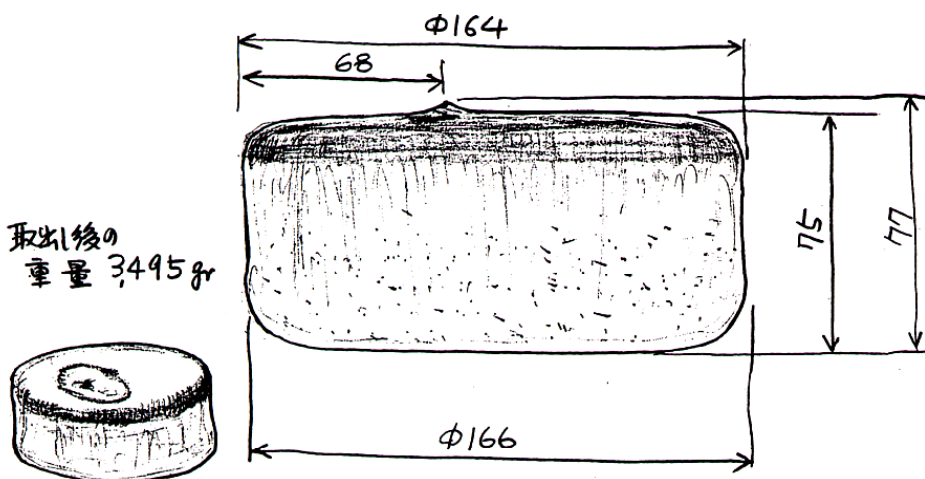
Light -induced Lifetime Degradation of Multicrystalline Silicon Cast Wafers
 (M. Dhamrin and T. Saitoh, 29th IEEE PVSC, 2002)



*Performance Change of Boron-doped Multicrystalline Silicon Solar Cells
after annealing, after degradation and after recovery annealing step*
(M. Dhamrin and T. Saitoh, 29th IEEE PVSC, 2002)

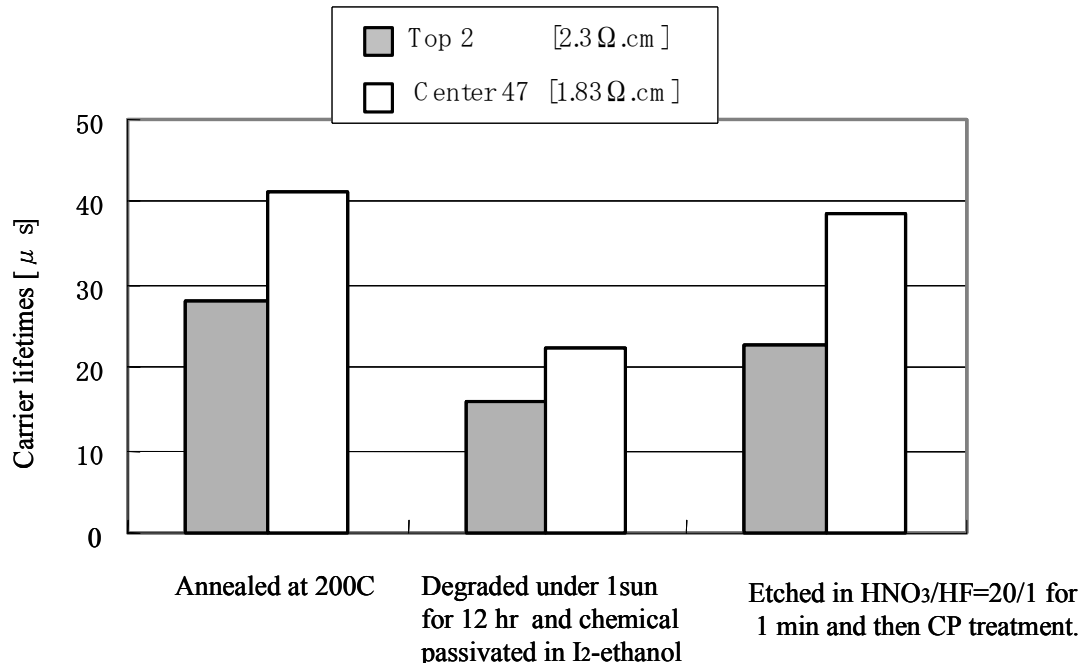


An Experimental Fabrication of Ga-doped Cast Ingot

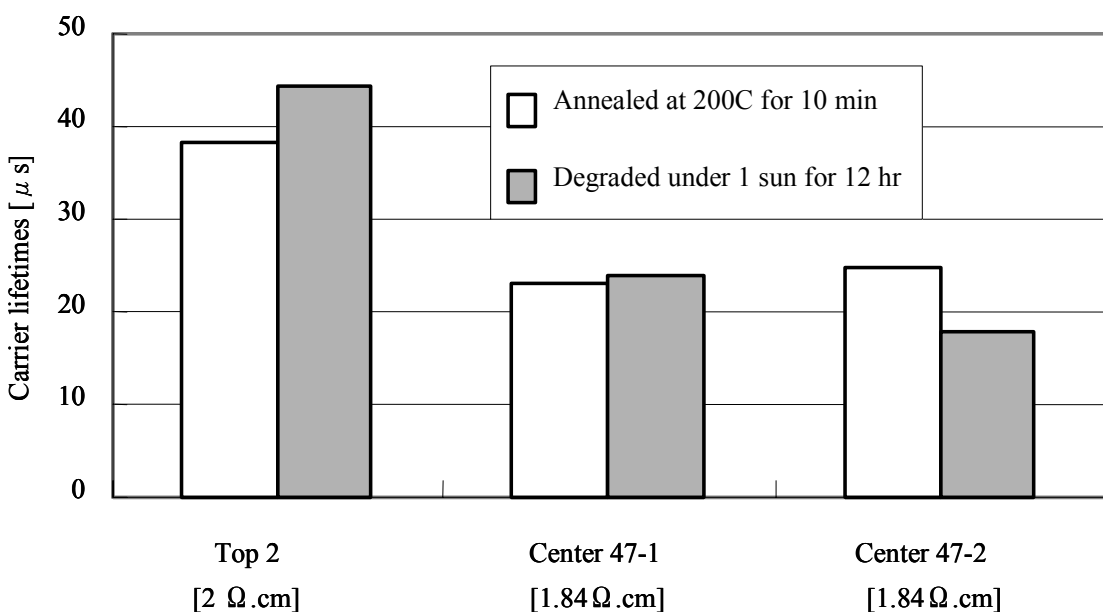


Ingot weight : 3.5 kg, added Ga:0.2 g

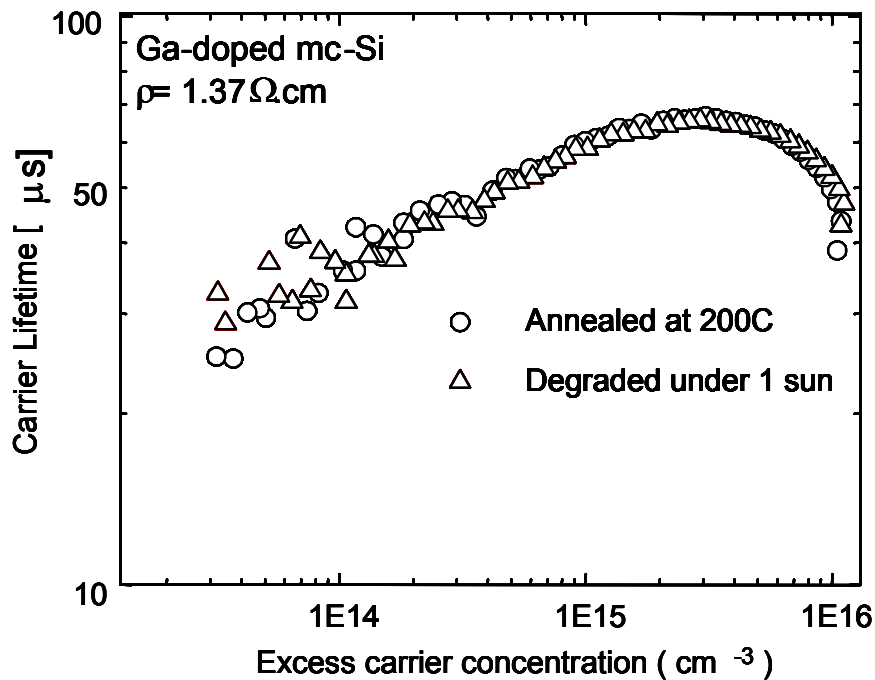
Effect of Surface Removal on Effective Lifetime during Chemical Passivation



Light Degradation of Another Ga-doped Cast Crystals
(Chemical passivation after etching in HNO₃/HF=20/1 for 1 min)



*Carrier lifetime vs. Excess Carrier Concentration
before and after 12 hours illumination for Ga-doped mc-Si
(QSSPC, Sinton Consulting)*



Comparison between Ga and B-doped multicrystalline silicon cast wafers

Dopant	#	$\rho(\Omega \cdot \text{cm})$	Carrier lifetime (μs)			Surface preparation	Reference
			Annealed	Degraded	Ratio*		
B-doped (cast)	0.6	24	15	0.63	CP**	Marwan IEEE (2002)	Takaki (2001)
	0.76	17	11	0.65	CP		
	2.6	70	44	0.63	CP		
	1.6	163	111	0.68	SiN + H ₂		
Ga-doped (cast)	46	1.4	53	51	0.96	CP	Marwan (July 2002)
	47	1.8	25	18	0.72	CP	
	Top2	2.3	38	44	1.16	CP	
	Top1	2.0	47	30	0.64	CP	

* Ratio = degraded / annealed

** CP: chemical passivation after removing a surface layer in an HNO₃/HF solution.

REFERENCES

1. H. Fischer and W. Pschunder, "Investigation of Photon and Thermal Induced Changes in Silicon Solar Cells", Proc. of 10th IEEE Photovoltaic Specialists Conference, pp.404-411 (1973)
2. J. Schmidt, A. Aberle and R. Hezel, "Investigation of Carrier Lifetime Instabilities in Cz-Grown Silicon", Proc. of 26th IEEE Photovoltaic Specialists Conference, 13-18 (1997)
3. S. Glunz, S. Rein, W. Warta, J. Knobloch and W. Wettling, "On the Degradation of Cz-Silicon Solar Cells", Proc. 2nd World Conference on Photovoltaic Solar Energy Conversion, pp.1343-1346 (1998)
4. T. Saitoh, T. Wang, H. Hashigami, T. Abe, T. Igarashi, S. Glunz, W. Wettling, A. Ebong, B. Damiani, A. Rohatgi, I. Yamasaki, T. Nunoi, H. Sawai, H. Ohtsuka, Y. Yazawa, T. Warabisako, J. Zhao and M. Green, "Light Degradation and Control of Low-resistivity Cz-Si Solar Cells", Tech. Digest of 11th International Photovoltaic Science and Engineering Conference, 1999, pp.553-556
5. S. Glunz, S. Rein, H. Knobloch, W. Wettling and T. Abe, "Comparison of Boron- and Gallium-doped p-type Czochralski Silicon for Photovoltaic Application", Progress in Photovoltaics 7 (6) 463-469 (1999)
6. T. Saitoh, H. Hashigami, S. Rein and S. Glunz, "Overview of Light Degradation Research on Crystalline Silicon Solar Cells", Progress in Photovoltaics 8, 537-547 (2000)
7. S. Glunz, S. Rein and J. Knobloch, "Stable Czochralski Silicon Solar Cells using Gallium-Doped Base Material", Proc. of 16th European Photovoltaic Solar Energy Conference, 1-5, 2000
8. A. Takaki, Y. Itakura, H. Hashigami, M. Dhamrin, S. Glunz and T. Saitoh, "Light-induced Lifetime Degradation in Hydrogenated Multicrystalline Cast Silicon Substrates", presented at 17th European Photovoltaic Solar Energy Conference, 2001
9. M. Dhamrin, T. Akihide, H. Hashigami and T. Saitoh, "Light-induced Lifetime Degradation of Commercial Multicrystalline Silicon Wafers", presented at 29th IEEE Photovoltaic Specialists Conference, 2002
10. C. R. Osterwald, A. Anderberg, S. Rummel and L. Ottoson, "Degradation Analysis of Weathered Crystalline Silicon PV Modules", presented at 29th IEEE Photovoltaic Specialists Conference, 2002
11. J. Schmidt, K. Bothe and R. Hezel, "Formation and Annihilation of the Metastable Defect in Boron-doped Czochralski Silicon", presented at 29th IEEE Photovoltaic Specialists Conference, 2002

ACKNOWLEDGEMENT

We would like to appreciate Dai-ichi Kiden Co. for supplying us Ga-doped silicon wafers.

Low-Cost Crystalline Silicon Wafers and Ribbons for Solar Cells (KOSI): A German Research Program

D. Karg¹, G. Hahn², K. Roy³

¹ Universität Erlangen-Nürnberg, Institut für Angewandte Physik, Staudtstr. 7, 91058 Erlangen, Germany

² Universität Konstanz, Fachbereich Physik, Postfach X916, 78457 Konstanz, Germany

³ Beratung Sonnenenergiotechnik, Lisztstr. 7, 74906 Bad Rappenau, Germany

ABSTRACT

The main topics of the German research program KOSI are defects in low-cost crystalline silicon wafers and ribbons, their influence on the performance of solar cells and the possibilities to prevent, getter or passivate them. Further on, the photovoltaic potential and the mechanical properties of the silicon wafers and ribbons are important fields of activity, respectively. The areas of research of the institutes and the contribution of the German photovoltaic industry are outlined. Examples of experimental results of the institutes are given.

INTRODUCTION

The photovoltaic program KOSI (*Kostengünstige kristalline Siliciumscheiben und -folien für Solarzellen* – low-cost crystalline silicon wafers and ribbons for solar cells) is a joint venture of eleven German institutes and three German companies. The program has been started in October 1999 and will be finished in September 2002. It is supported by the German Bundesministerium für Wirtschaft und Technologie. The co-operating institutes, their main areas of research and their main investigation techniques and technologies are:

Fraunhofer-Institut für Solare Energiesysteme, Freiburg (ISE)

- Processing of solar cells by Rapid Thermal Processing (RTP)
- Characterization tools: LBIC, μ -PCD, MFCA, FTIR, IQE

Universität Kiel, Technische Fakultät, Lehrstuhl Materialwissenschaften (UKI)

- Local solar cell characterization by the CELLO-technique
- Local material characterization by the Elymat-technique

Institut für Solarenergieforschung Hameln/Emmerthal (ISFH)

- Processing of solar cells by the MIS n^+ p solar cell process and by the low temperature inversion layer solar cell process.
- Characterization and optimization of hydrogen bulk passivation
- Characterization tools: μ -PCD lifetime mapping, QSSPC lifetime measurement, IQE-Mapping and L_{eff} -mapping

Universität Konstanz, Angewandte Festkörperphysik (UKN)

- Solar cell processing: standard process with flat or mechanically V-grooved surface, $POCl_3$ emitter, H-plasma bulk passivation, P- and Al gettering studies
- Characterization: μ -PCD lifetime mappings, LBIC-, IQE- and L_{eff} -mapping, Hall effect

Max-Planck-Institut für Mikrostrukturphysik (MPI)

- Localization and quantification of shunts in solar cells
- Characterization tools: Lock-in IR thermography, EBIC

Universität Göttingen, IV. Physikalisches Institut (UGÖ)

- Simulation of phosphorus diffusion
- Gettering of defects
- Dissolution kinetics of metal silicide precipitates
- Characterization tools: DLTS, TEM

Institut für Halbleiterphysik - innovations for high performance microelectronics Frankfurt/Oder (IHP)

- Electrical activity of crystal defects
- Characterization tools: EBIC (T), DLTS, PL

Technische Universität Bergakademie Freiberg, Institut für Experimentelle Physik (TUBA)

- Recombination at oxygen containing precipitates and clusters
- Investigations of the mechanical properties
- Characterization tools: LBIC, Scanning Infrared Microscope (SIRM), FTIR, SPV

Universität Erlangen-Nürnberg, Institut für Angewandte Physik (IAP)

- Electrically active defects in solar cells
- Influence of hydrogen treatments
- Characterization tools: DLTS, LBIC, FTIR, Mesadiode Analysis of Solar Cells (MASC), Hall effect

Universität Erlangen-Nürnberg, Institut für Werkstoffwissenschaften, Lehrstuhl für Mikrocharakterisierung (IWW)

- Correlation of the micro structure with the electrical behavior of solar cells
- Investigation of mechanical stress in solar cells
- Characterization tools: Micro-Raman, High Resolution and Analytical Transmission Electron Microscopy, EBIC

Access e.V. Materials and Processes

- Numerical simulation of solar cell processing
- Heat treatment experiments
- Image analysis of microstructure

The industrial partners and their contributions are:

Deutsche Solar GmbH (Bayer Solar GmbH)

- Supply of RGS and Baysix® material.
- RGS (Ribbon Growth on Substrate [1]) is a ribbon material directly grown out of the melt in the required thickness. Due to the fact that the solidification is perpendicular to the pulling direction, the achievable production rate is very high (approx. 10 cm/s).
- Baysix® [2] is a multicrystalline silicon, fabricated by directional solidification of square shaped silicon ingots.

RWE Solar GmbH (ASE GmbH)

- Supply of EFG material and solar cells.
- EFG (Edge defined Film fed Growth [3]) is a ribbon material directly grown out of the melt in the required thickness. The pulling speed is approx. 2 cm/min.

Shell Solar GmbH (Siemens Solar GmbH)

- Supply of TriSi material.
- TriSi (Tri-crystalline silicon [4]) is fabricated by the Cz-Si technology with a tri-crystal seed. In comparison to standard single crystalline Cz-Si, the achievable poly-free growth-rate and the mechanical stability are higher.

In addition, the industry partners contribute material and solar cell data, participate in the critical discussion of the results and analyze the results with respect to a direct process implementation.

TARGETS OF THE PROGRAM

The main targets of the program are:

- Characterization of new silicon materials (EFG under revised pulling conditions, TriSi, RGS) and reference materials (Baysix®, conventional EFG, Cz-Si), respectively.
- Investigation of the photovoltaic potential of the new silicon material.
- Proposals for
 - the decrease of wafer and cell production costs.
 - the improvement of the mechanical properties of the new silicon material.

DEFECTS, PASSIVATION AND GETTERING

Dislocations and grain boundaries

A main source of the lattice defects are the temperature gradients during crystal growth, which lead to mechanical stress and, as a consequence, to dislocations and grain boundaries. According to our investigations, only decorated dislocations are recombination active and thereby decrease the minority charge carrier lifetime and the solar cell efficiency.

A model of Donolato [5] describes the context of diffusion length and dislocation density. By combining this model with PC1D calculations (one-dimensional solar cell simulation program [6]), a correlation between IQE and the dislocation density can be created [7]. One important parameter of this correlation is the normalized dislocation recombination strength Γ (number of recombinations per unit time and length divided by excess charge carrier density and diffusion constant).

Investigations of experimental Baysix® material have shown that the dislocation recombination strength in areas close to the edges of the block is somewhat higher than in the middle of the block. This behavior explains the lower lifetime values of the areas with higher dislocation densities.

In addition, higher dislocation densities very close to the block bottom are associated with IQE-values that are higher than the IQE-values associated with low dislocation densities. This might be a hint for the existence of inversion channels, too (see also subchapter inversion channels). In general, these areas are removed before wafer cutting.

Investigations of the micro structure of TriSi wafers prior and subsequent to diffusion processes at different temperatures have shown that the dislocation density of the outer regions of TriSi wafers increases, if the applied temperature exceeds 1000 °C. This behavior is particularly obvious near to $\Sigma 9$ grain boundaries. Thus, for diffusion temperatures above 1000 °C, adapted conditions are required, especially for heating up and cooling off.

Due to the special growth conditions of EFG material, the carbon concentration is very high. According to TEM investigations, areas with high mechanical stress values have also a high density of twin boundaries. High Resolution Electron Microscopy (HREM) and Electron Diffraction X-Ray (EDX) investigations have shown that the carbon concentration is increased next to twin boundaries of EFG material. This could be an indication that the high mechanical stress values around twin boundaries could be caused by the incorporation of carbon.

Temperature dependent EBIC investigations [8] clearly proved the role of defect contamination for the recombination activity of extended defects in silicon. A model [9] describing the temperature behavior of the dislocation activity, gives quantitative access to the concentration of deep level impurities contaminating the dislocations. Measurements of the EBIC contrast require a low defect density, a condition that is often not fulfilled in mc-Si. For that case, measurements of the diffusion length versus temperature can serve to determine the mean defect activity in a certain area and to estimate the mean defect contamination.

The influence of a remote plasma passivation on the electrical recombination in multicrystalline solar cells has been investigated using different temperatures during the passivation (300 °C to 375 °C). At all investigated temperatures the recombination strengths of the dislocations are reduced, the most effective reduction occurring at the highest temperature. The decrease of the recombination activity at grain boundaries was even higher than at dislocations (up to 20 % increase of the internal quantum efficiency after the remote plasma passivation).

Impurities

There are several sources for impurities in ribbon, block-cast and Czochralski-grown silicon. The feedstock material contains impurities and in some cases even particles, too. The feedstock material is usually completely melted prior to the directional solidification or the crystal growth process. According to their segregation behavior, impurities (e.g. transition metals) are in a minor fraction re-incorporated into the material. Crucible and crucible coating are other impurity sources. In most cases carbon, oxygen, nitrogen and also metals are originating from these sources. Some of the defect sources are known and could be avoided, but sometimes, costs are prohibitive. Some other defects could probably be avoided, if the generation mechanism would be understood. During solar cell processing, the defect structure of the material changes due to the thermal treatments involved in these processes. New impurities, like dopants or gettering and passivating species, are introduced and the defect structure is significantly changed. The basic question is, which types of defects deteriorate the material quality most and which are less important.

In this program, primarily the behavior of chromium was investigated. Chromium is an impurity in some types of silicon crystals that can be introduced by the growing process. At room temperature, in boron-doped silicon, chromium forms the CrB-complex. Therefore, in boron-doped Si, Cr has two defect levels, one in the lower half of the band gap related to the CrB-complex ($E_T - E_V = 270$ meV), and another one in the upper half related to interstitial Cr ($E_C - E_T = 230$ meV) [10]. Due to the low binding energy of $E_B = 0.65$ eV, the complex starts to dissociate at temperatures higher or equal 50 °C.

DLTS and lifetime measurements of specially contaminated EFG material (resistivity: 3 to 5 Ωcm) have shown that the recombination strength of the CrB-complex is higher than that of the interstitial chromium [11]. The formation of the CrB-complex is very slow at room temperature and the dissociation starts at temperatures higher or equal 50 °C. Therefore, the CrB formation is highly sensitive to fluctuations of temperature. Fluctuations of temperature can be caused by e.g. light illumination and fluctuations of the ambient temperature.

Shunts

Shunts in the p-n junction of solar cells mainly decrease the fill factor and the open circuit voltage. This leads to a decrease of the solar cell efficiency. Unfortunately, the highly conductive n^+ -layer of silicon solar cells, acting like an equipotential surface, prevents a direct determination of the local fill factor and the open circuit voltage values.

One way to determine the local fill factor and open circuit voltage values is to measure the I-V characteristic of small diodes (MASC [12]) or small solar cells (MSC [13]) that are subsequently processed on the top of the solar cells. However, these investigation methods destroy the solar cells. Other non destructive, fast and sensitive methods are the Lock-in Thermography [14] and the CELLO-technique

[15]. By Lock-in Thermography, the local warming of solar cells on forward and reverse current is measured. For example, Lock-in Thermography investigations of RGS- and EFG-based solar cells have shown that after H-passivation, the forward dark current is decreased (EFG, RGS) and the deleteriousness of shunts is reduced (RGS).

The CELLO-technique (Solar CEL LOcal characterization) is an advanced LBIC measurement for the local characterization of solar cells. With the help of an extremely stable potential/current source the linear response to a local illumination is measured. Thereby, e.g. the local serial resistance, shunt resistance and open circuit voltage values can be determined.

From Lock-in Thermography and CELLO-technique, it is known that most of the shunts in solar cells are located close to the wafer edges. The reasons of the edge shunts are e.g. overlapping p-n junctions, sawing damage or crystal defects. A possibility to reduce the edge shunts, developed in this program, is applying liquid KOH to the edges and subsequently local heating [16].

Inversion channels

Some RGS based solar cells show very high short circuit current values. Nevertheless, the fill factor and open circuit voltage values are low. Furthermore, the apparently high diffusion length values do not match with the low lifetime values. These discrepancies can be explained by areas in the p-type bulk material, which show n-type conductivity and, therefore, are called inversion channels. The areas behave like an additional current collecting emitter. According to EBIC measurements, TEM and SIMS studies as well as etch experiments performed in this program, inversion channels are mainly caused by continuously decorated dislocations [17] [18]. Currently it is checked, whether it is possible to process solar cells on RGS material, having high short circuit current values and not too bad fill factor and open circuit voltage values.

Passivation using PECVD SiN_x

In the literature a model is proposed [19], which relates the high rates of passivation at temperatures above 700 °C to the release of hydrogen from the SiN_x-film, the injection of vacancies from backside Al alloying, and the retention of hydrogen at defect sites. To check, whether the concentration of vacancies in silicon does change during high temperature treatments, the concentration of vacancies was determined by the platinum diffusion method [20]. According to the achieved results, the following can be stated:

- There is no indication that vacancies are formed or annihilated during Al alloying of EFG material.
- By the platinum diffusion method, it is not possible to verify or exclude, whether vacancies can dissociate H₂-molecules or not.
- In comparison to Baysix® ([Vac] < 10¹² cm⁻³) and TriSi material ([Vac] ≈ 3 × 10¹² cm⁻³), the vacancy concentration is generally higher in EFG material ([Vac] ≈ (1-2) × 10¹³ cm⁻³). This could be the reason for the fast and very effective hydrogen passivation of EFG material.

In addition, non-conservative Ostwald ripening of extrinsic dislocation loops [21] [22] has been used to study vacancy injection from liquid Al:Si alloys. It could be concluded that no substantial vacancy injection occurred due to the presence or formation of the Al:Si melt since the ripening behavior of loops in uncovered silicon samples was practically the same.

Gettering

Gettering steps are very important for the improvement of the mc-Si wafers during solar cell processing. It could be clearly shown that highly doped P- and Al-layers can drastically improve the solar cell efficiency [23]. According to experimental investigations and simulations on Baysix®, Cz-Si and FZ-Si

material with different oxygen concentration, the gettering effect of e.g. cobalt is reduced at temperatures lower than 860 °C, if the oxygen concentration is high. This behavior is probably caused by oxygen-related defects, which prevent the cobalt to diffuse to the gettering layer.

Investigations of the gettering behavior of EFG material have shown that the charge carrier lifetime after hydrogen passivation can degrade under illumination [24], if the EFG material is not gettered prior to the hydrogen passivation [23] [24].

MECHANICAL PROPERTIES

Due to high temperature gradients during some crystal growth processes, the materials are mechanically stressed. Mechanical stress not only leads to dislocations and grain boundaries, but in extreme cases also to wafer cracks before and during solar cell processing. Residual stress in silicon causes a change of the elastic constants of the atoms and thereby leads to a change of the phonon and Raman frequencies. According to our Micro-Raman-Spectroscopy investigations, a complex stress distribution exists around the origin of regions in Baysix® ingots having a higher dislocation density. The maximum local mechanical stress differences in these regions are approximately 120 MPa.

The residual mechanical stress in EFG material is very high at the branching point of grain boundaries and in regions of a high density of twins. The difference of the local stress values can exceed 200 MPa. In contrast to EFG and Baysix material, TriSi material shows no local mechanical stress differences [25].

SOLAR CELL PROCESSING

One of the main tasks of the solar cell processing institutes ISE, ISFH and UKN is to check the photovoltaic potential of Baysix®, RGS, EFG and TriSi material, which can be achieved by using the following cell processing schemes:

- Rapid Thermal Processing (RTP) [26]
- MIS n⁺p Emitter [27]
- MIS Inversion Layer [28]
- Standard process with flat or mechanically V-grooved surface [29]

The highest efficiencies, obtained with the different standard process steps on Baysix®, EFG, RGS and TriSi material, are shown in table 1.

Rapid Thermal Processing (RTP)

The thermal budget (the integral of temperature over time) of solar cell processing can be considerably decreased by RTP processing. Therefore, by RTP processes, it may be possible to enhance the cell throughput, improve process control and save floor space. In this program, it is investigated, whether solar cells based on RGS, EFG and Baysix® can benefit from replacing the well established conventional quartz tube furnace diffusion by RTP.

By this replacement, it was managed to achieve an average solar cell efficiency of 8.4% in case of RGS and of 13.1% [30] in the case of EFG [30]. In the case of Baysix®, a deterioration and broadening of lifetime distribution due to RTP [31] was observed. With increasing diffusion temperature the average lifetime mainly decreases in the grain boundary regions and above 900 °C it drops below the initial lifetime. The reasons for this behavior are not understood up to now.

Table 1: Best efficiencies of differently processed solar cells based on Baysix®, EFG, RGS and TriSi material.

Solar cell process	Baysix®	EFG	RGS	TriSi
RTP	15.0%	14.9% [29]	9.0% [29]	-
MIS-IL	13.8%	12.0%	-	14.4%
MIS n ⁺ p	-	-	-	17.6%*
Standard process, flat surface	16.4%	15.3%	11.8% [28]	17.5%
Standard process, V-grooved surface	-	-	12.5%** [28]	-

* independently confirmed at FhG-ISE, Freiburg, ** independently confirmed at JRC Ispra

ACKNOWLEDGEMENT

This work is supported by the German Bundesministerium für Wirtschaft und Technologie under contract number 0329858 (Program KoSi).

References

- [1] H. Lange, I. A. Schwirtlich, *J. Crystal Growth* **104**, 108 (1990)
- [2] W. Koch, W. Krumbe, I. A. Schwirtlich, Proc. 11th EC PVSEC, Montreux, 518 (1992)
- [3] J. P. Kalejs in: *Silicon Processing for Photovoltaics*, Vol. II. Eds. C. P. Khattak, K. V. Ravi (Elsevier Amsterdam 1987) ch. 4
- [4] A. L. Endrös, R. Einzinger, G. Martinelli, Proc. 14th EC PVSEC, Barcelona, 112 (1997)
- [5] C. Donolato, *J. Appl. Phys.* **84**, 5 (1998)
- [6] P. A. Basore, D. A. Clugston, Proc. 25th IEEE PVSC, Washington, 377 (1996)
- [7] A. Lawerenz, M. Rinio, S. Riedel, M. Ghosh, M. Werner, H. J. Möller, Proc. 16th EC PVSEC, Glasgow, 1116 (2000)
- [8] M. Kittler, C. Ulhaq-Bouillet, *J. Appl. Phys.* **78**, 4573 (1995)
- [9] V. Kveder, M. Kittler, W. Schröter, *Phys. Rev. B* **63**, 115208 (2001)
- [10] H. Conzelmann, K. Graff, E. R. Weber, *Appl. Phys. A* **30**, 169 (1983)
- [11] O. Klettke, D. Karg, G. Pensl, M. Schulz, G. Hahn, T. Lauinger, Technical Digest of 12th International PVSEC, Jeju, 617 (2001)
- [12] C. Häßler, S. Thurm, W. Koch, D. Karg, G. Pensl, Proc. 13th EC PVSEC, Nice, 1364 (1995)
- [13] R. Baldner, H. Lautenschlager, C. Schetter, R. Schindler, W. Warta, Proc. 25th IEEE PVSC, Washington, 641 (1996)
- [14] O. Breitenstein, M. Langenkamp, K. R. McIntosh, C. B. Honsberg, M. Rinio, Proc. 28th IEEE PVSC, Anchorage, 124 (2000)
- [15] J. Carstensen, G. Popkirov, J. Bahr, H. Föll, Proc. 16th EC PVSEC, Glasgow, 1627 (2000)
- [16] M. H. Al-Rifai, J. Carstensen, H. Föll, Proc. 17th EC PVSEC, Munich, 1424 (2001)
- [17] G. Hahn, D. Sontag, C. Hässler, *Solar Energy Materials And Solar Cells* **72**, 453 (2002)
- [18] J. P. Rakotoniaina, O. Breitenstein, M. Langenkamp, M. Werner, G. Hahn, Proc. 17th EC PVSEC, Munich, 1444 (2001)
- [19] V. Yelundur, A. Rohatgi, J.-W. Jeong, A. M. Gabor, J. I. Hanoka, R. L. Wallace, Proc. 28th IEEE PVSC, Anchorage, 91 (2000)
- [20] M. Jakob, P. Pichler, H. Ryssel, R. Falster, *J. Appl. Phys.* **82**, 182 (1997)
- [21] J. K. Listaberger, K. S. Jones, J. A. Slinkman, *J. Appl. Phys.* **73**, 4815 (1993)
- [22] Y.-L. Huang, M. Seibt, B. Plikat, *Appl. Phys. Lett.* **73**, 2956 (1998)
- [23] P. Geiger, G. Kragler, G. Hahn, P. Fath, E. Bucher, Proc. 17th EC PVSEC, Munich, 1715 (2001)
- [24] L. Mittelstädt, S. Dauwe, A. Metz, R. Hezel, Proc. 17th EC PVSEC, Munich, 1311 (2001)
- [25] M. Becker, H. P. Strunk, to be published
- [26] S. Peters, H. Lautenschlager, W. Warta, R. Schindler, Proc. 16th EC PVSEC, Glasgow, 1116 (2000)
- [27] A. Metz, R. Hezel, Proc. 26th IEEE PVSC, Anaheim, 283 (1997)
- [28] K. Jäger, R. Hezel, *IEEE Trans. Electron. Devices* **ED-32**, 1824 (1985)
- [29] G. Hahn, C. Haessler, M. Langenkamp, Proc. 17th EC PVSEC, Munich, 1371 (2001)
- [30] S. Peters, C. Ballif, D. B. Borchert, V. Radt, R. Schindler, W. Warta, G. Willeke, C. Hässler, T. Lauinger, Proc. 17th EC PVSEC, Munich, 1319 (2001)
- [31] S. Peters, J. Y. Lee, C. Ballif, D. B. Borchert, S. W. Glunz, W. Warta, G. Willeke, Proc. 29th IEEE PVSC, New Orleans, 1814 (2002)

Front-side surface recombination analysis of 18%-efficient multicrystalline silicon solar cell

Yuji Komatsu, Yoshiro Takaba, Shuji Yasukawa, Satoshi Okamoto, and Masafumi Shimizu

Ecological Technology Development Center, SHARP Corporation,

282-1, Hajikami, Shinjo-cho, Kitakatsuragi-gun, Nara, 639-2198, JAPAN

tel: +81-745-65-1161, fax: +81-745-62-8254, e-mail: komatsu.yuji@sharp.co.jp

1. Introduction

Multicrystalline silicon (mc-Si) solar cell has been occupying more than a half part of the market of solar cells in these several years¹⁾. This superiority is expected to be also continued hereafter, because the one with the reasonable efficiency can be easily produced with moderate costs. On the other hand, the efficiency of mc-Si solar cell still stays inferior to that of monocrystalline silicon (c-Si) solar cell by several points, though its potential is as high as c-Si's. Therefore, the attempt to raise the efficiency of mc-Si solar cell is important, and the impact will be large when the attempt is successfully industrialized.

The typical efficiency of the factory product of mc-Si solar cell is about 14%. In the research trials, the efficiency of 19.8 % was recorded for 1cm² cell²⁾, 18.6% for 4cm² cell³⁾, and 17.4% for 25cm² cell⁴⁾. There is an efficiency gap between the factory product and the research results, and the efficiency over 18% for the area over 10 cm² has not been reported yet.

In this study, the development of device process is carried out with the project to attain high efficiency with a large-area mc-Si solar cell, under the support of NEDO. As a halfway result, the efficiency of 18.3% was attained for the area of 25 cm², using the substrate fabricated by Kawasaki Steel Corporation⁵⁾, which is also supported by NEDO under the same project.

In this paper, the analysis of the cell property is carried out focusing on the surface recombination velocity (SRV) of the front side. A prospect of the further improvement of the efficiency is also discussed.

2. Cell Structure and Characteristics

Figure 1 shows the schematic configuration of the mc-Si solar cell in this study. The p-type substrate which is fabricated by Kawasaki Steel Corporation⁵⁾ was used. The substrate has long diffusion length (L_e) of minority carrier in spite of low resistivity (ρ_s). L_e measured by surface photovoltage method is over 200 μm , and ρ_s is 0.7 $\Omega\cdot\text{cm}$.

For the front side of the cell, the surface was randomly textured using alkaline etchant. The front n⁺ layer was fabricated with phosphorus diffusion. The sheet resistance of the layer was 110 Ω/sq . A silicon nitride (SiN_x) film was deposited on the layer using plasma enhanced chemical vapor deposition. On the rear side, back surface field (BSF) was built in using a p⁺-layer with aluminum diffusion, and an aluminum contact was fabricated. The front fine line contact was fabricated through vacuum evaporation and photolithography. The dimension of the cell is 5 cm x 5 cm, and the thickness is 300 μm . Table I summarizes these device parameters.

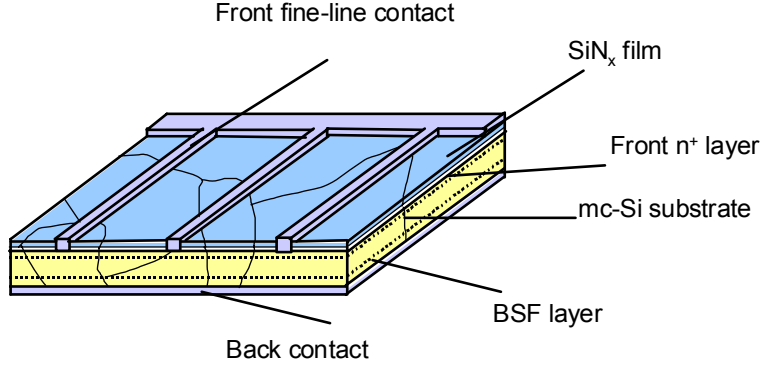


FIG1. Schematic configuration of the mc-Si cell.

Table I: Typical device parameters of the mc-Si solar cell in this study.

Substrate Resistivity	$0.7 \Omega\text{-cm}$
Carrier Lifetime	$20 \mu\text{s}$
Dffusion Length	$220 \mu\text{m}$
Front sheet resistance	$100 \Omega/\text{sq.}$
BSF sheet resistance	$15 \Omega/\text{sq.}$

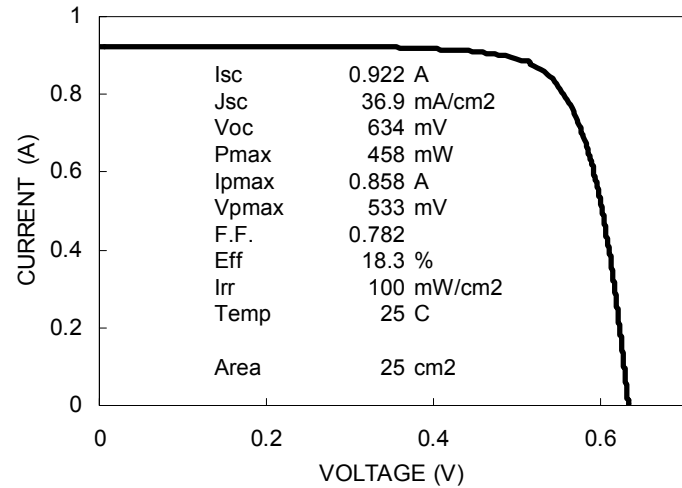


FIG2. Current-voltage characteristics of the mc-Si solar cell with the high efficiency of 18.3%.

Figure 2 shows the current-voltage characteristics of the cell with the highest efficiency. The efficiency of 18.3% was attained under the illumination of AM1.5, 100mW/cm^2 . The open circuit voltage (Voc) and the short circuit current density (Jsc) were 634 mV , 36.9 mA/cm^2 , respectively. The efficiency over 18% is the first report for the large size solar cell with the area over 10 cm^2 .

This result was obtained through several kinds of investigations into the cell process improvements in conjunction with the mc-Si substrates. In the discussion so far, analyses are attempted to reveal what kind of the improvements contributed to the high efficiency, especially attending to the surface recombination velocity (SRV) of the front side.

3. Analysis

3.1 c-Si solar cell

Preceding the analysis of mc-Si solar cells, SRV of high efficiency c-Si solar cells were analyzed based on the results obtained through our development in which the efficiency of 23.5% had been obtained for 25 cm^2 c-Si solar cell⁶⁾. In the development, a breakthrough was made in the improvement of the front SRV.

In the development of the c-Si solar cells⁶⁾, two kinds of front diffusion processes were examined.

Table II: Values of sheet resistance and solar cell characteristics through three different processes in c-Si solar cell analysis.

Process	sheet resistance (mA/cm ²)	J _{sc} (mA/cm ²)	V _{oc} (mV)	FF	Eff (%)
A	120	40.2	695	0.779	21.8
B	110	40.3	679	0.784	21.4
Optimized	120	41.1	694	0.823	23.5

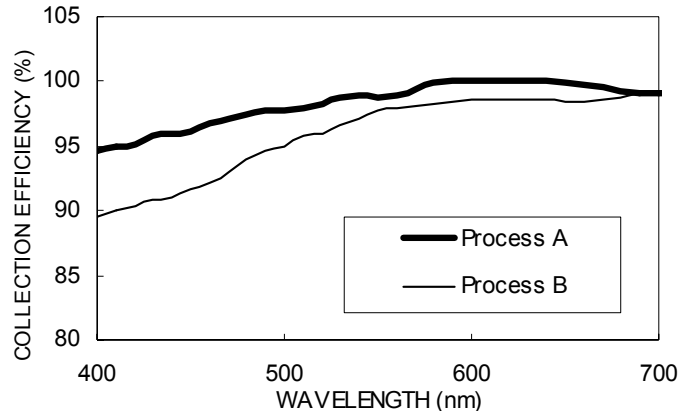


FIG. 3. Spectral collection efficiencies for the cells fabricated through processes A and B in c-Si cell analysis.

Table II shows the values of the sheet resistance and the solar cell characteristics through these two different processes, named process A and process B. Between these processes, the values of sheet resistance are controlled to be 110-120 Ω/sq., but the doping profiles are different. The V_{oc} of process A became 16 mV higher than that of process B. The process A was adopted into the optimized process with a large fill factor, and 23.5% was obtained in consequence of the improvement of the V_{oc}.

Figure 3 shows the spectral collection efficiencies of the cells fabricated through processes A and B. The collection efficiencies of the process A get higher than those of B in the range of 400-550 nm. In order to estimate the value of the front SRV, these values of spectral collection efficiencies were numerically simulated using PC-1D⁷⁾ with the device parameters for both processes A and B.

Figure 4 shows the comparisons of the measured and simulated results. In Fig. 4(a), the measured curve for process A and three simulated curves are drawn when SRV S = 1000, 5000, and 20000 cm/s. The most similar simulated curve to the measured one is when S = 5000 cm/s. In Fig. 4(b) for process B, simulated curves for S = 10000, 30000, and 100000 cm/s are drawn with the measured one, and it is the most similar when S = 30000 cm/s. This analysis suggests the SRV of process B is about 6 times larger than that of A.

The values of the front SRV were estimated in another point of view, using PC-1D by simulating V_{oc}. Figure 5 shows the front SRV dependence of the simulated V_{oc}. Each curve is calculated using the device parameters for each process. Except the profile of the n⁺-layer, same set of the device parameters was used for each curve. For both curves, the values of V_{oc} are shown to be

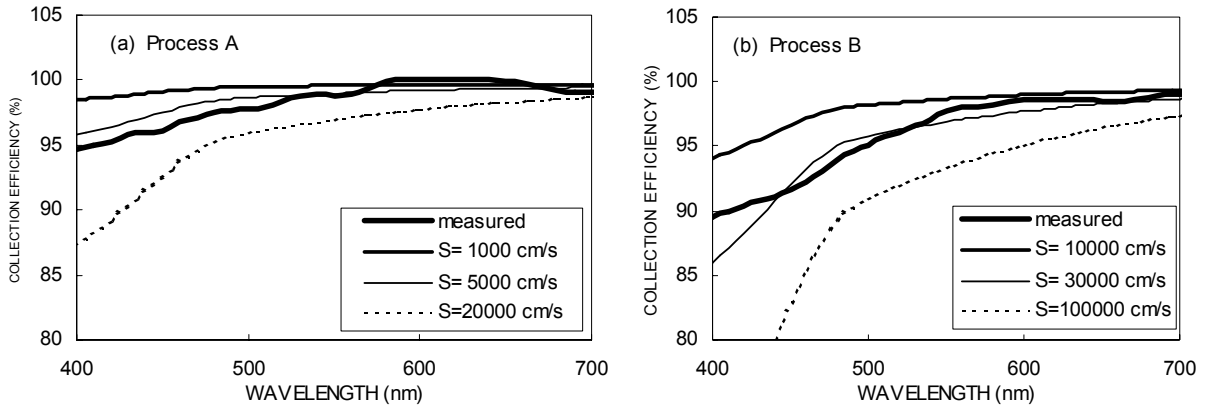


FIG. 4. Comparisons of the spectral collection efficiencies of the measured and simulated values.
(a) The measured curve for process A can be approximated to the simulated one when $S = 5000 \text{ cm/s}$.
(b) For process B, it can be approximated to when $S = 30000 \text{ cm/s}$.

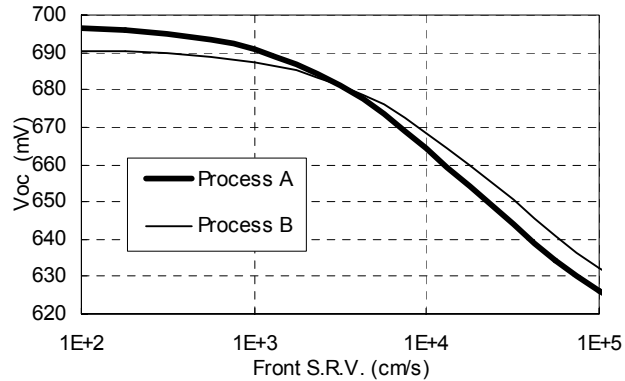


FIG. 5. Front SRV dependence of Voc for processes A and B in c-Si solar cell analysis. Adopting the Voc values of 695 mV for process A and 679 mV for process B, the values of the front SRV are fitted to be 800 cm/s and 4000 cm/s, respectively.

Table III: Simulated results of the front SRV. S1: calculated from spectral collection efficiency. S2: calculated from Voc . The rates $S1/S2$ are also described.

	Front S.R.V. (cm/s) calculated from collection efficiency (S1)	Voc (S2)	$S1/S2$
Process A	5000	800	6.25
Process B	30000	4000	7.5

reduced with the increasing SRV when $S > 10^3 \text{ cm/s}$. Adopting the Voc values of 695 mV for process A and 679 mV for process B, the front SRV are fitted to be 800 cm/s and 4000 cm/s, respectively.

Table III summarized the simulated results of the front SRV from different point of view. The SRV values estimated from the spectral collection efficiency (S1) do not correspond to those estimated from the Voc (S2), but the rates of $S1/S2$ are almost equal between processes A and B. In the analysis so far, this rate is considered to indicate the standard relationship between these two approaches, and it will be utilized for the simulation of mc-Si solar cell.

Table IV: Substrate properties, sheet resistance, and the cell characteristics of the mc-Si solar cell fabricated through the processes C, D, and C'.

Process	substrate	substrate resistance ($\Omega\text{-cm}$)	diffusion length (μm)	sheet resistance ($\Omega/\text{sq.}$)	Jsc (mA/cm ²)	Voc (mV)	F.F.	Eff. (%)
C	conventional	1.6	180	110	36.9	617	0.756	17.2
D	conventional	1.6	180	80	36.3	612	0.762	16.9
C'	Kawasaki St.	0.7	220	110	36.9	634	0.782	18.3

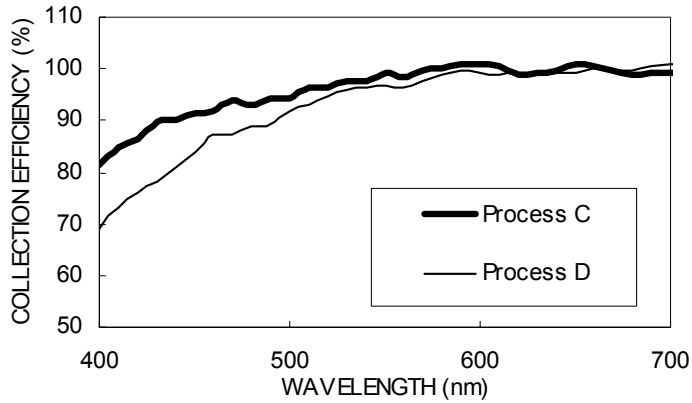


FIG. 6. Spectral collection efficiencies for the cells fabricated through processes C and D in mc-Si solar cell analysis.

3.2 mc-Si solar cell

In the analysis of the mc-Si solar cell, two kinds of front diffusion processes were examined, like in the case of the c-Si solar cell. Table IV shows the solar cell properties fabricated through these processes C, D, and C'. For processes C and D, the substrates fabricated by conventional cast method were used. The sheet resistance of process C is 110 $\Omega/\text{sq.}$, and that of process D is 80 $\Omega/\text{sq.}$, which is the only difference for the cell fabrication between the processes C and D. The value of Voc by process C was 5 mV higher than that by process D.

For the process C', the substrate fabricated by Kawasaki Steel⁵⁾ was used, and the cell fabrication processes are same as the process C. The value of Voc was 17 mV higher than that of process C.

Figure 6 shows the spectral collection efficiencies for the cells fabricated through processes C and D. The collection efficiencies of the process C became higher than those of D in the range of 400-500 nm. In the same way described in the analysis for c-Si solar cell, these values of collection efficiencies were numerically simulated using PC-1D in order to estimate the front SRV. Figure 7 shows the comparison of the measured and simulated results. In Fig. 7(a) for process C, the measured and three simulated curves are drawn when $S = 5 \times 10^4$, 2×10^5 , and 1×10^6 cm/s. The most similar simulated curve to the measured one is when $S = 2 \times 10^5$ cm/s. In Fig. 7(b) for process D, three simulated curves when $S = 1 \times 10^5$, 5×10^5 , 2×10^6 cm/s are drawn with the measured one, and it is the most similar when $S = 5 \times 10^5$ cm/s. This analysis suggests the front SRV of process C is about 2.5 times larger than that of D.

This result suggests that the passivating condition of the front surface in the process C is superior

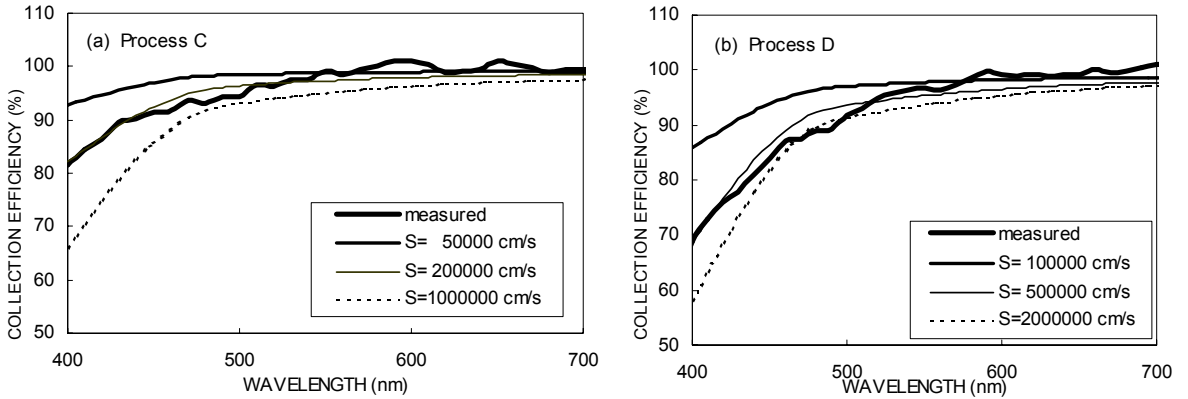


FIG. 7. Comparison of the spectral collection efficiencies of the measured and simulated values. (a) The measured curve for process C can be approximated to the simulated one when $S = 200000$ (2×10^5) cm/s, and (b) for process B, it can be approximated to when $S = 500000$ (5×10^5) cm/s.

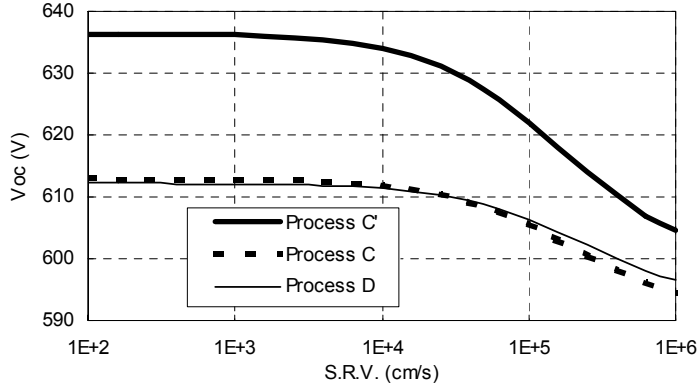


FIG. 8. Front SRV dependence of V_{oc} for processes C, D, and C' in mc-Si solar cell analysis. Applying the SRV values calculated in Fig. 7 divided by the approximate value of S_1/S_2 (~7) in Table III, $S_2=3 \times 10^4$ for processes C and C', and $S_2=7 \times 10^4$ for process D, the V_{oc} differences among C' (634 mV), C (617 mV), and D (612 mV) coincide with the results from Table IV.

to that of D. The SiN_x film on the n^+ -layer were deposited with the same process, therefore the difference in the passivating conditions is supposed to originate in the difference in the values of the sheet resistance. In other words, it was suggested that it is possible to reduce the front SRV by raising the sheet resistance of the front n^+ -layer.

The values of V_{oc} were also simulated by PC-1D for the processes C, D, and C'. Figure 8 shows the front SRV dependence of the simulated V_{oc} . The values of V_{oc} for processes C, D, and C' were calculated through the estimated SRV values in Fig. 7 divided by 7 which was the approximate value of S_1/S_2 in Table III. In Fig. 8, applying the SRV values of 3×10^4 cm/s for processes C and C', and 7×10^4 cm/s for process D, the V_{oc} differences among C', C, and D coincide with the results from Table IV. It can be concluded that the estimation of Fig. 8 was ensured to be proper through these comparisons.

The followings were shown in Fig. 8: The V_{oc} difference between the processes C and D is little when those SRV are almost equal. When $\text{SRV} > 1 \times 10^4$ cm/s, the reduction of SRV contributes much to the improvement of V_{oc} . For process C', V_{oc} can be further improved with lowerering SRV.

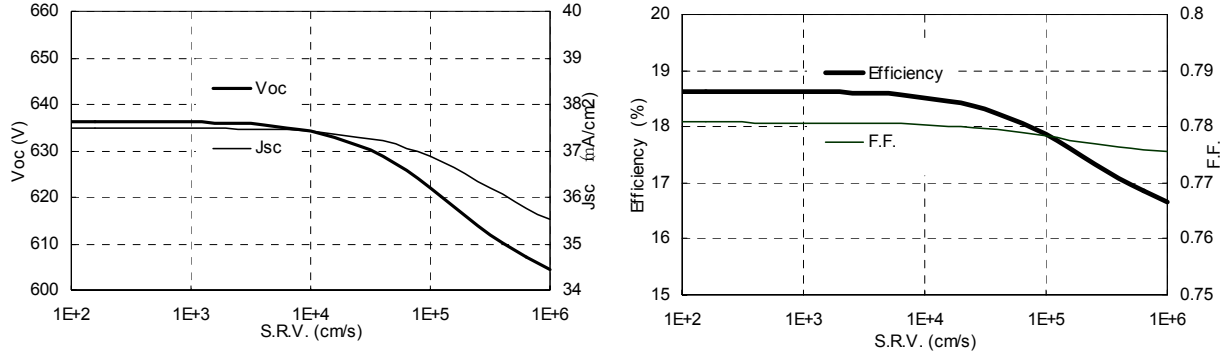


FIG. 9. SRV dependence of the solar cell characteristics simulated by PC-1D using the device parameters of the 18.3% cell shown in Table I.

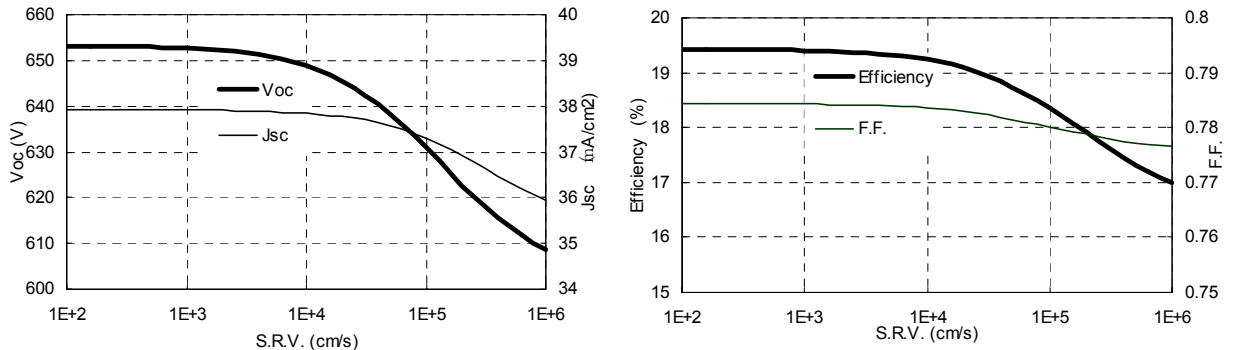


FIG. 10. SRV dependence of the solar cell characteristics in the case that the substrate quality is improved more with the resistivity of 0.5 Ωcm and the diffusion length of 300 μm.

4. Discussion

Figure 9 shows the SRV dependence of the solar cell characteristics simulated by PC-1D using the device parameters of the 18.3% cell shown in Table I. On the assumption that the front SRV of the fabricated cell is 3×10^4 cm/s, V_{oc} can be improved by 2-3 mV, and the efficiency can be improved by 0.3-0.4 points, with reducing the SRV to be less than 8×10^3 cm/s.

As the method to reduce the front SRV, the improvement of the film quality of SiN_x is the one possibility. As the other possibility, raising the sheet resistance is considered. But it is accompanied by the reduction of the surface doping density, which makes the formation of the ohmic contact difficult. Applying the selective emitter structure with highly doped area just beneath the contact, sheet resistance beneath the SiN_x can be raised, and the reduction of SRV is expected.

In the case that the substrate quality is more improved with the lower resistivity of 0.5 Ω-cm and the longer diffusion length of 300 μm, the SRV dependence of the cell characteristics can be calculated as Fig. 10. V_{oc} is improved to 640 mV and the efficiency is 18.6% if the SRV stays present value of $3 \sim 7 \times 10^4$ cm/s. Furthermore, V_{oc} can be improved to 653 mV and the efficiency can be 19.5% if the SRV can be also improved to be less than 3×10^3 cm/s, which suggests that the role of the SRV improvement is more important for higher-quality substrates.

Moreover, J_{sc} will be 2-3% increased if the light trapping structure like the honeycomb surface²⁾

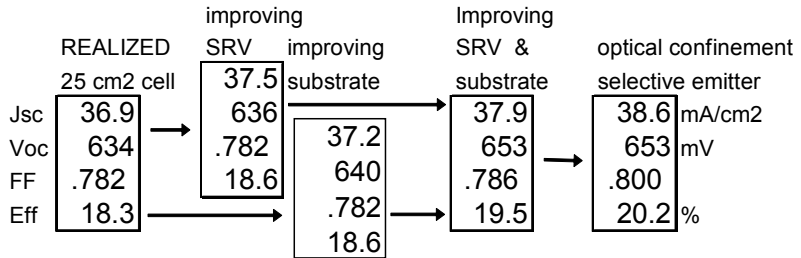


FIG. 11. Further improvements of the mc-Si solar cell characteristics.

is introduced. The selective emitter structure also has an effect to improve the fill factor because it reduces the series resistance. Considering these effects, the efficiency over 20% can be expected. Figure 11 summarizes the further improvements of the mc-Si solar cell characteristics.

Considering that the efficiency of 18.3% was realized for 25cm² cell, these improvements can be realized for the same size of the cell.

5. Conclusions

A multicrystalline silicon (mc-Si) solar cell with the efficiency of 18.3% with the area of 25 cm² was fabricated, using the substrate with the resistivity of 0.7Ω-cm and the diffusion length of 220 μm fabricated by Kawasaki Steel Corporation⁵⁾. An analysis of the solar cell characteristics was carried out, focusing on the surface recombination velocity (SRV) of the front side, applying the analyzed results of the high-efficiency monocrystalline silicon solar cells. Consequently, the front SRV of the mc-Si cell with 18% efficiency could be estimated to be 3x10⁴ cm/s. The efficiency is expected to be improved to 18.6% with the SRV reduction to 8x10³ cm/s. For the method to reduce the front SRV, raising the sheet resistance was nominated as a realistic method.

Furthermore, the guideline to improve the efficiency over 20% was displayed. To realize the efficiency over 20%, the selective emitter and the optical confinement structure should be introduced to the cell process, besides the quality improvement of the substrate.

Acknowledgment

This work was supported by the New Energy and Industrial Technology Development Organization (NEDO), as a part of the New Sunshine Program under the Ministry of Economy, Trade and Industry (METI), Japan.

References

- 1) PV News: No.2 and 3. (2002)
- 2) J. Zhao, *et al.*: Appl. Phys. Letters **73** (1998), 1991.
- 3) A. Cuevas, *et al.*: IEEE Transactions on Electron Devices, **ED-46** (1999) 2026.
- 4) H. Lautenschlager, *et al.*: Proc. of 26th IEEE Photovoltaic Specialists Conference (1997) 7.
- 5) S. Nara *et al.*: This workshop.
- 6) S. Okamoto, *et al.*: Proc. of 26th IEEE Photovoltaic Specialists Conference (1997) 255.
- 7) D. A. Clugston, *et al.*: Proc. of 26th IEEE Photovoltaic Specialists Conference (1997) 207.

Review on PV Low Concentration Devices

Carlos del Cañizo

Instituto Energía Solar – Universidad Politécnica de Madrid

ETSI Telecomunicación, Ciudad Universitaria, s/n. 28040 Madrid

Tel 34 91 544 10 60, Fax 34 91 544 63 41, e-mail: canizo@ies-def.upm.es

Abstract

This paper reviews the state of the art of static concentration, discussing its properties and its possibilities to become a real alternative for PV cost reduction. First, the principles of concentration are presented, stressing the fact that to be able to cast rays from a wide variety of directions, levels of concentration are limited to low values. Then, solar cell technologies for these ranges of illumination are evaluated, paying special attention to bifacial cells, of which there are some technologies close to industrialisation. A look is taken at some concentrator designs, highlighting their characteristics, and in particular to the PV Venetian prototype, a static concentrator for building integration in façades which reaches a concentration of 4.3, and whose cost is estimated in 2.02 €/Wp. The review finishes with some arguments that justify the advantages of static concentration for building integration applications, and also its feasibility for medium- and small-sized systems.

Introduction

Photovoltaic concentration reduces the need of solar cells by means of an optic system (a “concentrator”) that collects the incoming light and redirects it to a smaller solar cell. As solar cells are expensive devices and optic systems are much cheaper, a cost reduction of the PV system is expected. Indeed, concentration has always claimed to be an alternative for PV cost reduction.

Many research and demonstration activities have been performed to assess a wide variety of PV concentration technologies, but until now none of them has got to the point of becoming a real commercial product. Main reasons can be found in the difficulty of competing with traditional sources for large or medium-sized plants, and the lack of concentration cells, which are rarely available and at a high price due to the small market. Meanwhile, flat-plate technology has experienced a tremendous growth, both for stand-alone or grid-connected systems, but only in small scale applications.

Among PV concentration technologies that of static concentrators is the simplest one, quite similar to flat-plate technology because they also collect diffuse light and need no tracking, while saving some silicon. However, the levels of concentration a static concentrator can achieve are low, and so the question arises whether it is worth to develop such systems.

This paper reviews the state of the art of low concentration devices. First, the principles of concentration are presented, discussing the limits attainable by static concentration. Then, solar cell technologies for these ranges of illumination are evaluated, and concentrator designs shown. The review finishes with some arguments on the applications where static concentration can be competitive.

Principles of PV concentration

Optical concentration C_{opt} is defined as the ratio between the irradiance incident on the cell and that incident on the module aperture. It is always less than geometrical concentration C_g (the ratio between the concentrator aperture area and the solar cell area) due to the fact that the concentrator does not collect all the rays coming from the sky, and also due to optical losses in the concentrator itself.

Classic means of mapping remote points in the sky is to draw a sphere of radius unity (celestial sphere) with the concentrator in the centre (see Figure 1.a). The rays emitted by a point in the sky correspond to a direction of parallel rays incident on the concentrator, and so they are determined by the direction cosines p , q and r (related by $p^2+q^2+r^2=1$, so that only two of them are independent). The portion of the sky “seen” by the concentrator can be projected in the plane of the concentrator aperture, drawing a circle of radius unity where each point corresponds to a ray direction (p,q) . Figure 1.b shows this plane, called pq plane, and the projection of rays in an arbitrary instant, where three regions corresponding to solar beam, diffuse and albedo rays can be distinguished. The region A_p of rays collected by the concentrator is represented for axisymmetric concentrators that accept the rays that come within a cone of semiangle α (acceptance angle) with respect to the normal to the pq plane.

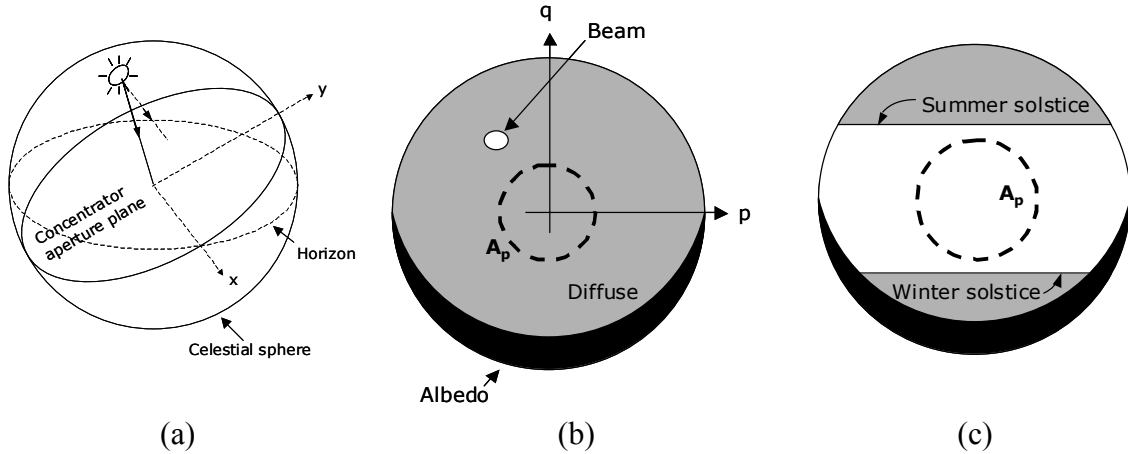


Figure 1. (a) Celestial sphere showing the projection of sun rays in the plane of the concentrator aperture. (b) pq plane for an arbitrary instant. (c) Sketch of pq plane for a static concentrator oriented to the equator and tilted an angle equal to the latitude.

So the target will be to design a concentrator able to collect as many rays as possible (and as energetic as possible) in a cell as small as possible. However, there is a limit imposed by the theorem of conservation of étendue, derived from the Second Law of Thermodynamics, that states that the maximum achievable concentration, when a medium of index of refraction n surrounds the receiver, is

$$C^{\max} = \frac{\pi n^2}{A_p} = \frac{n^2}{\sin^2 \alpha} \quad (1)$$

where the last equality only holds for axisymmetric concentrators. This limit can only be reached for isotropic illumination at the receiver [1].

Eq. (1) sets a limit to the achievable concentration for a given acceptance angle. For example, to reach $C^{max}=10$ the maximum acceptance angle of an axisymmetric concentrator is 18° , while for $C^{max}=100$ it reduces to 6° , assuming in both cases $n=1$ (air).

This trade-off between level of concentration and acceptance angle is responsible of the different strategies that we can plan:

-To reach high concentration levels, acceptance angle should be quite low, and to guarantee that the more intense beam rays are collected we need to track the system in 2-axes, so that the system points at the sun at any moment.

-If we want to relax the complexity of the tracking system, we can follow the sun in only one direction (1-axis tracking). The concentrator is not anymore axisymmetric. It will rather be linear. Then the concentration is smaller and the acceptance area larger. Now this area has an elongated shape capturing the sunrays for any position of the sun in the non-tracked direction.

-We can avoid the need of tracking with a static concentrator. Figure 1.c shows (qualitatively) the annual radiation distribution in the pq plane for a concentrator oriented to the equator and tilted an angle equal to the latitude. There is a central band with high radiance, corresponding to the sky region where the sun passes sometime during the year, whose limits are the projection of the sun's path on the two solstice days. Diffuse and albedo regions are also represented.

A concentrator collecting the beam rays during the whole year (that we do not know how to build) must collect all the rays in the white area of Figure 1.c. This area is 1.549 [2]. Therefore for a monofacial cell surrounded by a medium of $n=1$, $C^{max}=\pi/1.549=2.03$. A way to increase achievable concentration is to surround the receiver with a plastic of $n\approx 1.5$, that makes $C^{max}=4.57$. The limit of eq. (1) can be doubled with the use of bifacial cells because the angular spread at the receiver is doubled (from hemispheric to isotropic acceptance at the cell level), so that the figure of our example becomes $C^{max}=9.13$.

Real concentrators that we know how to build will present lower optical concentration. In any case, it has to be noted that we are always speaking of low levels of concentration. This is the price to pay if we want to have high acceptance angles and avoid the need of tracking. In last section we will see that, under certain conditions, these low levels will be enough to render static concentration attractive.

Solar cells for low concentration

Cell efficiency increases with concentration because photogenerated current, opencircuit voltage and fill factor increase. However, series resistance causes the fill factor and the efficiency to decrease at high current values. The maximum efficiency of a cell with a given series resistance occurs approximately when the ohmic drop equals the thermal voltage V_T :

$$J_L r_s \approx V_T \quad (2)$$

where the photocurrent is expressed in terms of current density $J_L(\text{mA/cm}^2)$ and the series resistance in terms of specific series resistance $r_s(\text{m}\Omega\text{cm}^2)$.

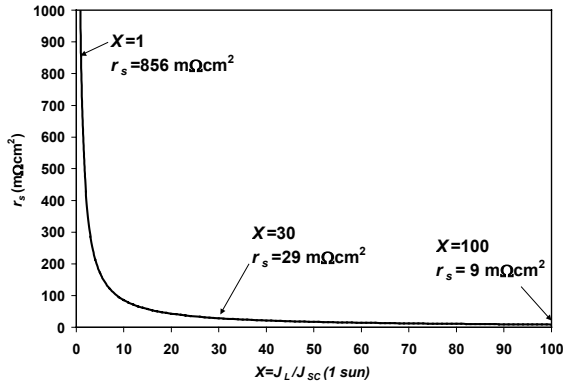


Figure 2. Requirements of series resistance vs. concentration to achieve maximum efficiency

for example, increasing the shadow factor from 8% to 18% is enough to reach an optimum for 4 suns.

As explained before, bifacial cells are attractive for concentration because they double concentration level. Bifacial cells were first fabricated by our Institute by the end of the 70s [4]. The interest in them has grown in the last years. On one hand, higher cell efficiencies have been achieved, and on the other, technologies are being adapted to bring bifacial cells closer to industrial conditions. As well as their use in static concentrators, it must be noted that “bifacial cells are very good monofacial cells”, in particular if the tendency to reduce wafer thickness consolidates, due to their low bulk recombination and their passivation schemes in both sides, good light trapping properties and symmetric metal deposition that avoids bending.

One direct application is the collection of the earth’s albedo. Flat modules made with bifacial cells encapsulated between two transparent covers can increase the power output by over 30-40% when placed in an adequate surroundings, such as a set of two white-painted wooden panels, or simply placed on a white-painted ground [5]. In reality we can consider an albedo-collecting module as a static concentrator, being the surroundings of the module part of the optical system. Several companies commercialised bifacial modules in the 80s and early 90s, and some installations, such as the one made in 1984 by Isofotón, a spin off company of our Institute, in San Agustín de Guadalix, of 40 kW, demonstrated the potential of bifacial modules.

To operate at medium or high concentration, cells of low series resistance are needed (see Figure 2), and that may need sophisticated technologies (vacuum evaporation of metals, for example) or novel designs (such as the Point Contact cell [3]).

The low concentration approach has the advantage that the series resistance reduction from that of 1-sun cells can be achieved simply by making the grid denser. For a typical screen-printed cell,

Table I summarises recent bifacial technologies, covering complex and expensive approaches, that lead to high efficiencies, as well as industrial or “pre-industrial” ones, that show the research effort currently being devoted to fabrication of cheap bifacial cells, appropriate candidates for static concentrators.

Table I. Bifacial cell technologies.

Institution	Efficiencies (frontal & rear illumination)	Cell characteristics	Ref.
Franhofer ISE	20.6%-20.2%	Rear contact cell with floating emitter. Evaporated contacts. FZ Si.	[6]
Georgia Institute of Technology	17%-11.6%	Screen-printed contacts. Passivation with RTO/SiN stacks. FZ Si.	[7]
Hitachi	15.5%-12.0%	Triode structure (with interdigitated n ⁺ and p ⁺ back contacts). Screen-printed contacts. MC Si.	[8]
	21.3%-19.8%	Triode structure (with phosphorus and boron back regions). Evaporated contacts. FZ Si.	[9]
IES-Polytechnic University of Madrid	19.1%-18.1%	Evaporated contacts. FZ Si, n-type, 20 Ωcm. Boron-diffused BSF.	[10]
	17.7%-15.2%	Same technology with Cz substrate	[11]
Institute for Solar Energy Research-Hameln	20.1%-17.2%	Evaporated contacts through masks. FZ Si. SiN _x passivation. Local Al BSF.	[12]
	15.0%-12.4% 14.6%-13.0%	Screen-printed contacts. SiN _x passivation. 100-140 μm thick Cz Si.	[13]
Lomonosov Moscow State University	16.3%-14.5%	Copper wire metallisation. Transparent conducting oxide passivation. n ⁺ np ⁺ structure on Cz-Si.	[14]
Sanyo HIT Power Double TM	Module of 15.2%-12.2% (estimated)	Heterojunction with Intrinsic Thin layer. n-type Cz. a-Si/c-Si heterojunctions.	[15]
Siemens Solar	~16%-9%	Screen-printed contacts. 150 μm thick Cz Si. Boron-diffused BSF.	[16]
SunPower	20.6%-15.2% 21.9%-13.9%	Back side point contact cells. Evaporated contacts. 160 μm FZ n-type Si.	[17]
University of Basque Country	12.0%-11.2%	Screen-printed contacts. Screen-printed boron BSF. 100 μm Cz Si.	[18]
University of New South Wales	15.0%-14.9%	Double-sided buried contact. SiN passivation and rear floating junction. FZ Si.	[19]

Concentrator designs

Classic optics imposes an unnecessary restriction for design, and is that of image forming, which means that each incident ray in the entry aperture is assigned to an incident ray in the cell. But for PV concentration we are not interested in the evolution of individual rays, but rather of bundle of rays carrying luminous power. This situation is better dealt with non-imaging optics, which was developed in the 60s to design the compound parabolic concentrator (CPC) [20].

Based on a number of theorems and design rules, different solutions can be found depending on the characteristics of the concentrator we are looking for. The typical procedure is to make a design in 2D and obtain a 3D version by rotational or linear symmetry, avoiding the complexity of designing optimal concentrators in 3 dimensions at the cost of lowering the concentration limit that can be achieved [21].

Other practical questions, such as manufacturing simplicity or thermal aspects, should also be taken into account. Regarding thermal aspects, in operation the solar cell temperature is above the ambient temperature in an amount approximately proportional to the luminous

power incident on it, and cell efficiency decreases with temperature. Although the impact of this effect in static concentrators is not as important as for medium or high concentration, heat dissipation should be considered. In the case of bifacial cells, special care should be taken, because the possibility of contacting the rear side with a heat-sink is precluded.

Table II lists some linear static concentrators developed in several laboratories, showing their profiles and commenting their most relevant characteristics. Designs look for compact and light devices, even though that may mean a decrease in concentration level.

Table II. Linear static concentrator prototypes

Concentrator	Characteristics	Ref.
Circular reflecting trough	Bifacial cells Cell temperature only 3-5 K over that of a 1 sun cell in similar conditions Power output enhancement of 40-45%	[22]
PEC-44D	Bifacial cells Modified CPC designed to supply power to a constant load A universal design $C_{opt}=2.5$ with $n=1$ (Madrid, Spain)	[23]
Roof tile static concentrator	Bifacial cells Rear surface mirror with tilted groove structure Using glass, cells 15°C over temperature of cells in a flat plate $C_{opt}=3.6$ with $n=1.5$ (Sydney, Australia)	[24]
2D-Compound Elliptic Lens	Monofacial solar cells Acrylic refractive lens $C_{opt}=1.75$ (Tokyo, Japan) Good performance on side-walls of a building	[25]
RX-RXI	Bifacial cells With glass, cell temperature 10°C higher than that of a flat module under the same conditions $C_g=4.3$ Interconnections can be placed in the gaps between cell borders and concentrator surfaces, which are not optically active	[26]

The RX-RXI concentrator presented in Table II has been developed in our Institute in the framework of the “PV Venetian store” project, funded by the European Union and lead by the PV company Isofotón. It has been designed by the Simultaneous Multiple Surface method [27], which provides highly compact devices. Although the RX-RXI concentrator would give better parameters with a plastic material, whose optical transmission is better than that of glass, the temperature drop from cell to ambient would be much larger, and the cell efficiency loss would be too important. That is why glass is preferred, besides the fact that it has better outdoors durability, and can be fabricated easily by extrusion.

In building integration the fundamental criteria of maximizing energy production has to compete with other aspects (practical and aesthetic ones). PV Venetian approaches this



Figure 3. PV Venetian prototype

market by offering a product resembling a Venetian store (see Figure 3), fully appropriate for integration in façades; although the whole module will be placed in vertical position each element can be tilted to the desired angle so optimising the collection of energy.

Indeed, it has to be pointed out that the typical cost reduction due to concentration becomes more and more

relevant as the module surface increases its tilt with respect to the optimum angle. For example, the electricity generated by a flat-plate on a south façade in Madrid would be 1.82 times less than that delivered if tilted an optimum angle of 30°, while for a linear static concentrator the energy output is practically constant with tilt angle [28]. The idea is that the optics can “compensate” the drawbacks of mis-orientation, which makes static concentrators very suitable for this kind of applications.

Will static concentrators become a real alternative?

Static concentration is supposed to compete mainly with flat module. The advantages come from the reduction in solar cell area. Supposing cell efficiency for a static concentrator similar to that of flat-plate cells, the area of solar cell reduces to $1/C_{opt}$. So, for $C_{opt}=2$ saving in cell area is 50%, while for $C_{opt}=4$ it increases to 75%. To be competitive, the cost of the rest of the system (optics, encapsulation) should be below the cost of that 50% or 75% of cell area that we are saving. Of course there are some questions, such as cell temperature inside concentrator or extra-cost of bifacial cells, that contribute to bring closer the costs of both alternatives.

For PV Venetian a detailed cost analysis has been carried out, breaking down cost in cell, concentrator and assembling components, and taking into account real efficiency. This analysis is based on Isofotón production experience and data collected from the glass manufacturer. A minimum yearly production in the range of 300-400 kWp has been considered in the calculations. In such conditions, a total cost of €2.02/Wp for the module has been obtained, which should be compared with the current cost (not price) of flat-plate modules. The later is around €3.5-4/Wp in large orders. It has now to be decided if there is a large enough cost reduction to become a driving force to initiate a high-volume production of PV Venetian concentrators.

Prospects have also been performed recently by Swanson [29], comparing a wide range of concentrator systems with flat-plate solutions, including static concentration. Its analysis considers four scenarios, combining medium-sized (100 kW- 10 MW) or small-sized (2-100 kW) systems, and high-solar-resource ($6.3 \text{ kWh/m}^2/\text{day}$) or low-resource ($4.5 \text{ kWh/m}^2/\text{day}$) areas. The parameters assumed for static concentrators are not far away from that achievable by the technologies presented in this review: concentration of 4, cell

efficiency between 21 and 17% with a cell cost 40% higher than that of flat-plate cells, and operating temperature 5°C over that of flat-plate.

With these assumptions, static concentration is always more cost-effective than flat-plate, both in the short term and in the long term (for which a reduction of costs is foreseen). In Swanson's analysis static concentration behaves well, in general, in comparison with other concentration systems (such as parabolic trough, Si point-focus Fresnel system or GaAs point-focus dish concentrator), being the best alternative of all for small-sized systems in low-solar-resource areas.

It can be concluded that static concentration is an alternative that should not be discarded due to its potential low cost, its reduction of wafer use and the consequent reduction of energy consumption and energy payback. There is a market for these systems, and a conjunction of research, development and industrialisation efforts is needed to make these prospects come true.

Conclusions

Among PV concentration technologies that of static concentrators is the simplest one, which do not need tracking systems while saving some silicon; however, only low levels of concentration can be achieved. Different technologies for cells and concentrators have been proposed, and demonstration prototypes have been fabricated and tested, looking for easy industrialisation. The potential of static concentration has been shown for different type of applications (small or medium-sized plants, building integration). The question remains whether the reduction of cost associated with static concentration is attractive enough so that an industry decides to develop commercial systems.

References

- [1] A. Luque, *Solar cells and optics for photovoltaic concentration*, Adam Hilger, Bristol, 1989.
- [2] A. Luque, *Solar Cells*, 3, 355-368 (1981).
- [3] R.A. Sinton, Y. Kwark, P. Greuenbaum and R.M. Swanson, *Proc. 18th IEEE PVSC*, New York, 61-65 (1985).
- [4] A. Luque, *Double-sided solar cell with self refrigerating concentrator*, US Patent 4 169 739, 1979.
- [5] A. Cuevas, A. Luque, J. Eguren and J. del Alamo, *Solar Energy*, 29(5), 419-420 (1982).
- [6] S.W. Glunz, J. Knobloch, D. Biro and W. Wettling, *Proc. 14th European PVSEC*, Barcelona, 392-397 (1997).
- [7] A. Rohatgi, S. Narasimha, A.U. Ebong and P. Dosi, *IEEE Trans. Electron Devices*, 46(10), 1970-1977 (1999).
- [8] T. Warabisako, K. Matsukuma, S. Kokunai, Y. Kida, T. Uematsu and H. Yagi, *Proc. 23rd IEEE PVSC*, Louisville, 248-251 (1993).
- [9] H. Ohtsuka, M. Sakamoto, K. Tsutsui and Y. Yazawa, *Prog. Photovolt.: Res. Applicat.*, 8(4) 385-390 (2000).
- [10] A. Moehlecke, I. Zanesco and A. Luque, *Proc. 1st World Conf. PV Energy Conversion*,

Hawaii, 1663-1666 (1994).

- [11] C. del Cañizo, A. Moehlecke, I. Zanesco and A. Luque, *IEEE Electron Device Lett.*, 21(4), 179-180 (2000).
- [12] A. Hübner, A.G. Aberle and R. Hezel, *Proc. 14th European PVSEC*, Barcelona, 92-95 (1997).
- [13] S. Steckemetz, A. Metz, R. Hezel, *Proc. 17th European PVSC*, Munich, 1902-1905 (2002).
- [14] G. Untila, A. Oipov, T. Kost, A. Chebotareva, M. Zaks, A. Sitnikov, O. Solodukha and A. Pinov, *Proc. 17th European PVSEC*, Munich, 1793-1795 (2002).
- [15] M. Taguchi, K. Kawamoto, S. Tsuge, T. Baba, H. Sakata, M. Morizane, K. Uchihashi, N. Nakamura, S. Kiyama and O. Oota, *Prog. Photovolt.: Res. Applicat.*, 8, 503-513 (2000).
- [16] K.A. Münzer, K.T. Holdermann, R.E. Schlosser and S. Sterk, *IEEE Trans. Electron Devices*, 46(10), 2055-2061 (1999).
- [17] C.Z. Zhou, P.J. Verlinden, R.A. Crane, R.M. Swanson and R. A. Sinton, *Proc. 26th IEEE PVSC*, Anaheim, 287-290 (1997).
- [18] J.C. Jimeno, V. Rodríguez, R. Gutiérrez, F. Recart, G. Bueno and F. Hernando, *Proc. 17th European PVSEC*, Munich, 1636-1639 (2002).
- [19] K.R. McIntosh, C.B. Honsberg and S. Wenham, *Proc. 2nd World Conf. PV Energy Conversion*, Vienna, 1515-1518 (1998).
- [20] W.T. Welford, R. Winston, *The optics of nonimaging concentrators*, Academic Press, New York, 1978.
- [21] J.C. Miñano, A. Luque, *Appl. Opt.*, 22, 2751-2760 (1983)
- [22] B. Mayregger, R. Auer, M. Niemann, A.G. Aberle and R. Hezel, *Proc. 13th European PVSEC*, Nice, 2377-2380 (1995).
- [23] J. Parada, *Desarrollo de módulos estáticos de concentración para conversión fotovoltaica*, PhD Thesis, UPM, Madrid, 1992.
- [24] S. Bowden, S.R. Wenham and M.A. Green, *Prog. Photovolt.: Res. Applicat.*, 3, 413-423 (1995).
- [25] K. Yoshioka, K. Endoh, M. Kobayashi, A. Suzuki, T. Saitoh, *Solar Energy Mat. Solar Cells*, 34, 125-131 (1994).
- [26] M. Hernández, R. Mohedano, F. Muñoz, A. Sanz, P. Benítez and J. C. Miñano, *Proc. 16th European PVSEC*, Glasgow, 2394-2397 (2000).
- [27] J. C. Miñano, J.C. González, *Appl. Opt.*, 31, 3051-3060 (1992).
- [28] R. Mohedano, P. Benítez and J.C. Miñano, *Proc. 2nd World Conf. PV Energy Conversion*, Vienna, 2241-2244 (1998).
- [29] R. M. Swanson, *Prog. Photovolt.: Res. Applicat.*, 8, 93-111 (2000).

A CONTACTLESS TECHNIQUE FOR MEASURING MINORITY-CARRIER PARAMETERS IN SILICON

R.K. Ahrenkiel and S.W. Johnston
National Renewable Energy Laboratory
1617 Cole Blvd., Golden, Colorado 80401 USA

Introduction

Characterization of minority-carrier parameters is a primary interest for a range of devices, including solar cells. For “on-line” testing needs, contactless techniques are mandatory, as any diagnostic requiring contact formation is impractical. Here, we will describe the resonance-coupled photoconductive decay (RCPCD) technique that has proven to be a valuable diagnostic for a number of semiconductor technologies.

This technique avoids some of the inherent limitations of microwave reflection. Our system is a pump-probe technique, using an optical pump and a microwave probe (400 to 900 MHz). These low frequency microwaves penetrate most silicon wafers with common doping levels. By varying the optical excitation wavelength, one can probe wafers of standard (300 to 400 μm) wafer thickness. Also, the method is very linear in sample photoconductivity, and we have observed a linear response over more than three orders of magnitude of excess carrier concentration. This attribute allows us to measure the carrier recombination lifetime over many decades of injection level, allowing the use of a procedure that is called injection-level spectroscopy (ILS).

The RCPCD technique was developed[1,2,3,4,5,6] at the National Renewable Energy Laboratory (NREL) and has been applied to more than 5000 samples, ranging from small-area thin films to 350- μm -thick, 250-mm-diameter silicon wafers. In addition, the lifetimes in semiconductor ingots of irregular shape have been successfully measured as no particular size or shape is required for the RCPCD analysis.

Theory of the Detection Process

A schematic representation of the apparatus is shown in Fig. 1. The sample is coupled to the electromagnetic field of a small antenna, a several-turn loop plus a rectangular copper box that is open on one end. The sample lies on an insulating, moveable platform, and the antenna configuration directs the microwave energy toward the box opening. The antenna-sample behave like an antenna array with active and passive elements. The antenna-sample coupling is commonly called impedance coupling. The complex impedance of the antenna can be described as a combination of radiation resistance and inductive reactance in this configuration. The antenna is placed in parallel with a small variable capacitor, and the two elements produce a circuit with a high quality factor (i.e. Q) at the parallel resonance of the circuit. When the semiconducting sample is coupled to the antenna, the mutual impedance modifies the input impedance of the antenna. We write the coupled impedance, Z_{in} , looking into the antenna terminals, as:

$$Z_{\text{in}} = Z_{\text{ant}} \frac{Z_{12}^2}{Z_s} \quad . \quad (1)$$

Here, Z_{ant} is the impedance of the isolated antenna, and Z_{12} is the mutual impedance. The quantity Z_s is the high-frequency impedance of the sample and depends on sample size and conductivity. The mutual impedance depends primarily on the antenna-sample spacing, but it also depends on the sample size and conductivity. In operation, the antenna-sample spacing is varied until a predetermined impedance is presented as the antenna input. The spacing varies from several centimeters for large wafers to a few mm for small-area thin films. Small changes in coupled reactance, produced by variable sample size, is accommodated by small adjustments in the parallel capacitor.

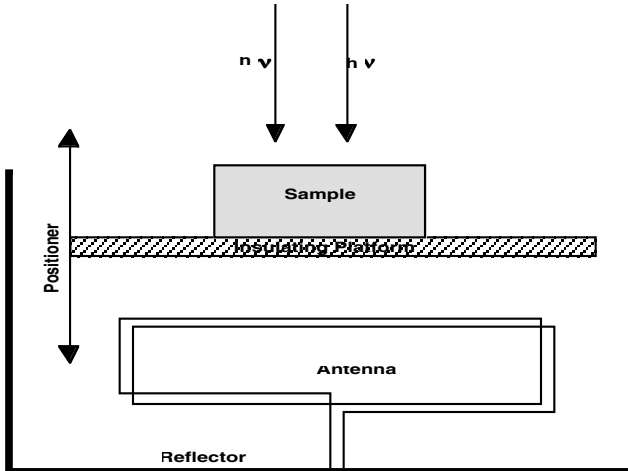


Fig. 1. Schematic of the samples chamber showing the relative positions of sample and antenna.

The antenna impedance, Z_{in} , is adjusted to match the input of a unidirectional coupler, usually 50 ohms. This is done by adjusting the sample positioner until the output of the coupler shows a null. The unidirectional coupler output is amplified by wide-bandwidth ac amplifiers, and then input to a high-frequency mixer module. This signal is mixed with a signal taken from the antenna driver circuit after the two signals are phase-matched. In operation, we use the dc component of the mixer output, and run that component through a wide-bandwidth dc amplifier before displaying the photoconductivity signal on an oscilloscope. The 2ω component has also been used (where ω is the oscillator frequency) to process the transient photoconductivity.

We can write the input impedance of the system under pulsed excitation as:

$$Z_{in} = Z_{ant} \cdot Z_{12}^2 [\sigma_s + \Delta\sigma(t)]. \quad (2)$$

Here, σ_s is the dark conductance of the sample, and $\Delta\sigma(t)$ is the pulsed photoconductivity of the sample. One can use pulse excitation energies such that: $\Delta\sigma_s(t) \gg \sigma_s$, and a linear response is still observed. To provide for the desired linearity and large dynamic range for $\Delta\sigma(t)$, we adjust $Z_{12} \ll Z_{ant}$. The photoconductive signal is then connected to a digitizing oscilloscope, where the signal voltage is:

$$V(t) = A Z_{12}^2 \Delta\sigma_s(t). \quad (3)$$

Here, A is the overall system gain and is 40 dB or more in our current apparatus.

The system, as shown, is sensitive to the movement of laboratory personnel in the room, as well as room lighting. To shield the apparatus from these disturbances, we enclose the entire sensor apparatus in a much larger conducting enclosure that is a resonant cavity at near the antenna resonant frequency. This enclosure does not degrade the signal and may, in fact, enhance the system sensitivity. The walls of the enclosure become nodes of the rf standing waves, and the sample is near an anti-node.

A variety of pulsed optical light sources have been used successfully with this system. These include xenon flash lamps and inexpensive light-emitting diodes. The sources of choice for research applications are YAG-pumped optical parametric oscillators (OPO), because these provide wide wavelength tunability for the variety of measurements that will be described here. The output intensities of these laser-based sources are usually much too large for most measurements, and they are reduced several orders of magnitude by calibrated neutral-density filters.

Frequency Response

Our primary system was designed for operation at about 400 MHz. The system response is optimum at the range of 415 to 425 MHz. The dimensions of the exterior enclosure are 46 cm wide, 38 cm high, and 61 cm long. The data of Fig. 2 were obtained using 150-mm, electronic-grade silicon wafers, with a 100-A-thick thermal oxide grown on the front surface. An optical excitation pulse is supplied from the OPO pumped by a tripled YAG laser (Coherent Radiation Infinity system). The wavelength of the OPO was set at 1000 nm so that nearly uniform depth excitation is produced. The OPO beam was reduced in intensity with a neutral-density filter (OD=2), and the incident photon flux is about 5.5×10^{12} photons/cm². The system was run over a range of frequencies from about 410 MHz to 430 MHz, to find the optimum operating frequency.

These measurements were performed to find the optimum operating frequency. The first set was done with the system completely sealed by fastening the top lid on the exterior chamber. Figure 2, curve A, shows the peak photoresponse of the system with the 150-mm, electronic-grade silicon wafer in the sample holder. The excitation area of the pulse is about 1.0 cm² at the sample, and the injected excess-carrier density is about 1.4×10^{14} cm⁻³. There is a peak in the response over the range of 415 to 420 MHz, which is the preferred operating frequency for these measurements. The system can be operated with the top of the exterior enclosure removed, but the open system is more susceptible to ambient electrical noise. Curve B shows the response to the same wafer, with the top removed and the enclosure open, and one sees a slightly lower response. However, this mode of operation is superior when one needs a very fast-turnaround measurement.

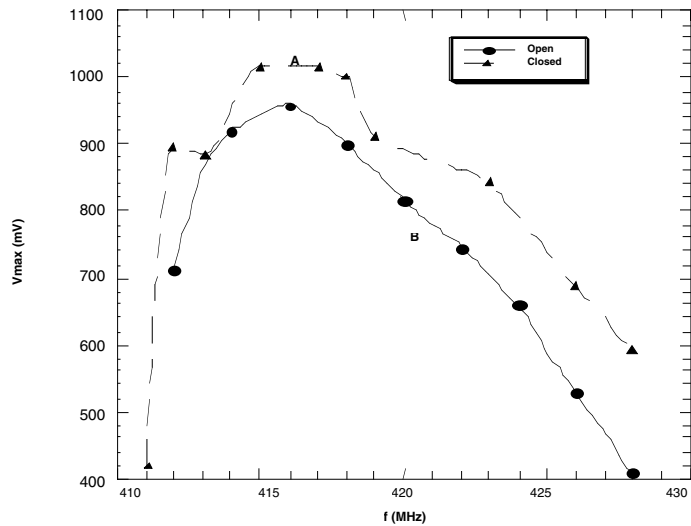


Fig. 2. System response for a 150 mm silicon wafer at a range of operating frequencies from 410 MHz to 430 MHz.

Theory of Photoconductive Decay

This RCPCD technique measures the transient ambipolar photoconductivity $\Delta\sigma(t)$ following pulsed excitation, which can be written as:

$$\Delta\sigma = q(\mu_n + \mu_p)\rho(x,t). \quad (4)$$

Here, μ_n (μ_p) are the electron (hole) mobilities, and $\rho(x,t)$ is the excess-carrier concentration. When recombination can be written in terms of a single lifetime, τ , we can write Eqn. (5) as:

$$\Delta\sigma = q(\mu_n + \mu_p)\rho(x)\exp(-t/\tau). \quad (5)$$

If the incident pulse is monochromatic, the conductivity has the following form:

$$\Delta\sigma(t) = qI_0(\mu_n + \mu_p)(1-\exp\{-\alpha[\lambda]W\})\exp(-t/\tau). \quad (6)$$

Here, $\alpha(\lambda)$ is the absorption coefficient of the material, I_0 is the incident optical density in photons/cm², and W is the sample thickness. We measure the ac. photocurrent driven by the microwave electric field. The photocurrent density per unit of electric field is then:

$$j(\omega, t) = qI_0(\mu_n + \mu_p)[1-\exp(-\alpha W)] \exp(-t/\tau). \quad (\text{amp/cm}^2) \quad (7)$$

From this result, we see that the pulse height per photon is proportional to the mobility sum, $\mu_n + \mu_p$. The time-integrated photoconductivity at a fixed wavelength as:

$$Q(\lambda) = \int_0^{t_{\max}} j(\omega, t) dt = qI_0[1-\exp(-\alpha W)]\tau(\mu_n + \mu_p). \quad (\text{amp/cm}^2) \quad (8)$$

Using the Einstein relationship, we can write Eqn. (8) as:

$$Q(\lambda) = \frac{q^2 I_0}{KT} \{1-\exp[-\alpha(\lambda)L]\}(L_n^2 + L_p^2). \quad (9)$$

For wavelengths that are strongly absorbed ($\alpha W \gg 1$), the integrated photoresponse is:

$$Q(\lambda) = \frac{q^2 I_0 L_a^2}{KT}, \quad (\text{Coulomb/volt}) \quad (10)$$

where $L_a \equiv \sqrt{L_n^2 + L_p^2}$, which is the root-mean-square diffusion length.

One can calibrate the data in terms of diffusion length.

Injection-Level Spectroscopy

The SRH recombination rate produced by a single-point defect at energy E_t in the forbidden gap is described by the well-known equation:

$$\frac{dn}{dt} = \frac{dp}{dt} = -\frac{\sigma_p \sigma_n v_{th} N_t [pn - n_i^2]}{\sigma_n \left[n + n_i e^{-E_t / kT} \right] + \sigma_p \left[p + n_i e^{-E_t / kT} \right]} \quad (11)$$

Here, n and p are the densities of free electrons and holes, respectively, and N_t is the defect density; σ_n and σ_p are the capture cross-sections for electrons and holes, respectively. Also, V_{th} is the thermal velocity, n_i is the intrinsic density, and E_i is the intrinsic energy. The SRH lifetime is not a single number, but a function of the electron and hole concentrations. The limits at low/high injection are:

$$\begin{aligned} \tau_{\text{low}} &= \frac{1}{\sigma_n N_t v_{th}} . \\ \tau_{\text{high}} &= \frac{1}{\sigma_p N_t v_{th}} + \frac{1}{\sigma_n N_t v_{th}} \end{aligned} \quad (12)$$

The ratio of the high-injection to low-injection lifetime is:

$$\text{ratio} = \frac{\sigma_n + \sigma_p}{\sigma_p}. \quad (13)$$

This ratio is a number that is usually unique to an impurity and is the basis of injection-level spectroscopy.

A batch of Czochralski-grown wafers, that were provided by a commercial vendor, were doped with transition metals, and the lifetime was measured over about three orders of magnitude of injection level. The wafer thicknesses averaged about 330 μm , and the resistivity was p-type and about 100 ohm-cm. Several of the wafers were run in the as-received condition and then processed to reduce surface recombination. The wafers were etched in dilute HF etch to remove the native oxide. This was followed by a rinse in deionized water and submersion in a methanol solution containing iodine [7]. In Fig. 3, the RCPCD lifetime measurement was made in the iodine/methanol solution, and the surface recombination effect was essentially eliminated.

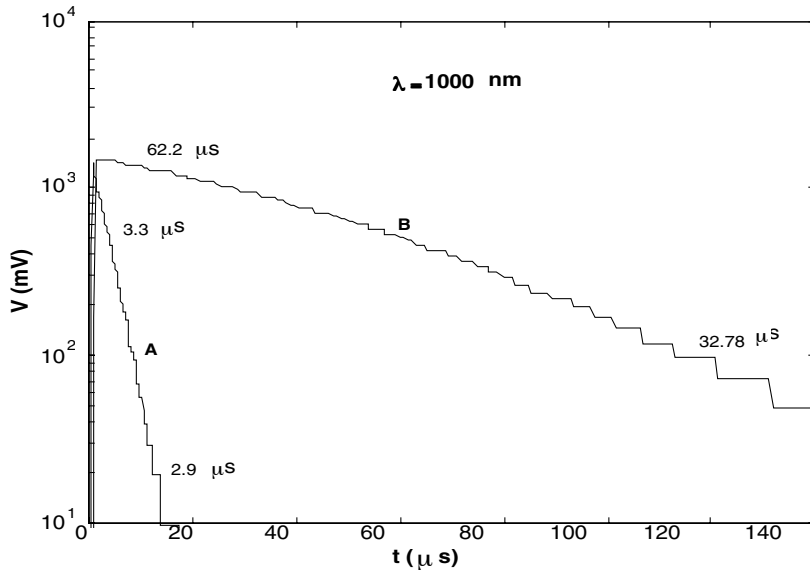


Fig. 3. RCPCD decay data for a Czochralski-grown wafer. A: As received from the vendor; B: After etching and while immersed in iodine/methanol solution.

Figure 4 shows the wafer measurement in air (curve A) and in iodine-methanol solution (curve B). Shown on curve A are the low- and high-injection lifetimes, respectively. Curve B shows that the lifetime increases over a factor of 10 when the surface is passivated. Assuming that $S=0$ for the treated wafers, the surface recombination velocity, S , is about $5.5 \times 10^3 \text{ cm/s}$ and the bulk, low- and high-injections lifetime are about 33 μs and 62 μs , respectively. Figure 4 shows RCPCD data from another wafer from the same lot that was doped with iron. This wafer was not immersed in iodine/methanol solution to eliminate surface recombination. Metallic iron was electrodeposited on the surface, and the wafer was then furnace annealed at 800°C for several hours. Prior to these lifetime measurements, the wafers were heated to about 250°C and quenched in water. Curve A shows the RCPCD data for the wafer prior to iron doping. The low-injection lifetime was 12.5 μs , and the high-injection lifetime was 18.9 μs . After Fe doping and the water quench to produce interstitial Fe, the data of curves B and C were obtained. Digitizing error prevents good data collection at lower injection levels, but the wafer was rerun with an additional neutral density filter of 3.0. This reduces the incident flux by a factor of 1000, and the data of curve C were produced. Here, the lifetime drops to 1.17 μs . The injection ratio is calculated to be 17.

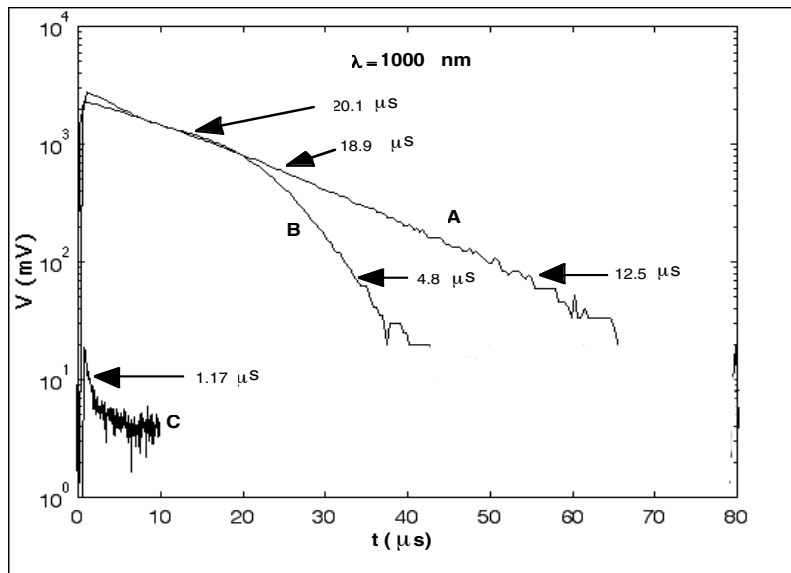


Fig. 4. RCPD data for a Czochralski-grown wafer from the same lot as the wafer of Fig. 3. A: As received; B: Diffusion of Fe into wafer and at higher injection levels; C: The wafer of curve B, but at the lowest injection levels.

One could obtain more precise data using the iodine-methanol treatment on all wafers, and getting the lifetime ratio with the surface effects removed. We can also use the ratio of 17 as an indicator of interstitial Fe, when the surface is unpassivated.

Summary

We have demonstrated the versatility of the contactless RCPD technique for a variety of semiconductor measurements. Other information that can be obtained from RCPD includes:

The spectral response of the semiconductor.

The specific sensitivity, S^* , of the semiconductor or photoconduction[8].

The photoexcitation spectra (PES) gives the relative absorption coefficient, α , of thin films.

The PES gives the absorption coefficient of deep impurity levels.

Other successful measurements that were not included here are:

A lifetime depth profile by excitation wavelength variation.

A defect level energy determination by combining injection-level spectroscopy and variable sample temperature.

In summary, the RCPD technique has been shown to be a very powerful, contactless method of semiconductor characterization.

Acknowledgements

The authors would like to thank R. Bhattacharya for doing the electrodeposition of transition metals on the silicon wafers used here. We would also like to thank Peter Sheldon of NREL for his support of the technique development work. This work was funded by the U. S. Department of Energy under contract # DE-AC36-83CH10093.

References

- [1.] R. K. Ahrenkiel, *Solar Cells and Solar Energy Materials* (in press).
- [2.] Ahrenkiel, R.K., Johnston, S.W., *Solar Cells and Solar Energy Materials*, **55**, pp. 59-73 (1998).
- [3.] Ahrenkiel, R.K., Johnston, S.W., *Mat. Res. Soc. Symp. Proc.*, Materials Research Society, **510**, pp. 575-581 (1998).
- [4.] U. S. Patent 5,929,652, Richard Ahrenkiel, July 27, 1999.
- [5.] U. S. Patent 6,275,06 Richard Ahrenkiel and Steven Johnston, August 14, 2001
- [6.] U. S. Patent 6,369,603, Steven Johnston and Richard Ahrenkiel, April 9, 2002.
- [7.] M'Saad, H., Michel, J., Lappe, J.J., Kimerling, L.C., *J. Electronic Materials*, **23**, p. 487 (1994).
- [8.] Bube, R.H. *Photoelectric Properties of Semiconductors*, Cambridge University Press, New York, p. 20 (1992).

**Application of synchrotron radiation based X-ray microprobe techniques
for the analysis of recombination activity of metals
precipitated at Si/SiGe misfit dislocations**

O.F.Vyvenko, T.Buonassisi, A.A.Istratov, and E.R.Weber

University of California, LBNL, 1 Cyclotron Rd., Berkeley, CA 94720, USA

M.Kittler and W.Seifert

IHP, Im Technologiepark 25, D-15236 Frankfurt (Oder), Germany

Transition metals are known to form precipitates in the vicinity of structural defects such as grain boundaries or dislocations. Metal precipitates often form band-like states near the middle of the band gap [1-3], thus providing an effective channel for minority carrier recombination. Additionally, these precipitates may be charged. This can provide an attractive electrostatic potential for minority charge carriers and increase the effective minority carrier capture cross-section of the precipitates by orders of magnitude [3, 4]. In order to develop a quantitative model describing the recombination activity of metal precipitates, one has to have data on both recombination activity and the size of individual precipitates or groups of similar precipitates. Until recently, the only tool which could in-situ assess recombination activity and chemical nature of the precipitates was Electron Beam Induced Current (EBIC) combined with the energy dispersive spectroscopy (EDS) mode of scanning electron microscopy (SEM). However, the detection limit of EDS was too low, about 0.1 to 1 at. %. In this study, we applied a combination of microprobe X-ray fluorescence (μ -XRF, see, e.g., [5]) and X-ray Beam Induced Current (XBIC, [6]) to the analysis of the recombination activity and space distribution of Cu and Fe in the vicinity of misfit dislocations in silicon/silicon-germanium structures. μ -XRF has several orders of magnitude better sensitivity than EDS.

The SiGe/Si structures consisted of a 2 μm thick $\text{Si}_{0.98}\text{Ge}_{0.02}$ layer sandwiched between a 2.5 μm silicon bottom buffer layer on (001) silicon substrate and a 2.5 μm thick silicon cap layer grown by chemical-vapor deposition (CVD). All samples were phosphorus doped with a concentration of shallow donors of 10^{15} cm^{-3} . A network of two perpendicular sets of 60° misfit dislocations running in <110> directions was observed at the interfaces between silicon and silicon germanium. The samples were intentionally contaminated with iron or copper by the diffusion annealing at 1000°C and 800°C, respectively. Additionally, one iron doped sample was treated in a remote hydrogen plasma reactor at 400°C for one hour and another got the same thermal treatment in an inert ambient. Further details of the sample preparation can be found elsewhere [7]. All investigated samples were pre-characterized by temperature dependent Electron Beam Induced Current (EBIC). Some results of EBIC investigation of the samples were reported in [7].

To perform XBIC/ μ -XRF studies, a 20 nm thick Pd or Au contact was thermally evaporated on the surface of the chemically cleaned samples. This thin contact neither significantly absorbed the x-rays, nor affected the penetration depth of the x-ray beam nor the sensitivity of the μ -XRF technique. Ohmic contacts were formed by rubbing gallium on the back side of the sample at its edges. The sample was mounted in an XRF sample holder, which could be moved in the X and Y directions with a step size of 0.1 μm by computer-controlled step motors. The Schottky contact on the front of the sample and the ohmic contact on its back surface were contacted by thin palladium wires, which were connected to a sensitive current amplifier.

The measurements were performed at Beamline 10.3.1 at the Advanced Light Source, Lawrence Berkeley National Laboratory. An intense X-ray beam from the synchrotron with approximately 3×10^{10} photons/s was focused in a $(1-2) \times (1-2) \mu\text{m}^2$ spot using elliptically bent multi-layer mirrors. The incident X-ray beam had a wide range of photon energies with a peak of intensity at 12.4 keV. The beam hits the sample surface under an angle of 45 degrees. The emanating X-ray fluorescence was detected by a Si:Li detector. As the penetration depth of the exciting X-rays was very large in silicon (about 250 μm), the sampling depth of the XRF technique was determined by the escape depth of the fluorescence x-rays of interest (36 μm for iron and 70 μm for copper). The sensitivity of the XRF tool depends on the accumulation time, t_a , in each point. For $t_a = 30\text{s}$ a single iron precipitate with a radius of 20-25 nm, or dissolved iron or copper in concentration of about 10^{14} cm^{-2} and $7 \times 10^{14} \text{ cm}^{-2}$, respectively, can be detected [5]. The absolute values of the impurity concentration are determined using calibration standards with known metal concentration.

Due to the large attenuation depth of the exciting radiation, XBIC sampling depth is determined primarily by the diffusion length of the excess minority carriers. Additionally, the inclined beam orientation leads to a shift of XBIC image with respect to the μ -XRF image in the direction of the beam projection on the sample surface. The excitation level of the XBIC experiments is similar to a low excitation regime of EBIC. Indeed, an X-ray photon flux of 10^{10} cm^{-2} with an energy of 12.4 keV corresponds to the electron current of 1 nA. However, the absorbed energy is spread over a 250 micron X-ray penetration depth, which is roughly 50 times greater than the penetration depth of the electrons of the same energy. Hence, the excitation conditions of XBIC-experiment correspond to approximately 20 pA electron beam excitation, i.e., a current which is considered a low excitation regime in EBIC.

No external bias was applied to the contact; the built-in voltage of the Schottky-diode was used to collect the charge carriers. Both μ -XRF and XBIC signals were measured simultaneously and were stored in a computer as a function of the (x, y) coordinates of the sample stage. These data could be later retrieved to plot the maps of minority carrier lifetime and metal impurity distribution, or to perform data analysis at any point within the scan.

Copper doped samples. XBIC and XRF Cu-K α maps of a SiGe/Si structure doped with copper are shown in Figs. 1a and 1b, respectively. Dark areas on the XBIC map correspond to a reduction of the diode current whereas the dark regions in the Cu-K α map correspond to an increased copper concentration. One can see that the dark contrasts in both images are grouped in two sets of mutually perpendicular straight lines correspondent to two sets of misfit dislocations. Individual copper-rich precipitates can be distinguished in many parts of the XRF-image. The XBIC image appears to be rather unsharp due to a large generation volume of the exciting beam. There is clearly a good correlation between the recombination activity and the copper concentration distributions, i.e., the higher is the intensity of the copper-related X-ray fluorescence, the lower is the XBIC current.

Fig. 2 shows an example of a quantitative treatment of the data presented in the Fig. 1. It compares the profiles of the copper concentration and of the XBIC current along the x-axis at y=9.4 mm in the Fig. 1. There is a good match between the copper distribution profile and the XBIC current profile. In Fig. 3, the XBIC contrast is plotted against the copper concentration determined from the XRF maps. The XBIC-contrast was calculated as the ratio $(I_0 - I_d) / I_0$, where I_0 is the XBIC-current value far away from the defect and I_d is the value of the XBIC current at the location of the precipitate. The maximum XBIC-contrast value observed in our samples was of

about 30% whereas the EBIC contrast of similar samples was up to 70%. Since the excitation level of EBIC and XBIC are rather close to each other, we believe that this discrepancy is due to a smaller fraction of the total current collected by the precipitates. Indeed, many of the carriers generated within a 250 μm path of the X-ray beam, penetrating into the sample at a 45 degree angle, will not be attracted by the space charge region around the metal precipitates and will diffuse straight to the Schottky diode.

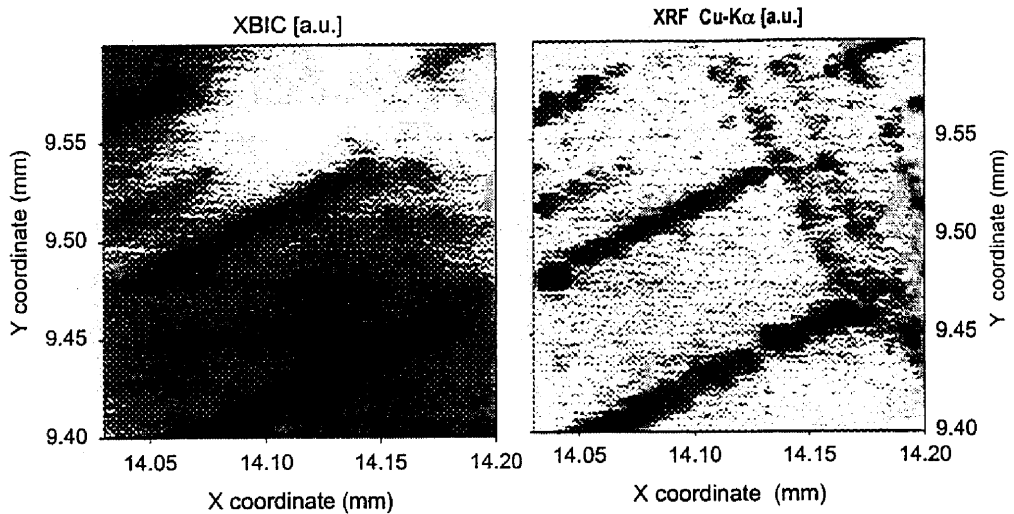


Fig. 1. XBIC (left) and μ -XRF map of the Cu- K α intensity distribution (right) of an area of a copper-doped Si-SiGe structure with misfit dislocations. Dark XBIC regions correspond to a reduction of the diode current whereas the dark Cu-K α regions correspond to increased copper concentration. A good correlation between the recombination activity and the copper concentration distribution is obvious.

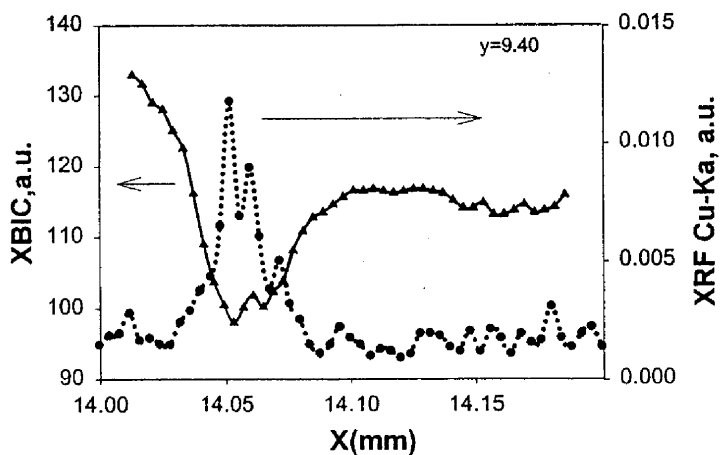


Fig. 2. XBIC and μ -XRF Cu- K α linear scans across a copper decorated misfit dislocation. The line scans are extracted from the maps in Fig. 1 along the horizontal axis at y=9.4 mm.

An exact theory of the XBIC-contrast with the particular generation function of the XBIC experiment has not been developed yet. Generally, it is known that the contrast measured by EBIC or XBIC is proportional or nearly proportional to the carrier recombination rate at the defect [8]. The recombination rate depends on the shape and size of the precipitates as well as on the origin of their electronic states in the band gap. A phenomenological model of EBIC-contrast due to sphere-shaped defect developed by Donolato [9] predicted the proportionality between the recombination strength of a defect and its radius in the limit of infinite recombination rate within the entire volume of the defect. In this case a sub-linear power dependence of the recombination strength, R_{e-h} , on the defect volume, V , would be observed, $R_{e-h} \sim V^{1/3}$. Since that does not agree with our observation, we conclude that Cu precipitates are not spherical, but platelets such as those observed by Istratov et al. [10]. Kittler et al. [11] and Plekhanov et al. [4] suggested that the recombination at the surface of plate-like precipitates is responsible for an extremely high recombination activity of the metal precipitates in silicon. In this case, according to the model [11], the recombination rate and the contrast must be proportional to the surface area of the precipitates, and a linear dependence of the recombination current on the number of atoms in the precipitate should be observed when changes of the precipitates volume are due to changes of their lateral dimensions rather than of their thickness. Note if the size (volume) of the precipitates remained unchanged and only thickness of the platelets increased with the increasing Cu concentration, then the XBIC-contrast would be independent on the local copper concentration in the sample. Since we observed a linear dependence, it is likely that Cu precipitates are platelets.

One can estimate from the Cu concentration at the dislocation lines determined from μ -XRF, from 10^{16} to $5 \times 10^{16} \text{ cm}^{-2}$, and the atomic density of Cu in copper-silicide, $6 \times 10^{22} \text{ cm}^{-3}$ [12], that if all Cu formed just one large platelet, then its thickness would be only 2 to 10 nm. This is close to the lowest thickness of Cu_3Si precipitates (2-5 nm) ever reported from TEM data [3]. In reality, it is very likely that our samples contain a large number of small platelets with the thickness equal or greater than 2-5 nm. In this case, it is unlikely that these precipitates overlap substantially, and hence the XBIC contrast is proportional to the number of the microprecipitates in a colony.

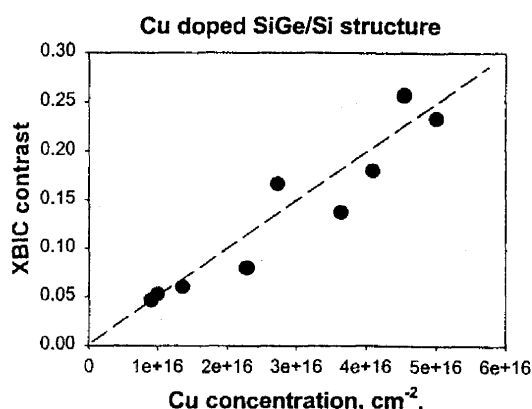


Fig.3. XBIC contrast versus XRF copper concentration as derived from the multiple line scan data similar to those shown in Fig.2.

Iron doped samples. XBIC maps of the Fe-doped samples showed strong contrasts of two perpendicular sets of misfit dislocation (Fig. 4a), running in $\langle 110 \rangle$ directions. Similar contrasts were observed in our EBIC experiments (not shown). XRF measurements revealed the appearance of Fe-K α and Fe-K β peaks in a proper ratio confirming the presence of iron in the sample that was treated in hydrogen plasma at 400°C. The iron concentration in the reference sample, which was diffused with iron but not passivated in hydrogen plasma, was below our detection limit. The iron concentration was found to be rather homogeneously distributed within dislocation bunches and was only 2-3 times larger than the detection limit of our set-up (about $5 \times 10^{13} \text{ cm}^{-2}$). That is why we were not able to measure the dependence of the XBIC contrast on iron concentration like presented in the Fig. 3 for Cu. A comparison of hydrogen-annealed and control Fe-contaminated samples suggested that some of the iron was gettered by the misfit dislocations during the hydrogen-diffusion anneal (1 hour at 400°C). This shows that the impact of remote hydrogenation on minority carrier diffusion length cannot be described by interaction of metals with hydrogen alone, but it is a more complicated process.

Taking the distance between dislocations of 1 μm , we estimated the number of iron atoms per 1 cm length of dislocation from the iron concentration obtained from XRF measurement as $10^{10} \text{ Fe/cm}^{-1}$, which is 2 order of magnitude greater than the linear atom density in silicon. This indicates that iron is likely to form clusters or microprecipitates along the dislocation line. In this case, the distance between the precipitates must be less than the spatial resolution of our measurement that is about 2 μm . Assuming that the precipitate form iron silicide, FeSi_2 , and taking its atomic density to be equal to $4 \times 10^{22} \text{ cm}^{-3}$ [12], one can estimate the largest expected size of such a small precipitate as 30-40 nm.

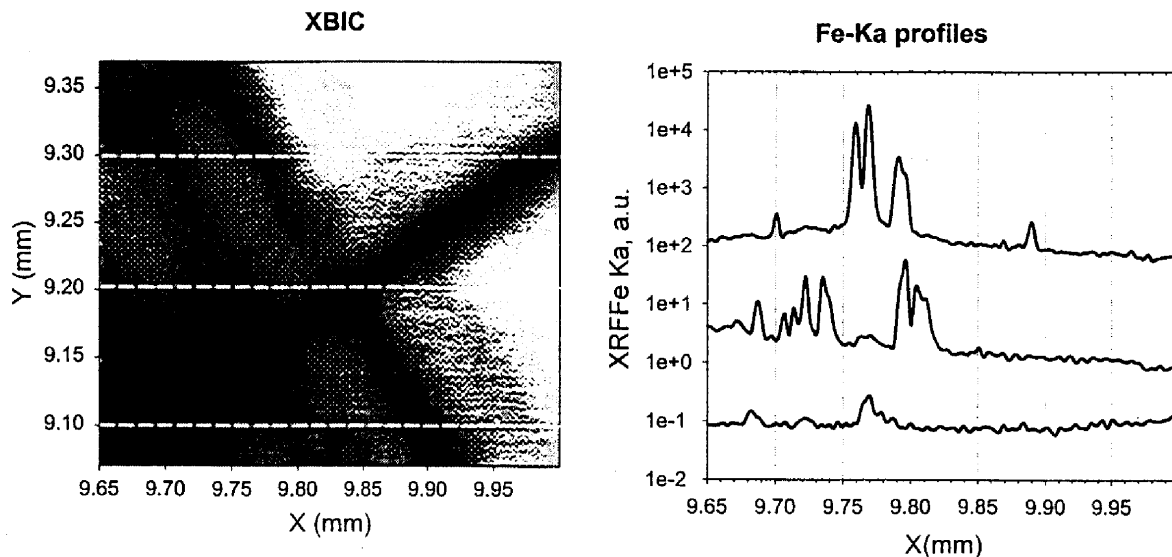


Fig. 4. XBIC (left) and μ -XRF map of the Fe- K α intensity distribution(right) of iron-doped Si-SiGe structure with misfit dislocations. No direct correlation between the recombination activity and the iron concentration distribution was found.

To find out if a separate precipitate can be detected we performed line scans instead of two-dimensional mapping. Additionally, the acquisition time per point was significantly increased. In this way, a larger iron signal was found in some regions of the sample, indicating the

presence of iron-containing precipitates. The results of that experiment are shown in the Fig.4b where three line scans of Fe-K α XRF-peak were measured along the dash lines drawn on XBIC-map Fig.4a. From a comparison of the XRF line profiles (Fig.4b) with the XBIC-map (Fig.4a) one can see that there is no obvious one-to-one correlation between the positions of the iron clusters observed in XRF scans and EBIC contrasts. A precise examination of all available data revealed that large iron precipitates can be frequently found at the edges of dislocation bunches or at the intersections of the dislocations of two perpendicular sets. However, a higher iron concentration did not lead to any significant increase of the XBIC contrast. Assuming spherical precipitates, we could estimate the radius of the large inactive precipitates from the absolute iron concentration in the peaks of the XRF profiles as from 100 nm to 250 nm. Since this is a very large size, we think that most likely it is not a single iron precipitate but rather clusters of precipitates of a smaller size described above.

This estimate for the sizes of iron-contained precipitates is similar to that observed in copper-doped samples. Therefore, the spatial resolution of our XBIC measurements is not the reason why they are not seen. The only explanation is that iron precipitates are not electrically active. It is possible that the electrical inactivity of the iron precipitates is the result of the hydrogenation; however, additional experiments are required to prove this hypothesis.

In summary, an analytical tool capable of in-situ measurements of recombination activity of defects and their chemical origin has been demonstrated in application to the studies of copper and iron contaminated misfit dislocations in silicon. A good correlation between the maps of the recombination activity and the density of the atoms in metal-contained precipitates was found. A proportionality between the XBIC-contrast and the impurity atom density was found for copper-doped samples, whereas some large and electrically inactive precipitates were found in the Fe-doped sample passivated in hydrogen plasma.

The funding for this research was provided by NREL, subcontract AAT-2-31605-03. The Advanced Light Source operations are funded by the Director, Office of Energy Research, Office of Basic Energy Sciences, Materials Sciences Division, of the US Department of Energy under Contract No. DE-AC03-76SF00098. The authors gratefully acknowledge fruitful discussions with S.A.McHugo, H.Hieslmair, G.D. Ackermann, R. Ynzunza, and Z. Hussein.

1. F. Riedel, J. Kronewitz, U. Gnauert, M. Seibt, and W. Schroter, *Solid State Phenom.* **47-48**, 359 (1996).
2. F. Riedel and W. Schroter, *Phys. Rev. B* **62**, 7150 (2000).
3. A. A. Istratov, H. Hedemann, M. Seibt, O. F. Vyvenko, W. Schröter, T. Heiser, C. Flink, H. Hieslmair, and E. R. Weber, *J. Electrochem. Soc.* **145**, 3889 (1998).
4. P. S. Plekhanov and T. Y. Tan, *Appl. Phys. Lett.* **76**, 3777 (2000).
5. S. A. McHugo, A. C. Thompson, C. Flink, E. R. Weber, G. Lamble, B. Gunion, A. MacDowell, R. Celestre, H. A. Padmore, and Z. Hussain, *J. Cryst. Growth* **210**, 395 (2000).
6. O. F. Vyvenko, T. Buonassisi, A. A. Istratov, H. Hieslmair, A. C. Thompson, R. Schindler, and E. R. Weber, *J. Appl. Phys.* **91**, 3614 (2002).
7. M. Kittler, C. Ulhaq-Bouillet, and V. Higgs, *J. Appl. Phys.* **78**, 4573 (1995).
8. C. Donolato, *Semicond. Sci. Technol.* **8**, 45 (1993).
9. C. Donolato, *Semicond. Sci. Technol.* **7**, 37 (1992).
10. A. A. Istratov and E. R. Weber, *Appl. Phys. A* **66**, 123 (1998).
11. M. Kittler, J. Larz, W. Seifert, M. Seibt, and W. Schroter, *Appl. Phys. Lett.* **58**, 911 (1991).
12. M. Ronay and R. G. Schad, *Phys. Rev. Lett.* **64**, 2042 (1990).

Locating losses due to contact resistance, shunts and recombination by potential mapping with the Corescan

A.S.H. van der Heide, J.H. Bultman, J. Hoornstra, A. Schönecker, G.P. Wyers, W.C. Sinke
ECN Solar Energy

P.O. Box 1, 1755 ZG, Petten, The Netherlands
Phone: +31 224 564723; Fax: +31 224 568214
E-mail: vanderheide@ecn.nl

Abstract

A visualization tool to locate losses in a solar cell can be very helpful in troubleshooting a non-optimal production line. Therefore, the Corescan has been developed, in which three different locating methods are incorporated, the Corescan, Shuntscan and the new V_{oc} scan. In this paper it is explained how the scan results have to be interpreted and it is shown that the sensitivity of the methods is more than sufficient. The unique V_{oc} scan method is introduced for the first time; this technique can locate recombination losses on cells that are almost complete (only the front contact has to be omitted). Several examples of how the Corescan instrument can be used for troubleshooting and process optimization are presented in this paper. These examples will help users of the instrument to relate measured scans with reasons for non-optimal processing.

Introduction

Normally, standard $J-V$ measurements are used to determine whether a production line is running properly. The process engineer must react when the $J-V$ fit results get below or above a certain threshold. The $J-V$ fit parameters themselves do not always reveal the real loss mechanism responsible for off-spec functioning of the process line, apart from loss due to shunts. It is difficult to determine whether a drop in fill factor is due to series resistance or recombination loss (see the Appendix and [1]). To distinguish between series resistance and recombination, an additional open circuit voltage measurement as a function of light intensity [2] is necessary. This separation of different loss sources is important, but not enough in itself to determine the real cause(s) for a lowered fill factor. This is much easier to do when also the loss locations on the cell can be determined for the different loss mechanisms.

A new way to find the loss locations has been presented recently [1,3]. The basic principle is to map the potential distribution on the front side of a solar cell, while operating the cell at conditions that enable separation of a specific loss type from the others. Using different conditions, it is possible to locate either losses due to series resistance (most importantly contact resistance), to shunts or to high recombination. These methods were patented [3] and incorporated in the Corescan, developed for industrial use and commercially available. The instrument is shown in Fig. 1. More details and on-line versions of Corescan publications are available at [4]. Corescan is derived from COntact REsistance scan, since

this is the most important scan mode. The three different scan modes of the Corescan are called Corescan, Shuntscan and V_{oc} scan.



Figure 1: Corescan instrument

The Corescan method is the only method that is able to determine the contact resistance over the entire cell surface. It has shown to be a very important and helpful tool, which makes reduction of the front side contact resistance easy. In case of contact problems it was found that the contact resistance is mostly very non-uniform. The distribution by itself can often be used to deduce the reason for poor contact.

The Shuntscan method is one of the few that is sensitive enough to enable shunt locating at the right (=forward) bias polarity. The main advantages compared to other forward bias methods, contact thermography [5], lock-in IR thermography [6] and CASQ [7], are the relative simplicity and lower costs of the Shuntscan.

The V_{oc} scan method will be presented here for the first time. It gives important information about differences in local diode behaviour over the cell. This method only works optimally when the front side metallization is omitted.

This paper discusses these three different potential mapping methods of the Corescan as well as their use in troubleshooting process optimization.

Corescan method

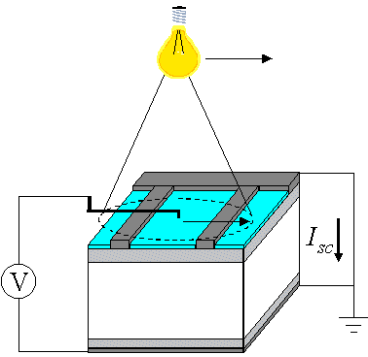


Figure 2: Schematic drawing Corescan method

The Corescan method (see Fig. 2), uses the fact that series resistance sources can be detected by potential differences that occur over these resistances while current is flowing in the device. In the Corescan, the current is generated by application of illumination while the cell is short-circuited externally. The potential at the front side is measured with a metal probe in direct contact with the surface, that is scanned across the cell. The size of the illuminated spot around the potential probe is not critical, as long as it is not smaller than a few finger separations. The contact resistance of a finger is proportional to the potential jump V_{ce} across the contact interface at the edge of the finger. This jump is the difference between the potential at the metal finger and the first point on the silicon adjacent to it (see Fig. 3). The proportionality factor is $1/i_c$, where i_c is the current flowing through the contact interface per unit length of finger. In formula form:

$$R_{cl} \equiv \frac{V_{ce}}{i_c} = \frac{V_{ce}}{dJ_{sc}},$$

where R_{cl} is the line contact resistance, J_{sc} is the short circuit current density within the beam and d is the distance between two fingers.

This line contact resistance is used instead of the more usual specific contact resistance ρ_c , because ρ_c is not so appropriate for screen printed contacts. This is because calculating ρ_c correctly involves the emitter sheet resistance below the finger and the assumption of a constant ρ_c across the finger width. However, the emitter sheet resistance below screen printed fingers increases to an unknown value during sintering due to dissolving of silicon, and the contact interface is very non-uniform. Instead of trying to separate the influence of ρ_c and emitter sheet resistance, the definition of R_{cl} includes both parameters in a single value. In fact, this is the only value of importance for the current output of the cell region between the fingers.

In the Corescan instrument, for practical reasons local illumination is used, the diameter of the beam is 9 mm. The probe is scanned perpendicular to the fingers with a resolution of 0.1 mm so that no finger is missed. To scratch through the isolating anti-reflection coating that is usually present on the front surface, the probe is continuously in contact with the surface during the scan and is made of a hard material (tungsten). By performing scan lines with a separation of 2 mm, it is possible to

obtain a potential map of the entire cell, which takes about 6 min for a 10 x 10 cm cell. An example of a scan line part is shown in Fig. 3.

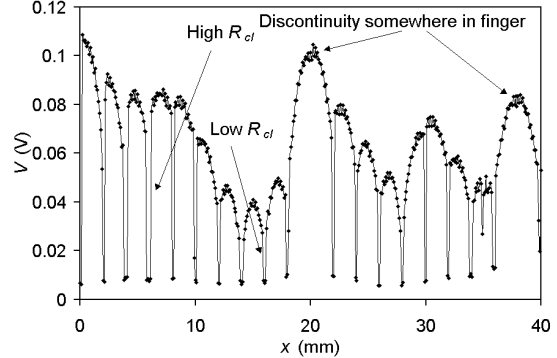


Figure 3: Part of one Corescan scan line

The potential jumps at the fingers due to contact resistance are clearly visible; the large spread in R_{cl} that is found on this cell is typical for cells that have a contact problem. The influence of other series resistance sources is also visible: the emitter sheet resistance causes a parabolic potential behaviour between the fingers and a finger discontinuity causes an effectively doubled finger spacing. The large non-uniformity of R_{cl} that is often found on solar cells causes high diode factors or second diode currents when fitting the $J-V$ curves, as is explained in the Appendix.

The minimum contact resistance that can be measured with the Corescan instrument can be calculated from the minimum measurable V_{ce} and maximum J_{sc} for the instrument. These values are 2 mV and 60 mA/cm², so for a typical finger spacing of 2 mm, the minimum R_{cl} is ~0.2 Ωcm. For reference: this would correspond to ρ_c ~2 mΩcm², assuming a constant ρ_c across the finger width and assuming a sheet resistance below the finger of 100 Ω. This accuracy of the Corescan is more than sufficient, since the influence of such a low contact resistance is negligible for illuminations up to 1 sun.

Before the Corescan method was developed, contact resistances could only be determined with the Transmission Line Model (TLM) method [8]. The TLM method is schematically shown in Fig. 4. The resistance is measured between one finger and other adjacent fingers. From the graph of resistance against distance, the emitter sheet resistance and contact resistance can be determined.

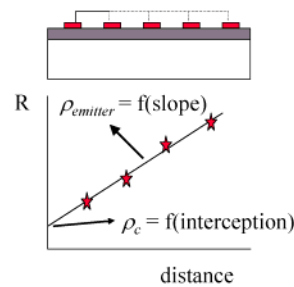


Figure 4: Principle TLM method

When the sheet resistance and contact resistance are assumed to be constant (which is often not the case), the points will be located on a straight line with a slope proportional to the sheet resistance and an intersection with the resistance axis proportional to the contact

resistance. The fingers have to be disconnected from the busbar to prevent parallel conduction. In practice this is usually done by laser cutting.

The advantages of the Corescan compared to TLM are that it is not necessary to assume the contact resistance to be the same for all fingers, it is not necessary to cut the cell, and the entire surface can be quickly measured.

Corescan application

In this section, Corescans will be shown for different causes of high (and non-uniform) contact resistance.

In the first example, 10 x 10 cm multi-crystalline silicon solar cells with silicon nitride were fired at different temperatures around an optimum value T . Contacts were applied by screen printing and co-firing of aluminum paste on the back side and silver paste on the front side. The cells are positioned on the belt with the busbars perpendicular to the belt direction.

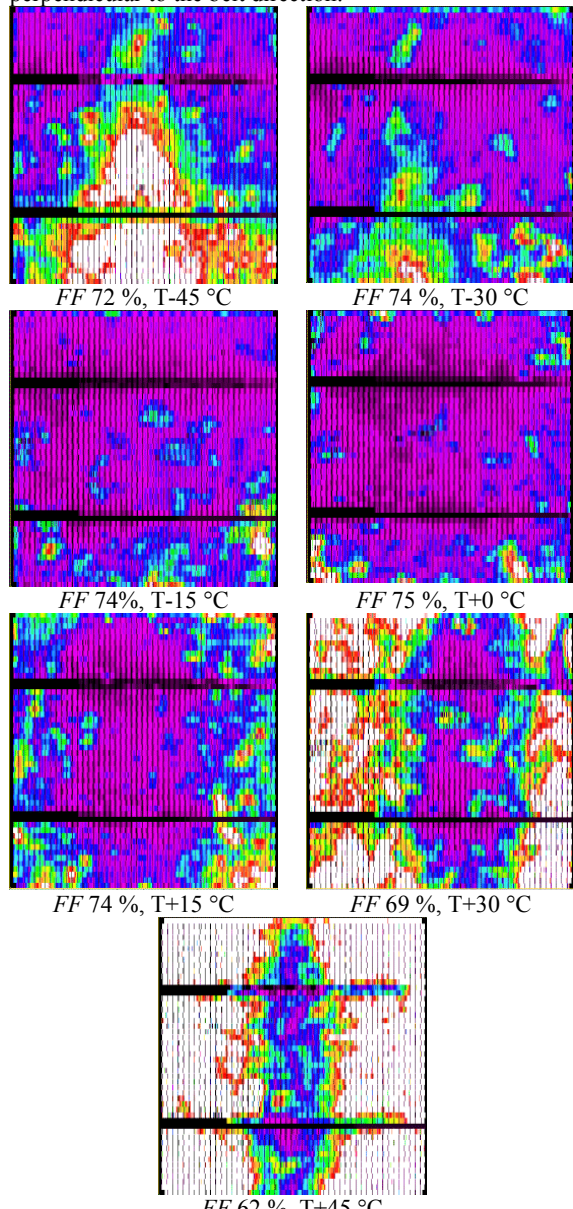


Figure 5: Corescans on cells fired at different set temperatures. Lighter areas have higher potential and thus higher contact resistance.

These scans show a large non-uniformity in R_{cl} which is due to cross-belt temperature differences. The middle region is the coolest: in this region it is too cold for good contact formation at low firing temperature, while it is the only region that has still good contact at high firing temperatures. This was enough reason to study the design of the furnace.

In IR firing furnaces, the belt is supported by fused quartz rods oriented in parallel with the belt direction. The IR lamps used for heating the cells are situated both above and below the belt. When the lamps below the belt are used, IR radiation will be blocked to some degree by the support rods, which could explain the observed temperature non-uniformity. By changing the position of cells during firing with respect to the support rod the high contact resistance region shifted over the cell. Therefore the conclusion was drawn that the center rod blocked too much IR radiation from the lamps below the belt.

Another example of temperature differences leading to R_{cl} uniformity is shown in Fig. 6. A Corescan is shown for a cell fired in a furnace with a belt having small quartz product supports. These support the products on the belt to prevent direct belt contact, and were suspected to cause contact resistance non-uniformity.

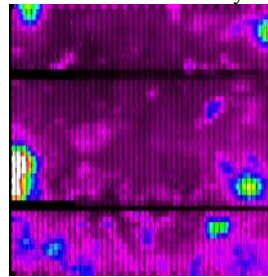


Figure 6: Corescan of a cell fired in a belt furnace, on a belt having quartz product supports. The positions exactly coincide with the supports.

It is clear from the Corescan that the temperature was too low indeed for good contact formation at the locations of the quartz product supports.

An emitter related contact problem is shown in Fig. 7, where a circle of increased contact resistance is visible.

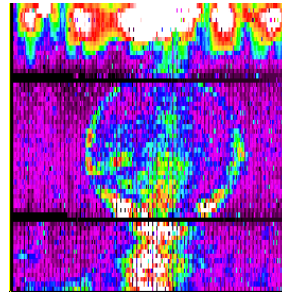


Figure 7: Circle of increased contact resistance due to locally less doped emitter

This circle is caused by application of dopant on the cell by spinning of a phosphorus containing fluid on both sides (the back side is overcompensated with aluminum later on). On the surface that was spun first, some fluid has been removed at the circle when dopant was applied to the second surface. Due to less dopant fluid the emitter resistance is increased, apparently to a value too high for good contact formation. Although this particular example may not be a very usual one, it is a good illustration of the effect of emitter non-uniformity, that can also be caused otherwise. These lateral doping variations become

especially important when lighter doped emitters are used in order to reduce recombination losses in the emitter. The next example is a contact problem caused by plasma etching of the solar cell edges for isolation (see Fig. 8).

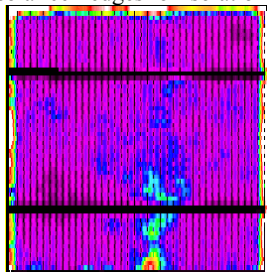


Figure 8: Increased contact resistance at the edges due to some emitter removal during plasma etching for edge isolation

The figure shows that the contact resistance is clearly increased near the edges of the front surface. Apparently some of the emitter on the front surface has been removed during the plasma etching, which was done immediately after emitter diffusion.

Some other causes for R_{cl} non-uniformity that have been identified so far are incomplete phosphorus glass removal, the presence of contamination on the silicon before contact firing, non-uniform TiO_x coating [1] and too low and non-uniform screen print pressure due to a wear dip on the screen printer vacuum chuck [9].

Shuntscan method

For the Shuntscan, the current necessary to detect shunts is generated by applying a bias across the cell with a power supply (see Fig. 9).

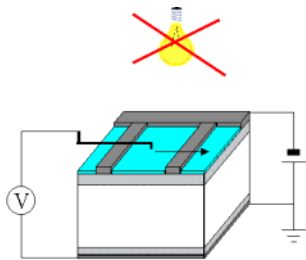


Figure 9: Drawing of the Shuntscan method

In order to study only shunt current flow, current generation by light is avoided by measuring in the dark. The current flowing through a shunt is supplied by the surrounding emitter area, and because the sheet resistance of the emitter is considerable, a potential decrease in the direction of the shunt will exist. In a Shuntscan this local potential decrease is detected; the magnitude of the shunt can be calculated from the potential gradients around it and the emitter sheet resistance.

To find the shunts that are important for the cell at normal operation, it is necessary to apply a forward bias to the cell. The reason is that not all shunts in solar cells are ohmic [10], so that shunts detected in reverse bias may not be shunts in forward bias. It is important to note that the Shuntscan is sensitive enough to detect shunts at forward bias. Except for lock-in techniques, the other methods that use heat detection to locate shunts have to use reverse bias to induce sufficiently high shunt

currents. This is used for example in case of detection with liquid crystals. The magnitude of the forward bias applied during the Shuntscan is adjustable; ideally it should be around the maximum power point (~ 0.5 V), but since the scratching of the probe itself induces some extra diode current due to surface damage it is better to use ~ 0.3 V. At that potential the diode is not conducting (even when scratched) and all currents are caused by shunts.

To calculate the current detection limit for the Shuntscan, the potential distribution $V(r)$ around a shunt must be calculated. To simplify the calculation, it is assumed that there are no fingers and that the cell is infinitely large. After the calculation for this simplified case, the influence of deviations of this model in case of real cells will be discussed.

The current flow to the shunt will be circle symmetric; the horizontal current i flowing in the emitter through a unit width is related to the shunt current I_{sh} and the distance r from the shunt (located at $r = 0$) by

$$i = \frac{I_{sh}}{2\pi r},$$

since the total current crossing the edge of any circle centered around the shunt is always I_{sh} (no current is lost).

The magnitude of i is Jt , where J is the current density of the horizontal current flow in the emitter with thickness t . At the current densities occurring in a solar cell, J is proportional to the electric field E ($= dV/dr$) and the conductivity σ ($= 1/\rho$, where ρ is the resistivity):

$$J = \sigma E = \frac{1}{\rho} \frac{dV}{dr}$$

So i can be expressed in terms of dV/dr as follows:

$$i = tJ = \frac{t}{\rho} \frac{dV}{dr} = \frac{1}{\rho_s} \frac{dV}{dr},$$

where ρ/t has been substituted by the emitter sheet resistance ρ_s .

Combining the expressions for i gives the following differential equation for $V(r)$:

$$\frac{dV}{dr} = \frac{\rho_s I_{sh}}{2\pi} \frac{1}{r},$$

which has the general solution

$$V(r) = \frac{\rho_s I_{sh}}{2\pi} \ln r + C.$$

As an example, $V(r)$ is drawn for two different I_{sh} values in Fig. 10.

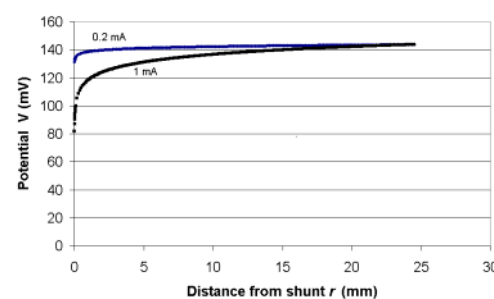


Figure 10: $V(r)$ for 2 different I_{sh} values; $\rho_s = 50 \Omega$.

The shunt with the larger I_{sh} clearly has a much larger area with lower potential around it.

The current detection limit of the Shuntscan can now be estimated; the smallest shunt that can be detected is determined by the smallest potential difference that can be detected when moving from “the shunt” to $r = 1.0$ mm (to stay between the fingers on a real cell). “The shunt” means here the point as closest as possible to it, since the potential probe itself has a finite diameter (in this case 0.2 mm). Taking r ‘at shunt’ = 0.1 mm, r ‘far away’ = 1.0 mm, $\rho_s = 50 \Omega$ and minimum $\Delta V = 5$ mV, the minimum detectable current for a single shunt turns out to be ~ 0.25 mA. Compared to a current at the maximum power point of a 10×10 cm cell of 3 A, this would mean 0.01 %, so that the sensitivity for a single shunts on an otherwise non-shunted surface is more than sufficient.

In practice, the ideal case of current flow only through one shunt and no current flow elsewhere does not exist. There will always be a small more or less homogeneous background, which cannot be detected by the Shuntscan. Therefore, the shunt resistance limit below which shunts will be found on a cell with the Shuntscan is lower than would be expected from this single shunt case. As a rule of thumb, cells with a shunt resistance below $1-2 \text{ k}\Omega\text{cm}^2$ are found to be interesting for Shuntscan investigation. This corresponds to the limit below which shunts have significant influence on the cell efficiency, so the Shuntscan sensitivity is also enough on real cells. In the case of a shunt at the Shuntscan detection limit of only 0.25 mA, the radius of influence is very small. Therefore, the potential distribution will not be much disturbed by the fingers that are present on real cells. However, when a shunt is larger, the potential distribution will be disturbed by the fingers, the degree of disturbing mainly depends on the contact resistance of the fingers around the shunt. The reason is that fingers are much better conducting than the emitter, and when the fingers around the shunt can supply enough current for the shunt, there is no flow of current in the emitter outside these fingers. An example of this is shown in Fig. 11, where the potential dip of 80 mV would be large enough to have a considerable influence radius without fingers (compare with Fig. 10).

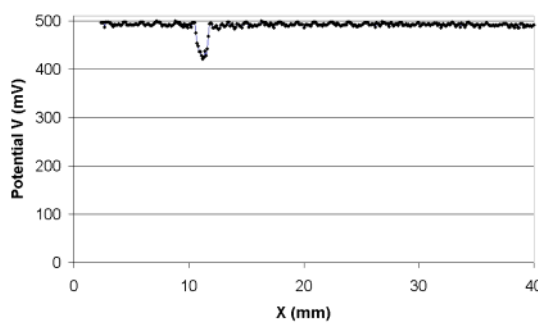


Figure 11: Confined influenced area by easy current supply by the fingers in case of low contact resistance.

However, when the fingers have a considerable contact resistance they cannot easily supply current for the shunt and the situation will be more like the one calculated without fingers. An example of this case is shown in Figure 12.

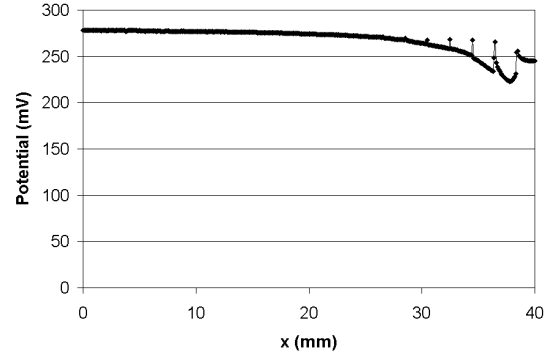


Figure 12: Potential distribution around shunt for large contact resistance, in this case the potential is more like the one without fingers.

In fact, a shunt is somewhat shielded if the fingers around it have a large contact resistance, reducing to some extent the current loss due to the shunt. This is comparable to the shielding of a shunt by emitter sheet resistance which was discussed recently in [11]. In that paper the influence of contact resistance was not taken into account.

Comparing Figs. 11 and 12, it is clear that the area with lowered potential around a shunt is not a good measure for the shunt magnitude on real cells. Another point to note is that the potential dip is not very sharp in Fig. 12. This is probably due to the fact that the probe was not scanned exactly across the shunt; the probe diameter of 0.2 mm also prevents the measurement of a very sharp peak.

Although actual potential distributions will always differ depending on the exact shunt location and metallization properties, it is in principle always possible to calculate the total current flowing through a shunt. The method is to perform a path integration of i along any closed path around the shunt that does not include a finger part:

$$I_{sh} = \oint \vec{i} \cdot \hat{n} ds = \frac{1}{\rho_s} \oint \nabla V \cdot \hat{n} ds .$$

i is written here in vector form and its inproduct with the inward normal to the integral path is taken, to account for the fact that i will generally not be perpendicular to the integral path (in the circle symmetric case, vector magnitudes were sufficient since i was perpendicular to the circle everywhere).

In practice, it is difficult to calculate the integral accurately since a very high lateral resolution is needed for the measurement of V in both x and y direction. However, a rough estimate which is sufficient for most purposes can be made with it.

In the near future, some detailed measurements will be made in an experiment to compare the absolute shunt current found with lock-in IR thermography with the value found with the Shuntscan.

To summarize, the Shuntscan can detect shunts at forward bias with sufficient degree of accuracy. It has been shown that the area with lowered potential around a shunt is not a good measure of its magnitude on a real cell, because the contact resistance of surrounding fingers is of influence as well. It is explained that the Shuntscan potential data can be used for quantitative analysis of shunts. In practice, the Shuntscan is mostly used in a qualitative way, some examples will be given in the next section.

Shuntscan application

Using the Shuntscan, several types of defects have been identified so far. In Fig. 13, a Shuntscan made on a 10 x 10 cm cell having a shunt resistance of $500 \Omega\text{cm}^2$ is shown.

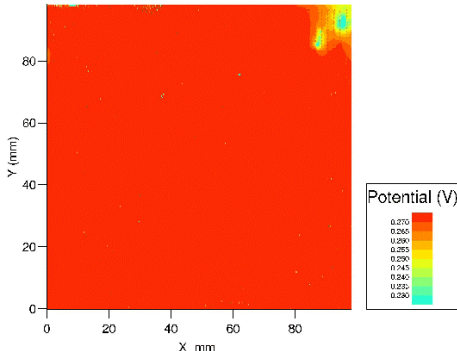


Figure 13 : Shuntscan on a multicrystalline silicon cell with shunts in the upper right corner.

It is clear that there are several shunts between the fingers in the upper right corner of the cell. After this corner was removed, the resistance increased to $3000 \Omega\text{cm}^2$, which is an acceptable value. In this case, the problem was probably base material related, e.g. SiC precipitates could be the reason.

In another experiment, both a Shuntscan and lock-in IR thermography picture were made for the same cell (see Fig. 14).

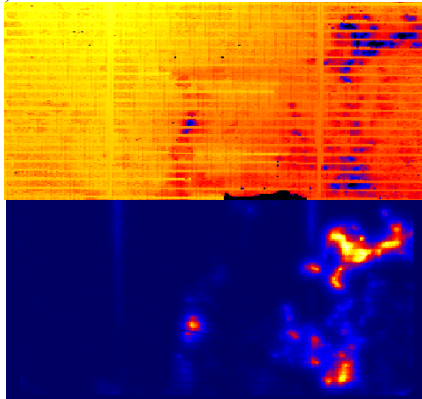


Figure 14: Comparison Shuntscan (upper picture) and lock-in IR thermography. The colors are inverted because a decrease in potential in the Shuntscan corresponds with an increase of the temperature measured by lock-in IR thermography.

It is clear that the methods agree about the shunt locations. The only difference is that shunts below metallization cannot be detected by the Shuntscan because the resistance of the metal is too low, while the heat produced by a shunt can be detected by lock-in IR thermography also below metal. An example of this is visible in Fig. 14 at the right busbar. For the cell in Fig. 14, the shunts were found to be due to material problems in the silicon base material, since scans on neighbouring wafers have shunts on the same locations.

Typical process related problems that were found on other cells are poor edge isolation, metal contamination on the front side of the cell and cracks.

V_{oc} scan method

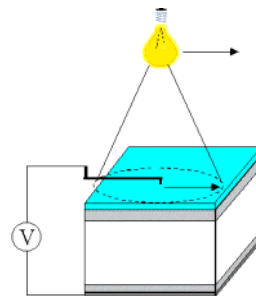


Figure 15: Drawing of the V_{oc} scan method

The V_{oc} scan principle (see Fig. 15) is simple and straightforward. A potential probe centered in a light beam is scanned over the front surface of a cell without front side metallisation, while the cell is in open circuit condition. The metallization has to be omitted to avoid smearing out of the potential. Although the scratching of the cell has been found to cause some V_{oc} loss by scanning a second time, the same distribution pattern is found again, so in that sense the result is reproducible. With the V_{oc} scan, a kind of local V_{oc} is measured, although the values measured can be considerably lower than for uniform illumination. The reason is that the light current generated in the beam can leak to the dark area around it. This effect is not present in case of uniform illumination, because the diode current at each location is compensated by the light current generated at the location itself. Lateral currents are therefore avoided and the local potentials reach higher values.

The result is that potential differences measured with the V_{oc} scan are exaggerated compared to the case of uniform illumination. The advantage is that differences are clearly visible; on the other hand, the current leakage makes the analysis of the scan method in a quantitative way difficult. Up til now, the V_{oc} scan has only been used as a qualitative tool.

V_{oc} scan application

In Fig. 16, the influence of the local absence of a back surface field (BSF) as measured by a V_{oc} scan is shown. The cell without front contact was fabricated with an aluminum back side, except for the regions at the back below the busbars, where silver was printed for soldering.

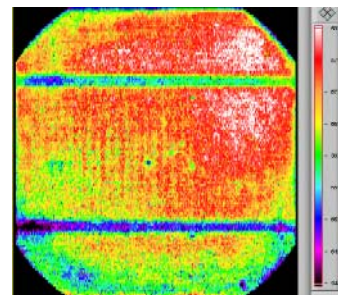


Figure 16: V_{oc} scan for a mono-crystalline cell. The potentials on the cell cover the entire color scale on the right, ranging from 540 to 580 mV.

V_{oc} is lower at the ‘back side busbars’ where no aluminum is present, due to less gettering and/or an

absence of BSF at these regions. In addition, V_{oc} on this cell turns out to be slowly increasing to the upper right, caused by emitter or BSF non-uniformity.

In another experiment, acid etched multi-crystalline cells were fabricated, among them some without front contact. The neighbouring complete cells had high J_{sc} values, but a low FF . A V_{oc} scan on one of the cells without front contact and a picture of the cell are shown in Fig. 17.

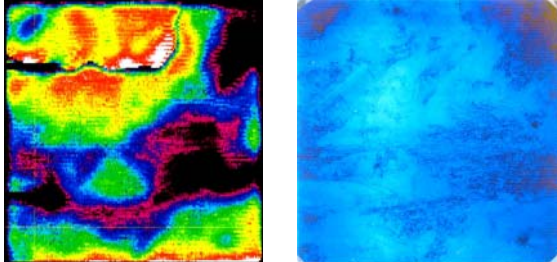


Figure 17: V_{oc} scan and picture for an acid etched cell. The coincidence between low V_{oc} (black regions) and etched defects is clear.

The scan demonstrates that areas where defects have caused extra etching are mainly responsible for the FF loss, since the measured V_{oc} is lower in these areas. A dark crack is also visible in the upper part of the scan, while it was not visible on the cell.

As the V_{oc} scan method is presented here for the first time, not many cells have been studied yet. However, these first results show that also the V_{oc} scan is a promising method for process optimization.

Conclusions

The different techniques based on potential mapping used by the Corescan are able to locate losses due to contact resistance, shunts and recombination in solar cells. The sensitivities of the methods are sufficient to find all significant locations.

An important fact found with the Corescan is that the cross-belt temperatures differences in a belt furnace can be significant, resulting in non-uniform contact resistance.

With the Shuntscan, shunts were detected related to base material problems, metal contamination and edge isolation problems. The influence of fingers on the measured potential distribution around a shunt was discussed, as well as the quantification of shunt current from measured potentials around a shunt.

The principle of the newly developed V_{oc} scan was explained, as well as its interpretation. With this V_{oc} scan, the influence of the local absence of a BSF on the back side was demonstrated. Acid texurization was found to be responsible for local fill factor loss of the silicon diode itself at defect locations visible by eye.

Summarizing, the Corescan instrument, equipped with the Corescan, Shuntscan and V_{oc} scan, has proven to be a valuable tool for troubleshooting and process optimization in industrial solar cell processing.

References

- [1] A.S.H. van der Heide, A. Schönecker, G.P. Wyers, W.C. Sinke, 16th European Photovoltaic Solar Energy Conference, Glasgow (United Kingdom), 1438 (2000)
- [2] R.A. Sinton, 9th NREL workshop on crystalline silicon solar cell materials and processes, Breckenridge (Colorado, USA), 67 (1999)
- [3] A.S.H. van der Heide, Dutch patent 1013204, priority date 4 October 1999, patent granted 5 April 2001, worldwide patent pending
- [4] <http://www.sunlab.nl>
- [5] O. Breitenstein, W. Eberhardt, K. Iwig, 1st World Conference on Photovoltaic Energy Conversion, Hawaii (USA) 1633 (1994)
- [6] M. Langenkamp and O. Breitenstein, 9th NREL workshop on crystalline silicon solar cell materials and processes, Breckenridge (Colorado, USA), 198 (1999)
- [7] J. Kabs and H.J. Möller, Proceedings 14th European Photovoltaic Solar Energy Conference, Barcelona (Spain) 2381 (1997)
- [8] G.K. Reeves, H.B. Harrison, IEEE Electron Device Letters, **3**, 111 (1982)
- [9] A.S.H. van der Heide, J.H. Bultman, J. Hoornstra and A. Schönecker, 12th Photovoltaic Science and Engineering Conference, Jeju (Korea), 591 (2001)
- [10] A. Kaminski, M. Langenkamp, O. Breitenstein, 14th European Photovoltaic Solar Energy Conference, Barcelona (Spain), 830 (1997)
- [11] J. Dicker, J. Isenberg and W. Warta, 17th European Photovoltaic Solar Energy Conference, Munich (Germany), 1567 (2001)
- [12] S. Bowden and A. Rohatgi, 17th European Photovoltaic Solar Energy Conference, Munich (Germany), 1802 (2001)

Appendix

An important consequence of the fact that R_{cl} is often found to be quite non-uniform is that the standard models to fit $J-V$ curves of solar cells are not capable to include recombination and series resistance in the right fit parameters. A clear demonstration of this effect is shown in Figure A.1, where the $J-V$ curve is calculated for a hypothetical cell having a region with good contact and an equally large region with bad contact. The applied method is to calculate $J-V$ curves for the area between two fingers for both a low R_{cl} and a high R_{cl} and averaging these $J-V$ curves. Averaging is done by taking $(J_{low\ R_{cl}} + J_{high\ R_{cl}})/2$ at each potential. The two curves are calculated assuming that the region between the fingers can be described by the following position-independent parameters: diode factor $m = 1.3$, $V_{oc} = 590$ mV, emitter sheet resistance = $50\ \Omega$.

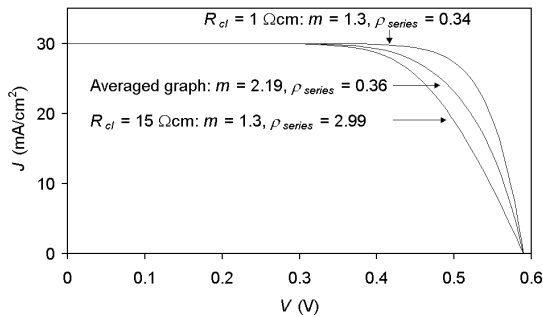


Figure A.1: Calculation of influence non-uniform R_{cl} on the J-V curve and fit parameters for a hypothetical cell having a region with good contact and a region with bad contact.

All curves were fitted and the parameters of the curves are indicated in the figure. It is found that the curves for the regions between the fingers are correctly fitted: the fitted m in both cases equals the m used as input, whereas the series resistance is almost increased by a factor of 10 for the high R_{cl} case (it is slightly less than 10 because the emitter sheet resistance is kept the same for both curves). However, fitting the J-V graph for the total cell results in a large increase of m , while the series resistance almost equals the value for the low R_{cl} case. So the very non-uniform potential distribution over the cell leads to an increase of the parameters describing recombination instead of the parameter for series resistance. Note that a uniform increase of the contact resistance was correctly handled in fitting (series resistance increases, m equals m used as input), only non-uniformity leads to problems. However, the non-uniform case is found to be the most occurring one in practice.

As is clear from the example just given, it is even possible to obtain $m > 2$ by R_{cl} non-uniformity, while m should be < 2 according to the standard (1-dimensional) solar cell model. Another paper discussing the fit problems in case of large series resistance non-uniformity was published recently [12]. That paper took line interruptions or non-printed areas as possible reasons for series resistance non-uniformity, non-uniform contact resistance was not mentioned however. The reason for the fact that the normal fit model is not functioning correctly is that the potential differences over the cell are not any more small compared to the thermal voltage q/kT of 25 mV at 300 K. Therefore the correct calculation of the cell output current gets non-linear while the normal fit model that accounts for series resistance with a lumped value ρ_{series} assumes linearity.

A solution that is sometimes used to account for the fit problems just mentioned is to introduce a series resistance that is not constant, but current dependent [12]. However, it is better to avoid the use of this concept by measuring V_{oc} as a function of light intensity [2] for the quantification of series resistance influence. Using the fill factor FF_{Rs0} of the “series resistanceless” J-V curve obtained with that method, and subtracting the fill factor FF of the normal J-V curve, the influence of series resistance on the solar cell J-V curve can be easily quantified by

$$\Delta FF_{Rs} \equiv FF_{Rs0} - FF,$$

By the use of ΔFF_{Rs} , the series resistance influence is characterized by a single value which gives a direct feeling for the efficiency loss due to series resistance.

As a demonstration a normal J-V curve and the series resistanceless curve of the same cell are shown for a cell with a high contact resistance region in Fig. A.2.

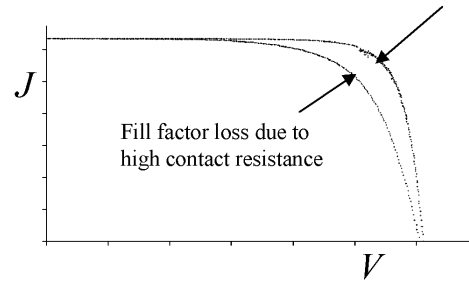


Figure A.2: Series resistanceless curve obtained from V_{oc} measurements as a function of light intensity, and the normal J-V curve. The cell is one with a high and non-uniform contact resistance, $\Delta FF_{Rs} = 11.3\%$.

When the FF difference between the curves is large as in the curves above, the Corescan is the appropriate method to find the locations or regions that are responsible for the fill factor loss.

Quantitative Shunt Investigations on Solar Cells by Lock-in Thermography

O. Breitenstein

Max Planck Institute of Microstructure Physics, Weinberg 2, D-06120 Halle, Germany

1. Introduction

If a one-dimensional modelling of a solar cell is performed e.g. by PC1D, one assumes that the properties of this cell are homogeneous across its whole area. Especially, the dark I-V characteristic is assumed to be the same in every position. In real solar cells, however, there are always local positions of an increased current density, which are called shunts. We will use the name "shunt" for all local maxima of the forward or reverse current density, independent on their geometry, even if they are no short circuits in the electrotechnical sense. It will turn out that there are shunts having a linear (ohmic) I-V characteristic and shunts having a non-linear (diode-like) one. Except for solar cells of very high quality, these shunts dominate the dark I-V characteristic under reverse bias and under low forward bias conditions.

Shunts may act in two ways in solar cells: I. In operation at the working point of the cell (usually near 0.5 V forward bias) all currents flowing through shunts are current losses, which cannot be fed out of the cell. Hence, shunts are reducing the fill factor (FF) and the open circuit voltage (V_{oc}) and thereby the efficiency of the cell. The detrimental influence of shunts on the efficiency is the stronger the lower the illumination level is [1]. II. If one solar cell in the string of a solar panel is shadowed, under unfavourable conditions this cell may become reverse-biased by the other cells in this string by more than 10 V, whereby a noticeable reverse current may flow through this cell. If there are local shunts acting under reverse bias, excessive heat may be produced in these positions leading to so-called hot spots, which may even destroy the cell or the solar panel [2]. Thus, shunts acting under reverse bias may limit the reliability of solar panels.

The dark I-V characteristic of solar cells is usually described by the so-called 2-diode model (see, e.g. Kaminski [3]), modelling the solar cell as the parallel action of two diodes, having two different ideality factors, and an ohmic parallel resistance R_p , completed by a series resistance R_s . Here the first diode describes the (usually homogeneous) diffusion current across the pn-junction. The second diode is attributed to point defect recombination in the space charge layer, which is sometimes modified by saturation effects [4] or trap-assisted tunneling or Pool-Frenkel effect [3] to explain ideality factors above two. Only the ohmic parallel resistance R_p is usually attributed to local shunts. This model assumes that the I-V characteristic of shunts should be ohmic, hence shunts acting under forward bias should also act under reverse bias and vice versa. We have already shown [5] and will demonstrate in the following that this assumption is true only for some fraction of all existing shunts. In good solar cells even the majority of shunts show a non-linear (diode-like) I-V characteristic. Typical origins of these shunts are contacts of the emitter-metallization to the base (Schottky type shunts) or local positions of high recombination activity like scratches, decorated crystal defects, or the edge of the cell. These non-linear shunts do not decrease R_p significantly and even may show a low reverse current. Nevertheless, they dominate the low bias part of the dark forward I-V characteristic and thus deteriorate especially the fill factor. Hence, their influence on the efficiency can only be estimated correctly if they are detected under forward bias conditions.

There are several techniques available allowing to image shunts in solar cells. Beam injection techniques are essentially EBIC (electron beam-induced current imaging, performed in the scanning electron microscope) and LBIC (light beam-induced current imaging, usually performed

on a x-y scanner). Here a focused beam of electrons or light excites minority carriers, which are separated by the pn-junction, and the current, usually measured under zero bias, is used to generate the image. Actually, EBIC and LBIC are used to image inhomogeneities of the diffusion length caused e.g. by crystal defects. However, if the excitation takes place near a strong shunt being active under zero bias, some part of the generated minority carriers are flowing across this shunt and not to the current amplifier, hence the surrounding of the shunt appears dark in the EBIC / LBIC image. If LBIC is performed in lock-in mode at different applied biases ("CELLO", [6]), shunts can be investigated even near the working point of the cell. However, one limitation of all beam injection techniques is that they do not allow to image shunts if they are lying below grid lines, which happens quite often. They share this disadvantage with PRAMP [7, 8], which measures the potential drop at the emitter surface near a shunt. Thermal shunt detection techniques do not have this limitation, since heat easily penetrates metallization layers. Here a bias is applied to the cell in the dark, leading to a current flow through the shunts, which leads to a local heating of the shunt positions. Hence, the operating conditions of the cell are simulated here in the dark by externally applying a bias. This procedure is justified by the fact that the illuminated I-V characteristic equals the dark characteristic parallel shifted by the short circuit current, if the series resistance R_s is correctly regarded (superposition principle). According to all our knowledge all kinds of shunts in silicon cells are acting both in the dark and under illumination. This statement is not true anymore for thin film and organic solar cells, where e.g. photoconducting barrier layers play a role.

The simplest way to image shunts thermally is to use low-cost thermochromic liquid crystal sheets [9, 10], which are commercially available e.g. from Edmund Scientific. Also infrared (IR) cameras have been used for the direct thermal imaging of shunts [2, 11]. The main problem with these stationary thermal imaging techniques is their limited thermal sensitivity, which is in the order of 100 mK. Note that silicon is a very good heat conductor. Hence, locally generated heat is instantly dissipated away from the shunt, leading to a blurred appearance of the imaged shunts and to a relatively low thermal contrast. Due to these halos in thermal images the real spatial resolution is often worse than the pixel resolution. For sensitivity limitations, with these stationary thermal techniques shunts could be imaged only under several Volts reverse bias, but not under a low forward bias near the operation point. Kaminski et al. [12] have averaged many IR images with and without applied bias and subtracted the results from each other. In this way they could image strong shunts under a relatively large forward bias. However, the blurred appearance of the images remained, and weak shunts under low forward bias remained invisible. So until recently there was simply no technique available to image shunts also under low forward bias conditions, and to measure the I-V characteristic of single shunts non-destructively in order to check the predictions of the two diode model. Lock-in thermography is the technique of choice which solves this problem and additionally improves the real spatial resolution of the images.

In this contribution the experimental technique of lock-in thermography is reviewed. Then the physical basics of a quantitative interpretation of lock-in thermography results in terms of thermally measuring shunt currents are presented. Finally some typical examples of quantitative shunt investigations are introduced.

2. The lock-in thermography technique

Lock-in thermography means that a periodically pulsed bias is applied to a solar cell, and the periodic temperature (T-) modulation at the surface is measured over many periods and processed

and averaged in every pixel according to the lock-in principle. So in contrast to stationary thermography this is a dynamic (a.c.) technique, which is not disturbed e.g. by T-drift phenomena. By averaging the result over many lock-in periods the signal-to-noise ratio (SNR) improves with the square root of the acquisition time and may become orders of magnitude better than the SNR of the primary T-measurement. In the past lock-in thermography was used mostly for non-destructive testing of mechanical components [13]. A special lock-in thermography technique showing a sensitivity below $100 \mu\text{K}$, which was able to investigate shunts in solar cells under low forward bias for the first time, was the Dynamic Precision Contact Thermography technique (DPCT, [14, 15]). This was a mechanically scanning and contacting technique, having the advantage of low costs but the disadvantage of long acquisition times of many hours. Therefore it did not become very popular. Modern lock-in thermography systems are based on highly sensitive focal plane array (FPA) thermocameras working either in the mid IR range ($3 \dots 5 \mu\text{m}$ wavelength) or in the long range ($8 \dots 10 \mu\text{m}$). There are several lock-in thermography systems on the market. One of it (called TDL 384 M 'Lock-in', by Thermosensorik GmbH Erlangen [16]) was developed in cooperation with Max Planck Institute of Microstructure Physics (Halle) and is specialized to the investigation of electronic components like solar cells. All investigations shown in this contribution are performed using this system. Therefore this system will be introduced here in some more detail.

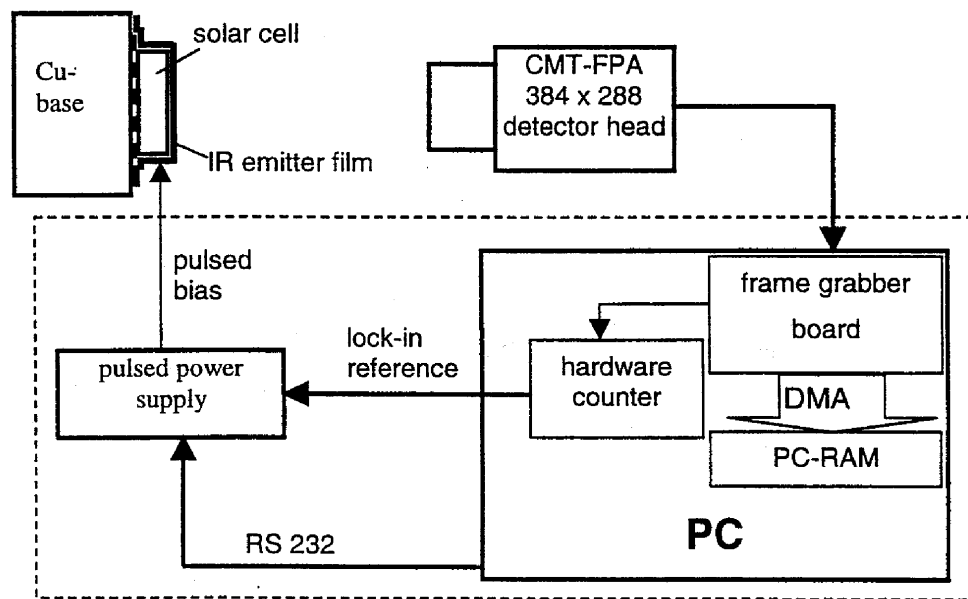


Fig. 1: Functional scheme of the TDL 384 M 'Lock-in' thermography system

As Fig. 1 shows, the system is based on a focal plane array (FPA) detector head, which is fabricated by AIM (Heilbronn) [17]. It contains a high resolution (384×288 pixel) detector array consisting from mercury cadmium telluride (MCT), which is sensitive between 3 and $5 \mu\text{m}$ wavelength and is cooled down to 70 K by a linear Stirling cooler. The image information is digitized in the detector head with an accuracy of 14 bit at a rate of 16 MPixel/s , leading to a full image frame rate of up to 140 Hz . If only some part of the image is read out, the frame rate may increase up to 800 Hz . A high frame rate is advantageous both for obtaining a good sensitivity of the measurement and a good spatial resolution (see next section). The image information is written by a frame grabber board by direct memory access (DMA) directly into the RAM storage

of the control PC, which for our system is a 2x700 MHz Dual Pentium III system running under Windows NT. The PC generates the lock-in reference trigger signal by using a hardware counter, which is directly triggered from the thermocamera, and it performs the actual lock-in correlation procedure on-line. The whole electronics unit is contained in a rugged roll container. During measurement the solar cell is covered by a 20 μm thin black-painted plastic film, which serves as an efficient IR emitter and is sucked to the Cu-base by a vacuum. Between the sample and the Cu-base a 100 μm thin woven Cu-net is placed, which distributes the vacuum laterally and serves as a heat diffusion barrier to the Cu-base. Only by using this barrier the results are independent on any heat conduction to the Cu-base.

The principle of the correlation procedure is shown in Fig. 2. Since the phase of the T-modulation signal is not constant, two-channel lock-in detection has to be used. In each of the channels every pixel information of every incoming image is multiplied by a weighting factor, which changes from image to image and may be positive or negative. The results are added up in two separate frame storages. In the first channel the weighting factors are approximating a sin function and in the other channel a -cos function. Thus, after the measurement the image stored in the first frame storage is proportional to the temperature modulation in-phase with the applied pulsed bias (0° -image, $T^{0^\circ}(x,y)$), and that in the other storage is proportional to the T-modulation phase-shifted against the bias pulses by -90° (quadrature image, $T^{-90^\circ}(x,y)$). From these two images, the phase-independent amplitude image $A(x,y)$ and the phase image $\Phi(x,y)$ can easily be calculated by the following relations:

$$A(x,y) = \sqrt{(T^{0^\circ}(x,y))^2 + (T^{-90^\circ}(x,y))^2} \quad \Phi(x,y) = \arctan\left(\frac{-T^{-90^\circ}(x,y)}{T^{0^\circ}(x,y)}\right) \quad (1)$$

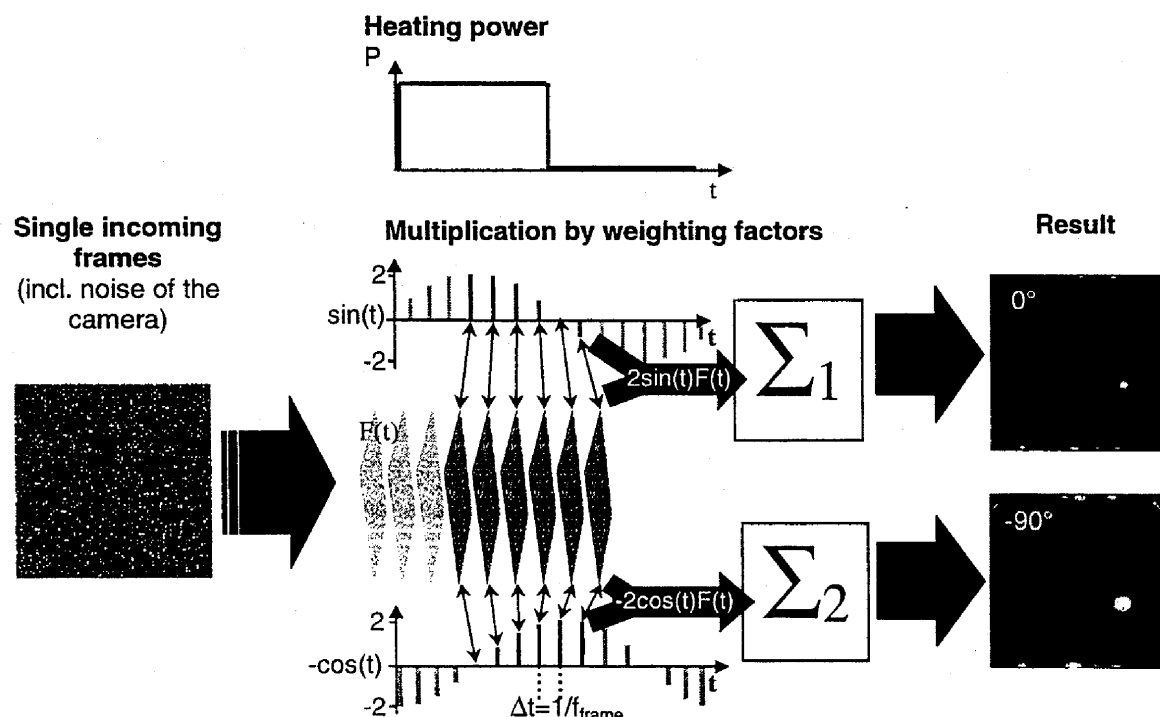
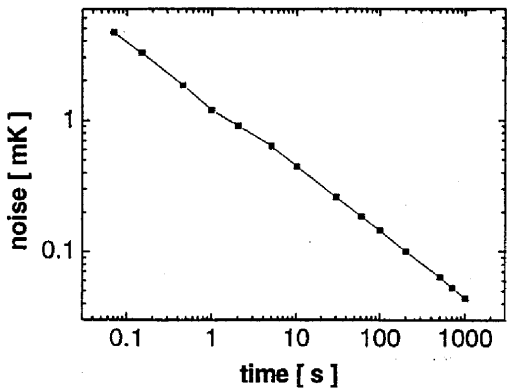


Fig. 2: Principle of the digital dual channel lock-in correlation procedure

Fig. 3: Amplitude noise level of the TDL 384 M 'Lock-in' thermography system as a function of the data acquisition time, measured at room temperature



A number of different IR objectives are available for the detector head. The most universal one is a f# 1.5 / 28 mm wide angle objective ("Weitwinkel MWIR"), which allows to use a wide range of object distances from 7 cm to ∞ , corresponding to an image size between 2 cm and ∞ . Hence, with this objective the best possible pixel resolution is about 50 μm , which still can be improved somewhat by using distance rings. There are special microscope objectives available leading to a pixel resolution down to 5 μm . The operation software allows to set the measurement parameters, to choose between different display types, to define and evaluate lines of interest or areas of interest, to perform automatic batch measurements e.g. for different biases (for measuring I-V characteristics, see below), to export the images as .bmp or .asc files (quantitatively scaled in mK), to create protocol sheets, and much more. Fig. 3 shows the measured dependence of the measured amplitude noise level of this system as a function of acquisition time. The noise level decreases with $1/\sqrt{t_{\text{acq}}}$ and reaches after 1000 s (17 min.) a level of about 44 μK .

3. Basics for the quantitative interpretation of lock-in thermograms

The differential equation for heat diffusion in a homogeneous body having a specific heat of c_p , a density of ρ , and a heat conductivity of λ is:

$$c_p \rho \frac{\partial T}{\partial t} = \lambda \Delta T + p \quad (2)$$

Here T is the time-dependent temperature field, Δ is the delta operator, t is the time, and p is the time-dependent field of the power density dissipated in the body. This is a linear differential equation, which has the property that a sum of two of its solutions is also a solution of the equation. Hence, time-dependent thermal fields of different heat sources are linearly superimposing. The simplest solution of (2), which holds e.g. for a plane harmonically oscillating heat source in an infinite 3-D body, is a plane thermal wave in z -direction:

$$T(z, t) = a \exp\left(-z \sqrt{\frac{i \omega c_p \rho}{\lambda}}\right) \exp(i \omega t) = a \exp\left(\frac{-z}{\Lambda}\right) \exp\left(i\left(\omega t - \frac{z}{\Lambda}\right)\right) \quad (3)$$

$$\text{with } \Lambda = \sqrt{\frac{2 \lambda}{\rho c_p \omega}}$$

Here a is an amplitude factor containing the power density of the source, ω is $2\pi f_{\text{lock-in}}$, and Λ is the so-called thermal diffusion length, which is proportional to $1/\sqrt{f_{\text{lock-in}}}$. For silicon at $f_{\text{lock-in}} = 3$ Hz, Λ is about 3 mm. Eq. (3) represents a strongly damped plane wave, whose amplitude decays in a distance of Λ by $1/e = 0.367$ and within a distance of one wavelength being $2\pi\Lambda$ by a

factor of 0.00187! This strong (frequency-dependent) damping, which basically also holds for other heat source geometries, is the reason for the improved real spatial resolution of lock-in thermography relative to stationary thermography. Whenever a sample is thin against the thermal diffusion length Λ , this sample may be regarded as "thermally thin" with respect to the lock-in frequency used. For such a 2-D sample the solution of (2) for an oscillating point heat source is [18]:

$$T(r, t) = a K_0 \left(r \sqrt{\frac{ic_p \rho \omega}{\lambda}} \right) \exp(i \omega t) = a \left(\ker \left(\frac{r\sqrt{2}}{\Lambda} \right) + i \text{kei} \left(\frac{r\sqrt{2}}{\Lambda} \right) \right) \exp(i \omega t) \quad (4)$$

Here K_0 is the modified Bessel function of second kind of order zero, which can be described by the real part $\ker(x)$ (describing the 0° -signal) and the imaginary part $\text{kei}(x)$ (describing the 90° -signal), a is an amplitude factor containing the power of the heat source, and r is the distance to the point source.

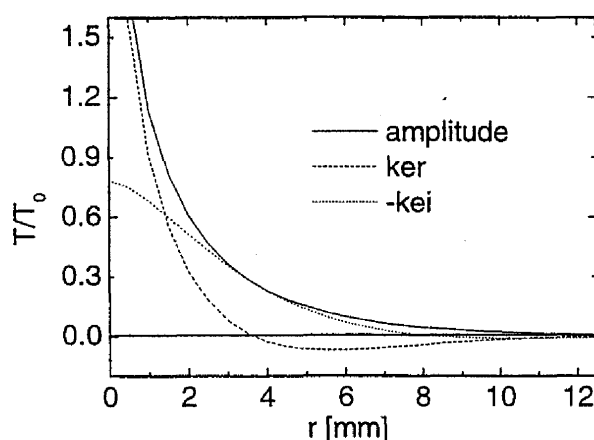


Fig. 4: Radial profile of the 0° -signal (\ker) and the -90° -signal ($-\text{kei}$) around a point heat source for $\Lambda = 3$ mm

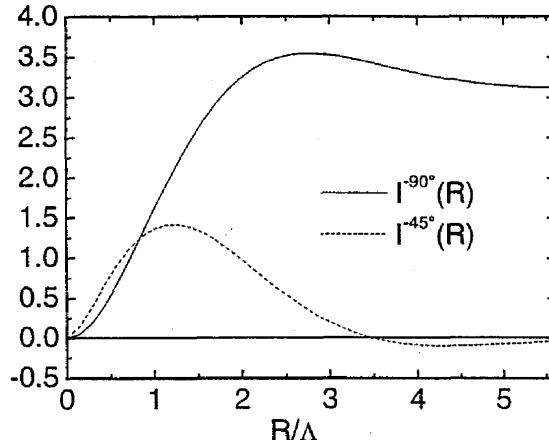


Fig. 5: Dependence of the plane integrals of the 0° - and the -90° signal around a point source on the radial integration boundary R

Fig. 4 shows the radial dependence of \ker and $-\text{kei}$ for a lock-in frequency of 3 Hz in silicon, together with the amplitude calculated by (1). It turns out that the 0° -signal (\ker) diverges in source position and shows a considerable overshoot into the negative, but the -90° -signal ($-\text{kei}$) shows only a single maximum in source position and nearly no overshoot. If a radial plane integral $I^{0^\circ, -90^\circ}(R)$ is calculated for these two signals in the surrounding of a point source up to a distance of R (see Fig. 5), its value approaches zero for the 0° -signal, but a well-defined value for the -90° -signal for large R . Hence, the plane integral of the -90° signal in a thermally thin sample around a point heat source is proportional to the power of this source, if all integration boundaries are sufficiently distant from the heat source:

$$P = C \iint_A T^{-90^\circ}(x, y) dx dy \quad (5)$$

Here A is the integration area and C is a scaling factor, which depends on the properties of the sample and on the measurement conditions. Eq. (5) is the base of the quantitative interpretation of

lock-in thermograms. If eq. (5) holds for a point heat source, it also holds for an arbitrarily shaped heat source (which can be thought as a superposition of many point heat sources) owing to the linear superposition properties of temperature fields. Especially, it also holds for the whole solar cell, where we know the total dissipated power by the current I_{cell} and the applied bias V_{cell} during the measurement. Performing the plane integration in (5) over a certain rectangular area is a trivial task using the "average value" option of the "area of interest" function, which is included e.g. in the lock-in thermography software. Thus, in order to measure the current through an isolated shunt I_{shunt} , the average value of the -90° signal $\overline{T_{shunt}^{-90^\circ}}$ has to be measured across a sufficiently large area A_{shunt} containing the complete T -field of this shunt, and the signal $\overline{T_{cell}^{-90^\circ}}$ has to be measured across the complete cell area A_{cell} . If there is a notable homogeneous current present, additionally the signal $\overline{T_{homogeneous}^{-90^\circ}}$ has to be measured in a region containing no shunts, which has to be subtracted from $\overline{T_{shunt}^{-90^\circ}}$ in order to obtain the net shunt current. Thus, the final rule for quantitatively measuring the current through a local shunt by lock-in thermography is:

$$I_{shunt} = I_{cell} \frac{\left(\overline{T_{shunt}^{-90^\circ}} - \overline{T_{homogeneous}^{-90^\circ}} \right) A_{shunt}}{\overline{T_{cell}^{-90^\circ}} A_{cell}} \quad (6)$$

This procedure can be repeated for different biases in order to measure local I-V characteristics of single shunts. Alternatively, it may be checked for any bias which dark current $I_{no\ shunts}$ would flow through a solar cell of of the same area A_{cell} , if it would not contain any shunts ("hypothetical cell"):

$$I_{no\ shunts} = I_{cell} \frac{\overline{T_{best}^{-90^\circ}}}{\overline{T_{cell}^{-90^\circ}}} \quad (7)$$

Note that for low biases the averaged temperature values used in (6) are increasingly influenced by statistical noise, hence this calculation becomes unreliable. Then for local shunts the qualitative LIVT procedure proposed by Konovalov [19] should be preferred, which just evaluates the signal peak value in shunt position T^{peak} . This procedure is based on the fact that this peak value is proportional to the dissipated power. Hence, dividing this peak value by the applied bias V_{cell} (in shunt position!) gives a number, which is proportional to the shunt current:

$$I_{shunt} = C^{LIVT} \frac{T^{peak}}{V_{cell}} \quad (8)$$

Here C^{LIVT} is a proportionality factor, which should be constant for a series of thermograms measured at different biases. This factor may easily be obtained by fitting the result of (8) to the result of (6) for a sufficiently large bias (e.g. 0.5 V), where the accuracy of (6) is still acceptable. The LIVT procedure (8) works both with the amplitude and with the 0° - and the -90° signals. However, the most appropriate signal is the 0° signal, because this has a sharp maximum and is not influenced by a homogeneous thermal signal contribution, which produces a pure -90° signal.

4. Quantitative shunt investigations

Fig. 6 shows results of the investigation of a typical commercial monocrystalline solar cell containing different types of shunts. All images are amplitude images. The measurements have been performed at +0.5 V forward bias (near the working point), at -0.5 V reverse bias (for checking the linearity of the I-V characteristics of the shunts, displayed in the same scaling as the thermogram for +0.5 V), and at -12V reverse bias (displayed in a different scaling). The acquisition time for the first images was about 10 min, but that for the last one was only some seconds. Shunts having a linear I-V characteristic should show the same brightness in the first two images. Indeed, two of the shunts (labelled A) are linear, but most of the other (e.g. B) are non-linear, hence they are not or only weakly visible under -0.5 V reverse bias. Nevertheless, under -12 V reverse bias hot spots become visible both for linear and for some non-linear shunts, hence also non-linear shunts may produce prebreakdown sites. Note that the signal at the dominant hot spots considerably exceeds the scaling range of 20 mK chosen here. Therefore they appear artificially blurred. Additionally to the dominant shunts, a large number of other weak breakdown sites become visible under -12 V reverse bias, which were invisible under low bias conditions. At the operation point at +0.5 V forward bias the wafer edge and the major grid lines become visible, hence also in these positions an excess forward current is flowing. As it was found also by Glunz et al. [20], the additional edge current is a recombination current flowing in the position where the pn-junction crosses the surface. A quantitative evaluation of the -90° image of the measurement at +0.5 V according to eq. (7) was performed. It lead to the conclusion that, if this cell would have no shunts at all, its forward current at +0.5 V would be about $I_{\text{no shunts}} = 69 \text{ mA}$, in contrast to the measured value of $I_{\text{cell}} = 96 \text{ mA}$. So about 27 mA are flowing at +0.5 V forward bias across all shunts visible in the left image of Fig. 6. Hence, this cell does not suffer seriously from shunts.

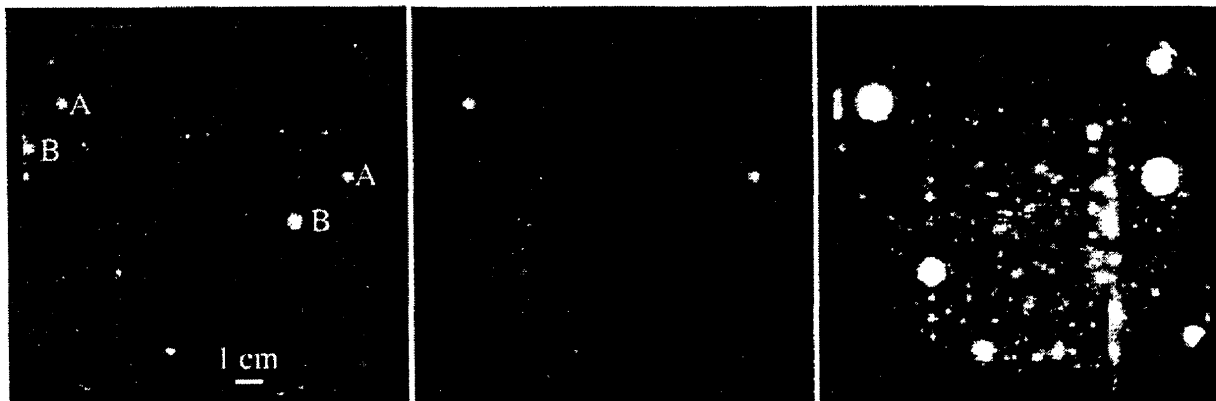


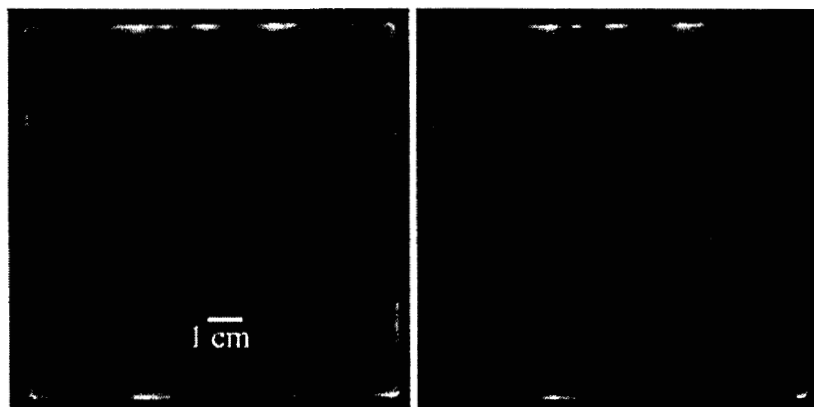
Fig. 6: Lock-in thermograms of a commercial $12.5 \times 12.5 \text{ cm}^2$ sized monocrystalline solar cell measured under +0.5 V forward bias (left), under -0.5 V reverse bias (middle, both scaled to 2 mK) and under -12 V reverse bias (right, scaled to 20 mK)

Results of the quantitative thermal measurement of the I-V characteristic of a shunt current under forward bias according to eq. (6) are shown in Fig. 7. This shunt was a non-linear one, similar to the shunts called B in Fig. 6, which was not lying below a grid line. The shunt current was independently measured at ECN Petten (Netherlands) by PRAMP [7], which measures the voltage drop between the shunt position and the neighbouring grid line at different biases. This voltage drop signal is proportional to the shunt current. In Fig. 7 the results of the thermal

measurements are compared with that of the PRAMP measurement, which were fitted to the thermally measured current only at +0.4 V. We see a very good agreement of the non-linear shape of the I-V characteristic of this shunt, as measured by these two independent techniques.

The final investigation was to estimate the quantitative influence of shunts on the efficiency of a solar cell as a function of illumination intensity. Here the sample was an experimental multicrystalline cell suffering from shunting due to residues of the emitter at the edge. Fig. 8 shows two lock-in thermograms (amplitude images) measured at +/- 0.5 V in the same scaling. It is visible that here most shunts are lying at the edges of this cell, and that in contrast to Fig. 6 most of these shunts show a linear I-V characteristic. The ohmic parallel resistance of this cell was $R_p = 14.6 \Omega$, which is not very low for a 100 cm^2 sized cell ($1.46 \text{ k}\Omega\text{cm}^2$). By analyzing the measured dark and illuminated I-V characteristics of this cell, the measured efficiency could be simulated from the dark I-V characteristic for any illumination intensity to an accuracy of below 1 % (relatively) by assuming the superposition principle and a constant series resistance of $R_s = 0.023 \Omega$. In the following we will construct the dark I-V characteristic, which this cell would have without any shunts, based on thermographic investigations. This allows us to estimate the influence of the shunts on the efficiency quantitatively.

Fig. 8: Lock-in thermograms of an experimental multicrystalline cell measured under +0.5 V forward bias (left) and under -0.5 V reverse bias (right), both scaled to 10 mK



Lock-in thermography measurements of this cell have been performed at 5 different biases between 0.4 and 0.55 V. Using the -90° images and eq. (7) the hypothetical I-V characteristic of this cell containing no shunts was estimated in this bias range, which is shown together with the measured characteristic in Fig. 9. For comparison also an exponential characteristic with an ideality factor of unity ("kT-current") is shown. In the measured characteristics the influence of the series resistance $R_s = 0.023 \Omega$ was corrected. It is visible that the cell without any shunts fairly well approximates the kT-current, whereas the ideality factor of the real cell is between 1.5 and 3.5 (influenced by R_p !) in this bias range. Hence, the lower the bias, the larger is the current

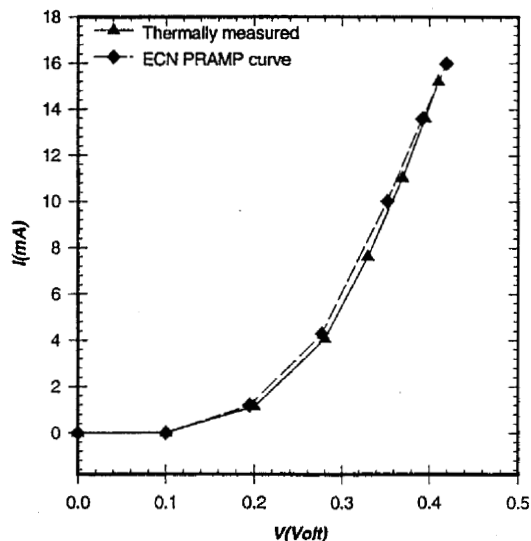


Fig. 7: I-V characteristic of a non-linear shunt measured thermally and by PRAMP

fraction flowing across the shunts and vice versa. Again, using the superposition principle and regarding $R_s = 0.023 \Omega$, the illuminated I-V characteristics were calculated for 4 illumination intensities between 100 and 600 W/m^2 from the hypothetical dark characteristic with no shunts shown in Fig. 9. The maximum power points have been determined and the resulting efficiencies are compared with those measured on the real cell as a function of illumination intensity in Fig. 10. The possible relative improvement of the efficiency by avoiding the shunts is about 6.1 %, 8.6 %, 11.6 % and 22.9 % for an illumination intensity of 600, 300, 200, and 100 W/m^2 , respectively. As expected and already shown before [1], the relative influence of shunts is the larger the lower the illumination intensity is. This tendency is most pronounced for linear (ohmic) shunts, but is also present for non-linear shunts like local recombination sites [20].

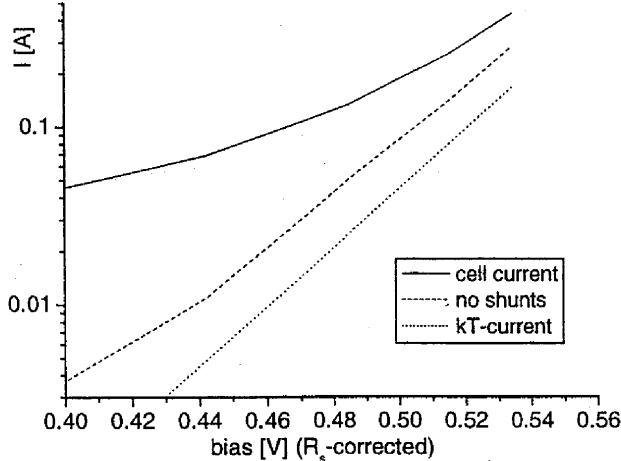


Fig. 9: Measured dark I-V characteristic of the cell of Fig. 8, hypothetical characteristic of the same cell with no shunts (based on thermographic measurements, both R_s -corrected), and kT-current

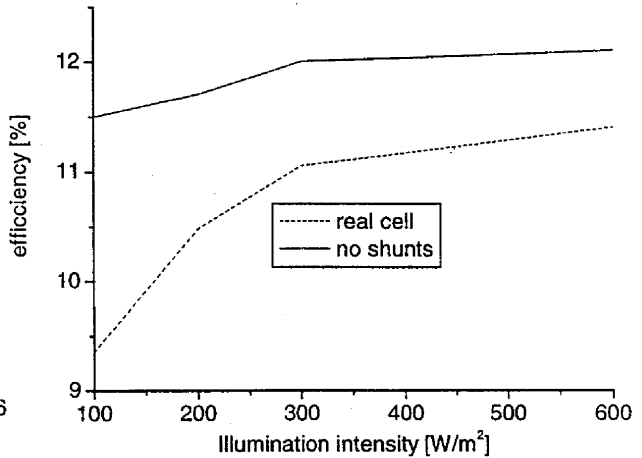


Fig. 10: Dependence of the efficiency of the real cell (measured) and of the hypothetical one with no shunts on the illumination intensity

5. Conclusions

If lock-in thermography measurements are performed at different biases, the results can be evaluated quantitatively in terms of a spatially resolved analysis of the dark I-V characteristic. So the characteristics of single shunts can be measured separately in a non-destructive way. Alternatively, by evaluating the signal of "good" regions of the cell away from the shunts, the properties of a hypothetical solar cell containing no shunts can be concluded and compared to that of the real cell. In this way the influence of the shunts on the efficiency can be concluded quantitatively for different biases, leading to a prediction about the possible degree of improvement if these shunts could be avoided. Since many shunts show a non-linear I-V characteristic, shunt investigations performed at a large reverse bias are not always able to predict the influence of shunts under forward bias correctly.

According to our experiences strong shunts, which seriously degrade the AM 1.5 performance, are always linear (ohmic) shunts. They may be caused e.g. by an incompletely opened emitter at the edge, by Al-contamination at the surface (producing tunnel-junctions between base and emitter), or by inversion channels crossing the bulk. The dominant residual shunts in well-processed cells are also edge shunts (recombination-induced), shunts below grid lines (Schottky-type or recombination-induced), and shunts caused by scratches or decorated crystal defects (both

recombination-induced). All these shunts usually show a non-linear I-V characteristic with a large ideality factor. Thus, as for ohmic shunts their relative influence on the I-V characteristic increases with decreasing bias resp. illumination intensity. Under AM 1.5 they only weakly degrade the cell performance, but they may considerably degrade the performance under weak illumination conditions [1, 20].

The author is grateful to J.P. Rakotoniaina, M. Al Rifai, and S. Neve (all Halle) and to A. van der Heide (ECN, Petten) for experimental cooperation. This work was supported by the BMWi project No. 0329858D (KoSi).

References:

- [1] O. Breitenstein, M. Langenkamp, 2nd World Conf. on Photovoltaic Energy Conversion, Vienna (1998) 1382
- [2] W. Herrmann, M.C. Alonso, W. Boehmer, K. Wambach, 17th Eur. PVSEC, Munich (2000) 1646
- [3] A. Kaminski, J.J. Marchand, H. Elomari, A. Laugier, Q.N. Le, D. Sarti, 25th IEEE PVSC, Washington DC (1996) 573
- [4] J. Beier, B. Voß, 23rd IEEE PVSC, Louisville (1993) 321
- [5] O. Breitenstein, M. Langenkamp, J.P. Rakotoniaina, J. Zettner, 17th Eur. PVSEC, Munich (2000) 1499
- [6] J. Carstensen, G. Popkirov, J. Bahr, H. Föll, 16th Eur. PVSEC, Glasgow (2000) 1627
- [7] A.S.H. van der Heide, A. Schönecker, G.P. Wyers, W.C. Sinke, 16th Eur. PVSEC, Glasgow (2000) 1438
- [8] O. Breitenstein, J.P. Rakotoniaina, A.S.H. van der Heide, 11th NREL Workshop on Crystalline Silicon Materials and Processes, Estes Park (2001) 253
- [9] J. Schmidt, I. Dierking, Prog. Photovolt: Res. Appl. **9** (2001) 263
- [10] C. Ballif, S. Peters, J. Isenberg, S. Riepe, D. Borchert, 29th IEEE PVSC, New Orleans (2002), in print
- [11] A. Simo, S. Martinuzzi, 21st IEEE PVSC, Kissimmee (1990) 800
- [12] A. Kaminski, M. Langenkamp, O. Breitenstein, 14th Eur. PVSEC, Barcelona (1997) 830
- [13] X.P.V. Mal dague: *Theory and Practice of Infrared Technology for Nondestructive Testing*, Wiley (New York) 2001
- [14] O. Breitenstein, W. Eberhardt, K. Iwig, 1st World Conf. on Photovoltaic Energy Conversion, Hawaii (1994) 1633
- [15] O. Breitenstein, M. Langenkamp, Sensors and Actuators A **71** (1998) 46
- [16] www.thermosensorik.com
- [17] www.aim-ir.com
- [18] H.S. Carslaw, J.C. Jaeger: *Conduction of Heat in Solids*, Clarendon, Oxford (1959)
- [19] I.E. Konovalov, O. Breitenstein, K. Iwig, Solar Energy Mat. & Solar Cells **48** (1997) 53
- [20] S.W. Glunz, J. Dicker, M. Esterle, M. Hermle et al., 29th IEEE PVSC, New York (2002), in print

Efficient characterisation techniques for industrial solar cells and solar cell materials

C. Ballif¹, S. Peters¹, T. Zerres¹, J. Isenberg², D. Borchert¹ and G. Willeke²

¹Fraunhofer ISE, Laboratory and Service Centre Gelsenkirchen, Haydnstr. 19, 45884 Gelsenkirchen, Germany

²Fraunhofer ISE, Heidenhofstr. 2, 79110 Freiburg, Germany

1 Introduction

As the photovoltaic industry is moving towards large volume manufacturing, a tighter monitoring of the different processing steps becomes crucial. It is therefore necessary to develop reliable and fast characterisation tools which can deal with large area substrates ($> 100 \text{ cm}^2$). Depending on their specifications, these tools can be implemented either in research laboratories, for troubleshooting purposes at the production sites, or directly for in-line control. So far, quite a number of new techniques have reached the laboratory stage and are starting to be used for process development and troubleshooting. Except for the end control of solar cell parameters, in-line controls are still limited, but several manufacturers intend to introduce new characterisation tools in their future production line. However, much of this development is proprietary or obtained in projects where only minimum information is disclosed. Consequently, only a few commercial systems are available for in-line control.

In the first part of this paper, we review some recent developments in measurement techniques, from material characterisation to solar cell properties determination. Then we outline the current status of process control in production lines and indicate some possible implementations in future production lines.

In the second part, some new measurement systems developed at the Fraunhofer ISE are presented. Some recent developments and possibilities of the carrier density imaging (CDI) technique, for a fast imaging of carrier lifetimes are outlined. A multiple head four-point probe system (FAKIR) for mapping of the sheet resistance on large area wafers is described. The FAKIR system allows a gain time by an order of magnitude compared to a single head four-point probe system. Examples of fast shunt detection using a set-up based on commercial liquid crystal (LC) sheets will be given, illustrating the power of this simple and low-cost technique.

Finally, we introduce a new technique for obtaining information on the metallisation properties of solar cells. This non-destructive technique is based on micro-wave photoconductivity decay ($\mu\text{W-PCD}$) measurements of complete solar cells operated at reverse bias. We show that the measured effective lifetime τ_{met} depends mostly on the local resistance between the measurement point and the metal grid, therefore containing information on the emitter sheet resistance and on the contact resistance between the metallisation and the emitter. Several examples illustrating metallisation failures and their effects on the τ_{met} maps are given.

2 Review of some recent characterisation techniques

A large number of techniques have been developed for semiconductor characterisation. An excellent review of these techniques can be found in ref. [1]. Many of these techniques, such as Fourier transform infrared spectroscopy (FTIR), deep level transient spectroscopy (DLTS), capacitance-voltage (C-V) measurements or resistivity profiling, are commonly used in photovoltaic research laboratories. One drawback of many of these techniques is that they are often time consuming or require special

sample preparation. They are therefore limited to small numbers of samples or small areas. This illustrates also the fact that quality control is a completely different problem in the semiconductor field, where low throughput but strict tolerance criteria have to be met.

The list of techniques presented here is certainly non-exhaustive. For some equipment, we indicated a few suppliers, although others might exist. Also, we will not review solar simulators, flash testers or cell sorters, because market surveys of these systems are already regularly presented in specialised magazines such as Photon International [2].

2.1 Wafer quality

Before wafering, ingots can be tested for resistivity by the eddy current technique [3] and for lifetime properties by microwave-photoconductivity decay (μ W-PCD) [3,4]. Cracks in the ingot can be detected by the scanning eddy current technique [4]. After wafering, a rigorous mechanical quality control has been introduced by some manufacturers. For instance, the German wafer supplier Deutsche Solar performs optically based control of their wafers to measure corrugation and thickness, and to detect cracks and edge chippings. The equipment has been developed by Henneke [6] and ACR [7].

Wafer breakage is an issue in some production lines. Thermosensorik [8] has developed a Wafer-crackDtec \circledR system, based on the thermal expansion of cracks after a light pulse and subsequent detection of the IR light passing through the wafer. The system is used by manufacturers of single-crystalline Si solar cells, but little experience with mc-Si has been reported. Optical detection systems for cracks down to 30 μ m width and 0.5 mm length have been developed [6]. Some other research directions include acoustic studies of stress in mc-Si wafers [9], or techniques like scanning eddy current where micro-cracks lead to a strong perturbation of the absorbed electromagnetic power. The last method is too slow for wafer mapping but could be applied for crack detection at the edge of wafers [5].

The PV scan system [10] can map dislocation densities by monitoring the light scattered from specially etched wafers.

Wafer resistivity can be checked by classical four-point probe or eddy current measurements [3]. However, for accurate resistivity measurements, thickness determination is necessary and can be obtained by optical techniques [6] or capacitive gauging [3].

The electronic properties of wafers before processing can be controlled using surface photovoltage (SPV) [11], μ W-PCD [3,4], charge density imaging technique (CDI), (see § 4.1), or quasi-steady-state photoconductance (QSSPC) [12-14]. The first three techniques allow a mapping of the wafer, whereas the QSSPC allows only single point measurements ($\sim 1 \text{ cm}^2$) with useful information on the injection dependence of the effective lifetime. Before saw damage etch, the effective lifetime is generally limited to about 3 μ s for 300 μ m thick wafers because of surface recombination. In the case of mc-wafers, μ W-PCD is well suited to determine the location of the wafer in the ingot (edge wafer, bottom or top part), because the extreme parts of mc-Si ingot generally exhibit initial bulk lifetime much lower than 3 μ s.

2.2 Following up the material quality evolution in the solar cell process

The change of material properties, namely the bulk lifetime τ_{bulk} , during the solar cell process can be monitored by etching consecutive wafers at the different stages of the process, passivating the wafer surfaces and measuring the lifetime with one of the techniques described in 2.1. This process is however, quite tedious and it would be better to analyse as-processed wafers. The values measured on as-processed wafers contain, after diffusion for example, information on the bulk lifetime, on the emitter properties, and on the backsurface recombination (which can be slightly passivated after one side diffusion, or a floating junction in case of POCl_3 diffusion). As all quantities are injection dependent, an extraction of the different parameters is difficult. If the bulk lifetime at the measurement

and the rear surface passivation at the measurement point are good enough, the emitter saturation current density can be estimated after diffusion with the QSSPC technique [13,15]. Possible implementations of this technique for in-line controls are discussed in ref. [13]. By performing spectral QSSPC at two different wavelengths it is also possible to evaluate the emitter spectral response [16].

To our knowledge, the only technique that can map the effective lifetime at each stage from the raw material to the finished product is μ W-PCD [17]. However, an extraction of important parameters such as τ_{bulk} , or effective surface recombination velocities, is difficult, so the method is essentially limited to studying the behaviour of low bulk lifetime areas. On devices, the effective diffusion length maps obtained in spectrally resolved light-beam induced current measurements (SR-LBIC) [18] can be correlated with lifetime maps. However, a major problem in comparing lifetime maps to L_{eff} maps is the control of the injection conditions which are usually too high [19] in μ W-PCD, whereas SR-LBIC measurements are performed in lower injection conditions, in the range of 10^{13} cm^{-3} , which is more relevant for the prediction of the cell short-circuit current.

2.3 Solar cells measurements

Global measurements

To complement the usual measurements of solar cell parameters (I_{sc} , V_{oc} , FF, η , $R_{\text{series}}(V_{\text{oc}})$, $R_{\text{shunt}}(0V)$), the recently developed Sun- V_{oc} technique [13,20] allows reconstruction of the I-V curve in a single flash without the influence of the series resistance. Dark I-V measurements can also accurately point out lumped series and parallel resistance problems, as well as second diode problems. However, edge effects can severely impact both the dark and the illuminated I-V curves [21-23]. Laser scribing and breaking of the edges ensures, for large area cells, a minor influence of the edges on the cell properties and much more consistent analyses of dark I-V curves [21], in addition to a possible FF increase. An important test for solar cells is the reverse voltage breakdown [24], which should be higher than at least -10V for cells encapsulated in modules, where the bypass diodes usually ensure a maximum reverse voltage in that range.

To evaluate the optical properties of the cell, the global reflection can be measured with the PV reflectometer [25,26]. When no global measurement is possible, we find it in general sufficient to measure the reflection at 6 different locations on the cell to achieve a representative reflection value of the entire cell, to which a 100% reflection on the bus bars is added.

A useful tool for the characterisation of solar cells is the determination of the large area internal quantum efficiency (IQE). We have developed, a special calibration procedure for large area external quantum efficiency (EQE) measurements, which are combined with the reflection data to give the IQE values. This procedure accounts for interference filter and lamp inhomogeneities, and for attenuation of the signal first harmonic in lock-in measurements when measuring large area cells. Our system allows a measurement at 31 wavelengths between 340 and 1200 nm on cells up to $15 \times 15 \text{ cm}^2$, with bias light up to 1 sun and measurement time between 3 and 6 min. Fig. 1 shows two examples acquired during process optimisation. The IQE at $\frac{1}{2}$ sun bias light of two cells processed from adjacent wafers but with two different types of AR layers are shown in fig. 1a. An absorption in the SiN layer of the second cell can be directly detected, since the 40 Ohm/sq emitter cannot account for the poor blue answer. Fig. 1b shows the IQE of cells (adjacent wafers) diffused at two significantly different temperatures. After SiN deposition and firing, the two groups of three cells have exactly the same long wavelength IQE, indicating that bulk-H passivation can level off differences in lifetime observed after diffusion. Note that, thanks to the calibration, the curves are perfectly smooth.

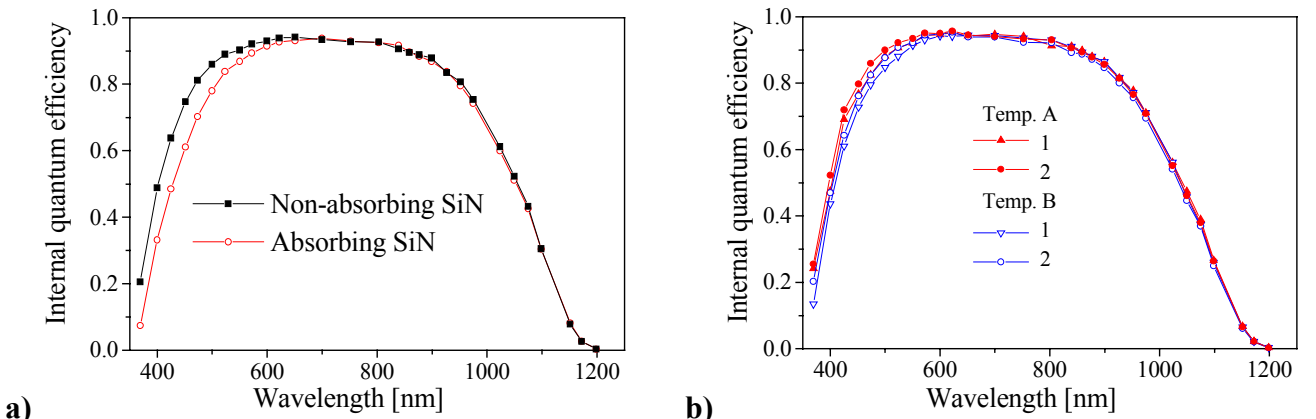


Fig. 1. Large area IQE curves of $12.5 \times 12.5\text{cm}^2$ samples. **a)** Adjacent solar cells with two different types of SiN. **b)** Sets of adjacent wafers diffused at different temperatures. After Al-SiN co-firing the cells exhibit the same IR-response.

Scanning or imaging of local properties

There is now a wide choice of scanning or imaging techniques to access the local properties of solar cells. Light beam induced current (LBIC) and spectrally resolved LBIC (SR-LBIC) images give information on the local current collection efficiency, with a direct estimation of the effective diffusion length in the case of SR-LBIC combined with reflection measurements [18,27]. Using a galvanometric scanner for beam deflection, ultra-fast LBIC scans can be performed; prototypes for the mapping of solar cells in a few seconds have been demonstrated [28]. τ_{eff} images can be obtained by $\mu\text{W-PCD}$ [17] but the interpretation of the results is not straightforward.

Shunts in solar cells can be detected with ultra-sensitive IR lock-in thermography [29,30] which is available commercially [8]. This technique has proven to be capable of detecting temperature differences in the μK range. Normal IR thermography and the use of liquid crystal sheet [21,31] allow in most cases a fast detection of the major shunts by the application of a reverse bias voltage. Shunts can also be detected using the RAMP mode of the Corescanner developed by ECN [32]. The strength of the Corescanner, which is now commercially available [33], lies however more in its ability to map locally the contact resistance between the fingers and the emitter, which is a significant progress towards the evaluation of firing processes and the detection of inhomogeneities. A drawback of the technique is that it is destructive. A new contactless mapping method ($\mu\text{W-PCD Met}$) to evaluate the metallisation properties will be discussed in the last part of this paper.

Some innovative mapping measurements

The CELLO technique is based on local light perturbation of globally illuminated solar cells operated at different voltages [34]. It yields information on most of the solar cell local properties, including R_s and R_p . Current distribution across the solar cell surface have been analysed using SQUIDs [35,36]. Magnetic investigations of the electrical activities of grain boundaries in mc-Si are reported in ref. [37]. Phase sensitive LBIC [38] has been shown to be sensitive to local impedance properties. Room temperature photoluminescence (PL) studies of mc-Si wafers have shown a correlation between lifetime and band-to-band recombination PL, whereas areas with high dislocation densities showed a defect PL band at 0.8 eV [39,40].

Ultra-high resolution ($6\mu\text{m}$) LBIC IQE measurements combined with measurements of the local dislocation densities have allowed the measurement of the dislocation recombination strength in processed mc-Si wafers [41]. This study illustrates perfectly the complex nature of defects in mc-Si,

where impurities, precipitates, dislocations and grain boundaries make the prediction of the evolution of the lifetime during processing highly difficult.

3 Process monitoring in production

3.1 Today

One unique in-line control is the final measurement of the illuminated I-V characteristics (using a flash tester or a continuous solar simulator). Tests of the cell at reverse bias have been introduced by some manufacturers in the same measurement step.

Visual controls at the different stages ensure an approximate evaluation of the saw damage etching, phosphorus glass removal, AR layer deposition and metallisation quality. The stability of the process can be regularly checked by analysing samples drawn from the line. Typical controls on selected wafers include, for instance:

- Weighing the wafers for saw-damage etch removal.
- 4 point probe measurements of the emitter sheet resistance.
- Ellipsometry (on polished wafers) for the determination of the refractive index and nominal thickness (Note: the thickness can be different on textured wafers).
- Metallisation: check of the grid conductivity with 4 wire measurements, weighing for the amount of paste deposited. Profilometry for the determination of finger height.
- Shunt thermography (IR, IR lock-in, LC sheet).
- Contact resistance scanning.

3.2 Tomorrow

A modern production line could control more tightly the evolution of its process by incorporating several in-line controls. This theme is, for instance, addressed in the Fast-IQ European project [5], dedicated to improving quality control in the PV industry and to inventing adapted automated systems for in-line measurements. Several manufacturers are also developing their own control systems in confidential collaboration with industrial partners. It is therefore possible that some of the techniques discussed here, as well as techniques unknown to the authors, are already tested or implemented at production sites.

It is not obvious which techniques will be implemented in tomorrow's production lines for several reasons. Firstly, many manufacturers think that regular controls on selected wafers are sufficient in a robust process, and that the cost of in-line control might not cover any efficiency gain. Secondly, as the solar cell results are linked not only to the process parameters, but also to the raw material supply which can be highly variable, it is a huge task to adjust effectively the process parameters to achieve optimum final solar cell results. This requires wafer tracking and the introduction of elaborate statistical control process (SCP) procedures. However, for a production volume of 50 MW/year, a modest 1% relative gain in efficiency might be worth one million euros, which shows that the issue is worth investigating thoroughly. Some of the possible in-line controls are:

- QSSPC lifetime measurements can be introduced at several points for in-line control [13]. The emitter quantum efficiency can be estimated by spectral QSSPC after emitter diffusion [16]. Only discrete points with a resolution in the cm^2 range can be measured.
- Fast $\mu\text{W-PCD}$ [3] lifetime line scans can be performed at the different steps.
- The flash CDI technique presented in part 4.1 could allow imaging the lifetime properties of the whole wafer in less than a second [42].

- First results indicate that organic surface contamination can be detected by Kelvin probe measurements [44].
- Single point contactless measurements of the emitter sheet resistance could be performed by surface resistance analyses (Ref 1, p39). Contactless surface charge profiling (SCP) [45-47] has been recently shown [48] to be able to measure the surface doping concentration of diffused mc-Si wafers and could therefore be a good control indicator for the diffusion process. Inductively coupled coils [13] and eddy current techniques can also yield information on the sheet resistance, but the effect of substrate conductivity can bias the results.
- At the different production stages (etch, AR layer, metallisation) the global reflection properties can be analysed using a fast PV reflectometer [26].
- Metallisation interruption can be monitored by optical recognition and commercial systems are already available [49].
- Sun- V_{oc} measurement at the end of the flash of the solar simulator can be used to check for series resistance problems [13,20].
- On complete solar cells, IR thermography of reverse biased cells is fast enough [17] to image localised shunts at a rate of about 1 cell every 2 to 3 seconds.
- The distribution of diffusion lengths on final devices can be obtained by ultra-fast LBIC [28] scans.
- Cracks in solar cells can be detected using the commercial system CrackDtec® [8]: by monitoring the temperature distribution in the cell with an IR-camera after a light pulse, cracks are characterised by disturbed heat distribution in the cells.
- Optical sorting of solar cells for aesthetic flaws like missing parts of the contact grid, taints in the anti-reflection layer, or wrong colours has been reported in the European project VISOLAR [50]. In the same project, optical systems for the detection of cracks after front tabbing of cells have significantly improved breakage losses.

4 Some recent developments at the Fraunhofer ISE

4.1. Carrier density imaging (CDI)

The principle of a lifetime imaging technique based on free-carrier absorption of IR-light has been demonstrated by Bail et al. [51]. By introducing lock-in processing of the signal, much shorter lifetimes can be measured, as shown by Riepe et al. [52]. In the CDI technique, a hotplate (black body) emits IR radiation, which is transmitted through the silicon sample. A fast CCD-camera sensitive in the mid-infrared ($\lambda \sim 3.5\text{-}5 \mu\text{m}$) measures the IR-transmission. The IR-absorption and hence the transmission, is modulated by excess free-carriers generated by the chopped light of a semiconductor laser ($\lambda = 917\text{nm}$) whose intensity is chosen to yield a generation close to 1 sun conditions (AM1.5g). The laser excitation frequency is in the Hz range, ensuring steady-state conditions. For each pixel, the lock-in signal is proportional to the local free-carrier excess concentration Δn and hence to the lifetime. After calibration of the system [52] the effective lifetime τ_{eff} is obtained.

Figure 2 illustrates the power of this technique by comparing lifetime images obtained with the CDI system (a) with those obtained by $\mu\text{W-PCD}$ (b). In one minute a complete CDI map of a $10\text{x}10 \text{ cm}^2$ mc-Si wafer has been obtained with a $350\mu\text{m}$ resolution, whereas $\mu\text{W-PCD}$ scanning at $740\mu\text{m}$ resolution requires high-injection to achieve a reasonable scanning time, and even then is an order of magnitude slower. The higher injection used in the $\mu\text{W-PCD}$ measurements explains the differences in the lifetime values with otherwise all features perfectly reproduced.

The CDI technique can be applied to as-cut or to diffused wafers as well [42]. However, to obtain a good signal/noise ratio for low effective lifetimes, a larger number of image frames have to be

processed and the measurement time becomes significantly longer. For in-line lifetime imaging of wafers, two approaches can be followed [42]. By flashing the samples with a high intensity flash, lifetime images could be obtained in a time as short as 16 ms (fig. 2c), but with higher injection conditions. Another approach is statistical: as many data points are acquired (288^2 in this case), it is still possible to reduce the lock-in measurement time to a minimum value, by imposing a noise criteria on the lifetime distribution, rather than on the lifetime measured at individual pixels [42].

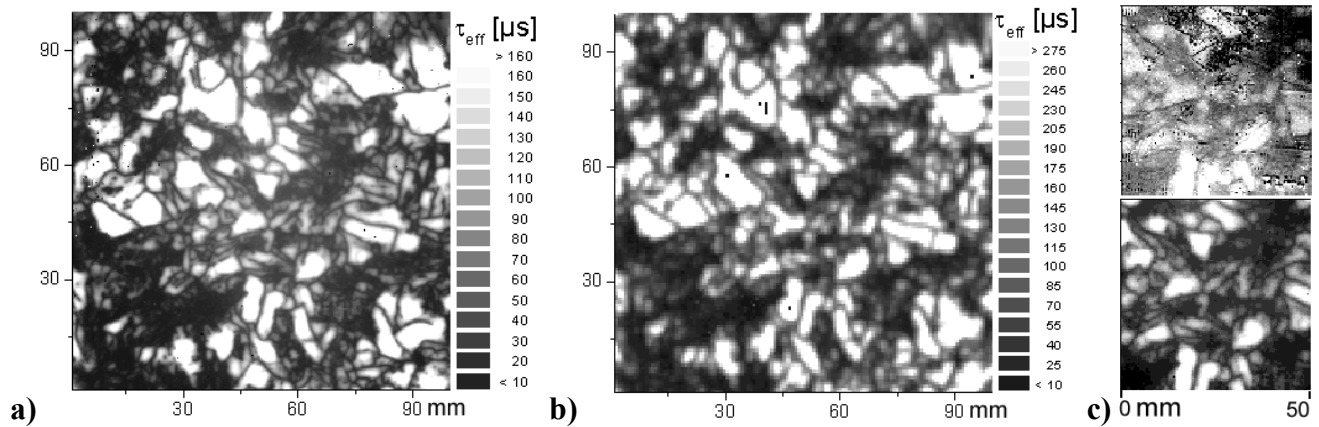


Fig. 2. Lifetime maps of a surface passivated mc-Si sample. **a)** CDI images (resolution 350 μm) obtained in 1 min. **b)** μW -PCD measurement (resolution 740 μm). **c)** Top = flash CDI imaging (16 ms). Bottom = lock-in imaging (48 s).

4.2 Sheet resistance mapping: the FAKIR system

In POCl_3 diffusion where the wafers are densely packed to reduce the production costs, or in an in-line diffusion furnace where edge effects can influence the wafer temperature, the value and homogeneity of the emitter sheet resistance ρ_s have to be controlled carefully.

For samples drawn from the production line or in the laboratory, four point probe measurements are the most common. The drawback of single head systems is the lengthy measurement time because the head has to be moved to the different measurement locations. We have recently built a system which reduces the measurement time by a factor of 9 [53]. The basic idea is to use an array of 100×4 needles, shown in fig. 3a. An I/O card integrated into the computer controls a relay box, which in turn connects or disconnects the different sets of needles to a 4-wire multimeter. In fig. 4b, the

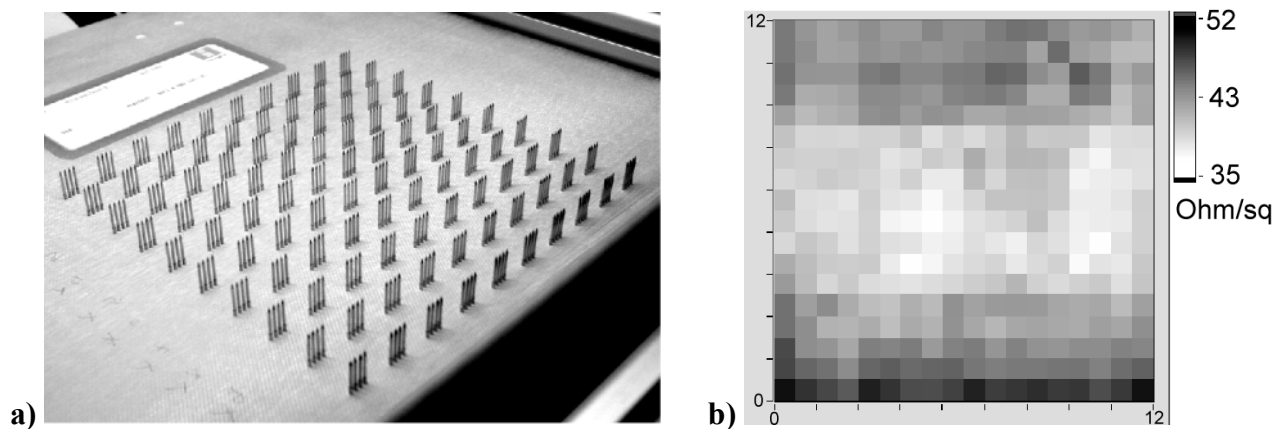


Fig. 3. **a)** Photo of the needle array of the Fakir system. **b)** Map of the emitter sheet resistance on a $12.5 \times 12.5 \text{ cm}^2$ mc-Si wafer after emitter diffusion.

emitter sheet resistance of a diffused $12.5 \times 12.5 \text{ cm}^2$ mc-Si wafer shows strong lateral variations linked to an inhomogeneous optical heating of the sample. The image resolution was doubled by automated translations along the x and y axis. For most applications, a resolution of 10×10 or 9×9 points is sufficient to detect inhomogeneities.

The simple concept of the system makes it easily adaptable to other measurement geometries. Our prototype uses low-cost steel needles, whose quality is sufficient to measure clean emitters. By using tungsten-carbide needles which can penetrate through the native oxide, measurements of substrate resistivity or of emitters through the phosphor glass are also possible.

4.3 Shunt detection using a fast low-cost set-up

Temperature sensitive liquid crystal sheets [31] can be used to detect shunts in solar cells. We have recently developed and optimised a new set-up [21] which detects shunts in reverse biased solar cells using low cost commercial liquid crystal (LC) sheets held in close contact with the solar cell by vacuum. The set-up, described in fig. 4, is easy to operate and allows high throughput even with a manual loading of the wafers (typically 1 cell every 12 seconds). The sensitivity and system performance achieved with this LC system are comparable to those of a conventional infrared camera (0.1° Kelvin resolution). The advantages of our set-up are its low cost and ease of use. In our laboratory, it has quickly become an invaluable tool for fast shunt localisation.

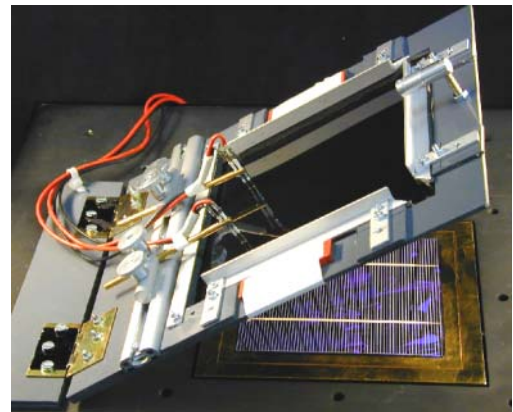
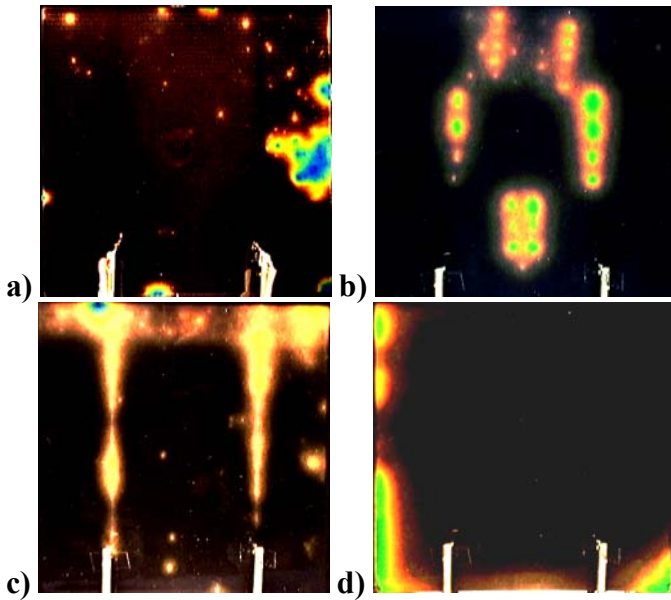


Fig. 4. Prototype for the imaging of shunts in solar cells. When the frame is closed, the vacuum brings the LC sheet into thermal contact with the solar cell surface and the front bus bars are contacted. After application of V_{bias} , a stable temperature distribution over the cell surface, and hence a stable shunt image, is obtained in about 1-2 sec.

Fig. 5. “The horror shunt museum”. All images are taken at reverse bias between -3 and -10V . **a)** Shunts caused by improper handling during processing. **b)** Localised shunts induced by diamond scribing on the fingers of the solar cell. **c)** Overfiring of the metallisation. **d)** Edge shunts stemming from an improper edge isolation process.

A frequently addressed point is whether the reverse bias shunts detected with the LC sheet technique are the same as the shunts revealed at the working point of the solar by ultra-sensitive IR lock-in thermography. From our experience, the correlation is not always perfect, but most major problems can be identified with the less sensitive LC sheet set-up, in particular if high reverse voltages are applied. This is because the non-ideal local I-V characteristics in forward bias are likely to be accompanied by similar non-idealities at reverse bias (lower local voltage breakdown). In particular, on mc-Si solar cells

series resistance effects, cells with reduced FF always show strong features at reverse bias. Furthermore, the presence of localised shunts in solar cells indicates a problem with either material quality (cracks at the edges, highly contaminated areas) or processing (edge isolation, contamination of the emitter, overfiring of the contacts, soldering of the tabs). The images of fig. 5 illustrate some typical shunt problems.

4.4 μ W-PCD to detect metallisation failure

In this part, we introduce a new contactless mapping technique which can yield information about the metallisation properties of solar cells. It is based on the use of μ W-PCD applied to reverse biased cells and can be applied to virtually any kind of solar cell.

In ref. [17], we showed that μ W-PCD can be used to map complete solar cells, but the measured effective lifetime τ_{eff} , was influenced by the local series resistance R_{loc} between the excited area and the rest of the solar cell. After a high intensity laser pulse, when the cell is reverse biased with a voltage V_{bias} , a recombination current will flow between the excited area (now at a positive voltage $V_{\text{loc}} \sim 0.7$ - 0.8 V) and the rest of the solar cell through R_{loc} . Immediately after the pulse, the current extracted from the excited area will be given by $I = (V_{\text{loc}} - V_{\text{bias}})/R_{\text{loc}}$, and the change in total excited carrier concentration can be monitored using a standard μ W-PCD set-up.

To first approximation, the decay time measured at reverse bias τ_{met} is given by [54]

$$\tau_{\text{met}} \sim (R_{\text{local}} \times q \times Q_0) / (V_{\text{loc}} - V_{\text{bias}}) \quad (1)$$

where Q_0 is the initial excess number of carriers induced by the laser pulse and q the elementary charge. On condition on equation (1) is of course that τ_{met} must be larger than τ_{bulk} .

We have observed experimentally the linear dependence of τ_{met} on the laser pulse intensity and its inverse dependence on the voltage. R_{loc} contains information about the metal-emitter contact resistance, emitter sheet resistance and backsurface contact. Fig. 6 illustrates the method, by showing the forward bias (left) and reversed bias (right) maps of a 12.5×12.5 cm 2 solar cell with a severe screen-printing failure (lower right part missing). The forward bias image is mainly influenced by τ_{bulk} and the grain structure is clearly resolved. The darker round spots under the bus bar are silver pads on the backside. τ_{eff} is reduced at the pads because of higher backsurface recombination. On the reverse bias image at the right (different τ scale), regular structures are observed where the grid lines are present. In this case,

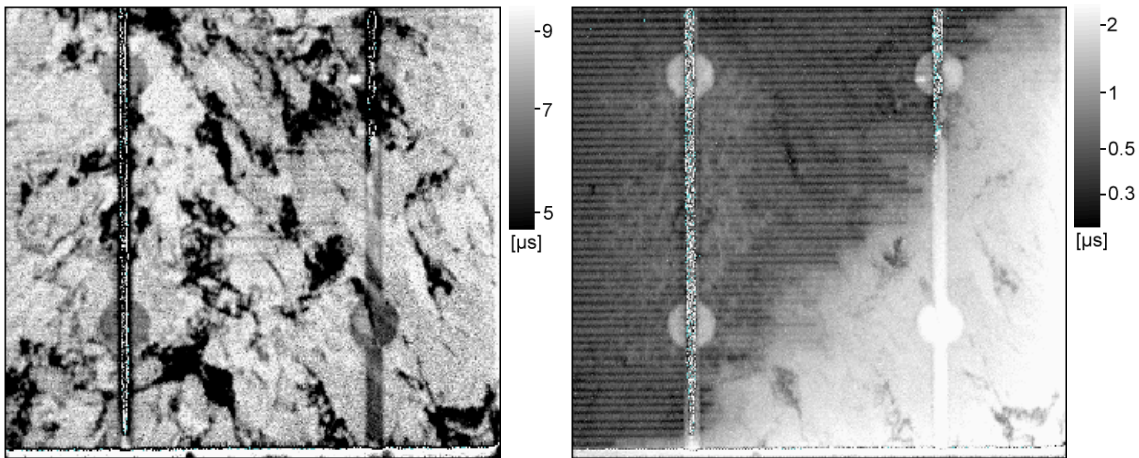


Fig. 6. μ W-PCD scans of the same solar cell at different V_{bias} . Left) $+0.6$ V. Right) -10 V)

a higher τ_{met} is observed at the backside Ag pad, indicating a more resistive contact between Ag and p-Si than for Al. The area with the metallisation problems also shows much higher τ_{met} , and τ_{bulk} influences τ_{met} more strongly.

Fig.7 shows a mc-Si solar cell with 78.2% FF. The reverse bias image is perfectly homogeneous, except for three lighter spots corresponding to finger interruptions (left part of the cell). The first τ_{met} detected word (ISE) is shown above the figure legend. To increase locally R_{loc} , we intentionally interrupted the Ag fingers at the various locations with a diamond scribe. As the current must now travel a longer way through the resistive emitter before reaching the metallisation, a higher τ_{met} is measured.

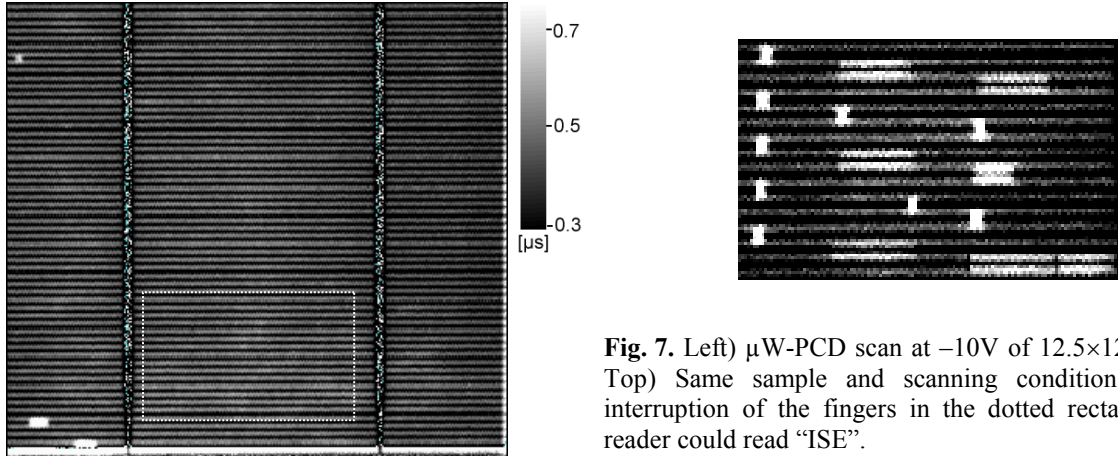


Fig. 7. Left) μ W-PCD scan at $-10V$ of $12.5 \times 12.5 \text{cm}^2$ Si solar cell. Top) Same sample and scanning conditions, after intentional interruption of the fingers in the dotted rectangle. An observing reader could read “ISE”.

Acknowledgements

We would like to thank the equipment suppliers and solar cell manufacturers for supplying information on this topic. The CDI measurements of fig. 2 have been performed by S. Riepe.

References

- [1] D. K. Schroder, “Semiconductor material and device characterization” Wiley-Interscience, ISBN 0-471-24139-3, (1998).
- [2] Photon International, Aachen, Germany, www.photon-international.com
- [3] Semilab, Budapest, Hungary, www.semilab.com.
- [4] FeNIX system, (ex-Janus von Amecon) of Accent Optical Technical Technologies, Bend, Oregon, www.accentopto.com.
- [5] FAST-IQ “Fast inline characterisation tools for crystalline silicon material and cell process quality control in the PV-industry”, Project Reference: ERK6-1999-00002, in the EESD part of the 5th EU Program. See also [2], [9],[46], [26].
- [6] HENNEKE, System Entwicklung, Zülpich, Germany, www.seh-zuelpich.de.
- [7] ACR Automation GmbH, Niedereschach, Germany. www.acr.de.
- [8] THERMOSENSORIK GmbH, Erlangen, Germany, www.thermosensorik.de.
- [9] A. Belyaev, S. Lulu, I. Tarasov, S. Ostapenko, J. P. Kalejs, ”*Stress Diagnostics in mc-Si Wafers Using an Acoustic Technique*”, to be pub. in Proc 29th IEEE PVSC, New-Orleans (2002).
- [10] B. Sopori, B. W. Chen, Y. Zhang, T. Hemmschoot, J. Madjdpour, ”*Extending PVSCAN to Meet the Market Needs for High-Speed, Large-Area Scanning*”, Proc. 9th Si Colarado Workshop, Breckenridge 1999, pp 135-141.
- [11] A. Castaldini, D. Cavalcoli, A. Cavallini and M. Rossi, ”*Surface photovoltaic analysis of crystalline silicon for photovoltaic applications*”, Sol. Energy Mat. Sol. Cells, **72** (2002), 559.
- [12] R.A. Sinton and A. Cuevas, ”*Contactless determination of I-V characteristics and minority carrier lifetimes in semiconductors from quasi-steady-state photoconductance data*”, Appl. Phys. Lett. **69** (1996), 2510.
- [13] R. A. Sinton, ”*Possibilities for Process-Control Monitoring of Electronic Material Properties During Solar-Cell Manufacture*” Proc. 9th Si Colarado Workshop, Breckenridge 1999, pp. 67-73.
- [14] Sinton Consulting, Boulder, USA.
- [15] A. Cuevas, ”*The effect of emitter recombination on the effective lifetime of Silicon Wafers*”, Sol. Energy Mat. Sol. Cells **57** (1999), 277.
- [16] A. Cuevas, R.A. Sinton, M. Kerr, D. Macdonald and H. Mäckel, ”*A contactless photoconductance technique to evaluate the quantum efficiency of solar cell emitters*” Sol. Energy Mat. Sol. Cells, **71** (2002), 295.
- [17] C. Ballif, S. Peters, D. Borchert, ”*Lifetime mapping of solar cells and control of the effective surface recombination velocity by application of a bias voltage*”, Proc. 17th EU-PVSEC, München 2001, pp 1408-1411.
- [18] W. Warta, J. Sutter, B. F. Wagner, R. Schindler, Proc. 2nd WCPEC, Vienna 1998, p 1650.
- [19] C. Ballif, S. Peters, D. Borchert, C. Hässler, J. Isenberg, R. Schindler, W. Warta, and G. Willeke, ”*Lifetime investigations of degradation effects in processed multicrystalline silicon wafers*”, Proc. 17th EU PVSEC, München 2001, pp 1818-1821.

- [20] R.A. Sinton and A. Cuevas, "A Quasi-Steady Open -Circuit Voltage Method for Solar Cell Characterisation", Proc. 16th EU PVSEC, Glasgow 2000, 1152.
- [21] C. Ballif, S. Peters, J. Isenberg, S. Riepe, and D. Borchert, "Shunt imaging in solar cells using low cost commercial liquid crystal sheets", to be pub. in Proc. 29th IEEE PVSC, New-Orleans (2002).
- [22] S. Glunz et al. "High-efficiency silicon solar cells for low-illumination applications", to be pub. in Proc 29th IEEE PVSC, New-Orleans (2002).
- [23] A. Hauser, G. Hahn, M. Spiegel, H. Feist, O. Breitenstein, J.P. Rakotonainaina, P. Fath, and E. Bucher, "Comparison of different techniques for edge isolation", Proc. 17th EU PVSEC, München (2001), pp. 1739-1742.
- [24] W. Herrmann, M.C. Alonso, W. Böhmer, and B. Proisy, "Improvement of photovoltaic modules - Measures for withstanding electrical and thermal effects caused by reverse biasing of cells-", in Proc. IMOTHEE workshop, 5th EU Program, Cologne, 2002.
- [25] B. Sopori, Y. Zhang, R. Faison, J. Madjdpor, "Principles and Applications of Reflectometry in PV Manufacturing", NICH Report No. CP-520-31003 (2001).
- [26] B.L. Sopori, Y. Zhang, J. Madjdpor, M. J. Romero, C. Frederic and K. Holdermann, "Monitoring Texture Etching Process in Si Solar Cell Production", to be pub. in Proc 29th IEEE PVSC, New-Orleans (2002).
- [27] W. Warta, "Defect and impurity diagnostics and process monitoring", Sol. Energy Mat. Sol. Cells **72** (2002), 389.
- [28] M. Acciarri, S. Binetti, A. Racz, S. Pizzini, G. Agostinelli, "Fast LBIC in-line characterization for process quality control in the photovoltaic industry", Sol. Energy Mat. Sol. Cells **72** (2002), 417.
- [29] M. Langenkamp and O. Breitenstein, "Fast shunt hunting in solar cells with highly sensitive lock-in IR-thermography", Proc. 9th Si Colarado Workshop , Breckenridge, (1999), pp. 198-201.
- [30] O. Breitenstein, M. Langenkamp, F. Altmann, D. Katzer, A. Lindner, and H. Eggers, "Microscopic lock-in thermography investigation of leakage sites in integrated circuits", Rev. Sci. Instr. **71** (2000), 4155.
- [31] J. Schmidt and I. Dierking, "Localization and Imaging of Local Shunts in Solar Cells Using Polymer-dispersed Liquid Crystals", Prog. in Photovoltaics **9** (2001), 263.
- [32] A.S.H. van der Heide, A. Schönecker, G.P. Wyers, and W.C. Sinke, "Mapping of contact resistance and locating shunts on solar cells using Resistance Analysis by Mapping of Potential (RAMP) techniques", Proc. 16th EU PVSEC, Glasgow 2000, pp.1438-1442.
- [33] SUNLAB, Petten, The Netherlands, www.sunlab.nl.
- [34] J. Carstensen, G. Popkirov, J. Bahr, and H. Föll, "Cello: an advanced LBIC measurement for solar cell local characterisation", Proc. 16th EU PVSEC, Glasgow 2000, pp. 1627-1630.
- [35] E. Soika, E. J. Koriath, H.J. Möller, "Investigation of the Current Distribution in Solar Cells Using a SQUID Microscope", Proc. 17th EU-PVSEC, München (2001), pp.1783-1786.
- [36] T. Schurig, J. Beyer, D. Drung, F. Ludwig, A. Ludge, S. Riemann "NDE of semiconductor samples and photovoltaic devices with high spatial resolution utilizing SQUID photoscanning", Inst. Electron. Inf. & Commun. Eng, **85** (2002), p.665-9.
- [37] J. Beyer, Q. Zhong, and TH. Schurig, "Noninvasive investigation of defects in multicrystalline silicon and photovoltaic devices by photomagnetic detection using superconducting quantum interference device magnetometers", Appl. Phys. Lett. **77**, (2000) 3107.
- [38] Th. Pernau, P. Fath, E. Bucher, "phase-sensitive LBIC analysis", to be pub. in Proc. 29th IEEE PVSC, New-Orleans (2002).
- [39] I. Tarasov, S. Ostapenko, V. Feifer, S. McHugo, S. V. Koveshnikov, J. Weber, C. Haessler and E. -U. Reisner "Defect diagnostics using scanning photoluminescence in multicrystalline silicon", Physica B: Condensed Matter, **273-274**, (1999), 549.
- [40] I. Tarasov, S. Ostapenko, W. Seifert, M. Kittler and J. P. Kaleis, "Defect diagnostics in multicrystalline silicon using scanning techniques", Physica B: Condensed Matter, **308-310** (2001), 1133.
- [41] M.Rinio, S.Peters, M.Werner, A. Lawerenz, H.J.Möller, "Measurement of the Normalized Recombination Strength of Dislocations in Multicrystalline Silicon Solar Cells" Sol. State Phenomena, **8284** (2002), 701.
- [42] J. Isenberg, S. Riepe, S.W. Glunz, W. Warta, "Carrier Density Imaging (CDI): A Spatially Resolved Lifetime Measurement Suitable for In-Line Process-Control", to be pub. in Proc. 29th IEEE PVSC, New-Orleans (2002).
- [44] A. Castaldini, D. Cavalcoli, A. Cavallini and M. Rossi "Surface analyses of polycrystalline and Cz-Si wafers", Sol. Energy Mat. Sol. Cells **72** (2002), 425.
- [45] P. Roman P, J. Sta, S. Fakhouri, M. Brubaker, J. Ruzyllo, "monitoring using noncontact surface charge profiling", J. Appl. Phys. **83** (1998), 2297.
- [46] FAaST™ 200 and 300 series: Near Surface Doping of Semiconductor Diagnostics, Inc, Tampa, USA, www.sdtampa.com.
- [47] QSC 7200-RC, of QC Solutions, Inc., Billerica, USA, www.qcsolutions.com.
- [48] A. Castaldini, D. Cavalcoli, A. Cavallini and M. Rossi, "Scanning Kelvin probe and surface photovoltage analysis of multicrystalline silicon", Materials Science and Engineering B **91-92** (2002), 234
- [49] NV ICOS VISION SYSTEMS, Heverlee, Belgien, www.icos.be
- [50] VISOLAR – "Production Integrated Visual Inspection and Quality Prediction for Solar Cells and Modules", Public Final Report of ESPRIT (2000) HPCN PST Activity 28514.
- [51] M. Bail, J. Kentsch, R. Brendel, M. Schulz, "Lifetime mapping of Si wafers by an infrared camera for solar cell production" Proc. 28th IEEE PVSC, Piscataway 2000, pp.99- 103.
- [52] S. Riepe, J. Isenberg, C. Ballif, S.W. Glunz, and W. Warta "Carrier density and lifetime imaging of silicon wafers by infrared lock-in thermography", Proc. 17th EUPVSEC, München 2001, pp 1597-1599.
- [53] T. Zerres, C. Ballif, D. Borchert, and S. Peters "High speed mapping of sheet resistance on large area wafers: the Fakir system", Proc. 17th EU PVSEC, München 2001, pp 1590-1593.
- [54] C. Ballif et al. manuscript in preparation.

Microscopic properties of copper in silicon: theoretical predictions

S.K. Estreicher and D. West

Physics Department, Texas Tech University, Lubbock, TX 79409-1051

ABSTRACT

First-principles molecular-dynamics simulations of Cu pairs, copper-hydrogen complexes, and copper-oxygen interactions in Si are used to predict stable configurations, binding energies, electronic structures, local and pseudo-local vibrational modes, and formation dynamics. The results are compared to the available experimental data.

INTRODUCTION

Copper is a common and feared impurity in Si. It easily contaminates a sample during chemomechanical polishing, etching (if the acid contains Cu), and other processes. It is also a major component of metallic interconnects on computer chips. Copper can be voluntarily introduced by indiffusion at high temperatures followed by rapid quenching. The solubility of interstitial copper (Cu_i) in Si is low, and it tends to precipitate at vacancy-like defects, stacking faults, grain boundaries, oxygen precipitates, or the surface of the sample.[1-6] The precipitates tend to be stable, electrically active, and impossible to passivate. Their formation is facilitated by the very low activation energy for diffusion of Cu_i^+ , measured [7] to be 0.18eV, close to the predicted value.[8]

If Cu_i encounters a (pre-existing) vacancy, it becomes substitutional. Cu_s has three levels in the gap[9,10]: $Cu_s^{0/+}$ at $E_v+0.20$, $Cu_s^{-/0}$ at $E_v+0.41$ eV, and $Cu_s^{-/-}$ at $E_c-0.17$ eV. Channeling data [11] in *n*-type Si show two Cu-related centers following 300 and 600°C anneals, respectively. The high-temperature center, Cu at an undistorted substitutional site, is seen in *n*- and *p*-type, CZ and FZ Si. It anneals out with 2.9eV activation energy. Upon hydrogenation, three $\{Cu_s, H_n\}$ complexes (n=1,2,3) are seen by DLTS.[12]

The EPR NL58 center[13] has two equivalent Cu atoms, probably in the -1 charge state. The best fit to the angular-dependence of the spectrum suggests tetragonal symmetry, which implies that the two copper atoms must be one lattice constant apart. This center is only seen at low temperatures and anneals out irreversibly at room temperature.[14] To date, it has not been identified.

A photoluminescence (PL) band with zero-phonon line (ZPL) at 1014meV has been identified as a trigonal Cu pair[15,16] and quantitatively correlates[17,18] with a Cu-related DLTS peak at $E_v+0.100$ eV. Its dissociation energy[19], 1.02 ± 0.07 eV, is about twice what one would expect from a Coulomb-bound donor/acceptor pair. DLTS measurements[19] of the field-dependence of the hole emission-rate do not show the Poole-Frenkel effect expected for a Cu^-/Cu^+ center. This implies that some degree of covalent interaction is present. These considerations also rule out the $\{Cu_i, Cu_i\}$ pair since the two interstitials would be positively charged and could not be covalently bound. The $\{Cu_s, Cu_s\}$ pairs can also be ruled out as it would not reorient easily under uniaxial stress as observed by PL.[15] The only option left is the trigonal $\{Cu_s, Cu_i\}$ pair.

A very similar PL band labeled *Cu_0 [20,21] appears in dislocated (vacancy-rich) samples, in samples treated at high temperatures, as well as in samples with low Cu concentrations. Its ZPL is at 944meV and the center appears to be associated with a DLTS level at $E_v+0.185$ eV. Very little else is known about it. In some samples, both PL bands coexist (Fig.1, left). The $\{Cu_s, Cu_i\}$ and the *Cu_0 PL bands show sharp phonon sidebands separated by 7.05 meV= 57 cm $^{-1}$ and 6.42 meV= 52 cm $^{-1}$, respectively (Fig.1, right). This implies the presence of a copper-related pseudo-local vibrational

mode (p-LVM), that is a localized mode with frequency lower than that highest lattice mode, the Gamma phonon.

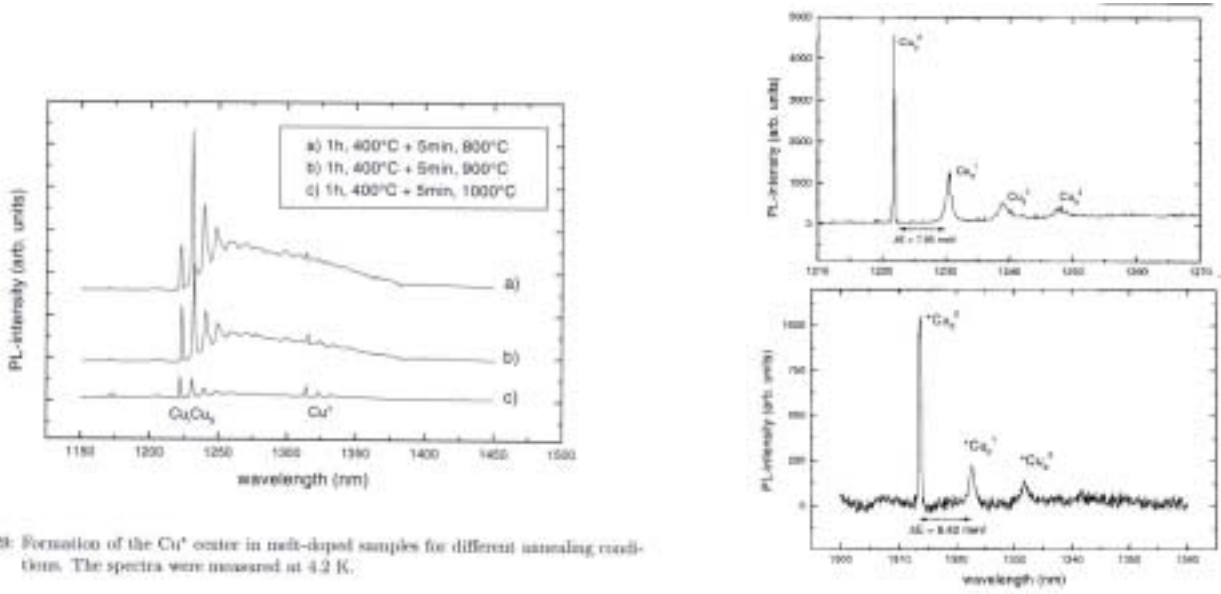


Figure 2.29: Formation of the Cu⁺ octer in melt-doped samples for different annealing conditions. The spectra were measured at 4.2 K.

Fig. 1: PL spectra of the {Cu_s,Cu_i} pair (Cu₀) and the *Cu₀ defect (left) and the phonon sidebands (right).

In this work, first-principles molecular-dynamics (MD) simulations in periodic 64- and 128-host atoms cells are used within the SIESTA package.[22] The electronic problem is solved within self-consistent local density-functional theory. The exchange-correlation potential is that of Ceperley-Alder[23] as parameterized by Perdew and Zunger.[24] *Ab-initio* pseudopotentials in the Kleinman-Bylander[25] form are used. For the valence orbitals, the basis sets consist of numerical linear combinations of atomic orbitals ranging from single-zeta (SZ) to double-zeta with polarization functions (DZP). For example, with an SZ basis set, each Si atom has one 3s and three 3p orbitals; with a DZP basis, each Si atom has two 3s, two sets of 3p's and one set of 3d's, that is 13 orbitals. Unless specified otherwise, our dynamic runs (constant-temperature, T>0) involve SZ basis sets and the *k*-point sampling is limited to *k*=0. The static results (T=0K) are done with DZP basis sets and a *k*-point sampling extended to a 2x2x2 Monkhorst-Pack[26] mesh. The (harmonic) vibrational frequencies are calculated using linear response theory.[27] This method allows the entire dynamical matrix to be extracted from derivatives of the density matrix relative to atomic coordinates. No atom needs to be physically displaced in order to calculate the frequencies.

Earlier calculations[28,29] have shown that the 3d¹⁰4sp⁰ configuration of the free Cu⁺ ion changes to 3d^{10-x}4(sp)^x when copper is inserted into Si, allowing copper to interact covalently with the host crystal, with impurities, and defects. The value of *x* is in the range 1<*x*<2 depending on the level of theory, the basis set, and of course the site of copper. The energy gained when Cu_i encounters a (pre-existing) vacancy and becomes substitutional is 2.7eV at the *ab-initio* Hartree-Fock level[28] (in the +1 charge state) and 2.8eV with SIESTA[29] (in the 0 charge state), close to the 2.9eV obtained from the channeling data.[11] Substitutional Cu is on center with four Cu-Si bonds of length 2.240Å, very close to the equilibrium Si-Si bond length. In the neutral charge state and at this level of theory, no significant relaxation or symmetry-lowering distortion of the complex is apparent.

COPPER PAIRS

Three Cu pairs have been described[30] in silicon. $\{Cu_s, Cu_i\}$ has Cu_s at a virtually undistorted substitutional site and Cu_i just off the T site, slightly displaced toward Cu_s . The Cu-Cu bond length is 2.338Å, within ~0.1Å of the Si-Si one. The calculated binding energy is 1.16eV, very close to the measured[19] 1.02eV (the smaller number reported earlier[30] was obtained with $k=0$ only). A second pair results from the trapping of a (pre-existing) vacancy, $\{Cu_s, Cu_i\} + V \rightarrow \{Cu_s, Cu_s\} + 2.26eV$ and has two coppers at adjacent substitutional sites with virtually no crystal distortion. The Cu-Cu separation is 2.275Å. A third copper pair, about 0.22eV higher than $\{Cu_s, Cu_s\}$, has the copper atoms at second-nearest substitutional sites and is therefore orthorhombic. This third pair does not appear to be very distinct from two isolated Cu_s impurities and will not be discussed any further. We calculated the dynamical matrices of the $\{Cu_s, Cu_i\}$ and $\{Cu_s, Cu_s\}$ pairs in the 64-cell, as well as that of the $\{Cu_s, Cu_s\}$ pair in the 128-cell to establish cell size effects. A comparison of the modes in the two cells (with and without $\{Cu_s, Cu_s\}$) shows that the key features are very similar.

There are four p-LVMs associated with each copper pair. In the 64-cell: (1) the lowest p-LVM is at $73cm^{-1}$ for $\{Cu_s, Cu_i\}$ and $79cm^{-1}$ for $\{Cu_s, Cu_s\}$. The two Cu atoms move *together* along the trigonal axis, in a way that preserves the Cu-Cu bond length. The frequencies are close to the observed phonon replicas at 57 and $52cm^{-1}$, respectively; (2,3) two degenerate modes have the Cu atoms moving perpendicular to each other in the $\{111\}$ plane. These wag modes are at $108cm^{-1}$ for $\{Cu_s, Cu_i\}$ and at $104cm^{-1}$ for $\{Cu_s, Cu_s\}$; (4) the highest p-LVMs, at $213cm^{-1}$ for $\{Cu_s, Cu_i\}$ and $251cm^{-1}$ for $\{Cu_s, Cu_s\}$, have the two Cu's moving against each other along the trigonal axis. **Note:** in the 128-cell, the four p-LVMs of $\{Cu_s, Cu_s\}$ are at 68, 104 (doublet), and $263cm^{-1}$, respectively. Watkins *et al.*[31] report weak phonon replicas at 16.4 and 25.1meV (132 and $202cm^{-1}$, respectively) in the PL spectrum of $\{Cu_s, Cu_i\}$. The latter could be the calculated mode at $213cm^{-1}$.

The localization of the p-LVMs can be quantified from the eigenvectors of the dynamical matrix. For each mode, these eigenvectors show the relative displacement of all the atoms in the cell. Their magnitudes give the relative amplitude of the displacement of each atom during the vibrational motion. In Fig.2, the total amplitude associated with the two Cu atoms in $\{Cu_s, Cu_s\}$ is plotted as a function of the mode. For the $68cm^{-1}$ mode in the 128-cell, over 70% of the total displacement of all the atoms involves the two Cu impurities. This fraction is almost 60% for the $263cm^{-1}$ mode and about 30% for the wag modes, indicating that these four modes are highly localized despite their proximity to lattice phonons. In the case of the $\{Cu_s, Cu_i\}$ pair in the 64-cell, the corresponding fractions are about 50%, 30%, and 30%. As for the second-nearest $\{Cu_s-Si-Cu_s\}$ pair in the 64-atom cell, no copper-related mode is more than 20% localized. A comparison of the modes in the perfect cell and that containing $\{Cu_s, Cu_s\}$ shows that phonons are repelled by the copper-related p-LVMs.

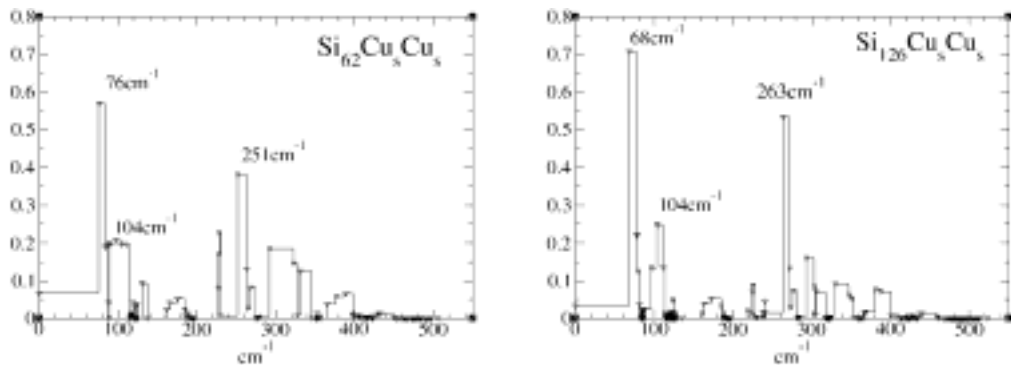


Fig. 2: The localization of p-LVMs is quantified using the eigenvectors of the dynamical matrix.

The $\{\text{Cu}_s, \text{Cu}_i\}$ pair has C_{3v} symmetry. The 73cm^{-1} mode is an A_1 mode and will therefore couple to the PL. The wag modes are degenerate E modes which do not couple to the PL. The mode at 282cm^{-1} , also an A_1 mode, should show up in the PL band, but is very close to the (broader) fourth phonon replica of the 73cm^{-1} mode. The PL band shown in Fig.1 (right, top) has been experimentally associated with the $\{\text{Cu}_s, \text{Cu}_i\}$ pair, and has phonon sidebands at 57cm^{-1} . Thus, we find only one mode with the right symmetry and frequency which explains the observed sidebands.

The $\{\text{Cu}_s, \text{Cu}_s\}$ pair has D_{3d} symmetry and the 79cm^{-1} (68cm^{-1} in the 128-cell) mode is an A_{2u} mode which should not produce sidebands.[32] For the ZPL to exist, the product of the irreducible representations of the ground (electronic) state times the dipole moment times the excited state must contain the totally symmetric representation, A_{1g} . For the phonon replicas to be visible, the product must also include the irreducible representation of the phonon. This is impossible if the phonon is *ungerade*, as is the case here. Thus, if the ZPL is seen, the phonon replicas should not and vice versa. The wag modes at 104cm^{-1} must also be rejected for symmetry reasons. Finally, the A_{1g} mode at 263cm^{-1} will couple but it is too high to generate the observed sidebands. We see three possibilities.

1. The ${}^*\text{Cu}_0$ center is *not* the $\{\text{Cu}_s, \text{Cu}_s\}$ pair. But if experiment shows that this defect contains two copper atoms and is trigonal, then the $\{\text{Cu}_s, \text{Cu}_s\}$ pair seems to be the only possibility ($\{\text{Cu}_i, \text{Cu}_i\}$ is not bound). Further experimental studies are planned in collaboration with the Dresden group.
2. There are *several (electronic) excited states* near each other, both *gerade* and *ungerade*. This is possible since the bonding of Cu_s involves some *sd* hybridization. As noted earlier,[28-30] even Cu_i^+ does not have the full $3d^{10}4(sp)^0$ structure but is $3d^{10-x}4(sp)^x$ with $x \sim 1$. The population analysis suggests that in $\{\text{Cu}_s, \text{Cu}_s\}$, each Cu binds to three Si neighbors, then tries to optimize the Cu-Cu bond. This includes some (*gerade*) σ -bond contribution from $4s-4s$ overlap as well as (*ungerade*) π -bond contributions involving the $3d_{yz}$ and $3d_{zx}$ orbitals. These have antibonding orbitals as well. If the excited electron goes sometimes into one, and sometimes into another, one could see both the ZPL and the phonon replicas.
3. The excited state is a *doublet*. The population analysis shows that the highest-occupied orbital is a singlet (doubly occupied in the 0 charge state) and the lowest-unoccupied orbitals are a pair of doublets. Therefore, the ground state is an orbital singlet in the 0 and +1 charge states. But upon excitation or trapping of an electron, the defect becomes an orbital doublet, is Jahn-Teller unstable, begins to distort and the symmetry drops. It returns to D_{3d} as soon as the electron is emitted or drops back to the ground state. The dynamic coupling between a non-degenerate ground state and a degenerate excited state would lower the symmetry. Then, this p-LVM becomes A_1 and the mode couples to the PL.

COPPER-HYDROGEN COMPLEXES

Cu_s forms whenever Cu_i encounters a pre-existing vacancy, a reaction which releases 2.8eV.[28-30] The four Cu-Si bonds are weak but covalent. Since no lattice strain is apparent around Cu_s , we estimate that the bond strength of each of the four Cu-Si bonds is of the order of $2.8\text{eV}/4=0.7\text{eV}$. MD simulations at $T=1,000\text{K}$ in cells containing copper as well as one, two, three, or four H interstitials show that H always moves straight toward Cu_s without disturbing Si-Si or Cu-Si bonds.

Systematic geometry optimizations were performed to find all the minima of the potential surface for one up to four H interstitials near Cu_s . This includes H bridging a Cu-Si bond or an adjacent Si-Si bond, H at the anti-bonding (AB) site of Si ($\text{Cu}_s\text{-Si-H}_{AB}$), H bound only to Cu_s , and all the combinations when more than one H is present. These calculations involved DZP basis sets and multiple k -point sampling. The lowest-energy configurations have Cu-H bonds with no Si participation: $\{\text{Cu}_s, \text{H}_1\}$, $\{\text{Cu}_s, \text{H}_2\}$, and $\{\text{Cu}_s, \text{H}_3\}$ have Cu_s 5-, 6-, and 7-fold coordinated, respectively.

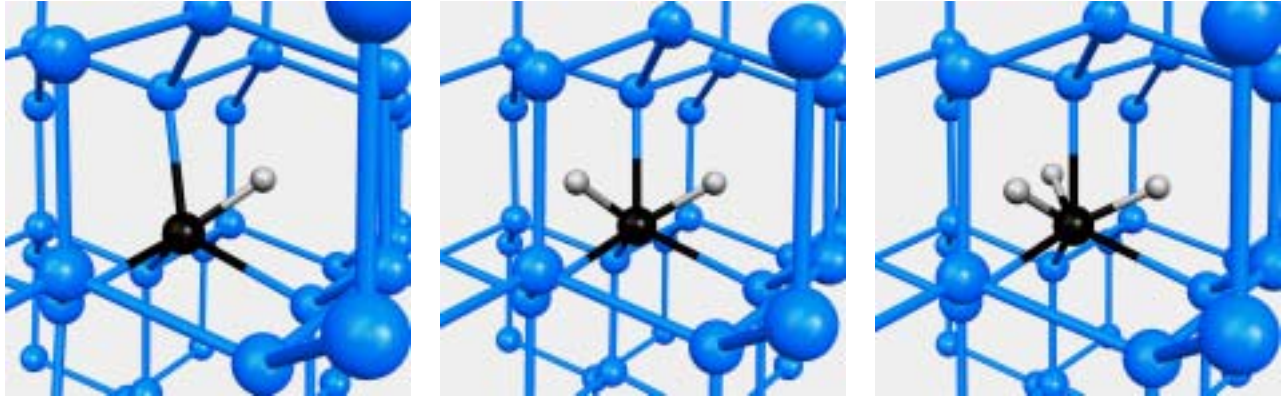


Fig. 3: The $\{\text{Cu}_s, \text{H}_1\}$, $\{\text{Cu}_s, \text{H}_2\}$, and $\{\text{Cu}_s, \text{H}_3\}$ complexes in Si.

Metastable configurations exist, but only at $T=0\text{K}$. To check their stability, we raised the temperature of the cell (typically 500-1,000K), let the system evolve freely for about 1,000 time steps, then quenched to see if the configuration has changed. In all cases, we found that a single configuration survives, the one shown above. In particular, the $\text{Cu}_s\text{-Si-H}_{\text{AB}}$ configurations do not survive our heat treatment. This configuration has been proposed[33] for $\{\text{Ni}, \text{H}_n\}$ complexes, but it is not clear if these calculations included the possibility of H bound directly to the transition metal.

In almost all H-impurity complexes in Si,[34] hydrogen is bound to (or predominantly to) a host Si atom adjacent to the impurity, sometimes in a bonding or bond-centered (BC) configuration, sometimes at an AB site. It is unusual for H to bind directly to the impurity in a manner that does not involve any Si participation. There is no experimental information about the structure of $\{\text{Cu}, \text{H}_n\}$ complexes, but infrared absorption spectra of the $\{\text{Pt}, \text{D}\}$ pair[35] show no trace[36] of the expected ^{29}Si and ^{30}Si isotope lines, were D bound to a Si atom.

The binding energies ΔE_n , ($n=1, \dots, 4$) of the $\{\text{Cu}_s, \text{H}_n\}$ complexes were calculated relative to isolated neutral hydrogen: $\{\text{Cu}_s, \text{H}_{n-1}\} + \text{H}_{\text{BC}} \rightarrow \{\text{Cu}_s, \text{H}_n\} + \Delta E_n$. For $n=1$, 2, and 3, the binding energies are the virtually identical, $\sim 1.6\text{eV}$. These binding energies are very similar because Cu_s induces no lattice relaxation or strain since the Cu-Si bond length matches very well the Si-Si bond length: the binding energy of H comes only from the formation of a covalent Cu-H bond. Realizing the Si-H_{AB} configuration would involve breaking one of the Cu-Si bonds (0.7eV) and displacing a Si atom to the plane of its nearest neighbors at some additional cost in energy. Thus, for the $\text{Cu}_s\text{-Si-H}_{\text{AB}}$ configuration to become energetically favorable, its binding energy would have to exceed $1.6+0.7=2.3\text{eV}$. But H at the AB site of Si forms a rather weak bond. A similar argument can be made for other configurations that involve a bond between Si and H. Therefore, it is not surprising that H prefers to bind to the copper. The key is that Cu_s is not a $3d^{10}$ species and can form many different hybrids with its $3d$ and $4sp$ orbitals.

The case of $\{\text{Cu}_s, \text{H}_4\}$ is different. This complex forms at $T=0\text{K}$ with all four H's bound to Cu_s , which is 8-fold coordinated (to 4 Si and 4 H atoms). However, the binding energy ΔE_4 is only 0.6eV . This complex is unstable. Room-temperature MD runs show that the H wag modes bring pairs of H's close to each other. They overlap and the complex dissociates into Cu_s and 2 interstitial H_2 molecules.

We calculated the LVMs for the $\{\text{Cu}_s, \text{H}_n\}$ complexes, $n=1, 2, 3$. The modes have low symmetry and the frequencies have values that are unusual for H-related modes in Si. $\{\text{Cu}_s, \text{H}_1\}$ has a stretch mode at 1731cm^{-1} and a wag mode at 577cm^{-1} . As the number of H atoms in the complex increases, the various modes couple in a complicated way. The four LVMs associated with $\{\text{Cu}_s, \text{H}_2\}$ are at

1529, 1511, 944, and 758cm^{-1} , and the six LVMs associated with $\{\text{Cu}_s,\text{H}_3\}$ are at 1653, 1587, 1455, 1290, 1192, and $1,144\text{cm}^{-1}$.

Thus, the $\{\text{Cu}_s,\text{H}_n\}$ complexes differ from other impurity-hydrogen complexes in Si in several ways. *First*, hydrogen binds directly to the TM, not to a Si atom near it: there is no Si-H overlap. *Second*, the binding energies (relative to isolated H_{BC}) are almost the same for $\{\text{Cu}_s,\text{H}_n\}$ with $n=1,2,3$. Cu_s does not distort the surrounding host crystal much at all, and the binding energy comes almost exclusively from the formation of a Cu-H bond. *Third*, copper traps three hydrogen interstitials, but if a fourth H binds, the complex dissociates into Cu_s and two interstitial H_2 molecules. Thus, if enough H is present, Cu_s becomes a machine that fabricates H_2 . These molecules have been observed[37-39] but how they form is not understood.[40] While Cu_s is not present in these H_2 studies, some unidentified catalyst may be involved. *Fourth*, the DLTS studies show that H shifts the Cu_s levels in the gap but does not passivate it. It has been suggested[41] that TM are passivated by four H interstitials. The present work shows that this is not the case for Cu_s . *Fifth*, the calculated LVMs are in a frequency range that is normally not associated with H-related defects in Si.

COPPER-OXYGEN INTERACTIONS

Oxygen (in CZ-Si) and carbon (in FZ-Si) are the two most common impurities in Si. Copper-carbon bonding is rarely, if ever, realized in nature. However, copper oxides exist, interstitial oxygen (O_i) is a common impurity, especially in CZ-Si. Copper (and other TM impurities) tend to precipitate at oxides.[6] Therefore, we also considered the interactions between Cu_i and O_i and well as Cu_i and the A-center ($\{\text{O},\text{V}\}$ complex). These results are preliminary.

Cu_i is attracted to O_i but does not form a covalent bond with it. Cu_i prefers the slightly larger void at the interstitial site near O_i , very much like the interstitial H_2 molecule does. In fact, the binding energy of $\{\text{O}_i,\text{Cu}_i\}$ (0.31eV) is very close to that of $\{\text{O}_i,\text{H}_2\}$ (0.25eV). This is enough for Cu_i to trap near O_i at low temperatures. The experimental signature of such a center would consist of a shift in the IR line associated with O_i . Isolated O_i has a characteristic asymmetric stretch at 1136cm^{-1} (our calculated mode is at 1133cm^{-1} for the D_{3d} configuration). When Cu_i or H_2 are adjacent to O_i , the Si-O-Si bond puckers toward the impurity and the frequency drops. In the case of H_2 , the measured O_i mode is at 1075cm^{-1} .[39] If Cu_i is nearby, the Si-O-Si bond puckers even more and the calculated O_i frequency drops to 886cm^{-1} . The structure is shown in Fig.4 (left).

Constant-temperature dynamics show that if Cu_i is placed near the A-center, copper moves into the vacancy and displaces O. MD simulations lead to a configuration where Cu is almost on center at the substitutional site and O bridges a reconstructed Si-Si bond. The lowest-energy configuration corresponds to the $\{\text{Cu}_s,\text{O}_i\}$ complex consisting of Cu_s and O_i bridging an *adjacent* Si-Si bond (Fig.4, right). Cu_s and O_i very far apart is only 0.13eV higher, but isolated Cu_i (in the 0 charge state) far away from the A-center is 1.23eV higher than $\{\text{Cu}_s,\text{O}_i\}$. These numbers are all from the 64-cell with k -point sampling reduced to the Gamma point.

SUMMARY

First-principles studies of fundamental interactions involving copper in Si show that the chemistry of this impurity is much richer than commonly assumed. Interstitial copper becomes substitutional if a vacancy is provided, and the binding energy ($\sim 2.8\text{eV}$) is larger than that of any of the Cu-impurity complex we considered so far.

Substitutional copper traps interstitial copper and forms the $\{\text{Cu}_s,\text{Cu}_i\}$ pair with C_{3v} symmetry. The binding energy (1.16eV) is close to the measured one ($1.02 \pm 0.07\text{eV}$). The p-LVMs of this complex include a mode very close to the observed phonon sidebands in the PL spectrum.

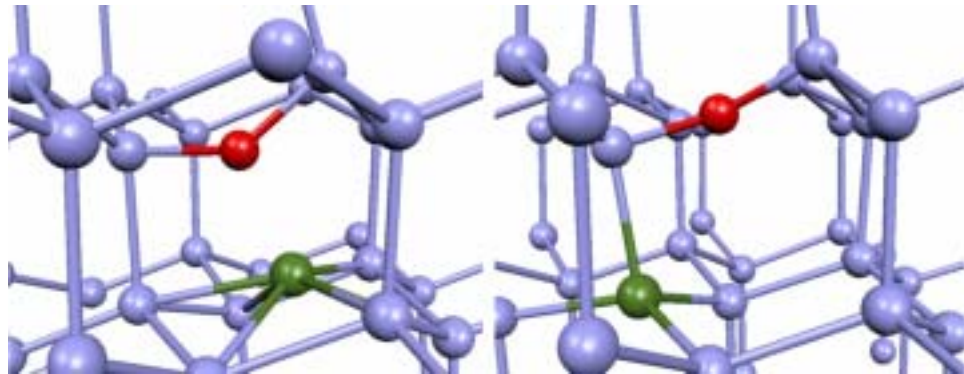


Fig. 4: Left: the $\{\text{Cu}_i, \text{O}_i\}$ complex. Right: Cu_i -- A-center interactions lead to a $\{\text{Cu}_s, \text{O}\}$ complex.

Note that isolated BC copper has been proposed[42] as the center responsible for the 1014meV PL band. Our calculations show that copper is unstable at the BC site, which is *not* a local minimum of the potential energy. Hydrogen, with Si-H \sim 1.4Å, fits at the BC site, but copper, with Si-Cu \sim 2.3Å, does not.

If $\{\text{Cu}_s, \text{Cu}_i\}$ traps a vacancy, it becomes $\{\text{Cu}_s, \text{Cu}_s\}$ at a gain of 2.3eV. This pair exhibits four p-LVMs but only the one at 263cm $^{-1}$ should give rise to sidebands in PL spectra. The A_{2u} mode at 68cm $^{-1}$ could couple as well, but only under special conditions. It is possible that this pair is not the one reported as $^*\text{Cu}_0$.

Substitutional copper can trap up to three H interstitials with $E_b\sim$ 1.6eV. H binds directly to Cu, with no Si participation. The LVMs of all the $\{\text{Cu}_s, \text{H}_n\}$ complexes have been calculated. When a fourth H traps at $\{\text{Cu}_s, \text{H}_3\}$, the $\{\text{Cu}_s, \text{H}_4\}$ complex dissociates into Cu_s and two H_2 molecules.

Finally, the interactions between Cu_i and O_i are weak but should lead to a new O_i mode at 886cm $^{-1}$ visible at low temperatures. When O_i comes close to the A-center, it displaces O, resulting in Cu_s and a nearby O_i . Thus, Cu is attracted to oxygen but does not form covalent bonds with it. Oxygen much prefers to bind to Si, but copper benefits from either a larger free volume or the opportunity to become substitutional itself.

ACKNOWLEDGEMENTS

The work of SKE is supported in part by a contract from NREL, a grant from the Welch Foundation, and a research award from the Humboldt Foundation. Many thanks are due to Texas Tech's High Performance Computing Center for generous amounts of computing time.

REFERENCES

1. A. Mesli and T. Heiser, Defect and Diffusion Forum **131-132**, 89 (1996).
2. A.A. Istratov and E.R. Weber, Appl. Phys. A **66**, 123 (1998).
3. A.A. Istratov, R. Sachdeva, C. Flink, S. Balasubramanian, E.R. Weber, Sol. St. Phenom. **82-84**, 323 (2002).
4. S.M. Myers and D.M. Follstaedt, J. Appl. Phys. **79**, 1337 (1996).
5. M.B. Shabani, T. Yoshimi, and H. Abe, J. Electrochemical Soc. **143**, 2025 (1996).
6. S.A. McHugo, A. Mohammed, A.C. Thompson, B. Lai, and Z. Cai, J. Appl. Phys. **91**, 6396 (2002).
7. A.A. Istratov, C. Flink, H. Hieslmair, E.R. Weber, T. Heiser, Phys. Rev. Lett. **81**, 1243 (1998).
8. D.E. Woon, D.S. Marynick, and S.K. Streicher, Phys. Rev. B **45**, 13383 (1992).
9. H. Lemke, Phys. Stat. Sol. (a) **95**, 665 (1986).

10. S.D. Brotherton, J.R. Ayres, A. Gill, H.W. van Kesteren, and F.J.A.M. Greidanus, *J. Appl. Phys.* **62**, 1827 (1987).
11. U. Wahl, A. Vantomme, G. Langouche, J.G. Correia, and ISOLDE Collaboration, *Phys. Rev. Lett.* **84**, 1495 (2000); U. Wahl, A. Vantomme, G. Langouche, J.P. Araújo, L. Peralta, and J.G. Correia, *Appl. Phys. Lett.* **77**, 2142 (2000).
12. S. Knack, J. Weber, and H. Lemke, *Physica B* **273-274**, 387 (1999).
13. P.N. Hai, T. Gregorkiewicz, C.A.J. Ammerlaan, and D.T. Don, *Phys. Rev. B* **56**, 4620 (1997).
14. C.A.J. Ammerlaan, private communication.
15. J. Weber, H. Bauch, and R. Sauer, *Phys. Rev. B* **25**, 7688 (1982).
16. M.H. Nazaré, A.J. Duarte, A.G. Steele, G. Davies, and E.C. Lightowers, *Mater. Sci. Forum* **83-87**, 191 (1992).
17. H.B. Erzgräber and K. Schmalz, *J. Appl. Phys.* **78**, 4066 (1995).
18. S. Knack, J. Weber, H. Lemke, and H. Riemann, *Physica B* **308-310**, 404 (2001).
19. A.A. Istratov, H. Hieslmair, T. Heiser, C. Flink, E.R. Weber, *Appl. Phys. Lett.* **72**, 474 (1998).
20. K.G. McGuigan, M.O. Henry, E.C. Lightowers, A.G. Steele, and M.L.W. Thewalt, *Sol. St. Com.* **68**, 7 (1988).
21. G. Davies, R. Harding, T. Jin, A. Mainwood, and J. Leung-Wong, *E-MRS* (6/2001), Symp. B.
22. D. Sánchez-Portal, P. Ordejón, E. Artacho, J.M. Soler, *Int. J. Quant. Chem.* **65**, 453 (1997); E. Artacho, D. Sánchez-Portal, P. Ordejón, A. García, J.M. Soler, *Phys. Stat. Sol. (b)* **215**, 809 (1999).
23. D.M. Ceperley and B.J. Adler, *Phys. Rev. Lett.* **45**, 566 (1980).
24. S. Perdew and A. Zunger, *Phys. Rev. B* **32**, 5048 (1981).
25. L. Kleinman and D.M. Bylander, *Phys. Rev. Lett.* **48**, 1425 (1982).
26. H.J. Monkhorst and J.D. Pack, *Phys. Rev. B* **13**, 5188 (1976).
27. J.M. Pruneda, S.K. Estreicher, J. Junquera, J. Ferrer, P. Ordejón, *Phys. Rev. B* **65**, 075210 (2002)
28. S.K. Estreicher, *Phys. Rev. B* **60**, 5375 (1999).
29. S.K. Estreicher, D. West, and P. Ordejón, *Sol. St. Phenom.* **82-84**, 341 (2002).
30. S.K. Estreicher, D. West, J.M. Pruneda, S. Knack, and J. Weber, *MRS Proc.* (3/2002, in print).
31. S.P. Watkins, U.O. Ziemelis, M.L.W. Thewalt, and R.R. Parsons, *Sol. St. Comm.* **43**, 687 (1982).
32. G. Davies, *Phys. Rep.* **176**, 83 (1989).
33. R. Jones, S. Öberg, J. Goss, P.R. Briddon, and A. Resende, *Phys. Rev. Lett.* **75**, 2734 (1995).
34. S.K. Estreicher, *Mater. Sci. Engr. R* **14**, 319 (1995).
35. S.J. Uftring, M. Stavola, P.M. Williams, and G.D. Watkins, *Phys. Rev. B* **51**, 9612 (1995).
36. M. Stavola, private communication.
37. E.E. Chen, M. Stavola, W. Beal Fowler, and P. Walters, *Phys. Rev. Lett.* **88**, 105507 (2002).
38. E.E. Chen, M. Stavola, W.B. Fowler, and J.A. Zhou, *Phys. Rev. Lett.* **88**, 245503 (2002).
39. E.E. Chen, M. Stavola, and W.B. Fowler, *Phys. Rev. B* **65**, 245208 (2002).
40. For a review, see S.K. Estreicher, *Acta Phys. Polonica A* (in print).
41. J.-U. Sachse, E.Ö. Sveinbjörnsson, N. Yarykin, and J. Weber, *Mat. Sci. Engr. B* **58**, 134 (1999).
42. M. Nakamura, S. Ishiwari, A. Tanaka, *Appl. Phys. Lett.* **73**, 2325 (1998); M. Nakamura, *Appl. Phys. Lett.* **73**, 3896 (1998); M. Nakamura and H. Iwasaki, *J. Appl. Phys.* **86**, 5372 (1999); M. Nakamura, *Appl. Phys. Lett.* **79**, 2904 (2001).

Interstitial H₂ in Si: A Nearly Free Rotator After All

Michael Stavola, E Elinor Chen, W Beall Fowler, J Anna Zhou,^a and Peter Walters^b

Department of Physics and Sherman Fairchild Laboratory, Lehigh University
Bethlehem, Pennsylvania 18015, USA

Abstract. Interstitial H₂ in Si has given rise to a number of perplexing puzzles since the discovery of its vibrational spectrum. The absence of an ortho-para splitting for the H₂ line and an apparent low-symmetry found in stress experiments misled several researchers, including the present authors, into thinking that interstitial H₂ must have a barrier that prevents rotation. Our discovery of a new vibrational line for interstitial HD in Si and its interpretation establish that interstitial H₂ in Si is a nearly free rotator. The insights provided by these results lead to simple, in retrospect, explanations of the microscopic properties of interstitial H₂ and an O-H₂ complex in Si.

1. Introduction

In the early 1980s, interstitial H₂ molecules were suggested to play an important role in semiconductors [1-4]. Nonetheless, the H₂ molecule in a semiconductor was not observed directly until recently when vibrational lines for the H₂, HD, and D₂ molecules in GaAs [5] and Si [6-8] were discovered. In addition to the isolated H₂ defect, an O-H₂ complex is formed when the H₂ molecule becomes trapped near an oxygen impurity in Czochralski-grown Si [7]. These experimental results have motivated a number of theoretical studies of the microscopic properties of interstitial H₂ in semiconductors [9-13]. Interstitial H₂ and the O-H₂ complex in Si are shown in Fig. 1.

In spite of these exciting recent advances, a number of results for the H₂ molecules led to apparently contradictory conclusions. The Raman band of the H₂ molecule in GaAs is split into two components, 8 cm⁻¹ apart, with an intensity ratio of ~ 3:1 (ref. 5). These lines were assigned to ortho and para H₂, whose frequencies differ because of ro-vibrational coupling. This interpre-

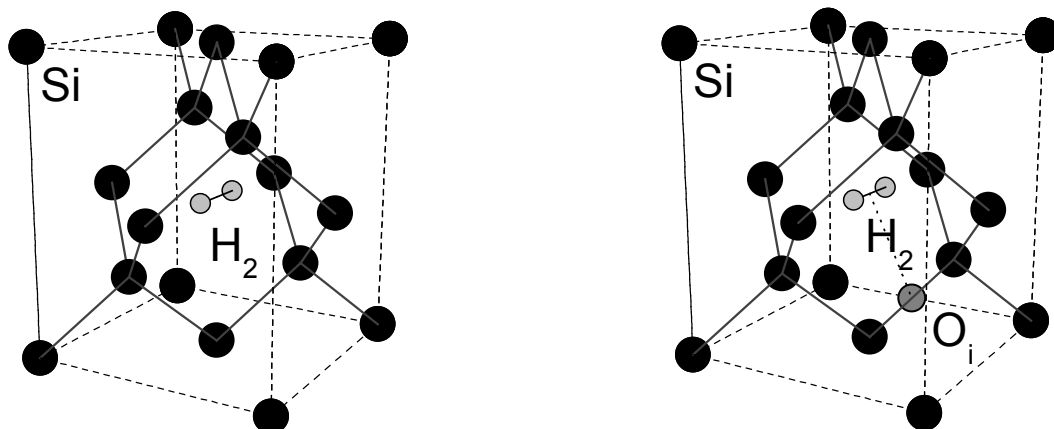


Figure 1. Interstitial H₂ and the O-H₂ complex in Si.

tation leads naturally to the conclusion that H₂, sitting at a T_d interstitial site in GaAs, is freely rotating. In contrast to the situation in GaAs, the H₂ molecule in Si gives only a single, sharp, H₂-vibrational line at 3618.4 cm⁻¹ and no evidence for an ortho-para splitting in its IR absorption spectrum [6,12]. To explain the absence of an ortho-para splitting, it was suggested that there must be a barrier that prevents rotation of the molecule [12]. Uniaxial stress results for the 3618.4 cm⁻¹ line of interstitial H₂ in Si were interpreted in terms of an orientationally degenerate defect with low symmetry, reinforcing the suggestion that the H₂ molecule is static [14]. However, several theoretical calculations for H₂ at a tetrahedral interstitial site in Si find that <100>, <111>, and <110> orientations have similar energies, making it surprising that the H₂ molecule does not rotate [9-12]. Furthermore, recent molecular dynamics calculations indicate that the H₂, HD and D₂ molecules in Si behave as nearly free rotators, bouncing within the interstitial region [13]. This conclusion is supported by our own model calculations [15] which suggest a rotational barrier of only ~ 0.01 eV, more than an order of magnitude smaller than argued [12] would be needed for consistency with a static model.

In addition to the 3618.4 cm⁻¹ line for H₂ in Si, vibrational lines due to HD and D₂ were discovered at 3265.0 and 2642.6 cm⁻¹ (4.2K), respectively, by infrared (IR) absorption [6, 7] and Raman [8] spectroscopies. Studies of HD in Si have led to additional puzzling results. In Si that contains both H and D, the HD vibrational line was reported to be weaker (by a factor of 7.5), relative to the intensities of the H₂ and D₂ lines, than would be estimated for a random pairing of H and D in the sample [16]. And the position of the 3265.0 cm⁻¹ HD line lies 85 cm⁻¹ to higher frequency than is predicted from the observed positions of the H₂ and D₂ lines and a simple model of the anharmonicity of the molecular vibration [14]. There are similar problems with the intensities and positions of the HD lines of the O-HD complex.

New experimental results described in this paper show that interstitial H₂ in Si is actually a nearly free rotator after all [17, 18]. This conclusion leads to the solution of the perplexing puzzles associated with H₂ and the O-H₂ complex [19] in Si.

2. Key to understanding H₂ in Si: the vibrational modes of HD

H₂ is a fascinating molecule with properties that are determined by the symmetry requirements of its total wave function [20]. H₂ consists of two identical nuclei with nuclear spin $\frac{1}{2}$. If the nuclear spins are antiparallel, the nuclear wave function has odd parity, and, therefore, the rotational wave function must have even parity (with even values of the rotational quantum number J). If the nuclear spins are parallel, the nuclear wave function is even, and, therefore, the rotational wave function must be odd (with odd values of J). The nuclear spins are usually coupled only weakly to their environment, so the nuclear spin state can remain unchanged for very long times. These considerations result in there being two separate H₂ species, ortho and para, with even and odd nuclear-spin states, respectively, that do not thermalize on the time scale of many experiments. The ortho and para H₂ species have different rotational levels and spectra. D₂ behaves similarly except that in this case, because the nuclear spin of a deuteron is 1, the total molecular wave function must be symmetric. HD, however, is different because the nuclei are no longer identical, and the symmetry of the nuclear spin state does not restrict the rotational states that are possible.

The considerations above, valid for a freely rotating H₂ molecule, have been thought to be irrelevant for H₂ in Si because distinct ortho and para species were not observed in the

vibrational spectra of the defect. On the contrary, the following results for HD in Si show the importance of molecular rotation. Fig. 2 shows spectra, measured as a function of temperature, for Si that contained H and D [17]. As the temperature is increased, the 3265.0 cm^{-1} line previously assigned [6] to isolated HD becomes weaker while a new line at 3191.1 cm^{-1} grows in with an activation energy of $71 \pm 4\text{ cm}^{-1}$. (We have also examined the vibrational spectra of H_2 and D_2 in Si and find that the 3618.4 and 2642.6 cm^{-1} lines simply shift and broaden without the appearance of any additional lines as the temperature is increased.) The difference in frequency between the 3265.0 and 3191.1 cm^{-1} lines is sufficiently close to the 71 cm^{-1} activation energy measured for the appearance of the new 3191.1 cm^{-1} line for us to consider these energies to be the same, within error. Therefore, the 3265.0 and 3191.1 cm^{-1} lines are attributed to transitions originating from two different initial states, with an energy difference of 73.9 cm^{-1} , to a common excited state (Fig. 3).

For an interatomic separation, $r = 0.788\text{ \AA}$, consistent with a theoretically predicted [10-12] extension of $\sim 0.04\text{\AA}$ from the free-molecule value, one obtains a rotational energy $\hbar^2/(\mu r^2)$ of 80.7 cm^{-1} for HD. This value is close to that observed here for the difference in frequency (73.9 cm^{-1}) of the 3265.0 and 3191.1 cm^{-1} lines observed for HD. That this energy difference lies close to the rotational energy of a free HD molecule strongly suggests that the 3265.0 and 3191.1 cm^{-1} lines are due to ro-vibrational transitions and that the HD molecule, while vibrating as a whole within a small interstitial region, rotates nearly freely.

The results and conclusions for HD in Si must also be consistent with the behavior of H_2 and D_2 . The new absorption line for HD at 3191.1 cm^{-1} that is seen at elevated temperature lies close

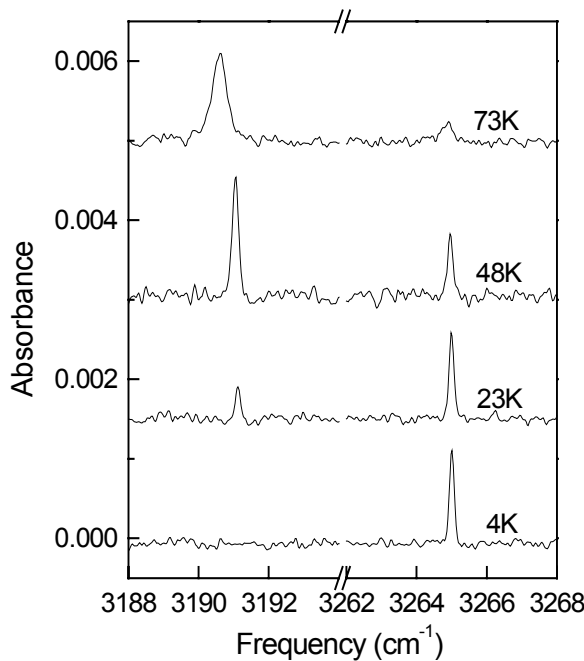


Figure 2. Spectra measured as a function of temperature for the 3265.0 cm^{-1} and 3191.1 cm^{-1} absorption lines assigned to the interstitial HD molecule in Si.

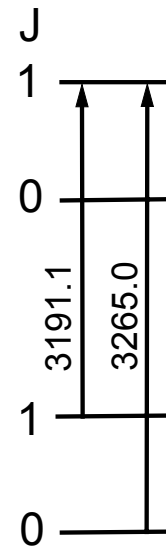


Figure 3. Energy level diagram for the ro-vibrational transitions of HD in Si.

to the frequency position (3180 cm^{-1}) predicted from the positions of the H_2 and D_2 lines and a simple model of the anharmonicity of the hydrogen molecule [14]. Therefore, our results suggest that it is the new 3191.1 HD line and the 3618.4 and 2642.6 cm^{-1} lines of H_2 and D_2 that arise from similar transitions. Furthermore, the new 3191.1 cm^{-1} HD line is more intense than the 3265.0 cm^{-1} line, resolving the problem of the HD absorption being anomalously weak. For H_2 and D_2 , the requirement that only rotational states with either odd or even parity exist depending on the parity of the nuclear-spin state makes ro-vibrational transitions with $\Delta J = 0, 2 \dots$ the only possibilities. For HD, there is no corresponding requirement, so all rotational states may exist. We therefore suggest that the 3618.4 , 3191.1 , and 2642.6 cm^{-1} lines all arise from purely vibrational transitions with $\Delta J = 0$ and that the 3265.0 cm^{-1} line involves a $J = 0$ to $J = 1$ transition that is possible only for HD. These considerations lead to the energy level diagram for HD shown in Fig. 3. The 3265.0 cm^{-1} line seen at 4.2K corresponds to a $J = 0$ to $J = 1$ transition, obeying the $\Delta J = \pm 1$ free rotator selection rule for a dipole-allowed transition, and thus includes one rotational quantum more than the purely vibrational transition. The 3191.1 cm^{-1} line that is observed once the $J = 1$ state is thermally populated corresponds to a $J = 1$ to $J = 1$ transition. Thus $\Delta J = 0$ and this transition corresponds to the purely vibrational transitions that must also occur for the *homonuclear* molecules H_2 and D_2 where transitions with $\Delta J = \pm 1$ are not possible.

The $\Delta J = \pm 1$ selection rule for allowed dipole transitions of a free rotator is found to be broken for the $J = 1$ state of HD where we see only a J-conserving transition, and not for the $J = 0$ state because the $J = 0$ to $J = 0$ transition is not observed in our spectra. To explain these selection rules, we note that in tetrahedral symmetry, $J = 0$ becomes A_1 , while $J = 1$ becomes T_2 . A_1 to A_1 transitions remain electric dipole forbidden in the tetrahedral field, while T_2 to T_2 transitions become electric dipole allowed. Therefore, the selection rule for rotational transitions of a free rotator, $\Delta J = \pm 1$, is broken in tetrahedral symmetry for the $J = 1$ state but not for the state with $J = 0$.

If we apply these selection rules for J to H_2 and D_2 , we immediately recognize that only the nuclear-spin configurations that correspond to the initial states with $J = 1$, ortho for H_2 and para for D_2 , will give rise to IR absorption lines. Thus the absence of an ortho-para splitting in the IR spectra of H_2 and D_2 is explained naturally by the selection rules for J found from our ro-vibrational spectra for HD. Surprisingly, ortho and para species also were not seen in Raman spectra measured for H_2 and D_2 in Si [8]. Recent Raman experiments, however, do reveal ortho-para splittings and additional new surprises [21].

3. Confirmation of the rotational motion of H_2 and D_2 in Si: uniaxial stress results

Uniaxial stress results for the H_2 and D_2 vibrational lines, previously interpreted in terms of a non-rotating defect [14], can be reinterpreted to confirm our model of a nearly free rotator [18]. The shifts and splittings of the H_2 and D_2 vibrational lines for different orientations of the applied stress are shown in Fig. 4. Here the data for H_2 and D_2 are plotted together with the frequency axes, left for D_2 and right for H_2 , shifted so that the zero-stress frequencies of the D_2 and H_2 lines coincide. The 3618.4 and 2642.6 cm^{-1} transitions both show sizeable stress splittings, with the remarkable characteristic that the line splittings seen for H_2 and D_2 are nearly identical.

The static model that previously was assumed to fit the stress data for the 3618.4 cm^{-1} H_2 line [14] does not explain the isotope independence of the stress splittings seen for H_2 and D_2 and

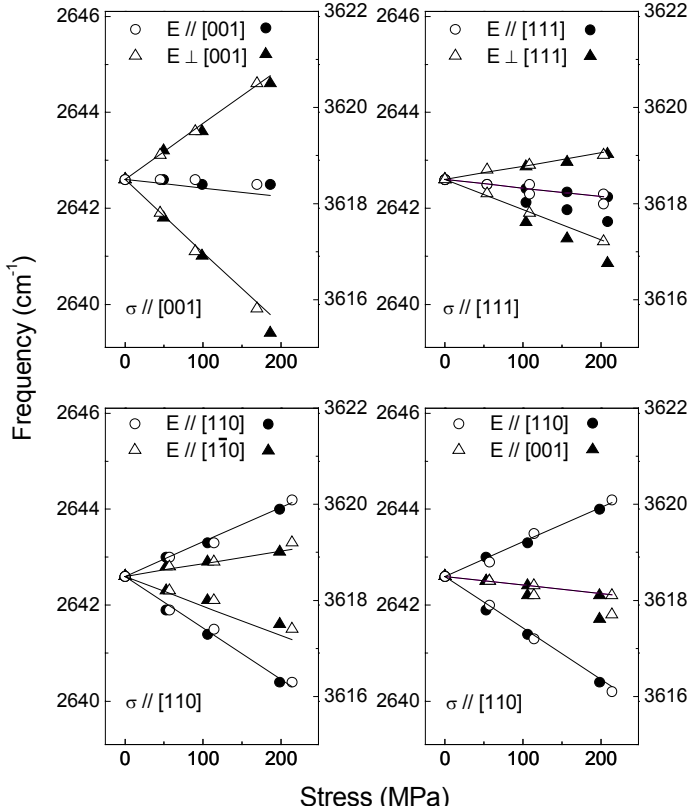


Figure 4. Stress-induced frequency shifts vs the magnitude of the stress applied along the high symmetry crystal directions for the 3618.4 cm^{-1} and 2642.6 cm^{-1} lines assigned to interstitial H_2 and D_2 in Si. The left scales correspond to data measured for D_2 (open circles and triangles) and the right scales correspond to the data measured for H_2 (filled circles and triangles).

also predicts the existence of additional weak lines that are not observed. Our proposal that the IR transitions of interstitial H_2 and D_2 in Si are allowed only when the molecule is in the $J = 1$ rotational state [17] suggests a new interpretation of the stress results in which it is the $J = 1$ rotational state of the H_2 molecule that is split by stress. Kaplyanskii [22] has determined the splittings of the representations of the T_d point group for stresses applied along the high-symmetry crystal directions and also the intensities of transitions between the split states. The IR transitions seen for H_2 (and D_2) when in the $J = 1$ rotational state are T_2 to T_2 transitions. To fit our data, we have assumed that the T_2 rotational states associated with the ground and excited vibrational states show the same splittings under stress and that there is a small hydrostatic shift of the center of gravity of the split lines. The straight lines drawn in Fig. 4 are the result of a least squares fit to the stress data for the 2642.6 cm^{-1} D_2 line. The experimental data for the positions, relative intensities, and polarization selection rules are in excellent agreement with the results expected [22] for a T_2 to T_2 transition of a defect with full tetrahedral symmetry.

The fit to our stress data for D_2 also provides a reasonable fit to the data for H_2 shown in Fig. 4. This absence of an isotope dependence, while initially puzzling, is a natural result of the splitting of a degenerate rotational level, in the present case $J = 1$. To first order in perturbation theory, the uniaxial-stress splitting arises from a perturbing potential energy whose effect is calculated from the matrix elements of rotational wave functions. Both the potential energy and the rotational wave functions are isotope independent, so the resulting splittings are as well.

Uniaxial stress results establish that the 3618.4 and 2642.6 cm^{-1} absorption lines seen for interstitial H_2 and D_2 in Si are due to vibrational transitions between ro-vibrational states with rotational quantum number $J = 1$ (T_2 in T_d symmetry). The absence of an isotope dependence for the line splittings is a *signature* of the lifting of the degeneracy of the rotational states by stress.

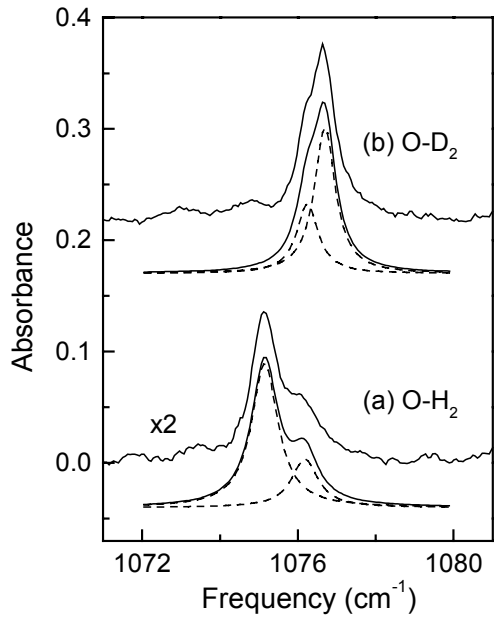


Figure 5. IR absorption spectra (4.2K) of the oxygen modes of (a) the O-H₂ and (b) the O-D₂ complexes in Si. Fits to the line shapes are shown. The samples are Cz Si into which H or D had been introduced, followed by an anneal at room temperature for at least one week to produce the complexes.

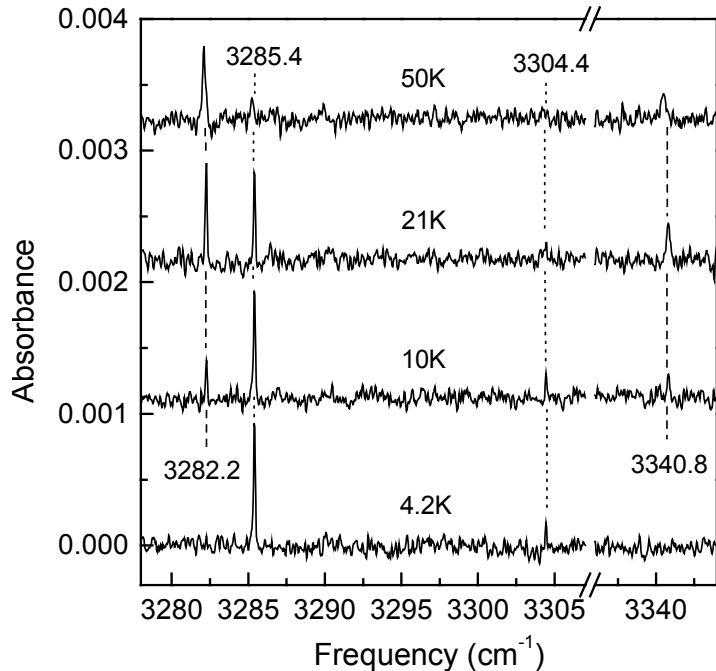


Figure 6. Spectra measured as a function of temperature for the 3282.2, 3285.4, 3304.4, and 3340.8 cm⁻¹ absorption lines assigned to the O-HD complex in Si. The vibrational lines present at 4.2K are indicated with the dotted vertical lines. The lines that appear at elevated temperature are indicated with the dashed vertical lines.

4. The O-H₂ complex in Si

An O-H₂ complex is formed in Czochralski-grown (Cz) Si when H₂ migrates and becomes trapped by an O impurity (Fig. 1) [7, 23]. O-H₂ gives rise to two near-lying oxygen modes (Fig. 5) and to high-frequency H₂ modes [7, 19]. These results were interpreted previously in terms of two O-H₂ complexes with different structures [7]. Our results for H₂ in Si [17] suggest a new model in which the H₂ molecule in the O-H₂ complex is a nearly free rotator and that both para-H₂ and ortho-H₂ are trapped by O impurities [19].

In the studies of HD in Si described above, we found a new vibrational absorption line that appears at elevated temperature (T>20K). In the experiments described here, vibrational spectra were measured as a function of temperature for Cz Si into which H and D had been introduced to search for new lines that might be associated with the O-HD complex. Fig. 6 shows spectra for the O-HD complex. As the temperature is increased above 4.2K, the 3285.4 and 3304.4 cm⁻¹ lines previously assigned to O-HD [7] become weaker while two new lines at 3282.2 and 3340.8 cm⁻¹ grow in. The joint appearance of the two new lines of O-HD at 3282.2 and 3340.8 cm⁻¹ as the temperature increases, while the two lines at 3285.4 and 3304.4 cm⁻¹ both weaken, shows

that all of these lines are due to the same defect complex. Similar to this finding for O-HD, we also conclude that the related vibrational lines of O-H₂ cannot be due to two complexes with different structures [19].

Our conclusion that only one O-H₂ structure is being observed suggests that the two near-lying oxygen lines observed for O-H₂ are due to the ortho and para states of the H₂ molecule in the complex, and similarly for O-D₂. This possibility was originally considered by Pritchard *et al.*, but was rejected in favor of an alternative model [7]. Fig. 5 shows spectra of Cz-Si samples measured after the indiffusion of (a) H and (b) D and an anneal at room temperature to produce the complexes. In spectra (a) and (b), two strong near-lying oxygen lines are seen. For the O-H₂ complex, spectrum (a) was fit by two lines with Voigt shapes and with the intensities of the two components being 3:1. For the O-D₂ complex, spectrum (b) was again fit by two lines with Voigt shapes, but with the intensities of the two components being 2:1. This analysis of the intensities of the oxygen modes of the O-H₂ and O-D₂ complexes is in excellent agreement with the previous results of Pritchard *et al.* [7]

The relative intensities of the two oxygen modes, 3:1 for O-H₂ and 2:1 for O-D₂, are consistent with the ratios expected for ortho to para complexes, where the ratios of the intensities are given by the ratios of the degeneracies of the ortho and para nuclear-spin states [20]. These results, and the knowledge that isolated, interstitial H₂ and D₂ in Si exhibit rotational motion [17, 18], lead us to conclude that there are two near-lying oxygen lines for the O-H₂ (and O-D₂) complex because the oxygen vibrational frequency depends on whether its H₂ (or D₂) partner is in the ortho or para state.

Our studies of the high-frequency H₂ and D₂ lines of the O-H₂ and O-D₂ complexes show that each complex has at least three high-frequency modes [19]. These can be understood as transitions of ortho and para H₂ and D₂ trapped by oxygen. The important differences between the isolated interstitial molecules and H₂ and D₂ trapped by O are that the presence of the O atom lowers the symmetry of the neighboring interstitial site, splitting the J = 1 rotational states and also making H₂ (and D₂) vibrational transitions in the J = 0 rotational state electric-dipole allowed. The splittings of the high-frequency modes of O-H₂ and O-D₂ and the intensities of the lines can be understood in the context of this model.

5. Conclusion

Previous studies of interstitial H₂ in Si have led to a number of perplexing questions, with a particularly controversial issue being whether H₂ in Si is static or is a nearly free rotator. The key to the solution of this problem is the discovery of a new IR absorption line for HD in Si at 3191.1 cm⁻¹ [17]. The line previously observed for HD at 3265.0 cm⁻¹ is reassigned to a ro-vibrational transition that can occur only for the heteronuclear HD molecule. These results and their interpretation lead to the conclusion that interstitial H₂ in Si is a nearly free rotator. Uniaxial stress results for H₂ and D₂, which were taken previously as evidence for a static defect [14], actually provide a strong confirmation of the rotation of interstitial H₂ [18]. Furthermore, the microscopic properties of an O-H₂ complex in Si can be understood in terms of ortho and para H₂ molecules that become trapped by O impurities [19].

6. Acknowledgments

We thank G. D. Watkins for numerous helpful discussions and F. S. Ham for group theoretical insights. This work was supported by NSF Grant No. DMR-0108914, the NSF REU program, and NREL Award Nos. ACQ-9-29639-02 and AAT-2-31605-04.

References

- a Current address: Lucent Technologies, Holmdel, NJ 07733
b Current address: University of Rochester, Rochester, NY 14627
- [1] Mainwood A and Stoneham A M 1983 *Physica* **116B** 101
 - [2] Corbett J W, Sahu S N, Shi T S, and Snyder L C 1983 *Phys. Lett.* **93A** 303
 - [3] Hall R N 1985 *J. Elect. Mat.* **14a** 759
 - [4] Estreicher S K 1995 *Mat. Sci. Eng. R* **14** 319
 - [5] Vetterhöffer J, Wagner J, and Weber J 1996 *Phys. Rev. Lett.* **77** 5409
 - [6] Pritchard R E, Ashwin M J, Tucker J H, and Newman R C 1998 *Phys. Rev. B* **57**, 15048
 - [7] Pritchard R E, Ashwin M J, Tucker J H, Newman R C, Lightowers E C, Binns M J, McQuaid S A, and Falster R 1997 *Phys. Rev. B* **56** 13118
 - [8] Leitch A W R, Alex V, and Weber J 1998 *Phys. Rev. Lett.* **81** 421
 - [9] Okamoto Y, Saito M, and Oshiyama A 1997 *Phys. Rev. B* **56** 10016
 - [10] Van de Walle C G 1998 *Phys. Rev. Lett.* **80** 2177
 - [11] Van de Walle C G and Goss J P 1999 *Mater. Sci. Eng. B* **58** 17
 - [12] Hourahine B, Jones R, Öberg S, Newman R C, Briddon P R and Roduner E 1998 *Phys. Rev. B* **57** 12666
 - [13] Estreicher S K, Wells K, Fedders P A and Ordejón P 2001 *J. Phys.: Condens. Matter* **13** 6271
 - [14] Zhou J A and Stavola M, *Phys. Rev. Lett.* **83**, 1351 (1999); Zhou J A, Chen E, and Stavola M 2000, *Phys. Rev. Lett.* **84** 4778
 - [15] Fowler W B, Walters P and Stavola M 2002 *Phys. Rev. B* to be published
 - [16] Newman R C, Pritchard R E, Tucker J H, and Lightowers E C 1999 *Phys. Rev. B* **60** 12775
 - [17] Chen E E, Stavola M and Fowler W B 2002 *Phys. Rev. Lett.* **88** 105507
 - [18] Chen E E, Stavola M, Fowler W B and Zhou J A 2002 *Phys. Rev. Lett.* **88** 245503
 - [19] Chen E E, Stavola M and Fowler W B 2002 *Phys. Rev. B* **65** 245208
 - [20] Eisberg R and Resnick R 1985 *Quantum Physics of Atoms, Molecules, Solids, Nuclei and Particles*, 2nd ed. (New York: Wiley)
 - [21] Lavrov E and Weber J, private communication
 - [22] Kaplyanskii A A 1964 *Opt. Spectrosc. (USSR)* **16** 557
 - [23] Markevich V P, Suezawa M, and Sumino K 1995 *Mater. Sci. Forum* **196-201**, 915; Markevich V P and Suezawa M 1998 *J. Appl. Phys.* **83** 2988

Industrial systems for hydrogen passivation using hydrogenated amorphous SiNx layers

Silvia Roth, Roth & Rau Oberflächentechnik AG, Gewerbering 3 + 10, D-09337 Hohenstein-Ernstthal

A high throughput industrial PECVD reactor for deposition of passivating SiN layers is presented. It is shown that high quality SiN layers are deposited using a novel remote microwave plasma technology as well as that the equipment fulfils the demands of the photovoltaic industry for high throughput and long time process stability under production conditions.

1. INTRODUCTION

Amorphous hydrogenated silicon nitride (SiN) layers, deposited by Plasma Enhanced CVD processes have been demonstrated to be - besides good anti-reflection layers - excellent means for surface passivation [1]. Moreover, in a mc-Si cell processing scheme in which the metallization pattern is printed on the SiN layer and subsequently is fired through the layer by means of a short high-temperature step, the minority charge carrier lifetime in the bulk of the mc-Si can improve significantly. This improvement of the quality of the bulk is due to diffusion of hydrogen from the SiN layer into the silicon during the firing step [2,3].

For these reasons and since more and more mc-silicon is used in solar cell production there is a great interest from the silicon PV industry in the process of PECVD deposition of SiN. An industrial PECVD reactor must meet the following requirements of the PV industry:

- Significant improvement of the cell efficiency of at least 10% compared with a conventional TiO₂ antireflective coating
- High process stability and reproducibility
- High throughput
- Low cost/wafer
- Easy implementation into automatic production lines

SiNA is a continuous operating industrial PECVD reactor, which has been developed to provide equipment, which fulfils the demands imposed by the PV industry (Figure 1).



Figure 1: View of a SiNA system

2. SYSTEM

The system consists of 5 vacuum chambers, an entry load-lock chamber, a heating chamber, a deposition chamber with linear remote plasma sources, a cooling of chamber and an exit load-lock chamber, in which trays with a number of wafers are sequentially processed (see Figure 2). The throughput of this system reaches from 640 wafers/hour (wafer size 8" x 8") to 1960 wafers/hour (wafer size 4" x 4").

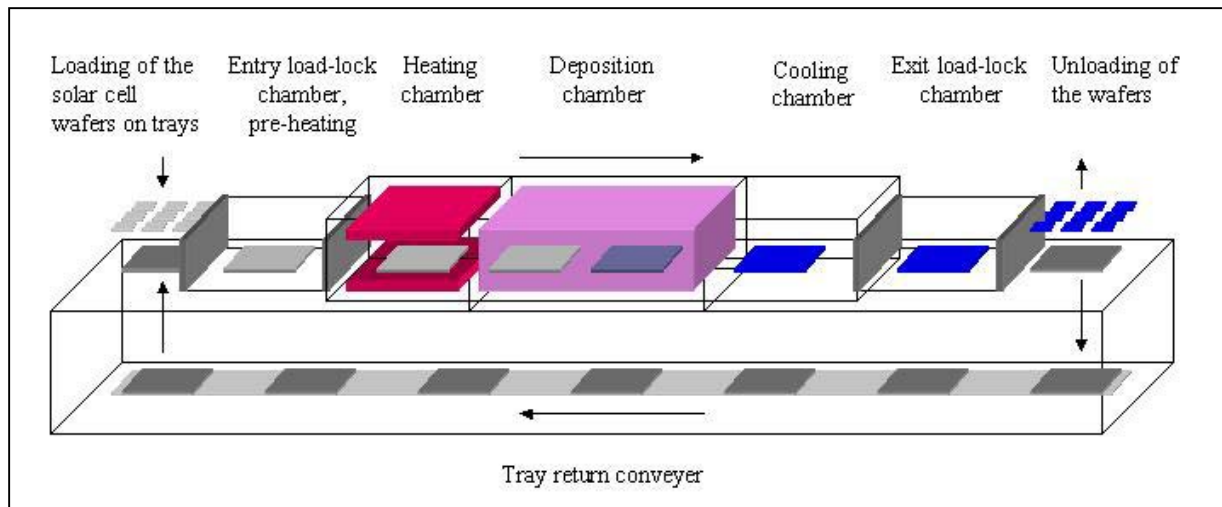


Figure 2: Scheme of construction and functional principle of SiNA systems

In the entry chamber, the wafers are pre-heated by means of IR-lamps. In the heating chamber the wafers attain the deposition temperature of typically 350...400°C. The deposition takes place in the central part of the system, where the trays with the wafers under- or overpass an array of 4 linear plasma sources. Both process directions of the wafers – face up or bottom up – are possible as well. The “bottom-up” version is the preferred process direction for production since there is no contamination of the wafers by spelling of loose particles from parasitic layers in the deposition chamber. The plasma sources in the reactor are novel remote microwave plasma sources, developed by Roth & Rau for the SiN deposition process [4]. The plasma sources consist of a quartz tube with a Cu antenna inside reaching from one wall of the deposition chamber to the other. The quartz tube separates the antenna from vacuum. The source is operated at a microwave frequency of 2.45 GHz. The microwaves are coupled from both sides and propagate along the antenna. A high density, uniform plasma is excited around the quartz tube over a length up to 1 m. The source also includes an arrangement of permanent magnets for electron confinement in the plasma. Typically a NH₃/SiH₄ gas mixture is used depending on the process technologic demands in the pressure range of 0.08 to 0.5 mbar. The deposition process takes place in the afterglow range of the plasma. Using an array of 4 plasma sources the deposition rate is typically 40 nm/min. The deposition arrangement is schematically shown in Figure 3.

In comparison with older and more conventional direct plasma sources, this remote plasma source has the following advantages.

- Wafer handling is more convenient since the wafers do not need an electrical contact with any electrode. Therefore the process does not depend on the wafer size or any wafer material properties

- Due to the GHz frequency at which the source is operated the plasma self-bias is very low. Consequently the ion bombardment of the wafers does not cause a deterioration of the surface.
- The utilisation of the process gases (silane and ammonia) is very efficient. The dissociation rate (depletion) in the plasma of both gases is more than 90 %. The deposition efficiency, that is the fraction of the process gases that is converted in SiN on the wafers, is about 4 % [5]

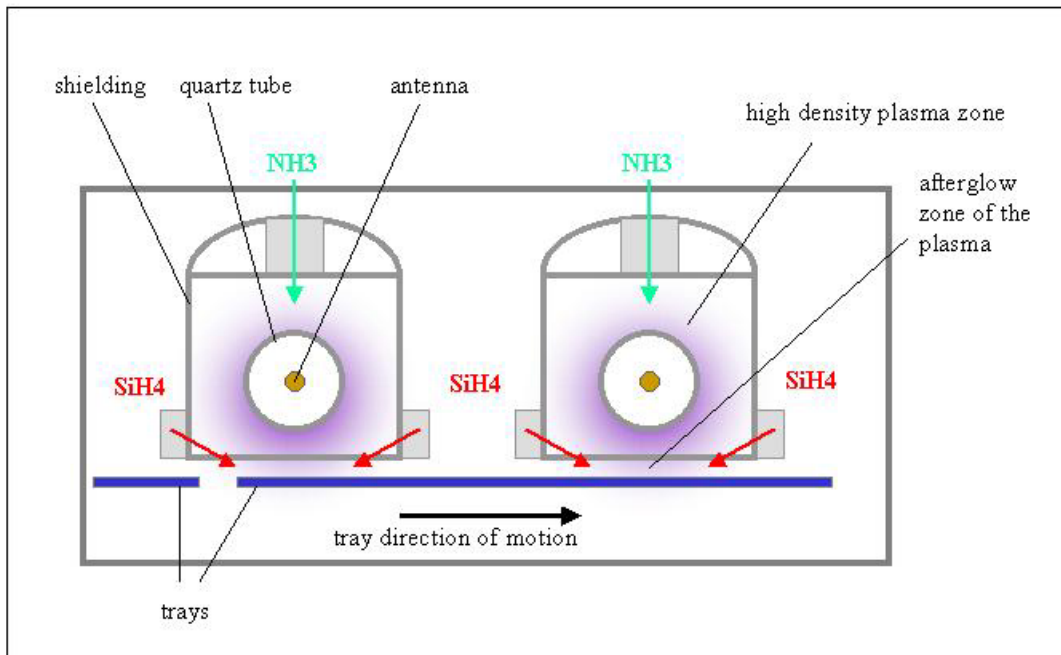


Figure 3: Scheme of the plasma source arrangement

Before the wafers enter the exit load lock chamber, they cool down in the forth chamber. The load-lock chambers and the deposition chamber have individual pumping systems such that the evacuation of the chambers is not a limiting factor for the throughput. The limiting factors for the throughput are the deposition time and the time needed for loading and unloading of the trays. The cycle time for loading is 90 s.

In order to meet the requirements of the different cell line capacities 3 system sizes are available. The capacities are summarized in table 1.

Wafer size / mm ²	SiNA ^{MINI}	SiNA	SiNA ^{PLUS}
100 x 100	300	1200	1960
125 x 125	192	800	1440
150 x 150	144	640	1000
200 x 200	108	360	640
Pieces / tray (125 x 125 mm ²)	16	20	36
Loading cycle time	300	90	90

Table 1: SiNA and SiNA^{PLUS} system sizes

3. SOLAR CELL RESULTS

Production tests have been carried out on mc-silicon wafers provided by different suppliers and made by different technologies. Basing on the experiences with the smaller pilot system operating at the Netherlands Energy Research Centre ECN different process recipes have been developed for the different materials.

For optimum solar cell performance the optical properties as well as the passivation properties have to be optimised in the deposition process. Usually the required film thickness is in the range of 70...80 nm and the refractive index about 2.1. The deviation of the film thickness must be less than +/- 5%. A deviation of the refracted index is acceptable in the range of < +/- 2,5%.

Variable process parameters are the NH₃/SiH₄ ratio in the process gas, process temperature, process pressure, microwave power and transportation speed of the trays. The optical and passivation properties are controlled by gas ratio, process temperature and process pressure. The uniformity of the layers mainly depends on the absolute values and balance of microwave power on both sides of the plasma sources. By varying the transportation speed the deposition rate is controlled.

The most important parameter for adjustment of the refractive index is the NH₃/SiH₄ ratio. In Figure 4 the dependence of the refractive index on the gas ratio is shown.

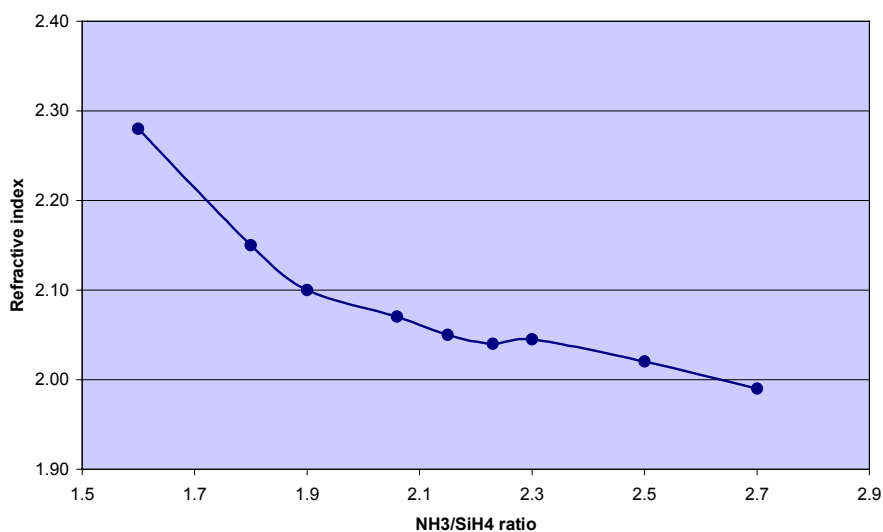


Figure 4: Refractive index in dependence on the NH₃/SiH₄ ratio (T = 350C; p = 0,15 mbar; MW power 2x 1500W for each plasma source)

Figure 5 and 6 show the uniformity of film thickness and refractive index in dependence on the position of the tray perpendicular to the moving direction of the trays. The wafers had a size of 208 x 208 mm². In moving direction no inhomogeneity has been observed.

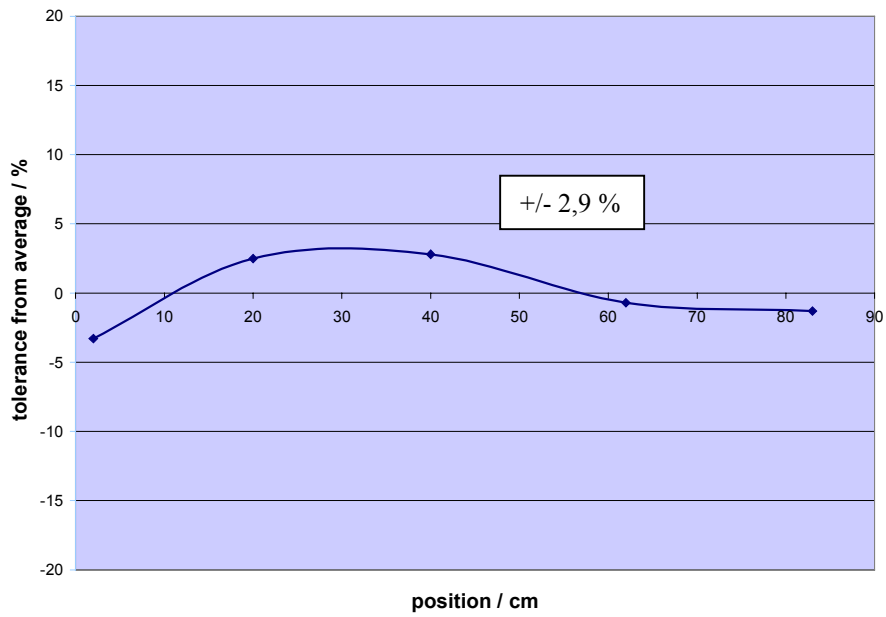


Figure 5: Film thickness uniformity over the tray perpendicular to the moving direction

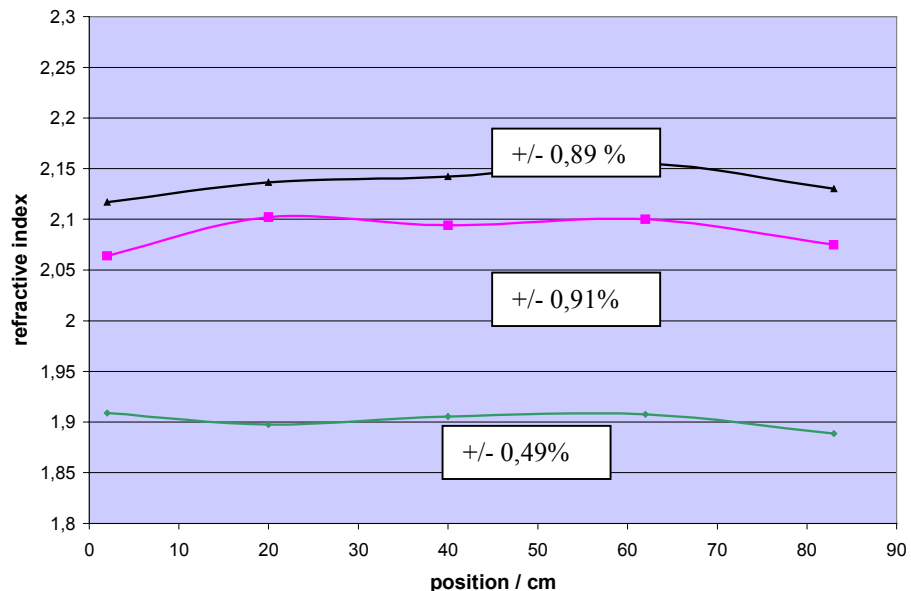


Figure 6: Refractive index in dependence on the position on the tray perpendicular to the moving direction of the tray for NH3/SiH4 ratios of 2,5, 1,9, 1,8

We have investigated film thickness uniformity and refractive index uniformity over a time interval of 8 hours operation under production conditions. The wafer size was 125 x 125 mm², 36 wafers have been processed on a tray. Film thickness and refractive index are an average of the values measured on wafers from 9 positions on the tray (Figures 7 a and b).

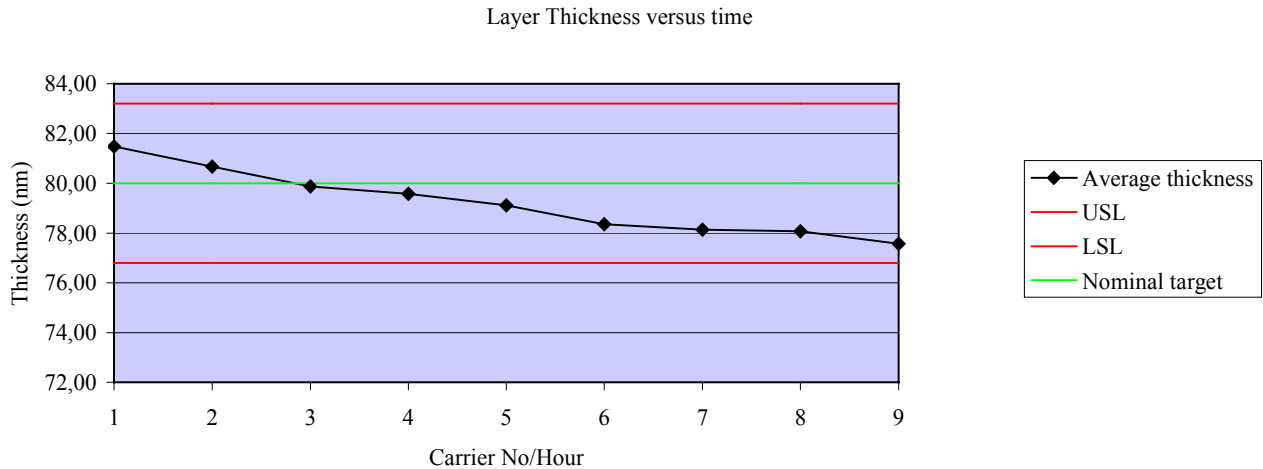


Figure 7a: Film thickness vs. time during 8 hours operation; the LSL to USL range is +/- 4% of the nominal target of 80 nm film thickness

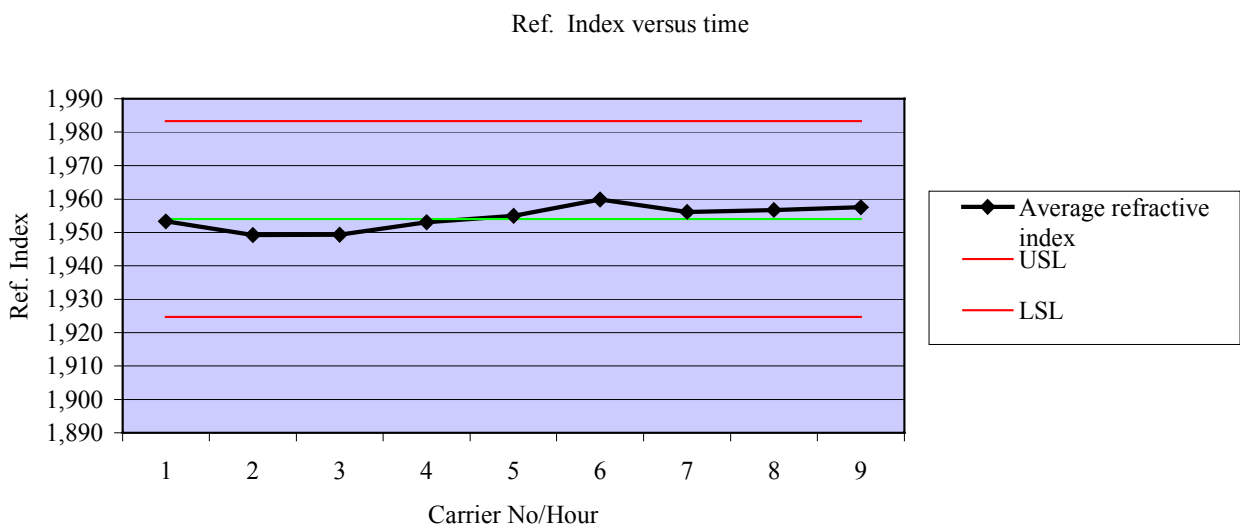


Figure 7b: Refractive index vs. time during 8 hours operation, the LSL to USL range is +/- 1,5% of the average value

The mean improvement of the cell efficiency caused by the passivation effect of the SiN layer is in the range of 10...20% compared with a conventional TiO₂ antireflective layer. Besides the deposition process the gain depends on the quality of the mc-silicon material and parameters of the firing step. Concerning the deposition process the passivation properties strongly depend on the NH₃/SiH₄ ratio on the process gas. We have investigated gas ratios from 1 to 4. We have observed two process windows for passivating SiN. With silane rich gas mixtures (ratio between 1,3 and 1,8) as well as with ammonia rich gas mixtures (> 2,7) good passivation properties can be achieved. Figure 8 shows some typical results for process recipes. The deposition process has been carried out at the same process temperature and the same process pressure. Different suppliers have provided the mc-materials.

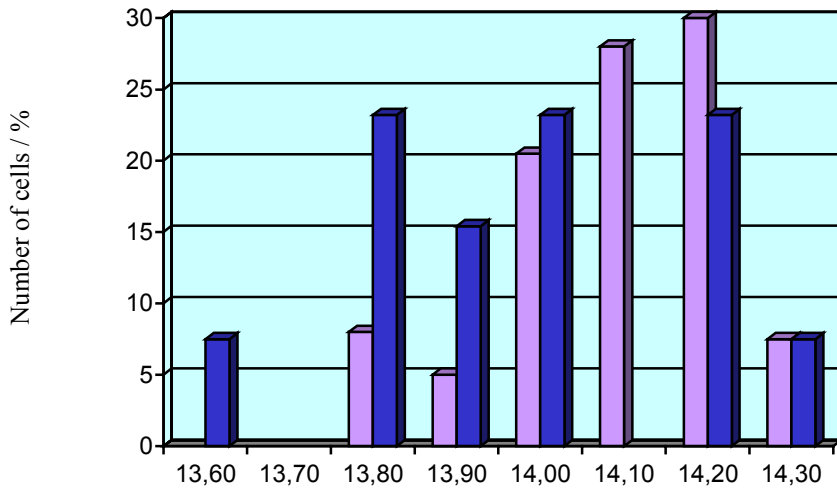
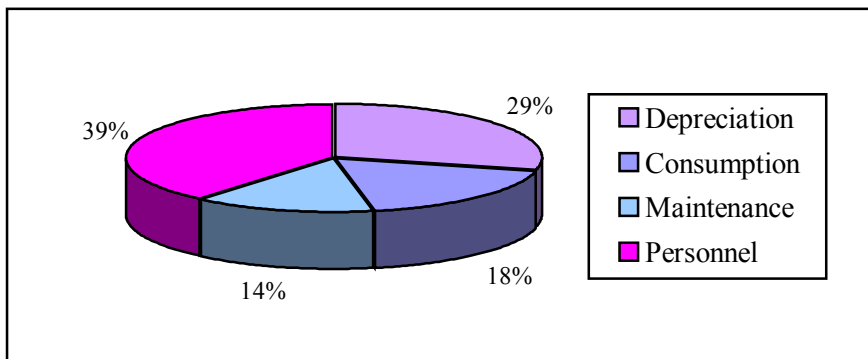


Figure 8: Total efficiency of cells in % of 2 test runs processed with silane rich gas mixture (violet bars) and ammonia rich gas mixture (blue bars)

4. COST SITUATION

Since the success of a technology in industrial application always depends on its cost we want to give a short overview on the cost situation. In table 2 all costs for operation of the large-scale industrial PECVD equipment SiNA^{PLUS} are summarized. The calculation is based on a 365 days / 24-hour production cycle and German prices for labour, facilities and consumables are applied. The wafer size is 125 x 125 mm² and the efficiency has been calculated with 14,5%.

Equipment	SiNA ^{PLUS}
Capacity	9,475 Million wafers/year (wafer size 125 x 125 mm ²) ~ 20 MW/year
Total cost / year	780.000,00 €
Cost per wafer	0,095 €
Cost per Watt	0,042 €



5. SUMMARY AND OUTLOOK

Roth & Rau have jointly developed a high throughput industrial scale PECVD reactor. This PECVD reactor has been successfully implemented into mc-Si solar cell processing for deposition of amorphous silicon nitride. It is shown that with this PECVD process, SiN can be grown which not only acts as a good AR coating, but which can also improve the quality of the bulk mc-Si material if the deposition is followed by a suitable heat treatment. The ‘firing through’ process significantly increases the lifetime of minority charge carriers in the bulk of the mc-Si, leading to an average increase of the cell efficiency of about 1% absolute.

We have performed 8-hour shift production tests on mc-Si wafers in which we have investigated the process stability and reproducibility of the properties of the SiN layers. These tests have shown a very good stability of the process under production conditions over long time.

The growing of PV as one option in the market of regenerative energies will mainly depend on cost reduction for production of solar cells and modules. Besides the cost reduction for the silicon material the production lines must produce more effectively. In-line concepts like SiNA offer new options for automation of the cell production lines and for implementation of other processes. Roth & Rau is going to develop a plasma-etching reactor for phosphor glass removal using a dry plasma etching process prior to the SiN deposition. The prototype will be installed next.

ACKNOWLEDGEMENTS

We would like to thank Dr. Wim Soppe and Arthur Weeber of ECN and Alexander Hauser of the University Konstanz for their support in process development, solar cell processing and efficiency measurements.

- [1] J. Schmidt, A.G. Aberle, *J. Appl. Phys.* **85** (1999) 3626.
- [2] W. Soppe, A. Weeber, H. de Moor, W. Sinke, T. Lauinger, R. Auer, B. Lenkheit and A.G. Aberle, Proc. 2nd World Conf. and Exhibition on Photovoltaic Solar Energy Conversion (1998) 1826.
- [3] J.E.A. Elgamel, *IEEE Trans. Electr. Devices* **45** (1998) 2131.
- [4] Patent No. DE 198125558
- [5] W.J.Soppe, B.G.Duijelaar, S.E.A.Schiermeier, A.W.Weber, A.Steiner, F.M.Schuurmans, Proc.3rd World Conf. And Exhibition on Photovoltaic Solar Energy Conversion (2000)

Isolated N and N pairs in silicon

J.L. McAfee and S.K. Estreicher

Physics Department, Texas Tech University, Lubbock, TX 79409-1051

ABSTRACT

First-principles molecular-dynamics simulations are used to study the configurations, binding energies, and electronic structures of isolated N and N pairs in Si. All the N-related local vibrational modes are predicted.

INTRODUCTION

Nitrogen-related defects in Si have not been studied as extensively as many other light impurities, probably because the semiconductor industry has been avoiding this impurity for decades. This has changed, and crystal growers now often add nitrogen to the ambient. This results in material with better mechanical strength and lower densities of grown-in defects, but also in N-related defect centers. In PV materials, thin nitrogen layers often serve as anti-reflection coatings. These layers, grown by exposure to an ammonia plasma, are hydrogen rich. The layer then serves as a source of H for bulk passivation during later anneals. Little information of microscopic nature is available about the details of the interactions taking place and about the role of N. An ongoing collaboration involves microscopic experimental studies (mostly based on Fourier-Transform Infrared Absorption (FTIR) spectroscopy) and first-principles calculations. The first step for theory is to identify the defects associated with the ingredients present, namely H, N, and native defects. Further, C will have to be considered as well, as it is often the most abundant impurity in the host crystal (passivation tends to be much less efficient in O-rich material).

Systematic studies must start with the identification of all the possible stable structures of isolated interstitial nitrogen (N_i), N-vacancy interactions leading to substitutional nitrogen ($\{N,V\}=N_s$), N-N pairs including two interstitials ($\{N,N\}_i$), the interstitial-substitutional pair ($\{N,N,V\}=\{N_2,V\}$), and the substitutional-substitutional pair ($\{N,V,N,V\}=\{N_2,V_2\}$). These defects are discussed below, but some results are still preliminary. In addition to the lowest-energy configurations and the binding energies, the electronic structures are obtained as well as all the N-related local vibrational modes (LVMs) which are critical to the identification of the defects by FTIR. Ongoing research focuses on the interactions between these defects and hydrogen, as well as the relevant dynamics.

In this work, first-principles molecular-dynamics (MD) simulations in periodic 64- and 128-host atoms cells are used within the SIESTA package.[1] The electronic problem is solved within self-consistent local density-functional theory. The exchange-correlation potential is that of Ceperley-Alder[2] as parameterized by Perdew and Zunger.[3] *Ab-initio* pseudopotentials in the Kleinman-Bylander[4] form are used. The basis sets consist of numerical linear combinations of atomic orbitals ranging from single-zeta (SZ) to double-zeta with polarization functions (DZP). The k -point sampling is limited to $k=0$ for dynamic runs and extended to a $2\times 2\times 2$ Monkhorst-Pack[5] mesh for static calculations. The vibrational frequency analysis is carried out within linear response theory.[6] This method allows the entire dynamical matrix to be extracted from derivatives of the density matrix relative to atomic coordinates. No atom needs to be physically displaced in order to calculate the frequencies.

ISOLATED NITROGEN IN SILICON

Systematic geometry optimizations of a range of plausible configurations for N_i in Si resulted in the identification of only one stable structure, shown in Fig.1 (left). N_i binds to three Si atoms, forming a split-<100> structure with almost identical N-Si bond lengths: 1.77, 1.78 and 1.79 Å, respectively. In the 64-cell, the split is not exactly along <100> but makes a 15° angle toward <110>. This could be a consequence of the small cell size, and we are checking the result in a larger cell. Were the split exactly along <110>, the symmetry of the defect would be C_{2v} . The tetrahedral (T) or hexagonal (H) interstitial sites are not local minima of the energy, and neither are the bond-centered site or the split <110> configuration. Two LVMs are associated with this defect, a Si-N stretch at 873 cm⁻¹ and a wag mode at 725 cm⁻¹ (see Table 1). We have not yet determined the activation energy for diffusion or the diffusion path of N_i .

If N_i encounters a pre-existing vacancy, it becomes N_s with an energy gain of 2.64 eV. This binding energy is substantially smaller than the vacancy formation energy (~4 eV [7]), which means that N_i will not displace a host atom to become substitutional. N_s has C_{3v} symmetry (Fig.1, right). Nitrogen moves away from the center of the vacancy along a trigonal axis by 0.73 Å and its three Si nearest neighbors (NNs) are displaced in such a way the N is almost trigonal and planar ($\sim sp^2$). The 4th and 5th electrons sit in the $2p_z$ lone pair which points toward the center of the vacancy. The A_1 mode at 504 cm⁻¹ has N_s moving up/down the trigonal axis and the degenerate E modes at 664 cm⁻¹ are N wag modes perpendicular to it (see Table 1). The fourth Si NN to the vacancy has a single electron in a dangling bond, which strongly suggests that it is a trap for an electron or hole. It is also a very likely trap for H. At present, we only considered the neutral charge states of all the defects.

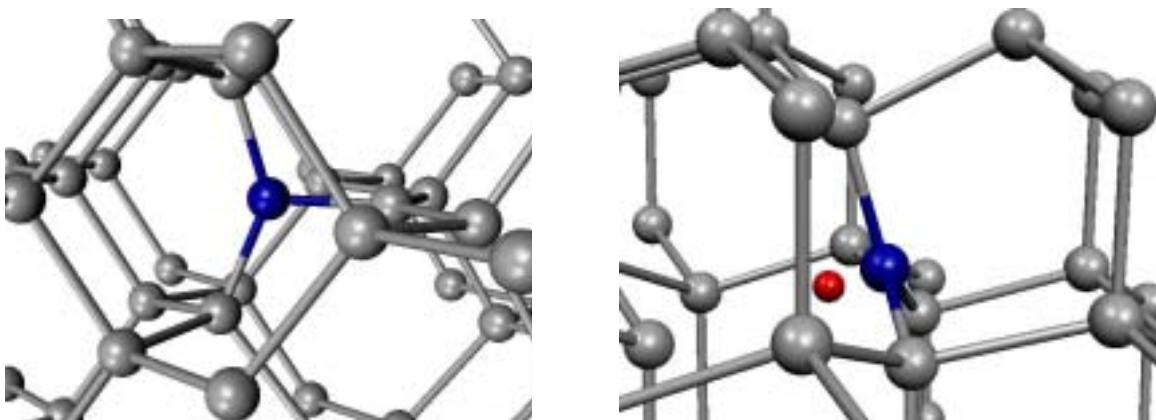


Fig.1: Lowest-energy configuration for N_i (left) and N_s (right) obtained in the 64-cell (Gamma point) with a DZ basis set on N and DZP on the Si atoms. The small ball shows the perfect substitutional site.

NITROGEN PAIRS IN SILICON

A total of seven N-N dimers were studied and three stable structures identified. The interstitial-interstitial pairs investigated include the interstitial N₂ molecule at the H site and at the T site, the structure proposed by Stein[8] which consists of two Ns at adjacent puckered bond-centered (BC) sites, and the D_{2h} configuration proposed by Jones[9] (it is shown in Fig.2, left). The latter is the most stable configuration. The N₂ molecule at the T site is 4.63 eV higher and the N₂ molecule at the H site dissociates into two N's at adjacent T sites which is 4.90 eV above the stable N_i . Finally, the Stein

structure is also metastable by 4.24eV. Therefore, we find that only one interstitial {N,N} pair is stable. We will refer to it as the {N,N}_i pair. The associated LVMs are listed in Table 1. Two FTIR lines[9] associated with this complex are very close to our predicted values.

The interactions of {N,N}_i with V or of N_s with N_i lead to the formation of the {N₂,V} complex (Fig.2, center). The former reaction releases 0.67eV and the latter 0.90eV. The symmetry of {N₂,V} is C_{2v} and its LVMs are given in Table 1. The N-Si and N-N bond lengths are 1.82Å and 1.46Å, respectively.

Finally, {N₂,V₂} results from the reactions {N₂,V}+V or {N,N}_i+V₂, since {N,V} is very unlikely to be mobile. The energetics are: {N₂,V}+V→{N₂,V₂}+2.86eV and {N,N}_i+V₂→{N₂,V₂}+3.79eV. The {N₂,V₂} complex looks very much like two adjacent N_s structures, and there is no overlap between the two N atoms.

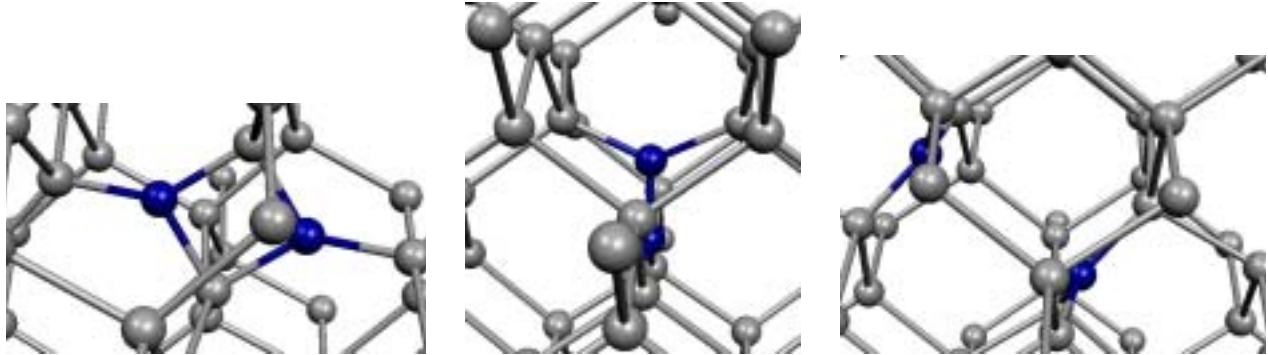


Fig.2: Lowest-energy configuration of the {N,N}_i (left), {N₂,V} (center), and {N₂,V₂} (right) complexes obtained in the 64-cell (Gamma point) with a DZ basis set on N and DZP on the Si atoms.

DISCUSSION

Isolated N and {N,N} pairs form relatively simple defects in Si. A single configuration exists for N_i (the split-<100>), N_s (a trigonal center with a Si dangling bond), {N,N}_i (Fig.2, left) {N_s,N_i}={N₂,V} (Fig. 2, center), and {N_s,N_s}={N₂,V₂} (Fig. 2, right), respectively. All these complexes have characteristic LVMs, but only those of N_s (one mode) and {N,N}_i (two modes) have been identified experimentally so far. For those three modes, our predictions are all very close to the measured values (Table 1). Ongoing work deals with formation energies and with the interactions between these centers and interstitial hydrogen.

complex	mode	this work (cm^{-1})	<u>Others (cm^{-1}) [9]</u>	<u>observed [9]</u>
N _i	n/a	873		
	n/a	725		
N _s	<i>E</i>	664	677	653[10]
	<i>A_I</i>	504		
{N,N} _i	<i>A_g</i>	1036	933	
	<i>B_u</i>	934	919	962.1
	<i>A_g</i>	705	769	
	<i>B_u</i>	730	689	765.6
{N ₂ ,V}	<i>A_I</i>	875	975	
	<i>E</i>	773	580	
	<i>B₂</i>	577	n/a	
{N ₂ ,V ₂ }	<i>E_u</i>	670		
	<i>E_g</i>	664		

Table 1: Calculated and measured (when available) LVMs for N-related complexes in Si.

ACKNOWLEDGEMENTS

The work of SKE is supported in part by a contract from NREL, a grant from the Welch Foundation, and a research award from the Humboldt Foundation. Many thanks are due to Texas Tech's High Performance Computing Center for generous amounts of computing time.

REFERENCES

1. D. Sánchez-Portal, P. Ordejón, E. Artacho, J.M. Soler, Int. J. Quant. Chem. **65**, 453 (1997); E. Artacho, D. Sánchez-Portal, P. Ordejón, A. García, J.M. Soler, Phys. Stat. Sol. (b) **215**, 809 (1999).
2. D.M. Ceperley and B.J. Adler, Phys. Rev. Lett. **45**, 566 (1980).
3. S. Perdew and A. Zunger, Phys. Rev. B **32**, 5048 (1981).
4. L. Kleinman and D.M. Bylander, Phys. Rev. Lett. **48**, 1425 (1982).
5. H.J. Monkhorst and J.D. Pack, Phys. Rev. B **13**, 5188 (1976).
6. J.M. Pruneda, S.K. Streicher, J. Junquera, J. Ferrer, P. Ordejón, Phys. Rev. B **65**, 075210 (2002)
7. See e.g., J.L. Hastings, S.K. Streicher, and P.A. Fedders, Phys. Rev. B **56**, 10215 (1997).
8. H.J. Stein, MRS Proc. **59**, 523 (1986).
9. R. Jones, S. Öberg, F. Berg Rasmussen, and B. Bech Nielsen, Phys. Rev. Lett. **72**, 1882 (1994).
10. H.J. Stein, Appl. Phys. Lett. **47**, 1339 (1985).

Theory of Copper Impurities in Silicon
D. West and S. K Estreicher

(Please contact S. K. Estreicher for copy of this paper)

HOT WIRE CHEMICAL VAPOR DEPOSITION OF SILICON NITRIDE FILMS FOR CRYSTALLINE SILICON CELL EMITTER PASSIVATION

J. K. Holt^a, M. Swiatek^a, D. G. Goodwin^a, A. M. Gabor^b, and Harry A. Atwater^a

^aDepartment of Applied Physics, California Institute of Technology, Pasadena, CA 91125

^bEvergreen Solar, 259 Cedar Hill Street, Marlboro, MA 01752

ABSTRACT

The stoichiometry and hydrogen content of hot-wire-grown silicon nitride was examined as a function of SiH₄/NH₃ flow ratio. The effect of post-deposition hydrogenation treatment on overall film hydrogen content was determined. The hydrogen release properties in Si-rich and N-rich nitride layers were characterized by annealing treatments. Hot-wire nitride layers were deposited onto diffused emitter String Ribbon silicon substrates, producing cells with comparable J_{SC}, V_OC, FF, and efficiency to those fabricated using plasma CVD nitride layers.

INTRODUCTION

Silicon nitride acts as an effective anti-reflection (AR) coating for solar cells due to its high refractive index, tunable in the range from 1.8-2.5. These films may also serve as passivation coatings for surface and bulk defects in the underlying silicon, due to the large fraction of hydrogen that may be incorporated (up to 25 atomic %).¹ The conventional means for depositing silicon nitride films uses plasma enhanced chemical vapor deposition (PECVD). Another promising technique for low temperature SiN_x growth is hot-wire CVD (HWCVD), also known as catalytic CVD (Cat-CVD).² As compared with PECVD, HWCVD offers the advantages of high deposition rate,³ as the process can take place at pressures higher than those at which a plasma can be sustained. In addition, it has been demonstrated that the process is compatible with large area deposition by careful design of gas delivery and filament geometry.⁴ The deposition of high hydrogen content nitride films by HWCVD for photovoltaic applications has been recently demonstrated.^{5,6}

EXPERIMENT

The system used in the deposition of SiN_x is a high vacuum chamber with a base pressure of order 10⁻⁹ Torr. Source gases, consisting of SiH₄ (diluted to 1% in He) and NH₃ are introduced through a gas inlet and decomposed on a W wire (0.5 mm dia, 12 cm length, 1800°C temperature). Flow rates of the various gases range from 4-48 sccm, with SiH₄/NH₃ ratios ranging from 1-8%, and pressures in the range of 20-100 mTorr (higher pressures are possible, but were not explored in this study). Under these conditions, growth rates range from 16-52 Å/min, limited largely by the use of dilute SiH₄; rates of up to 0.14 µm/min have been demonstrated with the use of pure SiH₄ and NH₃ ambients.⁶ A substrate heater is located approximately 5 cm from the wire, and a shutter is used to protect substrates from the evaporation of impurities from the wire during its initial heating; growth temperatures were approximately 300°C for this study. The substrates used were lightly-doped p-type (350 Ω-cm), double-side polished, float-zone Si.

RESULTS

A series of different SiH_4/NH_3 flow ratios (FR) were used to examine the effects on film properties. The films to be described were grown at a substrate temperature of 300°C for a period of 40 min, with a wire temperature of 1800°C and a total pressure of 100 mTorr. Fig. 1 provides the Fourier Transform Infrared (FTIR) transmission spectra for a series of four SiN_x films grown under SiH_4/NH_3 flow ratios of 1, 2, 4, and 8%. The most prominent feature in the transmission spectrum is the Si-N absorption around 860 cm^{-1} . Also evident from Fig. 1 is that the majority of H is bound to N for the 1, 2, and 4% flow ratios, while at 8%, H is mostly bound to Si. The refractive index, as determined by single wavelength (633 nm) ellipsometry, increases from 1.8 up to 2.5, with the 4% flow ratio film being the closest to stoichiometric silicon nitride ($n = 2.0$). To complement these FTIR measurements, Rutherford Backscattering (RBS) and Hydrogen Forward Scattering (HFS) measurements were made to determine the stoichiometry and hydrogen content of a select number of SiN_x films. The films chosen for analysis were the 1% and 8% flow ratio films, in addition to two films grown at a flow ratio of 6% (all other conditions identical)[†], one of which was subjected to a post-deposition H_2 treatment. The post-deposition H_2 treatment was carried out under conditions identical to SiN_x deposition, but with the replacement of SiH_4 and NH_3 with H_2 at the same 100 mTorr total pressure. Table 1 provides a summary of the RBS and HFS film analysis. As expected, an increase in the Si/N ratio in the film was observed as the SiH_4/NH_3 flow ratio increased. All values are greater than the value of 0.75 expected of stoichiometric silicon nitride, although the value of ~1 obtained with FR = 1% is attributed to the presence of SiO_2 . There is a slight decrease in the Si/N ratio after the post-deposition H_2 treatment, suggesting an etching effect of H on the Si of these Si-rich nitride layers. Also revealed by HFS is an increase in the overall atomic percentage of H as the flow ratio (or Si/N) increases, supporting the idea that SiH_4 is the primary source of this H at these flow ratios. It is noteworthy that the 1% film contains a large percentage of oxygen (23%), while it is absent in films grown at higher flow ratios. This has been attributed to post-deposition absorption of water by the nitride film.⁷

For applications where hydrogenated SiN_x is to be used as a passivation coating, the mobility of bound hydrogen is critical as it is thought that the degree of passivation (as measured in minority carrier lifetime) depends the amount of hydrogen released from the SiN_x film.⁸ As a means to study hydrogen release from SiN_x , two of the films described previously were chosen. In order to observe the effects of H release from N versus Si, the 2% and 8% flow ratio films were selected. Each film was annealed for 5 minutes at temperatures of 400°C, 600°C, and 800°C. Between each anneal, the sample was allowed to cool to room temperature, after which FTIR measurements were made to monitor to release of H from the SiN_x film. Fig. 2 shows the FTIR spectra at the various annealing temperatures for the 8% (Si-rich) film, along with an estimate of the H concentration, determined by the use of absorption cross sections.¹ This figure reveals only a slight reduction in the H bound to Si up to 600°C, with a total reduction of 80% after the 800°C anneal. For the 2% (N-rich) film, a steady reduction in the H bonded to N is seen as the anneal temperature is increased, with an overall reduction of 70% after the 800°C anneal. This

[†]FTIR analysis of the 6% flow ratio films revealed that H was bonded predominantly to Si, as in the 8% case.

difference in hydrogen release kinetics can have important implications for the choice of annealing treatments (temperature, time).

To evaluate the quality of hot-wire-deposited silicon nitride layers relative to their plasma CVD counterparts, films were deposited onto String Ribbon substrates provided by *Evergreen Solar* (Marlboro, MA). Film growth conditions were 3% SiH₄/NH₃ at a total pressure of 70 mTorr for a growth period of 1 hour. The hydrogen content was estimated to be, at minimum, 10 at.% by comparison with previously grown films. The samples were p-type (resistivity of 3 Ω-cm), with a thin phosphorous-diffused n-type layer on top. Due to the large area of the substrates (15 cm x 8 cm), a filament array had to be used to improve thickness uniformity. It has been observed⁴ that if the filament spacing is at most half the filament-to-substrate distance, then non-uniformity associated with the filament array is eliminated. With this design criterion in mind, the filaments were spaced 2 cm apart, with a wire-to-substrate separation of 5 cm. Samples grown using this wire array exhibited a thickness variation of approximately 150 Å from the center to edge.

Three nitride samples with an average center thickness of 830 Å were chosen for subsequent processing by *Evergreen Solar*. The nitrided samples had a thick aluminum layer deposited on back by a screen-printing process using a commercially available aluminum paste. The samples were then annealed in a belt furnace to form the back contact as well as release H from the nitride layer. Upon fabricating front contacts, the cell's electrical properties were measured. Table 2 provides the short circuit current density (J_{SC}), open circuit voltage (V_OC), fill-factor (FF), and efficiency (η) for a representative hot-wire (HW) nitride cell versus a similarly processed plasma nitride cell produced by *Evergreen*. The hot-wire nitride cell is comparable in electrical properties (with the exception of J_{SC}) to the plasma nitride cell. Further improvements in J_{SC} might be expected with the use of more uniform nitride coatings.

CONCLUSIONS

Varying the SiH₄/NH₃ ratio from 1-8% produced silicon nitride films ranging in refractive index from 1.8-2.5, with hydrogen content ranging from 9-18 atomic %. Transmission measurements using FTIR revealed a transition in the bonding of H (N-H to Si-H) as the flow ratio was increased beyond 6% SiH₄/NH₃. As this ratio was increased, the overall H-content increased in the film, suggesting that SiH₄ is the primary source of H under these conditions. A film deposited with a low flow ratio of 1% revealed a prominent Si-O-Si feature, suggesting oxidation. This result was further confirmed with RBS, indicating 23 atomic % oxygen incorporation in the film. Annealing studies revealed different kinetics for H release from Si versus N, important in the selection of an appropriate annealing treatment. String Ribbon silicon cells produced with hot-wire-grown silicon nitride layers show comparable electrical properties to those produced with plasma nitride layers.

REFERENCES

- [1] W. Lanford and M. Rand, *J. Appl. Phys.* **49**, 2473 (1978).
- [2] H. Matsumura, *Jpn. J. Appl. Phys.* **37**, 3175 (1998).
- [3] B. Nelson, E. Iwaniczko, A. Mahan, Q. Wang, Y. Xu, R. Crandall, and H. Branz, *Thin Solid Films* **395**, 292 (2001).

- [4] A. Ledermann, U. Weber, C. Mukherjee, and B. Schroeder, *Thin Solid Films* **395**, 61 (2001).
[5] J. Holt, M. Swiatek, D. Goodwin, and H. Atwater, *Mat. Res. Soc. Symp. Proc.* **715**, A10.2.1 (2002).
[6] J. Moschner, J. Schmidt, and R. Hezel, *29th IEEE Photovoltaic Specialists Conference Proceedings*, New Orleans (2002).
[7] B. Stannowski, M. van Veen, and R. Schropp, *Mat. Res. Soc. Symp. Proc.* **664**, A17.3.1 (2001).
[8] V. Yelundur, A. Rohatgi, A. Ebong, A. Gabor, J. Hanoka, and R. Wallace, *J. Elect. Matl.* **30**, 526 (2001).

Table 1. Summary and comparison of RBS and HFS film analysis.

FR	t (nm)	n	Si/N [RBS]	[H] at.% [HFS]	atomic density [RBS] (at/cc)	oxygen content (at.%)
1%	62	1.8	0.99	9.3	8.2×10^{22}	23%
6%	209	2.2	1.3	16	7.5×10^{22}	0%
6% + H ₂	185	2.1	1.1	16	8.4×10^{22}	0%
8%	129	2.5	2.2	18	6.2×10^{22}	0%

Table 2. Comparison of electrical properties for hot-wire versus plasma nitride cells.

cell type	J _{SC} (mA/cm ²)	V _{OC} (mV)	FF	η (%)
HW nitride	29.99	579	0.712	12.4
Plasma nitride	30.92	584	0.709	12.8

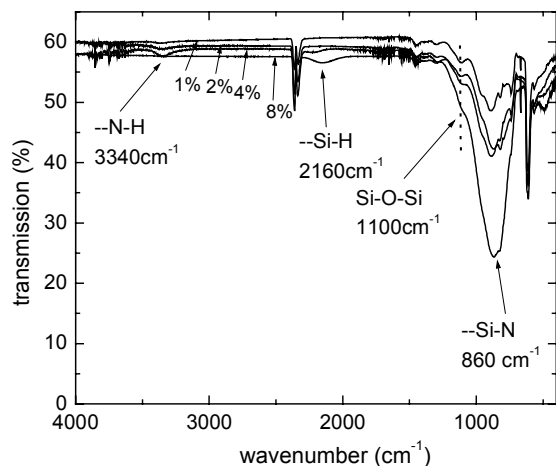


Fig. 1. FTIR transmission spectra of films grown under different SiH₄/NH₃ flow ratios (indicated in %).

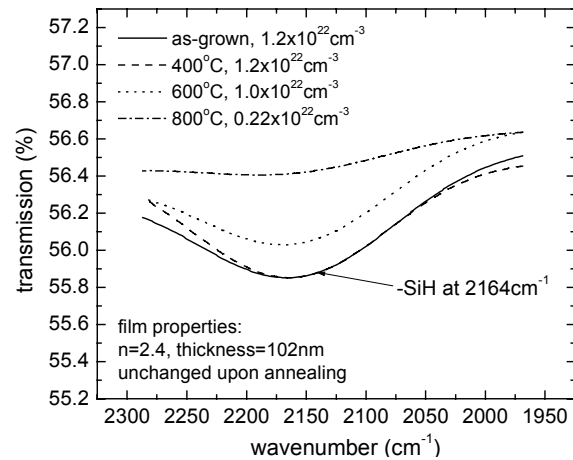


Fig. 2. FTIR spectrum at various annealing temperatures (5 minute anneal at each temperature) for a film grown with 8% SiH₄ in NH₃; corresponding hydrogen concentrations at each temperature are listed.

New method of solar grade silicon production

V.V. Zadde, A.B. Pinov, D.S. Strebkov

INTERSOLARCenter, 2, 1-st Veshnaykovsky proezd, 109456, Moscow, Russia.

Tel. (+7095) 171-19-20, fax: (+7095) 171-96-70

E.P. Belov, N.K. Efimov, E. N. Lebedev, E.I. Korobkov

SRC RF GNICHTEOS, 38, sh. Entuziastov, Moscow, 111123, Russia

D. Blake, K. Touryan

National Renewable Energy Laboratory (NREL), Denver, USA

1. Introduction

One of the main advantages of photovoltaic solar cells (PVC) is their ecological clarity of direct conversion of solar energy to electricity. For wide spreading of PV technologies it is necessary to ensure that there is no environment pollution at the stage of PVC-s manufacturing, beginning from producing of polysilicon feedstock [1].

The objective of this project is creation of ecologically clean method for production of solar grade polysilicon feedstock (SGPF) as raw material for PVCs, and also raw material for producing monocrystalline silicon, which is used in electronic industry.

Semiconducting silicon made from polycrystalline silicon is base material for electronic and electrotechnical industry, which produce millions discrete and integral devices, microprocessors. More than 80% of computing, radio-, video-, robotics, telecommunication, controlling automatisation and PV and other equipment are manufactured with use of monocrystalline silicon.

World production of PVC-s reached 300 MW in 2001. From this amount about 80% is produced from polycrystalline silicon. To produce 1 MW of PVCs using modern technologies it is required 13 tons of SGPF [2]. According to more optimistic prognoses, this amount will decrease to 10 tons per 1 MW produced. For PVCs polycrystalline silicon with less purity, than for electronic industry, so named scrap. Usually, scrap is not more than 10% of electronic grade polycrystalline silicon. During last years, growth of world production of PVCs was bigger than production of scrap, therefore world reserves of scrap is almost depleted and it is necessary to create new way for production of solar grade SGPF.

Forecast for demand and delivery of polycrystalline silicon on world market is presented at fig.1 [3]. You can see that delivery of SGPF will be less than demand within next 10 years. Annual world demand in SGPF in 2010 can be 16-32 thousand tons; at the same time the delivery will be only 8 thousand tons.

To produce such amount of solar grade SGPF with cost less than 20 USD per kg new approaches are required, which ensure less energy consumption and higher ecological cleanliness comparing to conventional methods.

Main obstacle for mass production of PVCs is high cost of SGPF. If the cost will decrease in several times, the cost of PVCs could decrease twice as less up to 1 USD per watt peak. In this case cost from PV stations will be competitive with cost of energy produced by conventional methods.

In [4] it is noted that silicon can be “oil of 21 century”, because 1 kg of polycrystalline silicon used in filmed α -Si PVCs can produce during its lifetime the same amount of energy that can be produced from 100 tons of oil. However, this example is not typical for polycrystalline PVCs, because in α -Si PV cells the silicon film with thickness 1 μm is insignificant part from total thickness of the cell, which consists mainly from stainless steel and glass. Modern PVCs from crystalline silicon have thickness \sim 350 μm . At this thickness and efficiency 15%, to produce 1 MW of solar cells it is required 13 tons of polycrystalline silicon (or 1 kg for 100 W module). If

accept average number of peak-hours during a day equal 5, then during a year it will produce ~182 kWh, and during 30 years – 5475 kWh of energy. At electricity price 0.1 USD per kWh, the cost of energy produced will be 547.5 USD; for these money ~1.5 tons of petroleum can be bought. Let's assume that 1 kg of oil produces 9 kWh of heat and efficiency of conversion it to electricity is 30%. Then, to produce 5475 kWh of electricity about 2 tons of oil will be required; the same amount of energy can be produced by 1 kg of SGPF used for manufacturing of PVCs. Market price of solar modules is now ~3.5 USD/W, thus 100 W module price is 350 USD and pay-back period is about 19 years. Thus, already today the increase of solar cells production is economically expedient. Forecasted decrease of PV cells and modules price will decrease payback period to 10 years.

2. Known methods of pure silicon producing.

There are 2 SGPF producing methods dominated:

- with use of hydrogenous reduction of trichlorsilane SiHCl_3 , named “Siemens-process [5], and
- disproportionation for producing of monosilane SiH_4 , developed by Union Carbide Co.[6]

In the world about 80% of polycrystalline silicon is produced using first method and 20% using second method. Block-schemes of these processes are presented at fig. 2 and 3.

In the Siemens process the SiHCl_3 is produced in boiling bed reactor as results of exothermal interaction of powdered metallurgical silicon with HCl. The vapor-gas mixture obtained is separated through filtration and condensation, and HCl and H_2 are recycled. The condensate is separated and SiHCl_3 is purified through multilevel rectification. Purified SiHCl_3 mixed with H_2 is directed to rod reactor for producing SGPF, where only 30% of SiHCl_3 is converted to SGPF. Main amount of SiHCl_3 remains in balanced mixture and along with other matters is removed from the reactor. Further this mixture is separated cryogenically and products of separation are directed to recycle. This process is complex, energy consuming and ecologically dangerous.

SGPF production process developed by “Union Carbide Co” started from hydrochlorination of metallurgical silicon in boiled bed reactor. Only silicon is spent, and SiCl_4 from all stages of the process is returned to hydrochlorination, ensuring maximal return of Si and Cl into the process. After separation of H_2 , SiHCl_3 is multi-rectified and directed to disproportionation , where SiH_4 is obtained. The SGPF is obtained through pyrolysis of SiH_4 at temperature 800°C in rod reactor with special design.

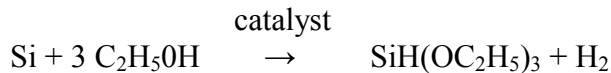
Disadvantages of this method are conducting the process in chemically aggressive media at high pressure and temperature, which require costly equipment made from heat-resistant and chemically inert materials. The presence of chemically aggressive Cl compounds leads to transfer of admixtures from the equipment walls (sides) to monosilane and create ecological danger.

In former USSR, beginning from 1983, the main method of producing of high purity SiH_4 , and then SGPF, was catalytical disproportionation of triethoxysilane $\text{SiH}(\text{OC}_2\text{H}_5)_3$ [7]. Block-scheme of used technological process presented at fig. 4. Raw material for producing of $\text{SiH}(\text{OC}_2\text{H}_5)_3$ were SiHCl_3 and dehydrated ethanol. The process of synthesis of $\text{SiH}(\text{OC}_2\text{H}_5)_3$ and desorption of HCl is implemented in film type apparatus. This method was realized in “Kremni polimer” plant in Zaporozhie city (Ukraine) and production volume of SiH_4 was 12,6 t per year. From the monosilane was produced SGPF through pyrolysis, and then high-resistant monocrystals for nuclear particles detectors and IR-receivers were produced by float zone technique.

Disadvantage of this method are: high consumption of ethanol, big amount of wastes, use of energy consuming method of monosilane rectification at liquid nitrogen temperature and use of ecologically dangerous Cl-containing materials.

3. Main features if the new method.

In the new alcoxysilane method of SGSF production the technology existed in the plant “Krasny polimer” was partially used. The block-sheme of the method of producing of SGPF through monosilane is presented on fig.5.. At the first stage as raw material powdered metallurgical silicon and dehydrated ethyl alcohol is used instead of trichlorsilane.

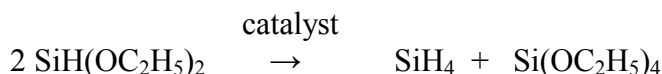


It is noted, that purity degree of powdered metallurgical silicon has no such importance as in case of synthesis of trichlorsilane, thus less expensive silicon with purity 98% can be used. The reaction is conducted in high-boiled silocsan liquid at presence of Cu-based catalyst at atmospheric pressure and temperature not less than 180°C. At low pressure not reacted alcohol is removed, which prevents conversion of triethoxysilane to tetraethoxysilane. At optimal conditions 85-90% of $\text{SiH}(\text{OC}_2\text{H}_5)_3$ is obtained, and the rest is diethoxysilane.

At the second stage the triethoxysilane is converted into silane and tetraethoxysilane according reaction:



Small amount of produced diethoxysilane is converted into silane according to reaction:



Unlike to existing in “Kremni polimer” plant technology, at disproportionation of $\text{SiH}(\text{OC}_2\text{H}_5)_3$ stage better catalyst was used and also the process of purifying of monosilane was modified. This allowed to implement disproportionation at ambient temperature, increased equipment efficiency and reduced energy consumption. New method has stage of tetraethoxysilane hydrolysis; this allows to receive valuable by-products, and to return waterless alcohol to the stage of $\text{SiH}(\text{OC}_2\text{H}_5)_3$ synthesis. The waterless ethyl alcohol is obtained without additional reagents due to absorption of water by tetraethoxysilane. At this stage more than 95 % of ethyl alcohol is recycled and it is required to add only 5% of ethyl alcohol into the process.

The main advantage is absence of Cl in the process, eliminating the possibility of ingress of Cl-contained contamination to environment. Moreover, all stages of the silan purifying and pyrolysis are conducted at ambient temperature or at lower temperatures, down to temperature of the silan liquefaction; these reduce the risk when work with monosilane.

Every admixtures of elements of III-V group, which present in metallurgical silicon, are converted to saturated metalorganic compounds without link element-hydrogen and, thus, are not disproportionated with creation of volatile hydrids like dibonran, phosphine and arsine. In this case main polluting admixtures in monosilane are high-boiled ethoxysilanes. Ethoxysilanes and aother metalorganic compounds are removed at the next stage by adsorption of admixtures by liquid tetraethoxysilane cooled to -60°C. Final purity of monosilane 99,999% is reached by adsorption of tracking admixtures by activated charcoal and final purifying on chucks with chemisorbent. Such purifying guarantees content of carbon and oxygen at level less than 1.10^{15} at/sm³ and characterized by minimal energy consumption and material capacity. Big temperature difference between main substance and carbon-containing admixtures simplifies the purifying process at stages of ethoxysilane and monosilane purifying. In table boiling temperatures if these substances are presented.

Table.

Nº	Name of substance	Boiling temperature at pressure 1 atm
1	Carbon oxide	- 192
2	Carbon dioxide	- 78,6
3	Methan	- 161,5
4	Ethan	- 88,6
5	Ethylene	- 103,7
6	Ethyl alcohol	+ 78,5
7	Triethoxysilane	+ 131,5
8	Tetraethoxysilane	+ 168,5
9	Monosilane	- 112

For producing SGPF the monosilane is pyrolysed at 800-850°C; the process can be implemented in rod reactor or in reactor with “boiling” layer of seed silicon particles. In second case the pyrolysis process requires minimal energy at level 10 kWh/kg.

4. Characteristics of main and by-products

Main production for the new method of SGSF production are:

- Monosilane and monosilane mixtures with other gases,
- Electronic grade polycrystalline silicon,
- SGPF for PV industry.

The technological process allows to change assortment and shares of the products in total amount depending on market situation.

High quality of monosilane and SGPF are confirmed by measurements. The admixtures presence is at the level of sensitivity of modern instruments. Specific resistance of monocrystalline silicon samples produced by float zone technique is more than 10 000 Ω.sm, and life time of minority carriers is up to 1000 μs.

At the same time there is 24 kg of tetraethoxysilane per 1 kg of monosilane in the yield. To transform it to other useful materials several technologies were elaborated:

- As result of hydrolysis of tetraethoxysilane, silica sols are produced; they can be used as coupling agent at manufacturing transfer-molds, for textile and construction materials strengthening, for creation of composite and other new materials. After thermal treating of silica sols Si dioxide is obtained; it can be used for manufacturing of fibre-optic and quartz wares
- Through organomagnesium synthesis of tetraethoxysilane wide used silicone polymers are obtained
- By thermal-oxidation of tetraethoxysilane superfine silicon dioxide (white soot) is obtained; it is used as a filler material

5. Possibilities of perfection of the new method

At annual yield of silicon 10000 tons about 240000 tons of tetraethoxysilane will be produced; this is close to current world tetraethoxysilane annual production. Currently accepted tetraethoxysilane production scheme [9], presented on fig. 6, in many respects coincides with alcoxysilane technology of monosilane production. For creation of joint manufacture it is expedient to combine 2 schemes to one, which should be close to scheme presented on fig.5. To do this it is necessary to create conditions for maximal yield of di-and triethoxysilane during the first stage of alcoxysilation of silicon; in this case the main product will be silicon and materials produced from tetraethoxysilane.

At the initial stage of industrial scale use of this new technology at SGSF production volumes about 1000 tons annually, in the existing production of tetraethoxysilane only part of metallurgical silicon can be converted into triethoxysilane according to scheme presented on fig.7.

Another approach for the problem solving is selection of new catalysts and conditions of silicon and alcohol interaction ensuring increase of diethoxysilane yield and decrease of tetraethoxysilane amount in disproportionation reaction.

Part of tetraethoxysilane can be converted into triethoxysilane through hydration:



Realization of this method will allow to return the tetraethoxysilane into technological process for increasing of the monosilane yield.

Comparing to using of traditional catalysts, more effective can be implementation of plasma catalysis with use of nonequilibrium plasma generated by various types of electrical discharges.

Literature

1. Tsuo Y.S., Gee J.M., Menna P., Strebkov D.S., Pinov A., Zadde V. Environmentally benign silicon solar cell manufacturing. 2-nd World Conference and Exhibition on Photovoltaic Solar Energy Conversion, 6-10 July, Vienna, Austria, pp.1199-1204, 1998.
2. Bernreuter J., The Time Pressure is Enormous, Photon International, September, pp. 26-32, 2001.
3. Maurits J. Polycrystalline Silicon – World Demand and Supply. Eight Workshop on Crystalline Silicon Solar Cell Materials and Processes, NREL, Colorado, August, pp. 10-17, 1998.
4. Strebkov D.S., Zadde V., Pinov A., Touryan K., Murphy L., Crystalline Silicon Technologies in CIS Countries. 11th Workshop on Crystalline Silicon Solar Cell Materials and Processes, Colorado August, pp.199-207,2001.
5. O'Mara W.C., Herring R.B., Hunt I.P., Handbook of Semiconductor Silicon Technology, pp.33-77, Noyes Publications, Park Ridge, NJ (1990)
6. Union Carbide. Base Gas Condition for use Silane Process. Report DOE/JPL-954343-21, Nat. Tech. Inform. Center, Springfield, VA, 1981.
7. Kleschevnikova S.I., Dubrovskaya G.A., Rumyantseva E.I. Plastmassy, 1965, № 3, p. 14-16.
8. Strebkov D.S., , Pinov A. Zadde V., Tsuo Y.S., Touryan K., Murphy L., Gee J.M. Polysilicon production in the Commonwealth of Independent States. Eight Workshop on Crystalline Silicon Solar Cell Materials and Processes, NREL, Colorado, August, pp. 18-21, 1998.
9. Klein L.C., Woodman R.H., Key Engr. Mater., 115, pp. 109-124 (1996).

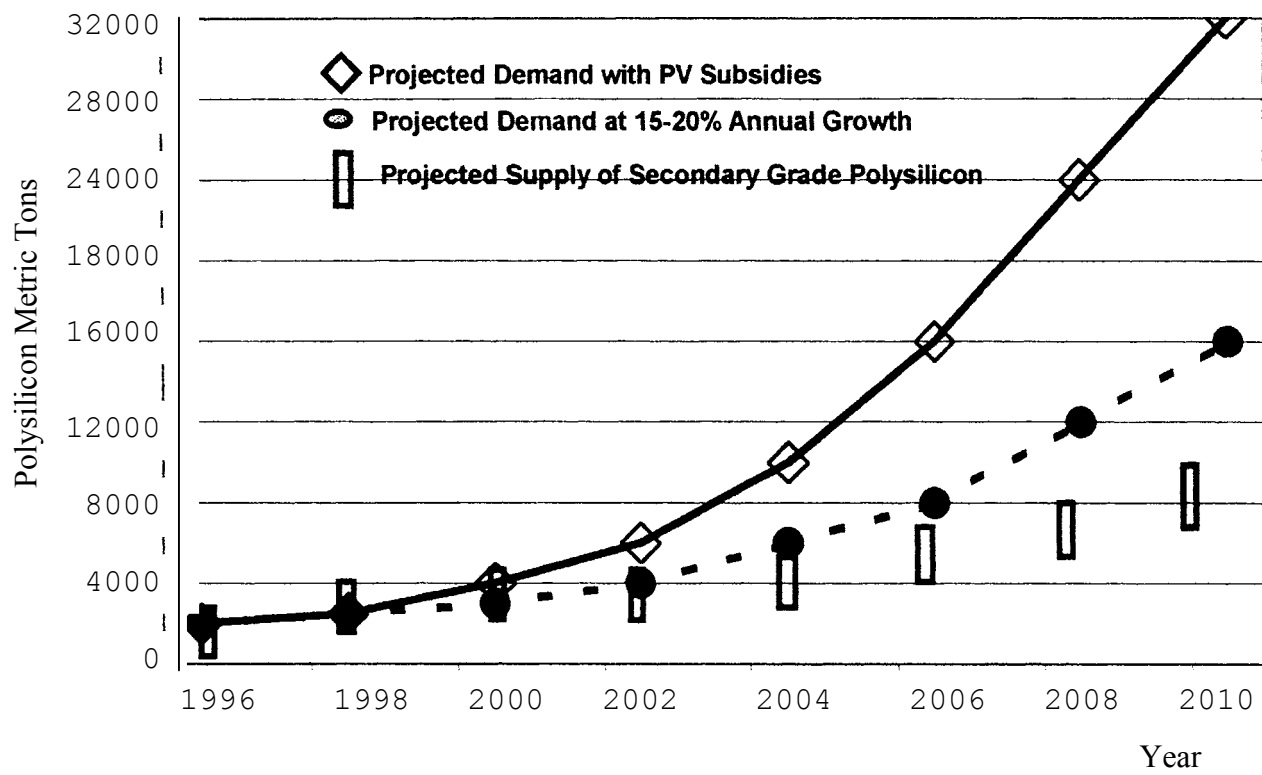


Figure 1. Forecasted PV Feedstock Demand and Secondary Polysilicon Supply in Metric Tons by Year.

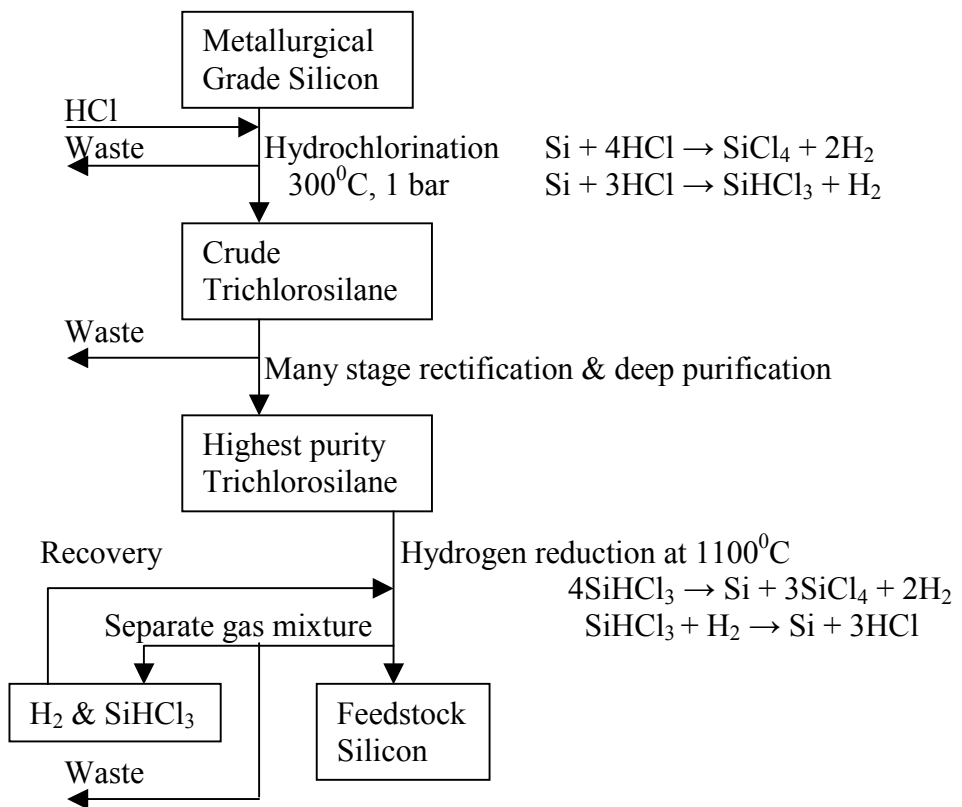


Figure 2. Schematic of semiconductor grade silicon produced (Siemens process).

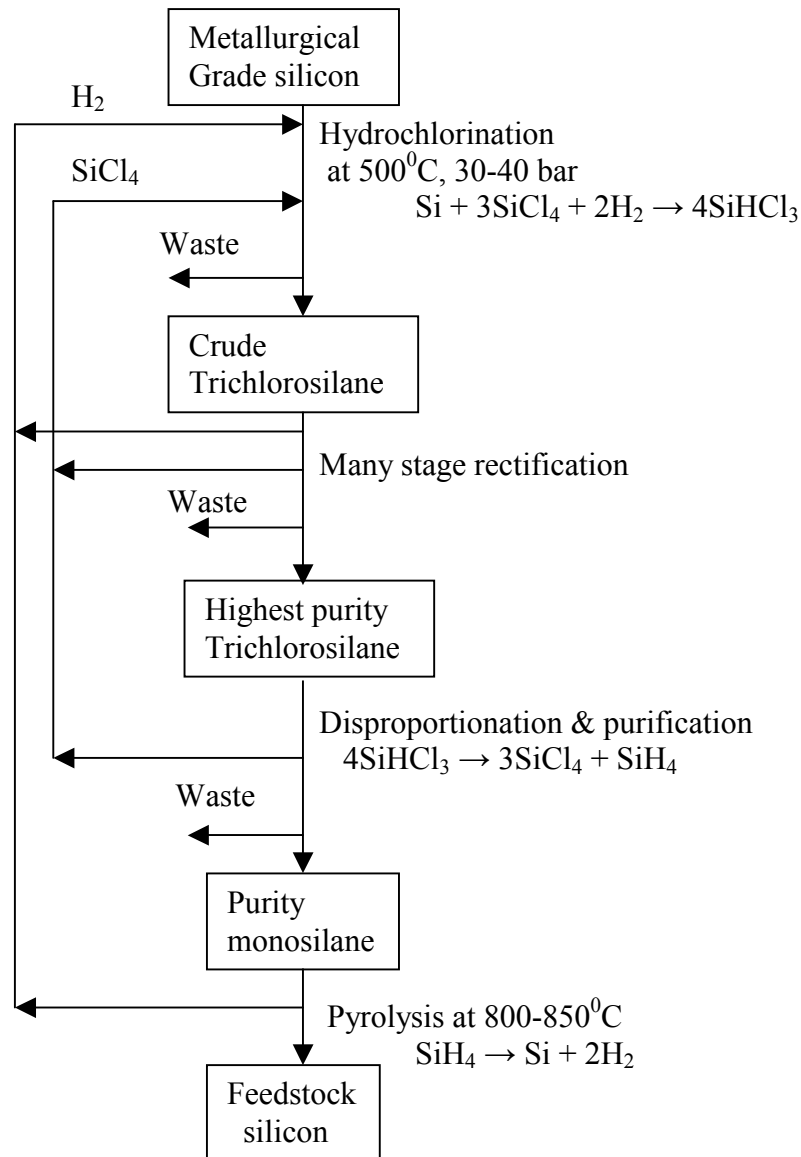


Figure 3. Schematic of semiconductor grade silicon produced (Union Carbide).

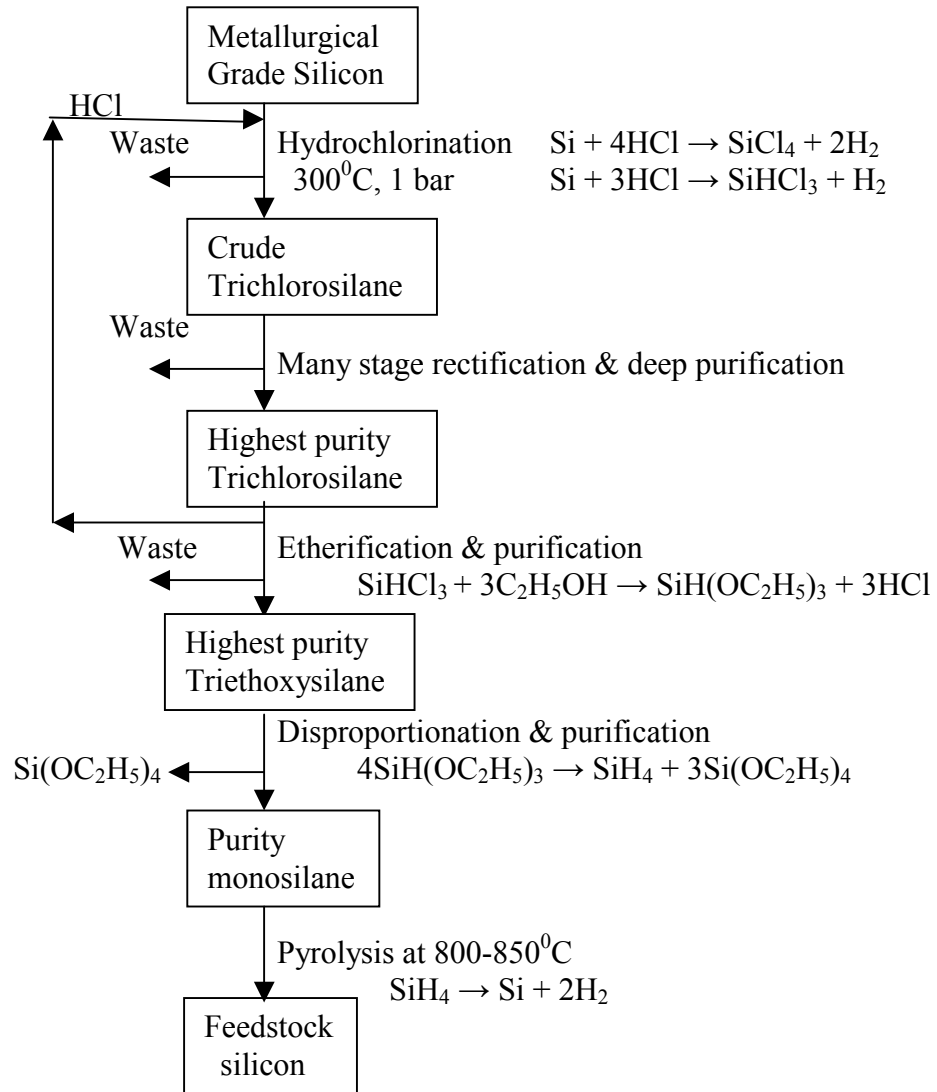


Figure 4. Schematic of semiconductor grade silicon produced through monosilane in former USSR.

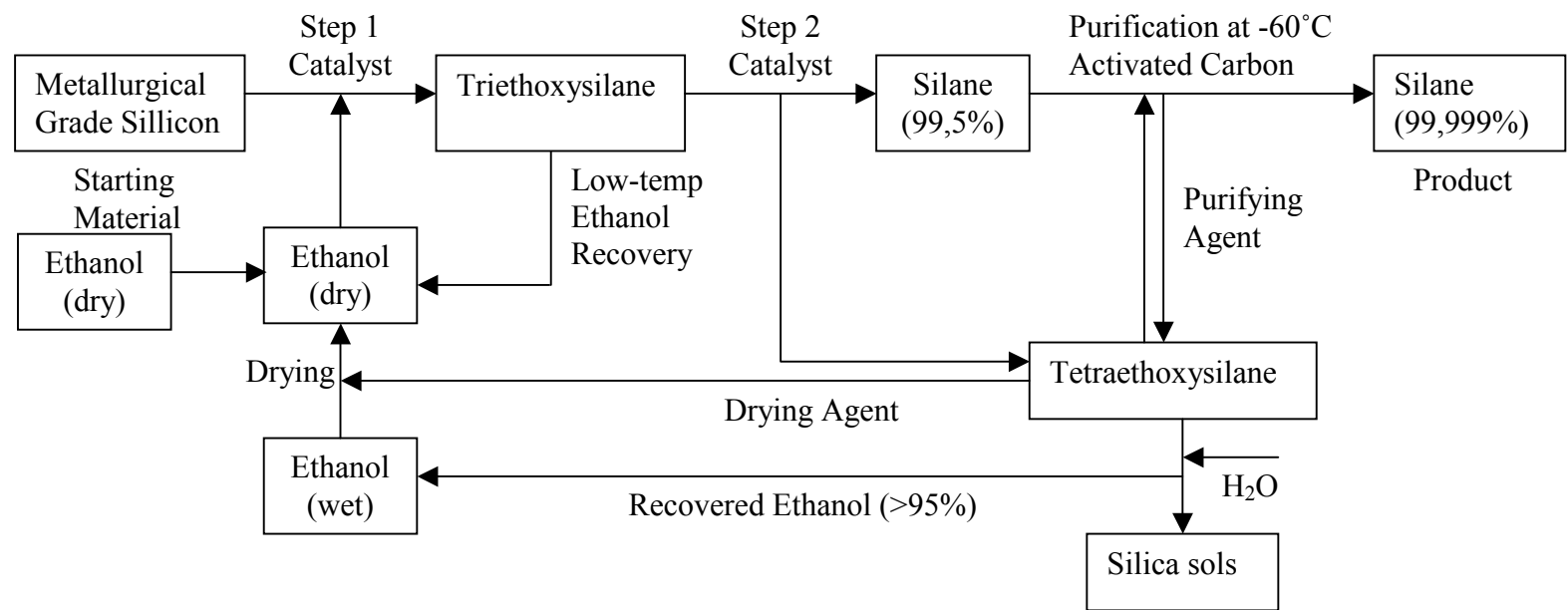


Figure 5. Scheme of new silane production process

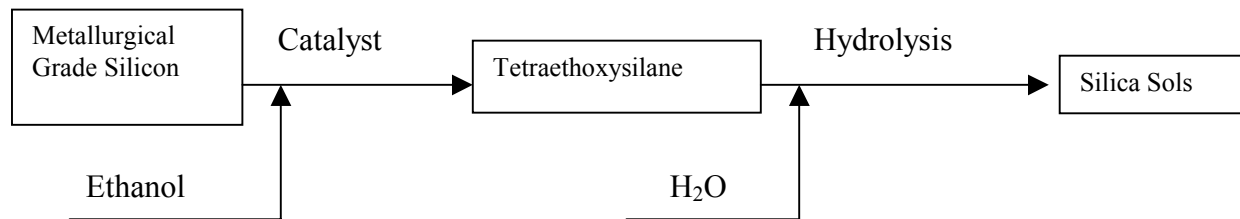


Figure 6. Existing Process for Production Silica Sols.

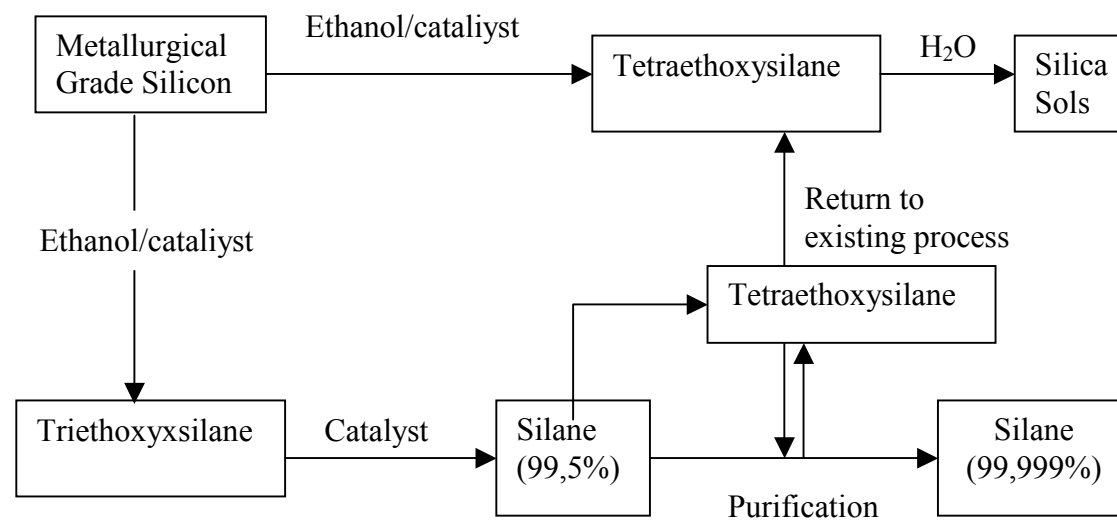


Figure 7. Schematic combined process for producing silane and silica sols.

A Luminescent Anti Reflective Coating

Stephen Nicoletti

Department of Applied Science, University of Arkansas at Little Rock
Little Rock, AR 72204

Robert Engelken

College of Engineering, Arkansas State University
Jonesboro, AR 72467

Roger M. Hawk

Department of Applied Science, University of Arkansas at Little Rock
Little Rock, AR 72204

Introduction

Due to its high refractive index, ZnS has been used as an anti-reflective coating for high efficiency solar cells. ZnS is also common to many inorganic phosphors[1]. It should therefore be possible to fabricate fluorescing anti-reflective coatings with a ZnS type phosphor. A fluorescing anti-reflective coating would evolve longer wavelengths from shorter wavelengths, possibly increasing photo current since[2]:

$$J_L \propto \int \lambda \phi(\lambda) d\lambda$$

We have shown that a ZnS type phosphor can be used to fabricate fluorescing anti-reflective coatings. However whether the luminescent coating increases or decreases photo generated current was not shown.

Method: Thin films of ZnS and ZnS:Cu,Al were resistively evaporated at 10^{-5} torr from a graphite crucible onto glass substrates at Arkansas State University (ASU). The evaporated films had a milky-brownish color on glass, perhaps due to preferentially evaporated trace Cu_xS which would inhibit luminescence. To check that the ZnS:Cu,Al films fluoresced, transmission through the glass substrate was analyzed with an Elmer Perkins Fluorescent Spectrometer model FS100. The results are shown in Figure 1 for a .64um thick film of ZnS:Cu,Al. Figure 2 shows the relative percent energy absorbed and emitted on the excitation and emission bands of ZnS:Cu,Al [3]. Comparison of Figure 1 and Figure 2 shows that the absorption and emission bands of the resistively deposited film correspond to the absorption and emission bands of the ZnS:Cu,Al proving that the resistively deposited films maintained fluorescence. Thin films of ZnS:Cu,Al were then resistively evaporated at 10^{-5} torr from a graphite crucible onto etched p-type silicon substrates at ASU. This was followed by PECVD deposition of 2.2um of SiO₂. 2.2um of SiO₂ was also deposited on etched p-type silicon substrates. An Ocean Optics model OOII spectrometer was used to measure the reflectance off samples of SiO₂ – p type Si (Figure 3) and SiO₂ – ZnS:Cu,Al – p type Si (Figure 4). The ripple in each figure is sequential constructive and destructive interference due to reflections at the two SiO₂ surfaces. Comparison of the two figures proves that the ZnS:Cu,Al is an effective ARC in the 550nm to 650nm range for the SiO₂ – Si interface.

A Gaertner L117 Manual Ellipsometer was used to measure the refractive index of the resistively deposited ZnS:Cu,Al. The refractive index was $2.39 \pm .15$, which is only slightly lower than the accepted value of ZnS refractive index for films in the .2um to .4um range[4]. It was assumed that ZnS and ZnS:Cu,Al have identical refractive indices at all wavelengths. A Perkin-Elmer Lambda 19 spectrophotometer was used at ASU to measure absorbance vs. wave length for sample 017 of ZnS and samples 019 and 022 of ZnS:Cu,Al. Ripple in the absorbance curves at longer wavelengths, due to consecutive constructive/destructive interference between the resistively deposited films and the glass substrate, was used to calculate the thickness [5] t of the ZnS film (t = .64um) and the ZnS:Cu,Al sample 019 (t = 1.33um) and ZnS:Cu,Al sample 022 (t = .37um). Absorption coefficient (α) vs. wavelength (λ) was obtained for the ZnS and ZnS:Cu,Al samples by dividing the thickness of each film into its spectrophotometer data: Figure 5 is ZnS; Figures 6 and 7 are ZnS:Cu,Al. Since the transmittance through a film $T = I e^{-\alpha l}$, where I is the incident intensity and l is the film thickness, the α vs. λ

Figure 1 ZnS:Cu,Al Measured EX/EM

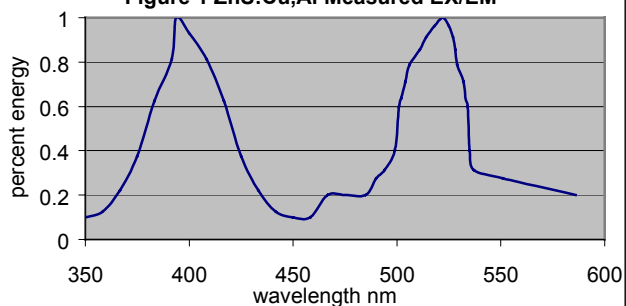


Figure 2: ZnS:Cu,Al Excitation/Emission

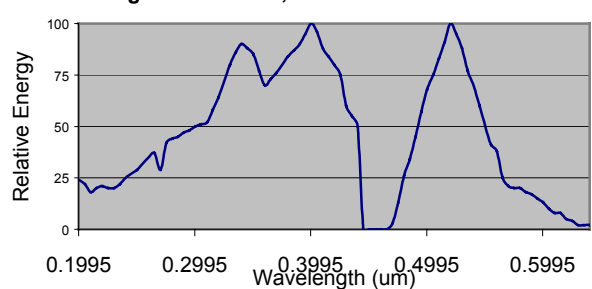


Figure 3 Reflectance w/o ZnS:cu,Al

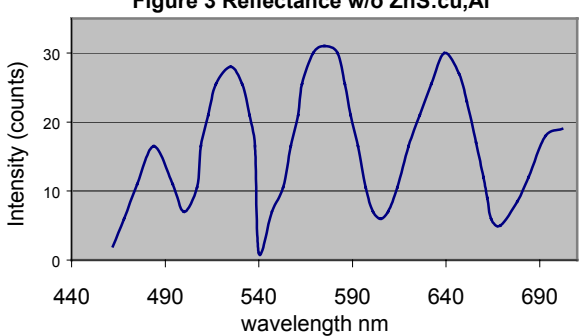


Figure 4 w/ZnS:Cu,Al

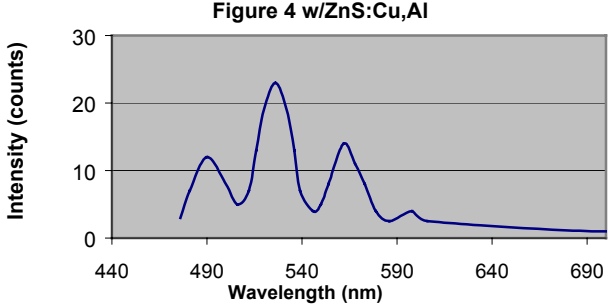


Figure 5 Absorption/length vs. Wavelength ZnS

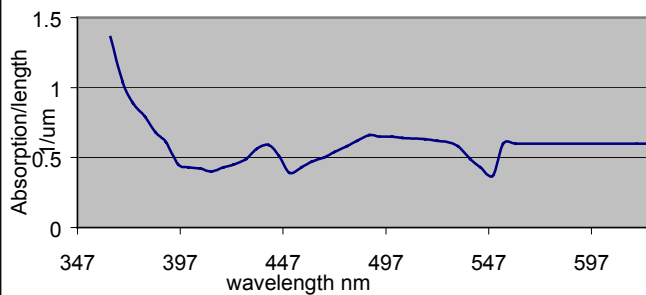


Figure 6 Absorption/length vs. Wavelength ZnS:Cu,Al

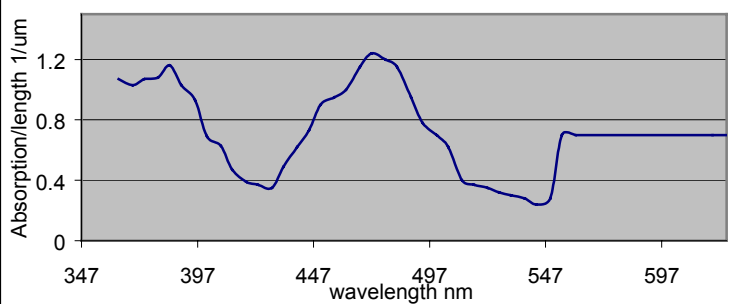
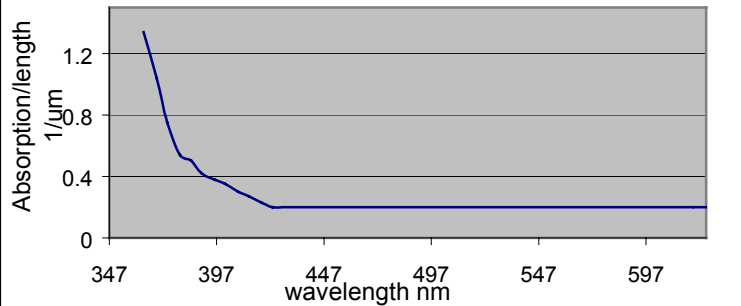
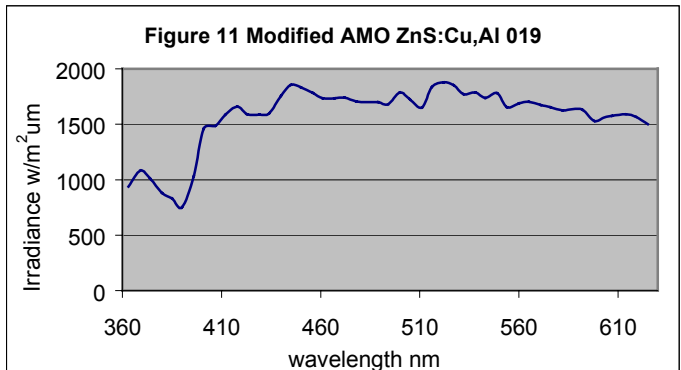
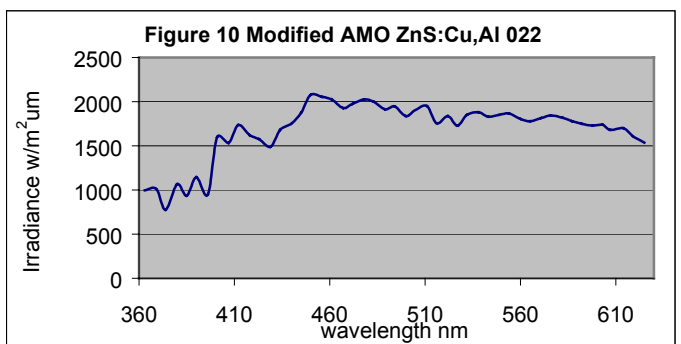
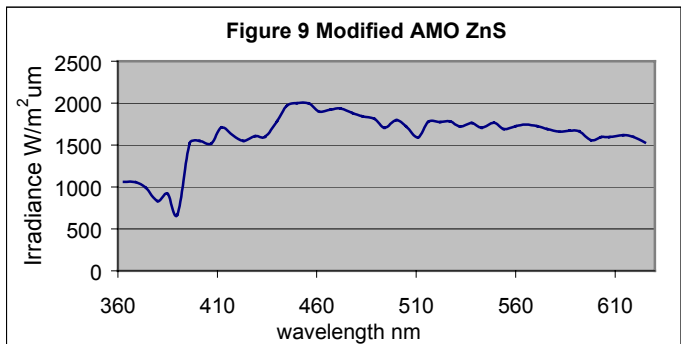
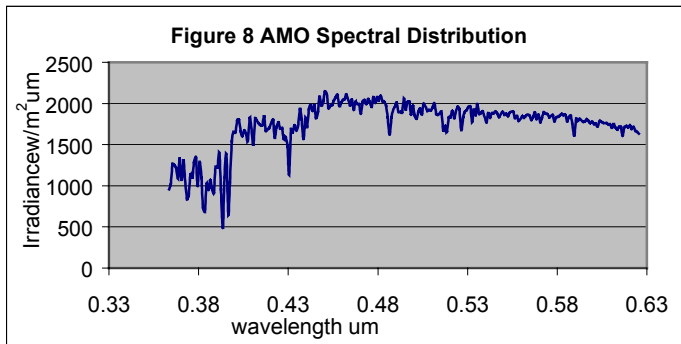


Figure 7 Absorption/length vs. Wavelength ZnS:Cu,Al





curves were applied as a filter to the AMO spectral distribution assumed incident on .125um thick films of ZnS and ZnS:Cu,Al. In this way the modified AMO distributions for ZnS:Cu,Al (Figure 10 and Figure 11) and ZnS (figure 9) were generated. Figure 8 shows the AMO spectral distribution[2]. On (325nm, 625nm), $\int \lambda \phi_{\text{mod}}(\lambda) d\lambda$ for ZnS:Cu,Al sample 022 is 1.8% larger than for ZnS.

However, on the same interval $\int \lambda \phi_{\text{mod}}(\lambda) d\lambda$ for ZnS:Cu,Al sample 019 is 1.5% smaller than for ZnS.

Conclusions:

Photo luminescent films of ZnS:Cu,Al were resistively evaporated onto glass and p-type silicon substrates. The films were shown to maintain fluorescence and act as anti-reflective coatings for the glass-silicon interface. Spectrophotometer data was used to generate modified AMO spectral distributions for light transmitted through .125 um films of ZnS and ZnS:Cu,Al and $\int \lambda \phi_{\text{mod}}(\lambda) d\lambda$ was numerically determined on (360nm,630nm). However, no conclusion as to the sign of this integral can be made from this limited number of samples analyzed. Annealing the resistively deposited films in an inert atmosphere may drive the Cu and Al impurities into their equilibrium position within the conduction band to impurity level energy gap. Therefore annealing may increase the phosphors' absorption and emission thereby increasing photogenerated current. Since copper and aluminum are problematic for long-term solar cell use, future work will also involve identifying ZnS type phosphors with smaller diffusion coefficients.

Acknowledgement

The authors would like to thank Errol Porter at The University of Arkansas, Fayetteville HiDEK facility for help with the PECVD of SiO₂.

References

1. OsramSylvania, Phosphor Data Sheet, 2000.
2. L.D. Partain, "Solar Cells and Their Applications", Wiley and Sons, 1995.
3. OsramSylvania, Technical Information Bulletin, Phosphor 1260, ZnS:Cu,Al, 2000
4. Crystran Corp., ZnS Data Sheet, 1995.
5. W.R. Runyan, "Semiconductor Measurements and Instrumentation", McGraw-Hill, 1975.

HOT-WIRE CHEMICAL VAPOR DEPOSITION FOR EPITAXIAL SILICON GROWTH ON LARGE-GRAINED POLYCRYSTALLINE SILICON TEMPLATES

M. Swiatek Mason, C.M. Chen and H.A. Atwater
Thomas J. Watson Laboratory of Applied Physics
California Institute of Technology, Pasadena, CA 91107.

INTRODUCTION

Hot-wire chemical vapor deposition (HWCVD) has recently been shown to be a promising method for fast, low-temperature epitaxy [1, 2]. We investigate the low-temperature ($<600^{\circ}\text{C}$) epitaxial growth of thin silicon films by HWCVD on polycrystalline template layers formed by selective nucleation and solid phase epitaxy (SNSPE). Previously, we showed that direct deposition by HWCVD on SiO_2 produced small grains ($\sim 40\text{-}80 \text{ nm}$), even with the addition of H_2 to a diluted mixture of 1% silane in He [3]. By varying the gas flow rates and the wire-to-substrate distance, we are now able to grow 300 nm thick epitaxial layers at $T=400^{\circ}\text{C}$ on silicon [100] substrates with an $\text{H}_2:\text{SiH}_4$ ratio of 70:1. Transmission electron microscopy confirms that the films are epitaxial with a periodic array of stacking faults. SNSPE layers formed by the use of nickel nanoparticles as nucleation sites for the solid-phase crystallization of phosphorus-doped amorphous silicon on SiO_2 display grain sizes on the order of $100 \mu\text{m}$, and have been successfully used as seed layers for epitaxial growth by molecular beam epitaxy at 600°C [4,5]. We will discuss the microstructural properties of epitaxial films grown on silicon substrates and SNSPE template layers and their suitability for photovoltaics applications.

EXPERIMENT

Silicon films of 300 nm thickness were grown on silicon (100) and SiO_2 substrates and SNSPE templates by HWCVD using hydrogen and diluted silane in He at an $\text{H}_2:\text{SiH}_4$ ratio of 70:1 at a total gas pressure of 170 mTorr. A tungsten filament of 0.5 mm diameter was heated to 1850°C and placed 4 cm from the substrates. These conditions were chosen to produce amorphous silicon films on SiO_2 , similar to those investigated by Seitz et al. [2]. Growth temperatures of $350^{\circ}\text{C} - 450^{\circ}\text{C}$ were chosen to investigate the effect of different levels of hydrogen surface passivation on the resulting epitaxial films. Substrates were ozone cleaned for 10 minutes and HF-dipped; to reduce surface contamination, ultrahigh purity gas mixtures were used and the base pressure of the growth chamber was below 10^{-6} torr.

RESULTS

Cross-sectional transmission electron microscopy of films grown on silicon (100) substrates at 400°C confirms the presence of epitaxial growth, as shown in Figure 1. The rough film-substrate interface is believed to have been caused by etching of the surface during growth by atomic hydrogen produced by the wire [3]. The roughened morphology of the silicon substrate in cross-section may be due to the presence of hydrogen platelet defects arising from the diffusion of hydrogen into the film during growth. Epitaxy continues to a thickness of approximately 240 nm, after which the film becomes highly twinned. The epitaxial films exhibit a periodic array of stacking faults which gives rise to the higher-order spots seen in the diffraction pattern in Figure 2.

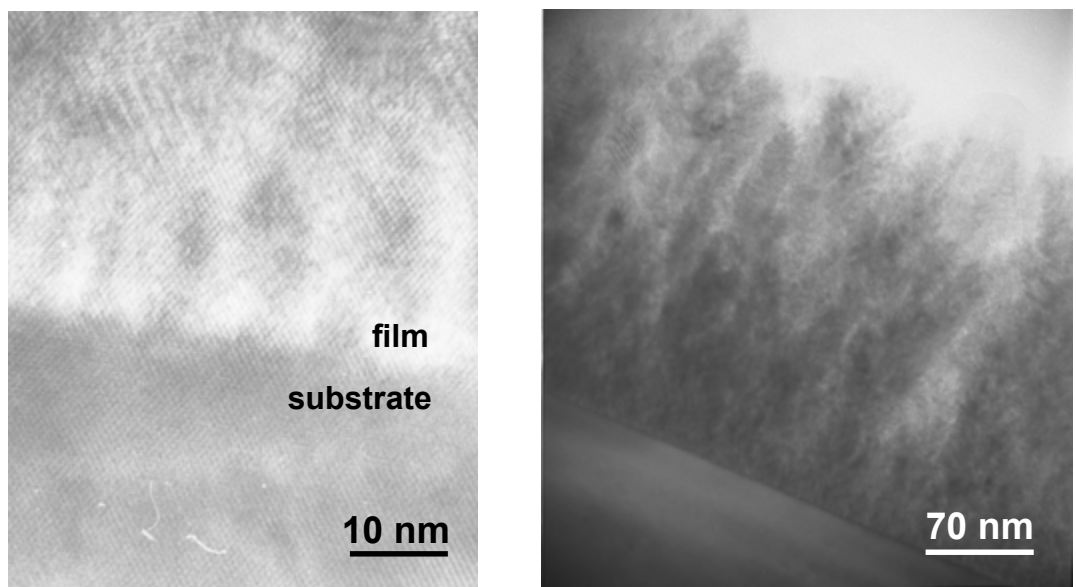


Figure 1. Cross-sectional TEM of Si on Si (100) at 400°C. (a) Interface between Si (100) and HWCVD epitaxial film. What appear to be hydrogen platelet defects are evident in the substrate. (b) Films become highly twinned after a thickness of approximately 240 nm.

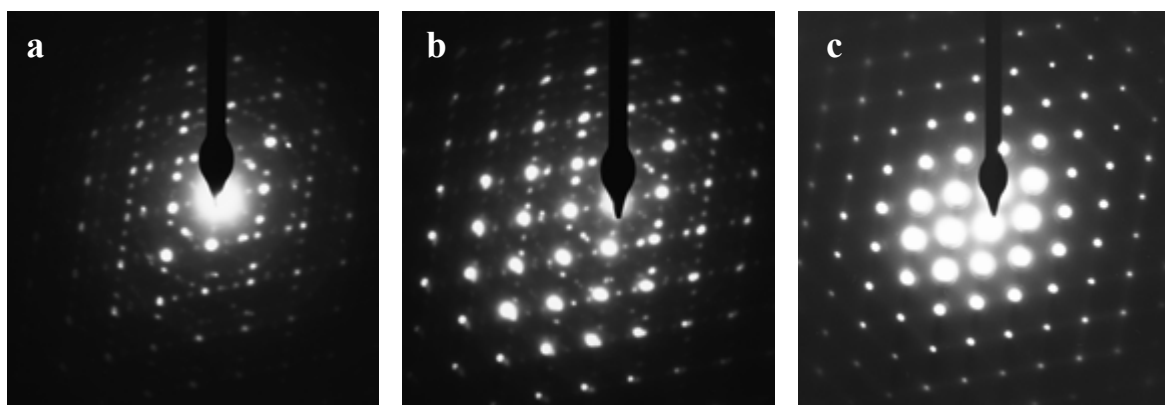


Figure 2. Selected area diffraction patterns. (a) HWCVD film and amorphous glue layer. (b) HWCVD film and Si (100) substrate. (c) Si (100) substrate. Higher order spots in (a) and (b) are due to a periodic array of stacking faults in the epitaxial film and twinning in the uppermost regions of the film.

Epitaxial films on SNSPE templates were investigated through plan-view transmission electron microscopy. The results, seen in Figures 3 and 4, are consistent with low-temperature epitaxy on the scale of the 100 μm grains of the SNSPE templates. Epitaxial breakdown is observed in the diffraction pattern of the HWCVD film, but some of the underlying higher-order diffraction spots are visible, making it likely that the underlying film has a morphology similar to that observed in the HWCVD films on Si (100). The effect of the orientation of the underlying grain structure of the SNSPE template on the morphology of the HWCVD film can be seen in Figure 4.

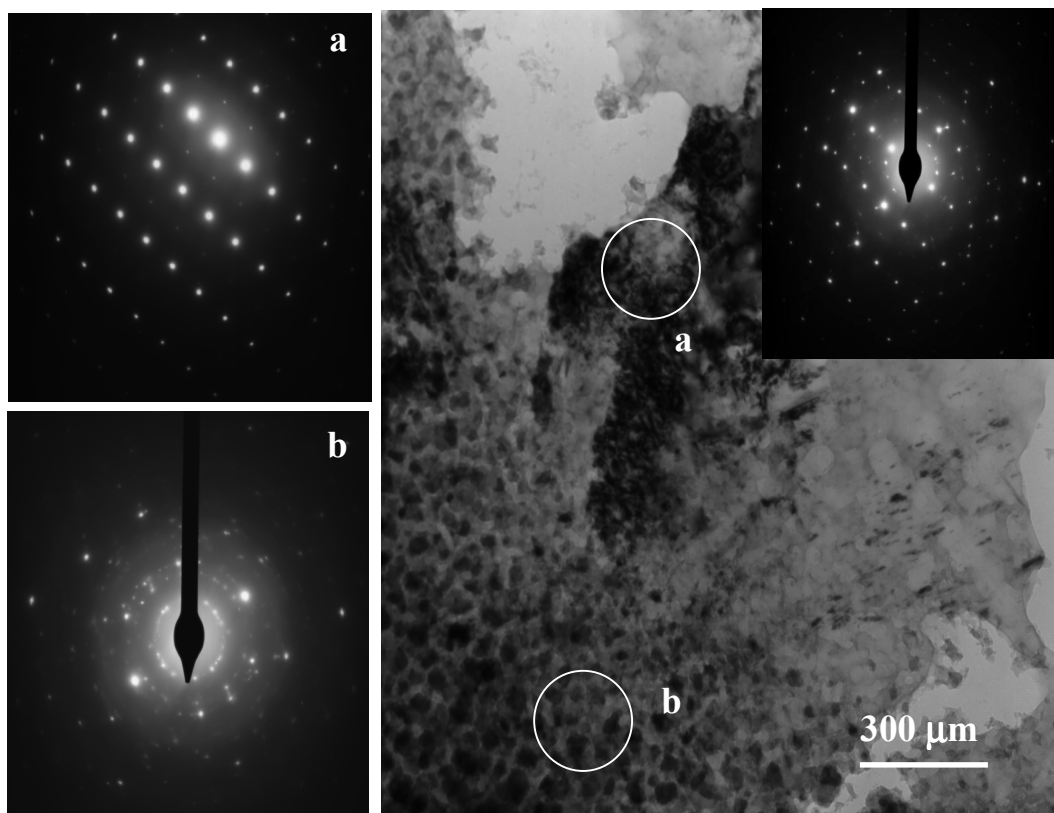


Figure 3. Plan-view TEM of HWCVD epitaxial film on SNSPE template. (a) Selected area diffraction pattern from underlying SNSPE template. (b) Selected area diffraction pattern from HWCVD film on SNSPE template. (c) Bright-field image indicating selected area diffraction regions. Inset: diffraction from entire area.

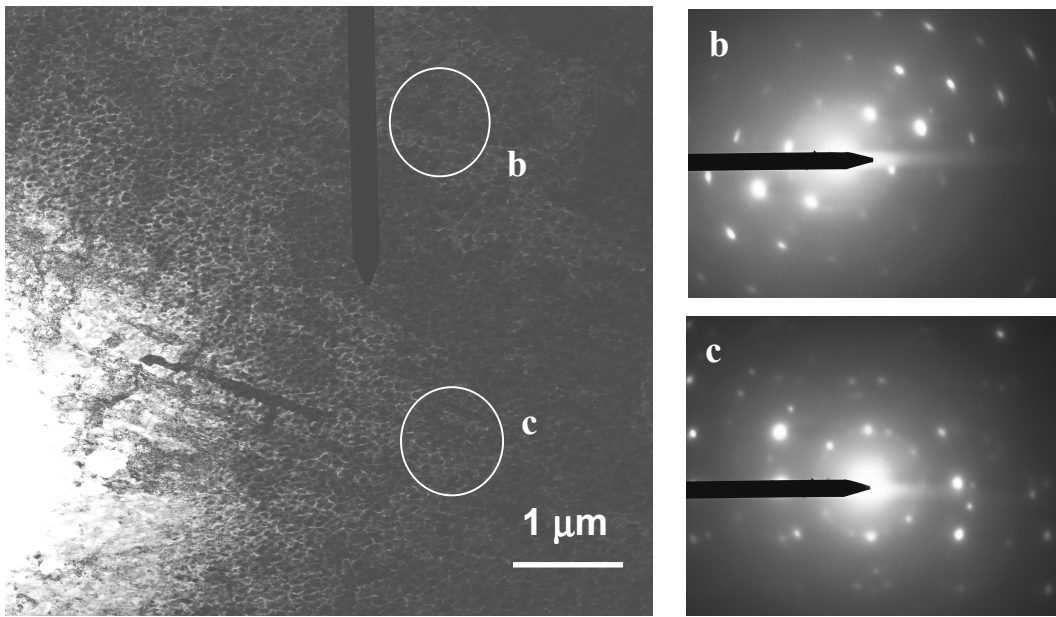


Figure 4. (a) Bright-field image of HWCVD film on SNSPE template showing selected area diffraction regions. (b) HWCVD film on (100)-oriented grain. (c) HWCVD film on grain of different orientation.

CONCLUSIONS

Epitaxial films characterized by a periodic array of stacking faults have been grown at high hydrogen dilution by HWCVD on Si (100) substrates. The limiting thickness for epitaxy is shown to be approximately 240 nm at a growth temperature of 400°C, after which the films exhibit a high degree of twinning. Evidence has been presented for epitaxial growth on SNSPE templates with 100 μm grains. Epitaxial growth on these templates could lead to the development of large-grained thin-film polycrystalline photovoltaic devices. Future work includes efforts toward increased growth rates (currently only 0.05 Å/s) and evaluation of the minority carrier lifetimes of the SNSPE templates and resulting epitaxial films to determine their suitability for photovoltaic applications.

REFERENCES

1. J. Thiesen, E. Iwaniczko, K.M. Jones, A.H. Mahan, and R. Crandall, *Appl. Phys. Lett.* 75, 1999.
2. H. Seitz and B. Schröder, *Sol. State Comm.* 116, 2000.
3. J.K. Holt, M. Swiatek, D.G. Goodwin, R.P. Muller, W.A. Goddard III, and H.A. Atwater, *Thin Solid Films* 395, 2001.
4. C.M. Chen, Ph.D. thesis, California Institute of Technology, 2001.
5. R.A. Puglisi, H. Tanabe, C.M. Chen and H.A. Atwater, *Mat. Sci. Eng. B* 73, 2000.

PROCESS FOR PRODUCTION OF SILANE

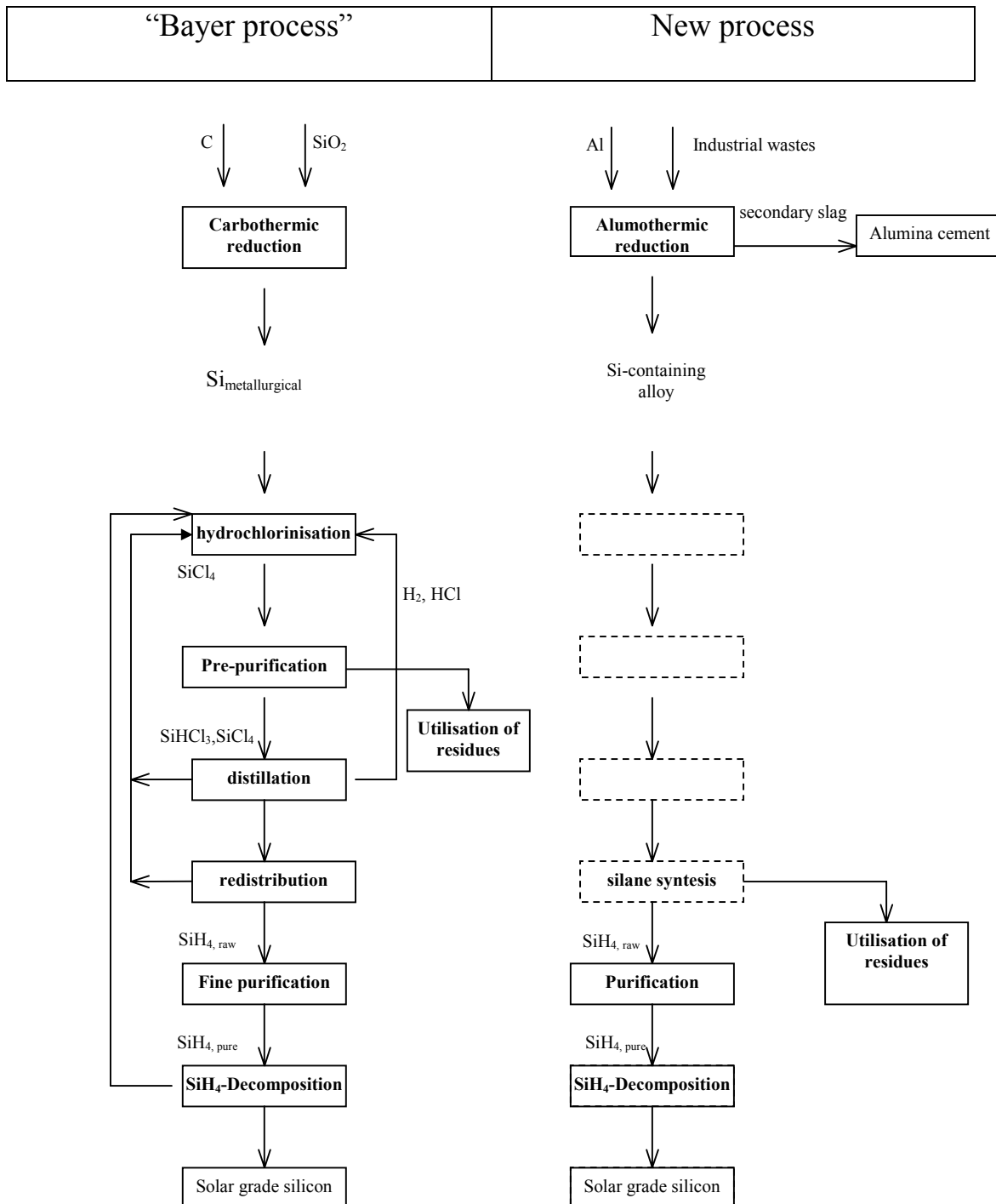
Marat. F. Tamendarov

Institute of Physics and Technology, Ministry of education and Science,
Almaty, 480082, Kazakstan, E-mail: tamendar@sci.kz

At present, there are two well-known techniques for silane production: simultaneous reduction and oxidation of trichlorosilane over a catalyst, and the reaction of silicon-containing alloy such as magnesium silicide with an acid aqueous solution. The former process, having the advantage of producing a high purity silane, involves a set of complicated steps that leads to high cost of the product. In contrast, the latter process is the best and the easiest to be realized among other methods because it requires neither expensive reducing agent, no low temperatures or elevated pressures. However, it poses a problem of low yield of silane.

This paper intends to report a process for production of silane, at a low cost and a high yield, suitable for forming thin layer silicon structures and high purity poly- and single crystalline silicon for a variety of applications, such as electronics and photovoltaics. The process of silane production, considered in this work, comprises the aluminothermic reduction of silica of industrial wastes, to obtain a silicon-containing alloy. The alloy used in the process is composed of at least two metals and silicon. Silane is produced under the interaction of silicon-containing alloy in the form of fine powder with hydrochloric acid at ambient temperatures. The reaction rate is very high and in average the reaction takes from several seconds to several minutes to be completed. The amount of the silane gas generated and identified as monosilane (SiH_4) was found corresponding more than 80% of the silicon content of the alloy. The purification of silane may be carried out by known methods such as low temperature processing and by the use of adsorbent. It is noticeable that in unrefined silane only traces of diborane, the most hard-to-remove impurity, are detected. The advantages of this process are low energy consumption, high yield of silane, simple production steps that enable reduction of product cost, effective utilization of industrial wastes.

Bayer evaluated different ways for the production of solar grade silicon [1]. The technology stages in comparison with “Bayer process” are shown in Figure 1.



References

1. P. Woditsch, Wolfgang Koch, “Solar grade silicon feedstock supply for PV industry”, Solar Energy Materials & Solar Cells, **72**, (2002), 11-26.

Injection-Dependent Lifetime Studies of Copper Precipitates in Silicon

Daniel Macdonald¹, Willi Brendle¹, Andres Cuevas¹ and A. A. Istratov²

¹Dept. of Engineering, Australian National University, Acton, ACT 0200, Australia.

²Dept. of Materials Science and Engineering, University of California, Berkeley, CA 94720.

Abstract – Copper precipitates have been deliberately formed in single-crystal silicon wafers in order to study their impact on carrier lifetimes. The injection-dependence of the measured lifetimes of samples with different dopant type and resistivity reveals the presence of both shallow and deep levels associated with the precipitates, in support of previous DLTS studies. Although such precipitates are expected to produce a continuous range of interacting energy levels, a simple model using only one shallow and one deep Shockley-Read-Hall recombination centre results in a consistent fit across all samples.

1. INTRODUCTION

Metallic precipitates are often a dominant recombination centre in multicrystalline silicon wafers, and are therefore of critical importance in solar cells. In general, these precipitates contain several different metallic species, as well as other impurities such as oxygen and carbon. Unfortunately, their diverse composition means that controlled studies of these ‘native’ precipitates are difficult. In order to learn about the recombination behaviour of precipitates, it is therefore desirable to study those that contain only a single metallic species.

Recently, Sachdeva *et al.*[1] found that conditions which initiate precipitation of Cu in p-Si simultaneously give rise to a sudden decrease in the diffusion length. By contrast, the diffusion length decreases more evenly with increasing Cu concentration in n-Si, in which precipitation occurs easily, even for low Cu concentrations[2,3]. These facts suggest that, of the various possible forms Cu can take in Si, Cu precipitates tend to dominate the carrier lifetime when present. This dominance, coupled with the fact that the conditions that bring about precipitation are fairly well understood, makes them an ideal candidate to study precipitate-driven recombination.

One of the most important electronic features of precipitates in general is that they produce states in the forbidden gap which occupy a range of energy

levels, as opposed to discrete, single-energy states typically caused by interstitial metal atoms. Cu precipitates are no exception, as shown by modelling of DLTS spectra by Schröter *et al.*, who identified a defect band from $E_C - 0.2\text{eV}$ to $E_C - 0.5\text{eV}$ [4-6]. They were also able to conclude that these states were ‘band-like’ rather than localised, meaning that they interact with one another directly through carrier hopping.

As a result, a rigorous recombination model for such distributed, interacting states would be quite complex. In this present study, we have approximated them with two non-interacting Shockley-Read-Hall recombination centres. The net impact of the interactions between the states and their non-discrete distribution are then lumped into a relatively small set of ‘effective’ energy levels and cross-sections. Despite the apparent crudeness of this simple model, the results indicate that it can indeed provide a good explanation of the measured injection-dependent lifetimes.

2. EXPERIMENTAL TECHNIQUES

Most of the Cu contaminated samples were prepared at the Australian National University (ANU). An additional sample from the University of California, Berkeley (UC) was originally prepared for Cu precipitation studies published elsewhere[1].

A critical aspect of preparing the samples is to ensure that most of the Cu is in fact precipitated in the bulk of the wafers, and not at the surfaces or present interstitially. As mentioned, bulk Cu precipitation occurs spontaneously in n-Si[7], even for low Cu concentrations, due partly to the position of the Fermi level causing the precipitates to be negatively charged or neutral. In p-Si however, precipitation only seems to occur when the Cu concentration exceeds a critical level that is approximately equal to the acceptor concentration plus 10^{16}cm^{-3} [7].

Hence, in this study, the n-Si sample contains a relatively low bulk Cu concentration of $1 \times 10^{14}\text{cm}^{-3}$,

while the p-Si samples have $3 \times 10^{16} \text{ cm}^{-3}$ Cu to ensure precipitation in even the most heavily doped sample ($1\Omega\text{cm}$, or $N_A=1.5 \times 10^{16} \text{ cm}^{-3}$). A further p-Si sample ($250\Omega\text{cm}$) with a lower Cu concentration of $1 \times 10^{14} \text{ cm}^{-3}$ is also included.

The ANU samples were $<100>$ FZ-Si implanted with 70keV Cu⁶³ isotopes at 100°C to reduce the formation of an amorphous layer. Doses were chosen to give the desired bulk Cu concentrations after annealing. The implant was 3×3cm in size to allow accurate lifetime measurements.

After implantation and cleaning, the samples were annealed at 900°C for 54 minutes to distribute the Cu evenly. At this temperature, the solid solubility limit of Cu in silicon is more than 10^{17} cm^{-3} , safely above the target values[8]. 54 minutes is sufficient for the Cu to diffuse 10 times the thickness of the thickest wafer, ensuring a uniform distribution within the wafer bulk. The samples were then etched to remove residual implant damage or Cu pile-up at the surfaces.

For each resistivity, control samples were processed in parallel. In all cases the lifetimes of the control samples were at least an order of magnitude greater than those with Cu, meaning the latter are not affected by surface or Auger recombination, furnace contamination, or the lifetime of the starting material.

The preparation of the sample from UC is described in detail elsewhere[1]. The most important features are that it was p-Si $12\Omega\text{cm}$ CZ, prepared by dipping in dilute CuF₂ solution and then annealing at 900°C. This resulted in a bulk Cu concentration of $2.2 \times 10^{17} \text{ cm}^{-3}$ (as determined by the solubility limit), sufficiently high to ensure precipitation after cooling.

To passivate the surfaces, all samples were coated with plasma SiN films[9]. Lifetime measurements were then performed using the Quasi-Steady-State PhotoConductance technique (QSSPC)[10] coupled with a generalised analysis[11]. Since the sample prepared at UC was significantly smaller (100mm^2) than the inductive coil used, special silicon samples of the same shape and size were prepared to re-calibrate the apparatus.

3. RECOMBINATION MODEL

The Shockley-Read-Hall model provides a basis for calculating the injection-dependence of the carrier

lifetime if the energy level and the capture cross sections of a defect are known. It is generally expressed in terms of the capture time constants for electrons and holes τ_{n0} and τ_{p0} , which are related to the recombination centre density N_{SRH} through $\tau_{n0}=1/(N_{SRH} c_n)$ and $\tau_{p0}=1/(N_{SRH} c_p)$. The parameters c_n and c_p are equal to the product of the thermal velocity and capture cross section for each carrier type. Details of the model can be found elsewhere[12].

In attempting to model the lifetime curves dominated by Cu precipitates, we have chosen two non-interacting levels at the extremes of the range suggested by Schröter: E_C-0.2 and E_C-0.5eV. The values of c_n and c_p for each level are unknown, and have been treated as fit parameters. It should be remembered that, in general, the only parameters that can be unambiguously determined from such fits are the *product* of the defect density and c_n or c_p . Since in this case we do not know the precipitate density by other means, the parameters reported are only relative, not absolute. Hence we may only really determine the ratio of c_n and c_p . Furthermore, as mentioned above, since the two energy levels used only approximate the likely energy distribution, the ratio of c_n and c_p for each level should be thought of as an *effective* parameter.

These limitations may at first appear to make the modelling somewhat pointless. However, there are two important constraints that make it less ambiguous. Firstly, the density of defects at the E_C-0.2 and E_C-0.5eV levels are forced to be equal for each sample. This merely reflects the fact that the precipitates are considered to be physically identical in each sample. Secondly, since the capture cross-sections are not expected to change either, the same set of c_n and c_p values are used for all of the samples. An important exception to this requirement is the E_C-0.5eV level in the n-Si case, as discussed below.

Finally, the primary purpose of this modelling exercise is not just to determine c_n and c_p ratios, but to determine whether, at least for the case of Cu precipitates, the continuous distribution of energy levels can be reasonably well approximated by a single shallow and a single deep SRH level. This is highly relevant for future attempts to characterise precipitates.

Resistivity	Type	N_A or N_D (cm^{-3})	Fermi level $E_C - E_F$ (eV)	N_{Cu} (cm^{-3})	N_{SRH} (arb.)	$E_C - 0.2\text{eV}$ level $c_n (\text{cm}^3 \text{s}^{-1})$	c_p	$E_C - 0.5\text{eV}$ level c_n	c_p
250Ω FZ	p	5×10^{13}	0.78	3×10^{16}	3.3×10^{14}	2.2×10^{-9}	5.5×10^{-8}	2.7×10^{-9}	1.6×10^{-10}
"	"	"	"	1×10^{14}	3.5×10^{12}	"	"	"	"
12Ω CZ	"	1.1×10^{15}	0.86	2.2×10^{17}	7.5×10^{14}	"	"	"	"
1Ω FZ	"	1.5×10^{16}	0.93	3×10^{16}	2×10^{14}	"	"	"	"
20Ω FZ	n	2×10^{14}	0.31	1×10^{14}	1×10^{13}	"	"	2.2×10^{-10}	3.3×10^{-9}

Table I. Parameters for the 5 samples in Figure 1 containing Cu precipitates. The parameters in italics are involved in the SRH fitting process.

4. RESULTS AND DISCUSSION

Figure 1 shows the injection-dependent lifetime measurements for all of the samples in this study. The corresponding dopant densities, total Cu concentrations and fit parameters are shown in Table I. Note that the same energy levels and c_n and c_p values are used for all of the samples (except the n-Si wafer, as discussed below). The only parameters that are altered between samples are the dopant density, which is known, and the nominal recombination centre density (the same value is used for both energy levels). This final parameter simply shifts the curves vertically.

The two energy levels used were $E_C - 0.2\text{eV}$ and $E_C - 0.5\text{eV}$. However, self-consistent fits are also possible with other pairs of deep and shallow energy levels. It is also difficult to unambiguously determine from the modelling if the levels are in the upper or lower band-half, although the change of cross-sections observed for the n-Si sample, discussed below, strongly suggests they are in the upper half. The $250\Omega\text{cm}$ p-type sample allows us to state with certainty that the deep level must be further than 0.33eV from either band edge, while the shallow level must be at most 0.33eV from either band. Future work with a larger range of samples, and combination with Temperature Dependent Lifetime Spectroscopy (TDLS)[12] performed at Fraunhofer ISE, will pinpoint the band-halves and energy levels more exactly.

Nevertheless, although limited at this stage, the results are consistent with those of Schroter *et al.*, and tend to confirm that Cu precipitates are responsible for the poor lifetimes in both n-Si and p-Si in this and other studies[13].

Importantly, the fact that the shapes of the curves are qualitatively correct for each resistivity indicates that the two-level SRH model describes the data well. An

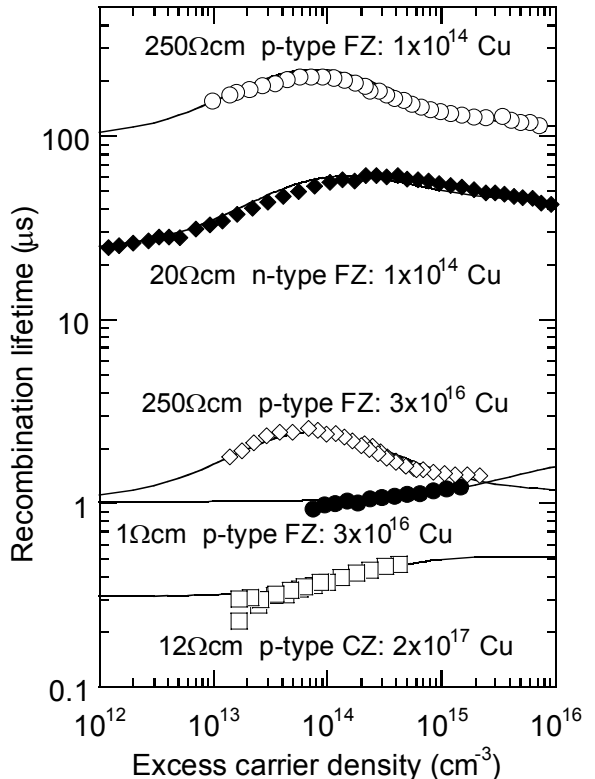


Figure 1. Measured lifetimes for wafers of various resistivities containing Cu precipitates, and two-centre SRH model fits.

obvious feature is that the higher resistivity wafers show a hump-like shape. This reflects the fact that the shallow level at $E_C - 0.2\text{eV}$, which dominates in high injection, decreases the lifetime with increasing carrier concentration. In the more heavily doped samples, the shallow level has a much flatter dependence, although this is not clear in the measured data because high-injection could not be achieved. By contrast, the deep level, which dominates at low injection, causes a strongly increasing lifetime for all resistivities. This is indeed typical of many systems that involve simultaneous deep and shallow levels[12,14].

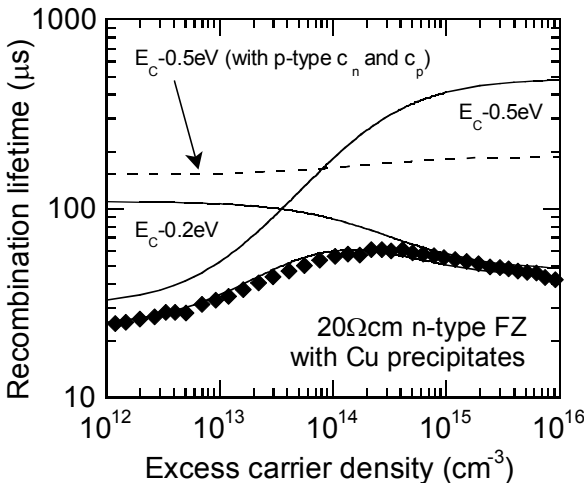


Figure 2. Fit for the 20Ωcm n-type sample showing contributions from shallow and deep levels. The dashed line represents the deep level with the values of c_n and c_p as used for the p-type samples.

Figure 2 shows the relative contribution of the deep and shallow levels for the n-type sample. In this case, it was not possible to obtain a satisfactory fit with the c_n and c_p values used for the p-type samples, as shown on the Figure. For this sample, the Fermi level lies in between the two SRH levels, whereas in all other samples the Fermi level is well below both (see Table I). Since the charge state of the precipitate would therefore be different in the n-type sample, it is in fact physically reasonable to expect the capture cross sections to change. Specifically, this level would become more negatively charged, and therefore less attractive to electrons and relatively more so for holes. Consistent with this, the value of c_n of the deep level used in the modelling decreased by an order of magnitude, while c_p increased. It is not clear why the shallow level remains unchanged, since presumably it should also be affected by the change in charge. It should be kept in mind that the cross sections could be different again for differently doped n-Si, since the extent of charging would change.

Another interesting aspect of the results relates to the 250Ωcm p-type sample with low Cu concentration. As discussed above, it is not necessarily expected that the Cu would precipitate easily in such a sample. However, the lifetime curve can be accurately fitted using the same parameters as the other p-type wafers. It seems likely then that at least some of the Cu in this sample has precipitated, and that these precipitates dominate the lifetime. Note that the

recombination centre density N_{SRH} used to model this sample, which is proportional to the precipitate density, is two orders of magnitude lower than the sample with a greater Cu concentration.

5. CONCLUSIONS

Irrespective of the complex nature of interacting, distributed energy levels associated with Cu precipitates in silicon, their impact on carrier lifetimes can be adequately described by two non-interacting SRH recombination centres. A reasonably good fit was obtained using levels at E_c -0.2 and E_c -0.5 eV, which correspond to previously identified upper and lower edges of Cu-related defect bands. This finding helps to confirm that Cu precipitates are indeed responsible for the minority carrier lifetime degradation in p-Si and n-Si.

ACKNOWLEDGEMENTS

The authors acknowledge the assistance of colleagues in the Dept. of Electronic Materials Engineering, ANU: Prof. J. Williams and M. Conway for help with ion implantation, and Prof. C. Jagadish and H. Tan for access to the PECVD reactor. This work has been supported by the Australian Research Council.

REFERENCES

- [1] R. Sachdeva, *et al.*, *Appl. Phys. Lett.* **79**, 2937-2939 (2001).
- [2] A. A. Istratov and E. R. Weber, *J. Electrochem. Soc.* **149**, G21-G30 (2002).
- [3] A. A. Istratov and E. R. Weber, *Appl. Phys. A* **66**, 123-136 (1998).
- [4] W. Schroter, *et al.*, *Mater. Sci Eng. B* **72**, 80 (2000).
- [5] A. Sattler, *et al.*, *Solid State Phenom.* **63-64**, 369 (1998).
- [6] M. Seibt, *et al.*, *Phys. Status Solidi A* **166**, 171 (1999).
- [7] C. Flink, *et al.*, *Phys. Rev. Lett.* **85**, 4900-4903 (2000).
- [8] E. R. Weber, *Appl. Phys. A* **30**, 1-22 (1983).
- [9] M. J. Kerr and A. Cuevas, *Semicond. Sci. Technol.* **17**, 166-172 (2002).
- [10] R. A. Sinton and A. Cuevas, *Appl. Phys. Lett.* **69**, 2510-2512 (1996).
- [11] H. Nagel, *et al.*, *J. Appl. Phys.* **86**, 6218-6221 (1999).
- [12] S. Rein, *et al.*, *J. Appl. Phys.* **91**, 2059-2070 (2002).
- [13] K. Stewart, *et al.*, *11th Workshop on Crystalline Silicon Solar Cell Materials and Processes* (Estes Park, Colorado, 2001) 212-215.
- [14] D. Macdonald, *et al.*, *J. Appl. Phys.* **89**, 7932-7939 (2001).

Nanoscale Investigations of Polycrystalline Silicon for Photovoltaic Applications

R. Zhang¹, G. Duscher¹, J. Rand², and G. A. Rozgonyi¹

¹Department of Materials Science and Engineering, North Carolina State University, Raleigh, NC;

²AstroPower, Inc., Newark, DE

ABSTRACT

Electron Beam Induced Current (EBIC) and preferential etching techniques were applied to study intragrain inclusions in polycrystalline silicon sheet solar cell material. Subsequent Transmission Electron Microscope (TEM) measurements revealed the size and configuration of inclusions, extended defects generated in the vicinity of inclusions, and a unique void defect. Electron Energy Loss Spectroscopy (EELS) was used to identify the chemical composition of particles contained within a single void.

INTRODUCTION

Solar cells generate electricity from clean and inexhaustible sunlight without producing any contamination. For solar application, polycrystalline silicon is a promising candidate for its low fabrication costs while maintaining moderate conversion efficiency. The conversion efficiency of solar cells made with polycrystalline silicon is limited by not only grain boundary (GB) interfaces, but also intragrain defects (subgrain boundaries, dislocations, impurity precipitates, etc.) acting as recombination centers [1, 2]. This paper reports on the investigation of intragrain inclusions in polycrystalline silicon.

EXPERIMENTAL

AstroPower produces a polycrystalline Silicon-Film™ sheet used for the fabrication of solar cells. The top of the sheet is P-type polycrystalline silicon with columnar grains, ranging in size from 100 μm to 5mm. The total sheet thickness ranges from 600 to 800 μm [3]. The electrical properties were studied using EBIC measurements, performed in a Scanning Electron Microscope (SEM) operating at 30 KV with an electron beam intensity of 1 nA. After EBIC measurement, the samples were stripped of their Al contact layer and preferentially etched (Wright etch), prior to imaging with a Normaski microscope or SEM to reveal any structural defects. Finally, samples were thinned by ion-milling for TEM imaging and EELS analyses performed using a JEOL 2010F electron microscope.

RESULTS AND DISCUSSION

Figures 1 (A) and (B) shows Normaski and corresponding EBIC images of the same region, while (C) is a magnification of the area denoted by a box in (A), and (D) is an SEM image after Wright etch. From Fig. 1 (B), it is clear that grain boundaries have various electrical activities, ranging from very weak to strong. However, the strongest recombination center observed by EBIC, see Fig. 1 (B), is the large dark intragrain spot. Preferential etching revealed this recombination center as an irregular-shaped depression, possibly originating from an inclusion. This assumption was confirmed by further study on the same set of samples using SEM, Fig.1 (D), with the core of inclusion clearly visible. Note that there are many dislocations surrounding this microdefect due to the associated strain field. Since this type of inclusion, exhibiting high recombination activity is commonly observed in the polycrystalline silicon sheet material, it is necessary to study its origin, composition, and electrical behavior.

TEM was chosen for its high resolution and chemical identification capability. From the TEM images taken at different locations with various magnifications, see Fig. 2, the size of the inclusions may vary from 20-100 nm and may even form agglomerates up to a size of 1 μm , while the local density may reach around 20/ μm^2 .

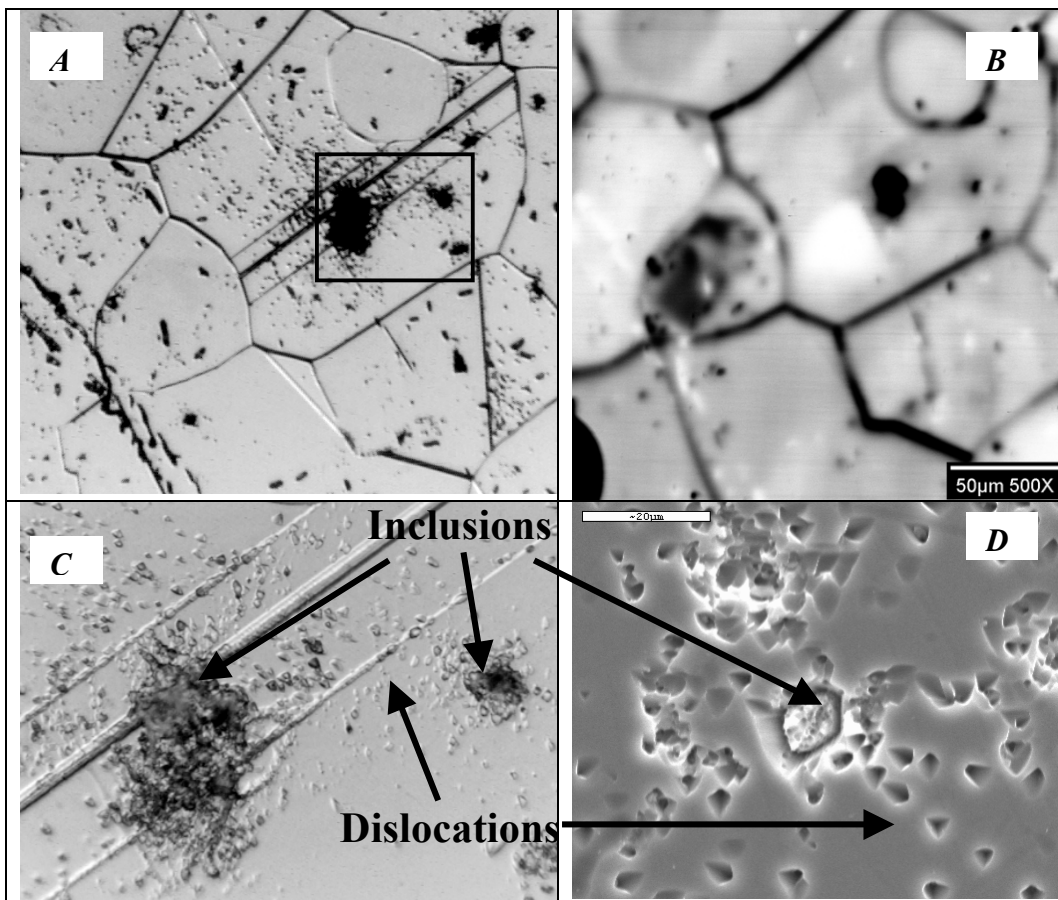


Figure 1. Normaski and corresponding EBIC images on the same region are shown in (A) and (B), respectively, while (C) magnifies a part of (A) detonated by a box, showing the presence of inclusions of various sizes, and many surrounding dislocations. (D) is an SEM image taken on a different region.

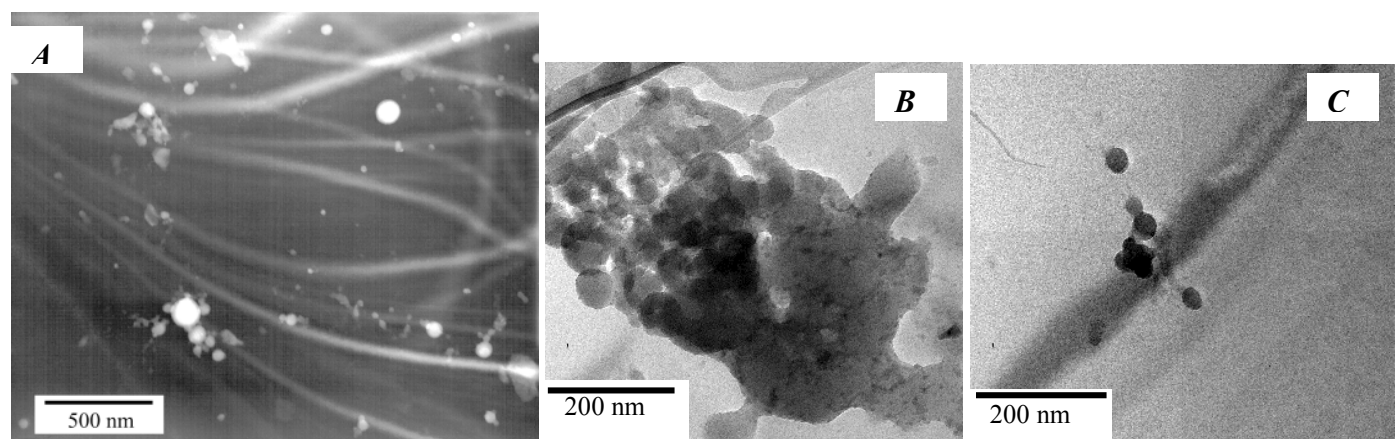


Figure 2. (A) dark field TEM image shows the size distribution of inclusions (20-100 nm), as well as their density. (B) and (C) are bright field TEM images of the inclusions of extreme sizes (large vs. small). Note the agglomerate of inclusions of about 1 μm in (B).

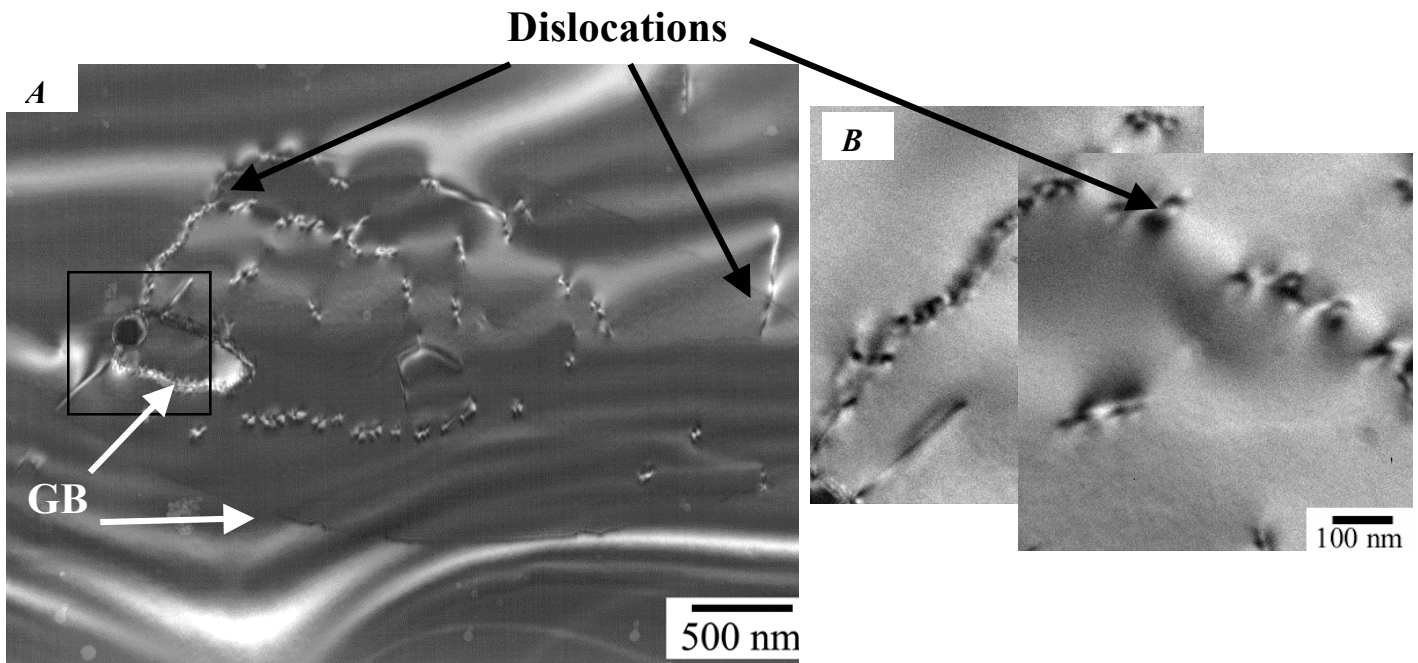


Figure 3. (A) shows a weak beam dark field image of one specific inclusion. There are grain boundary and dislocations in the vicinity of the inclusion. (B) is the magnified view of a section of dislocation network.

We now focus our discussion on one specific inclusion inside the box in Fig. 3 (A), which is a weak beam dark field image, containing bright stress lines generated by the inclusion (the dark circle). With higher magnification, you can see that some of the lines are discrete dislocations forming low-angle GBs, see Fig. 3 (B), others are continuous high-angle GBs, see Fig. 4 (A). The box in Fig. 3 (A) denotes the region shown in Fig. 4 at higher magnification. Note that the single inclusion is, in fact, a large void containing many small particles. The octahedral shape of the void suggests its possible origin: agglomeration of point defect during the rapid crystallization process. Subsequently, supersaturated impurities (O, C, and metals) heterogeneously precipitate along the boundary of the void.

EELS analyses were performed on the void periphery regions indicated by the small black squares in the Z-contrast image of Fig. 4 (C). Qualitative chemical composition results of the EELS analyses are superimposed on Fig. 4 (A). The major elements identified inside the particles are Si, C and O, indicating the possible chemical compositions of particles: SiC or SiO_x. Note that C is also present in the neighboring grain boundary, resulting from C diffusion along GB. Transition metal Cr is found in some particles, as well as within neighboring grain boundaries. Note that the nature of the void was confirmed by a continuous EELS spectrum with no peaks identifiable.

Since the Z-contrast imaging reveals local differences in atomic number of elements present, it is suitable for the study of the interaction between void and impurities. The white Z-contrast observed in Fig. 4 (C) indicates the presence of impurities, whose Z is higher than that of the Si host, possibly transition metals, localized both within and outside of the void. If more specifically, we can see that heavy elements are mostly segregated within the small particles and surrounding GBs from the comparison of Fig. 4 (A) and (C).

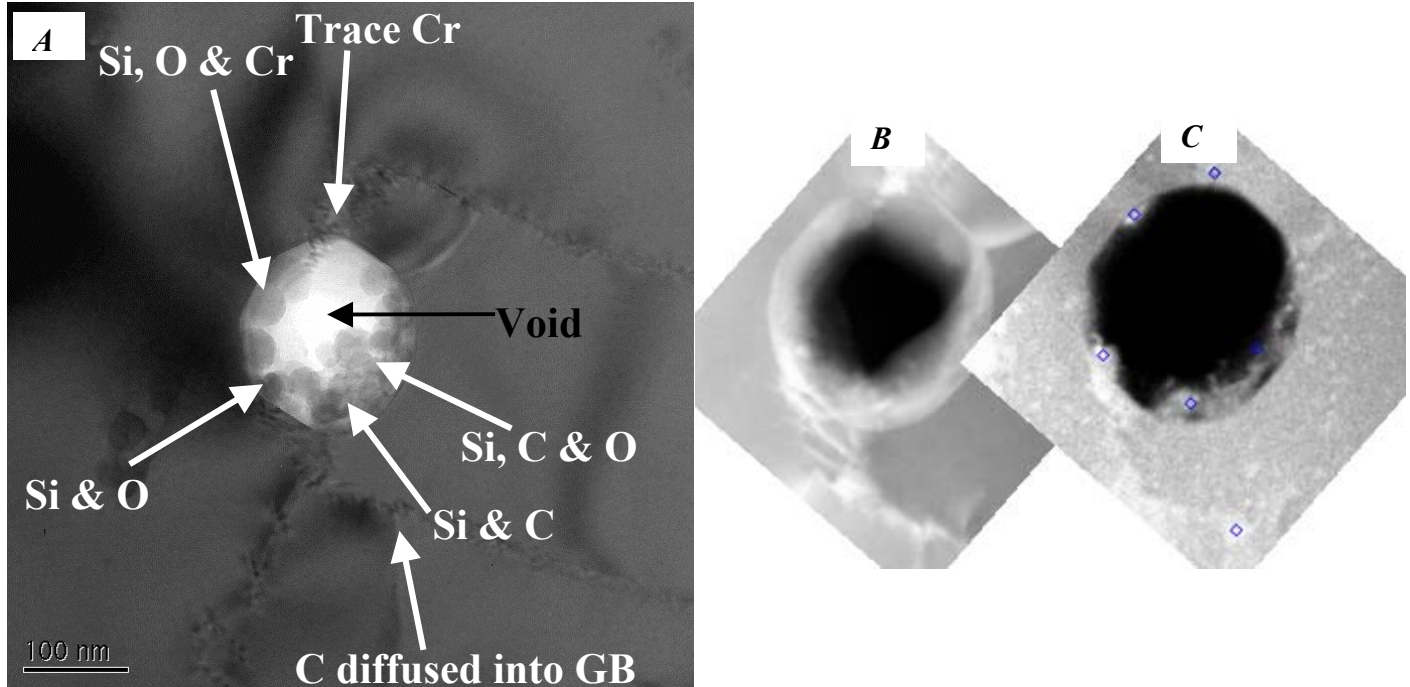


Figure 4. (A) is a magnified dark field view of the region enclosed by a square in Fig. 3 (A), showing that the inclusion is actually a void enclosing many small particles. (B) and (C) are the corresponding bright field and dark field images, respectively, with (C) being a Z-contrast image whose contrast indicates some elemental differences. EELS analyses were also performed on regions with bright contrast in (C), and indicated by the arrows in (A).

SUMMARY

We have found a strong correlation between the results from TEM measurement and those from EBIC and preferential etching. Inclusions are chemically identified as SiC and SiO_x, and rich with transition metals (e.g., Cr) as observed using EELS analyses. Due to the fact that extrinsic defects decorated with transition metals can behave as deep level traps, the inclusions should exhibit strong recombination activity, as confirmed by EBIC contrast. For the large inclusions, clusters of dislocations are generated in the neighboring region, due to the associated strain field, which is again consistent with the preferential etching study.

ACKNOWLEDGEMENTS

The authors gratefully acknowledge the help of Alex Kvit and Haiyan Wang with TEM operation, and valuable discussions with Ernest Van Dyk.

REFERENCES

- [1] Werner, M., Weber, E.R., McHugo, S., Hieslmair, H. and Chapman, K.L.: Solid State Phenomena Vols. **47-48** (1996) 449-454.
- [2] Ihlal, A., Rizk, R., Voivenel, P. and Nouet, G.: J. Phys. III France **5** (1995) 1371-1382.
- [3] Culik, J. S. et al, "Progress in 15-MW Single-Thread Silicon Film Solar Cell Manufacturing System", 17th ECPVSEC, Munich, October 2001.

Infrared Residual Stress Polariscopic for Solar Cell Inspection

Shijiang He and Steven Danyluk

The George W. Woodruff School of Mechanical Engineering

Georgia Institute of Technology

And

Sergei Ostapenko

University of South Florida

This research addresses the non-contact measurement of in-plane residual stresses in thin silicon sheet by two complementary infrared transmission systems. A full field infrared phase stepping polariscope with a fringe multiplier using a pair of partial mirrors developed at the Georgia Institute of Technology, and a scanning linear polariscope system which scans samples with a IR laser and records a point-by-point measurement developed at the University of South Florida. As part of this study five samples of EFG silicon sheet grown by ASE Americas were measured by these two methods. The results show a good correlation between the two techniques with the same level and statistical variation in the residual stress distribution.

Some of the details that have needed to be examined included the analysis of the influence of crystal anisotropy on the IR transmission in silicon. The photoelastic effect for the (100), (010) and (001) orientations was developed to describe the relationship between the stress and the dielectric impermeability tensors. For the (001) and (111) orientations, the stresses are related to the photoelastic parameters by an effective stress-optical coefficient which may be angle dependent.

In addition, the thickness of the silicon samples was measured by an LH/F-200 SAM system which was developed as part of the research effort. A focused longitudinal acoustic pulse with a repetition rate of 20KHz was used to scan the samples while in DI water. The acoustic pulses are reflected from the front and back surfaces, received by the transducer and converted back to voltage pulses. Time-of-flight data were measured and used to obtain thickness maps on EFG wafers. The maximum thickness variation caused by anisotropy is about 20%.

Achieving High Dopant Concentrations in Si: First Principles Simulations.

Scott A. Centoni, Babak Sadigh, Maria-Jose Caturla,
George H. Gilmer and Tomas Diaz de la Rubia

Lawrence Livermore National Laboratory, Livermore, CA 94550

ABSTRACT

In this paper we discuss methods to obtain high dopant concentrations during processing of Si devices. The possibility of increasing the solubility of B in Si by misfit stress is investigated. The enthalpy of B atoms is calculated, with and without stress, using density functional theory. A second approach, the trapping of excess dopant atoms during deposition of Si, is also considered. For this purpose, the enthalpies of several dopant species in sites near the surface are calculated.

1 INTRODUCTION

The design of efficient and compact Si devices can be facilitated by device processing simulations, provided the models are based on accurate kinetics to describe fabrication, including the diffusion and interactions of dopants and point defects [1]. In recent years the models of Si processing have improved significantly, due in part to data generated by quantum mechanics calculations based on density functional theory (DFT).

DFT calculations can also suggest new techniques for fabricating devices. The trend in integrated circuit fabrication is to pack the chips with higher densities of components, requiring high doping densities to provide sufficient current flow. We present DFT calculations of stress and its influence on equilibrium dopant concentrations that predict extremely large enhancements with biaxial stress from film/substrate misfit on the order of 1% [2]. Higher equilibrium solubility reduces the fraction of implanted dopant atoms that are in clusters and precipitates, and hence electrically inactive.

Another technique for doping at high concentrations is to deposit Si together with the dopant by chemical vapor deposition (CVD), or by co-deposition during molecular beam epitaxy (MBE) of silicon. In this way, the dopant is inserted without the need for energetic collisions with the Si crystal lattice. Therefore very little diffusion of dopant atoms or defects occurs, reducing the opportunity to form clusters and precipitates. The incorporation of impurities during deposition is strongly enhanced by surface segregation, and for this reason we will examine the energies of several dopant atoms in the vicinity of the surface.

2 STRESS AND B SOLUBILITY

During the past two decades much attention has been directed towards the study of the electronic properties of strained Si, as it has become possible to grow epitaxial interfaces between lattice mismatched materials; e.g. Si/Si_{1-x}Ge_x heterostructures [3]. The Si-B binary phase diagram indicates that for temperatures lower than 1200°C, the solid solubility of B in Si is smaller than 1 atomic percent [4]. Beyond this concentration, the excess B atoms form precipitates of the so-called SiB₃ phase. This phase has a complicated structure based on distorted boron-rich icosohedral clusters [4]. Assuming that the B concentration is dilute, the phase boundary between the bulk Si and SiB₃ phases is expressed as

$$[B]_{\max} = A \exp\{ -(\Delta E_B - \mu_B - E_F)/kT\},$$

where $\mu_B = [E(B_3Si) - E(Si)]/3$, and $[B]_{\max}$ is the maximum soluble B concentration in Si, E_B is the energy of an isolated negatively charged B impurity, $E(B_3Si)$ and $E(Si)$ are the total energies per atom of the B₃Si and pure Si phases respectively, and A is a temperature independent prefactor which includes the vibrational entropy. The explicit appearance of the Fermi level E_F is due to the charge of the B

impurity. At finite temperatures, however, E_F depends on the dopant concentration, and we can derive the expression

$$[B]_{\max} = \sqrt{An_i(T)} \exp \left\{ -(\Delta E_B - \mu_B - E_{mid})/2kT \right\}$$

where n_i is the intrinsic carrier concentration and E_{mid} is the level at midgap [2].

We calculate the terms in the exponential in the above equation from first principles using the VASP plane-wave pseudopotential code [5] with Vanderbilt's ultrasoft pseudopotentials [6], supplied by G. Kresse and J. Hafner [7]. To calculate ΔE_B , we use a 128 atom supercell. The experimental ESL of B over the range 900° to 1325°C, exhibits Arrhenius behavior, i.e. $[B] \propto \exp(-E/kT)$, where $E = 0.73 \pm 0.04$ eV [8]. We can thus neglect the variation with strain of A and the chemical potential μ_B , in expression for $[B]_{\max}$ above.

Figure 1a depicts the change in ΔE_B and E_{mid} with bi-axial strain. It is shown that both these quantities depend linearly upon strain in such a way as to raise the B solubility for $\varepsilon < 0$. But the change in E_{mid} with strain is an order of magnitude larger than the change in ΔE_B . Hence the strain dependence of the solubility of B in Si is determined to a large extent by the explicit response of the Si band structure to shear stress.

Figure 1 shows both GW and LDA results for the strain dependence of E_g and E_{mid} , from which we can conclude that LDA is very accurate for the strain dependence of the band structure of Si, in spite of its failure to correctly predict the Si band gap at equilibrium.

The intrinsic carrier concentration n_i in Si can be written as $n_i(T, \varepsilon) = \rho(T, \varepsilon) \exp(E_g/2 kT)$, where $\rho(T, \varepsilon)$ is a well-known function of the electronic density-of-states of Si, near the top of the valence band and the bottom of the conduction band.

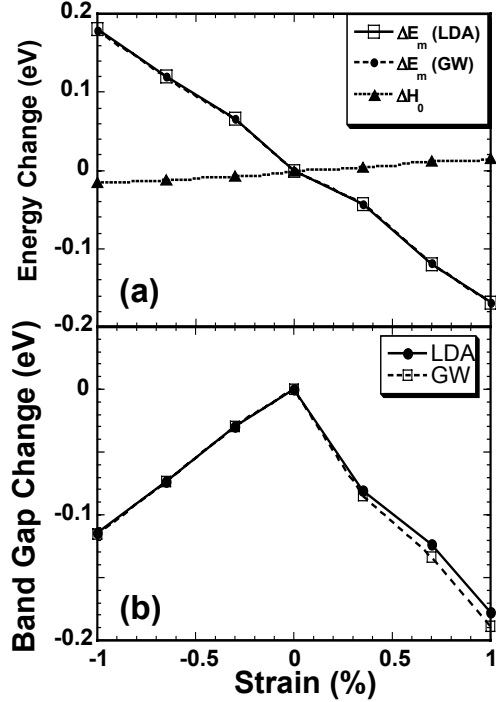


Figure 1. (a) shows the strain dependence of E_{mid} as well as ΔE_B . (b) shows the strain dependence of the band gap. All energies are relative to the cubic phase.

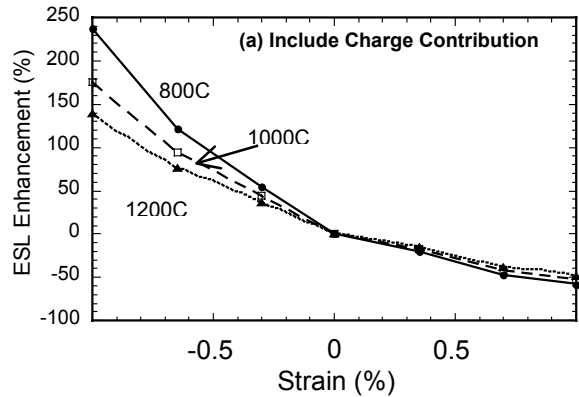


Figure 2. The enhancement of the solubility of boron as a function of strain at three temperatures.

From the above equation for $[B]_{\max}$ we can now calculate the strain dependence of the B solubility in Si (see Fig. 2a). We find that compressive bi-axial strain enhances the ESL of B dramatically. A 1% reduction in a_{parallel} can raise $[B]_{\max}$ by more than 150% at 1000°C. This is a remarkable result. Calculations were performed omitting the dependence of the Fermi level on the strain, and these showed a mere 15% increase in the

ESL at 1000°C, with 1% bi-axial compression. The opposite effect is expected for positively charged dopants such as As, where tensile strain would be expected to increase solubility.

3 SEGREGATION OF DOPANTS

Though the solubility limit of carbon in Si is only about $3 \times 10^{17} \text{ cm}^{-3}$ [9], films have been grown using MBE having concentrations as high as 10^{22} cm^{-3} , or 20% [10]. Tersoff used an empirical potential to examine a possible explanation for this based upon an increased solid solubility near the surface, which is frozen in as the film grows [11]. He predicted an equilibrium concentration limit near the surface of around $3 \times 10^{21} \text{ cm}^{-3}$, close to the MBE value above.

Crystal growth is inherently a non-equilibrium process, and trapping of a species at concentrations far above its maximum equilibrium value is always possible. The amount trapped will depend on the rate of crystal growth compared to the rate at which the impurity can diffuse away from the moving crystal surface. During MBE growth of Si with the co-deposition of dopant atoms, diffusion away from the surface is difficult or nearly impossible, since the evaporation rate for most dopants is small. Either they accumulate on the surface, or they are trapped in the growing crystal.

A high concentration of dopant present at the surface increases the probability for dopant incorporation at advancing step edges. The energies of dopant atoms in sites near the surface can play an important role in trapping. Relatively low energies in these sites permit the large surface accumulation of dopant atoms to become incorporated at high concentrations in this region. Then, as the crystal grows, and the potential energies of the dopant atoms increase, their ability to hop to lower energy sites closer to the surface is impeded by the presence of several crystalline layers. Dopants with the lowest energies in these sites are expected to exhibit the highest supersaturations in the crystal.

We have calculated the energies of atoms at the surface sites by similar methods to those described above. A 4x4x7 slab of silicon was

modeled, using periodic boundary conditions in the lateral directions (see Fig. 3).

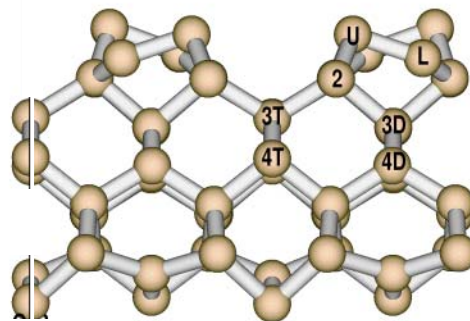


Figure 3. Atomic sites near the surface of a Si crystal. U and L are the upper and lower atoms of the tilted surface dimer, 2 indicates atoms in the second layer, 3T and 4T the third and fourth layer sites below the trench, and 3D and 4D are the sites below the dimer.

Energies obtained for dopant atoms in sites near the surface are shown in Fig. 4. The symbols indicate the sites marked in Fig. 3. We will discuss the differences in the behavior of the different dopant atoms in a forthcoming publication, together with comparisons with MBE data on trapping in excess of equilibrium solubilities. But the tendency to segregate at near-surface sites is common to all four dopants. It may be significant that the highest concentration relative to bulk Si solubility is found for MBE growth of C co-deposited with Si, since C has low energy surface sites, as seen in Fig. 4.

4 CONCLUSIONS

We have investigated two techniques to increase dopant concentrations in Si. The first involves ion-implanting B atoms into a strained layer of Si, grown epitaxially on the (001) surface of a slightly smaller pseudomorphic compound, such as ZnS. We attribute this effect largely to the charge of the B impurity in Si.

The second approach is to co-deposit silicon with the dopant atoms, using CVD or MBE methods. Dopant atoms may be trapped in the growing crystal at concentrations up to five orders of magnitude greater than their equilibrium solubility. We examined segregation of the dopant at sites near the surface of the crystal, and found some sites near

the surface where the concentration of the impurity would be enhanced by several orders of magnitude. Tersoff's results showing that there is a tendency for dopants to segregate in this region is qualitatively correct, although the various dopant species have very different behavior [11]. Strong segregation implies that a large dopant concentration is in the region being encompassed by the growing crystal, therefore likely to be trapped.

Acknowledgments

This work was supported by the Office of Basic Energy Sciences, Division of Materials Science, U.S. Department of Energy, and was performed under the auspices of the U.S. Department of Energy by the University of California, Lawrence Livermore National Laboratory under Contract No. W-7405-Eng-48.

REFERENCES

- [1] T. E. Haynes, ed., "Defects and Diffusion in Silicon Tehcnology", MRS Bull. **25**, (6) 2000, pp. 14-50.
- [2] B. Sadigh, T. J. Lenosky, M.-J. Caturla, A. A. Quong, L. X. Benedict, and T. Diaz de la Rubia, Appl. Phys. Lett. **80**, 4738 (2002)
- [3] M. M. Rieger and P. Vogel, Phys. Rev. B **48**, 14276 (1993), and S. E. Laux, J. Appl. Phys. **80**, 2234 (1996).
- [4] R. W. Olesinski and G. J. Abbaschian, Bull Alloy Phase Diagrams **5**, 478 !984).
- [5] G. Kresse and J. Hafner, Phys. Rev. B **47**, 558 (1993); G. Kresse and J. Furthmuller, Comput. Mater. Sci **6**, 15 (1996), .
- [6] D. Vanderbilt, Phys. Rev. B **41**, 7892 (1990).
- [7] G. Kresse and J. Hafner, J. Phys.: Condens. Matter **6**, 8245 (1994)
- [8] A. Armigliato, D. Nobii, P. Ostoja, M. Servidori, and S. Solmi, Semiconductor Silicon, Proc. Series P.V. 77-2 (Electrochemical Society, Princeton, 1977), pp. 638
- [9] O. Madelung, ed., Physics of Group IV Elements and III-V compounds, vol. 17a (Springer-Verlag, 1982).
- [10] H. Rucker, M. Mdthfessel, E. Bugiel, and H. J. Osten, Phys. Rev. Lett. **72**, 3578 (1994).
- [11] J. Tersoff, Phys. Rev. Lett. **74**, 5080 (1995).

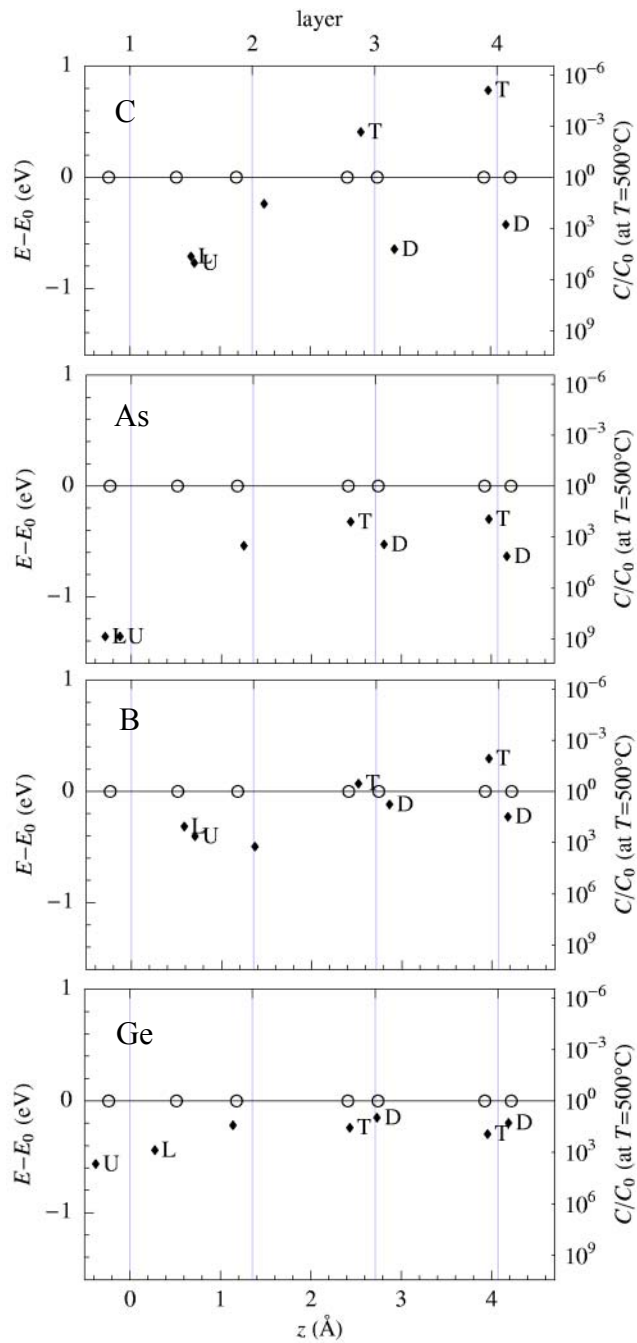


Figure 4. Energies of substitutional dopant atoms in sites near the surface, relative to their energies in the bulk Si. See Fig. 3 for identification of the sites corresponding to the symbols.

solar-grade silicon by a direct route based on carbothermic reduction of silica: requirements and production technology.

L.J. Geerligs⁽¹⁾, G.P. Wyers⁽¹⁾, R. Jensen⁽²⁾, O. Raaness⁽²⁾, A.N. Waernes⁽²⁾, S. Santén⁽³⁾, A. Reinink⁽⁴⁾, and B. Wiersma⁽⁴⁾.

⁽¹⁾Energy research Centre of the Netherlands (ECN); ⁽²⁾Sintef Materials Technology, Norway; ⁽³⁾ScanArc Plasma Technologies AB, Sweden; ⁽⁴⁾Sunergy BV, Netherlands. Email: solsic@ecn.nl

Abstract

In the European projects SOLSILC and SPURT, a process is developed for the production of solar grade silicon (SOG-Si) by carbothermic reduction of silica, based on very pure raw materials. The purity of the raw materials greatly reduces the requirements on purification of the silicon, from dopants and other impurities. This paper reports the technology used for the Si production, which is suitable for the available high purity silica and carbon materials. It also reports results from the carbon removal process, which brings the carbon content of the silicon from several hundred ppmw to below 5 ppmw. Finally, it discusses experiments on the allowable impurity concentrations in SOG-Si feedstock for directional solidification. Segregation observed during directional solidification is better than previously published, and allowable concentrations of Fe and Ti are similar to what was previously published for monocrystalline material by Westinghouse Corp.

1. Introduction

The amount of feedstock required for silicon solar cells is increasing by several thousand metric tons per year. The two present sources of silicon for PV are limited: reject and waste silicon from the electronics industry is about constant and limited to 3000 mt/a, and the excess production capacity in the same industry is presently 10000 mt/a but expected to disappear in a few years. Therefore, around 2004 one or more sources of dedicated “solar grade silicon” (SOG-Si) must be available. Nevertheless, firm plans for large scale SOG-Si production plants have not yet been announced.

There are two main approaches towards the production of SOG-Si: i) try to make the production and purification of (halo)silane precursor gasses and their pyrolytic decomposition into high-purity Si as low-cost as possible, or ii) try to produce Si by inherently low-cost metallurgical procedures – for example, carbothermic reduction of quartz.

In the SOLSILC and SPURT projects, we are developing the production of SOG-Si by carbothermic reduction of silica, based on very pure raw materials. The purity of the raw materials greatly reduces the requirements on purification of the silicon, from dopants and other impurities. We have developed, at pilot scale, a Si production technology suitable for the available high purity silica and carbon materials. We have developed, at lab scale, a carbon removal process, which brings the carbon content of the silicon from several hundred ppmw to below 5 ppmw. We are in the process of optimising and scaling up this technology. The price goal is below 20 €/kg.

2. The SOLSILC Si production process

The idea of using high-purity raw materials for production of solar grade silicon by carbothermic reduction has been followed before by several groups¹. There are several ways in which the Si production in SOLSILC differs from these previous efforts. First, the SOLSILC route is the first to use both high purity quartz from natural sources as well as high purity carbon black, combined together in one process. In all previous work, either for at least one of the raw materials the purity was in fact not sufficient, or elaborate and probably costly purification methods were used (Table 1).

	SiO ₂	carbon
SOLSILC	cleaned powder from natural quartz	high-purity gas black
Dow Corning	lumpy quartz	oil black
Siemens	molten+fibre leached quartz	leached oil black
Kawasaki	leached water glass	gas black
Heliosil	sand/lumpy quartz	carbon black

Table 1. Raw material characteristics of “direct reduction” projects.¹

The result of the SOLSILC approach is that for acceptable costs, the impurity content of the raw materials is compatible with application as feedstock for ingot production. For the first time, raw materials are combined which have dopant (B, P) impurity levels below 1 ppm, and other contaminants in the 1-10 ppm range.

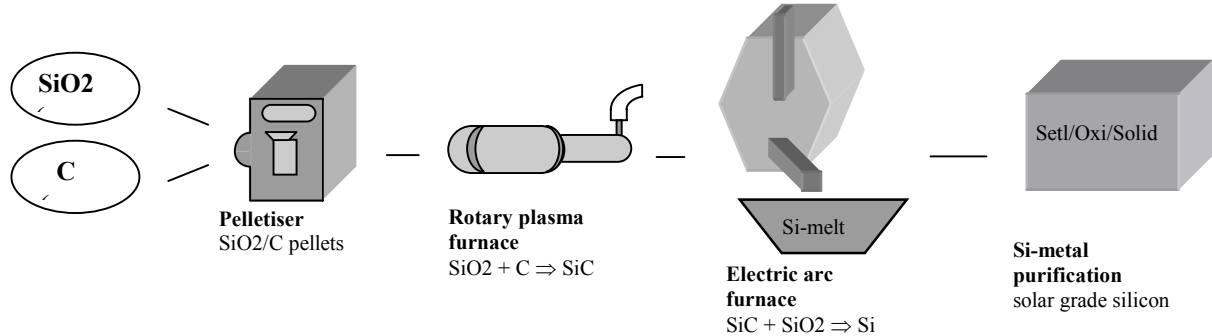


Fig. 1. Schematic process sequence of production of solar grade silicon in SOLSILC.

The second main difference of the SOLSILC Si production with previous attempts is the use of a two-step process (Fig. 1). Conventional Si production takes place in a submerged arc furnace, where the use of lumpy materials allows for the high gas flow rates (of CO and SiO) which occur during the process. High-purity raw materials in powdered form, however, have to be pelletized and are then less suitable for this conventional process. Consequently, the Si production has been separated in two process steps, the first producing SiC in a rotary plasma furnace (at Sintef, ref.²), and the second producing Si from this SiC in a submerged arc furnace (at ScanArc). Both these processes have been operated successfully, with the high-purity raw materials, at pilot scale. Within the available accuracy of chemical analysis (1-10 ppm) the first step does not add significant quantities of contamination. The submerged arc furnace and its environment are presently being upgraded for clean operation, to verify the same important issue for the second step of the process.

3. The Si purification

The liquid silicon which is produced by carbothermic reduction at high temperature (up to 2000 °C) contains a high concentration of dissolved carbon, usually several hundreds of ppm. Virtually all of this carbon has to be removed to make the Si suitable for ingot production. In the past this problem was tackled with a variety of techniques, varying from, e.g., plasma treatment to directional solidification.

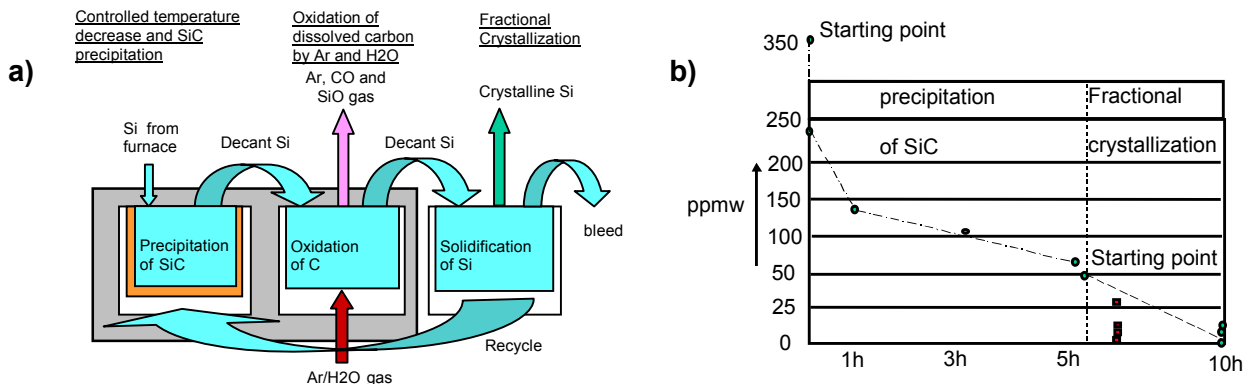


Fig. 2 a) process for carbon removal. b) results.

Fig. 2a shows the approach to carbon removal in the SOLSILC process. First, during a controlled cool-down the excess carbon is precipitated as SiC and separated. This results in Si saturated with carbon at the melting point (~70 ppmw). Next, by a combination of oxidative melt treatment and solidification, the carbon is reduced to less than 5 ppmw. Fig. 2b shows results. Typical carbon concentrations which have been obtained in the final Si are \leq 3 ppmw with a yield of 70%.

4. Evaluation of purity and requirements

The Si produced via the SOLSILC route is meant to be suitable as feedstock for directional solidification or Cz growth (after remelting, the material would also be suitable for ribbon growth). Contamination from the quartz and carbon black can be up to the 1-10 ppm level, whereas the limits allowed in Si wafers are around the 1 ppb level or lower. Hence, the segregation of contaminants to the liquid phase which occurs during directional solidification (DS) is essential in order to produce solar grade ingots. Equilibrium segregation coefficients have been listed, for example, by Hopkins or Schei et al.³. The actual segregation approaches these values closely during Cz growth, but may be different for DS of mc ingots.

To investigate this problem systematically, we have produced a number of purposefully contaminated ingots (similar to older work⁴). The feedstock for these ingots was electronic grade silicon doped with varying combinations and concentrations of contaminants either to simulate the quartz and carbon raw materials, or to provide model ingots for segregation and sensitivity studies of particular impurities. The ingots of ~10 kg were grown in a Bridgman-type directional solidification furnace at Sintef, according to industry-like procedures. The ingots were wafered by HCT AG and processed to solar cells in the industry-type process line at ECN⁵.

Fig. 3a shows short circuit current density for two ingots: one made from electronic grade silicon, and one with 10 ppmw Ti added to the Si feedstock for a Ti-sensitivity study. Fig. 3b shows the FeB profile⁶ in the uncontaminated ingot. With these ingots, the effective segregation during DS, and the effect of Ti and Fe on solar cell properties was estimated.

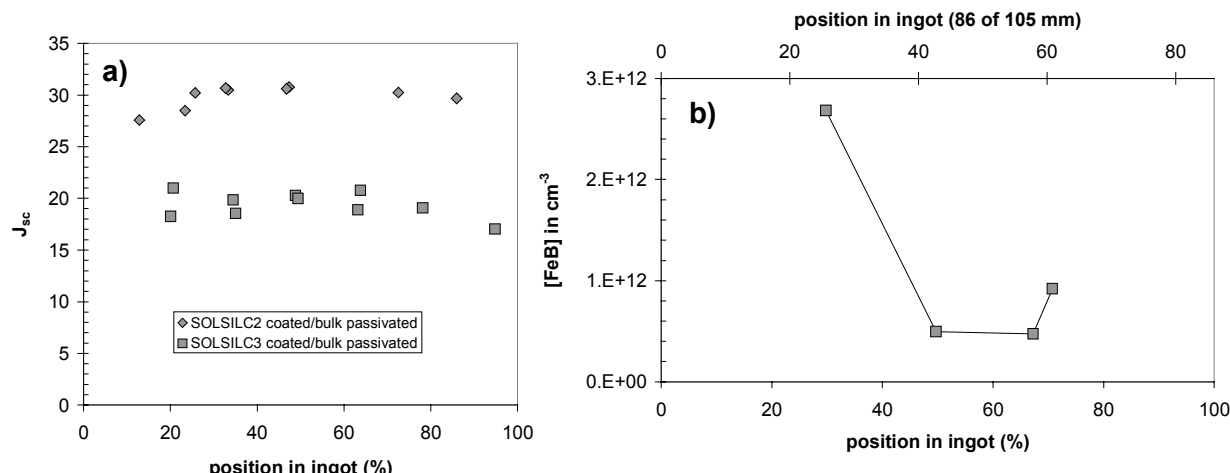


Fig. 3 a) J_{sc} in mA/cm^2 for uncontaminated feedstock (SOLSILC2, diamonds) and feedstock contaminated with 10 ppmw Ti (SOLSILC3, squares). b) FeB concentration in the uncontaminated ingot SOLSILC2 from lifetime measurements.

DLTS⁷ measurements of the Ti-contaminated ingot showed a number of traps, with concentrations of approx. $1\text{-}3 \cdot 10^{13} \text{ cm}^{-3}$. Unfortunately the oxygen content in this ingot was high due to air leak-in during growth, but because oxygen traps are usually not visible in DLTS in p-type material, we attribute the traps to 0.34-1 ppbw of Ti. The effective segregation coefficient then follows to be approx. 10^{-4} , decreasing to $2 \cdot 10^{-5} \text{ cm}$ as growth proceeds and gets slower. For comparison, the equilibrium segregation coefficient of Ti is $2 \cdot 10^{-6}$. In agreement with DLTS, chemical analysis could not detect Ti within the detection limit of 20 ppbw.

The $I_{sc}V_{oc}$ product of the cells from the Ti-contaminated ingot was 60% relative to uncontaminated reference cells. The work by Hopkins et al.⁸ reported a decrease to 60% relative efficiency for 1.7 ppbw Ti. Hence, these results do, at least, not disagree with each other. Another ingot from feedstock with 10 ppmw Ti as the main impurity and without the accidental oxygen contamination resulted in an $I_{sc}V_{oc}$ product between 70% and 80% relative to uncontaminated cells.

The Fe in the uncontaminated ingot is due to solid state diffusion from crucible and segregated material in the top of the ingot. There are just four data points in Fig. 4b but the magnitude as well as the shape of the profile are also found

systematically in commercial material.⁹ A wafer at 90% of ingot length had such low lifetime ($0.3 \mu\text{s}$) that the concentration of FeB could not be determined reliably. Judging from the lifetime it was several times 10^{13} cm^{-3} . These Fe-contaminated wafers were used to assess the effect of Fe on cell efficiency. The wafers in Fig. 4b with FeB up to $3 \cdot 10^{12} \text{ cm}^{-3}$ showed no significant reduction of cell performance. For the wafer at 90% position the efficiency reduction is at most $\sim 5\%$ relative. Again this is in rough agreement with Hopkins.

5. Discussion and conclusions

Finally, we conclude on some implications for solar grade silicon feedstock. From DLTS it appears that the segregation of Ti in directional solidification is very good, much better than the sparse reports in literature¹⁰ suggest. We also conclude that the model curves from Hopkins so far give a reasonable prediction also for present-day mc material and processing.

If we assume that the ratio of effective to equilibrium segregation coefficient for Fe will be the same as for Ti, this leads to the following requirement for feedstock for DS¹¹:

max allowable loss in cell efficiency (% relative)	impurity upper limits, in ppmw in feedstock	
	Ti	Fe
2 %	0.07	2.5
5%	0.2	8
10 %	0.4	25

Table 2. Tentative requirements for Fe and Ti in SOG-Si feedstock for mc ingot growth

Acknowledgements

This work was supported by the EU under contract nos. ERKG-1999-00005 and ENK6-CT-2001-30006, and by Novem under project nos. 146.110-020.1 and 0146-00-51-10-0018.

We gratefully acknowledge HCT AG for wafering our research ingots, NTNU and Øyvind Mjøs for assistance in production of the ingots and useful discussions, and the staff of ECN for cell production and characterisation. LJG would like to acknowledge discussions and input from the EU Sahara project.

References

-
- ¹ L.P. Hunt and V.D. Dosaj, 2nd European PVSEC, p. 98 (1979); H.A. Aulich et al., Proc. ECS vol. 86-1, p. 443 (1986); F. Aratani et al., 9th European PVSEC p. 462 (1989); M. Rustioni et al., Proc. flat-plate solar array project workshop on low-cost silicon, JPL-PUB-86-11, p. 297 (1986), and other papers therein.
- ² O.Raaness, R.Jensen, A. Arnstein Løvsland: Plasma Rotary Furnace. Norwegian patent 970735 18 February 1997.
- ³ R.H. Hopkins, Proc. flat-plate solar array project workshop on low-cost silicon, JPL-PUB-86-11, p. 15 (1986); A. Schei, J.Kr. Tuset, and H. Tveit, *Production of High Silicon Alloys* (Tapir Forlag, Trondheim, 1998).
- ⁴ R.H. Hopkins, in ref. 3; J. Fally et al., Revue Phys. Appl. 22, 529 (1987).
- ⁵ SiN_x ARC and firing-through of metallisation
- ⁶ determined by lifetime change after light soaking, see L.J. Geerligs, these proceedings, and references therein.
- ⁷ deep level transient spectroscopy
- ⁸ R.H. Hopkins, in ref. 3.
- ⁹ L.J. Geerligs, these proceedings
- ¹⁰ e.g., C.P. Khattak and F. Schmid, in *Silicon processing for photovoltaics II*, p. 285 (1987); N. Yuge et al., 11th Int. PVSEC, technical digest p. 115 (1999); M. Rustioni in ref 1.
- ¹¹ if, of course, the DS is comparable to the situation in the Crystalox furnace which we used in our experiments

RAPID ANODIC OXIDATION FOR DEPTH PROFILING OF SILICON

Oleg V. Sulima, Ralf Jonczyk, Neil L. Kirpalani, Puthur D. Paulson*, Sarbjit Datta, James A. Rand

AstroPower, Inc., Solar Park, Newark, DE, 19716-2000

**Institute of Energy Conversion, 451 Wyoming Road, Newark, DE. 19716-3820*

Abstract. A rapid anodic oxidation process was developed for precise iterative thinning of Si layers. After optimization of the electrolyte and oxidation parameters, a homogenous 100-nm thick oxide was formed within 6 min at 150V. Doping profiles were determined by measuring sheet resistance in samples that were intermittently thinned by anodic oxidation.

INTRODUCTION

Measurement of doping profiles in Si devices is extremely important to develop new and control current technological processes. The most commonly used methods to determine doping profiles in Si are Secondary Ion Mass Spectroscopy (SIMS), electrochemical CV-profiling (ECVP) and spreading resistance analysis (SRA) on beveled surfaces. These methods require complicated and expensive equipment and time-consuming sample preparation: polishing for SIMS and ECVP, beveling for SRA. Moreover, SIMS cannot measure the distribution of electrical carriers, both SIMS and ECVP are limited to very small areas, and SRA is only suitable for materials with a uniform planar impurity distribution.

It is, however, often necessary to measure Si samples having a rough surface and/or macro planar heterogeneity of the carrier distribution, as for example poly- or multicrystalline Si wafers or sheets for solar cells. For this type of material one can use the four-point probe method similar to SRA on beveled surfaces. Obviously, for planar depth profiling, a reproducible thinning of the analyzed material is required. Theoretically, a very stable and slow chemical etching process can be used. Practically, however, this is not possible due to the uncontrolled etching rate at surfaces composed of multiple grains and having a complicated relief structure.

Perhaps the best and the simplest solution for this case, is anodic oxidation of the Si surface followed by selective oxide etching. Anodic oxidation is reproducible, planar, orientation independent, and is practically independent on conductivity type as well as doping concentration. Also, it does not require complicated equipment. The main problem with anodic oxidation is a relatively long time (about an hour) necessary to form a reasonably thick oxide (about 100 nm) using electrolytes cited in the literature [1]. This work was aimed at developing of faster anodic oxidation through optimization of chemical composition of electrolytes and oxidation regime (applied voltage and final current).

EXPERIMENTAL

The setup for anodic oxidation is shown in Fig.1. 40 x 40 mm² Si wafers with p- or n-type surface layers and different surface morphologies were used in this work.

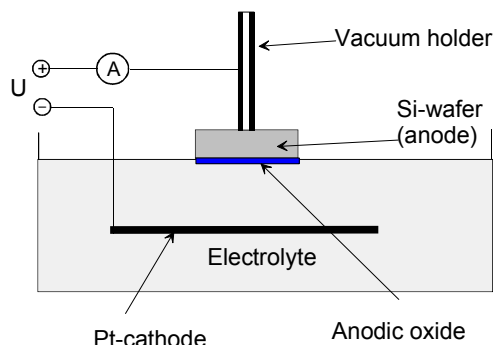


Fig. 1 Setup for anodic oxidation.

The sample is held with metal vacuum tweezers from the backside. The front side of the sample is exposed to the electrolyte. Special precautions have to be taken to avoid the electrolyte creeping towards the vacuum tweezers on the backside of the sample such as often occurs when a high electrostatic field is applied.

Prior to anodic oxidation the wafers were cleaned using HF and dried with nitrogen. No visible residual layers were observed on the surface of the wafers after this cleaning. Anodic oxidation was performed in electrolytes with the following components:

- (i) A component to provide a suitable ionic conduction in the electrolyte. In this work we studied a concentrated HNO_3 , 5 % tartaric acid aqueous solution, as well as nonaqueous (0.04N) solutions of KNO_3 or NH_4NO_3 .
- (ii) A component to decrease the dissolution of the anodic oxide. In this work ethylene glycol (EG) was used.
- (iii) A catalyst to accelerate the process of oxidation (optionally). Tungsten was used in this work.

The anodic oxidation process consisted of two parts (Fig.2): (a) a galvanostatic part (within 6 min in the optimized electrolyte) with a constant current density (J_0) and increasing voltage from 0 V to V_A , and (b) a potentiostatic part with a constant applied voltage (V_A) and a current density falling from J_0 to the final value J_f .

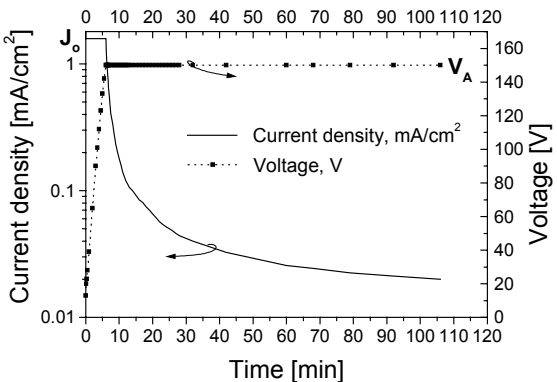


Fig.2 Current density and voltage vs. oxidation time in a (0.04N)- NH_4NO_3 : EG electrolyte with tungsten. 150 V is applied.

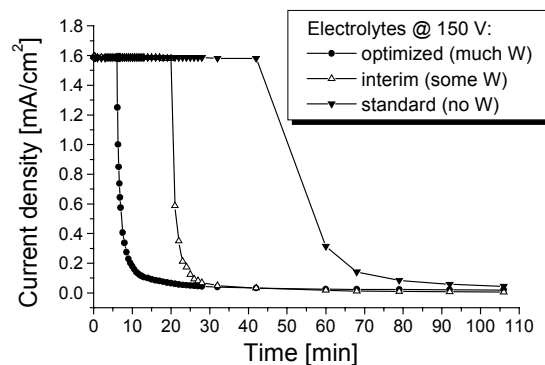


Fig.3 Current density vs. oxidation time at 150 V in a (0.04N)- NH_4NO_3 : EG electrolyte showing the effects of including different amounts of diluted tungsten.

An important criterion for anodic oxidation, is the duration of the galvanostatic part. The drop in current indicates that formation of a continuous oxide film on the surface is complete. Though the oxide film continues to grow at lower currents, the growth rate decreases substantially. Also, as it was determined for anodic oxidation of GaSb [2], a lower J_f is advantageous for homogeneity of the oxide. However in this work, the homogeneity of the Si oxide after the end of the galvanostatic part was good (at least by a visual control), and we terminated the oxidation process at this point.

After preliminary experiments without tungsten, we found that an electrolyte consisting of nonaqueous (0.04 N) solution of NH_4NO_3 in ethylene glycol provides the shortest galvanostatic part compared to electrolytes using HNO_3 , KNO_3 or tartaric acid. Therefore, this electrolyte was chosen as the basis for further studies. In the text below this electrolyte is referred as “standard”.

Fig. 3 displays the influence of diluting tungsten in the standard electrolyte on the oxidation process. The galvanostatic part in the standard electrolyte is reduced from 42 minutes to 6 minutes. The relative change of tungsten in the electrolytes was determined by Inductively Coupled Plasma Optical Emission Spectroscopy (ICP-OES). One can assume that tungsten works as a catalyst accelerating the process of oxidation.

To determine the oxide thickness on polished Si wafers, spectroscopic ellipsometry measurements were carried out using a J.A. Woollam Variable Angle Spectroscopic Ellipsometer. For thinning of Si, however, not only the oxide thickness but also the amount of consumed silicon is important. The thickness of consumed Si was determined by performing a local oxidation, selective anodic oxide etching and measuring the step height between oxidized and no-oxidized parts. This thickness was found to be approximately 50 % of the oxide thickness.

Voltage applied to the sample is the main parameter determining the thickness of the anodic oxide. The higher the voltage, the thicker the oxide. In general, anodic oxidation of Si is characterized by a relatively small thickness/voltage ratio of oxidation (several Ångströms per Volt) that is advantageous to study very thin layers. However, the process becomes time consuming when micron or more thick layers have to be

studied. Many oxidation steps are necessary in this case because application of high voltage (>200 - 250 V) and thus using of larger steps is technically difficult. As it is shown below, not only the oxide thickness, but also the oxidation rate depends on applied voltage. Unfortunately, the oxidation rate decreases with voltage. Thus oxidation at high voltages results in thicker oxide layers, but the time involved might be unreasonably large.

Fig.4 shows that the galvanostatic part of the oxidation process increases with applied voltage. The thickness/voltage ratio measured at the end of the galvanostatic part was determined to be approximately 0.6 nm/V. As the duration of the galvanostatic part increases with the voltage, the growth rate of the oxide falls. Fig.5 demonstrates that the oxidation rate at 250 V is only one third of that at 100 V.

This is important to consider in developing a Si-thinning process. For example, what is better for oxidation of 450 nm of Si: to make (i) less low-rate long-time high-voltage oxidations or (ii) more high-efficiency short-time low-voltage ones? To oxidize 450 nm one needs to apply 450 nm / 0.6 nm/V = 750 V. This voltage can be composed from three 250 V (method A), five 150 V (method B) or ten 75 V (method C) oxidations.

Let us assume that the post-oxidation processing that includes selective etching of the anodic oxide, rinsing, drying and adjustment for the new oxidation requires 5 min. According to Fig.5, three 250 V oxidations will last $3 \times 23 = 69$ min, five 150 V oxidations – $5 \times 6 = 30$ min and ten 75 V oxidation – $10 \times 2.4 = 24$ min. As method A requires three post-oxidation processes, the total process time is $15 + 69 = 84$ min. For method B which requires 5 post-oxidation processes, only $25 + 30 = 55$ min will be necessary. Though oxidations in method C require the least time, 10 post-oxidation processes are necessary making the total time of $50 + 24 = 74$ minutes. Thus method B is optimal for the above example. In this work, the voltage of 150 V was normally used for the depth profiling.

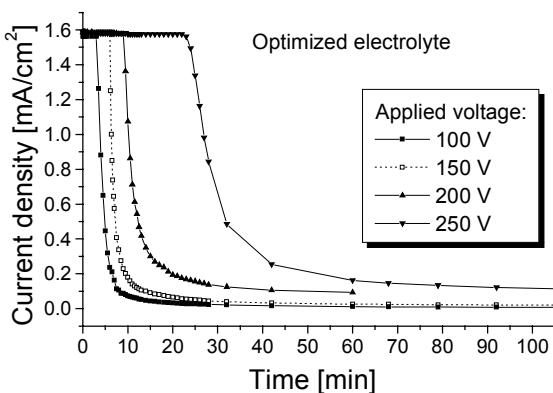


Fig.4 Current density vs. oxidation time in an optimized (0.04N)-NH₄NO₃ : EG electrolyte at different voltages.

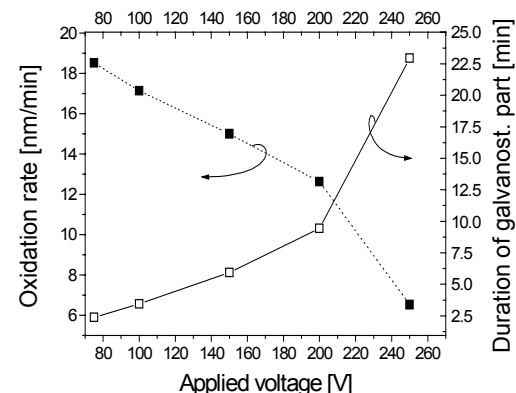


Fig.5 Duration of the galvanostatic part and oxidation rate vs. applied voltage in an optimized (0.04N)-NH₄NO₃ : EG electrolyte.

SHEET RESISTANCE AND DOPING PROFILING IN SILICON

Diffused emitters formed by phosphorous or boron diffusion into p- or n-type Si, respectively, were studied by the above-described method. Four-probe measurements were carried out after each oxidation/etching step. Figure 6 shows an example of the sheet resistance profile of an n-type B-diffused emitter with a surface roughness of about 5 - 10 μm . As the highly doped layers near the surface are removed during the oxidation/etching, the sheet resistance increases. A sharp drop in resistance is observed when the base layer is reached, thus showing the position of the pn-junction. This was verified by measuring the polarity of the sample with a thermoelectric probe. Similar profiles were obtained for single crystal and polycrystalline P-diffused emitters with a surface roughness of about 5 - 10 μm and 50 - 60 μm , respectively.

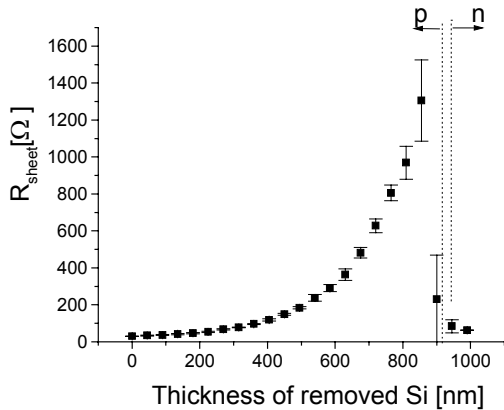


Fig.6 Distribution of sheet resistance in a boron-diffused layer obtained by means of the anodic oxidation depth profiling. 6-min long steps at 150 V were used.

The resistivity ρ_i of the layer removed at an i -step can be calculated as follows: $\rho_i = \left(\frac{1}{R_i} - \frac{1}{R_{i-1}} \right) \Delta h$,

where R_i is sheet resistance of the layer removed at an i -step and Δh is a thickness of the removed layer (45 nm in our case). To determine the concentration of holes or electrons in the layers from ρ_i values, one can use the Solecon calculator [3] that is based on carrier mobility values derived by W. Thurber et al.

To check the accuracy of the above-described method, some samples were measured by means of anodic oxidation depth profiling and electrochemical CV-profiling. The latter was performed using the newest CVP21 profiler from Dage Electronic Europa-Vertriebs GmbH [4]. Both methods showed practically the same depth of the pn-junction (about 600 nm) and a good match in carrier concentration (Fig. 6).

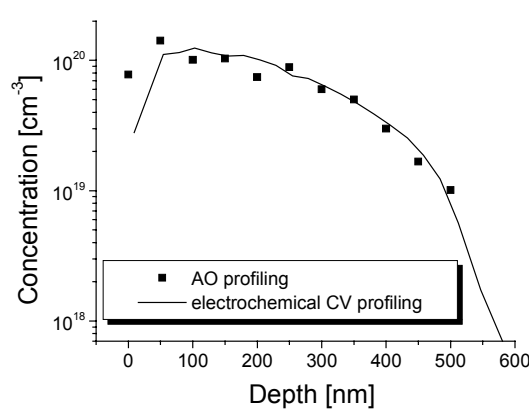


Fig.7 Carrier concentration in a boron-diffused layer (different from shown in Fig 6) determined by means of the electrochemical CV and anodic oxidation depth profiling.

CONCLUSIONS

A rapid anodic oxidation process of silicon was developed. Due to optimization of the electrolyte and oxidation regime, a homogenous 100-nm thick oxide was formed within 6 min at 150V. The rapid anodic oxidation can be successfully used for depth profiling of silicon wafers without complicated and expensive equipment. In addition, wafers with rough surfaces and heterogeneous distribution of doping can be studied.

ACKNOWLEDGEMENTS

The authors wish to thank T. Wolff from WEP, Furtwangen, Germany for the electrochemical CV-profiling of several samples, V. DiNetta from the Institute of Energy Conversion, Newark, Delaware for AFM measurements, as well as our colleagues from AstroPower: E. Addo and A. Tata for ICP-OES measurements, B. Grems and A. Holmes for supplying of some types of samples, M. Mauk and P. Sims for useful discussions.

REFERENCES

- [1] S.K. Sharma, B.C. Chakravarty, S.N. Singh, B.K. Das, D.C. Parashar, J.Rai, and P.K. Gupta , J. Phys. Chem. Solids, v.50 (7), 679-684 (1989)
- [2] O.V. Sulima, A.W. Bett, and J. Wagner, J.Electrochem. Soc., v.147 (5), 1910-1914 (2000)
- [3] See Web-site <http://www.solecon.com/sra/rho2ccal.htm>
- [4] See Web-site <http://www.dage.de>

DIRECT WRITE PROCESSING FOR PHOTOVOLTAIC CELLS

Tanya Rivkin, Calvin Curtis, Alex Miedaner, John Perkins, Jeff Alleman and David Ginley
National Renewable Energy Laboratory, 1617 Cole Blvd, Golden, CO 80401

ABSTRACT

Direct writing of solar cell components is an attractive processing approach. We have fabricated a 6.8% Si solar cell using silver ink based electrodes. Ohmic contact through the antireflection (AR) coating was obtained with pure Ag electrodes at 850 °C. We also report on highly conductive silver metallizations and initial results on direct-write TCO demonstrating a 100-micron spatial resolution produced by inkjet printing.

INTRODUCTION

A key issue in developing next generation photovoltaics is the ability to develop low cost production techniques and maintain or improve device quality. Ink jet printing of metalorganic (MO) and nanoparticle based inks as precursors potentially offers the ability to deposit high quality electronic materials with the desired spatial resolution [1]. Versatility in the formulation of the liquid inks allows fine tuning of the compositions and control of doping levels of the materials produced so as to optimize the device performance.

We have previously demonstrated silver layers with conductivities near bulk that were spray-printed from solutions of MO precursors and from composite MO/nanoparticulate silver precursors [2]. Using composite precursors results in much greater deposition rates. In both cases high adhesion strength to Si and to glass substrates was obtained without employing adhesion promoters such as glass frits or metallic adhesion layers.

For direct write contacts to be useful in photovoltaics applications they must form a low-resistance ohmic contact with the underlying semiconductor through any intervening layers. This requirement is especially challenging when the contact is fabricated on top of an antireflection coating such as the typically employed Si₃N₄[3]. In screen-printed contacts glass frits are incorporated in the Ag paste. These frits are believed to "burn" through the insulating layers at relatively low temperatures (~700 °C) facilitating ohmic contact between Ag and Si [4]. Analogously, nanosized glass frits could be incorporated in the Ag inks for inkjet and spray printing. In our initial experiments, however, we used pure MO-silver inks and studied the effect of high temperature annealing on contact resistance. Here we report on inkjet

and spray-printed silver contacts to Si solar cells with and without Si₃N₄ AR layers.

Transparent conducting oxides (TCO) represent another key solar cell component especially for thin film solar cells. These may also be amenable to direct write processing. MO inks or colloidal nanoparticle suspensions can be developed based on known precursors for virtually all known TCO compounds. Here we also report on initial results on the direct writing of transparent conducting oxides. ZnO and SnO₂ were successfully printed from concentrated colloidal nanoparticulate precursors. In addition, MO precursors containing both In and Sn sources were employed to directly deposit conducting ITO films.

SPRAY-PRINTED CONTACTS TO SI

Silicon substrates with a diffused p-n junction, with and without a Si₃N₄ AR layer were provided by Evergreen Solar. The substrates were briefly etched in 10% aqueous HF prior to Ag deposition. MO (MO) silver inks were prepared by dissolving 2 mol (4.2g) of silver-(hexafluoroacetylacetone)(1,5-cyclooctadiene) (Ag(hfa)COD) in 5 ml of toluene. 1.0 μm thick Ag layers were spray-printed from the Ag-MO ink onto heated substrates at 400 °C in air using a hand-held Vega 2000 airbrush. TLM grids (Figure 1) were patterned from the sprayed silver layer using photolithography and chemical etching in concentrated nitric acid.

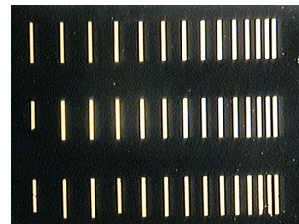


Figure 1. TLM pattern of Ag contacts fabricated on the n-type surface of Evergreen Solar material (the image is 2x).

For Si substrates without the AR coating, an ohmic contact with relatively low contact resistance of 0.4 mΩ • cm² was formed immediately during Ag deposition. For the substrates coated with silicon nitride, the Si₃N₄ dielectric layer electrically insulated the as-deposited silver contacts from Si and each other.

No current could be initiated between the contact pads by application of an external voltage up to 20 V, above which breakdown of the insulating layer was observed.

After the initial electrical testing, the samples containing AR coatings were annealed in a tube furnace in air at 600 °C, 750 °C, 800 °C and 850 °C for times ranging between 2 min and 1 hour. Due to surface tension phenomena, the originally continuous Ag layers broke into islands in the course of firing (SEM Figure 2). To form a continuous contact, another 2-micron thick layer of Ag was spray-printed on top of the already fired Ag pattern at 400°C and patterned using photoresist and etching, as before. Annealing at temperatures between 600 °C and 800 °C for a period of time from 2 minutes to 1 hour did not result in formation of ohmic contact, however the breakdown voltage for the annealed films was reduced to 1 V.

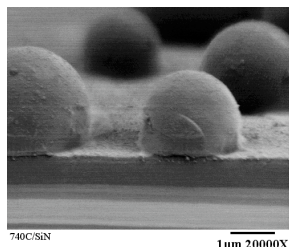


Figure 2. Ag layer breaks into isolated balls in the course of annealing at elevated temperatures

Ohmic contact between Ag and Si was obtained, however, in the samples annealed at 850 °C for times as short as 5 minutes. The best contact resistance achieved was $4 \text{ m}\Omega \cdot \text{cm}^2$. Following the contact resistance measurement, the Ag layer was removed by a prolonged etch in nitric acid, revealing the surface of the substrate under the contact. The signs of the interaction between the substrate and Ag layer were evident by microscopic examination (Figure 3).

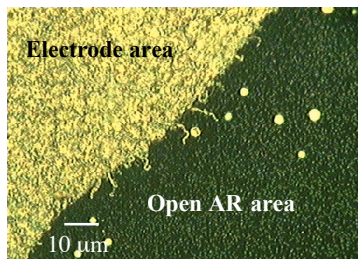


Figure 3. Optical micrograph of Ag printed on Si_3N_4 -coated Si, annealed at 850°C and then etched, showing that the ink derived Ag burned through the AR coating.

An experimental 1cm^2 solar cell was prepared with spray-printed Ag contacts. The Ag grids were fabricated in a similar fashion as the

TLM patters described above (Figure 4). The back Al contact ($1 \mu\text{m}$ thick) was deposited by e-beam evaporation after the first Ag grid was fabricated and prior to the high-temperature annealing step. The front and the back contacts were co-fired at 850 °C for ~ 10 minutes.

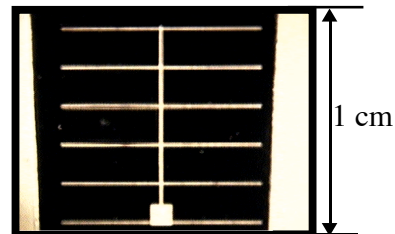


Figure 4. Si solar cell fabricated with spray-printed Ag burned through the silicon nitride layer

This resulted in simultaneous alloying and ohmic contact formation of the front and the back contacts with Si. Again, the Ag layer broke into isolated islands in the course of the annealing. A second Ag layer was spray-deposited and patterned over the original grid in order to provide continuous front contact. The performance parameters of the fabricated cell are enumerated in the Table 1.

Table 1. The performance parameters of the cell with spray-printed front contacts.

Voc	0.5476 V
Jsc	26.762 mA/cm ²
FF	46.16%
Eff	6.76%

The low fill factor (FF) is probably due to high series resistance resulting from insufficient thickness of the front and back contact metallizations. This initial experiment demonstrates the feasibility of printed Ag contacts on Si solar cells and shows significantly that the metal-organic ink is capable of burning through the AR coating to form a low-resistance ohmic contact.

INKJET-PRINTED SILVER ELECTRODES

The MO Ag inks were printed using a Microfab drop-on-demand inkjet printer. In this system the drops are stimulated at the tip of a glass capillary by an acoustic wave produced by a piezoelectric actuator. The frequency, and to some degree, the volume of the generated drops, can be controlled by an operator. Such flexibility in printing parameters helps in controlling deposition rate and resolution of a printed line. When printing parameters are optimized, the most important factors that limit the line resolution are the size of the drop-generating

orifice and the wetting properties of the ink on the surface of a substrate. Our MO Ag inks (Ag(hfa)COD in organic solvents) were printed on glass, Si and Si_3N_4 coated Si substrates using a 50 μm jet. The best line resolution (100 μm) (Figure 5) was achieved with butanol-based ink (highest viscosity solvent) printed on heated (120 $^{\circ}\text{C}$) glass substrates.

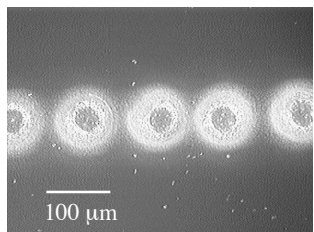


Figure 5. Individual 100 μm Ag drops printed on glass at 120 $^{\circ}\text{C}$ with the Microfab inkjet printer using Ag(hfa)(COD) /butanol ink.

The printed precursor lines turned into pure Ag during the following annealing step at 250 $^{\circ}\text{C}$ in air. The toluene-based inks demonstrate lower resolution but may be printed at temperatures above that required to decompose the precursor, thus directly producing Ag patterns without the need for postdeposition annealing (Figure 6).

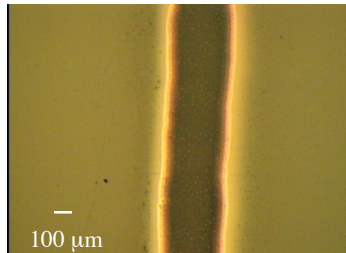


Figure 6. 300 μm wide Ag line printed on glass at 200 $^{\circ}\text{C}$ with the Microfab inkjet printer using Ag(hfa)(COD) /toluene ink.

The homogeneous MO inks are very compatible with the inkjet-printers. High quality conducting lines are produced with MO inks, but the deposition rates are rather low (300 \AA - 500 \AA per pass). Thus we are developing alternate precursors that are capable of higher deposition rates. Two approaches are currently being evaluated. One is using alternate MO precursors capable of higher solubility in suitable solvents. Second is using concentrated suspensions of Ag nanoparticles.

Applying the former approach we have attained concentrations of up to 8M of Ag with a Ag-trifluoroacetate precursor in water. This is four times higher concentration than that attained for (silver-(hexafluoroacetylacetone)(1,5-

cyclooctadiene) and should lead to deposition rates up to 2000 \AA per pass. The new concentrated ink was printable by inkjet and demonstrated pure silver deposits upon decomposition in air at 250 $^{\circ}\text{C}$. Poor wetting of the substrate by the ink in our original printing experiments led to non-uniform distribution of the printed precursor making it difficult to evaluate the average thickness of the Ag deposit. Follow-on work will focus on optimizing ink rheological properties and the substrate surface to produce uniform layers.

Key to the latter approach is stabilizing concentrated Ag suspensions. A certain degree of agglomeration would be tolerable, however aggregates with sizes greater than 5 microns would constrict the flow of the precursor through the orifice of the inkjet reducing line resolution and increasing the chance for clogging of the orifice of the inkjet. Surface stabilization of the nanoparticles with organic surfactants may alleviate the agglomeration through stabilizing the suspension of the nanoparticles. Developing stabilized nanoparticle inks has a potential to result in much greater deposition rates than the highest possible for MO precursors. Initial results with composite nanoparticulate/MO precursors of Ag have shown that it is possible to attain up to 10 μm thick layers with conductivities within factor of two of that for bulk Ag.

INKJET-PRINTED TCO

Water-based colloids of ZnO and SnO_2 from NYACOL were printed on Pyrex glass substrates at 125 $^{\circ}\text{C}$ and 800 Hz deposition rate (800 drops per second). Narrow (100 μm) and thick (5 μm) lines were printed in a single pass (Figure 7). As-printed pure ZnO and SnO_2 particulate precursors are not conductive. Annealing in a reducing atmosphere as well as introducing doping elements (such as Al for ZnO and F for SnO_2) via intermixed MO compounds will be used to control the doping level in the printed oxides. In this approach, small amounts of water-soluble MO precursors are added to the colloidal suspension. The MOD reagent is uniformly dispersed in the colloid providing a uniform supply of doping elements. When printed and annealed above the decomposition temperature of the MO precursor the dopant is free to diffuse into the oxide particles. Also during the anneal the individual particles sinter together in a conducting continuum. For nanoparticles this occurs at lower temperatures than normal because of surface energy considerations. Both reducing anneal and doping via MO will increase carrier concentrations and thus improve conductivity of the printed TCOs.

Conducting ITO films were also printed from a commercial (CHEMAT) MO ITO precursor in hexanes. 100 μm lines of the precursor were

printed at 50 - 75 °C on Pyrex glass slides. Rectangular patterns of the precursor were produced by printing individual lines with 20-micron overlap.

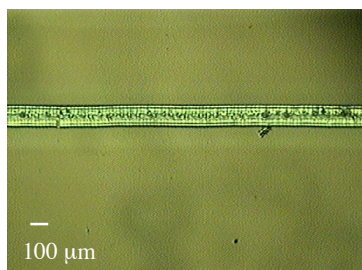


Figure 7. 100 μm SnO₂ line printed on glass at 125°C with the Microfab inkjet printer using NYACOL colloidal tin oxide precursor

The printed precursor patterns were decomposed by annealing in air at 300 °C. The solid and transparent 1000 Å thick films thus produced had a resistivity of 300 Ohm·cm. Annealing in air at 700 °C significantly improved the resistivity reducing it to 0.03 Ohm·cm. A further improvement in resistivity down to 0.004 Ohm·cm was achieved with a one-hour reducing anneal in argon at 400 °C.

With these initial experiments, we demonstrated that low resistivity transparent ITO patterns can be inkjet printed from MO precursors. Also high deposition rates and good resolution were obtained for colloidal TCO precursors.

SUMMARY

Metal contacts and transparent conducting oxide layers were printed from MO and nanoparticulate precursors. High quality materials can be achieved by printing liquid precursors under atmospheric conditions. Using direct write techniques such as inkjet printing may eliminate expensive steps of vacuum deposition, photolithography and etching, significantly reducing the cost of solar cell fabrication. In addition, the ability to control the composition of the precursors in real time can lead to tremendous flexibility in controlling the conductivity and doping levels spatially. Ink formulation and process optimization are underway to produce higher quality materials and more efficient devices by direct write techniques.

REFERENCE

1. K.F. Teng, R.W.V., *Metallization of Solar Cells with Ink Jet Printing and Silver Metallo-Organic Inks*. IEEE Transactions on Components, Hybrids, and Manufacturing Technology, 1988. **11**(3): p. 291-297.
2. C.J. Curtis, D.L.S., A. Miedaner, J. Alleman, T. Rivkin, J.D. Perkins and D.S. Ginley. *Spray and inkjet printing of hybrid nanoparticle-metal-organic inks for Ag and Cu metallizations*. in *Materials Research Society Symposium*. 2002.
3. Duerinckx, F.S., J., *Defect passivation of industrial multicrystalline solar cells based on PECVD silicon nitride*. Solar Energy Materials and Solar Cells, April, 2002. **72**(1-4).
4. Nijs, J.D., E.; Szlufcik, J.; Poortmans, J.; Frisson, L.; De Clercq, K.; Mertens, R.; Van Overstraeten, R.; Ghannam, M., *Recent improvements in the screenprinting technology and comparison with the buried contact technology by 2D-simulation*. Solar Energy Materials and Solar Cells, June, 1996. **41-42**: p. 101-117.

Effects of Dislocations on Minority Carrier Lifetime In Dislocated Float Zone Silicon

A. Karoui, R. Zhang, G. A. Rozgonyi, T. F. Ciszek*

*Materials Science and Engineering Dept.
North Carolina State University, Raleigh, NC 27695-7916*

**NREL, Golden, CO, 80401*

Abstract: We present a correlation of Microwave Photoconductance Decay minority carrier lifetime with dislocation density in high purity Float Zone silicon. Electron Beam Induced Current (EBIC) images were carefully aligned to lifetime maps and depth profiling of individual defect electrical activity was done by varying the bias of Schottky diodes. The data presented provides a relationship between lifetime variations and EBIC contrast, based on dislocation density and impurity decoration in the near surface zone.

INTRODUCTION

Although Float zone (FZ) Si ingots grown in NREL are pure and have the highest minority carrier lifetime [1], they suffer high yield losses due to breakage and mechanical failure during PV device processing. As a means to merge the benefits of both high lifetime FZ and the mechanically tougher CZ wafers, a joint NCSU/NREL program is underway using combinations of oxygen and nitrogen doping to maintain the high minority carrier lifetime, while improving the hardness by blocking dislocation movement. We report on longitudinal (parallel to growth axis) and radial changes in dislocation density and electrical activity in connection to minority carrier lifetime. Previously, dislocation "lineage" were revealed by x-ray topography (XRT) imaging and a correlation was established with Microwave Photoconductance Decay (μ PCD) carrier lifetime [2]. As expected the highest lifetimes correspond roughly to areas of lowest dislocation density. In this poster, the dislocations are examined via EBIC imaging in connection with lifetime variations due to the level of dislocation impurity content.

RESULTS AND DISCUSSION

The measured lifetime distribution in the top portion of a longitudinal slug cut from a dislocated FZ Si ingot, on which a Schottky diode array was made, is given in Fig. 1. Note that most of the lifetime distribution is between 100 to 300 μ s, while the maximum is about 400 μ s. The EBIC images in Fig. 2 were obtained with a variable bias in a region with ~170 μ s lifetime. Since the contrast of EBIC images is lowered in the bulk, see Fig. 2(d), we conclude that the dislocations in the near surface are contaminated. According to C-V measurements it appeared that the impurities introduced in the material at room temperature diffused about ~3 μ m depth down the dislocations. Impurity free "clean" silicon dislocations are not expected to act as carrier recombination centers at room temperature [3, 4] and, therefore, are not visible with room temperature EBIC. The fact that the impurities were introduced during room temperature

polishing of the surfaces limits their extent in the bulk, as verified with the variable bias EBIC. The extrinsic impurities were identified with DLTS, which showed that Fe exists at a level of $1\text{E}13$ to $2\text{E}14 \text{ cm}^{-3}$ and Cu at a level of $1\text{E}13 \text{ cm}^{-3}$ [5].

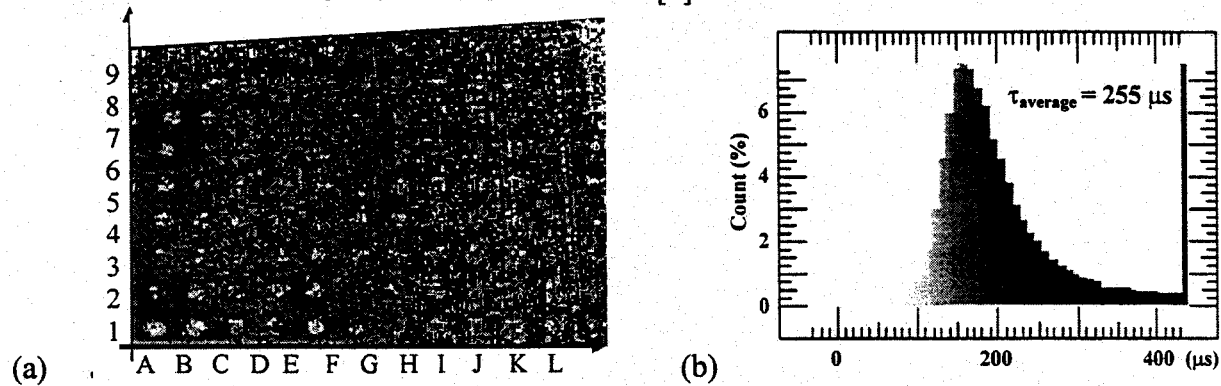


Fig. 1: (a) Lifetime map and (b) histogram of dislocated FZ sample cut from the region close to the ingot neck with superimposed the image of the diode array used in EBIC measurement. Note that the bar at $430 \mu\text{s}$ in the histogram represents the accumulated measured lifetimes above that value.

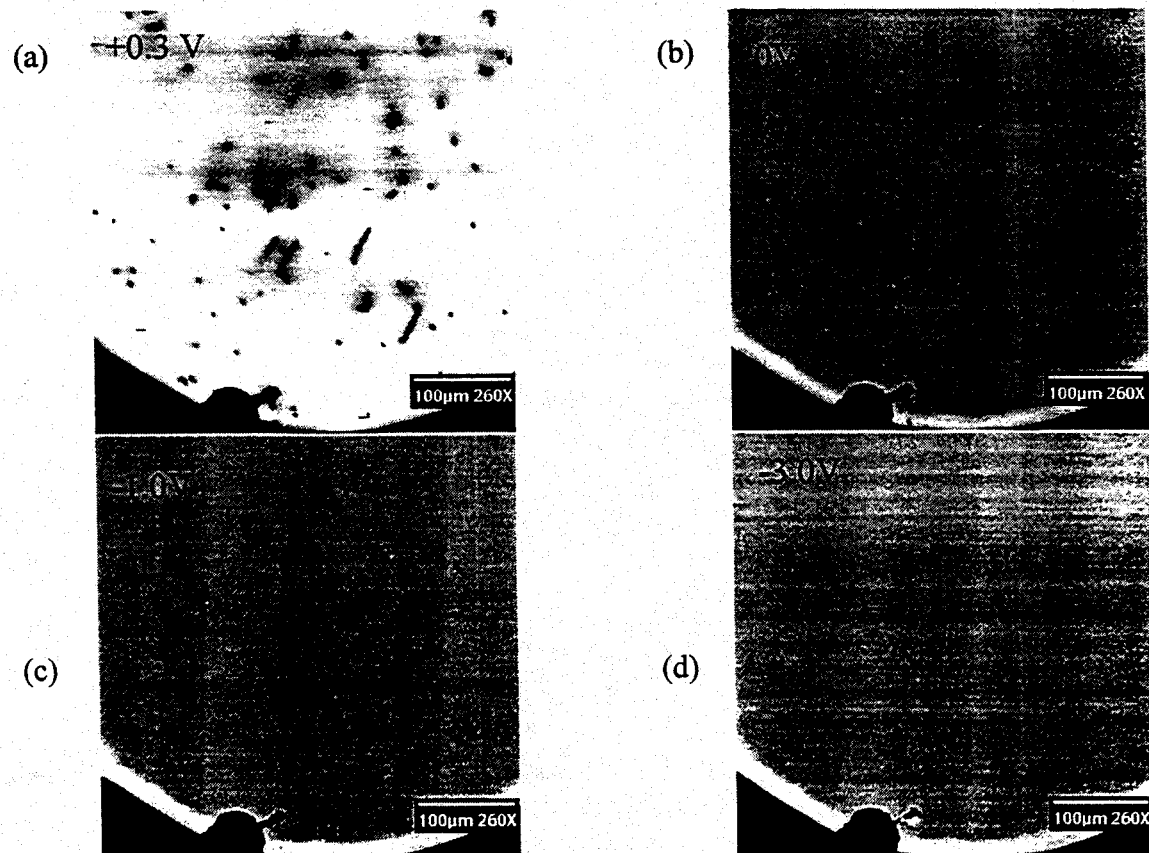
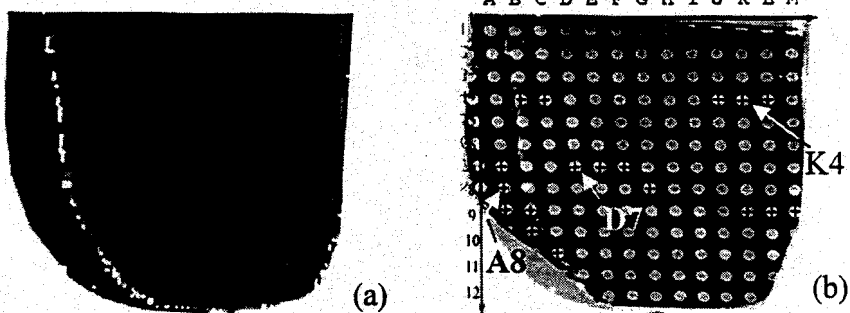


Fig. 2: EBIC images of a diode taken at different bias voltages. The diode is located in the ingot neck portion, in a region where the lifetime is about $170 \mu\text{s}$, diode E2 in Fig. 1 (a).

The results obtained in the ingot bottom region differ slightly from the neck region in that low lifetime does not simply suggest a high dislocation density but also different type of dislocations leading to different characteristics of the EBIC contrast. Stronger EBIC contrast and wider extent of the recombination centers indicate dislocations with stronger impurity gettering ability. The shape and the contrast of the EBIC features can provide information on the dislocation character.

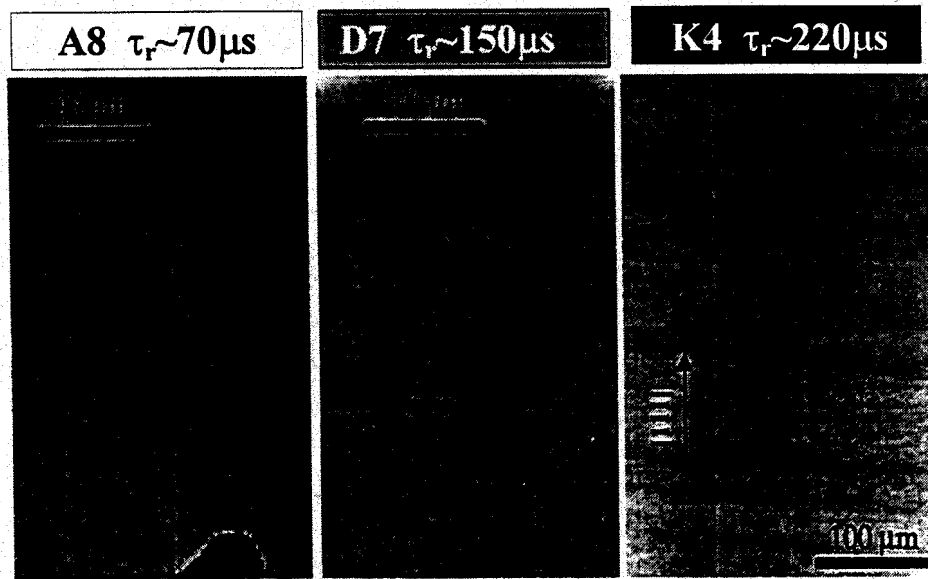
Fig. 3: μ PCD Lifetime map of the bottom of an axial slug cut from an FZ ingot with a high density of dislocations. The gray scale in this map matches that of the histogram in Fig.1(b).



As shown in Fig. 3, the left side of the ingot is characterized with a low lifetime $\sim 70\mu\text{s}$ (diode A8) and a high dislocation density [2]. Dislocation multiplication may have occurred by interaction with small impurity clusters which also reduce the lifetime and the EBIC baseline current, compare Fig. 4(a) to Fig. 4(c). The EBIC contrast of features in diode D7 appear sharper, many of which are circular or linear in shape, see Fig. 3(b), while the EBIC spots in diodes A8 and K4 appear weaker, and in the case of A8 more diffuse. It should be noted that the less sharp EBIC features (due to dislocations decorated with extrinsic impurities at the top portion) occur in a region (i.e., A8) where the lifetime is intrinsically low.

In the low dislocation area K4 the contamination is also present in the near surface (sensed by the dislocation carrier recombination activity) and the bulk is relatively cleaner than A8 region, according to the higher EBIC background current and the higher μ PCD lifetime. Nonetheless, the shallow contamination partially screens the bulk lifetime component when measured by μ PCD.

Fig. 4: Enlargement of portions of the EBIC images of diode A8, D7 and K4 shown in Fig. 3(b), where there is a clear lifetime variation (70 , 150 and $220\mu\text{s}$ respectively). Note that the [111] growth direction is parallel to the diode surface. The gray scale in the label boxes matches the lifetime gray scale provided in the histogram in Fig.1(b).



CONCLUSION

The minority carrier lifetime correlated previously with XRT images, is further studied in connection to EBIC data. The EBIC measurements at various biases have shown that a contamination occurred in the first 2-3 microns at most. This shallow contamination, was instrumental in decorating the dislocations which then allowed electrical evaluation of the dislocations strength and electrical activity field and the correlation with minority carrier lifetime. Indeed, the dislocation EBIC related features exhibited a characteristic shape that is location-dependent and varies with lifetime regions. In the highly dislocated region of the ingot neck, the lifetime is the lowest, while in region D7 of moderate lifetime (in the middle of the bottom of the ingot) dislocations appear as strong gettering center. Finally, in the low dislocation density region (K4) the lifetime is intrinsically high, due to a lower density of gettered impurities. Thus the lifetime degradation is proposed to be not caused by the dislocations only, but also to the distribution of impurities.

Acknowledgements: This work was carried out under the project "Optimization of Silicon Crystal Growth and Wafer Processing for High Efficiency and High Mechanical Yield", sponsored by NREL, contract #: AAT-2-31605-05.

References:

- [1] T. F. Ciszek, T.H.Wang, R.W.Burrows, T.Bekkedahl, M.I.Symko, and J.D.Webb, Solar Energy Materials and Solar Cells 41 /42, p.61 (1996).
- [2] G. A. Rozgonyi, A. Karoui, L. Kordas, and T. F. Ciszek, *NREL 11th Workshop*, Ed. B.L.Sopori, Estes Park, Co, Aug. 19-22, 2001, p.18.
- [3] Z.J. Radzimski, T.Q. Zhou, A.B. Buczkowski, and G.A. Rozgonyi, Appl. Phys. A 53 (1991) 189.
- [4] M. Kittler, C. Ulhaq-Bouillet-C, V. Higgs, J. Appl. Phys., 78, (7), 4573 (1995).
- [5] Quarterly Report of NREL Grant no: AAT-2-31605-05.

PARTITIONING EFFECTS IN RECRYSTALLIZATION OF SILICON FROM SILICON-METAL SOLUTIONS

E.A. Good, T.H. Wang¹, T.F. Ciszek¹, R.H. Frost², M.R. Page¹, and M.D. Landry¹

1. National Renewable Energy Laboratory, Golden, CO 80401

2. Colorado School of Mines Metallurgical and Materials Engineering Dept., Golden, CO 80401

ABSTRACT

The objective of this work is to investigate various silicon-metal eutectic systems that selectively retain detrimental impurities, such as Ni, Co, Fe, Cr, in the melt so that silicon may be purified. We studied possible interactions in the melt and in the silicon crystal between impurity elements and solvent metals that lead to reduced or enhanced impurity partition relative to the respective silicon-impurity binary systems. Systems such as Al-Si, Cu-Si, and In-Si show promises of reduced impurity incorporations in recrystallized silicon, which are good candidates for further investigation besides Ga-Si, Au-Si, and Ag-Si.

INTRODUCTION

One of the major issues facing PV manufacturers today is the supply and cost of solar-grade silicon (SoG-Si) with low detrimental metal impurity concentrations. As we reported in a previous publication [1], a novel approach to purifying metallurgical grade silicon (MG-Si) in lieu of the conventional distillation of chlorosilanes is silicon-metal solution growth. Figure 1 shows a simple phase diagram of a binary silicon-metal eutectic system. As the temperature is lowered from above the liquidus line, silicon precipitates out along the left axis with a low metal content according to the metal's solubility in silicon at the liquidus/composition interception temperature.

When solidifying silicon from an almost pure silicon melt, impurities contained in the silicon melt also incorporate into the silicon lattice according to their respective impurity-silicon binary solubilities at the silicon melting point. However, if we use some metals as solvents to dissolve silicon, one can recrystallize silicon at a much lower temperature and impurities contained in the silicon-metal solutions will also incorporate at the lowered temperature. The use of a metal solvent dilutes these impurities in MG-Si, thus the incorporation into the recrystallized silicon will be proportionally less. Furthermore, most impurities exhibit retrograde solubility in silicon with peaks around 1300°C. Some of the most harmful elements in metallurgical-grade silicon such as, Ni, Co, Fe, and Cr, have their solubility in silicon decreased by more than one order of magnitude from that at the silicon melting point if the crystallization is done at temperatures below 800°C instead. Many metals form eutectics with silicon at much lower temperatures than the silicon melting point. These include Ag, Al, Au, Cu, Ga, In, Sb, Sn, Zn, etc. One would prefer those of which with low or no detrimental effects on solar cell performances and with moderate slope of the liquidus line to afford fast recrystallization of silicon.

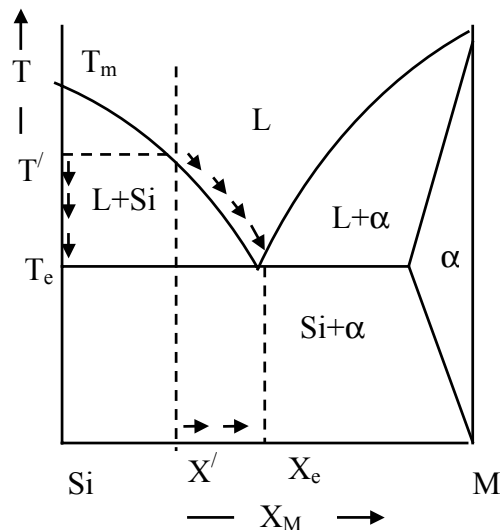


Figure 1 – Simple binary eutectic phase diagram for a silicon-metal system. Arrows illustrate growth along liquidus curve yielding precipitation of Si.

Interactions between an impurity and the metal solvent in a silicon-metal solution could change the impurity's chemical potential, thereby altering its partition coefficient. An attractive interaction retains the impurity in the solution by the solvent, and vice versa. These can be studied by means of the regular solution model in combination with experimental data.

In addition to dilution and interaction effects, a third mechanism could account for the reduced incorporation of some electrically active impurities into the silicon lattice. The law of mass action or Fermi energy level restriction reveals a type of interaction between an ionized impurity and the electrically active solvent element in the recrystallized silicon. This phenomenon could lead to either reduced or enhanced impurity segregation coefficient depending on the impurity's defect energy levels and the silicon Fermi energy level that is determined by incorporation of the solvent metal.

CRYSTAL GROWTH

Bulk crystals of silicon were grown in a 10kHz induction heated furnace with a charge size nearly 300g (Fig. 2). Compositions were selected from phase diagrams for each system such that silicon recrystallization takes place at or around 900°C. Electronic-grade silicon doped with impurities, at levels comparable to MG-Si, was used for precise control of initial impurity contents (e.g. B $\sim 2 \times 10^{18}$ atoms/cc). Kryopolous growth, as described by Brice [5], from (100) seeds yielded single crystal and multicrystalline samples depending on the growth conditions.

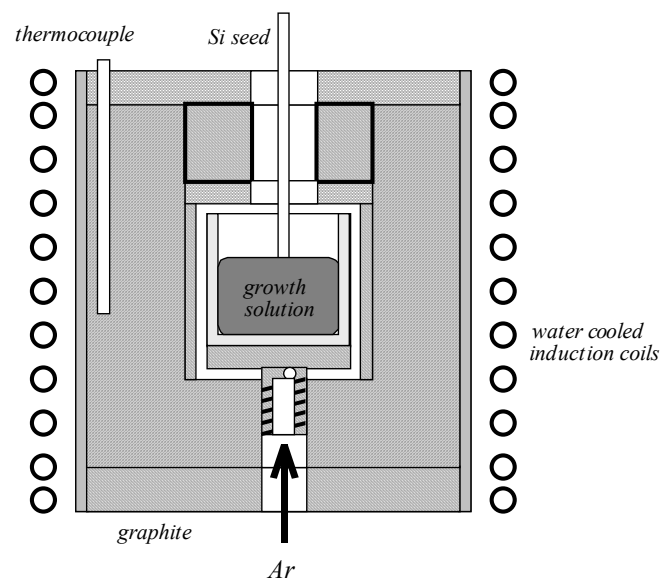


Fig. 2 Experimental setup for recrystallization



Figure 3 - Silicon-aluminum melt and multicrystalline growth



Figure 4 - Single crystal silicon grown from Si-Al



Figure 5 - A longitudinal cross-section of a single crystal silicon sample

INTERACTION IN THE MELT - THE REGULAR SOLUTION MODEL

When solidifying silicon from a Al-Cu-Si ternary solution, the chemical potentials of respective elements in the liquid phase must be equal to those in the solid phase. The chemical potential of individual element is determined by its activity (the ratio of an element's fugacity in the mixture at equilibrium to the fugacity in its pure state), which is the product of activity coefficient and composition

fraction. Using the regular solution model, the interaction parameters between the three components at 1173K are experimentally obtained as, $\Omega_{\text{SiAl}}^l = 2.430\text{RT}$, $\Omega_{\text{SiCu}}^l = 2.469\text{RT}$, $\Omega_{\text{AlCu}}^l = -0.103\text{RT}$. Therefore, the segregation coefficient of Al for growth of silicon from Al-Cu-Si mixture can be derived [2],

$$k_{Al} = \frac{x_{Al}^s}{x_{Al}^l} = \frac{\gamma_{Al}^l}{\gamma_{Al}^s} = \frac{\exp[2.430(x_{Si}^l)^2 - 0.103(x_{Cu}^l)^2 - 0.142x_{Si}^lx_{Cu}^l]}{8991}.$$

Similarly for Cu, we have:

$$k_{Cu} = \frac{x_{Cu}^s}{x_{Cu}^l} = \frac{\gamma_{Cu}^l}{\gamma_{Cu}^s} = \frac{\exp[2.469(x_{Si}^l)^2 - 0.103(x_{Al}^l)^2 - 0.064x_{Si}^lx_{Al}^l]}{3.98 \times 10^7}.$$

Because both Ω_{SiAl}^l and Ω_{SiCu}^l are large positive numbers, Si-Al and Si-Cu interactions are of repulsive nature (with higher heat of mixing). Ω_{AlCu}^l is negative, however, implying an attractive interaction between Al and Cu (with lower heat of mixing). Therefore, Cu in the growth solution will not only dilute Al, but also will retain Al in the liquid, thus providing greater control for Al doping. Other Si-metal solvent combinations may be explored in a similar fashion to reduce incorporation of more detrimental impurities using harmless metals as solvents.

INTERACTION IN THE CRYSTAL - THE FERMI ENERGY MODEL

When choosing metal solvents, its conductivity type in silicon is very important. At growth temperature, solvent metal atoms incorporated into the silicon crystal ionize to give a Fermi energy level in silicon (determined by solvent concentration and growth temperature). If an acceptor-type solvent is chosen, other impurities of the same acceptor-type but with energy levels above the Fermi level will not be able to ionize, thus reducing these acceptor impurities' incorporation. Similarly, if the solvent is of donor-type, other donor-type impurities with energy levels below the Fermi Energy will not be able to ionize. The ratio of the impurity solubility from such an impurity-solvent-silicon system to that from an impurity-silicon binary system is given by [3,4]:

$$\text{for acceptor-type impurities with acceptor-solvent: } \frac{[A]}{[A_{bi}]} = \exp\left(\frac{E_F - E_{imp}}{kT}\right),$$

$$\text{for donor type impurities with donor-solvent: } \frac{[D]}{[D_{bi}]} = \exp\left(\frac{E_{imp} - E_F}{kT}\right),$$

where the subscript *bi* stands for impurity-silicon binary system, and E_{imp} is the impurity energy level.

The adverse effect is also true. For example, if a solvent is of acceptor type, other impurities of donor-type with energy levels above the Fermi level will be easily ionized to act as donors, so their concentration could be enhanced compared to impurity-silicon binary system.

CHARACTERIZATIONS

Bulk silicon samples grown from eutectic systems: Al-Si, Cu-Si, and In-Si were analyzed for impurity concentrations. Depth profiling by secondary ion mass spectroscopy (SIMS) was preformed on longitudinal cross-sections to achieve true bulk impurity measurements. Figure 6 depicts a SIMS measurement about 50μm into the bulk of a single crystal sample grown from an aluminum melt. From this profile, any non-uniform edge and interface effects can be ignored, as the concentrations appear constant. Table 1 shows that impurity concentrations observed in the crystals grown from Si-metal solutions are quite different from the source levels and from dilution considerations from the intended doping (B, Cu, and Al). The unintended impurities (Mn and Fe) also deviate from even the binary solubilities. Solvents like Ag, Au, and Ga will also be studied for interactions with targeted impurities.

Table 1 – SIMS Bulk Impurity Data for Three Eutectic Systems

	<i>B</i> (intent.)		<i>Cu</i> (intent.)		<i>Al</i> (intent.)		<i>Mn</i> (unint.)		<i>Fe</i> (unint.)	
	SIMS	Source	SIMS	Melt	SIMS	Melt	SIMS	Sol. [7]	SIMS	Sol. [7]
<i>Si-Al</i>	2×10^{17}	2×10^{18}	2×10^{15}	2.0×10^{20}	8×10^{18}	*	1×10^{17}	5×10^{14}	2×10^{16}	2×10^{15}
<i>Si-Cu</i>	4×10^{18}	2×10^{18}	1×10^{15}	*	2×10^{16}	8.0×10^{20}	8×10^{14}	7×10^{14}	3×10^{15}	3×10^{15}
<i>Si-In</i>	2×10^{17}	2×10^{18}	1×10^{15}	1.2×10^{21}	7×10^{14}	5.1×10^{20}	3×10^{14}	6×10^{15}	2×10^{15}	1×10^{16}

* Solvent Metal

CONCLUSIONS

Recrystallization from some silicon-metal eutectic systems offers promises for solar-grade silicon feedstock production with several possible purification effects. These effects include: lowering crystallization temperatures, diluting impurity concentrations, attractive impurity-solvent interactions in the solutions, and repulsive impurity-solvent element interactions in the silicon crystal resulting rejection of impurity at the growth interface. Future work will be conducted to systematically determine interaction parameters for all of the major eutectic systems and to complete investigations into the Fermi energy effect on impurity partition.

ACKNOWLEDGEMENTS

Valuable contributions to this work from the staff of NREL's Silicon Materials Team within the National Center for Photovoltaics are greatly appreciated. Financial support was made possible from a task order agreement between the Colorado School of Mines and the National Renewable Energy Laboratory: No. KCQ-0-30600-20. Robert Reedy and Matthew Young of NREL's measurements and characterization team conducted SIMS analysis.

REFERENCES

- [1] T.F. Ciszek, T.H. Wang, M.R. Page, P. Menna, R.E. Bauer, E.A. Good, and J.A. Casey in: *Proceedings of the 11th Workshop on Crystalline Silicon Solar Cell Material and Processes*, Ed: B.L. Sopori (August 2001 NREL/BK-520-30838), pp. 150-154.
- [2] T.H. Wang and T.F. Ciszek, "Impurity Segregation in LPE Growth of Silicon from Cu-Al Solutions," *J. of Crystal Growth* **174** (1997) pp.176-181
- [3] R.A. Swalin, *Thermodynamics of Solids*, Wiley, New York, 1962, p.305
- [4] H.F. Wolf, *Semiconductors*, John Wiley & Sons, New York, 1971 p. 201. W.C. O'mara, R.B.
- [5] O.F. Devreux, *Topics in Metallurgical Thermodynamics*, Krieger Publishing Company. Malabar, Florida.1983. pp. 95-107
- [6] J.C. Brice, *Crystal Growth Processes*, John Wiley and Sons, New York, 1986, p. 137.
- [7] M. Neuberger, S.J. Welles, *Silicon*, DS -162, October 1969.

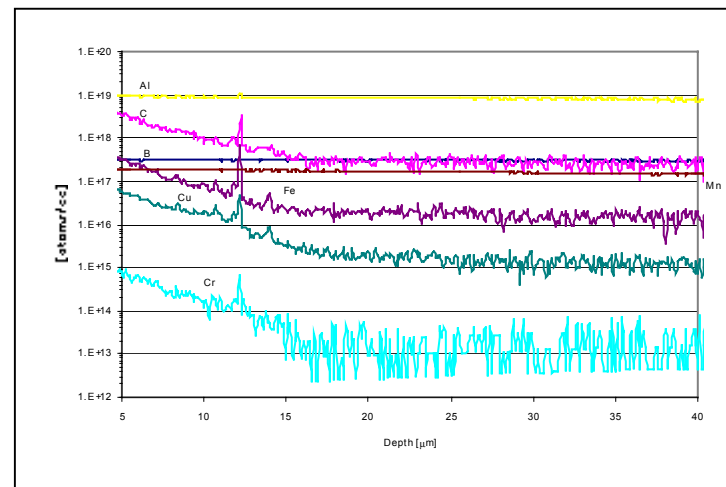


Figure 6 – SIMS impurity data for single crystal silicon grown from Al solution.

Measurement of Lattice Vacancy-Type Defects in Crystalline Si by a Au Labeling Technique

A. T. Fiory and N.M. Ravindra

Department of Physics, New Jersey Institute of Technology, Newark, N.J.

R. Kalyanaraman

Department of Physics, Washington University, St. Louis, Mo.

V. C. Venezia

Phillips Research, Leuven, Belgium.

B. L. Sopori

National Renewable Energy Laboratory, Golden, Co.

Vacancy densities and vacancy binding energies have been quantitatively determined by a Au labeling technique for single crystal Si damaged by high-energy ion implantation. When Au is diffused into the defective Si material, Au atoms are preferentially trapped at vacancies and small vacancy clusters. The volume concentration has been quantitatively calibrated to be 1.2 Au atoms per vacancy (denoted as calibration factor $k = 1.2$). The technique is potentially capable of obtaining vacancy concentrations in as-grown and processed solar cell Si material by diffusing Au from the surface. Of particular interest is vacancy injection associated with the formation of Al backside contacts. Introduction and diffusion of the Au species and Au profiling is discussed in the context of applying a Au labeling technique to problems where vacancies play a role in solar cell processing, such as hydrogen passivation and contact formation.

Introduction

Electrically active lattice defects in solar cell Si can be largely passivated by hydrogenation. Vacancies, which contribute 2 acceptor and 2 donors levels, are endemic to most starting Si materials grown by rapid solidification from the melt. Vacancy concentrations are also correlated with oxygen and carbon impurity levels.

During solar cell processing, additional vacancies are injected by the thermal processing to form the backside contact with Al metallization. Vacancies, as well as other defects, act as traps, which affect the diffusion of H in Si. The apparent diffusivity of H in Si is thus material sensitive, as shown in Fig. 1 [1]. The measurements yield an effective trap-limited diffusivity of H. Diffusion of H in the presence of fixed and mobile traps has been modeled by Zhang [2]. Trap concentrations on the order of 10^{13} to 10^{14} cm^{-3} were obtained by fitting diffusion profiles in float zone (FZ) Si. Trap concentrations in the 10^{17} cm^{-3} range can be inferred from model fits to diffusion of H introduced by ion implantation into cast polycrystalline (CP) and edge defined film growth (EFG) solar Si. These traps are likely to include vacancies or vacancy clusters.

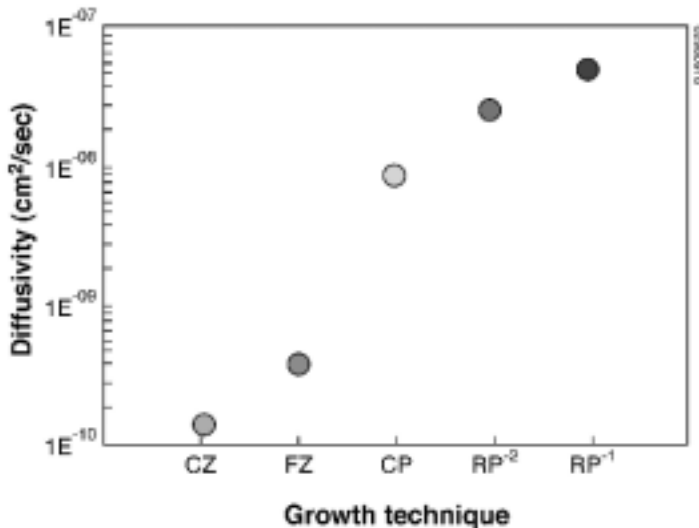


FIG. 1. Apparent diffusivities of H in Si materials grown by Czochralski (CZ), float zone (FZ), cast polycrystalline (CP), and several recrystallized ribbon (RP) methods [Source: Refs. 1, 2].

The vacancies presumably agglomerate to form clusters after thermal processing. A number of methods have been used to sense the presence of vacancies. Positron annihilation S-parameter measurements have been useful for qualitatively profiling the density of open-volume defects [3].

Au Labeling in Implant-Damaged Si

Previous studies of vacancies in Si exploited the selective precipitation of Au at vacancies and vacancy clusters [4-8]. In these works the source of the Au was a surface implanted layer. Figure 2 shows the Au concentration obtained in Si damaged by a 2 MeV, 10^{16} cm^{-2} Si^+ implant. The diffusion times at 750 °C are shown in the legend. The Au concentrations are in excess of the Au solid solubility of $2 \times 10^{14} \text{ cm}^{-3}$ at 750 °C. Transmission electron microscopy (TEM) studies indicate the presence of fcc Au precipitates [5]. The Au concentration profiles obtained by RBS and TEM were found to be in good agreement. Importantly, it was shown that the ratio of Au atoms to vacancies,

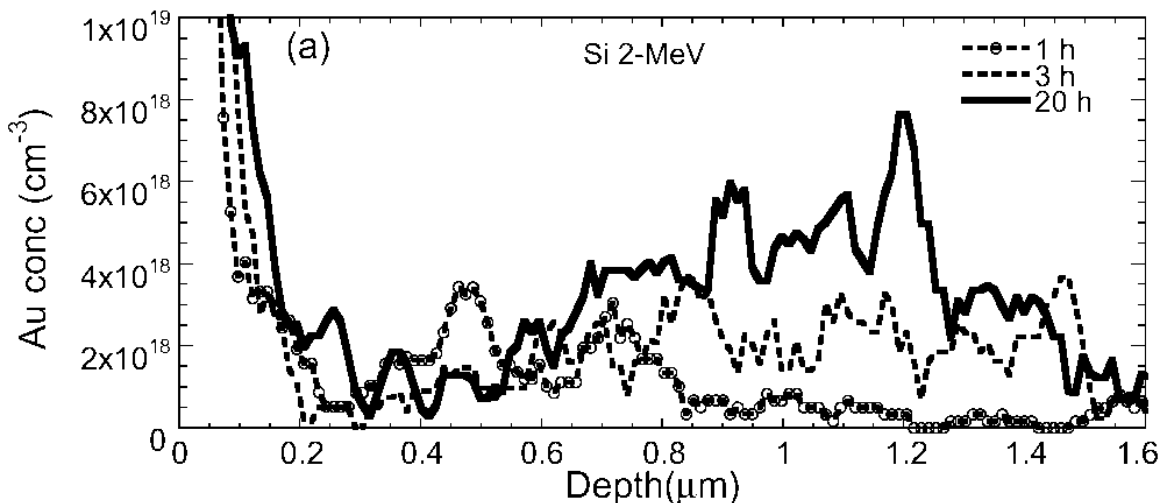


FIG. 2. Au concentration profile in high-energy implanted Si, determined by Rutherford backscattering spectrometry (RBS) with a 2.8-MeV ${}^4\text{He}^{2+}$ analysis beam [Source: Ref. 8].

i.e., the calibration factor for the Au labeling technique, is given by $k = 1.2$. The characteristic time, τ , for the vacancies to become saturated with Au atoms, was found to scale with vacancies [6] as

$$\tau = 3.2 \times 10^{-11} \text{ cm}^2 \text{ s} [v], \quad (1)$$

where $[v]$ is the areal density of vacancies in the profiled region [8]. Thus data such as the solid curve in Fig. 2, which corresponds to annealing up to saturation of Au in the vacancy region, is a quantitative measure of the vacancy concentration profile in Si.

Au Labeling in Solar Cell Si

A deposited Au film was also used for Au labeling and yielded similar findings as for ion-implanted Au [9]. Au-Si clusters were observed to be formed at the surface, since the film provided an excess quantity of Au, as compared to ion-implanted doses.

Although it requires special sample preparation, one could introduce Au in solar cell Si material by depositing a thin Au film on the surface. The method will entail a surface-clean preparation of the Si surface and deposition under clean conditions to avoid an oxide interfacial diffusion barrier. For studying the effect of Al-diffused contacts, the Al film would be removed by etching prior to the Au deposition.

Au diffusion into the Si is assumed to follow a trap limited diffusion mechanism, where the Au diffusivity varies inversely with the vacancy concentration. The equilibration is also limited by the solubility of Au at the anneal temperature ($2 \times 10^{14} \text{ cm}^{-3}$ at 750 °C). Assuming a diffusion time of $\tau = 1 \text{ hr}$, the depth, d , to which the Au labeling will reach saturation can be estimated by scaling Eq. (1) as $[V] = [v] / d$, where $[V]$ is the mean volume density of vacancies. This relationship between the depth d and $[V]$ is plotted in Fig. 3.

The model shown in Fig. 3 suggests that a depth of 100 μm can be probed for a vacancy concentration of 10^{16} cm^{-3} .

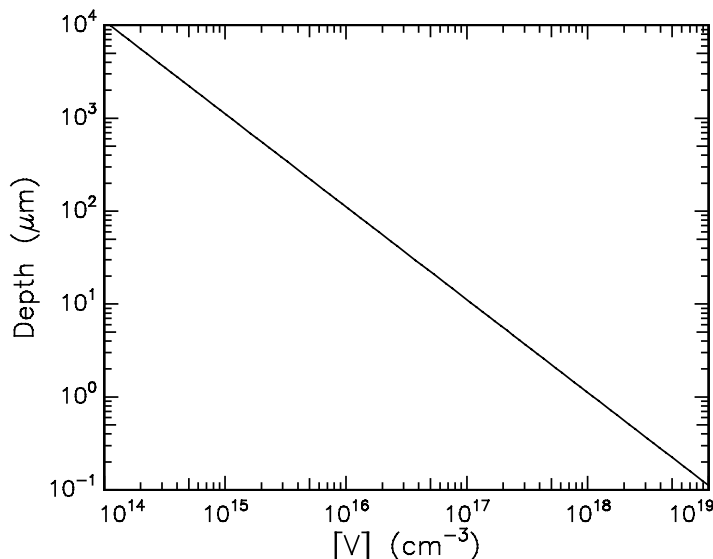


FIG. 3. Relationship between probed depth and vacancy volume concentration for Au diffusion at 750 °C for 1 hr. Model is estimated from Au labeling result of Eq. (1).

Au Profile Measurement

Vacancy concentrations may be considerably lower in processed solar Si, when compared to the high-energy ion implanted Si of Refs. 4-9. However, the Au concentration profiles can also be determined by secondary ion mass spectroscopy (SIMS), which has greater sensitivity than the RBS method. The depths probed by SIMS are nominally unlimited, a further advantage over RBS. The sensitivity of SIMS is expected to correspond to a mean Au volume concentration of 10^{15} cm^{-3} [10].

The vacancy concentration near the surface will be perturbed by the Au/Si diffusion reaction. A peak and shoulder structure in the Au profile near surface region is observed with the Au implantation method, as can be seen in Fig 2.

Conclusions

Au labeling has been proposed for quantitatively determining vacancy concentrations in solar cell Si materials. It will be necessary to study whether the thermal treatment required to diffuse the Au would also ripen or perturb the vacancy distribution under study. Such effects were determined to be negligible in the case of vacancies introduced in crystalline Si by ion implantation damage. Controlled deposition of the Au film could provide a reliable and reproducible surface source of Au diffusion. Studies of Al contact formation entail removal of the Al film, to avoid further reaction and eutectic formation, and deposition of a Au film. The Al processing will be restricted to approximately 400 °C, which is below the Al spiking temperature. Study of the redistribution of the Al during the Au diffusion would also be of interest.

References

1. "Silicon Device Processing in H-Ambients; H-Diffusion Mechanisms and Influence on Electronic Properties", B. L. Sopori, Y. Zhang, and N. M. Ravindra, J. Electron. Mat. **30**, pp. 1616-1628 (2001).
2. "Modeling hydrogen diffusion for solar cell passivation and process optimization", Y. Zhang, Ph.D.Thesis, New Jersey Institute of Technology (2002).
3. "Impurity and Defect Characterization in c-Si by Positron Beams," K. G. Lynn and M. H. Weber, 10th Workshop on Crystalline Silicon Solar Cell Materials and Processes, pp. 71-82 (NREL, 2000).
4. "Depth profiling of vacancy clusters in MeV-implanted Si using Au labeling", V.C. Venezia, D.J. Eaglesham, T.E. Haynes, A. Agarwal, D.C. Jacobson, H.-J. Gossman, and F.H. Baumann, Appl. Phys. Lett. **73**, 2980 (1978).
5. "Quantification of excess vacancy defects from high-energy ion implantation in Si by Au labeling, R. Kalyanaraman, T. E. Haynes, V. C. Venezia, D. C. Jacobson, H.-J. Gossman, and C. S. Rafferty, Appl. Phys. Lett. **76**, 3379 (2000).
6. "Binding energy of vacancy clusters generated by high-energy ion implantation and annealing of silicon", V. C. Venezia, L. Pelaz, H.-J. L. Gossman, T. E. Haynes, and C. S. Rafferty, Appl. Phys. Lett. **79**, 1273 (2001).
7. "Binding energy of vacancies to cluster formed in Si by high-energy ion implantation", R. Kalyanaraman, T. E. Haynes, O. W. Holland, H.-J. L. Gossman, C. S. Rafferty, and G. H. Gilmer, Appl. Phys. Lett. **79**, 1983 (2001).
8. "Quantitative Depth Profiles of Vacancy Cluster Defects Produced by MeV Ion Implantation in Si: Species and Dose Dependence," R. Kalyanaraman, T.E. Haynes, D.C. Jacobson, H.-J. Gossman, and C.S. Rafferty. Mat. Res. Soc. Symp. Proc. **610**, B9.4 (2000).
9. "Evolution of Vacancy Supersaturations in MeV Si Implanted Silicon," V.C. Venezia, Ph.D. Thesis, University of North Texas, Denton, TX (May, 1999).
10. The Au detection limit of $\sim 10^{15} \text{ cm}^{-3}$ of Au is based on SIMS with a Cs beam at 5-keV energy and 60° incident angle (Evans East, private communication).

Comparison of Shunt Imaging by Liquid Crystal Sheets and Lock-in Thermography

O. Breitenstein, J.P. Rakotonaina, J. Schmidt*

Max Planck Institute of Microstructure Physics, Weinberg 2, D-06120 Halle, Germany

*Institut für Solarenergieforschung Hameln/Emmerthal (ISFH), Am Ohrberg 1,
D-31860 Emmerthal, Germany

1. Introduction

Thermographic techniques are able to image local shunts in solar cells [1-3]. An external bias is applied to the cell in the dark, and the currents flowing locally through the shunts are leading to a local heating of the surface of the cells, which may be detected thermographically. Note that shunts may act in two different ways to solar cells: I. Under forward bias (near the working point of the cells) shunts are increasing the dark forward current, thus degrading the fill factor and the open circuit voltage of the cells [4]. II. If a single solar cell in a module is shadowed, it may become reverse-biased by the other illuminated cells in the string by up to 13 V [2]. If there are local shunts in this cell being active under reverse bias, in these positions excessive heat may be produced (hot spots), which may lead to a thermal destruction of the module.

In the past it was generally assumed that shunts should have a linear (ohmic) I-V characteristic. In this case indeed shunts acting under forward bias would be the same which produce hot spots under reverse bias, hence reverse bias shunt imaging also would reveal the dominant shunts acting at the working point. Then for quantitatively estimating the influence of shunts, it would be sufficient to consider the parallel resistance of the cell measured at low bias. In recent investigations, however, it has turned out that a large fraction of shunts may show a non-linear (diode-like) I-V characteristic [5]. In this case reverse-bias shunt imaging would produce misleading results with respect to the influence of shunts under operation of the cells.

The thermal sensitivity of classical (stationary) infrared (IR) thermography is in the order of 20... 100 mK. This is sufficient to image shunts in silicon cells under a few Volts reverse bias, but shunts under forward bias usually produce such a low amount of heat that they cannot be imaged in this way. Lock-in thermography improves the sensitivity of thermal investigations by 2-3 orders of magnitude, since it averages the oscillating thermal signal over thousands of single IR measurements [3, 5]. Moreover, lock-in thermography suppresses the action of lateral heat conduction, hence it improves the effective spatial resolution compared to stationary thermography, and it can be evaluated quantitatively in terms of shunt currents flowing [4].

Unfortunately, lock-in IR thermography is a very expensive technique. The easiest and cheapest, though quite insensitive, hot spot detection technique is to apply a sufficiently large reverse bias to the cell and gently glide with your fingers across the surface of the cell. In this way hot spots can be sensed. With this simple technique is it possible to locate the dominant shunts acting under reverse bias up to an accuracy of, say, 5 mm. Unfortunately this technique produces no images. The use of nematic liquid crystal (LC) layers under crossed polarisers is also known as a cheap thermography technique [6]. For this investigation the sample should be thermostatted, but it may be hard to ensure a homogeneous covering of the surface, and after investigation the liquid has to be removed. Recently, Schmidt et al. [7] have demonstrated the application of polymer-dispersed liquid crystal sheets as an easy-to-use thermographic technique to detect shunts under reverse bias. These low-cost sheets are sucked together with the cell to a heat sink, thereby producing images of the dominant shunts under reverse bias. Practically the same technique is being used also at FhG-ISE by Ballif et al. [8] using commercially available

sheets from Edmund Scientific. The aim of this work is to compare this low-cost liquid crystal sheet thermography technique with the IR lock-in thermography technique on some typical silicon solar cells.

2. Experimental

Two cells have been selected for this comparison. Cell No. 1 was a 19.5 cm^2 sized float-zone silicon solar cell fabricated by means of a high-efficiency cell process. In this cell 4 scratches have been made at the surface with a diamond scribe in order to produce strong shunts intentionally. Cell No. 2 was one $5 \times 5 \text{ cm}^2$ sized quarter of a $10 \times 10 \text{ cm}^2$ commercial monocrystalline Czochralski silicon solar cell. For the liquid crystal (LC) investigations the cells were sucked by a vacuum to a thermostatted brass heat sink and covered by the LC sheets. Two different liquid crystal sheets have been used: On sample No. 1 a non-commercial one having a temperature range of $25 \dots 26^\circ\text{C}$ was used [9], and on sample No. 2 a commercial one purchased by Edmund Scientifics having a temperature range of $35 \dots 36^\circ\text{C}$. The temperature of the heat sink was stabilized at 25 and 35°C , respectively, and the colour pattern was photographed. Under forward bias in both cases no visible signal could be obtained. Under reverse bias, starting from -3V hot spots became visible, which were fully resolved at $-7 \dots -10\text{ V}$ reverse bias. Lock-in thermography investigations have been made at a lock-in frequency of 24 Hz using the TDL 384 M 'Lock-in' thermography system made by Thermosensorik Erlangen [10]. Here the cells were covered by a thin black-painted plastic IR emitter film vacuum-attached to the surface and measured at room temperature both under forward and under reverse bias. The acquisition time for each image was about 30 minutes for the forward bias images and below 1 minute for the reverse bias ones. Local I-V characteristics have been measured thermally (LIVT [11]) by repeating the lock-in thermography measurement at different biases and evaluating the results according to the image integration method, which was described in [4].

3. Results

Figs. 1 and 2 show greyscaled images of the LC investigation and lock-in thermography images of both samples at reverse bias together with lock-in thermography images measured under $+0.5\text{ V}$ forward bias. In some images the shape of the cell is indicated by dashed lines. The colour scale of the LC sheets goes from black across red, yellow and green, to blue. Unfortunately, in grayscale presentation this colour scale behaves non-monotonically, hence the blue colour representing the highest temperature appears darker again. Therefore the strongest hot spots in the LC images are showing a dark dip in shunt position.

In cell No. 1 the four scratches (A through D), which are aligned in cross shape, represent the dominant hot spots. Under reverse bias these hot spots are visible both in the LC investigation and in lock-in thermography. However, the spatial resolution of lock-in thermography is clearly better. Another weak hot spot E is visible in lock-in thermography at the edge of the cell, which was lying just outside of the photographed region in the LC image. It is visible in both techniques that hot spot D is the strongest and A the weakest of these four. The lock-in thermography investigation under $+0.5\text{ V}$ forward bias shows that in this cell indeed all hot spots imaged under reverse bias are also shunts under forward bias.

Cell No. 2 showed a weaker shunting activity than cell No. 1. Therefore a larger reverse bias of -10 V was applied here in order to see not only the dominant hot spot in LC imaging (Fig. 2, left). One dominant and two minor hot spots (see arrows) are visible in the LC image, which are

all lying in the interior of the cell. This result indicates that the edge of this cell should be well-passivated. Interestingly, the halo around the dominant spot appears larger here than that around the spots visible in Fig. 1. Note, however, that the visual appearance of the hot spots in LC imaging strongly depends on the heating power and on the illumination conditions as well as on the time left after switching on the power to the cell. The hot spots visible in LC imaging are also visible with a better spatial resolution in lock-in thermography (Fig. 2, middle). Additionally some more hot spots become visible here, which remain invisible in the LC image since they are too weak or are lying in the halo region of the dominant hot spot. The most interesting result is that the forward bias thermogram of this cell (Fig. 2, right) looks very different to the reverse bias one. Under forward bias the dominant shunts are lying at the edge of the cell, whereas the dominant shunt under reverse bias is only a weak one under forward bias. Additionally, there is some shunting activity under grid lines in the upper right part of the cell, which is totally invisible under reverse bias. This proves that in this case reverse bias shunt imaging using LC sheets would not reveal the dominant shunts acting under operation of this cell. This behaviour has been found also in other solar cells [5], hence in well-processed solar cells an ohmic behaviour of shunts is rather an exception than the rule.

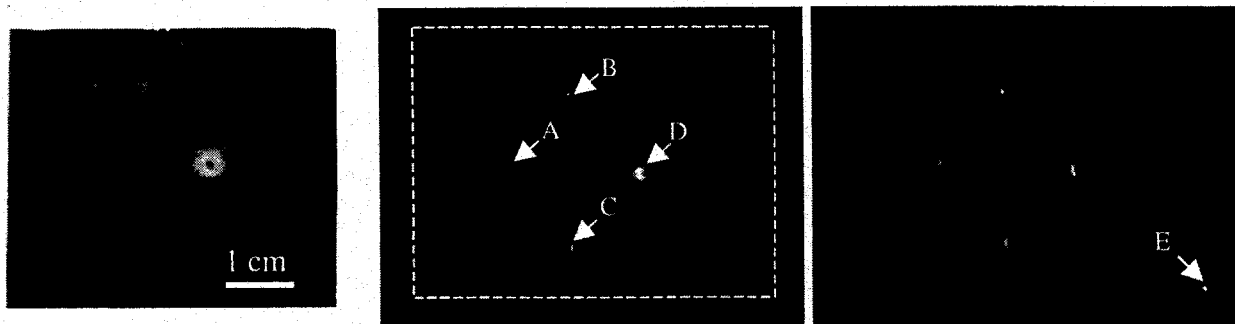


Fig. 1: Cell No. 1 containing 4 scratches. Left: liquid crystal (LC) image under -7V reverse bias, middle: lock-in thermogram under -7V reverse bias (0 ... 100 mK), right: lock-in thermogram under + 0.5 V forward bias (0 ... 5 mK).

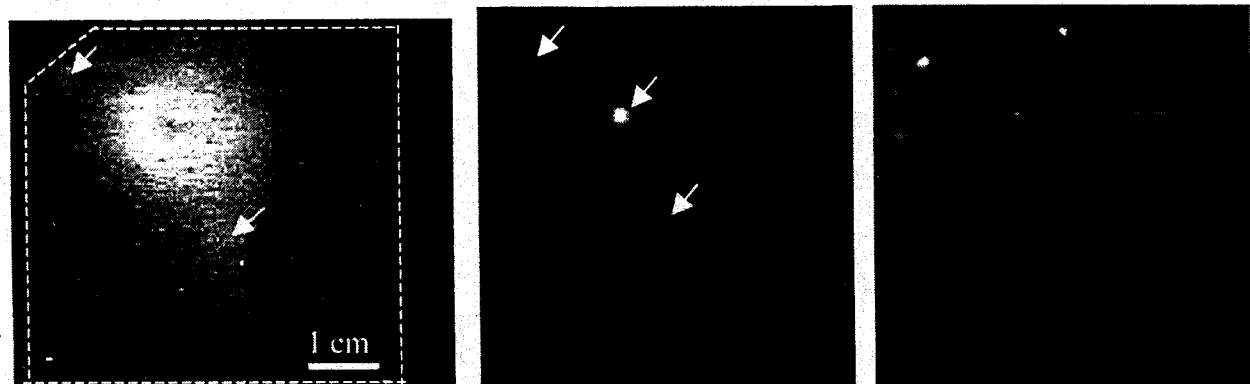


Fig. 2: Industrial solar cell No. 2. Left: liquid crystal (LC) image under -10V reverse bias, middle: lock-in thermogram under -10V reverse bias (0 ... 200 mK), right: lock-in thermogram under + 0.5 V forward bias (0 ... 4 mK).

Finally it should be checked whether the shunts in sample No. 1 are indeed showing a linear I-V characteristic. Using lock-in thermography local I-V characteristics may be measured thermally (LIVT [11]). This technique is based on the fact that the thermal signal is proportional to the dissipated power. The thermal signal phase-shifted by -90° to the pulsed excitation may be

averaged over a sufficiently large region around a shunt, leading to a quantitative measurement of the shunt current [4]. The result in Fig. 3 shows that neither the forward nor the reverse bias characteristics of the shunts in cell No. 1 behave linear. Thus, even in this case, where a qualitative agreement between forward and reverse bias shunt investigation has been found, the reverse bias shunt investigation does not allow to draw quantitative conclusions as to the action of these shunts under operation conditions. Even here the action of the shunts is not sufficiently described by the parallel resistance of the cell.

4. Conclusions

It has been shown that for reverse bias hot spot investigations LC sheet thermography is an interesting alternative for lock-in thermography, delivering basically the same results with a lower spatial and temperature resolution, but at a fracture of the costs. However, these results are not representative for the behaviour at the working point under forward bias, which can only be investigated by lock-in thermography. In one of the investigated cells having stronger shunts at least a qualitative correspondence between the behavior in both polarities has been found, but in the other cell the behaviour was dissimilar even qualitatively. The quantitative thermal measurement of local I-V characteristics of shunts is possible only by lock-in thermography. Thus, LC sheet thermography is sufficient for detecting hot spots under reverse bias, but for optimizing the fill factor and V_{oc} lock-in thermography has to be used.

This work has been supported by BMWi project No. 0329858D (KoSi). The cooperation with Thermosensorik GmbH (Erlangen) is acknowledged.

References:

- [1] A. Simo, S. Martinuzzi, 21st IEEE PVSC, Kissimmee (1990) 800
- [2] M. Danner, K. Büchner, 26th IEEE PVSC, Anaheim (1997) 1137
- [3] O. Breitenstein, M. Langenkamp, K.R. McIntosh, C.B. Honsberg, M. Rinio, 28th IEEE PVSC, Anchorage (2000) 124
- [4] O. Breitenstein, M. Langenkamp, Proc. 2nd World Conf. on Photovolt. Energy Conv., Vienna (1998) 1382
- [5] O. Breitenstein, M. Langenkamp, J.P. Rakotonaina, Proc. 17th Eur. Photovolt. Solar Energy Conf., Munich 2001, 1499
- [6] G. Färber, R.A. Bardos, K.R. McIntosh, C.B. Honsberg, A.B. Sproul, Proc. 2nd World Conf. on Photovolt. Energy Conv., Vienna (1998) 280
- [7] J. Schmidt and I. Dierking, Progr. Photovolt: Res. Appl. **9** (2001) 263
- [8] C. Ballif, S. Peters, J. Isenberg, S. Riepe, D. Borchart, 29th IEEE PVSC, New Orleans 2002
- [9] obtained from M. Pranga, K.L. Czuprynski, S.J. Klosowicz, Warsaw, Poland
- [10] www.thermosensorik.com
- [11] I.E. Konovalov, O. Breitenstein, K. Iwig, Solar Energy Mat. and Solar Cells **48** (1997) 53

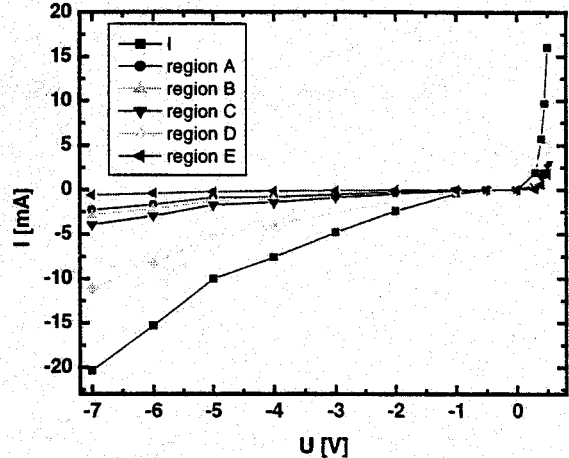


Fig. 3: Measured current (I) and thermally measured shunt currents of shunts A ... E of cell No. 1

LEAKAGE CURRENT IN P-N JUNCTIONS CONTRIBUTED BY METALLIC PRECIPITATES VIA THE SCHOTTKY EFFECT

M. D. Negoita and T.Y. Tan

Department of Mechanical Engineering and Materials Science
Duke University
Durham, NC 27708-0300

Abstract

Leakage currents are important factors affecting the operation of p-n junction devices. For bipolar transistors and solar cells fabricated using Si, it is well known that metallic precipitates located in the junction charge depletion region can have a dominant effect on the leakage currents. In the present work, we model the electrical activity of such precipitates by examining the effect of the Schottky current contributions under forward and under reverse junction biasing conditions.

Introduction

To model the electrical activity of metallic precipitates inside the depletion region of the p-n junction, a cylindrical diode, 2μ in length and 2μ in diameter, with the p-n junction at the middle of its long dimension, is considered. A spherical precipitate 100\AA in diameter is placed at the n-side of the depletion region of the diode along its center cord. The cylindrical symmetry of the diode and the spherical symmetry of the precipitate allowed the problem to be formulated and solved for a longitudinal planar section passing through the center of the precipitate, see in Fig.1. This enables a steady-state two-dimensional model of the p-n junction to be used instead. To account for the metal-Si junction property, the Schottky effect model [1] is used.

Formulation of Problem

Physically, we note that the precipitate charges-up with the same charge as the majority carrier and creates its own electric field. This field on the one hand, and the p-n junction field together with the gradients of carrier concentrations on the other, balance each other so that a steady state is reached. Which factor is dominant is strongly dependent on the bias condition and will be made clear in the solution of the problem. The precipitate charging process is not limited by the supply of carriers in the depletion region (even under reverse bias) because for the amount of charges accumulated on the precipitate surface is extremely small. However, the overall effect of the charged precipitate on the device band structure and carrier transport phenomena in the depletion region can be very strong because this charge is confined in the very small volume of the precipitate, and hence the electric field emerging or entering the precipitate has values comparable with the electric field of the p-n junction itself.

A set of the standard steady-state semiconductor equations with dependent variables (ϕ_e, ϕ_h, ψ) , where ϕ_e, ϕ_h are the electron and hole quasi-Fermi levels respectively and ψ is the electric potential, have been used as governing equations for the carrier transport phe-

nomena in Si, while the boundary conditions at the Si-metal interface have been derived from the thermionic emission theory described in detail elsewhere [2]. The mathematical model consists of two continuity equations and Poisson's equation posed in the bounded domain representing the device geometry with two ohmic contacts and the Si-metal interface.

Results and Discussion

The problem has been solved numerically using a general-purpose two-dimensional finite-element solver. The materials parameters used in the solution are summarized in Table 1. Three different cases, the forward biased, reverse biased, and the unbiased (equilibrium) p-n junctions have been analyzed. The carrier profiles for the three different cases and the structure of quasi-Fermi levels and electric potential demonstrate that the precipitate charges with the same charge as the majority carrier in Si. In steady-state, the precipitate, in our case charged negatively, creates its own electric field which repels majority carriers and attracts minority carriers. In transition from reverse bias to forward bias the effect of precipitate dynamically changes. As the device goes from reverse to forward bias the precipitate discharges and consequently the precipitate charge generated electric field decreases.

Forward bias at 0.2 V leads to the injection of carriers from Si into metal with a carrier flux density of $6.7 \times 10^{17} \text{ cm}^{-2} \text{ sec}^{-1}$ (corresponding to 107.2 mA/cm^2) at the Si-metal interface. This changes to $-5.3 \times 10^{14} \text{ cm}^{-2} \text{ sec}^{-1}$ (corresponding to 0.085 mA/cm^2) for a reverse voltage of -0.2 V. Reverse biasing leads to the injection of carriers from metal into Si. Thus, under forward and reverse biasing conditions, the precipitate serves respectively as carrier recombination and generation centers.

The total current at the device contacts is shown respectively in Fig. 2 and Fig. 3 for forward bias up to 0.2V and for reverse bias up to -0.2V. Carrier supply is one of the important factors acting in conjunction with the precipitate field.

The profiles of hole and electron quasi-Fermi levels and the electric potential are presented in Fig. 4. The plots show the band structure is distorted near the metal-precipitate interface for the two biasing regimes.

In conclusion, the electric activity of the metallic precipitate is dictated by the operating regime of the p-n junction. The precipitate dynamically turns from a generation center in a reverse biased p-n junction to a recombination center in a forward biased junction. Consequently, the presence of the precipitate in the depleted region of a reverse biased pn junction increases the leakage current and also increases the forward current for a forward biased pn junction as can also be seen in Fig. 3.

References

- [1] P.S. Plekhanov and T.Y. Tan, "Schottky effect model of electrical activity of metallic precipitates in silicon, Appl. Phys. Lett., vol. 76, pp. 3777-3779, 2000
- [2] E. H. Rhoderick and R.H. Williams, Metal-Semiconductor Contacts, Oxford University Press, 1988

Table 1. Material parameters

Parameter	Value
p-side doping, N_a^-	$4.5 \times 10^{15} \text{ cm}^{-3}$
n-side doping, N_d^+	$1 \times 10^{16} \text{ cm}^{-3}$
Hole lifetime, τ_p	$1 \times 10^{-7} \text{ sec}$
Electron lifetime, τ_n	$1 \times 10^{-7} \text{ sec}$
Precipitate radius, R_p	$5 \times 10^{-7} \text{ cm}$
Schottky barrier height between Si and metal ϕ_{Bn}	0.68 V

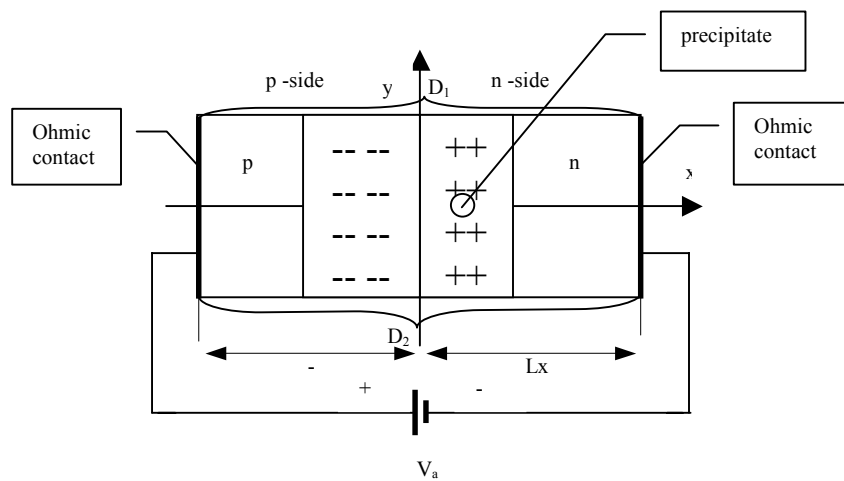


Figure 1. Schematic diagram of the device

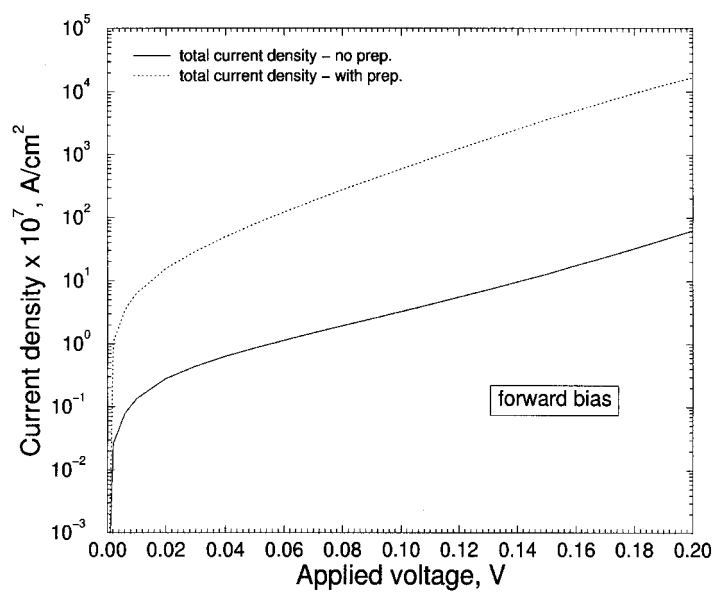


Figure 2. p-n junction current under forward bias.

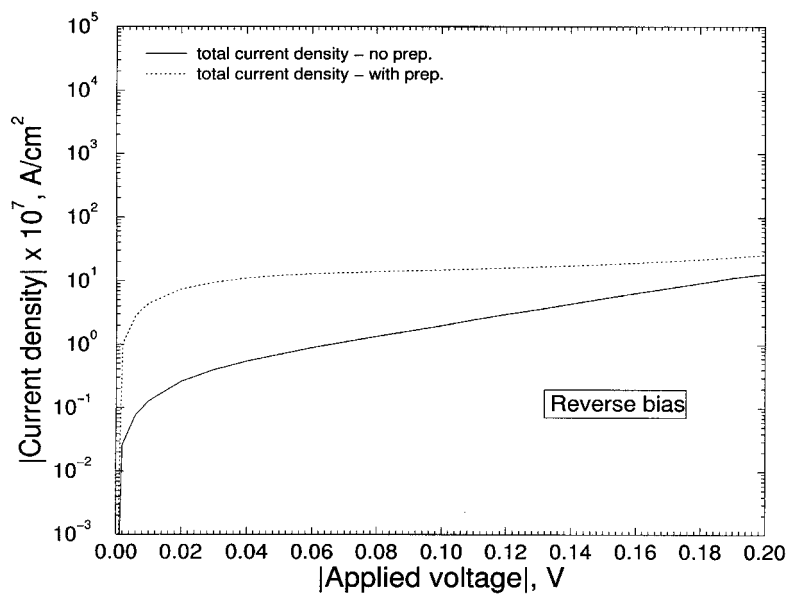


Figure 3. p-n junction current under reverse bias.

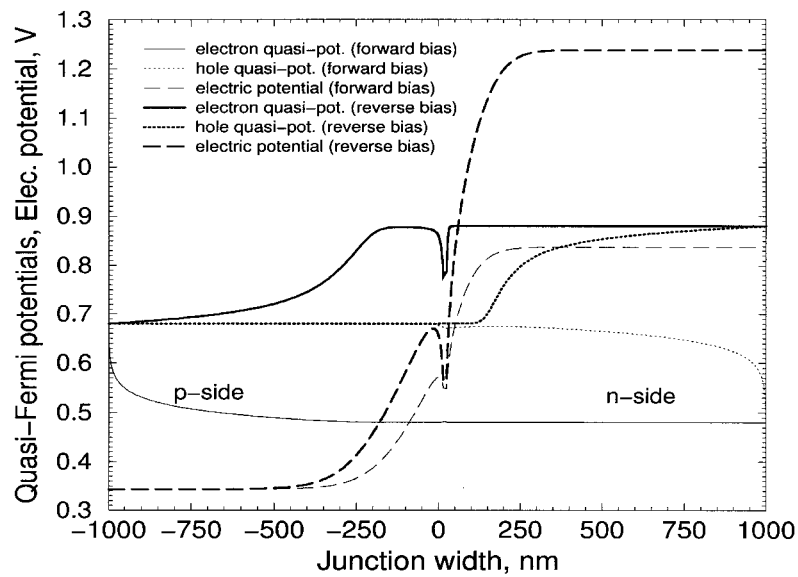


Figure 4. Band structure diagrams for forward bias at 0.2 V and reverse bias at -0.2 V.

Resonance Acoustic Diagnostics as a Characterizing Tool for Solar-Grade Cz-Si Wafers

A. Belyaev¹, S. Ostapenko¹ and T. L. Jester²

¹ University of South Florida, Center for Microelectronics Research, Tampa FL 33620

² Siemens Solar Industries, Camarillo, CA 93011

A resonance acoustic method has been developed experimentally and theoretically to characterize an elastic quality of as-grown and processed silicon for IC and PV application [1]. The acoustic approach is non-contact and non-destructive technique applicable for inspection of the full-size Si wafers. Entire cycle of the acoustic measurements can be performed within a few seconds which makes the method promising as in-line quality assurance tool. In this study, ultrasonic vibrations were excited into commercial 200 mm Cz-Si wafers using an external ultrasonic transducer and their amplitude was recorded using a scanning air-coupled acoustic probe operated in a non-contact mode. A schematic of the system is shown in the Figure 1. By tuning the driving frequency of the transducer, we observed the amplification of a specific acoustic mode, referred further as a “whistle” [2]. Typically, a resonance frequency of the whistle is observed at 12.7 KHz with a narrow frequency generation window of ~ 50Hz showing a variation between as grown and processed wafers. We noticed that a minimum amplitude of the transducer vibrations required to generate the whistle (amplitude threshold) is reduced by a factor of 10 in PV wafers compared to IC wafers of the same

diameter [2]. This can be attributed to a reduced thickness of the PV wafers versus IC wafers.

Spatial distribution of the whistle in 200 mm Cz-Si wafers was measured in a non-contact mode allowing for identification the mode with high-order flexural vibrations of a thin elastic circular plate (Fig. 2). The acoustic map clearly reflects C_4 symmetry of the (100) crystallographic plane of the wafer. Frequency and amplitude scans of the whistle mode can be used for fast in-line monitoring to separate wafers with high and poor elastic quality.

Theoretical modeling of the whistle in Si wafers of different diameter was performed [3]. In a case of 200mm wafers an excellent match with experimental resonance frequency was achieved. The calculations predicted resonance frequencies of the whistle in 150 and 300mm diameter wafers.

References

1. A. Belyaev, Master thesis, University of South Florida (2002).
2. S. Ostapenko and I. Tarasov, Appl. Phys. Lett., v. 76, 2217 (2000).
3. A. Belyaev and S. Ostapenko, Physica B, v. 310, 1137 (2001).

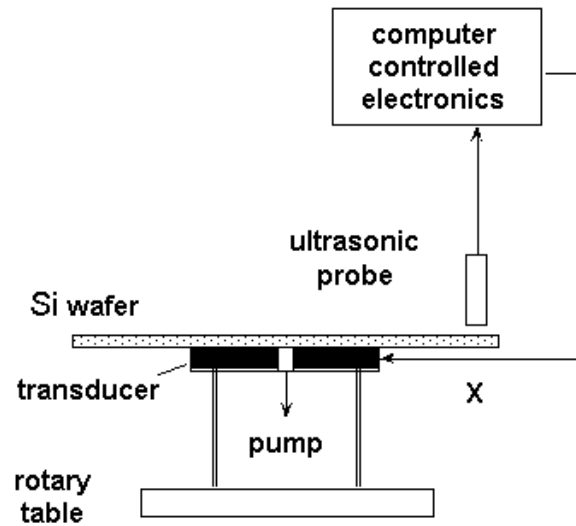


Figure 1. A schematics of the acoustic system for “whistle” monitoring.

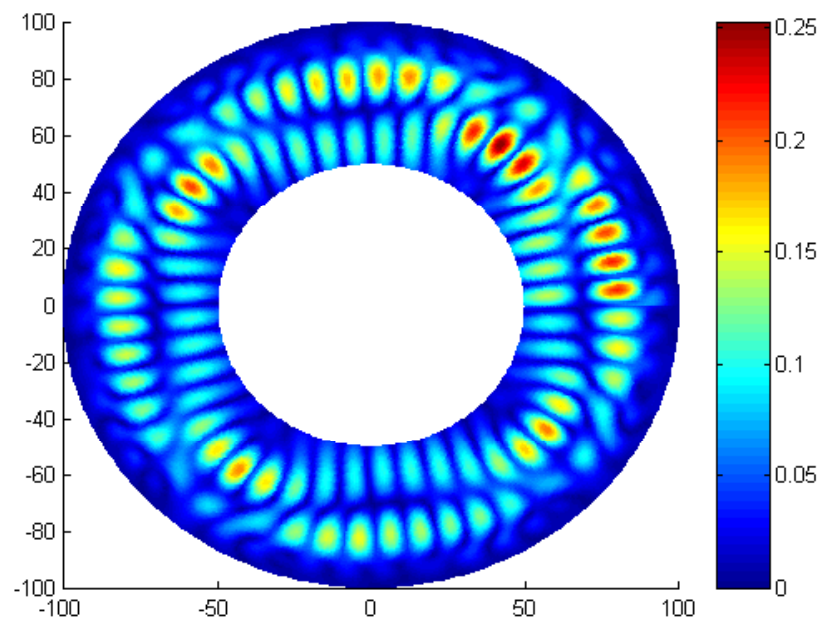


Figure 2. Spatial distribution of the “whistle” in 200mm Cz-Si wafers. Central part of the wafer (white area) was not measured due to interference with the transducer.

Rapid Thermal Processing Enhanced SiN_x-induced Defect Passivation in 15.9% Efficient Screen-Printed EFG Silicon Solar Cell

¹Ji-Weon Jeong, ¹Ajeet Rohatgi, ²B. R. Bathey, ²J. P. Kalejs

¹University Center of Excellence for Photovoltaics Research and Education, School of Electrical and Computer Engineering, Georgia Institute of Technology, Atlanta, GA 30332

²ASE Americas, Inc. 4 Suburban Park Dr. Billerica, MA 01821

Abstract

The conversion efficiency of 15.9% has been achieved on low-cost EFG ribbon Si solar cells. This represents the highest reported efficiency for EFG ribbon Si solar cells fabricated with manufacturable technologies, involving belt furnace diffusion, PECVD SiN_x antireflection coating, and screen-printed contacts. Rapid thermal firing cycles, with fast ramp-up and cooling rates, were optimized to enhance the PECVD SiN_x-induced hydrogen passivation of defects, back surface field, and contacts. Process optimization increased the bulk lifetime from ~2 μs to ~50 μs, resulting in 15.9% efficiency with a Voc of 615 mV, a Jsc of 33.7 mA/cm², and a FF of 0.769.

Introduction

Low-cost high-efficiency solar cells are the key to making photovoltaics (PV) a cost-effective energy option for the 21st century. EFG ribbon Si is one of the most promising candidates to achieve both low-cost and high-efficiency cells because of efficient use of Si feedstock; and elimination of mechanical sawing steps, deep surface damage etching, and kerf losses. However, due to the direct contact with the die and thermal stresses during crystal growth, EFG Si has a high density of crystalline defects such as dislocations, twins, and grain boundaries; relatively high concentrations of impurities such as carbon and transition metals¹. These defects and impurities act as carrier recombination sites and reduce the minority carrier lifetime in the as-grown EFG Si to typically less than 3 μs, which is not sufficient for high efficiency cells. Therefore, effective lifetime-enhancement techniques need to be implemented during cell fabrication to achieve high efficiencies.

Rapid thermal processing (RTP) has been used successfully in the laboratories for many Si solar cell fabrication steps such as shallow n⁺ emitter diffusion², high-quality oxide growth for surface passivation³, p⁺ aluminum (Al) back surface field (BSF)⁴, and screen-printed contact formation⁵. The use of RTP for solar cells is currently being investigated at the laboratory level because a continuous high throughput RTP machine is not yet available, although some equipment manufacturers are working on it. A conveyor belt furnace is preferred by the PV industry today due to its capability of continuous high-throughput processing. However, RTP provides a promising option for low-cost and high-efficiency Si solar cells in the near future because of fast processing, accurate temperature control, and beneficial optical effects due to high-energy photons in the visible and ultra-violet range⁶.

Figure 1 shows the efficiency progress of screen-printed manufacturable ribbon Si solar cells.

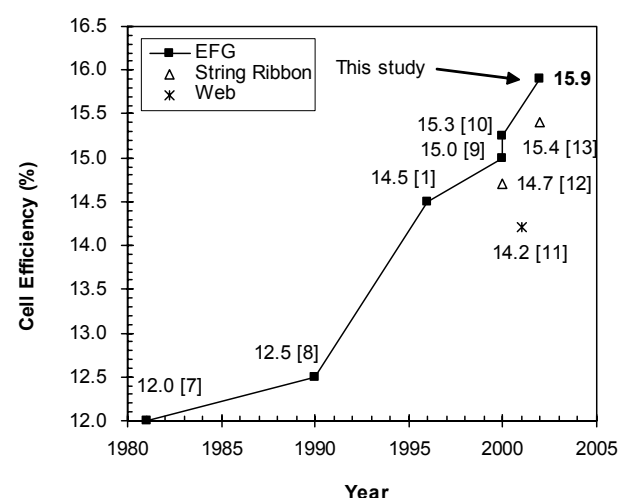


Figure 1. The efficiency progress of ribbon Si solar cells. Note: The number in brackets represents the reference.

The progress was very slow during 1980-1990 but, after 1990, cell efficiencies have increased quite rapidly. This is the result of improved understanding of loss mechanisms, gettering and defect passivation, and improved crystal growth and process technologies. Figure 1 shows that screen-printed ribbon Si cell efficiencies of 15.3% have been reported on EFG Si¹⁰, 14.2% on dendritic web Si¹¹, and 15.4% on String ribbon Si¹³. This paper reports on a record high efficiency (15.9%) cell on a low-cost ribbon Si using a cost-effective technology, involving screen-printing, SiN_x AR coating, and RTP.

Experimental

The 15.9% efficient EFG Si cell was fabricated on a ~300 μm thick and ~3 Ω-cm EFG Si using a very simple n⁺-p-p⁺ cell design. Cell fabrication involved phosphorus (P) diffusion in a conveyor belt furnace to form n⁺ emitter with a sheet resistance of 45-50 Ω/sq, which is suitable for screen-printed contacts. A silicon nitride (SiN_x) antireflection (AR) coating was deposited on top of the n⁺ emitter in a commercial low-frequency plasma enhanced chemical vapor deposition (PECVD) reactor. SiH₄, NH₃, and N₂ gases were used to deposit the SiN_x coating with an average refractive index of ~2.1 and thickness of ~775 Å. A commercial Al paste (FX-53-038 from Ferro Corp.) was printed on the entire backside and annealed at 750 °C in a single wafer RTP system, involving a fast ramp-up and cooling rates to promote and enhance PECVD SiN_x-induced hydrogen passivation of defects in EFG Si. Silver (Ag) grid was screen printed on top of the SiN_x AR coating and fired through it very rapidly at 700 °C in RTP to form the front contacts to the n⁺ emitter. Finally, the cells were annealed in forming gas at 400 °C for 10 min.

Results and Discussion

In order to support that the two-step RTP firing was critical in achieving record-high efficiency screen-printed EFG Si cells, additional EFG Si cells were fabricated using three different firing schemes: a) two-step firing in a conveyor belt furnace (simultaneous firing of the PECVD SiN_x and the screen-printed Al at 850 °C for 2min followed by 730 °C/10s firing for the screen-printed Ag contacts), b) co-firing at 730 °C in a conveyor belt furnace, and c) co-firing at 700 °C in the RTP system. Nine 2×2 cm² cells were fabricated on each 10×10 cm² EFG Si wafer, and several wafers were used for each process scheme producing 50-100 cells per process scheme. After fabrication, the cells were isolated by dicing and analyzed by lighted and dark current-voltage (I-V) measurements. Bulk lifetimes were measured before and after each process scheme by quasi-steady-state photoconductance (QSSPC) method to assess the process-induced lifetime change.

Figure 2 shows bulk lifetime and cell efficiency after the four different process schemes. Scheme d) involves the two-step RTP firing, which produced the best results. The starting or as-grown bulk lifetime of the EFG Si samples was only ~2 μs, which improved to a) ~13 μs after the two-step belt furnace firing process, b) ~18 μs after the co-firing process in the belt furnace, c) ~35 μs after the co-firing in the RTP, and d) ~48 μs after the two-step RTP firing process. Figure 2 also shows that a) the two-step belt furnace firing process resulted in an average efficiency of ~13% with a maximum of 13.8%, b) the belt furnace co-firing gave an average efficiency of 13.5% with a maximum of 14%, c) the RTP co-firing produced an average efficiency of 14.3% with a maximum of 15%, and d) the two-step RTP firing process resulted in an average efficiency of 15% with a

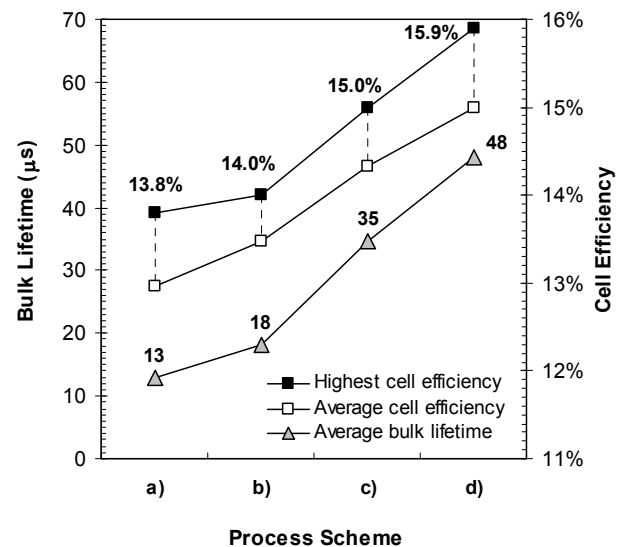


Figure 2. The bulk lifetime and cell efficiency of screen-printed EFG Si cells after four different firing schemes.

maximum of 15.9%.

Figure 3 shows the lighted I-V data for the highest efficiency (15.9%) EFG Si cell (verified by National Renewable Energy Laboratory). This cell had an open-circuit voltage (V_{oc}) of 615 mV, a short-circuit current (J_{sc}) of 33.7 mA/cm², and a fill factor (FF) of 0.769. Figure 4 shows an efficiency distribution of 61 screen-printed EFG Si cells fabricated in three different batches using the two-step RTP firing scheme. The average efficiency of the cells was found to be 15.0%, and many cells showed efficiencies over 15%. To establish the superiority of the two-step RTP firing over the industrial belt firing, we also fabricated as many as 71 screen-printed EFG Si cells. These cells were fabricated along with the two-step RTP fired cells using the same P diffusion, SiN_x AR coating, and screen-printed metals. But, co-firing of the SiN_x AR coating, Al on the back, and Ag grid on top of the SiN_x AR coating was performed in a conveyor belt furnace being used in a PV manufacture. The average efficiency of the co-fired cells was found to be 13.9% with a maximum efficiency of 14.7%, which is well below the two-step RTP firing scheme.

Following discussion explains how and why optimized RTP firing cycles contributed to record-high efficiency and why the two separate RTP firing cycles were used. First of all, the optimal hydrogenation temperature for the PECVD SiN_x-coated EFG Si was found to be 750 °C in RTP. This is the result of competition between the release/diffusion of atomic hydrogen from the SiN_x into the bulk Si and retention of hydrogen at defects. Less atomic hydrogen is incorporated into the bulk Si at lower temperatures while more atomic hydrogen evolves out of the defects at higher temperatures. Rapid cooling can reduce dehydrogenation of defects. This is why the belt-fired cells, where cooling was much slower than RTP, showed lower bulk lifetime and cell efficiency (Figure 2). Secondly, simultaneous firing of the SiN_x and Al enhanced hydrogenation of defects in EFG Si because vacancies generated by the Al alloying process increase the flux of hydrogen into the bulk Si and also split the molecular hydrogen into atomic hydrogen. We have explained and demonstrated this mechanism elsewhere¹⁴. Third, fast ramp-up rate in RTP, relative to belt furnace process, improves the uniformity and quality of Al-BSF⁴. Even though the optimum alloying temperature for the Al-BSF is 850 °C⁴, 750 °C was used in Step 1 to maximize the defect passivation or bulk lifetime enhancement.

Optimized screen-printed Ag contact firing at 700 °C (Step 2) also contributed to high efficiency because very short firing time with rapid cooling rate helped in retaining hydrogen at defects which was incorporated in Step 1. This was supported by bulk lifetime measurement, which showed only 1-2%

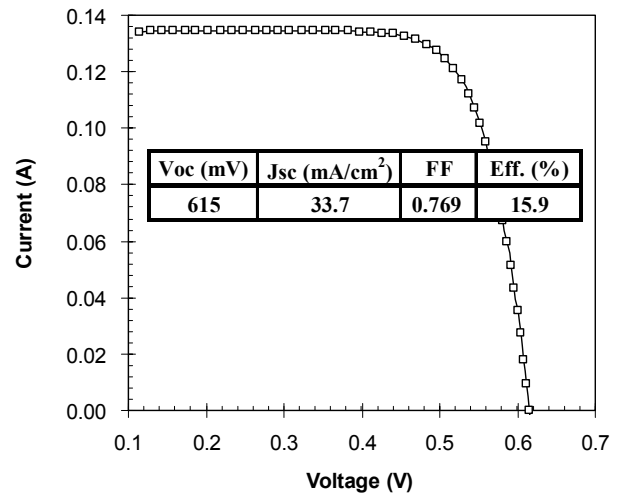


Figure 3. Current-voltage (I-V) curve for the 15.9% efficient screen-printed EFG ribbon Si solar cell, measured by National Renewable Energy Laboratory.

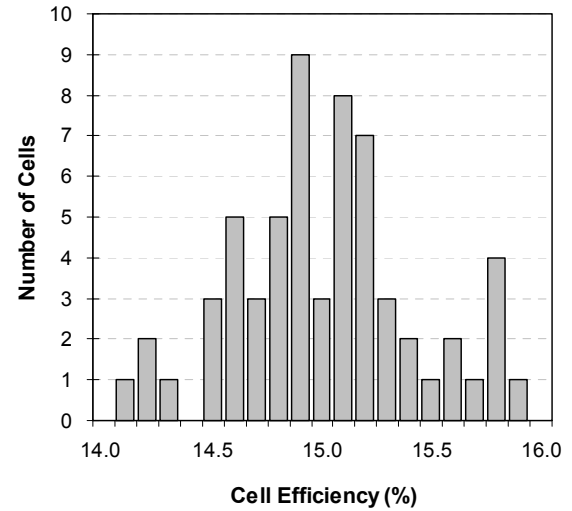


Figure 4. An efficiency distribution of 61 screen-printed EFG Si cells using the two-step RTP firing.

252

decrease in bulk lifetime after the RTP contact firing as opposed to 20-30% loss of bulk lifetime after contact firing in the belt furnace. In addition, rapid contact firing in RTP reduced junction shunting without degrading series resistance ($\sim 0.8 \Omega\text{-cm}^2$). This resulted in somewhat higher FF (~ 0.77) for RTP than the belt furnace firing. It was found that RTP co-firing at 750 °C severely degraded the screen-printed Ag contact quality and FF, while RTP co-firing at 700 °C did not produce maximum hydrogenation or bulk lifetime enhancement. That is why the two-step RTP firing was selected, which gave the highest bulk lifetime, reasonable BSF, and high FF, resulting in the 15.9% efficient screen-printed EFG Si cell.

Conclusion

In conclusion, screen-printed EFG Si cell efficiencies approaching 16% have been achieved using single layer SiN_x AR coating with no surface texturing. Fundamental understanding of process-induced hydrogenation of defects, BSF, and contacts in conjunction with two-step RTP firing scheme contributed to this success. In the first firing step at 750 °C, fast ramp-up rate improved the Al-BSF quality and contacts, simultaneous annealing of SiN_x and Al enhanced atomic hydrogen content of the bulk Si, and fast cooling rate improved the hydrogen retention or defect passivation. Very short and rapid firing at 700 °C in the second step improved the hydrogen retention at defects without compromising the contact quality. Enhanced defect passivation or bulk lifetime improved V_{oc} and J_{sc} while improved contact quality increased FF, resulting in the record-high efficiency screen-printed ribbon Si solar cells to date.

References

- ¹M. J. Kardauskas, M. D. Rosenblum, B. H. Mackintosh, and J. P. Kalejs, Proceedings of 25th IEEE Photovoltaic Specialists Conference, Washington, D.C., 1996, p. 383.
- ²B. Hartiti, A. Slaoui, J. C. Muller, R. Stuck, and P. Siffert, *J. Appl. Phys.*, **71**, 5474 (1992).
- ³P. Doshi, J. Moschner, J. Jeong, A. Rohatgi, R. Singh, and S. Narayanan, Proceedings of 26th IEEE Photovoltaic Specialists Conference, Anaheim, CA, 1997, p. 87.
- ⁴S. Narasimha and A. Rohatgi, Proceedings of 26th IEEE Photovoltaic Specialists Conference, Anaheim, CA, 1997, p. 63.
- ⁵H. El Omari, J. P. Boyeaux, and A. Laugier, Proceedings of 25th IEEE Photovoltaic Specialists Conference, Washington, D.C., 1996, p. 585.
- ⁶D. Ratakonda, R. Singh, L. Vedula, A. Rohatgi, J. Mejia, and S. Narayanan, *J. Electrochem. Soc.*, **144**, 3237 (1997).
- ⁷K. V. Ravi, R. C. Gonsiorawski, A. R. Chaudhuri, C. V. Hari Rao, C. T. Ho, J. I. Hanoka, and B. R. Bathey, Proceedings of 15th IEEE Photovoltaic Specialists Conference, Kissimmee, FL, 1981, p. 928.
- ⁸B. R. Bathey, C. E. Dube, J. P. Kalejs, and F. V. Wald, Proceedings of 21st IEEE Photovoltaic Specialists Conference, Kissimmee, FL, 1990, p. 687.
- ⁹V. Yelundur, J. Jeong, A. Rohatgi, M. D. Rosenblum, and J. I. Hanoka, Proceedings of 10th NREL Workshop on Crystalline Silicon Solar Cell Materials and Processing, Breckenridge, CO, 2000, p. 228.
- ¹⁰B. R. Bathey, J. P. Kalejs, M. D. Rosenblum, M. J. Kardauskas, R. M. Giancola, and J. Cao, Proceedings of 28th IEEE Photovoltaic Specialists Conference, Anchorage, AK, 2000, p. 194.
- ¹¹D. L. Meier, H. P. Davis, R. A. Garcia, J. Salami, A. Rohatgi, A. Ebong, and P. Doshi, *Solar Energy Materials and Solar Cells*, **65**, 621 (2001).
- ¹²V. Yelundur, A. Rohatgi, J. Jeong, A. M. Gabor, J. I. Hanoka, and R. L. Wallace, Proceedings of 28th IEEE Photovoltaic Specialists Conference, Anchorage, AK, 2000, p. 91.
- ¹³Giso Hahn, Alexander Hauser, Andrew M. Gabor, and Mary C. Cretella, Proceedings of 29th IEEE Photovoltaic Specialists Conference, New Orleans, LA, 2002, in press.
- ¹⁴J.-W. Jeong, M. D. Rosenblum, J. P. Kalejs, and A. Rohatgi, *J. Appl. Phys.*, **87**, 7552 (2000).

Measurement of the current distribution in the emitter region of solar cells by magnetic methods

R. Buchwald, E. Soika, M. Zschorsch, H.J. Möller

Freiberg University of Mining and Technology, Institute for Experimental Physics
Silbermannstr. 1, 09596 Freiberg, Germany

D. Drung, T. Schurig

Physikalisch-Technische Bundesanstalt, Abbestr. 2 – 12, 10587 Berlin, Germany

ABSTRACT

Damaged areas in the contact and emitter region of solar cells cause current losses. The localization of these areas is possible by a measurement of the magnetic field that is connected with the lateral current in the surface region under illumination. In this paper a new method is introduced which uses an inductive coil for the measurement of the field. The results are compared with the previously developed CASQ method which uses a superconducting SQUID sensor instead. Furthermore a faster numerical algorithm has been developed to derive the local current density from the magnetic field. Both the current distributions in the contact grid of solar cells and in pn – junctions are determined. Experimental results are presented for various damage situations that can occur in the emitter and contact region of solar cells.

1. INTRODUCTION

In previous papers it has been shown that one can measure the local current flow in the emitter and the contact grid of solar cells under illumination [1-5]. The method is based on the fact that currents which flow parallel to the surface of a solar cell produce a magnetic field that can be measured by sensitive magnetic field detectors. In the CASQ method a high temperature superconducting SQUID is used inside a specially designed liquid nitrogen cryostat. Topographical mappings of the magnetic field with a lateral resolution of about 300 - 500 μm have been obtained. A practical limitation of the method is that external magnetic stray fields have to be shielded. A newly developed system uses inductive coils for the measurement. In this case the current is generated by a pulsed laser beam and the resulting magnetic field is detected inductively. This method has a much higher lateral resolution of about 10 μm and is less sensitive to magnetic stray fields. Both techniques require the numerical calculation of the local current density from the measured magnetic field. This so called inverse problem cannot be solved in general but in the special case of a two dimensional current distribution, which is approximately given in the emitter and contact region of a solar cell [6]. We developed a fast numerical Fourier transformation method for the direct calculation of the current distribution.

In this paper mainly the current distributions in illuminated pn – junctions on multicrystalline wafers have been investigated. The experimental results show that in many cases the junctions do not collect and transport the current as expected. This is caused by inhomogeneities of the sheet resistance and by local shunts. The possible failure mechanisms can be investigated in detail by microscopic investigations of the underlying material structure. It is also shown that although the illumination conditions are different both experimental methods yield similar results when damaged regions due to shunts are analyzed.

2. EXPERIMENTAL PROCEDURE

A detailed description of the CASQ method has been given in references [1, 3]. In the present system the superconducting loop of the SQUID inside of the cryostat measures the B_z - component of the magnetic field perpendicular to the surface. This component is less critical to misorientations of the sensor and allows the highest lateral resolution, which is determined by the minimum distance between the SQUID sensor and the wafer surface. The wafer, either a solar cell or simply a pn – junction, is illuminated by a homogeneous light source and scanned in two directions below the SQUID. The voltage of the solar cells can be changed by a variable load resistance whereas pn – junctions without contacts are measured under open circuit conditions.

In the newly developed system the current is generated by a pulsed laser beam with a wavelength of 680 nm. The resulting alternating magnetic field is detected by an inductive coil with a diameter of about 0.7 cm. The pulse frequency in the present measurements is 1 kHz but can be increased to about 100 kHz which improves the sensitivity of the system. Since the spatial resolution is determined by the spot size of the beam (about 10 μm) the coil can be placed at a larger distance to the surface. This has the advantage that the three vector components of the field can be measured more easily. The electrical signals are filtered electronically so that stray fields from the environment can be strongly reduced and shielding is not required.

Assuming that the current density $\vec{j} = (j_x, j_y, 0)$ lies entirely in a thin sheet of thickness d the two-dimensional current distribution in the x-y plane and the magnetic field are related by the law of Biot – Savart in the following form

$$\vec{B}(\vec{r}) = \frac{\mu_0 d}{4\pi} \iint \frac{\vec{j}(\vec{r}') \times (\vec{r} - \vec{r}')}{| \vec{r} - \vec{r}' |^3} dx' dy'$$

where $\mu_0 = 4\pi \times 10^{-7}$ Tm/A is the permeability of the free space. The magnetic field is measured at a height z above the plane. The current density components j_x, j_y can be derived from these equations by a Fourier transformation method which will be described elsewhere [7].

Previous measurements with the CASQ method on solar cells have shown that mainly the currents in the contact grids can be detected. Therefore current losses due to broken contacts, high contact resistances to the emitter, shunts below contacts or at the edges of solar cells become visible in this way. Because of the limited lateral resolution of the method damaged regions of the emitter between the contacts could not be resolved in many cases. Therefore investigations of the pn – junction and emitter region were carried out without contacts. For this purpose Cz – and multicrystalline wafers with a diffused pn – junction only were produced and investigated.

3. EXPERIMENTAL RESULTS

Figure 1 shows the B_z - component of the magnetic field above a globally illuminated mono – and multicrystalline wafer with a diffused pn – junction. The underlying current distribution is the result of the local generation and recombination and the varying sheet resistance of the emitter. It is evident that the current distribution is less homogeneous in the multicrystalline wafer. In order to understand and analyze such distributions in more detail the current density components in the emitter plane were derived numerically from the magnetic field. Figure 2 shows the result for a monocrystalline wafer where the surface and emitter region have been damaged deliberately by scratches. The damaged areas become easily visible and produce a current pattern that consists of regions where either

the generation or the recombination is enhanced. Previous results for solar cells have shown that under an external load such a current distribution changes due to the increasing current flow through the parallel external resistance. However bad regions can be identified best in the open circuit case by the technique. Shunting currents can be determined quantitatively and measured as a function of the external voltage.

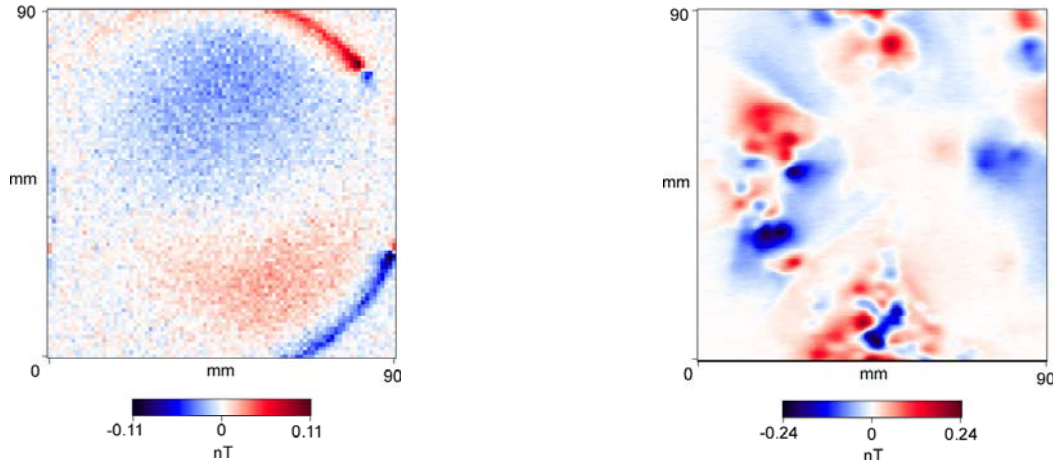


Figure 1 Topographical SQUID measurement of the B_z -component of the magnetic field of two illuminated wafers with a diffused pn-junction at a distance of about 1 mm above the surface. Monocrystalline Cz-wafer (left) and multicrystalline wafer (right).

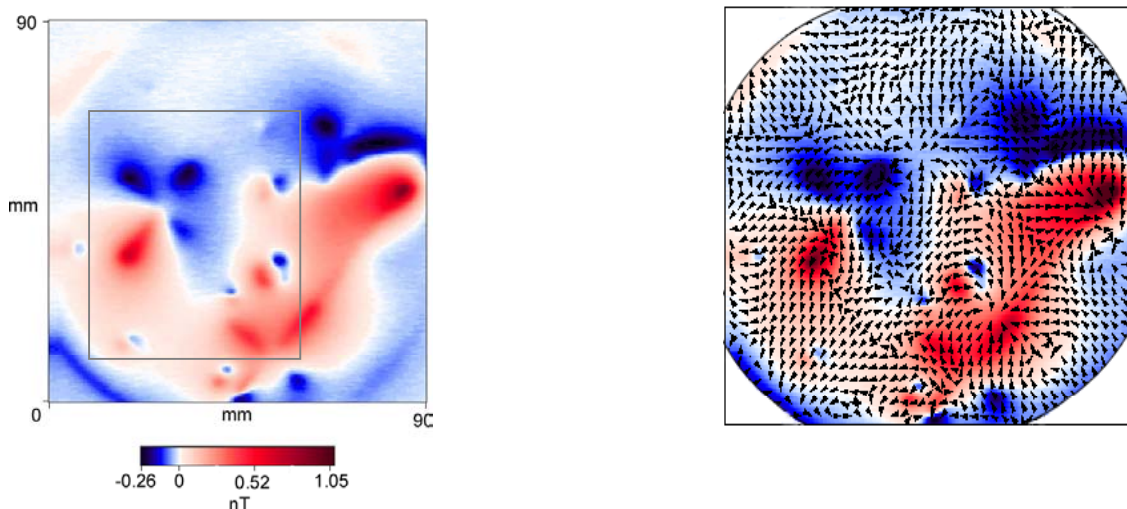


Figure 2 Topographical SQUID measurement of the B_z -component of the magnetic field of an illuminated diffused monocrystalline Cz-wafer (left) and corresponding current distribution (right). The wafer surface and underlying junction has been deliberately damaged by scratches at several positions. The marked region is also measured by the inductive coil method (see figure 3).

The experimental results obtained with the inductive coil system resemble the SQUID measurements and yield similar information. This is shown in figure 3 where a part of the same wafer as in figure 2 is measured with such a system. Instead of the vertical B_z - component the field components parallel to the surface (B_x and B_y) are measured here. Due to the higher spatial resolution more details become visible. The calculated currents yield partly a different distribution compared to figure 2. This is due to the different illumination conditions, since the wafer is illuminated by a focused laser beam here in contrast to the global illumination in the SQUID measurements. It is however possible in both cases to identify the areas where the current flow is concentrated because of a local shunt or a higher generation (encircled regions in figure 3). It can be seen that the mechanical damage of the surface by scratches influences the current flow in a complicated way which can be analysed in great detail by these methods. The inductive coil method has the advantage to be much simpler experimentally, it requires however higher local currents for detection compared to the SQUID system.

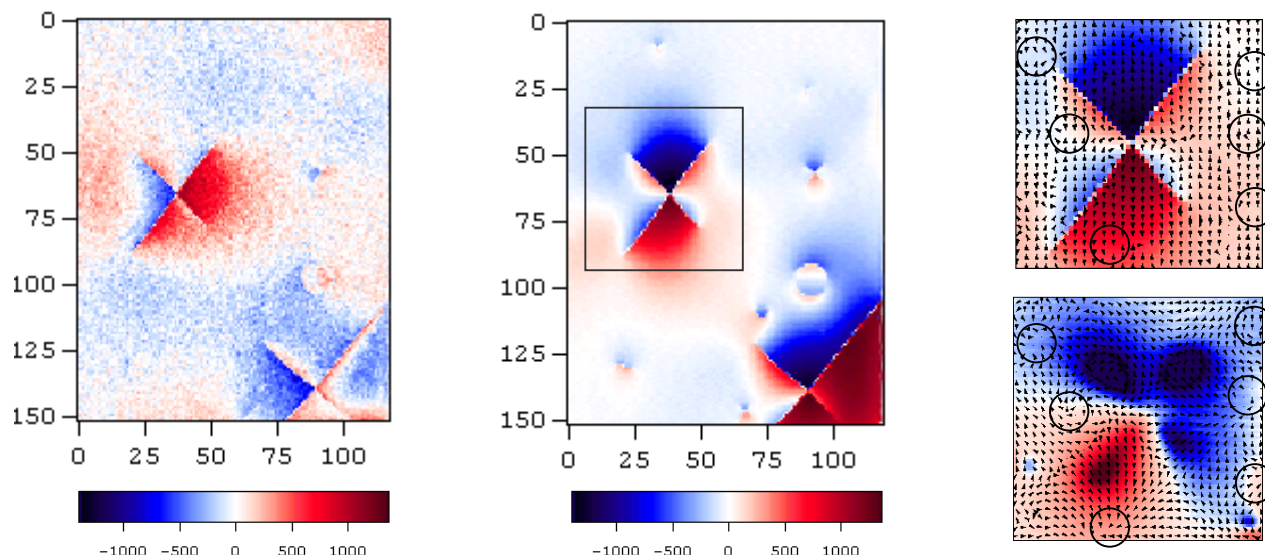


Figure 3 Inductive coil measurement of the B_x - (left) and B_y - (center) component of the magnetic field in the marked region of figure 2. The magnetic field is measured in relative units here. The top right, enlarged image shows the calculated current distribution for the marked region. For comparison the current distribution calculated from the B_z – component of figure 2 is depicted. Areas of current concentrations are encircled in both cases.

4. REFERENCES

- [1] J. Kabs, H.J. Möller, Proc. of the 14th EPSEC, Barcelona (1997), p. 2381
- [2] J. Kabs, H. J. Möller, Proc. 2nd World Conf. PVSEC, Vienna (1998) p. 82
- [3] J. Kabs, H. J. Möller, phys. stat. sol. (b) 22, (2000) 337
- [4] J. Koriath, H. J. Möller, Proc. of the 15th EPVSEC München (2002)
- [5] J. Kabs, H. J. Möller, Freiberger Forschungshefte (2002)
- [6] B.J. Roth, N.G. Sepulveda, J.P. Wikswo Jr., J. Appl. Phys. 65 (1), (1989) 361
- [7] E. Soika, H. J. Möller, to be published

ANALYSIS OF SHUNTS IN MULTICRYSTALLINE SILICON SOLAR CELLS USING MICROPROBE X-RAY FLUORESCENCE TECHNIQUE

T.Buonassisi, O.F.Vyvenko, A.A.Istratov, E.R.Weber
University of California, Berkeley, CA 94720

R.Schindler
Fraunhofer ISE, Freiburg, Germany

G.Hahn
University of Konstanz, Konstanz, Germany

Experimental procedures and sample preparation

Experiments were conducted at Beamline 10.3.1 of the Advanced Light Source (synchrotron facility) at the Lawrence Berkeley National Laboratory. This beamline was originally developed for high-resolution x-ray fluorescence microprobe (μ -XRF) studies. An intense x-ray beam from the synchrotron with approximately 10^{10} photons/s is incident on the sample, focused to an optimum spot size of $(1.2 \times 1.5 \times 2.5) \mu\text{m}^2$ by a pair of elliptically bent multilayer mirrors in Kirkpatrick-Baez configuration. The emanating x-ray fluorescence is detected by a Si:Li detector with a resolution of about 180 eV. The sampling depth of this technique is determined by the escape depth of the fluorescence x-rays of interest from the silicon matrix, typically between 10 and 100 microns depending on the element [1]. In order to correlate elemental distribution maps obtained by μ -XRF with minority carrier lifetime maps, x-ray beam induced current maps (XBIC, [2]) were measured in-situ simultaneously with μ -XRF. The advantage of XBIC is that it provides a direct and unambiguous correlation of the chemical nature and recombination activity of the defects. Additionally, XBIC proved to be an extremely helpful tool for finding the areas of interest on the solar cells. This can be achieved by taking a fast overview XBIC map using short accumulation times and large steps in x-y direction. Both μ -XRF and XBIC were performed on fully processed solar cells.

In our experiments, we used two types of fully processed solar cells: BaySix and RGS, pre-characterized with thermography of the forward biased cells [3] in order to find location of the shunts. The size of the BaySix cell was 45×45 mm, the size of the RGS cell was 20×20 mm.

Experimental results: analysis of the BaySix solar cell

XBIC mapping of large areas of the cell, performed with a relatively large step (50-100 microns), enables one to find the area of the shunt by correlating XBIC maps with the thermography and LBIC maps. Since the size of the "hot spot" on the thermography maps is typically around 0.5-2 mm, the task of correlating the XBIC, thermography, and LBIC maps with this accuracy was fairly straightforward. Figure 1 demonstrates a good correlation between XBIC and LBIC images of large area scans of a BaySix solar cell. Then, the area of the shunt was rescanned with a smaller step and a longer accumulation time in order to achieve the optimum XRF sensitivity.

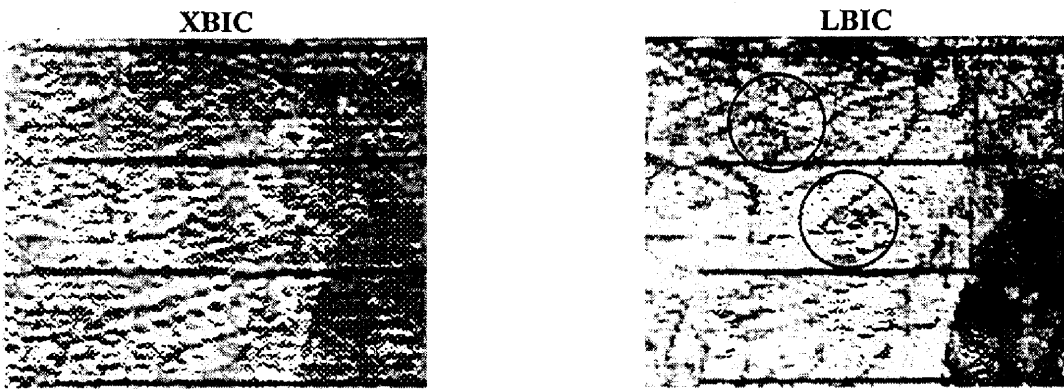


Figure 1 – Comparison of XBIC (left) and LBIC (right) maps of a 9x7mm region of a pre-characterized with thermography and LBIC BaySix solar cell. XBIC step size is 100 μm . The circles on the LBIC picture corresponds to areas where shunts was detected by the thermography measurements. Horizontal lines are contact grids; the distance between them is 2.125 mm.

The regions in the center of the map highlighted by the circles in Fig. 1 are of particular interest, as two separate shunts were found there by the thermography measurements. Detailed μ -XRF analyses were performed on these regions of interest. The μ -XRF map of the area which corresponds to the lower circled area in Fig. 1 is shown in Fig. 2 along with the XBIC map which was obtained during the same scan. The map of the shunt area circled in the upper half of Fig. 1 is shown in Fig. 3. In Fig. 2, a cluster of silver particles with the diameter of up to 10-20 μm was found within the area of the shunt. An examination of μ -XRF and XBIC images in the Figure 2 revealed that a dark XBIC contrast spot could be found for every silver particles visible on XRF-map. An optical microscope image of this area did not reveal any surface contamination, suggesting that these precipitates are located within the bulk of the material, possibly close to the surface given the strong fluorescence signal. This suggests that these metal particles may be responsible for the shunt.

Upon closer inspection of the area of interest using μ -XRF scans with longer accumulation times, it was found that the small silver precipitates also contain a small amount of titanium. Since the contact grid contains a significant amount of both silver and titanium, we conclude that the formation of shunts may be caused by the process of the contact strips deposition of the contact strips. Interestingly, these clusters of impurities occur not under the contact strips, but approximately at the midpoint between two contact strips, the closest of which is located nearly a millimeter away from the center of the cluster. Traces of iron could also be found at the Ag-Ti precipitates, which may further contribute to the lowering of the lifetime in this region of the cell.

Similar procedure has been applied for the investigation of another shunt on the same cell, circled in the upper part of the XBIC image of Figure 1. The experimentally obtained μ -XRF maps are presented in Fig. 3. Similarly to the first shunt, both iron and titanium were found.

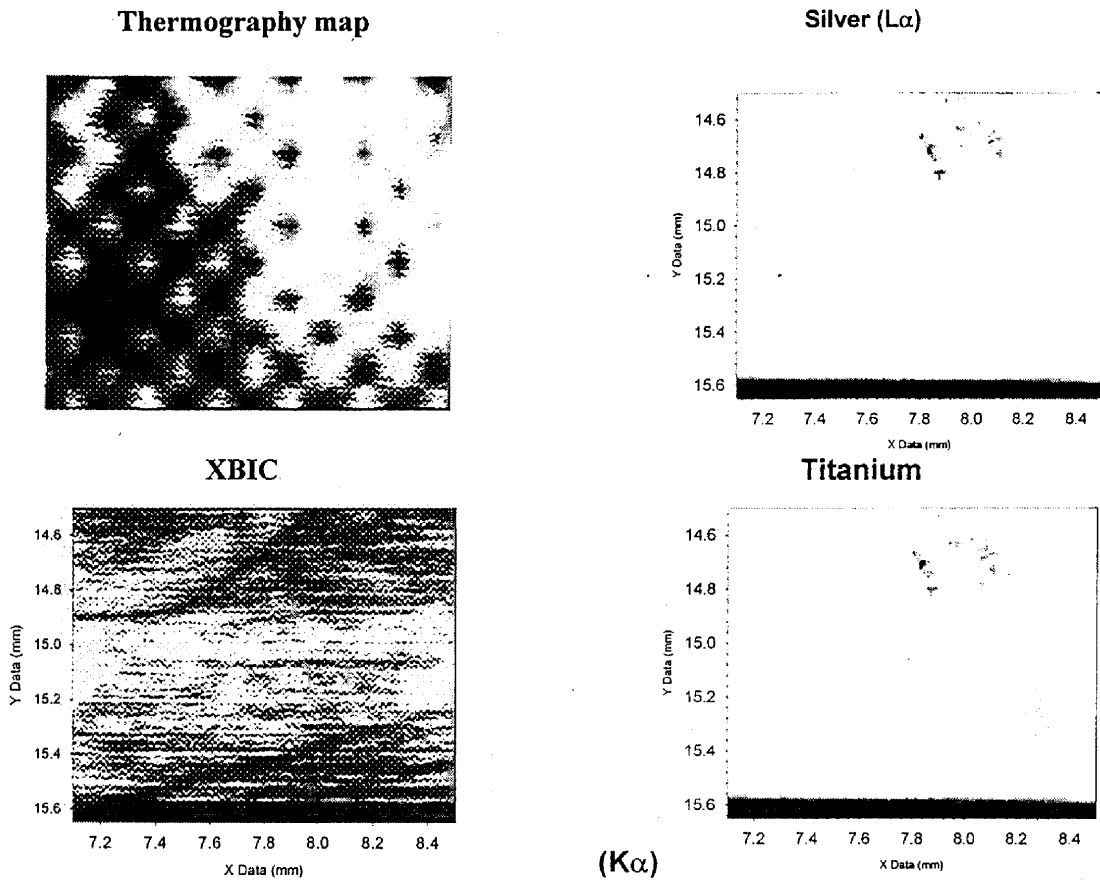


Figure 2 – Comparison of thermography (upper left), XBIC (bottom left), μ -XRF Ag-L α (top right), and μ -XRF Ti-K α (bottom right) maps of a fully processed Baysix solar cell mapped in the area of the lower shunt region shown in Fig. 1. The XRF/XBIC step size is 14 μm . The dotted structure in the thermography map is the result of the low resolution of this thermography scan, and not a physical effect.

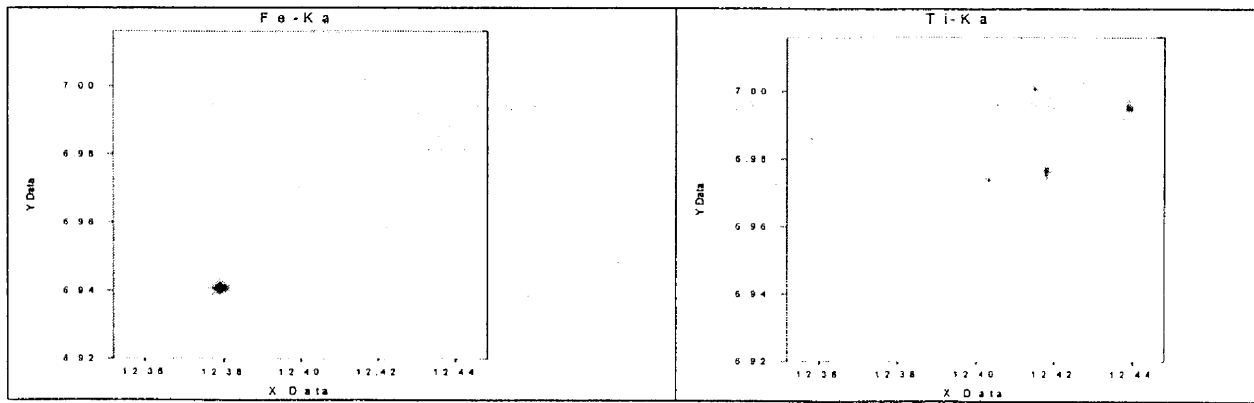


Figure 3 – μ -XRF Fe-K α (left) and Ti-K α (right) maps of a fully processed Baysix solar cell of the upper shunt region shown in the Figure 1. The step size is 3 μm . In this case a large precipitate consisting mainly of iron as well as numerous titanium spots were found in the area of a bright thermography contrast.

Experimental results: analysis of RGS solar cell

For the analysis of RGS material, the same experimental procedure was used. The area of a shunt was mapped using a combination of μ -XRF and XBIC (Figure 4). The areas of shunts had a strong XBIC contrast. μ -XRF mapping revealed several large clusters of titanium within the shunt location. Additionally, these precipitates contained small amount of silver, iron, and copper. All four of these metals could be reliably identified in X-ray fluorescence spectra by their $K\alpha$ and $K\beta$ lines, see Fig. 5.

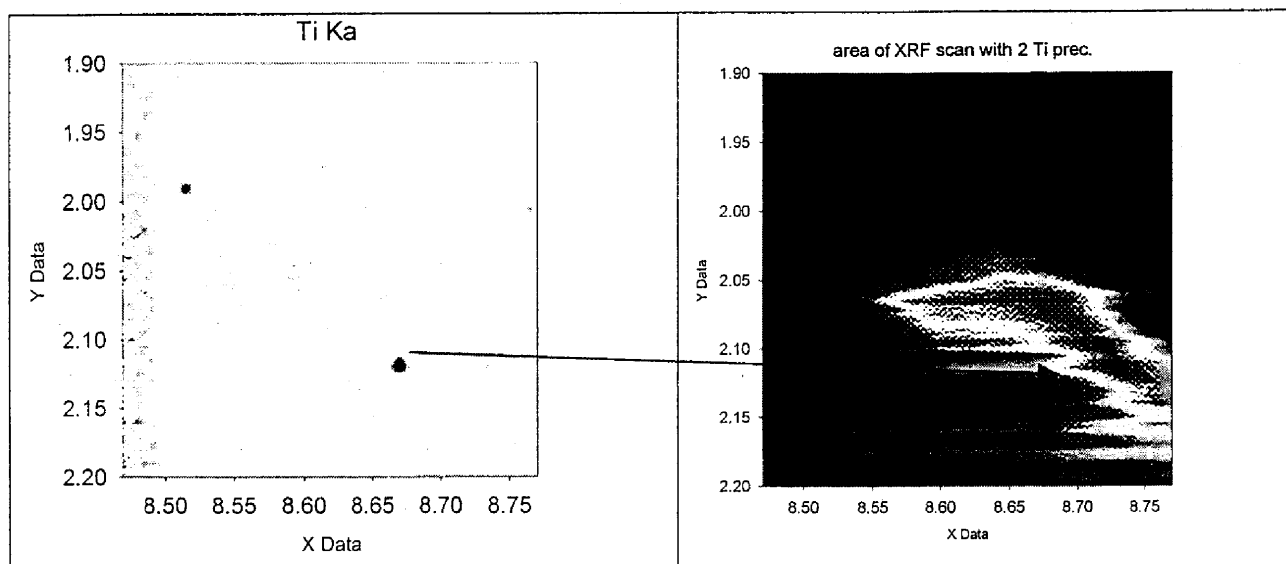


Figure 4. XRF (left) and XBIC maps taken around an area of a shunt in RGS material. Bright XBIC contrast is believed due to an enhanced minority carriers collection due to presence of channels of inverted conductivity type [4]. The position of the largest precipitate coincides with the location of the location of the current collecting channel.

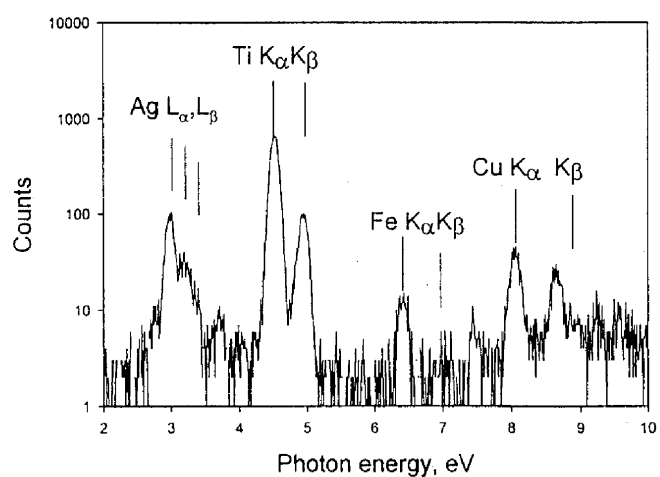


Figure 5. XRF spectrum taken from the largest "Ti"-precipitate shown in the Figure 5. Besides titanium, the precipitate contains silver, copper and iron.

Discussion and conclusions

XRF mapping of BaySix and RGS multicrystalline silicon samples revealed higher than average metal concentration at the shunt locations. Specifically, our investigations revealed the presence of silver, titanium, iron, and (in the RGS sample) copper at the location of the shunt, this suggesting that shunts are process-induced defects formed during deposition of the contact strips. Hence, our data indicate that (a) the shunts we measured contain, or could possibly even be determined by metal contamination, and (b) this metal contamination was process-induced. Unfortunately, the spatial resolution of thermography, which is the only technique capable of reliably detecting and mapping shunt locations, is much worse than the resolution of our X-ray microprobe technique. Therefore, we can only conclude that the metal concentration at the shunt location is higher than average, but cannot unambiguously prove that these metals clusters cause the formation of the observed shunts.

An important confirmation that Ag and Ti clusters cause the shunts would be the information on the depth of these precipitates from the sample surface. Indeed, the metal clusters should be within the depth of the p-n junction in order to affect its properties. The lack of any indications of these precipitates in an optical microscope suggest that these metal clusters are located inside of the solar cell, while the strong XRF signal indicates that these metal clusters are close to the wafer surface. However, so far we could not accurately measure the depth of these clusters from the wafer surface. At the present time, we are developing an experimental procedure which would enable us to obtain information not only on the spatial location of the precipitate, but also on its depth from the surface.

Acknowledgements

The authors would like to acknowledge O. Breitenstein of the Max-Planck-Institute of Microstructure Physics Halle for the thermography measurements on the RGS material, in addition to J. Isenberg and E. Schäffer of Fraunhofer ISE for the thermography and LBIC measurements on BaySix material, respectively. This study was made possible with the financial support from NREL, subcontract No. ATT-2-31605-03, AG-Solar project of the government of Northrhein-Westfalia, and from the German KOSI project.

References

1. S. A. McHugo, A. C. Thompson, C. Flink, E. R. Weber, G. Lamble, B. Gunion, A. MacDowell, R. Celestre, H. A. Padmore, and Z. Hussain, *J. Cryst. Growth* **210**, 395 (2000).
2. O. F. Vyvenko, T. Buonassisi, A. A. Istratov, H. Hieslmair, A. C. Thompson, R. Schindler, and E. R. Weber, *J.Appl.Phys.* **91**, 3614 (2002).
3. O. Breitenstein, K. Iwig, and I. Konovalov, *phys. stat. sol. (a)* **160**, 271 (1997).
4. O. Breitenstein, M. Langenkamp, and J. P. Rakotonaina, *Solid State Phenom.* **78-79**, 29 (2001).

Application of X-ray fluorescence technique to studies of aluminum gettering in silicon

O.F.Vyvenko, T.Buonassisi, A.A.Istratov, and E.R.Weber

University of California, LBNL, 1 Cyclotron Rd., Berkeley, CA 94720, USA

EXPERIMENTAL PROCEDURES AND SAMPLE PREPARATION

The samples used for this study were CZ silicon samples containing approximately $2.5 \times 10^{11} \text{ cm}^{-3}$ (sample Si11), and $1.8 \times 10^6 \text{ cm}^{-3}$ (sample Si6) of the oxide precipitates, formed by precipitating of $\Delta O_i = 6 \times 10^{17} \text{ cm}^{-3}$ and $\Delta O_i < 10^{16} \text{ cm}^{-3}$ of interstitial oxygen, respectively. The samples were doped with approximately $1.5 \times 10^{15} \text{ cm}^{-3}$ of boron. These samples were chosen because they contain sufficiently high density of precipitation sites for metals to mimic multicrystalline silicon, and at the same time the properties of the samples cleaved from the adjacent areas are very similar. After chemical cleaning of the samples and their intentional contamination with Cu or Fe, diffusion anneal was performed at a temperature of 1200°C in forming gas ($\text{N}_2 + 5\% \text{H}_2$) ambient for 30 min. The anneal was terminated by an air cool. After a chemical cleaning and etching, the samples were mapped by microprobe x-ray fluorescence (μ -XRF) at the Beamline 10.3.1 of the Advanced Light Source at Lawrence Berkeley National Laboratory. The typical measurement parameters were: scanned area of approximately $(100 - 300 \mu\text{m}) \times (100 - 300 \mu\text{m})$, focused X-ray beam size of approximately 1.4×2 to $2 \times 2.5 \mu\text{m}$, step size 2 to $3 \mu\text{m}$, accumulation time at each point from 1 to 7 seconds. Then, after another cleaning, a layer of aluminum with the thickness of 1.6 to $2.2 \mu\text{m}$ was deposited on the backside of the samples. Aluminum gettering anneal was performed at 800°C for 2 hours in forming gas ambient in a horizontal furnace. Then, the samples were mapped with μ -XRF again. Additionally, one of the Cu-contaminated samples was also mapped on the back side to prove that the backside aluminum layer has indeed gettered copper.

EXPERIMENTAL RESULTS: COPPER GETTERING

XRF map obtained after Cu contamination, presented in Fig. 1, revealed large clusters of copper of a typical size of 10-30 microns with a density of approximately $4 \times 10^4 \text{ cm}^{-2}$. Since the density of the oxide precipitates was at least 5-6 orders of magnitude higher, we believe that these copper clusters were associated with stacking faults or networks of dislocation loops punched out by the largest precipitates. Note that besides the large Cu clusters, there is a high background level of copper in Fig. 1, probably associated with small Cu agglomerates which could not be resolved in our measurements. Also note that the average Cu concentration in the sample, approximately $(2-3) \times 10^{15} \text{ cm}^{-3}$ according to the μ -XRF data, is much less than the solubility of copper at the diffusion temperature of 1200°C (approx. 10^{18} cm^{-3} , [1]). This indicates that the majority of copper had diffused to the wafer surfaces during cooling and was removed by chemical etching performed before the μ -XRF mapping. The structure and density of Cu clusters observed in Fig. 1 and the average copper concentration in the XRF map are in agreement

with the data reported by McHugo et al. [2], who used the same type of samples and similar Cu diffusion conditions in their study of thermal stability of copper precipitates in silicon.

The μ -XRF map obtained on Si11 sample after Al gettering is presented in Figure 2. Note that due to the lack of markers on the surface of the sample or distinctive features in the μ -XRF spectra, we could not find with sufficient accuracy the same area of the sample that was measured before etching. XBIC technique [3], which was successfully used for this purpose on mc-Si samples, does not work well on metal-contaminated CZ samples due to their spatial homogeneity and lack of characteristic features in minority carrier maps. Therefore, the area mapped in Fig. 2 does not match the area mapped in Fig. 1. However, since CZ samples are fairly homogeneous, we believe that there is no significant differences between the adjacent areas, and each XRF scan is a good representation of a typical metal distribution in the wafer. Fig. 2 revealed that the background Cu concentration has significantly reduced after Al gettering. The average background Cu concentration has reduced to below 10^{15} cm^{-3} . On the other hand, several clusters with high copper concentration were found. As it is known that Cu often forms precipitates and precipitate colonies in the near-surface area (see [4, 5] and references therein), it was suggested that the observed Cu clusters are most likely located at the sample surface. In order to verify this hypothesis, several microns were removed from the sample surface using silicon etch, and the sample was re-measured with μ -XRF. In agreement with our expectations, no copper clusters were found after etching, and the background signal was very low.

In order to prove that the backside aluminum layer is an efficient getter for copper, the backside of the Cu-contaminated sample Si11 was mapped with μ -XRF after Al gettering. The local Cu concentrations in the Al layer was in the 10^{18} cm^{-3} range, which indicates that the segregation coefficient of Cu in Al is at least 10^{-3} at 800°C . However, the accurate value of the segregation coefficient could not be determined since the copper concentration measured at the front side of the sample was at or below the detection limit. To the best of our knowledge, it is the first direct confirmation of the efficiency of aluminum backside gettering for copper.

XRF maps taken on a Cu-contaminated sample with 10^6 cm^{-2} of oxide precipitates before and after aluminum gettering (not shown) did not contain well defined clusters of copper as those in Fig. 1. A summation of the counts at each point over the full scan area, plotted in Fig. 3 as the total number of XRF counts versus the XRF energy, enabled us to obtain a quantitative measure of the efficiency of gettering. Besides the Cu K α peak at 8047.78 eV, the XRF spectrum in Fig. 3 contains a strong Ni K α peak at 7478.15 eV. This indicates that unintentional nickel contamination had occurred in our furnace during diffusion of copper. Fig. 3 shows that the height of the Cu K α peak reduced below the background level after gettering, which indicates a decrease of Cu concentration by a factor of 6-8 or greater. At the same time, the amplitude of the Ni K α peak has only partially (by less than a factor of 2) decreased after gettering.

EXPERIMENTAL RESULTS: FE GETTERING

Fe gettering experiments were performed on a sample with 10^{11} cm^{-3} of oxide precipitates (Si11). μ -XRF maps were homogeneously gray with more or less equal concentration of iron everywhere, and without any characteristic features. After Al gettering, the μ -XRF maps remained as featureless as before gettering, while the average iron concentration in the sample had decreased. XRF spectra obtained by summation of data points in μ -XRF maps before and after gettering are plotted in Fig. 4. Besides Fe K α peak at 6403.84 eV, a K α peak of Ni at 7478.15 eV is also observed in the spectrum. We attribute the Ni-related peak to the unintentional nickel

contamination stemming from our diffusion furnace. Comparison of the plots before and after gettering shows that Al gettering is not as effective for Fe as for Cu for the same gettering conditions. Notice the 58% reduction in Ni concentration, whereas only a 33% reduction in Fe is observed. This, however, should not be interpreted as an insignificant segregation coefficient of iron in aluminum. In our opinion, the observed low iron gettering efficiency is not an indication of a low segregation coefficient of Fe in Al (literature data suggest that iron can indeed be efficiently gettered by Al (see, e.g., [6, 7])), but a reflection of a relatively low, in comparison with Cu, diffusivity and solubility of iron. Since the equilibrium solubility of iron at 800°C is approximately 5×10^3 times lower than at 1200°C , the iron clusters formed during iron in-diffusion cannot all be dissolved all at the same time during the gettering anneal. The concentration of the dissolved iron quickly reaches its equilibrium solubility at 800°C , $2.8 \times 10^{12} \text{ cm}^{-3}$. As soon as this iron is gettered by the aluminum backside, the dissolved iron concentration is replenished by further dissolution of the iron clusters. Hence, gettering of iron is kinetically limited by its solubility at the gettering temperature and its diffusivity. The possibility of such mechanism was pointed out by Plekhanov et al. [8], who concluded that it may take many hours to completely dissolve and getter iron clusters in a solar cell, if the total precipitated concentration exceeds the equilibrium iron solubility at the gettering temperature.

SUMMARY

Our experiments proved that aluminum gettering is very efficient for copper. While the segregation coefficient of Cu could not be accurately determined, it was estimated as better than 10^{-3} . The Cu clusters formed at stacking faults or dislocation networks in Cu-contaminated samples Si11 could be completely dissolved during gettering annealing at 800°C . However, a formation of Cu clusters in the near-surface area on the front side of the sample was also observed.

For iron, the efficiency of backside Al gettering for 2 hours at 800°C proved to be relatively low under our experimental conditions. This can be explained by much lower diffusivity of iron and its low solubility at the gettering temperature, which prevents fast dissolution of the iron clusters. No gettering-resistant clusters with the size detectable in μ -XRF maps was found after diffusion of Cu and Fe in CZ-Si at 1200°C .

This study was supported by NREL, subcontract AAT-2-31605-03.

1. E. R. Weber and N. Wiehl, in *Defects in Semiconductors II*, S. Mahajan and J. W. Corbett, Editors, p. 19, North-Holland, New York (1983).
2. S. A. McHugo and C. Flink, *Appl. Phys. Lett.* **77**, 3598 (2000).
3. O. F. Vyvenko, T. Buonassisi, A. A. Istratov, H. Hieslmair, A. C. Thompson, R. Schindler, and E. R. Weber, *J.Appl.Phys.* **91**, 3614 (2002).
4. A. A. Istratov and E. R. Weber, *Appl. Phys. A* **66**, 123 (1998).
5. A. A. Istratov and E. R. Weber, *J. Electrochem. Soc.* **149**, G21 (2002).
6. H. Hieslmair, S. A. McHugo, and E. R. Weber, in "25th IEEE Photovoltaic Specialists Conference", p. 441. IEEE, Washington D.C. (1996).
7. S. H. Ahn, S. Zhao, A. L. Smith, L. L. Chalfoun, M. Platero, H. Nakashima, and L. C. Kimerling, in *Defects in Electronic Materials II*, J. Michel, T. Kennedy, K. Wada, and K. Thonke, Editors, p. 169, Mat. Res. Soc., Pittsburgh (1997).
8. P. S. Plekhanov, R. Gafiteanu, U. M. Gosele, and T. Y. Tan, *J. Appl. Phys.* **86**, 2453 (1999).

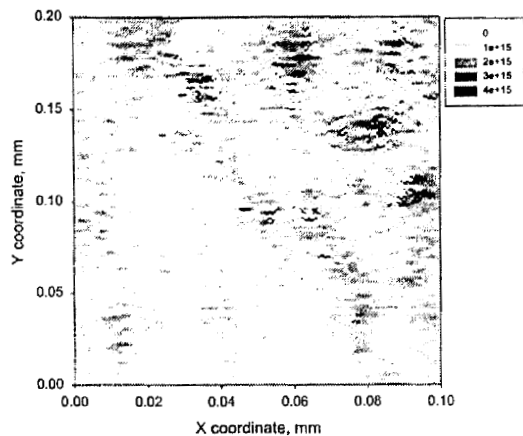


Fig. 1. μ -XRF scan of Cu-contaminated sample Si11. The X and Y coordinates are given in mm. The copper concentration in the legend is in cm^3 . The measurement was performed after copper was diffused at 1200°C , and the sample was chemically cleaned.

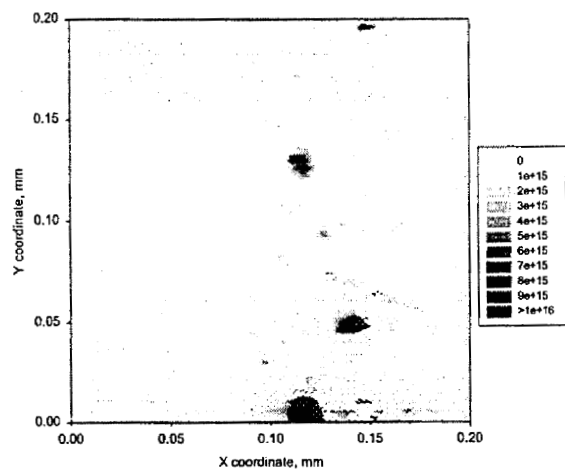


Fig. 2. μ -XRF taken on Cu-contaminated sample after Al gettering (2 hours at 800°C). Cu concentrations in the legend are in the units of cm^3 .

Comparison of Cu-contaminated Si6
Before and After Al Gettering

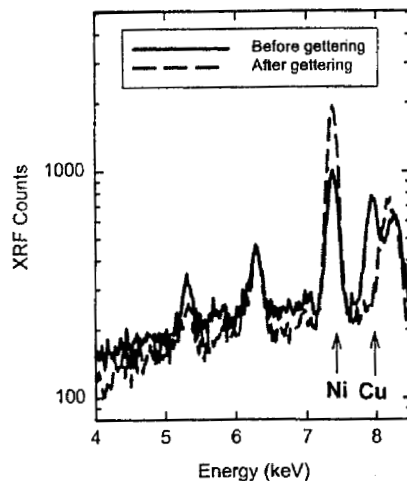


Fig. 3. XRF spectra obtained by summation of all data points in the maps in the previous figure before and after gettering. It is seen that the Cu peak is no longer distinguishable on the background noise after gettering. However, the unintentional nickel contamination remains strong, and the amplitude of the Ni peak was only partially decreased by the gettering.

before and after gettering

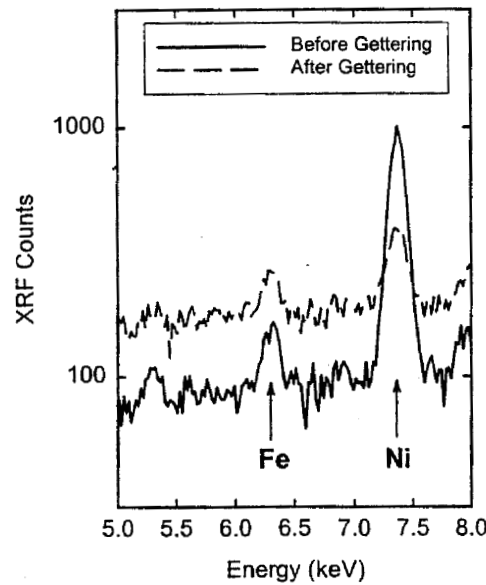


Fig. 4. XRF scan of the sample with $2.5 \times 10^{11} \text{ cm}^{-3}$ of oxide precipitates, intentionally contaminated with iron and measured before and after Al gettering. Unintentional nickel contamination is also present.

Investigation of Oxygen Precipitates and Associated Stacking Faults in Polycrystalline Sheet Silicon and Their Impacts on Solar Cell Performance

Jinggang Lu, James Rand, Ralf Jonczyk*, George Rozgonyi*

Materials Science and Engineering Department, North Carolina State University, Raleigh, NC 27695

**Astropower Inc., Newark, DE 19711*

Abstract:

Oxygen precipitates (OP) and associated defects, such as punch out dislocation loops and stacking faults (SF), can act as minority recombination centers and degrade solar cell performance. In this experiment, two groups of samples with high and low oxygen concentration were used to study oxygen precipitation phenomenon in sheet silicon. Both as-grown and processed samples were examined by Fourier transform infrared spectroscopy (FTIR), EBIC, PCD and etching/optical microscopy. It was found that during solar cell processing, the interstitial oxygen concentration decreased from $16.6 \times 10^{17} \text{ cm}^{-3}$ for the high oxygen sample (HO) and from $11.0 \times 10^{17} \text{ cm}^{-3}$ for the low oxygen sample (LO). EBIC measurements show that the intra-grain current collection I_C of the HO sample is worse than that of the LO sample. The difference is more prominent for large grain regions. The same regions examined by EBIC were etched and checked by optical microscopy. A high density of stacking faults was found inside the large grain of the HO sample, while no isolated oxygen precipitates or SF was observed in the LO wafer. To correlate these defect results with photovoltaic performance, the samples were also studied by the microwave PCD method. It was found that, while the large grain region of the LO wafer consistently exhibited high lifetime, no consistent correlation was found between the grain size and the minority lifetime of the HO wafer. In conclusion, a high interstitial oxygen concentration in an as-grown wafer will give rise to a high density of SF, which decreases the minority carrier lifetime. It is suggested that, to achieve high lifetime material, in addition to increasing the grain size, it is important to keep the O_i concentration below about $12 \times 10^{17} \text{ cm}^{-3}$.

1. Introductions:

As grain boundaries and dislocations are always present in polycrystalline silicon and these defects can act as gettering sites for transition metals, the metals will precipitate by employing proper post-diffusion annealing. As a result, the lifetime of the polycrystalline silicon materials will be mainly limited by the presence of the extended defects, such as grain boundaries, oxygen precipitates, dislocations, SF and metal precipitates. In the polycrystalline sheet silicon materials, the O_i usually reaches 10^{18} cm^{-3} and will precipitate during cell processing. It is well known that OP and SF can act as minority carrier recombination centers, especially when decorated by transition metal species, which is the case in the sheet silicon materials.

It is well known that carbon¹ and nitrogen² can enhance oxygen precipitation, as well as iron³, if its concentration reaches 10^{14} cm^{-3} . Dislocations can also enhance oxygen precipitation by providing heterogeneous nucleation sites. All these impurities and defects

appear in polycrystalline sheet silicon materials with carbon and nitrogen at their saturation. The iron concentration is on the order of 10^{13} cm^{-3} . In this paper, we will focus on the influence of the initial O_i concentration on the oxygen precipitation process.

2. Experiments:

Two groups of wafers with different initial oxygen concentration were grown at Astropower. Wafers were boron doped with a resistivity of 2-3 ohm cm and a thickness of about 800 um. The grain size ranges from 100um to 2mm. For detailed information regarding the sheet silicon materials, refer to Ref. 4. A conventional solar cell process is used at AstroPower, including a phosphorous diffusion, silicon nitride antireflection coating, and screen printed metals. In addition, two novel, high temperature gettering steps are being evaluated as part of the standard processing sequence. The gettering steps and phosphorous diffusion were used on the samples under study here.

The initial O_i concentration of the high and low O_i samples is 16.6 and $11.0 \times 10^{17} \text{ cm}^{-3}$ respectively. Room temperature FTIR measurements were performed on Bio-Rad FTS-6000 spectroscope to investigated the oxygen precipitation by monitoring the change of the O_i concentration. Samples were double-side chem-mechanical polished. The spectral resolution was set at 2 cm^{-1} . A calibration factor of $3.14 \times 10^{17} \text{ cm}^{-2}$ was used to calculate the O_i concentration from the intensity of the 1107cm^{-1} peak.

Microwave PCD lifetime mapping was performed on the double side polished wafers. Before measurement, samples were boiled in piranha solution and then dipped in 10% HF solution for 10 minutes to passivate the surface. The step size of the mapping was 0.1 mm. A 904 nm GaAs laser with a penetration depth of 30 um for Si was used as injection source. After PCD measurements, Al-Schottky diodes were prepared on the polished surface for EBIC measurement. EBIC measurements were performed at room temperature with an accelerating voltage of 20 KV and a probe current of about 0.2 nA. Following EBIC measurements, the samples were etched in Secco solution for 2 min and examined under Normaski microscope.

3. Results and Discussions:

Room temperature FTIR spectra, see Fig. 1, shows that after solar cell processing, the interstitial oxygen concentration decreases dramatically. The broad peak spanning from $850-1100 \text{ cm}^{-1}$ is believed to be related to nitrogen precipitates. The interstitial oxygen concentrations are summarized in Table. 1, which shows that more interstitial oxygen precipitated in the HO sample.

Sample	HO	LO
As-grown	16.6	11.0
Processed	5.6	4.1
Difference	11.0	6.9

Table 1. O_i concentration in the as-grown and processed wafers. Unit in 10^{17} cm^{-3}

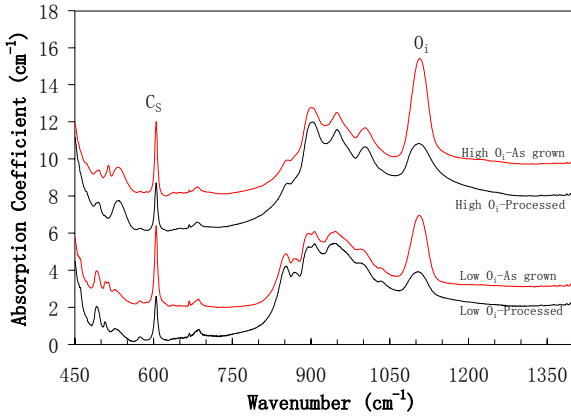


Fig. 1 Room temperature FTIR spectra of the HO and LO samples.

Figures 2(a) and 2(b) are the EBIC and corresponding etching/optical micrographs of a large grain region of the HO processed sample, which show a very good correlation. The high defect density region correspondingly exhibits low current collection efficiency (dark region), and vice versa. From Fig. 2(c), it is evident that most of the defects are stacking faults, while in Fig. 2(b) the SF density inside the large grain is higher than that of the small grain. Also, near the grain boundaries there are few SF. Due to the volume difference between SiO_2 and silicon matrix, silicon self-interstitials I_{Si} are generated during oxygen precipitation process. These self-interstitials can nucleate on the oxygen precipitates and form stacking faults. Because the dimension of the SF denuded zone around grain

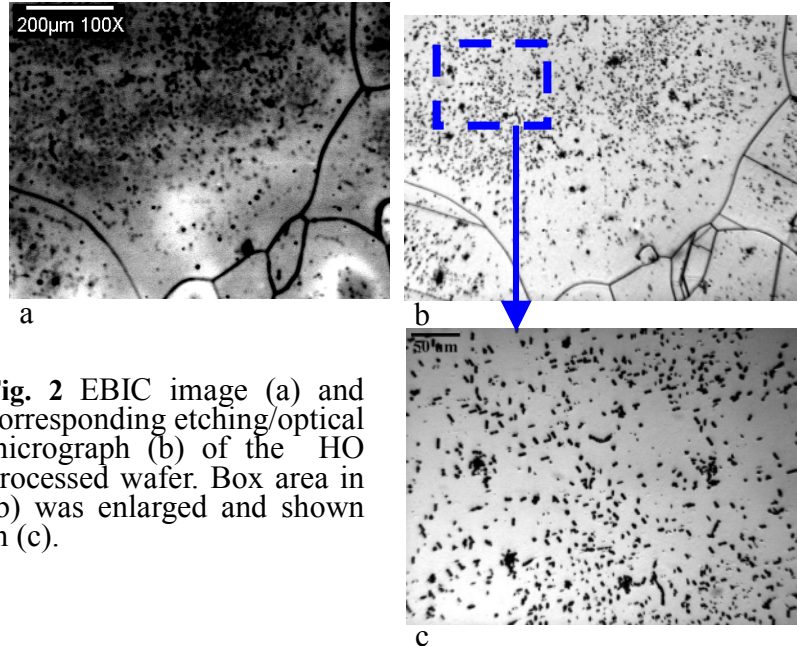


Fig. 2 EBIC image (a) and corresponding etching/optical micrograph (b) of the HO processed wafer. Box area in (b) was enlarged and shown in (c).

boundaries is about 50-100um and the total diffusion length of O_i is about 15um in the solar cell processing, the distribution of SFs is not determined by the interstitial oxygen, but arises from some fast-diffusion species (nitrogen, I_{Si} or transition metals). The reason why no SF formed near the grain boundaries might be (1) grain boundaries can act as the sink for silicon self-interstitials and results in low I_{Si} supersaturation degree, and so no SF can nucleate. (2) Grain boundaries can gettering carbon, nitrogen and iron which can enhance oxygen precipitation. Due to the grain boundaries gettering, the concentrations of carbon and nitrogen are lower at the near grain boundary region than the intra-grain region, thereby reducing the SF formation.

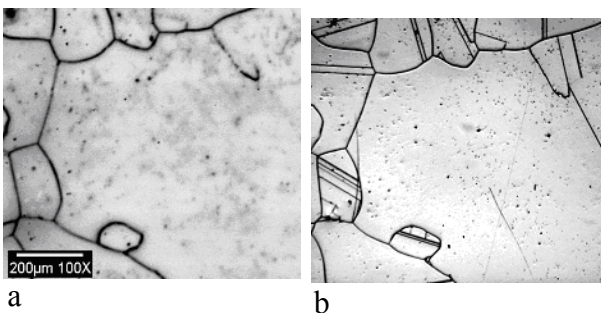


Fig. 3 EBIC (a) and corresponding etching/optical micrograph (b) of the LO processed wafer. The large grain is clean and no SF formed in the large grain.

The EBIC and corresponding etching/optical micrographs of a large grain region of the LO processed sample are shown in Figures 3(a) and 3(b). Note the absence of the dark region inside the large grain in the EBIC picture. Etching pits picture shows that there are only dislocations and oxygen precipitates appeared inside the large grain. No SF were found in the LO processed wafer. Also, in some regions of the sample, no isolated oxygen precipitates (hillock)

were found. This fact implies that even with the assistance of nitrogen and carbon, oxygen precipitates still can only nucleate along the dislocation or grain boundary because of the lower O_i supersaturation.

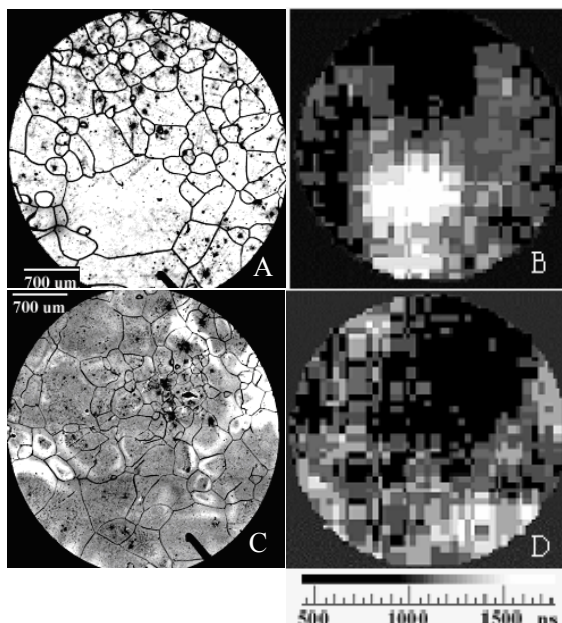


Fig. 4. EBIC picture and the corresponding PCD lifetime mapping of the LO (A and B) and HO (C and D) processed wafers.

Figures 4(A) and 4(B) show the EBIC picture and the corresponding PCD lifetime mapping of the LO processed sample. Note that the lifetime is well correlated with the grain size. In the small grain region, in addition to more grain boundaries, there are more black spot dislocation clusters. The grain boundaries and the dislocation clusters lower the lifetime dramatically. Inside the large grain, the lifetime reaches its highest value because there is no grain boundaries and fewer intra-grain defects.

Figures 4(C) and 4(D) are the EBIC and corresponding PCD lifetime mapping of the HO processed sample. Although the lifetime is also mainly influenced by the grain size, the correlation is not as consistent as the LO processed sample. This is likely due to the high density of SF formed inside the large grain of the HO processed sample which decreases the lifetime.

4. Conclusions:

A high interstitial oxygen concentration in the as-grown sheet material will give rise to a high density oxygen precipitates and SF, which will decrease the minority carrier lifetime. It is suggested that, in order to achieve high lifetime material, in addition to increasing the grain size, it is important to keep the initial O_i concentration below about $12 \times 10^{17} \text{ cm}^{-3}$.

References:

1. F. Shimura, J. Appl. Phys., **59** (1986) 3251
2. Q. Sun, K. H. Yao., and H.C. Gatos, J. Appl. Phys., **71**, (1992) 3760
3. J.Jablonski, et al, Materials Sci. Forum, **196-201**, (1995) 1859
4. J. S. Culik et a., "Progress in 15-MW Single-Thread Silicon Film Solar Cell Manufacturing Systems", 17th ECPVSEC, Munich, October 2001

A Study of Contact Resistance and Cell Performance of Selective-Emitter Screen-Printed Silicon Solar Cells Using a Self-Doping Paste

M. Hilali¹, J.-W. Jeong¹, and A. Rohatgi¹

¹University Center of Excellence for Photovoltaics Research and Education,
School of Electrical and Computer Engineering, Georgia Institute of Technology, Atlanta, GA 30332-0250

Abstract

Screen-printed selective-emitter solar cells have been fabricated on FZ Si with efficiencies of ~16.5%. A self-doping paste was used on 100 Ω/sq . emitter to form the selective emitter. A much lower contact resistance was obtained for the self-doping paste PV168 compared to conventional pastes on 100 Ω/sq . Contact resistance for the PV168 self-doping paste on a 100 Ω/sq . was ~1.5 $\text{m}\Omega\cdot\text{cm}^2$ which is comparable to that of a conventional paste on a 40 Ω/sq . emitter (~0.96 $\text{m}\Omega\cdot\text{cm}^2$). The co-fired selective-emitter cell using PV168 showed a ~0.1% improvement in absolute efficiency over the 2-step fired conventional cell. Due to the lightly-doped emitter in the selective-emitter cell, the blue response of the IQE was better, contributing to 0.6 mA/cm^2 improvement in the short-circuit current. The fill factors for both conventional and selective-emitter cells were very close, 0.776 and 0.775 respectively, indicating the effectiveness of the self-doping paste PV168. The selective-emitter cells had an unoptimized silicon nitride passivation. Improved oxide or nitride passivation is expected to increase the performance of the selective-emitter cells even further.

Introduction

The self-doping Ag paste introduces the P dopant into the underlying Si when fired at a temperature above the Ag-Si eutectic (~830°C). This contact formation technique makes use of the lightly-doped emitter, which should improve the short-wavelength response. A lightly-doped emitter should also improve the effectiveness of the front-surface passivation. Self-doping paste is fired at higher temperatures (900°C set point in a belt furnace), which forms a good Al BSF simultaneously. Hence, a 2-step firing process is not necessary and both front and back contacts can be co-fired simultaneously. Previous work showed that firing temperatures below the Ag-Si eutectic do not give good fill factors (FFs) due to high series resistance or poor ohmic contact on the front [1]. Also, a fast firing in the belt furnace showed much superior results as compared to slow firing at ~900°C because of reduced junction leakage current (J_{o2}) [1]. Thus, it was established that the firing temperature and the belt speed are critical to the performance of the selective-emitter cells using the self-doping paste. Contact resistance of 0.26 $\text{m}\Omega\cdot\text{cm}^2$ has been previously reported on a 73 Ω/sq . emitter and 12 $\text{m}\Omega\cdot\text{cm}^2$ for a 93 Ω/sq . emitter [2, 3]. The aim of this work is to minimize the contact resistance of the PV168 self-doping paste on 100 Ω/sq . emitter and demonstrate high efficiency screen-printed selective-emitter cells.

Experimental

Two types of solar cells (4 cm^2) were fabricated on p-type 0.6 $\Omega\cdot\text{cm}$ 300- μm thick (100) float-zone (FZ) Si wafers: one involving conventional pastes (Table 1) and the other involving the self-doping paste PV168 (Table 2). In Table 1, the first cell is a conventional screen-printed cell with a 40-45 Ω/sq . homogeneous emitter using the commercially available paste A, which gave a 16.38% efficient cell. This cell was fabricated using a 2-step firing process: 850°C/2 min. for the Al BSF (back-surface field) and 752°C/40 sec. for the front contact firing. The next two cells in

Table 1 had 100 Ω/sq . emitter and the front and back contacts were co-fired using conventional screen-printed pastes A and B under identical conditions (900°C) to those used for firing the self-doping paste PV168. The cells in Table 2 involve the self-doping paste on emitters of different sheet resistance values (100, 110, 120, 130, and 150 Ω/sq .). All the cells in this set were co-fired (front contact and back Al BSF) at 900°C at the firing conditions optimized to give good ohmic contact on a 100 Ω/sq . emitter. After cleaning the wafers, the emitters for all the cells were diffused in a POCl_3 tube furnace. After the removal of the phosphorus glass, a SiN_x single layer antireflection coating (SLARC) was deposited with a refractive index of 1.98 and a thickness of 850 Å. The front-contact grid was screen-printed on top of the SiN_x , and the front and back metal contacts were either co-fired, or a 2-step firing process was used as explained previously. All screen-printed contacts were fired in a belt-line furnace. In order to assess the quality of the contacts, contact resistance measurements were performed using the transfer length method (TLM) [4] on contact resistance test patterns screen-printed and fired simultaneously with the front-metal grid.

Results and Discussion

A. Contact Resistance Analysis

In order to investigate the quality of the front metal contacts, contact resistance measurements were performed. Figure 1 shows contact resistance measurements for two conventional pastes on 40 and a 100 Ω/sq . emitters. For the 40 Ω/sq . emitter, paste A gave a low contact resistance of 0.96 $\text{m}\Omega\cdot\text{cm}^2$ which increased to ~21 $\text{m}\Omega\cdot\text{cm}^2$ for the 100 Ω/sq . emitter. Paste B produced even higher contact resistance (1.65 $\text{m}\Omega\cdot\text{cm}^2$ on the 40 Ω/sq . emitter and ~23 $\text{m}\Omega\cdot\text{cm}^2$ on the 100 Ω/sq . emitter). Paste A gave lower contact resistance values (as low as 2 $\text{m}\Omega\cdot\text{cm}^2$ on 100 Ω/sq .) when fired at temperatures slightly higher than the optimized temperature (900°C) for PV168 suggesting that it also contains some phosphorus. However, high temperature firing of paste A degrades the cell performance resulting in lower open-circuit voltage (V_{oc}) and higher n factor and leakage current.

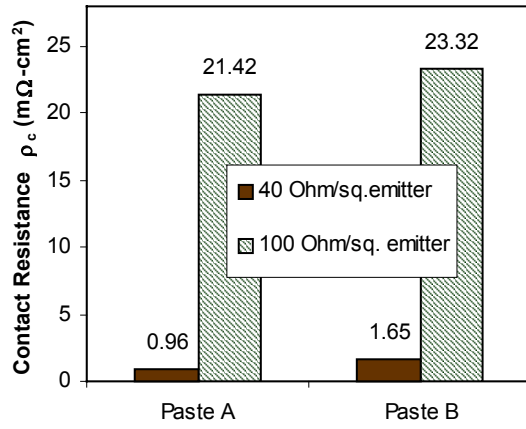


Figure 1: Contact resistance values for conventional pastes (A and B) on 40 and 100 Ω/sq . emitters.

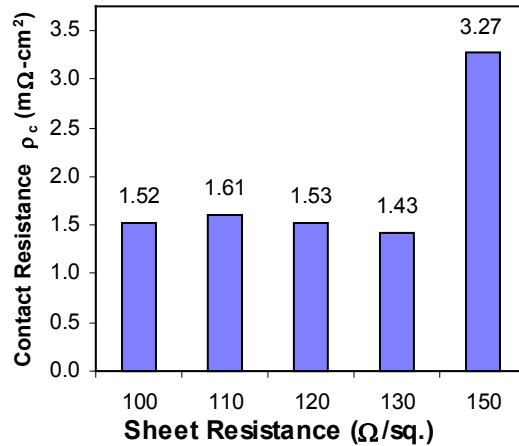


Figure 2: Contact resistance values for PV168 on emitters of different sheet resistance.

Figure 2 shows contact resistance values for the PV168 self-doping paste on emitters of different sheet resistance. The contact resistance is around 1.5 $\text{m}\Omega\cdot\text{cm}^2$ for sheet resistance values in the range of 100-130 Ω/sq . and is comparable to that of a conventional paste on a 40 Ω/sq . emitter.

The contact resistance for the self-doping paste starts to increase rapidly ($3.27 \text{ m}\Omega\cdot\text{cm}^2$) when the sheet resistance increases to $150 \Omega/\text{sq}$.

B. Cell Data and Analysis

Light and dark I-V measurements were performed to analyze the performance of the cells. As shown in Table 1, the conventional cell with $40 \Omega/\text{sq}$. homogeneous emitter has a fill factor of 0.776 and a reasonably good series resistance of $0.886 \Omega\cdot\text{cm}^2$ (cell 2-step-40). Cells A-100 and B-100 in Table 1 are fabricated with conventional pastes A and B on $100 \Omega/\text{sq}$. emitter. These cells showed a very high series resistance and low FFs of 0.5-0.6.

Table 1: Cells fabricated using conventional front metal pastes A and B.

Cell Name	V _{oc} (mV)	J _{sc} (mA/cm ²)	FF	Eff (%)	n factor	R _s ($\Omega\cdot\text{cm}^2$)	R _{sh} ($\Omega\cdot\text{cm}^2$)
2-step-40	635.3	33.20	0.776	16.38	1.11	0.886	1,507
A-100	619.5	33.00	0.594	12.14	1.07	4.812	18,297
B-100	571.6	32.89	0.536	10.08	2.62	3.208	15,078

Selective-emitter cells in Table 2 and Figure 3 show that the series resistance increases with the increase in emitter sheet resistance. However, for the $100-130 \Omega/\text{sq}$. emitters, the series resistance is only dictated by the higher emitter sheet resistance and not by the contact resistance as shown by Figure 2. The FF also decreases slightly and systematically as the emitter sheet resistance increases. Thus, the performance of these selective-emitter cells (Table 2) could be improved significantly by the optimized front metal contact grid design using finer gridlines in conjunction with smaller grid spacing. The front metal grid used in this study was optimized for the $40 \Omega/\text{sq}$. emitter.

Table 2: Front metal contact self-doping paste PV168 on emitters of different sheet resistance.

Cell Name	V _{oc} (mV)	J _{sc} (mA/cm ²)	FF	Eff (%)	n factor	R _s ($\Omega\cdot\text{cm}^2$)	R _{sh} ($\Omega\cdot\text{cm}^2$)
PV168-100	627.1	33.90	0.775	16.47	1.01	1.003	3,353
PV168-110	622.0	33.40	0.769	15.95	1.01	1.171	8,222
PV168-120	626.5	33.60	0.766	16.13	1.01	1.225	9,681
PV168-130	625.4	33.30	0.765	15.93	0.99	1.293	88,757
PV168-150	617.90	33.50	0.7562	15.67	1.00	1.357	13,111

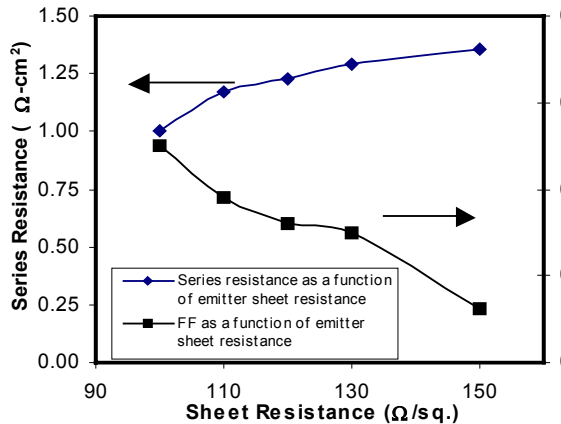


Figure 3: Series resistance and fill factor (FF) as a function of emitter sheet resistance.

Figure 4 shows the IQE plot for the conventional cell with $40 \Omega/\text{sq}$. homogeneous emitter and a selective-emitter cell with a $100 \Omega/\text{sq}$. emitter. The short-wavelength response of the co-fired selective-emitter cell is superior to that of the 2-step fired conventional cell, resulting in

0.6 mA/cm² improvement in the current. The long-wavelength response of both cells is almost identical indicating the same BSF quality. The short-wavelength response can be improved further by better surface passivation because the SiN_x SLARC used in this study was not optimized for lowest surface recombination velocity.

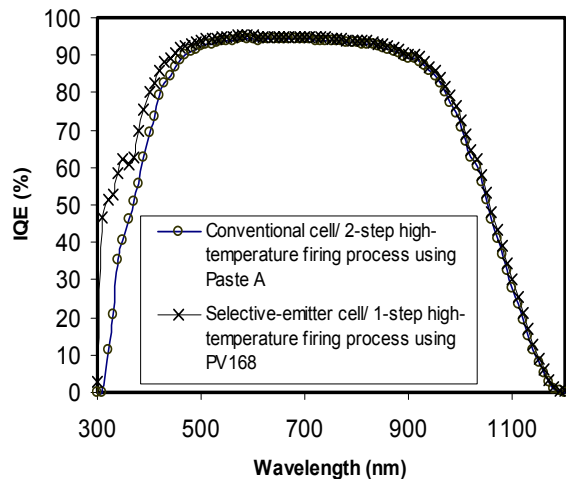


Figure 4: IQE plots for the conventional paste 2-step fired cell on a 40 Ω/sq. emitter and the selective-emitter cell using PV168 on a 100 Ω/sq. emitter.

Conclusion

Contact resistance measurements show that the PV168 Ag paste can achieve reasonably low contact resistance on $\geq 100 \Omega/\text{sq}$. emitter with the appropriate firing conditions. Contact resistance values are comparable ($< 2 \text{ m}\Omega\cdot\text{cm}^2$) to those of conventional Ag pastes on a $40 \Omega/\text{sq}$. emitter. Screen-printed selective-emitter cells with an efficiency of $\sim 16.5\%$ were achieved on FZ silicon with $0.6 \text{ mA}/\text{cm}^2$ enhancement in J_{sc} over the conventional $40 \Omega/\text{sq}$. cells. Fill factors were ~ 0.775 for both selective-emitter and conventional cells. Improved surface passivation and optimized grid design can increase the efficiency of selective-emitter cells significantly over the conventional cells.

Acknowledgements

The authors wish to thank Alan Carroll of DuPont Microcircuit Materials for providing the PV168 self-doping Ag paste. This work was supported by NREL contract No. AAT-2-31605-02.

References

- [1] M. Hilali, J. -W. Jeong, A. Rohatgi, D. L. Meier, and A. F. Carroll, "Optimization of self-doping Ag paste firing to achieve high fill factors on screen-printed silicon solar cells with a $100 \Omega/\text{sq}$. emitter," *Proc. of the 29th IEEE PVSC*, May 2002, in press.
- [2] D. L. Meier, H. P. Davis, R. A. Garcia, J. A. Jessup, and A. F. Carroll, "Self-doping contacts to silicon using silver coated with a dopant source," *Proc. of the 28th IEEE PVSC*, 2000, pp. 69-74.
- [3] D. L. Meier, H. P. Davis, R. A. Garcia, J. A. Jessup, P. Hacke, S. Yamanaka, and J. Salami, "Self-doping silver contacts for silicon solar cells," *Proc. 11th Workshop on Crystalline Silicon Solar Cell Materials and Processing*, August 19-22, 2001, pp. 129-136.
- [4] Deiter K. Schroder, *Semiconductor Material and Device Characterization*, John Wiley & Sons, Inc., 1990, pp. 119-120.

Greater Than 15% Efficient Screen Printed Solar Cells with Porous Silicon Anti-Reflection Coating

Ben Damiani and Ajeet Rohatgi

University Center of Excellence for Photovoltaics Research
Georgia Institute of Technology

Abstract

Porous silicon anti-reflection coatings for silicon solar cells provide an alternative to conventional plasma techniques. Porous silicon is applicable to all silicon crystals and allows for reduced processing times. This paper reports on the development of a novel process sequence that incorporates porous silicon as a first step and produces 15.3% screen printed RTP cell efficiency (confirmed by NREL) in less than 35 minutes on FZ Si. Fill factor (FF) degradation is avoided because the metal contacts are formed at the end and are not exposed to a chemical etching solution. Firing Ag contacts through porous silicon is shown to make good ohmic contact to the emitter. This process involved short RTP firing of screen printed contacts on the porous silicon layer that enabled better control of the reflective properties and resulted in high FF's of ~0.787, V_{oc} 's of ~618 mV, 31.5 mA/cm² J_{sc} , and efficiencies in excess of 15%.

Introduction

Crystalline silicon continues to be the most widely used substrate for commercial solar cells. Incorporating porous silicon texturing into solar cell fabrication has received increased attention in the photovoltaic community because of its promise of increased efficiency, ease of fabrication, and low fabrication costs [1,2]. The use of porous silicon as an anti-reflection coating (ARC) has received the most attention due to ease of integration with current solar cell processing [1,3,4]. Other uses of porous silicon have been explored including band gap modification, surface passivation and light trapping / diffusion for solar cell structures [3]. Selective emitter formation is an added benefit that could result from porous silicon etching at the end of a solar cell fabrication sequence [3]. However, deep emitter junction, unstable surface passivation, and fill factor degradation of screen printed (SP) metals could hurt the cell performance if porous silicon is formed as a final processing step. Other approaches to incorporate porous silicon texturing form the porous silicon layer prior to metal contact formation but are constrained by good ohmic contact [5]. That is why, unlike other studies, the objective of this work is to form the porous silicon layer prior to emitter diffusion and metal contact formation. In this approach the challenge is to manage the change in reflectivity during subsequent high temperature processing and series resistance due to the high resistivity and wide band gap of porous silicon. RTP is used in this study to maintain appropriate reflectance after high temperature processing.

Experimental

Solar cells are fabricated using the dopant oxide solid source (DOSS) technique [6] to form an n⁺ emitter in both a conventional furnace (CF) and in an RTP system. Diffusion

glass removal is avoided in DOSS processing [6]. Porous silicon layers were formed on Si substrates prior to phosphorus emitter diffusion by chemical etching (stain etching) technique comprised of HF acid and HNO_3 acid, rather than electro-chemical etching. Porous silicon etching time was limited to < 10 seconds. Screen printed Al BSF was formed for rear surface passivation. A Ag grid was SP on top of the porous silicon and fired through it in a belt furnace (BF) or RTP to form the front contacts. Spreading resistance analysis (SRA) was performed to obtain diffusion profiles. Porous silicon etching is performed as the first step in all solar cell fabrication techniques described in this paper.

Results and Discussion

Phosphorus emitter diffusion employed a limited source DOSS diffusion; therefore analysis of the diffusion profile through a porous silicon layer needs consideration. Figure 1 shows a dopant profile for a planar sample and a sample with a porous silicon layer subjected to the same CF diffusion cycle. A spin-on coated wafer with a 6% P_2O_5 concentration was used as a DOSS diffusion source at $\sim 925^\circ\text{C}$ for ~ 1 hour. The porous silicon etched sample showed lower surface concentration and shallower diffusion depth compared to the planar control ($\sim 0.5\mu\text{m}$ and $0.95\mu\text{m}$, respectively). Thus porous silicon acts as a diffusion limiter not a barrier. Therefore, proper diffusion profiles can be tailored by changing the temperature, spin-on dopant concentration, or time of diffusion. Figure 2 compares the internal quantum efficiency (IQE) and reflectance curves of a SP porous silicon solar cell subjected to a CF diffusion cycle and a standard screen printed cell. The standard cell consists of a $\sim 40\ \Omega/\text{sq}$. POCl_3 emitter with a full Al BSF on a $1.3\ \Omega\text{cm}$ FZ and a SiN_x single layer ARC. Figure 2 shows that the porous silicon sample has an inferior reflectance with a minimum of $\sim 10\%$ at 600nm . The BSF is also inferior because the Al was fired in a belt furnace rather than RTP. The weighted reflectance is 17.4% as compared to 12.4% for the SiN_x coated standard cell. However, the blue response is much better for the porous silicon sample. This is partly

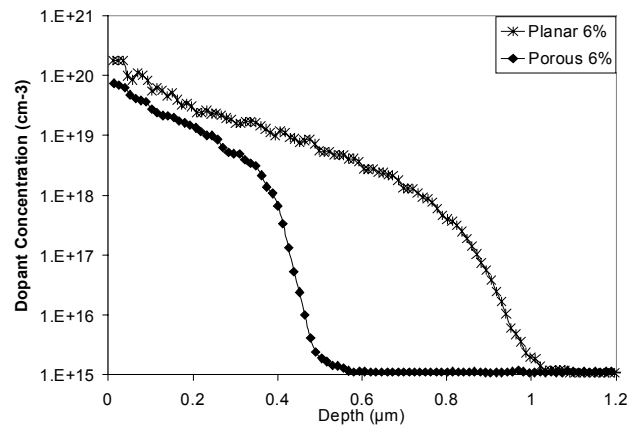


Figure 1. Phosphorus dopant concentration diffused at 925°C using 6% P_2O_5 .

100%
80%
60%
40%
20%
0%

● IQE (A)
○ Refl. (A)
— Std. IQE
— Std. Refl.

Process	V_{oc}	J_{sc}	FF	Eff.
Std. SP	626	33.9	0.786	16.7
Process A	624	29.9	0.749	14.0

Figure 2. IQE and Reflectance curves for the standard screen printed solar cell and a porous silicon ARC solar cell (Process A).

due to the higher sheet resistance and in-situ oxide passivation in the DOSS emitter. In order to realize the full benefit of the improved blue response the front surface reflectance needs to be optimized. It is clear from Fig. 2 that during high temperature processing the porous silicon layer reflectance curve undergoes changes. Initial weighted reflectance was ~11.5% but increased to 17.4% after CF processing. Therefore, initial reflectance needs to be optimized to minimize the final reflectance profile. However, initial results showed no direct correlation between initial porous silicon reflectance and finished solar cell reflectance in CF processing.

In an effort to reduce fabrication time (~1 hour diffusion cycle in a CF) and improve the porous silicon layer reflectance, use of an RTP is explored. DOSS diffusion was performed in an RTP at 880°C or 900°C for 3 minutes. Better control of the diffusion ambient and shorter cycles time are realized in RTP processing that can help to minimize reflectance changes for the porous silicon layer. Figure 3 shows the resulting reflectance curves for samples subjected to various RTP processes. Samples subjected to a 725°C RTP heat cycle in nitrogen ambient prior to the diffusion cycle showed only a slight blue shift in reflectance minimum wavelength but not in the minimum reflectance value. However, the sample that received no RTP heat treatment prior to emitter diffusion showed a substantial jump in minimum reflectance to ~10%, similar to the afore mentioned CF process.

The CF and RTP solar cell fabrication sequences used in this study are shown in Figure 4. CF process (A) gave a SP cell efficiency of 14% along with the IQE shown in Fig. 2. This process took ~3 hours. Process sequence (B) was developed to fabricate solar cells in the RTP in approximately 17 minutes after initial cleaning. This process resulted in a much improved front surface reflectance compared to Process A, as shown in Fig. 3. However, to maintain the low reflectance of porous silicon, no BSF step was implemented in Process B because prolonged exposure to the oxygen ambient (~2 minutes) for BSF formation was found to degrade the front surface reflectance. This resulted in somewhat inferior red response (see Fig. 5) and lower cell efficiency of 13.7%.

Process C implements a novel sequence that provides a proper BSF formation simultaneously with the emitter formation. Figure 5 shows the resulting IQE and reflectance curves for the RTP processed solar cells with porous silicon ARC. Process C allows for BSF formation to match the standard process because RTP DOSS diffusion temperature is 880°C, which simultaneously forms a good Al BSF on the rear. In process

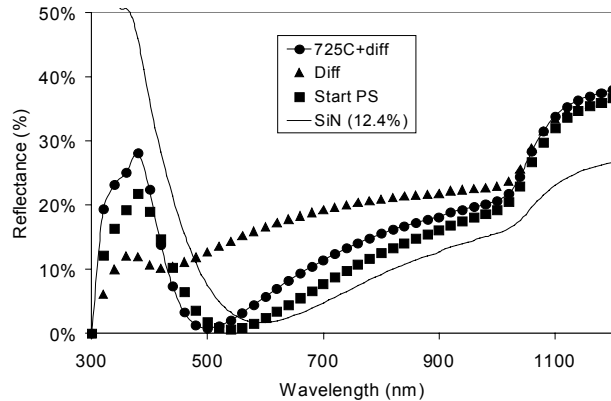


Figure 3. Reflectance curves for SiN_x and porous silicon ARC's subjected to RTP processing.

Process A Clean 15 minutes	Process B Clean 15 minutes	Process C Clean 15 minutes
Porous Silicon Etch 6 seconds	Porous Silicon Etch 6 seconds	Porous Silicon Etch 6 seconds
CF DOSS Emitter 150 minutes	RTP 725°C 6 minutes	RTP 725°C 6 minutes
SP Al BSF + Bake + Fire 8 minutes (BF)	900°C RTP DOSS Diff. 6 minutes	SP Al BSF + Bake 2 minutes
SP Ag + Bake + Fire 8 minutes (BF)	SP Al BSF + Bake 2 minutes	880°C RTP DOSS Diff. 6 minutes
	SP Ag+Bake+Fire 700°C 3 minutes (RTP)	SP Ag+Bake+Fire 700°C 3 minutes (RTP)
Total Time ~3 hours	Total Time ~32 minutes	Total Time ~32 minutes
V_{oc} J _{sc} FF Eff. FZ 624 29.9 74.9 14.0 Cz 614 29.2 74.6 13.4 Mc 619 26.9 75.5 12.5	V_{oc} J _{sc} FF Eff. FZ 603 28.6 76.2 13.2 FZ 592 30.1 77.0 13.7	V_{oc} J _{sc} FF Eff. FZ 618 31.5 78.7 15.3

Figure 4. Process sequence diagram for porous silicon ARC solar cells using DOSS processing

B, Al firing temperature was only 700°C for 1 second. A 15.3% efficiency is obtained using process C, an improvement of greater than 1% absolute efficiency over process A and process B. This is the highest reported efficiency for a porous silicon solar cell to our knowledge. FF degradation is avoided by not exposing the SP metal contacts to porous silicon etching. The solar cells processed by porous silicon and RTP in < 35 minutes achieved FF's in excess of 78% and efficiency of 15.3%. Note that the efficiency is ~1% lower than the standard cells with PECVD SiN_x coating. Further optimization can reduce the gap between the two.

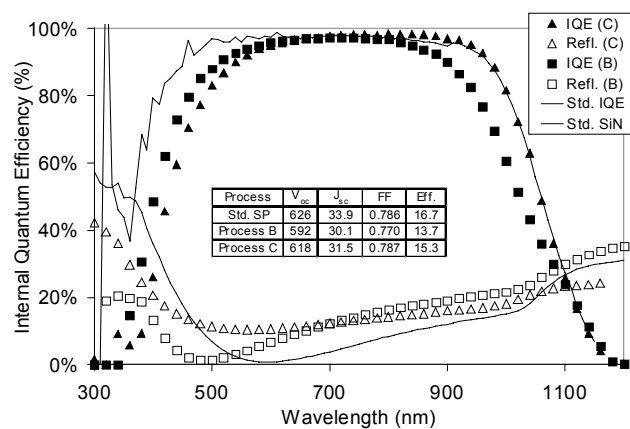


Figure 5. IQE and Reflectance curves for the standard screen printed solar cell and porous silicon ARC solar cells (Process B and Process C).

Conclusion

Innovative silicon solar cell processing using porous silicon texturing for ARC and RTP resulted in greater than 15% SP solar cells fabricated in less than 35 minutes. All processing steps used in fabrication are industrially viable. The porous silicon layer provides a uniform coating that has a violet appearance on the entire wafer surface. RTP pre-treatment in N₂ stabilizes the porous silicon layer. In addition, a short simultaneous RTP heat treatment is used to form the n⁺ emitter and p⁺ BSF simultaneously without appreciably degrading the porous silicon reflectance. Finally SP through the porous silicon layer forms good ohmic contacts resulting in FF's of ~0.78.

Acknowledgements

This work was supported by DOE contract #DE-FC36-00G010600 and NREL contract #AAT-2-31605-02.

Reference:

- [1] R. Bilyalov, L. Stalmans, L. Schirone, and C. Lévy Clément, IEEE Trans. on ED, **46**, p.2035, 1999
- [2] J. Szułufcik, F. Duerinckx, E. Van Kerschaver, and J. Njis, Proceedings of the 17th EC PVSEC, 2001
- [3] R. Bilyalov, R. Lüdemann, W. Wetling, L. Stalmans, J. Poortmans, J. Njis, L. Schirone, G. Sotgiu, S. Strehlke, and C. Lévy Clément, Sol. Energy Mat. and Solar Cells, **60**, p.391, 2000
- [4] R. Lüdemann, B. Damiani, and A. Rohatgi, Proceedings of the 28th IEEE PVSC, 2000
- [5] R. Bilyalov, Z. Matic, J. Poortmans, F. Schomann, and W. Schmidt, Proceedings of the 28th IEEE PVSC, p. 291, 2000
- [6] T. Krygowski and A. Rohatgi, IEEE Trans. on ED, **45**, p.198, 1998

mc-Si: relation between ingot quality and cell efficiency

L.J. Geerligs

Energy Research Centre of the Netherlands (ECN), Solar Energy,
PO Box 1, 1755 ZG Petten, the Netherlands. email: geerligs@ecn.nl

Abstract

We have investigated and compared material properties and solar cells of several common multicrystalline ingots. Apart from the contaminated end parts of the ingots the cell quality correlates well with the as-received lifetime, and the lifetime profile through the ingot correlates with the distribution of defect densities in the material. The as-received lifetime after light soaking is a reasonable predictive parameter for cell performance for the complete ingot if the major impurity in the end parts is iron, and if the oxygen concentration is low. A high oxygen concentration of 15-20 ppma in the bottom parts of some ingots, instead of the more common 5-10 ppma for that position, correlates with a strong reduction of cell efficiency.

1. Introduction

The properties of solar cells produced from multicrystalline silicon (mc-Si) wafers show a significant variation. The purpose of this work is to understand the part of this variation which is due to material properties, and to see whether the understanding can be generic, independent of manufacturer. This may help to minimize the variation as much as possible e.g. through optimized processing or directions for optimized ingot growth. We investigated 8 ingots from 4 manufacturers. Characterisation of carbon, oxygen, FeB, lifetime, defects, and traps (by DLTS¹) was compared to cell results. Results from two types of ingots (denominated A and B) are presented. Because many studies focus on material with high concentrations of a particular kind of defect, a characterization of commonly used mc-Si also helps to put such studies into context. This paper reports only on the commercially used part of the ingots (i.e., not the discarded edges). The paper finishes with tentative qualitative conclusions.

2. Material characterization

It is well known that the oxygen concentration decreases slowly from bottom to top of an ingot. In most of the ingots the oxygen is everywhere below 10 ppma, and in most of the material even below 5 ppma. Fig. 1a shows that the ingots of type A show much higher maximum oxygen concentrations of around 20 ppma in the bottom.

The carbon concentration in most ingots is high: about 7-11 ppma with relatively flat profiles. Carbon is known to precipitate not very easily. Indeed, the observed carbon concentrations caused no noticeable shunting of cells ($R_{sh} > 1000 \Omega\text{cm}^2$), neither in clean parts of the ingot nor in metal-contaminated parts.

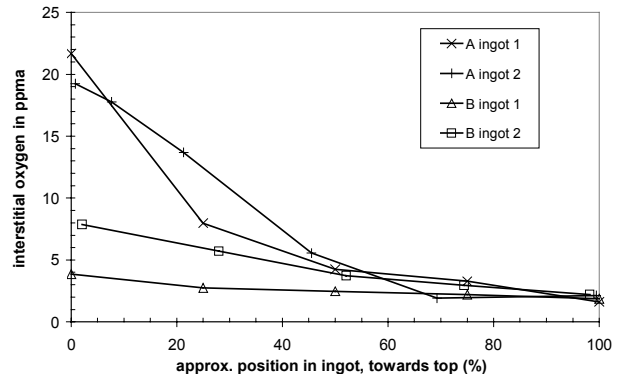


Fig 1. Interstitial oxygen, measured by FTIR, measurement error is approx. 1-2 ppma.

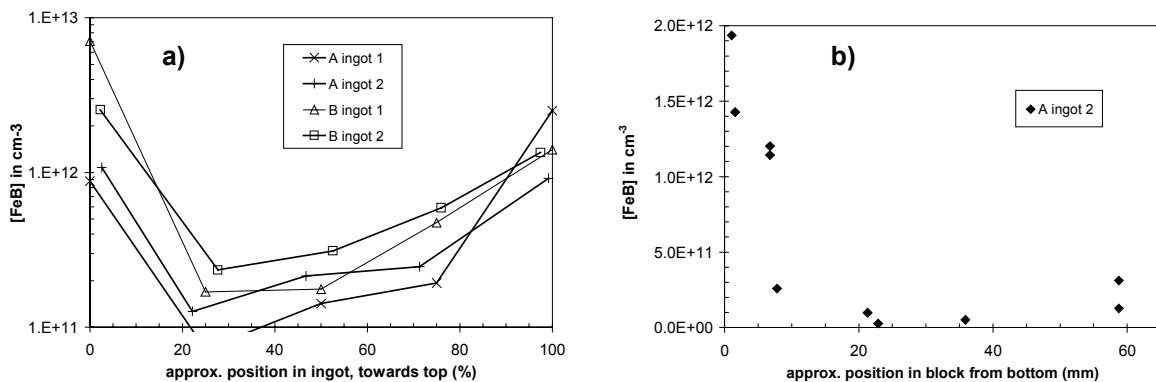


Fig 2. a) FeB pair concentration estimated from lifetime change after light soaking. b) FeB profile in bottom of ingot A2, measurements from 3 blocks. Errors in calculation of FeB may be a factor 2. Note that the position in b) is in mm.

The effective lifetime of the ingots was measured by QSSPC² as a function of position in the ingots. The *shapes* of these lifetime profiles vary significantly among the ingots. However, in at least the center 60% of all investigated blocks,³ the QSSPC lifetime is at least tens of microseconds, up to more than 100 μ s in several cases.

Top and bottom of all ingots show the well-known reduction of lifetime. This is attributed to diffusion into the solidified silicon of metallic impurities⁴, and (in the bottom only) to oxygen-related defects. The impurities in the bottom of the ingots originate from the crucible and/or its coating. The impurities in the top originate from impurities dissolved in the liquid silicon, which have segregated to the very top layer of the ingot, and after solidification diffuse ‘backwards’. Bottom and top metallic contaminants therefore need not be the same.

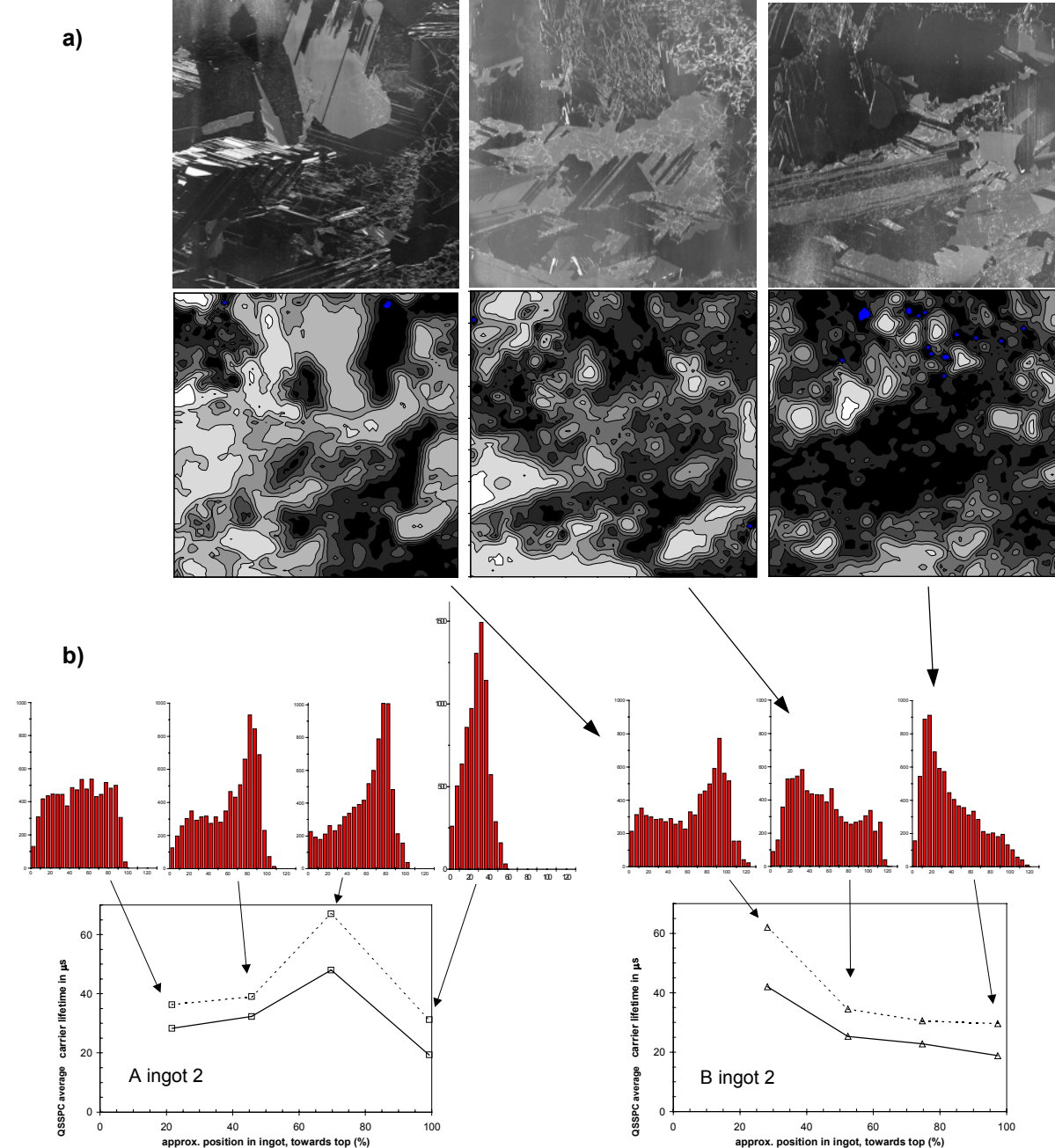


Fig 3. Spatially resolved lifetime measurements by MFCA. a) correspondence between images of defect density and the lifetime maps. Three examples are given, from ingot B2. b) correspondence between density distributions and QSSPC lifetime profile through the ingot. The lifetime scale for 2D maps as well as histograms is 0-130 μ s.

As a convenient probe of this solid state diffusion, the FeB concentration can be measured by lifetime change after light soaking (see, e.g., ref⁵). The resulting estimated FeB concentration profiles are given in Fig. 2a. The diffusion depth of Fe is about 30 mm, and most of the contaminated silicon is cut away from ingots before wafering. Some 10 mm of contaminated top and bottom however usually remains in the block for wafering.⁶ Fig. 2b shows a detail of the FeB profile in ingot A2. The sharp drop of concentration in a few mm is remarkable. The non-zero level of FeB in the center of the ingots, and the slow increase towards the top, may be due to a small feedstock contamination (~0.01 – 0.1 ppma) in combination with a segregation coefficient of around 10⁻⁴.⁷ The maximum observed levels of FeB due to this phenomenon are around 10¹³ cm⁻³. Such a high concentration causes a dramatic decrease of lifetime (to, e.g., 3-4 μ s for 10¹³ cm⁻³). However, since Fe can be easily gettered this low lifetime is not, by itself, predictive of poor cell results.

For the large central part of the ingots, neither solid-state diffused impurities nor oxygen can be the cause for the observed lifetime profile. Fig. 3a shows spatially resolved lifetime variations of three wafers measured by MFCA,⁸ and the corresponding visual images after a defect etch. As far as we could qualitatively determine in many measurements like these, the low lifetime areas always correspond to high defect density areas. These are mostly in the form of a fine crackle-type network, apparently strings of dislocations. Fig. 3b shows histograms of MFCA lifetime measurements and the corresponding QSSPC lifetimes. Apart from bottom and top wafers, the width of the histograms is approx. constant (105-120 μ s); only the shape changes. It appears, therefore, that lifetime profiles in the ingots (apart from bottom, and sometimes top) are determined by the evolution of the defect distributions. This is related to solidification and cool-down parameters,⁹ which are particular for ingot growth techniques and manufacturers.

3. Cell results and lifetime after emitter diffusion

Fig. 4 shows illustrative examples of cell results and QSSPC lifetime after the normal emitter diffusion (in a belt furnace), as well as after the same furnace anneal without emitter dopant source (“anneal only”). It is clear that in both ingots, gettering makes a difference with the “anneal only” situation, only for the top and bottom parts¹⁰. The improvement in the bottom of ingot B2 is very significant, which we attribute to the fact that DLTS showed that Fe is the major in-diffused impurity, and oxygen concentration is low (<8 ppma). The lifetime limiting impurities can therefore be easily gettered. The phenomenon of best performance in the bottom of the ingots was found in both ingots of type B.

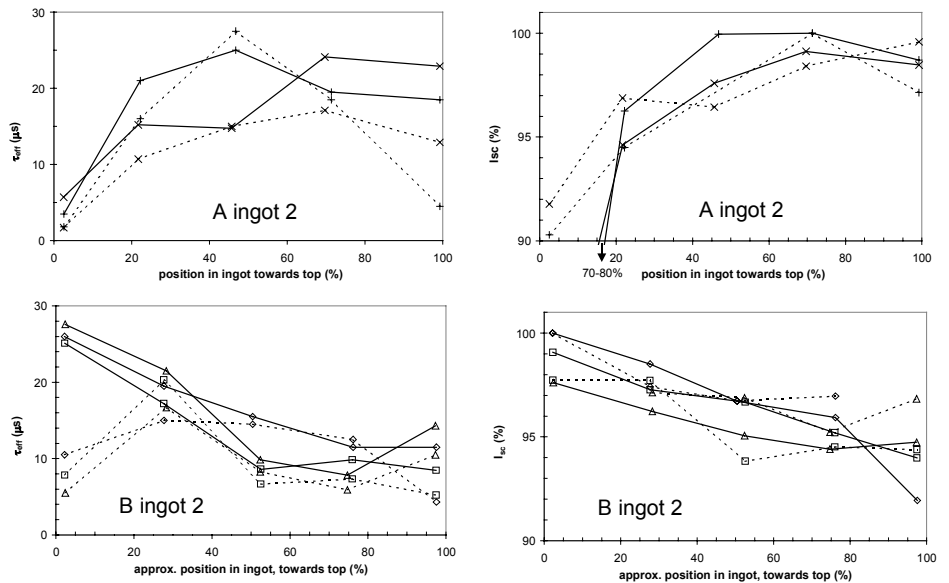


Fig. 4. left: Lifetime after emitter diffusion (solid lines) and after the thermal profile for emitter, but without dopant source (dashed lines). right: I_{sc} relative to maximum of ingot, of cells without SiNx ARC (solid lines) and with SiNx ARC (dashed lines). Maximum I_{sc} corresponds to about 21.5 and 30.5 mA/cm², respectively.

Top graphs: ingot A2, bottom graphs: ingot B2.

In ingot A2 the improvement of the bottom due to gettering is only modest. Oxygen and in-diffused impurities are compared with I_{sc} in Fig. 5. The strong decrease of I_{sc} towards the bottom of ingot A2 is not as abrupt and short-ranged as the FeB profile, so it is more likely due to (or at least, related to) the oxygen contamination. However, it should be noted that DLTS showed that Fe was not the major in-diffused impurity in this case. A high oxygen concentration in the bottom and accompanying reduced cell performance was found in both ingots of type A.

The agreement of the I_{sc} curves with lifetime profiles after emitter diffusion is obvious. The as-received lifetime after light soaking for ingot B2 (Fig 6) is also a reasonable qualitative predictor for the I_{sc} .

4. Discussion and conclusions

The lifetime after emitter diffusion (Fig.4), and in specific cases as-received (Fig.6), is a good qualitative predictive parameter for cell efficiency. This lifetime evolution through the ingot is largely determined by crystal defect distribution (Fig.3), i.e. by thermal parameters during ingot growth. The effect of hydrogen passivation on this defect activity (difference with and without SiN_x ARC in Fig. 4) is, in the presented experiments, small.

It is apparently feasible to reduce oxygen concentrations to below 10 or even 5 ppma in a complete ingot, and choose crucible and/or coating which release only Fe into the ingot (example: ingot B2). Such ingots are then largely free of problems due to bottom/top contamination and yield homogeneous cell results. Optimizing thermal parameters during production of such ingots should allow for further lifetime and efficiency improvement.

In agreement with ref.¹¹, an oxygen concentration above about 10 ppma rapidly becomes detrimental (Fig 5 and similar results for ingot A1). In the largest part of any material the oxygen concentration is low and not obviously harmful.¹²

These experiments do not show whether the observed impact of defect density is caused by precipitates (in particular, precipitates decorating dislocations), or the impact of oxygen is due to interaction with metal impurities.

Acknowledgements

We gratefully acknowledge the kind supply of wafers from known ingot positions by the manufacturers, the processing and characterisation by staff of ECN, and valuable discussions with staff of ECN, G. Hahn, and D. Macdonald. This work was supported by Novem under project nr. 146.110-020.1

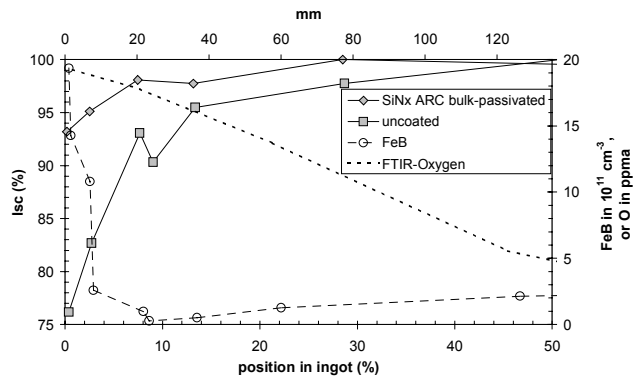


Fig. 5. Oxygen and FeB trends (right scale) and relative cell I_{sc} (left scale) in the bottom of ingot A2. I_{sc} for uncoated cells (squares) and cells with hydrogen-passivation by SiN_x ARC (diamonds) is shown.

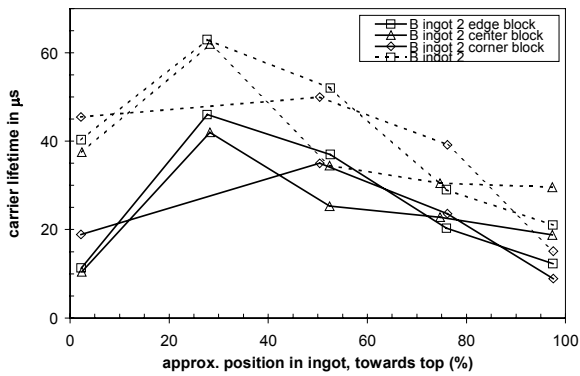


Fig. 6. As-received lifetime of ingot B2. Before light soaking: solid lines, after: dashed lines.

¹ Deep Level Transient Spectroscopy

² Quasi Steady State PhotoConductivity. Sinton WCT-100. This lifetime is an area-averaged quantity.

³ with the exception of one ingot which was apparently grown from heavily contaminated feedstock

⁴ M. Acciarri et al., 13th European PVSEC, p. 1336 (1995).

⁵ D. Macdonald and A. Cuevas, 11th workshop on crystalline silicon solar cell materials and processes, p. 24 (2001).

⁶ We have verified in one ingot that the edge blocks indeed show a FeB profile consistent with this model.

⁷ L.J. Geerligs, these proceedings.

⁸ Modulated Free Carrier Absorption, methodology as in A. Schönecker et al., J. Appl. Phys. 79, 1497 (1996).

⁹ D. Franke et al., 2nd world conference on PVSEC, p. 108 (1998).

¹⁰ This result may have been influenced by contamination introduced during processing, which however does not invalidate the subsequent discussion.

¹¹ The rate of precipitate nucleation is a high power of the oxygen concentration, see *Handbook of Semiconductor silicon technology*, eds. O'Mara, Herring, and Hunt (Noyes publications, 1990). Perhaps related to this, a threshold of around 14 ppma for the detrimental effects of oxygen was reported by. S. Martinuzzi et al., 13th European PVSEC, p. 1382 (1995).

¹² Perhaps so low that boron-oxygen defects will not be very relevant for mc-Si.

Development of a Novel Phosphorus Spray Diffusion System for Low Cost Silicon Solar Cells

K. Nakano, A. Hariharan and K. Matthei
GT Solar Technologies, Nashua, NH 03063

D.S. Kim, A.D. Upadhyaya and A. Rohatgi
University Center of Excellence for Photovoltaics Research and Education
Georgia Institute of Technology, Atlanta, GA 30332

Abstract

Phosphoric acid was used as an n-type doping source for making an emitter. Cold spray method has been adopted because it does not need complicated and corrosive heating system. The key spray parameters such as belt speed, flow rate of carrier gas, concentration of phosphoric acid and angle of spray nozzles are optimized to get uniform and reproducible sheet resistance of the emitter. Diffusion process has been studied by firing spray coated silicon wafer in the belt furnace. Screen-printed solar cells using the emitter formed by spray method have been fabricated and compared with conventional POCl_3 diffused emitter. Screen printed/spray diffused cells gave impressive cell efficiencies up to 16.6 % on 1 Ωcm FZ, which is nearly equal to POCl_3 emitter cells (~16.9%). Compared to POCl_3 emitter cell, the spray diffused cells showed slightly lower quantum efficiency at short wavelength and slightly higher emitter saturation current density ($\sim 3.59 \times 10^{-13} \text{ A/cm}^2$ as opposed to $2.73 \times 10^{-13} \text{ A/cm}^2$). Further optimization can eliminate this small difference in efficiency.

Introduction

Batch type diffusion process with POCl_3 is very common for junction formation in PV industries because of low contamination and availability of equipment from semiconductor industry. However, the cost and throughput of POCl_3 diffusion system are not very satisfactory due to prolonged heat treatment and excessive wafer handling including wafer insertion into quartz boats. To meet the requirements of the PV industry, Low-Cost, High-Throughput and High-Mechanical Yield, an inline type diffusion process and equipment are desirable. Although various phosphorus diffusion techniques [1,2,3] have been reported for PV applications, no study on cold phosphorus spray has been conducted. The spray of phosphoric acid offers many advantages over the conventional diffusion technology due to its simplicity and low cost. In order to develop standard inline diffusion process/equipment for PV, we have developed a promising diffusion process with spray method and demonstrated high efficiency solar cells.

Experiment

1. Spray System

A spray system with two spray nozzles was developed for spraying phosphoric acid at GT solar. Nitrogen was used as a carrier gas to spray phosphoric acid for doping source. Pick-up rate of each spray nozzle was calibrated and adjusted to give uniform sheet resistance across 4 inch x 4inch silicon wafers. The amount of phosphoric acid on the wafer was controlled by changing the belt speed and the concentration of spray source during the spray.

2. Preparation of phosphoric acid solution

Spray source were prepared by mixing commercial phosphoric with D.I. water. The weight percent of P_2O_5 was calculated using equation (1) when 1 ml of phosphoric acid is mixed with water.

$$\begin{aligned}\text{Percentage P}_2\text{O}_5 &= (\text{Weight of P}_2\text{O}_5) / (\text{Weight of H}_3\text{PO}_4 + \text{Weight of water}) \\ &= 1.041\text{g} / (1.69\text{g} + \text{Wg})\end{aligned}$$

where W is weight of water

3. Wafer cleaning

Silicon wafers were cleaned in 2:1:1 H₂O: H₂O₂: H₂SO₄ and 2:1:1 H₂O: H₂O₂: HCl solutions for 5 minutes followed by 3 minute DI water rinse after each cleaning. The surface of wafer shows hydrophilic characteristics after HCl cleaning. Some wafers were dipped in HF solution to obtain hydrophobic surfaces. Saw damage of as-cut wafers was removed by etching in 15: 5: 2 HNO₃: CH₃COOH: HF solution for 10 minutes. All the wafers were dried in vapor of isopropyl alcohol after cleaning.

4. Diffusion of phosphorus

The mixture of phosphoric acid and D.I. water sprayed on silicon wafer was at 200 °C for 5 minutes before firing in the belt furnace at high temperature. The firing temperature and belt speed were changed in order to get various sheet resistances and junction depths.

5. Measurement of emitter saturation current density (Joe)

Phosphoric acid was sprayed on both side of n-type 5000 Ωcm FZ wafer followed by firing in the belt furnace to diffuse phosphorus. SiNx was coated on diffused surfaces in a PECVD chamber operating at 13.56 MHz. Joe was measured by PCD method [4] on the emitters with 40Ω/□ sheet resistance. The emitters used for Joe measurement were formed by POCl₃ diffusion as well as spray diffusion with different concentration of phosphoric acid (2 ~ 15%).

6. Cell fabrication

P-type (100) 1Ωcm FZ as well as 1.3 Ωcm multi-crystalline silicon, grown by heat exchange method (HEM), wafers were used to fabricate screen-printed silicon solar cells. The emitter was formed by spray and POCl₃ diffusion. After phosphorus diffusion, the phosphorus glass was removed in dilute HF solution. Phosphorus diffused emitter was passivated by SiNx deposited by PECVD (Plasma Enhanced Chemical Vapor Deposition). Al paste was screen-printed at the back followed by sintering in RTP chamber to form a BSF. Front contact was formed by screen-printing Ag paste on the SiNx film followed by firing in the belt furnace or RTP.

Result and discussions

The pick-up rates of spray nozzles were calibrated before spray diffusion. The configuration of each spray nozzle was optimized to give uniform coating on silicon wafers. Molecules of solvent evaporate from the droplets and only phosphoric acid remains when volatile solvent is used as vehicle liquid. However, we used water solvent because phosphoric acid is miscible with water in all proportions.

Figure 1 shows the optical micrographs of the surface after phosphoric acid spray. Hydrophilic surfaces (a, b) were obtained during HCl cleaning due to oxidation of surface. The hydrophobic surfaces (c, d) were obtained when silicon dioxide was removed in HF. It was found that the surface state of the wafer is important for achieving good uniformity. The droplets of phosphoric acid become round and decrease surface area coverage on hydrophobic surface. It appears that uniform emitter cannot be formed on hydrophobic surface because phosphoric acid agglomerates without spreading out on the surface. However, the phosphoric acid on the hydrophilic surface spreads out and covers all surface with slight variation in thickness. Figure 1 indicates that

hydrophilic surface is better than hydrophobic surface when water based phosphoric acid used as a spray source.

The dependence of sheet resistance on diffusion temperature is shown in Figure 2. The concentration of phosphoric acid and belt speed were 15 % and 5cm/sec, respectively. The sheet resistances of $20\text{--}50 \Omega/\square$ were easily obtained by changing the diffusion temperature in the IR belt furnace. The silicon surface showed dark brown color after diffusion regardless of diffusion temperature.

The effect of spray parameters on sheet resistance is shown in Figure 3. The sheet resistance data demonstrate two different trends depending on the concentration of phosphoric acid. The sheet resistance of emitter decreases as the belt speed increases for P_2O_5 concentrations above 8.54% while the sheet resistance increases at lower P_2O_5 concentrations. It seems that phosphoric acid reacts with silicon and produces phosphosilicate glass during drying and ramping up to diffusion temperature. More phosphoric acid on the surface produces thicker glass, which limits diffusion of phosphorus into the silicon at low belt speed and high P_2O_5 concentrations. Different colors after diffusion support that the glass thickness is different for different concentration of phosphoric acid. Decrease of sheet resistance starts at lower belt speed when low concentration of phosphoric acid is sprayed. The figure suggests at low P_2O_5 concentrations, the diffusion is controlled by the amount of phosphoric acid on the wafer, which is lower at higher belt speed.

The cell parameters are summarized in table 1. Two different Ag pastes were used for front contact. $POCl_3$ diffused emitter maintained high efficiency regardless of type of Ag paste. The firing condition for each paste was optimized for $POCl_3$ diffused emitter which has deeper junction than the spray diffused emitter. It was found that the open circuit voltage and diode ideality factor of cells with spray diffused emitters was more sensitive to the type of paste used. The table shows that 2% phosphoric acid gives higher efficiency compared to 15% phosphoric acid partly because of low J_{sc} . The cells with spray-diffused emitter yielded lower open circuit voltages than those with $POCl_3$ diffused emitter, resulting in slightly lower efficiency. Impressive screen printed cell efficiencies of 16.6 % and 15.22% were achieved on FZ on HEM respectively, by 2% phosphoric acid. $POCl_3$ diffused FZ cells were ~16.9% and HEM cells were ~15%.

The IQE analysis in Figure 4 shows that spray-diffused emitter exhibited lower quantum efficiency at short wavelength than $POCl_3$ diffused emitter. This low quantum efficiency is caused by heavy doping effects and high recombination velocity due to high phosphorus surface concentration in the spray diffused emitter.

From Figure 5 it is seen that higher phosphorus concentration gives higher emitter saturation current density. This appears to be caused by high concentration of phosphorus at the surface. The emitter saturation current density for 2% phosphoric acid was measured to be $3.59 \times 10^{-13} A/cm^2$, which corresponds to voltage of 653 mV when the base effects are neglected. $POCl_3$ diffused emitter had J_{sc} of $2.73 \times 10^{-13} A/cm^2$.

LBIC scan of a cell with spray-diffused emitter is shown in Figure 5 along with cell parameters in order to study the uniformity of spray diffused emitter. The figure indicates that the emitters formed by spray are quite uniform.

Conclusion

We have demonstrated screen printed cell efficiencies of 16.6% on FZ and 15.22% on HEM with emitters formed by spraying 2% phosphoric acid in air at room temperature. The efficiency is only slightly (~0.3% absolute) lower than that of $POCl_3$ diffused emitter due to lower open circuit voltage or higher emitter saturation current density. Spray diffused emitter requires proper firing condition and paste selection because of shallow junction depth. Process optimization can further enhance the performance of cells with spray diffused emitter.

Reference

- [1] Parag Doshi and Ajeet Rohatgi, "18 % Efficient Silicon Photovoltaic Devices by Rapid Thermal Diffusion and Oxidation", IEE Trans. On Elec. Dev. Vol.45, no.8, pp.1710~1716, 1998.
- [2] S.Sivoththaman, W.Laureys, J.Nijs, and R.Mertens, "Rapid thermal annealing of spin-coated phosphoric acid films for shallow junction formation", Appl. Phys. Lett. Vol.71. no.3, pp392~394, 1997.
- [3] Mark D.Rosenblum, Jack I. Hanoka, US patent No. 5,527,389 , Jun. 18, 1996.
- [4] D.E.Kane and R.M.Swanson, "Measurement of saturation current by a contactless photoconductivity decay method", Conf. Record 18th IEEE PVSEC, pp.578-583, 1985

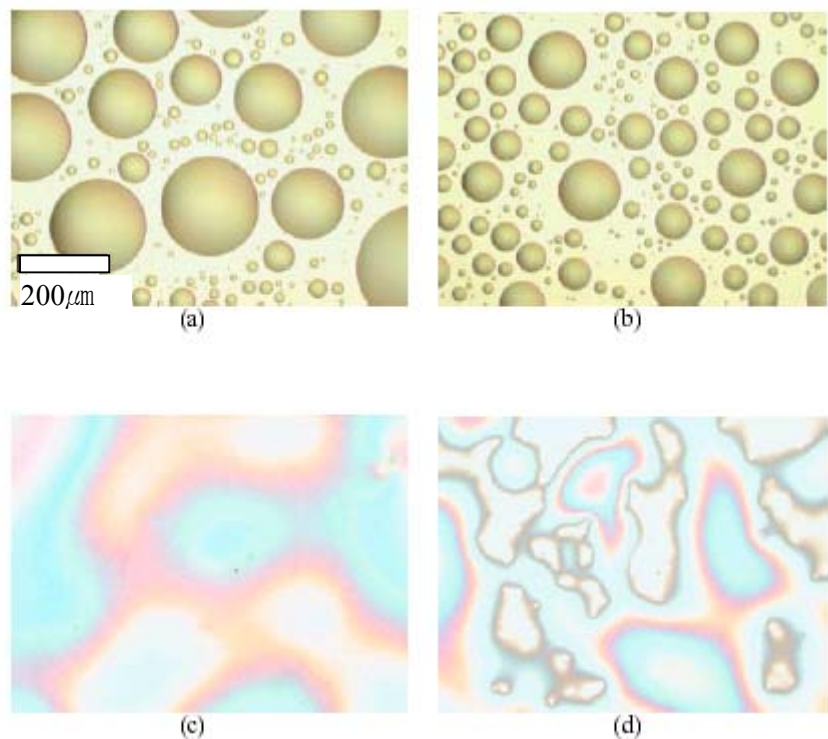


Figure 1. Optical microscope images of silicone surface coated with Phosphoric acid on hydrophobic (a,b) and hydrophilic (c,d). The belt speeds of spray system were 5cm/sec for (a,c) and 15 cm/sec for (b,d).

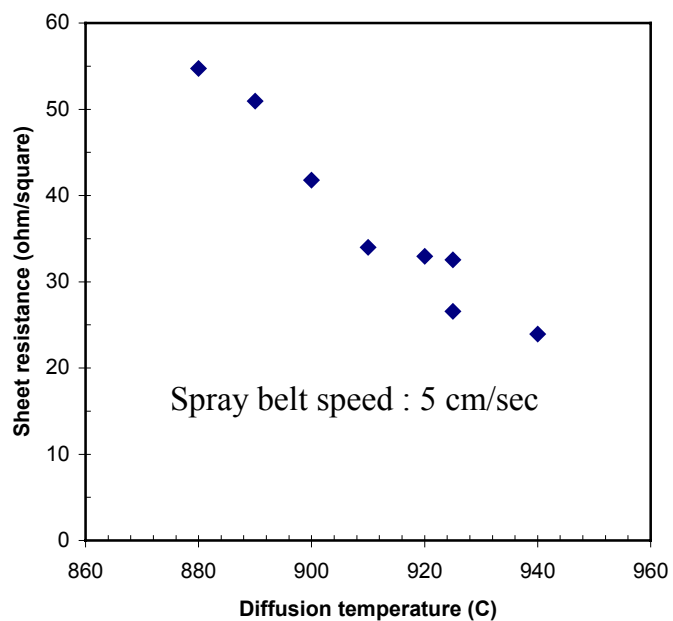


Figure 2. Sheet resistance as a function of diffusion temperature. The concentration of phosphoric acid is 15%.

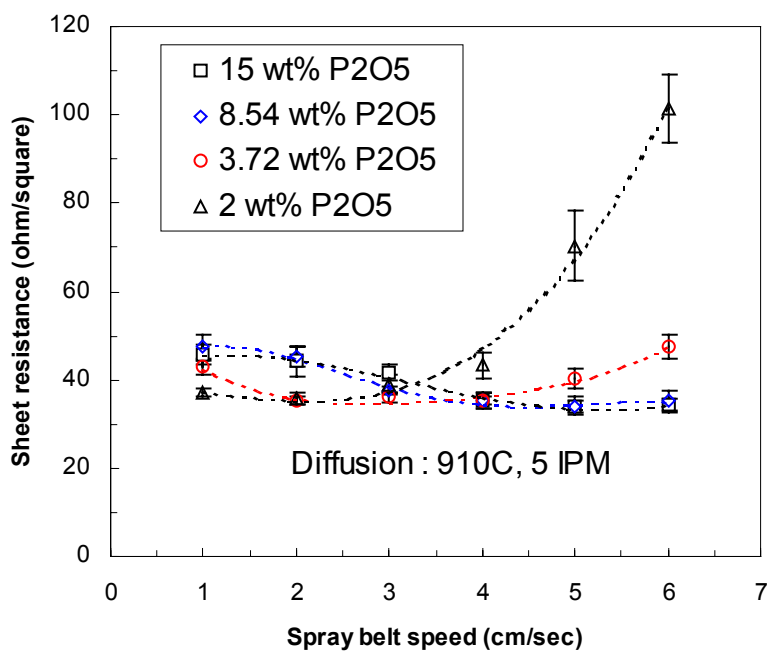


Figure 3. Sheet resistance as a function of spray belt speed.

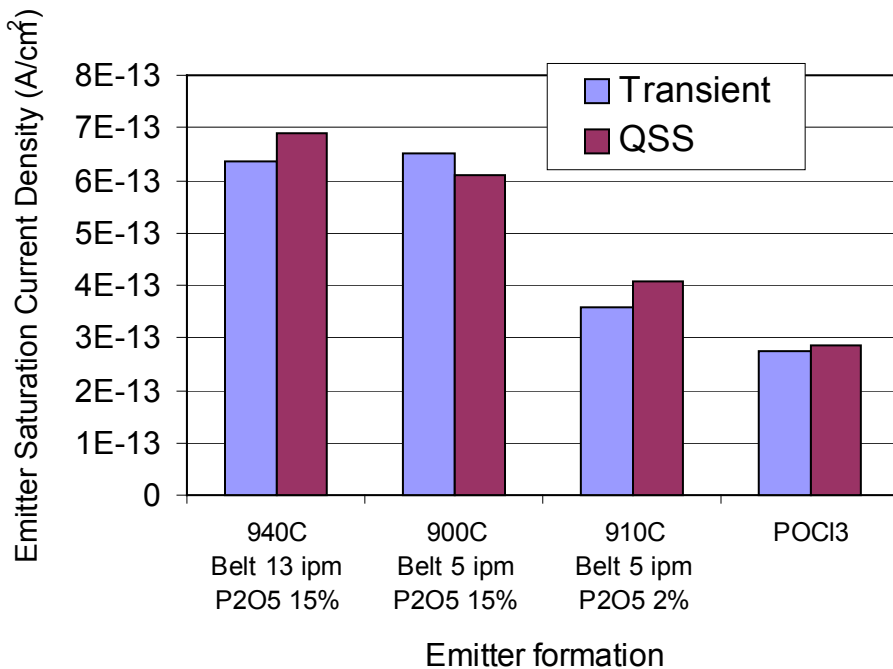


Figure 3. Effects of emitter diffusion parameters on emitter saturation current density.

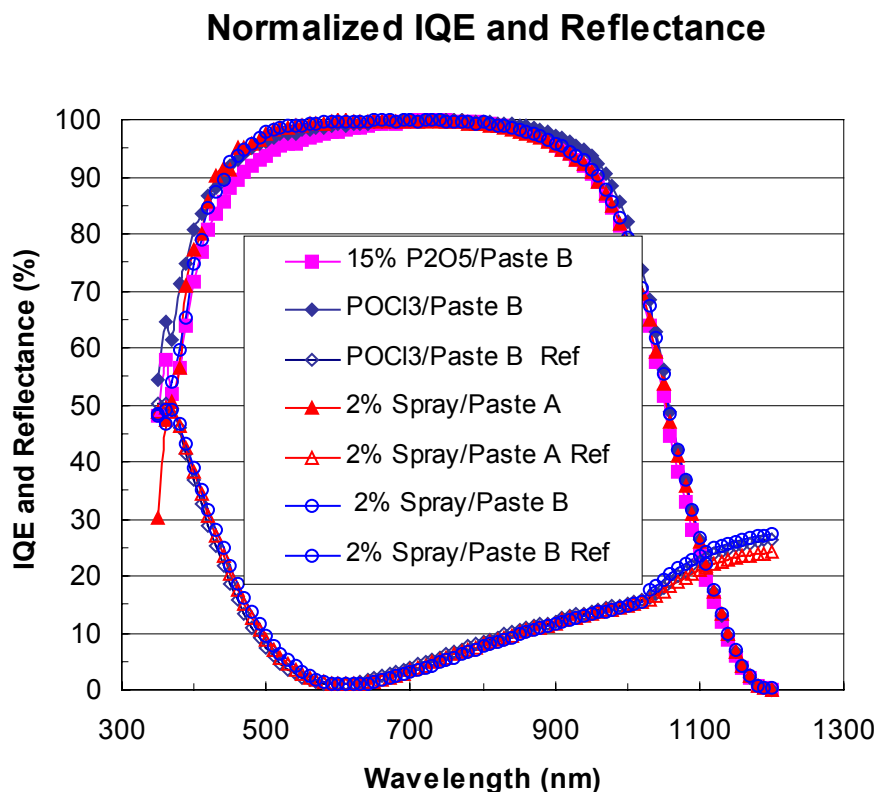
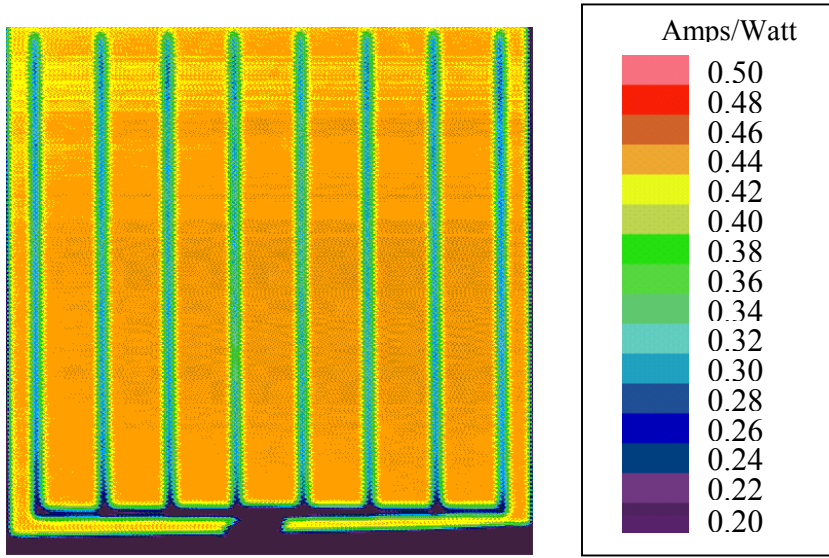


Figure 4. Internal quantum efficiency of cells.



Eff=16.2 %, Voc=615 mV, Jsc=33.4 mA/cm²

Figure 5. LBIC response of FZ silicon cells spray doped emitter.

Table 1. Light I-V data of cells on various emitters. Paste A and B were fired in RTP and IR belt furnace, respectively.

Cell ID	Wafer	Voc (mV)	Jsc (mA/cm ²)	FF (%)	Efficiency (%)	n factor	Emitter / Front contact
11F1-3-7	FZ	635	33.8	0.787	16.9	1.10	POCl ₃ / Paste A
11F1-4-2	FZ	632	33.6	0.784	16.6	1.15	POCl ₃ / Paste B
12F1-1-5	FZ	621	33.4	0.791	16.4	1.02	15 % P ₂ O ₅ / Paste A
12F1-2-5	FZ	619	33.2	0.773	15.9	1.13	15 % P ₂ O ₅ / Paste B
12H1-2	HEM	599	31.3	0.765	14.4	1.13	15 % P ₂ O ₅ / Paste A
12H2-2	HEM	586	30.9	0.697	12.6	1.98	15 % P ₂ O ₅ / Paste B
10F2-3	FZ	628	33.5	0.788	16.6	1.09	2 % P ₂ O ₅ / Paste A
10F3-4	FZ	621	33.0	0.762	15.6	1.31	2 % P ₂ O ₅ / Paste B
10H1-5	HEM	608	32.1	0.781	15.22	1.15	2 % P ₂ O ₅ / Paste A
10H2-4	HEM	597	31.4	0.757	14.18	1.33	2 % P ₂ O ₅ / Paste B

Two-Dimensional Simulations of Thin-Silicon Solar Cells

T.H. Wang, M.R. Page, and T.F. Ciszek

National Renewable Energy Laboratory
1617 Cole Blvd., Golden, CO 80401
[mailto: tihu_wang@nrel.gov](mailto:tihu_wang@nrel.gov)

1. Introduction

Quantitative analysis or numeric simulation on a cross-section of silicon devices offers many insights into understanding material problems and their effects on device performances as well as device structure optimizations. Such two-dimensional simulations on semiconductor devices are standard design practices and are routinely done with expensive software packages. The availability of less expensive software tools nowadays, such as MicroTec® [1] for 2D modeling of semiconductor devices, affords us a more detailed examination of polycrystalline thin-silicon materials and solar cells.

MicroTec® is based on the diffusion-drift model and does not include energy balance. It has a robust 2D semiconductor device simulator component that efficiently solves the Poisson equation and the continuity equation for electrons and holes with a finite difference technique on a rectangular grid. Only steady-state problems are possible, but the built-in models consider many physical effects such as bandgap narrowing, recombinations (Shockley-Read-Hall [SRH], Auger, radiative, and surface), impact ionization, band-band tunneling, photogeneration, metal-semiconductor contacts (ohmic and Schottky), and concentration- and field-dependent mobilities. This paper presents three case studies that are of interest to polycrystalline thin-silicon solar cell research, the so-called “bad” region effect, grain boundary effect, and device optimization using interdigitated contacts.

2. Inhomogeneity effect

A polycrystalline material having a “bad” region that is photoelectrically inactive and electrically conductive can lead to a severe shunting problem. Figure 1(a) is the schematic representing such a “bad” region of 1 μm in width and 10 μm in length in a 20- μm thick and 20- μm wide device. Simulation results in Fig. 1(b) show that the effect on cell performance really depends on the extent of the defects. Fig. 1(c) and (d) show the enhanced SRH recombination in the “bad” region and the resulting non-equilibrium electron and hole concentration distribution at $y=5 \mu\text{m}$.

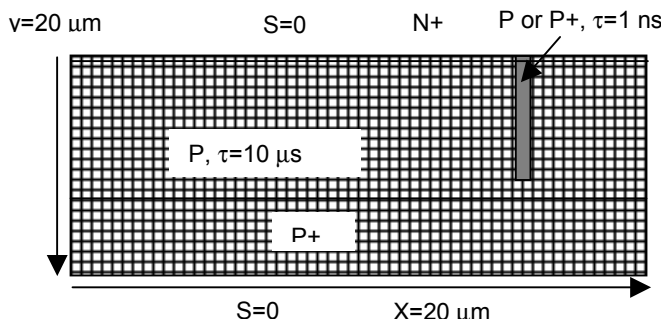


Fig. 1 (a) Model device cross-section with a “bad” region

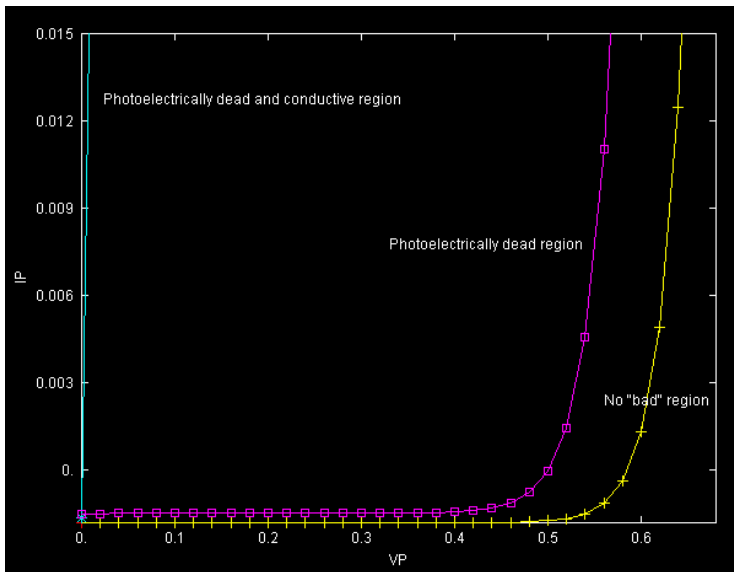


Fig. 1 (b) The corresponding I-V curves

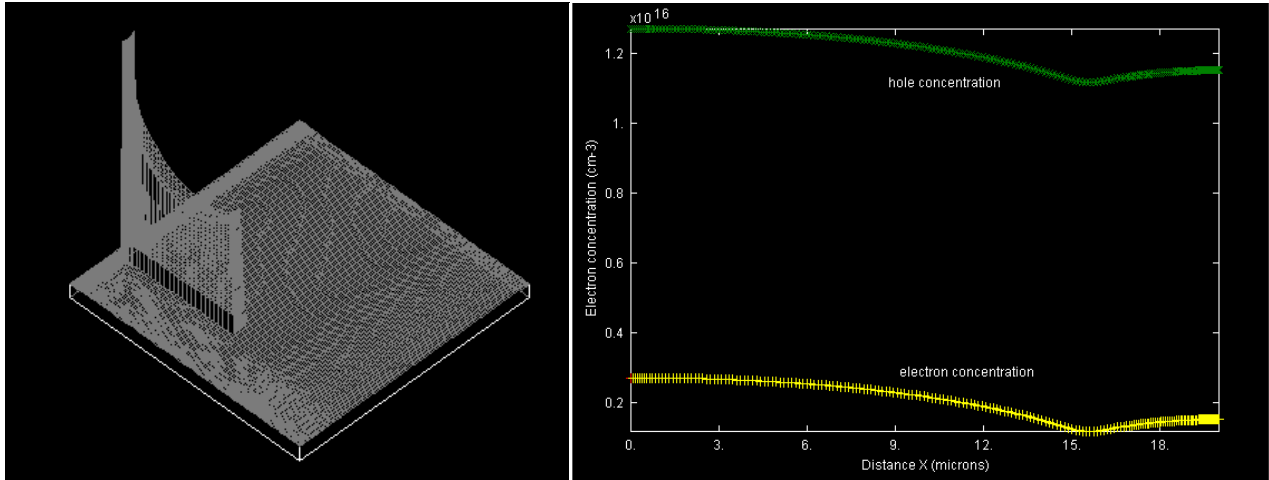


Fig. 1 (c) SRH recombination rate (cm^{-3})

Fig. 1 (d) electron and hole concentration at $y=5 \mu\text{m}$

If the “bad” region is only photoelectrically inactive (with a minority carrier lifetime of 1 ns) but not electrically conductive, then only a small impact is seen which is caused by increased dark current in the “bad” depletion region. However, if the region is also electrically conductive (represented by degenerate doping), the effect is catastrophic even if the “bad” region does not reach the back contact.

3. Grain boundary effect

The grain boundary recombination activity may be represented by an effective recombination velocity. Fig. 2 shows a sketch of a simple N+/P/P+ thin silicon device with a total thickness of 20 μm and an average grain size of 20 μm . The simulation domain consists of half of a grain (the cross-hatched area). The grain boundary runs vertically across the junction. The calculated IV curves are given in Fig. 3(left) with recombination velocities at the grain boundary varying from 10^2 to 10^6 cm/sec . It is seen that for a grain size of 20 μm , a recombination velocity lower than 10^4 cm/sec is necessary to avoid significant loss of performance. This velocity, however, has to be lowered to 10^3 cm/sec for a grain size of 2 μm , as shown in Fig. 3(right).

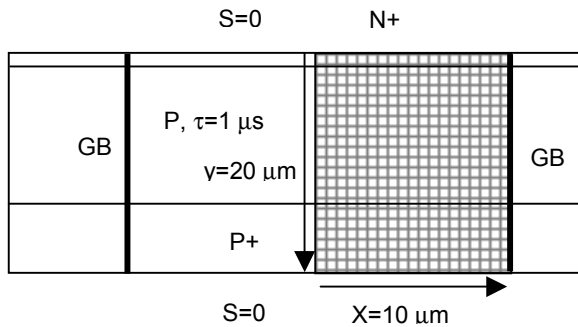


Fig. 2 Sketch of a polycrystalline silicon solar cell having a thickness of $20 \mu\text{m}$ and average grain size of $20 \mu\text{m}$. The shaded area is the simulation domain.

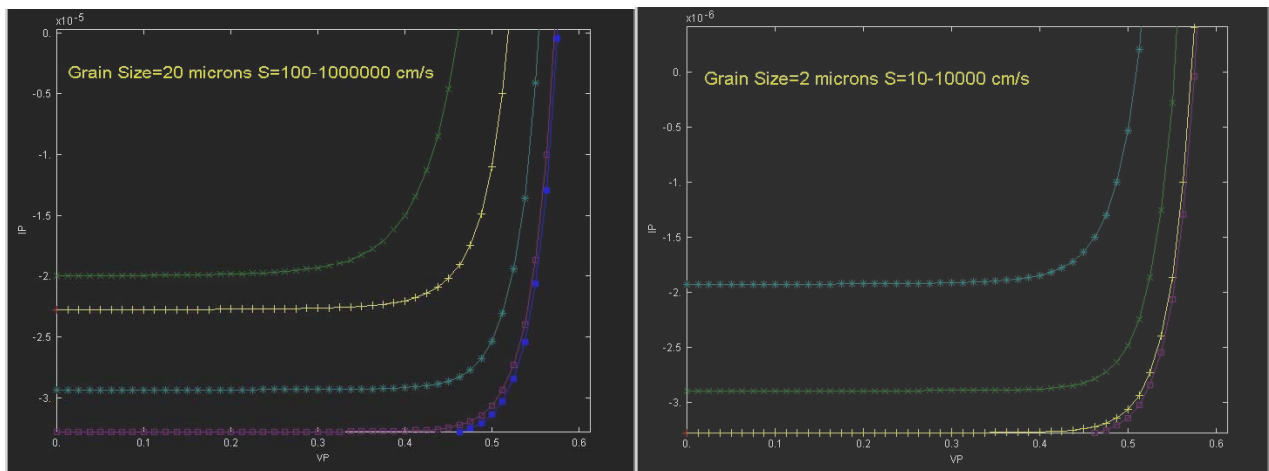


Fig. 3 (left) Simulated IV curves for a thin silicon solar cell with a grain size of $20 \mu\text{m}$. The curves from top to bottom are for recombination velocities of 10^6 , 10^5 , 10^4 , 10^3 , and 10^2 cm/sec , respectively. (right) Simulated IV curves for a thin silicon solar cell with a grain size of $2 \mu\text{m}$. The curves from top to bottom are for recombination velocities of 10^4 , 10^3 , 10^2 , and 10 cm/sec , respectively.

4. Optimizing device designs

A device structure of interdigitated contacts on the same surface of a thin-silicon film has many advantages over a conventional planar structure such as simplified processing and connections, especially when an insulating substrate is used that makes it possible to monolithically integrate cells to sub-modules.

Analytically speaking, the spacing between the alternating N- and P-contacts is limited by twice the effective diffusion length of the minority charge carriers. However, with 2D simulations, we may optimize the design, and a much larger spacing on the order of $100 \mu\text{m}$ can be used even when the diffusion length is only about $20 \mu\text{m}$, making screen-printing the contacts a possibility. Figure 4 shows some examples of varying device parameters and the corresponding I-V curves.

5. Conclusions

Two-dimensional simulation of thin-silicon solar cells is very useful to gain further understanding of material problems and their effects on device performances as well as to aid device design optimizations. Three case studies are presented on the so-called “bad” region effect, grain boundary effect, and device optimization using interdigitated contacts.

If a “bad” region is only photoelectrically inactive but not electrically conductive, then only a small impact is seen which is caused by increased dark current in the “bad” depletion region. However, if the region is also electrically conductive (represented by degenerate doping, not even reaching the back contact), the effect is then catastrophic. The effects of grain boundary recombination on device performances are examined with grain sizes of 2 and 20 μm respectively, and it is found that 10^4 cm/sec recombination velocity is adequate for 20 μm grain-sized thin silicon whereas a low recombination velocity of 10^3 cm/sec must be accomplished for a 2 μm grain-sized silicon. 2D simulation indicates that it is possible to design a thin-silicon device with interdigitated contacts that has an intercontact spacing large enough to use the screen-printing technique.

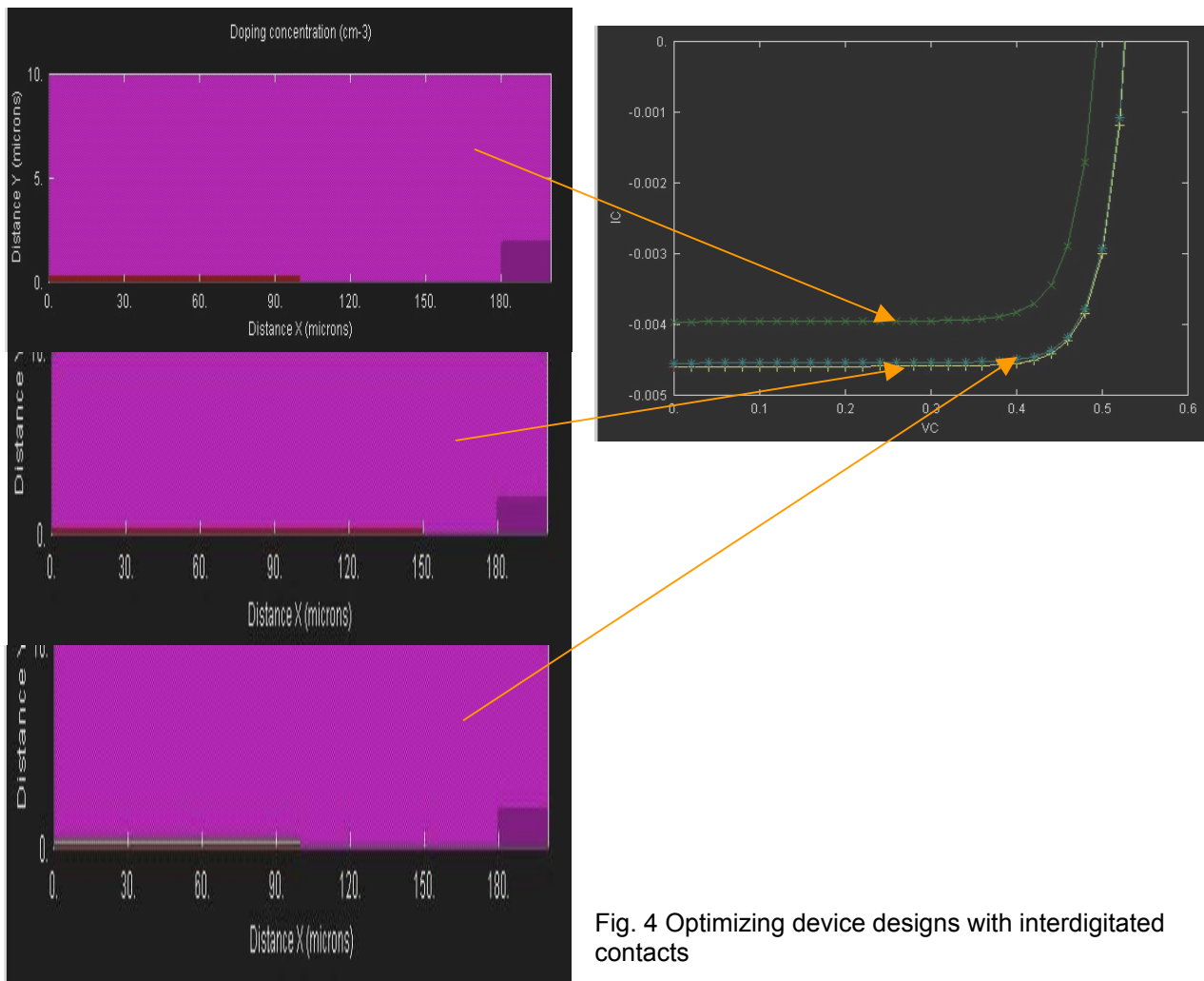


Fig. 4 Optimizing device designs with interdigitated contacts

Acknowledgement

This project was supported by the U.S. Department of Energy under contract No. DE-AC36-99-GO10337 to the National Renewable Energy Laboratory.

Reference

- [1] Siborg Systems Inc., *MicroTec User's Manual*, 1998

Wafer and Solar Cell Characterization by GT-PVSCAN6000

Bhushan Sopori, Jamal Madjdpour, and Chris Auriemma

National Renewable Energy Laboratory (NREL), 1617 Cole Boulevard, Golden, CO 80401

Keith Matthei, Kengo Nakano, Heiko Moritz, GT Solar, 472 Amherst St., Nashua, NH 03063
Email contact: moritz@gtsolar.com

Introduction

The PVSCAN is an instrument designed to characterize silicon solar cell materials and devices. It performs a host of measurements that yield spatial maps of dislocation density, grain distribution, reflectance, and photoresponses from near-junction and the bulk of a solar cell. The information it generates helps in both crystal growth and solar cell process design. It provides insight for developing better crystal growth conditions for minimizing defects, establish database on how substrate defects degrade the performance of the electronic devices, and examining the influence of various device fabrication processes on the device performance. It therefore leads to processes that can ameliorate the impact of defects and impurities on device performance. The PV industry recognized the importance of this instrument for solar cell processing development. Therefore, NREL has decided to upgrade the instrument to include commercial features such as large-area scanning capability, high-speed scanning, user-friendly/menu-driven operation, and automated data analysis. More features are now being added to the new version of the software to accommodate the needs of industry.

PVSCAN was available from NREL for many years. Recently, it has been licensed for commercial manufacture to GTSolar, Nashua, NH. PVSCAN6000 has a fully menu-driven operation with many upgraded features suitable for high-speed analyses. These features include:

- Larger scanning area (8 x 8 in. vs. 4 x 4 in.) with a resolution up to 25 μm
- Reduced the scanning time. PSCAN6000 is typically operated at 4 ips. This high-speed reduces the scanning time for most commercial Si solar cells to about 30 min.
- Display of distribution-plots of the measured parameters.

User Requested Capabilities

In addition to these, we have had requests from various users. In response, we are currently implementing several improvements as described below.

Capability of exporting data for all scans as text/csv files of position (X, Y) and intensity (Z) data. The updated software saves an additional set of scan files as text files in the SDMS folder for each scan type. These files can be renamed after the scan is completed.

Figure 1 shows line-scan plots of a defect-etched wafer taken from three different maps (at the same position of the wafer) using data-export capability. The three plots correspond to defect,

grain boundary, and reflectance maps. It is seen that defect and reflectance maps have excellent correlation. Furthermore, one can decipher segmentation of intragrain defect density, representative of grains with high and low densities. Also notice the occurrence of grain-boundary signals at the edges of each defect density segmentation.

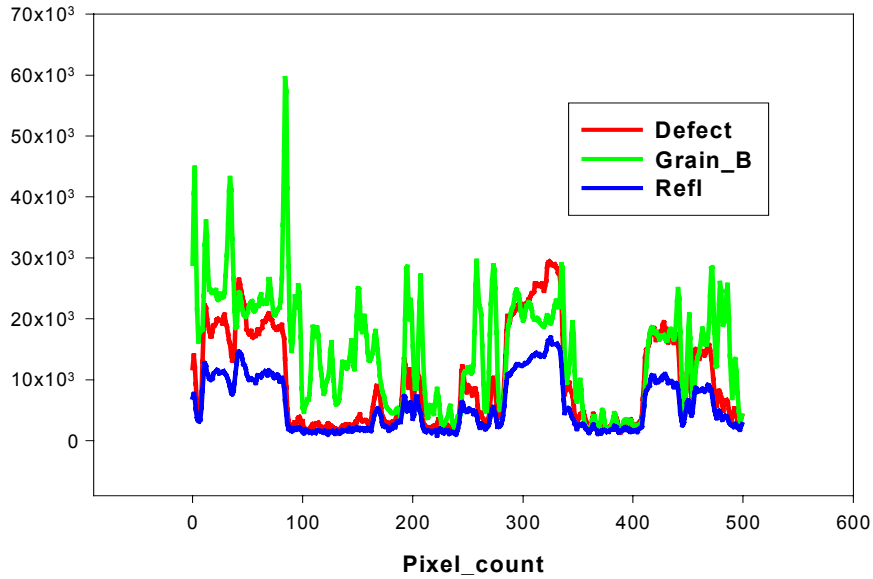


Figure 1. Line scans generated from cvs files of defect, grain boundary and reflectance files. The data are selected from the saved text files that contain data of the entire scan.

The size of the cvs file can be quite large for a large-area sample. To avoid handling excessive amounts of txt-data and save plotting time, we also save a txt file that contains data for one line scan. This line scan is selected to correspond to the central row of data (along Y direction) scan. Figure 2 shows a line scan, transposed to the map via any graphical package, and imposed on a defect map.

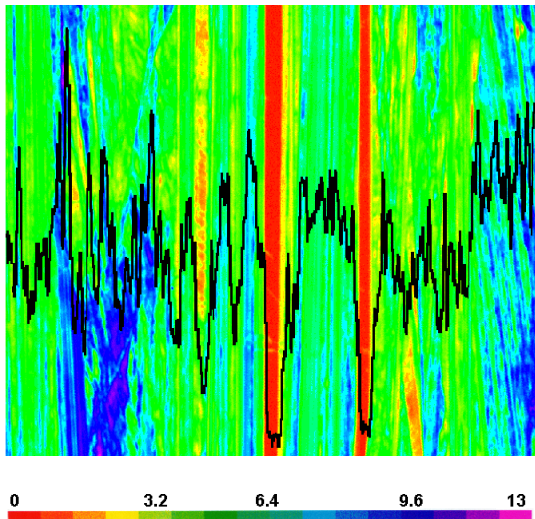


Figure 2. A line-scan superimposed on a defect map. The data for the central line are stored in a file that only saves information for the central row.

One of the recent improvements in the PVSCAN analysis is the ability to make defect maps without chemical-mechanical polishing. We are following two approaches to do this: one is for ribbon samples and the other for wire-sawn samples. For ribbon samples, we have adjusted our etching conditions to provide better defect delineation on striated surfaces of ribbons. Figures 3a and 3b compare etch pits generated on polished and as-grown ribbon samples. For wire-sawn samples, we are trying to identify a polishing chemical etch that can yield a smooth surface.

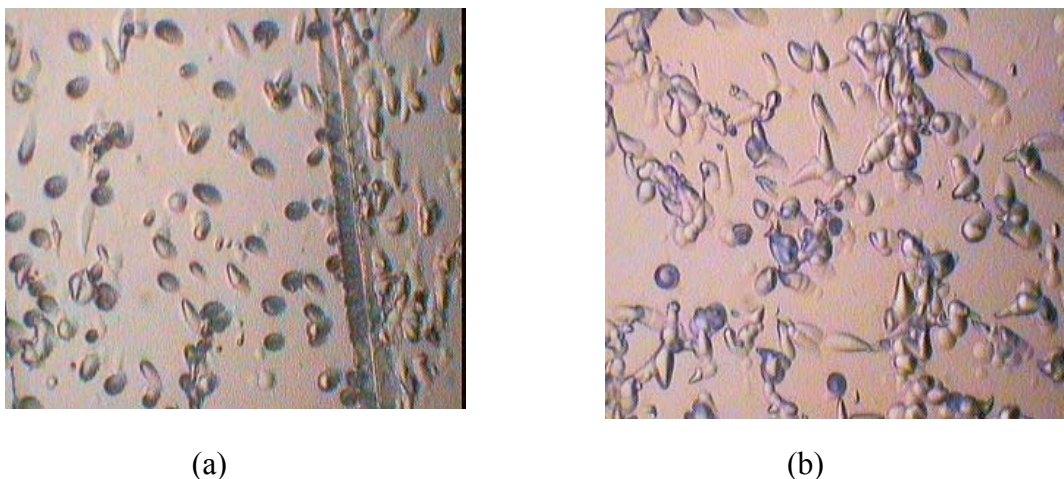


Figure 3. Defect delineation on EFG ribbon samples using Sopori etch: (a) sample was polished before defect etching, and (b) as-grown sample.

Because the as-grown surface of ribbons is not smooth, the defect-etched samples result in some extraneous scattering that can produce an error. We have compared average defect density of as-grown and polished samples to determine the error caused by lack of polishing. Figures 4, 5, and 6 show defect maps of three EFG ribbon samples. The sample in Figure 4a was polished and defect-etched, whereas samples in Figure 5a and 6a were only defect-etched. The defect distributions corresponding to Figures 4a, 5a, and 6a are shown in Figure 4b, 5b, and 6b. The average density of defects for samples of Figures 4, 5, and 6 are: 5.82 cm^{-2} , 6.65 cm^{-2} , and 4.77 cm^{-2} , respectively. Considering these numbers, there appears to be insignificant error resulting from a lack of polishing.

Higher sensitivity is needed for reflectance mapping so that low-reflectance, AR-coated cells can be mapped. In response to this, we have developed a new procedure for reflectance mapping that will enable mapping of total reflectance or as three different reflectance components, i.e., specular, near-specular, and diffuse component, either individually or in any combination.

SUMMARY

PVSCAN is now commercially available from GT Solar. It has many upgraded capabilities, such as ease of data handling and export, less sample preparation for defect mapping, separation of reflectance into specular, near-specular, and diffuse components, and higher sensitivity for reflectance to accommodate very low-reflectance AR coatings.

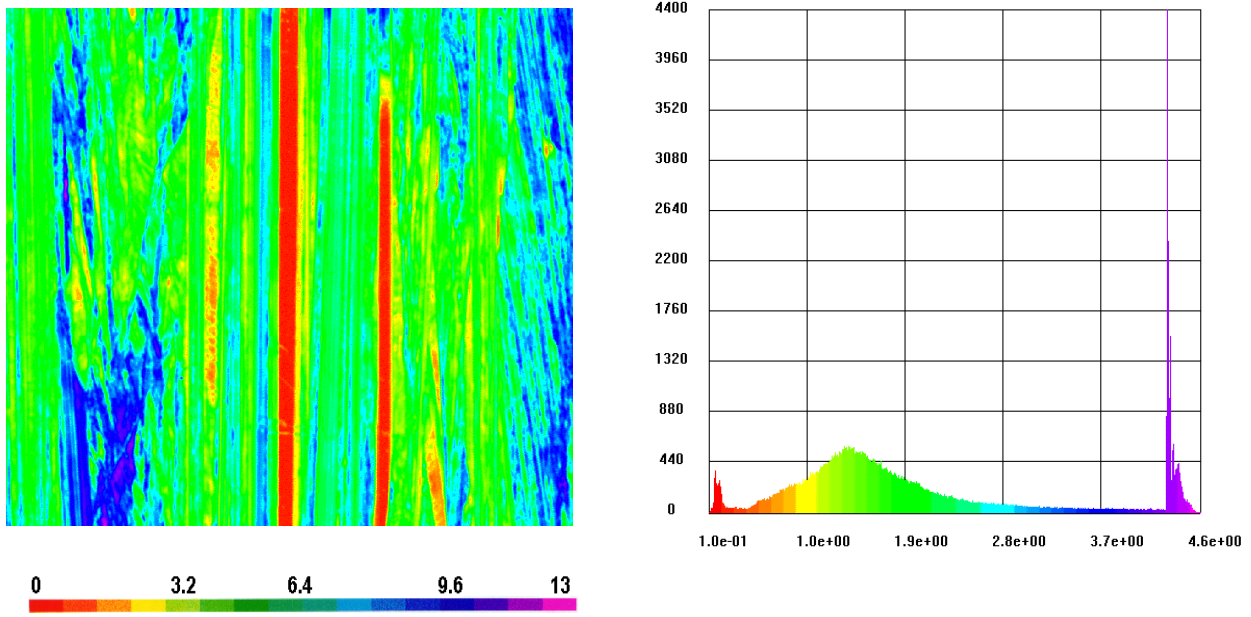


Figure 4. Defect map (a) and defect distribution (b) of a polished sample ribbon sample. Average defect density = 5.82 cm^{-2} . Scan area = $3.5 \times 3 \text{ in.}$

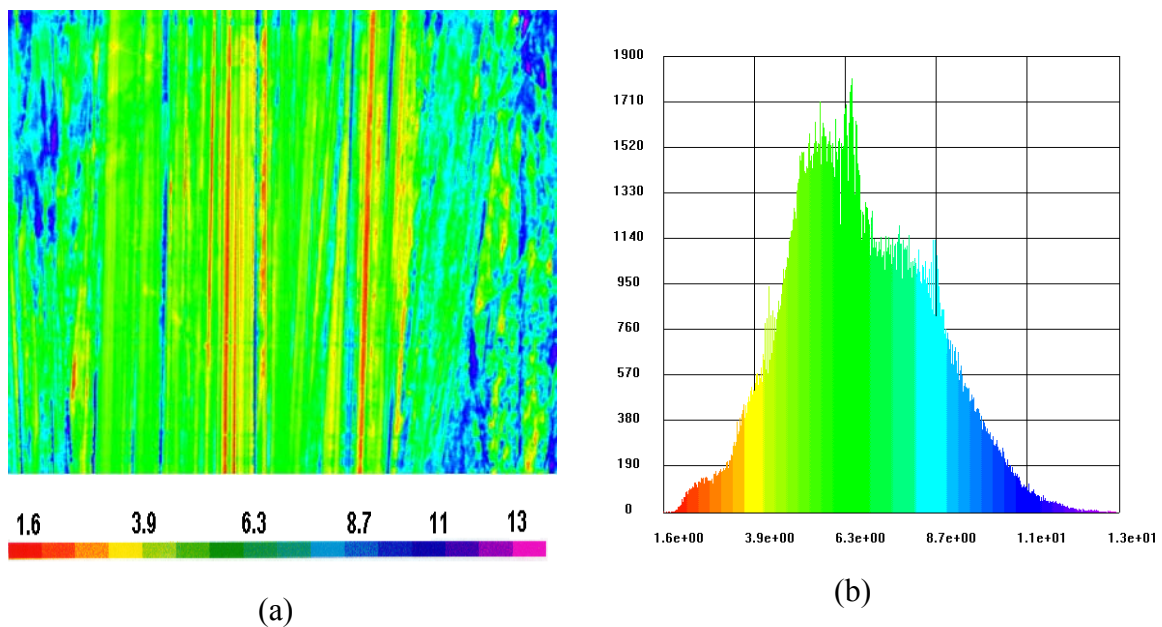


Figure 5. Defect map (a) and defect distribution (b), of an unpolished ribbon sample Ave defect density = 6.65 cm^{-2} . Scan area = $3.5 \times 3 \text{ in.}$

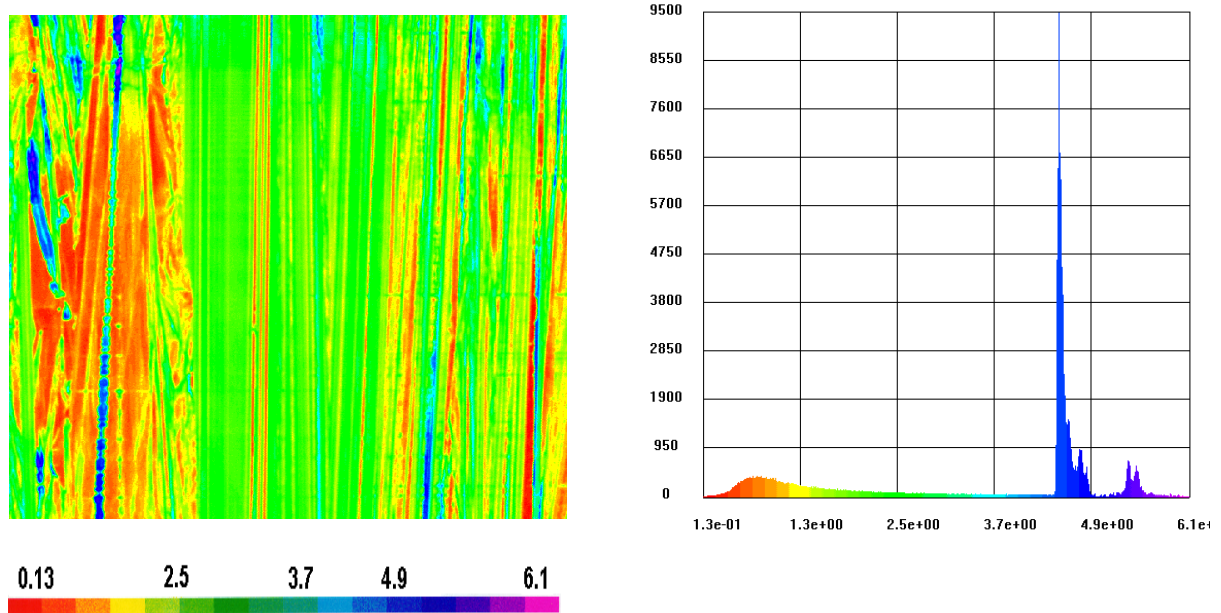


Figure 6. Defect map (a) and defect distribution (b) of an unpolished ribbon sample. Average defect density = 4.77 cm^{-2} . Scan area = 3.5 x 3 in.

Production Technology for Passivation of Polycrystalline Silicon Solar Cells

Julio A. Bragagnolo

NPC America Corporation, Dumont, NJ 07628

Bhushan Sopori

National Renewable Energy Laboratory

Erten Eser

Institute of Energy Conversion, University of Delaware

Tohru Hashimoto

NPC Incorporated, Tokyo, Japan

Ichiro Sugiyama

NPC Europe GmbH, Cologne, Germany

Abstract

Techniques for cost-efficient operation of $\text{SiN}_x:\text{H}$ systems with a capability for hydrogen passivation in a manufacturing environment are analyzed. We conclude that $\text{SiN}_x:\text{H}$ performance may be optimized by a variety of techniques, and that the cost and productivity of the deposition tool may be the determining factors in the industry's decision for a particular technique. PECVD constitutes the current benchmark. Dual magnetron reactive sputtering is a candidate to achieve industry acceptance.

Introduction

Shipments of solar electric power products based on crystalline-silicon materials reached 321.6 megawatts (MW) in 2001 [1], representing more than 82% of total solar cell shipments. More than 57% of the crystalline silicon capacity, as well as most of the 40% expansion in shipments from 2000 to 2001 and the announced future additions, are based on multicrystalline silicon wafers.

Multicrystalline silicon and other low-cost substrates used for commercial Si solar cells contain high concentrations of impurities and defects [2]. Fabrication of high-efficiency devices requires their concentrations be greatly reduced and/or their electrical activity be diminished. Because some of the processes, such as phosphorous diffusion and Al alloying (for formation of the n+/p junction and metal contact, respectively) can remove many impurities and defects by gettering, the completed cell carries significantly lower impurity and defect concentrations than the starting material. Consequently, these processes are designed to optimize impurity gettering in commercial solar cell fabrication. However, even after optimized gettering, significant amounts of impurities remain in the cell. Use of hydrogen passivation is one way to mitigate the effects of the residual impurities and defects [3].

A number of methods have been applied for hydrogenation of Si solar cells including ion implantation, plasma processing, forming gas anneal, and, more recently, PECVD nitridation. Crystalline-silicon cell manufacturing is converging on a set of standard production tools [4]. Typically used are CVD of antireflection TiO_2 or $\text{SiN}_x:\text{H}$ layers and printing and firing of a thick film paste (TFP) metallization. PECVD nitridation involves deposition of an antireflection $\text{SiN}_x:\text{H}$ layer, followed by screen printing and firing of the metallization through the nitride using a rapid thermal anneal (RTP). For multicrystalline silicon wafers, efficiency gains from the use of PECVD $\text{SiN}_x:\text{H}$ layers, as opposed to TiO_2 , are reported to be well over 10%. In an era of new

factories with capacities in the hundreds of MW, there are major opportunities for PECVD and other cost-effective SiN_x:H deposition tools.

This paper presents the key conclusions of a model that explains hydrogen diffusion during a SiN_x:H deposition process followed by RTP. We then review the major techniques for SiN_x:H deposition with intrinsic ability for impurity and defect passivation. We finally evaluate the performance potential of processes suitable for passivation in an industrial setting. As a result we determine that, in addition to PECVD, use of a dual magnetron reactive sputtering process has considerable potential in mass manufacturing of silicon solar cells.

Mechanisms of H Diffusion in a Nitridation Process

It is now known that a nitridation process involving PECVD SiN_x:H films produces bulk passivation of multicrystalline Si solar cells. It is generally contemplated that the passivation mechanism is the diffusion of hydrogen from SiN_x film into the Si, during deposition or during post-deposition anneal. Some authors have suggested that in a nitride process, hydrogenation occurs during RTP step when H released from SiN_x:H diffuses into Si [3,4]. This explanation does not consider H diffusion into Si during the nitridation itself. Recently, we have developed a model for diffusion of H in Si containing impurities and defects [5,6]. It shows, through quantitative modeling, that H can be introduced into traps near the surface of Si solar cells during nitridation. This “stored” H is de-trapped and redistributed during subsequent RTP anneal. This mechanism explains most observations related to solar cell passivation.

We have performed calculations for many cases, from which we can summarize some salient conclusions.

- In a two-step SiN_x:H passivation process, the deposition step is accompanied by a shallow diffusion of H, in which H is “stored” near the wafer surface. The process-induced-trap (PIT) density controls the profile of the H, whereas the bulk trap density determines the depth of such diffusion.
- In the anneal step, the source of H can be simply the in-diffused H. It may be pointed out that although H will be depleted out of SiN_x:H film during this step, there is no indication that any H from this film is going into the wafer. A simple redistribution of H is sufficient for effective passivation.
- The diffusion depth of H upon annealing is strongly controlled by the bulk trap density. For example, if the bulk trap density is $1E16 \text{ cm}^{-3}$, the H will permeate through the entire wafer in a 1s anneal at 800°C. This is in agreement with experimental observations [3].
- Because the trap density and distribution play a dominant role in the diffusion of H, it is clear that lower trap density material will require shorter anneal time or lower temperature. Likewise, higher predeposition temperatures during deposition can help introduce higher H content necessary to passivate higher trap and impurity concentrations. An interesting effect of the RTP step is that it can anneal out the plasma process-induced defects, making the H available for passivation.

To verify this theory, we measured the H profiles in the solar cell after PECVD nitridation and after subsequent RTP step in ASE America’s production solar cells. For these measurements, the SiN_x:H films were removed from solar cells with AR coating (no RTP) and after metallization firing (without affecting the H in the cell). Figure 1 shows the measured profiles that clearly demonstrate the presence of H in the solar cell after nitridation, and a redistribution of the

existing H. The H profiles match very closely those predicted by our theory. These results clearly suggest that any $\text{SiN}_x\text{-H}$ deposition process, that creates a surface damage and simultaneously exposes the surface to atomic H-containing ambient can produce a reservoir of H at the surface. Subsequent high-temperature process can release this stored H to passivate bulk defects and impurities.

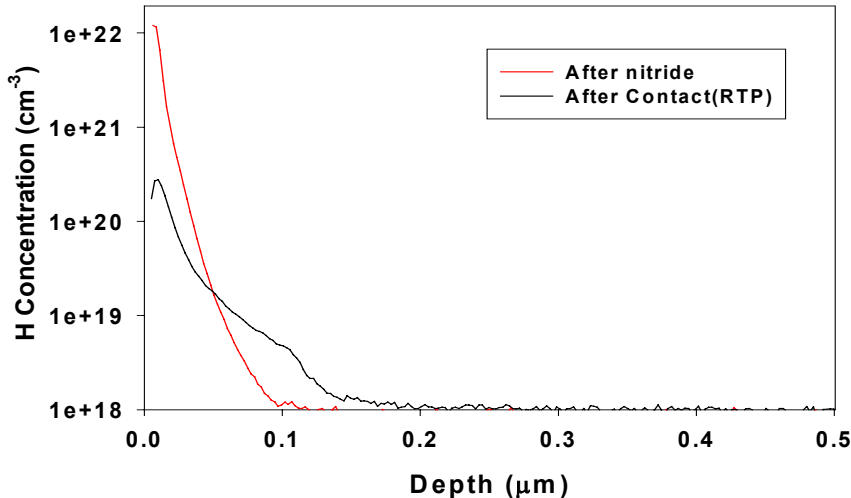


Figure 1: SIMS profiles of H in EFG ribbon samples: **Red:** after PECVD Si_3N_4 coating, **Black:** after contact firing (RTP).

Plasma Enhanced CVD $\text{SiN}_x\text{-H}$ Deposition and Properties

Amorphous silicon nitride (SiN_x) thin films have many applications in the semiconductor industry and in photovoltaics. SiN_x is an effective diffusion barrier against moisture and alkali impurities, which, when coupled with a high dielectric constant of 7.5, becomes an ideal candidate material for gate dielectric [7]. For solar cell and other advanced device applications in which low processing temperatures are required, SiN_x films are deposited by PECVD from a mixture of SiH_4 and NH_3 at process temperatures $\leq 400^\circ\text{C}$, which are compatible with commercial manufacturing processes [8]. The resulting films are hydrogenated amorphous SiN_x and are an excellent barrier against hydrogen out-diffusion.

Optical and electrical properties of the films depend on the structure and the chemistry defined by the Si-H, N-H, Si-N bond densities, Si-to-N ratio, and the amount of unbound H, resulting in a wide range of properties. Typically, for films deposited from SiH_4 and NH_3 , local bonding depends on the N-to-Si ratio “x” in the films [9]. For small x, the bonding configuration consists of isolated Si-H bonds, with no adjacent Si-N bond. As x increases, multi-N-bonded Si-H bonds dominate the structure. Finally, for $x > 1$, N-H bonds start to form and increase with x. Material properties of the SiN_x films, such as refractive index, ESR spin density, band gap and Urbach tail, can be adjusted across a wide range by changing N content. SiH_4 and N_2 can be used to deposit silicon nitride by PECVD, but these reactants typically yield silicon-rich films because of the relatively high bond energy of N_2 . SiH_4 and NH_3 depositions are normally carried out at pressures of 0.2 to 3 Torr, which yield growth rates of 20 to 50 nm/min. PECVD silicon-nitride films contain 15% to 30% of hydrogen bonded to either silicon or nitrogen [10].

The refractive index of SiN_x depends on processing parameters and stoichiometry. It is greater than 2.0 at 630 nm, which makes it an ideal single-layer AR coating for amorphous and crystalline solar cells [11]. PECVD SiN_x films are effective for surface passivation of silicon solar cells. Surface passivation effectiveness depends on the deposition method. Ion bombardment during deposition creates different defect types at the Si- SiN_x interface. Substrate temperature is a most important deposition parameter determining hydrogen content and is anti-correlated to the surface recombination velocity [12,13].

Bulk passivation of multicrystalline Si solar cells by PECVD $\text{SiN}_x\text{:H}$ films has been analyzed by Fukui, et al. [14]. The passivation mechanism is the diffusion of hydrogen from SiN_x film into the Si, during deposition or during post-deposition anneal, and the saturation of the dangling bonds associated with various defects in the material by this hydrogen. Fukui measured a decrease in the ESR spin density from $4 \times 10^{14} \text{ cm}^{-3}$ to $2 \times 10^{14} \text{ cm}^{-3}$ as a result of SiN_x coating of the solar cell from three different sources.

For microelectronic applications such as gate dielectrics, SiN_x films are required to have high resistivities and breakdown voltages. In a- $\text{SiN}_x\text{:H}$ films these electrical properties are inversely correlated to the hydrogen content of the films [15]. PECVD films with low hydrogen content can be obtained only at high substrate temperatures of $\geq 300^\circ\text{C}$. Electron cyclotron resonance PECVD (ECR-PECVD) [16] can yield low-hydrogen-content films at low temperatures and was originally developed for this application. In ECR-PECVD, a highly ionized plasma ($\sim 10^{16} \text{ m}^{-3}$) can be produced as a result of high electron temperatures because of the combined effect of the microwave radiation (2.45 GHz) and the magnetic field. In such nitrogen plasma, there is a high degree of dissociation of N_2 molecules, which allows gas phase reactions with SiH_4 molecules and results in a material with lower hydrogen content than is obtained with NH_3 . Recently, Soppe et al. investigated the application of ECR-PECVD deposited SiN_x films to surface passivation of silicon cells [17], showing that SiN_x films deposited from SiH_4 and NH_3 precursors onto FZ-Si result in a surface recombination velocity as low as 50 cm/s for a deposition temperature of 475°C . Recombination increases to 500 cm/s for a deposition temperature of 300°C , which is due presumably to the increase in the hydrogen content of the film from 12.8 at% at 475°C to ≈ 5 at%. This is consistent with what is observed in the case of PECVD SiN_x . The authors also demonstrated bulk passivation of microcrystalline Si solar cells by comparing device characteristics of annealed SiN_x -coated solar cells to the as-coated solar cells. Annealed solar cells showed a 1% average absolute higher efficiency than the as-deposited ones, indicating bulk passivation caused by hydrogen in-diffusion from the SiN_x .

Industrial Plasma Enhanced CVD $\text{SiN}_x\text{:H}$ Systems

An ECR-PECVD in-line system manufactured by Roth & Rau is the current industry benchmark. The Roth & Rau SiNA is a high-throughput, five-chamber continuous in-line system in which cells are transported on carriers. More detail about the system and its performance is given in reference [18]. Deposition is of the remote plasma type in which the linear level source operates at 2.45 GHz frequency. Water-cooled permanent magnets confine the NH_3 plasma and increase the ionization rate. SiH_4 is introduced at the substrate. For a film thickness of 80 nm, a cell tray can be loaded every 90 s into a system utilizing four linear sources in series. Standard operating temperature is 350°C , but it can be as high as 450°C .

Shimadzu (Japan) supplies a direct PECVD System. Shimadzu literature describes the reactor as a quasi-continuous, in-line system with four vacuum chambers isolated by gate valves. Substrate

trays preheated in an external oven are further heated in the load-lock chamber from the top and bottom via lamp heaters. From the load-lock chamber, the trays move into two process chambers in which SiN_x films are deposited on stationary trays heated by resistive heaters. Standard deposition temperature is 450°C, but can be as high as 550°C. Deposition is obtained by supplying microwave (90–460 kHz) power to an electrode facing the tray in the presence of a SiH_4 , NH_3 , and N_2 mixture. From the process chamber, the tray moves into the unloading chamber and is removed from the system. Effective deposition rate is quoted to be 200 Å/min, which gives, for an 800-Å film, an effective process time of 4 min. Other commercial reactors based on multi-tube batch systems have lower productivity.

Sputtered $\text{SiN}_x:\text{H}$ Deposition and Properties

Commercial viability for large-area, high-throughput manufacturing attracts interest in the sputtering process. Manufacturing of Si PV modules, thin-film transistor (TFT) arrays for large-area liquid crystal displays (LCDs), 2D imagers, scanners, and detectors all require low-cost deposition of SiN_x films. The advantages of sputtering versus PECVD include low-temperature processing, use of nontoxic gas, high deposition rate, low downtime due to direct deposition, and high homogeneity/uniformity on very large surfaces. Several researchers have studied, in detail, the reactive sputtering for silicon nitride films [19,20] for microelectronic applications such as oxidation masks, gate dielectrics, inter level insulators, and final passivation layers (see for example [21]), showing that the silicon-nitride film properties can be greatly varied with the preparation conditions.

Although reactive magnetron sputtering can be used to deposit silicon-nitride films for Si solar cells and in microelectronics, it has a number of limitations (such as arcing, disappearing anode and low deposition rate) that prevent its acceptance for large-scale manufacturing [22]. These problems can be addressed by the use of dual magnetron sputtering (DMS), in which an AC power having a frequency larger than 10 kHz is connected to the two targets so that they are driven alternatively positive and negative with respect to one another [23]. This arrangement permits each target to act as an anode for the other. If the reversal frequency is high enough, only a very thin layer of insulator will be formed on the target acting as an anode, and this very thin layer can be sputtered away. Note that when the target acts as an anode it collects electrons; these not only provide the return current for the sputtering process, but also discharge any supply accumulated positive charges on insulating islands on the target, thus reducing cathode arcing. TwinMag is such a DMS system that uses 40 kHz AC power [24]. The TwinMag sputtering system has high potential for fast and stable reactive deposition of $\text{SiN}_x:\text{H}$. The system used by Preu et al. to study AR and passivation effect of SiN_x films on Si solar cells is said to be capable of operating continuously for 310 hours at a dynamic deposition rate of 35 nm m/min [25]. This means that the layer thickness will be 35 nm if the substrate passes one TwinMag with a speed of 1m/min. Linear sources up to 3.75 m have been developed to coat 3.2-m-wide substrates with a thickness uniformity of $\pm 1.5\%$. The study demonstrated that SiN_x films reduced S_{eff} to < 1000 cm/s from 10^6 cm/s. Also, based on the measured open-circuit voltages, the deposition process did not introduce any damage to the emitter and/or the space charge region. The gain in the short-circuit current resulting from the AR effect was as high as 39%. It should be pointed out that even though the authors prepared hydrogenated SiN_x films by introducing H_2 into the sputtering gas, they did not determine the bulk passivation effect of such films on multicrystalline Si solar cells. Information on industrial sputtering systems such as a dual-magnetron sputtering system developed by Balzers Process Systems (BPS) [25] is limited.

Performance and Cost of SiN_x:H Deposition Tools

In the preceding sections, we have seen that PECVD and sputtered SiN_x layers can be fabricated with a large range of properties suitable for solar cell application. However, although hydrogenated SiN_x films were prepared by introducing H₂ into the reactive sputtering gas, no data are available on the effect of such films on bulk passivation multicrystalline Si solar cells.

Although the question of the applicability of sputtering to nitridation awaits experimental verification, our model for hydrogen diffusion during a SiN_x:H plus RTP deposition process predicts that sputter deposition is amenable to optimization for bulk passivation. We expect that the optimum near-surface conditions for shallow diffusion of H in the deposition step, and H “storage” near the wafer surface, can be obtained by careful tailoring of the PIT profile by controlled damage of a near-surface layer during sputtering.

The second key question about sputtering regards tool cost. In analyzing production tools, it is useful to employ the concept of cost of ownership (CoO), defined as “the full cost of embedding, operating, and decommissioning in a factory environment a process system needed to accommodate the required volume of product material” (SEMI Standard E-35: Cost of Ownership for Semiconductor Manufacturing Equipment). The algorithm for CoO (Equation 1) includes the fixed costs FC, the running costs RC, the yield cost YC, the equipment life L, throughput T, yield Y, and utilization U:

$$\text{CoO} = [\text{FC} + \text{RC} + \text{YC}] / (\text{L.T.Y.U}) \quad \text{Equation 1}$$

The CoO of PECVD silicon nitride deposited by the Roth & Rau machine has been calculated to be 0.04 €/Wp [18]. This value is lower than earlier estimates of [26], reflecting the progress in industrial PECVD technology.

The estimated CoO for sputtered silicon-nitride films has been estimated to be 0.043 €/Wp, comparable to the cost of PECVD films. However, a calculation from [25] of the area throughput of a sputtering system with two TwinMag sources in series suggests that a useful area of about 3.2 m² per min can be coated with SiN_x:H. Assuming 15%-efficient cells, we estimate a capacity of about 50 MW per year per 2,000-hour shift for such a machine. Such a high throughput can reduce the fixed costs (FC), which are a significant component of CoO. Conveniently, the process uses no SiH₄ or NH₃ gases. If the cost of silicon targets can be controlled, we expect that the ‘learning curve’ of industrial SiN_x:H sputtering will lead to CoO decreases for sputtering technology similar to those achieved in industrial PECVD nitride.

Conclusions and Recommendations

The review of the scientific literature and our current physical model presented earlier in this report suggest that the key solar cell bulk passivation properties of SiN_x films are, to a first order, independent of the processes used to deposit SiN_x films. In view of this fact, in choosing a particular process for the development of a commercial-scale SiN_x deposition system the primary criteria should be the suitability of that process to large-scale, high throughput manufacturing environment. PECVD SiN_x:H is the current technology of choice. Dual magnetron reactive sputtering from intrinsic silicon targets is a potential competitor. Continuous in-line sputtering is a well-developed technique to deposit thin films over large areas at high throughput. Sputtering from silicon targets in the presence of N₂ and H₂ avoids the use of dangerous gases such as SiH₄ and NH₃ which require care in handling, as well as complicated systems to safely dispose of them, especially when the utilization rates are as low as in the plasma-assisted deposition

systems. Dual magnetron reactive sputtering of insulators from elemental targets is the preferred sputter deposition technique of insulators because of its high deposition rate and stable operation over extended times.

The further development of both technologies requires increased knowledge of (1) the kinetics of H diffusion from the SiN_x film, and (2) the amount of hydrogen required to bulk passivate a typical multicrystalline silicon wafer, and (3) verification of bulk passivation by sputtered silicon nitride. Optimum operating parameters of a dual magnetron system need to be determined on a laboratory-scale, in-line system.

Acknowledgements

The authors are pleased to acknowledge contributions from Bob Reedy of NREL and J. Akita, H. Sato, M. Ito, and Y. Chikaki of the NPC Group.

References

- [1] PV News Vol. 21, Nos. 2 and 3, February and March 2002.
- [2] Bhushan Sopori, "Silicon solar cell processing for minimizing the influence of impurities and defects," to be published, *J. Elec. Mat.*
- [3] P. Sana, A. Rohatgi, J. Kalejs, and R.O. Bell, *Appl. Phys. Lett.* 64, 1994, p. 111 (1994).
- [4] "PVMaT Improvements in the BP Solarex Photovoltaic Module Manufacturing Technology", Annual Report, NREL/SR-520-29459, March 2001.
- [5] B.L. Sopori, Y. Zhang, and N.M. Ravindra, *J. Elec. Mat.* 30, 2001, p. 1616.
- (6) B.L. Sopori, Y. Zhang, and R. Reedy, "H diffusion for impurity and defect passivation: a physical model for solar cell processing," Presented at the 29th IEEE-PVSC, New Orleans, May, 2002.
- [7] Z. Lu, S. S. He, Y. Ma, G. Lucovsky, *J. Non-Cryst. Solids*, 187 (1995) 340.
- [8] D. S. Ruby, W. L. Wilbanks, C. B. Fleddermann, Proceedings of the 1st World Conference on Photovoltaic Energy, Waikoloa, Hawaii, 1994, pp. 1335-1338.
- [9] Y. Masaki, R. A. G. Gibson, and P. G. LeComber, *J. Appl. Phys.* 73, 5088 (1993).
- [10] S. Hasegawa, Y. Amano, T. Inokuma, and Y. Kurata, *J. Appl. Phys.* 75, 1493 (1994).
- [11] P. Doshi, G. E. Jellison, Jr., A. Rohatgi, *Appl. Opt.* 36, 7826 (1997).
- [12] Schmidt a A.G. Aberle, Crystalline Silicon Solar Cells – Advanced Surface Passivation and Analysis (University of New South Wales Press, Sydney, 1999).
- [13] L. Cai, A. Rohatgi, S. Han, G. May, and M. Zou, *J. Appl. Phys.* 83, 5886 (1998).
- [14] K. Fukui, K. Okeda, Y. Inomota, H. Takahashi, S. Fujii, Y. Fukawa and K. Shirasawa, *Solar Energy Materials & Solar Cells* 48, 219 (1997).
- [15] J. Kanicki, N. Voke, *Mater. Res. Soc. Symp. Proc.* 68, 167 (1986).
- [16] A. J. Flewitt, A. P. Dyson, J. Robertson, and W. I. Milne, *Thin Solid Films* 383, 172 (2001)]
- [17] W. J. Soppe et al., 16th European Photovoltaic Solar Energy Conference, Glasgow, 1-5 May (2000).

- [18] S. Roth, this Workshop
- [19] C. J. Mogab et al, J. Electrochem. Soc. 122, 815 (1975); T. Serikawa, and A. Okamoto, J. Electrochem. Soc. 131, 2928(1984).
- [20] F. C. Stedile, I. J. R. Baumvol, W. H. Schreiner, and F. L. Freire, Jr., J. Vac. Sci. Tech. A 10, 462(1992); I. Sugimoto, K. Yanagisawa, H. Kuwano, S. Nakano, and A. Tago, J. Vac. Sci. Tech. A **12**, 2859 (1994)]
- [21] S.A. Awan, R.D. Gould, and S. Gravano, Thin Solid Films 355&356, 456 (1999)].
- [22] R. A. Scholl, Society of Vacuum Coater. Proc. 33rd Ann. Techn. Conf. (1990) p 250.
- [23] J. Szczyrbowski, and G. Teschner, Society of Vacuum Coater. Proc. 38th Ann. Techn. Conf. (1995)].
- [24] S. Beißwenger, G. Bräuer, W. Dicken, J. Szczyrbowski, Surface and Coatings Technology 60. Proc. 3rd Intl. Conf. on Plasma Surface Engineering. (1993) p. 624.
- [25] R. Preu, J. Krempel-Hesse, D. Brio, D. Huljic, M. Mäckel and R. Lüdemann, 16th European Photovoltaic Solar Energy Conference, Glasgow, 1-5 May (2000)].
- [26] A.G. Aberle et al., 14th European PVSEC, Barcelona (1997), 1-6.

GT Reflectometer: Performance Testing/Error Analysis

Bhushan Sopori, Chris Auriemma, and Jamal Madjdpor

National Renewable Energy Laboratory (NREL), 1617 Cole Boulevard, Golden, CO 80401

Keith Matthei, Kengo Nakano, and Heiko Moritz, GT Solar, 472 Amherst St.,

Nashua, NH 03063

Email contact: moritz@gtsolar.com

INTRODUCTION

Reflectance spectroscopy is very well-suited for measuring physical parameters of semiconductor wafers, and of surface structures (continuous or patterned) deposited on them as thin films. We have developed a reflectometer (PV-Reflectometer) that can measure physical parameters of wafers, wafer surfaces, and other materials deposited during solar cell fabrication. Concomitantly, PV Reflectometer can also be applied for monitoring various cell fabrication processes. Specifically, this system can monitor the following processes steps:

- Wafer sawing
- Texture etching
- AR coating
- Front metal patterning (area and height of front metallization)
- Back metallization (reflectance of back metallization).

The PV Reflectometer can measure the reflectance spectrum of an entire wafer or cell in a very short time (typically < 100 ms). This spectrum is deconvolved to separate parameters that relate to various parts of the test wafer. Recently, we have built a commercial prototype reflectometer that is being loaned to PV Industry for evaluation and to provide feedback for fine-tuning to specific applications of each industry partner. The PV Reflectometer has been licensed by GT Solar, Inc., Nashua, NH, for commercial production (now called GT Reflectometer). Basic principles and the system configuration of the GT Reflectometer are described in earlier papers [1–3]. Here we will only briefly describe the system, and focus primarily on discussion of results of our investigations to assess repeatability and error analysis. We undertook this work to establish measurement accuracies of the system and relate them to expected ranges of variations in monitoring various processes.

PRINCIPLES/SYSTEM CONFIGURATION

The approach used in the GT Reflectometer is unique—it uses multiple, wide-angle light sources to illuminate the large-area sample, whereupon the light scattered normal to the sample is collected for analysis. This new approach makes the system quite simple, low-cost, and rapid, and it permits use of high-power sources to enable measurement of “optically averaged” parameter values for large-area solar cells and wafers. However, because only the light reflected in a direction normal to the sample must be collected, this approach demands that all the extraneous light be excluded. Such extraneous light includes non-normal components of the light

reflected from the test wafer, as well as the scattered light from parts of the instrument such as the wafer holder and mounting brackets. To accomplish this, the GT Reflectometer uses highly absorbing surfaces and a system of light-trapping baffles, resulting in an extremely high S/N ratio (of about 200). This allows the entire measurement and analysis to be made in less than 100 ms.

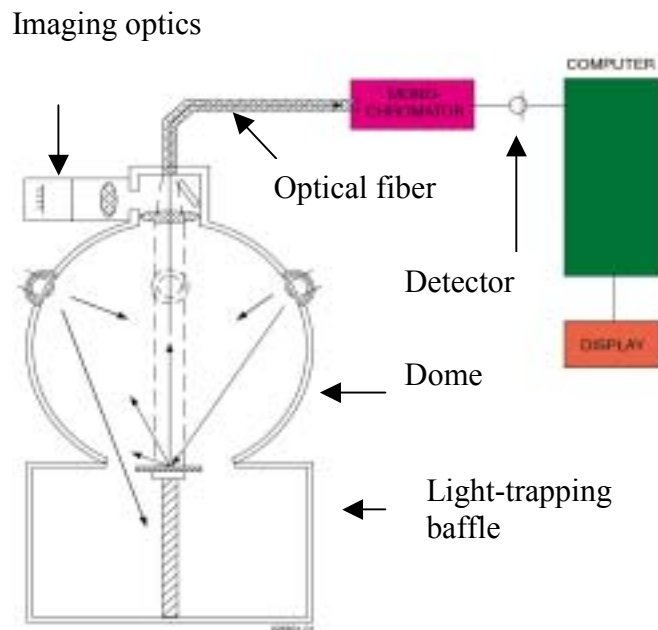


Figure 1. A schematic of the GT Reflectometer showing major parts of the system.

Figure 1 is a schematic of the GT Reflectometer. It consists of a highly absorbing spherical dome, about 12-18 inches in diameter, with openings at the top and at the bottom. The bottom opening terminates in an optical baffle that houses a platform to support the test wafer. The dome has four sets of diverging lights located on the upper side that illuminate the test wafer. Separate controllers balance the intensities of the lights. The entire system is designed to eliminate all possible scattering of the light except by the test wafer. The top side of the dome has a lens and an aperture assembly that couples the light reflected from the sample into a diode array spectrometer through an optical fiber. The spectrometer control, data taking/handling, calibration, and system control are done by a computer that generates the reflectance (R) versus wavelength (λ) plot for the test sample. The system operates in a broad spectral range that allows reflections from the front and back sides of the cell to be monitored. The setup shown in Figure 1 includes only the illumination source for measurement of the diffuse reflectance for rough or textured wafers/cells. A slightly different illumination source is used for planar cells.

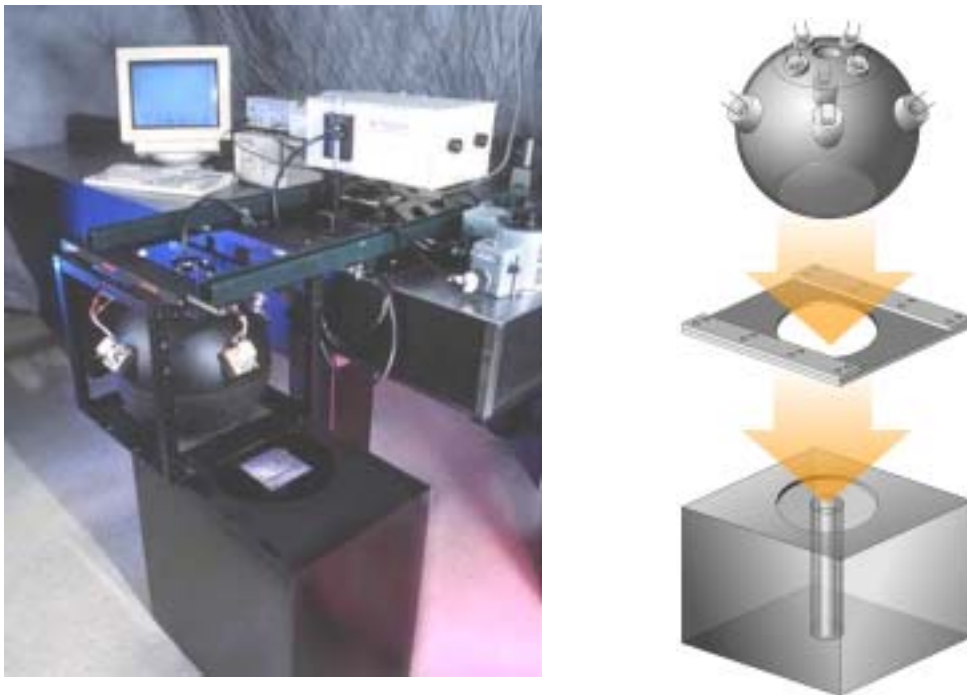


Figure 2. A photograph of a laboratory reflectometer (left) and an exploded schematic showing major optical parts (right).

RECENT IMPROVEMENTS

Recent developmental work involves some newer applications, system improvements to reduce the size, and detailed studies to evaluate measurement accuracy and sensitivities. Because a GT Reflectometer was designed to be a true production monitoring system, capable of very high throughput, we are performing detailed analyses to access the repeatability and reproducibility of the system. Here we will discuss repeatability tests that we have performed, and the corresponding changes incorporated in the system for production compatibility. These studies were carried out to identify and mitigate various mechanisms responsible for variations in the system performance. Some of the mechanisms we have evaluated follow.

1. Stability of the light sources/power sources:

Stability of the illumination is an important parameter in the accuracy of the optical measurements. This is particularly true for the GT Reflectometer because it uses eight lamps that can be connected in several configurations to produce diffuse or specular light sources. These lamps were tested individually for the output and determined to have sufficient stability, with a short-term variation of less than 0.1%. In the past, the lights were powered by AC sources consisting of autotransformers. Figure 3 shows 10 normalized spectra from a reference sample taken 1 min apart. It is seen that the variation is larger for shorter wavelengths, and that the maximum variation in the spectra is about 3%. It is useful to compare variation at a wavelength corresponding to the maximum intensity. This max-power wavelength (MPW) variation,

identified by the arrow in the figure, is seen to be 0.8%. Use of a DC power supply greatly reduces the variation in the spectra. Figure 4 shows variation in 10 spectra taken 1 min apart using a TiO₂-painted reference sample. The variation at the MPW is only 0.1%. This is a very low variation for any spectrometer or reflectometer.

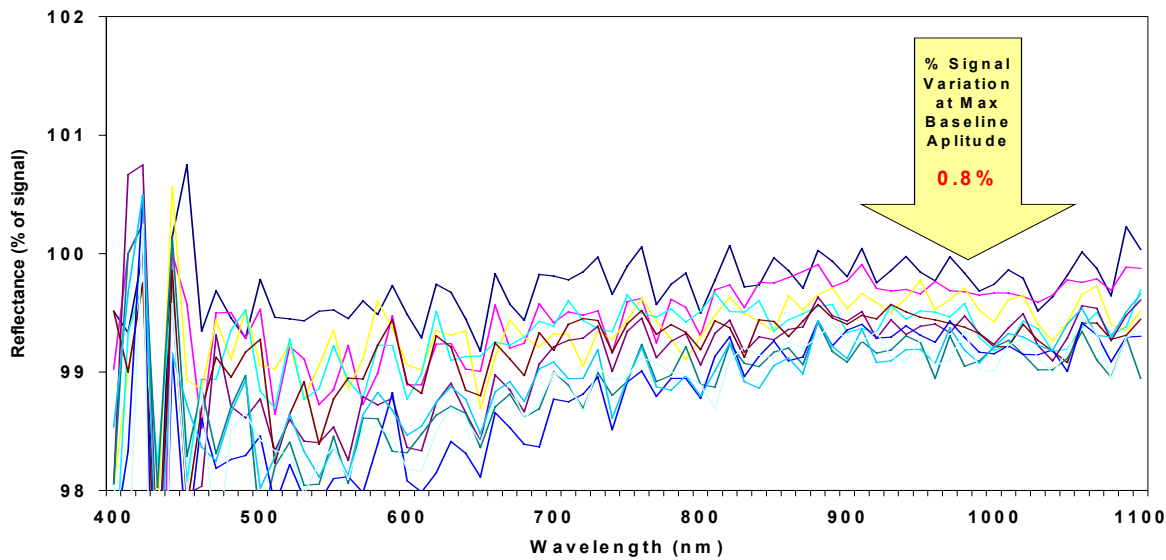


Figure 3. Ten reflectance spectra taken 1 min apart using AC power from low-cost autotransformers. Reference sample: Sprayed TiO₂.

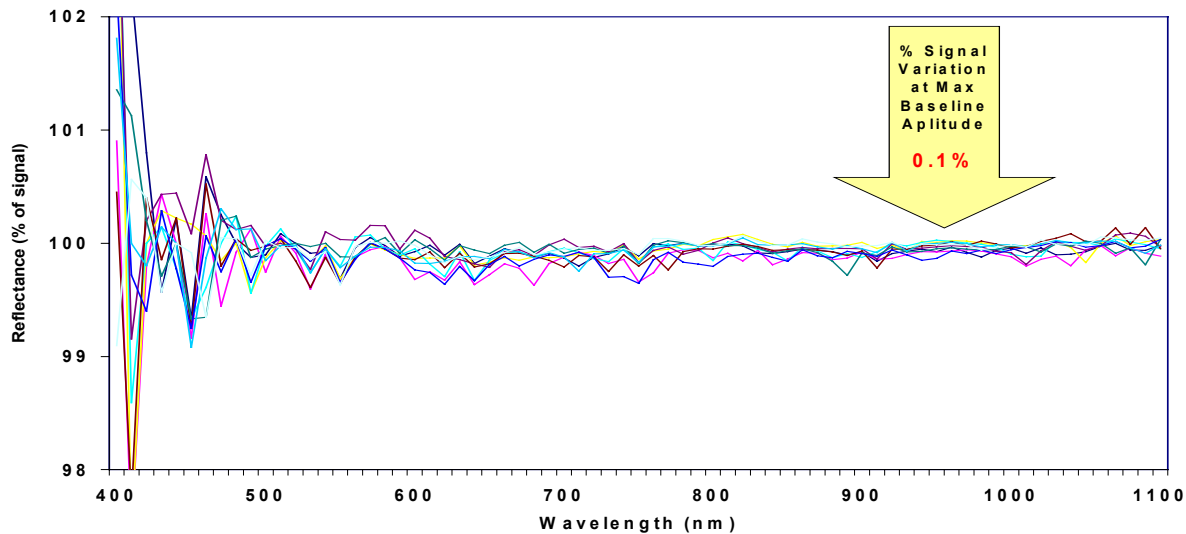


Figure 4. Ten reflectance spectra taken one minute apart using DC power supplies. Reference sample: Sprayed TiO₂

2. Stability of the reference: We have also evaluated three different reference samples. They consisted of a thick white paper, a Teflon sheet, and a TiO₂-rich paint. All reference samples had a matte finish. Figure 5 shows 10 spectra taken 1 min apart using a Teflon reference. The MPW variation is 0.3%. Figure 6 shows 10 normalized spectra taken with a white paper reference, which show MPW variation of 0.4%. These figures should be compared with Figure 4, which shows similar spectra for the new TiO₂-painted reference (with MPW variation of 0.1%). It is thus clear that our special paint (and its processing) produces a high-quality reference.

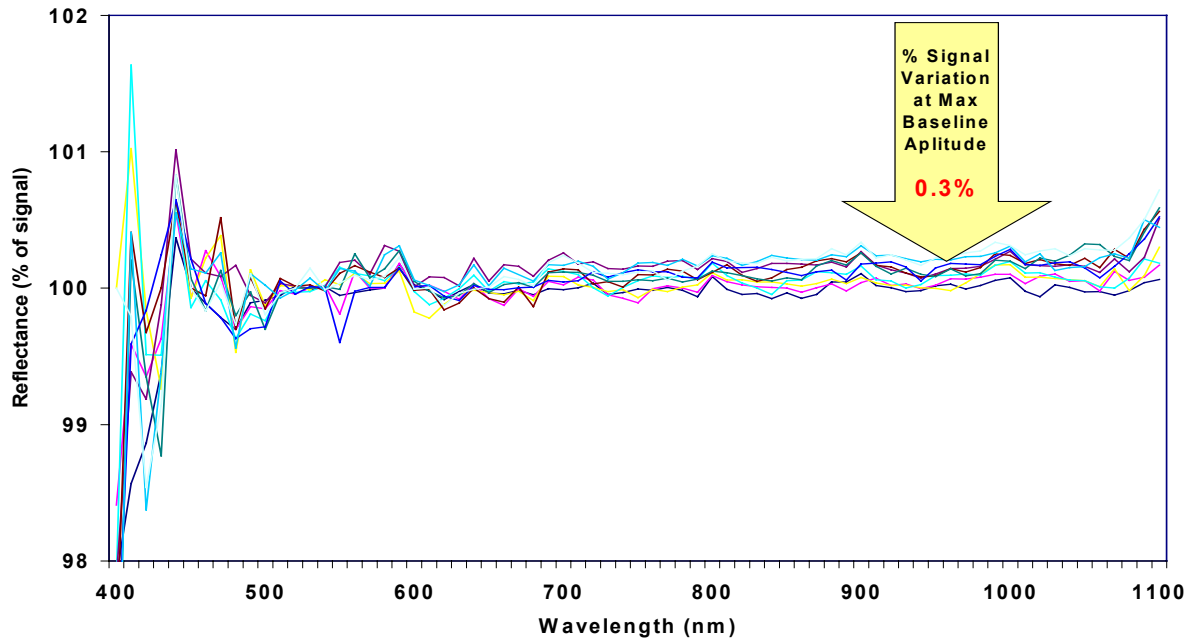


Figure 5. Ten normalized spectra taken with Teflon reference (DC power).

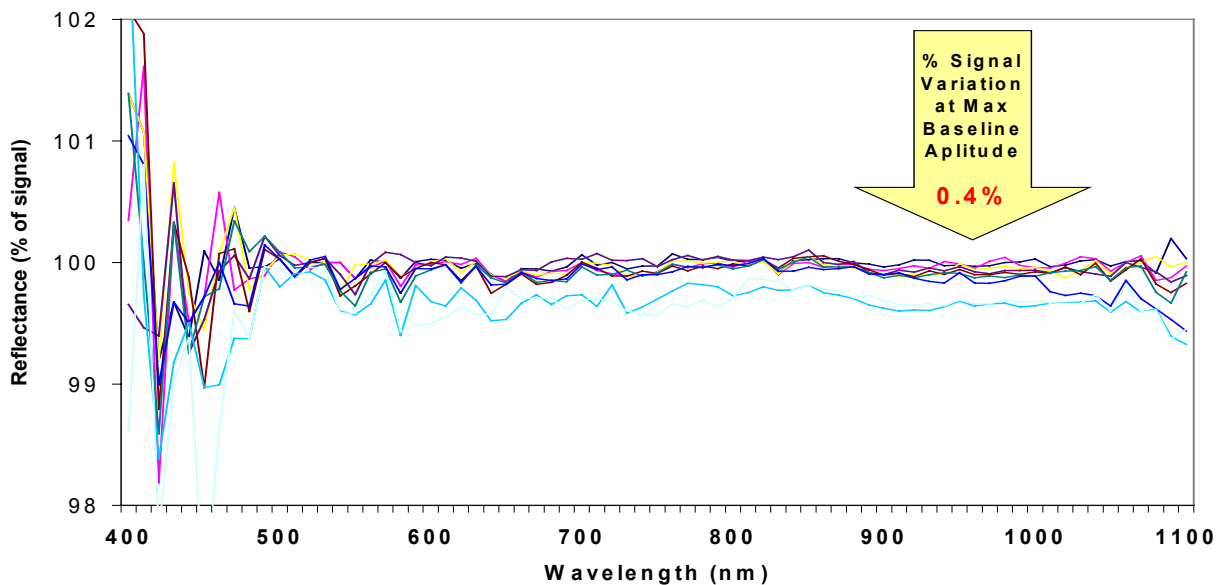


Figure 6. Ten normalized spectra taken with white paper reference (DC power).

3. Positioning of the test device within the reflectometer: GT Reflectometer is designed to have a relaxed sensitivity to positioning of the test. This feature helps in maintaining a high-throughput capability so that the wafers can be brought into the measurement chamber at a high speed. We have studied the sensitivity to lateral and vertical positioning of the wafer.
4. Duration of the test-wafer in the reflectometer: Figure 7 shows ten normalized spectra taken over a 1-hour period with the lights on for the entire test period. The resulting MPW variation is 0.3%.
5. System noise: The ultimate system noise is associated with the detector/amplifier combination. Because the light intensity is quite low in a short wavelength region, this noise is highest, in a range of 0.4-0.5 μm . Beyond 0.5 μm wavelength, the noise is considerably less than 0.1%

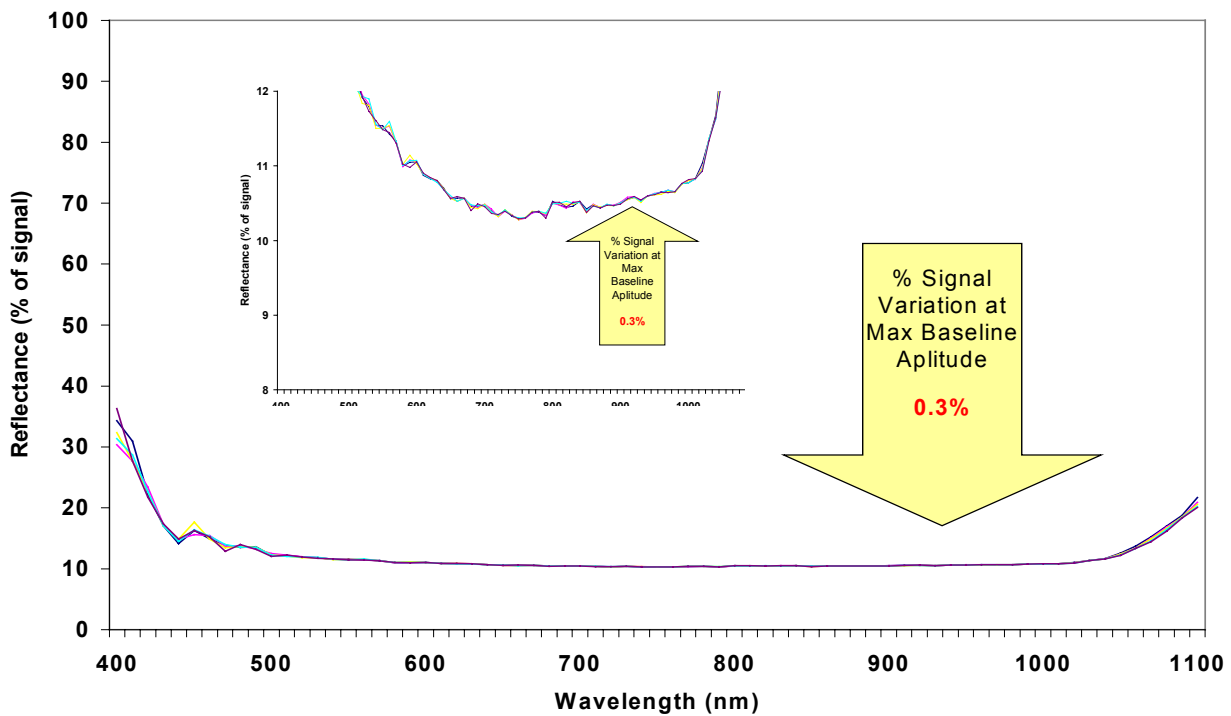


Figure 7. Variation in the spectra of a textured Si Wafer taken over a one-hour (DC power).

SUMMARY

We have carried out a performance/noise analysis of the GT Reflectometer. The results are summarized in Table 1. The dominant sources of noise were determined to be the lamp power supply and reference standard. A stabilized DC power supply and a new reference standard

(using spray on TiO₂-rich paint) have been incorporated in the new GT Reflectometer. These changes have improved the measurement accuracy to 0.1%.

Table 1. Summary of the Test Results

Test	Results (MPWV)
Stability of the light sources/power sources	Lamp stability :very high Power supply: AC ---- (0.8%--short term) DC ---- (0.1%--short term , 0.3 long term)
Stability of the reference Sample (<i>with DC power</i>)	White paper -- 0.4% Teflon -- 0.3% TiO ₂ -- 0.1%
Positioning of the test device within the relectometer <i>(note: these measurement correspond to AC power supply)</i>	Sensitivity to lateral location: < 2.5 within 5 mm Height sensitivity <2.5 % within 10mm
Duration of the test wafer in the reflectometer	Long term -- 0.3% Short term -- 0.1%
System noise	The ultimate system noise is associated with the detector/amplifier combination. A typical S/N system is about 200

REFERENCES

- [1] B. L. Sopori, "Principle of a new reflectometer for measuring dielectric film thickness on substrates of arbitrary characteristics," *Rev. Sci. Instrum.* **59(5)**, 725,1988.
- [2] Bhushan Sopori, Yi Zhang, Wei Chen, and Jamal Madjdpour, "Silicon solar cell process monitoring by PV Reflectometer," *IEEE PVSC, Anchorage, AK, Sept. 2000*.
- [3] Bhushan Sopori, U. S. Patent No. 6,275,295.

REPORT DOCUMENTATION PAGE

Form Approved
OMB NO. 0704-0188

Public reporting burden for this collection of information is estimated to average 1 hour per response, including the time for reviewing instructions, searching existing data sources, gathering and maintaining the data needed, and completing and reviewing the collection of information. Send comments regarding this burden estimate or any other aspect of this collection of information, including suggestions for reducing this burden, to Washington Headquarters Services, Directorate for Information Operations and Reports, 1215 Jefferson Davis Highway, Suite 1204, Arlington, VA 22202-4302, and to the Office of Management and Budget, Paperwork Reduction Project (0704-0188), Washington, DC 20503.

1. AGENCY USE ONLY (Leave blank)	2. REPORT DATE August 2002	3. REPORT TYPE AND DATES COVERED Conference Proceedings	
4. TITLE AND SUBTITLE 12 th Workshop on Crystalline Silicon Solar Cell Materials and Processes, Extended Abstracts and Papers, August 11-14, 2002			5. FUNDING NUMBERS WO97A700
6. AUTHOR(S) B.L. Sopori, Workshop Chairman/Editor			
7. PERFORMING ORGANIZATION NAME(S) AND ADDRESS(ES) NREL 1617 Cole Boulevard Golden, Colorado 80401			8. PERFORMING ORGANIZATION REPORT NUMBER
9. SPONSORING/MONITORING AGENCY NAME(S) AND ADDRESS(ES) National Renewable Energy Laboratory 1617 Cole Blvd. Golden, CO 80401-3393			10. SPONSORING/MONITORING AGENCY REPORT NUMBER NREL/BK-520-32717
11. SUPPLEMENTARY NOTES			
12a. DISTRIBUTION/AVAILABILITY STATEMENT National Technical Information Service U.S. Department of Commerce 5285 Port Royal Road Springfield, VA 22161			12b. DISTRIBUTION CODE
13. ABSTRACT (<i>Maximum 200 words</i>): The 12th Workshop will provide a forum for an informal exchange of technical and scientific information between international researchers in the photovoltaic and relevant non-photovoltaic fields. Discussions will include various aspects of impurities and defects in silicon—their properties, the dynamics during processing, and their application for developing low-cost processes for manufacturing high-efficiency silicon solar cells. The workshop will emphasize some of the promising new technologies in Si solar cell fabrication that can lower PV energy costs and meet the production demands of the future. It will also provide an excellent opportunity for researchers, in private industry and at universities, to prioritize mutual needs for future collaborative research. Sessions and panel discussions will review recent advances in crystal growth, new cell structures, new processes and process characterization techniques, and manufacturing approaches suitable for future manufacturing demands. Some presentations will address recent technologies in the microelectronics field that may have a direct bearing on PV. The three-day workshop will consist of presentations by invited speakers, followed by discussion sessions. In addition, there will be two poster sessions presenting the latest research and development results.			
14. SUBJECT TERMS: photovoltaics; solar cells; crystalline silicon; materials; processes; impurities; defects; low cost; manufacturing; microelectronics			15. NUMBER OF PAGES
			16. PRICE CODE
17. SECURITY CLASSIFICATION OF REPORT Unclassified	18. SECURITY CLASSIFICATION OF THIS PAGE Unclassified	19. SECURITY CLASSIFICATION OF ABSTRACT Unclassified	20. LIMITATION OF ABSTRACT UL